RGNZ/*MGPB*

Rudarsko-geološko-naftni zbornik

The Mining-Geological-Petroleum Engineering Bulletin



Godište XXXVII, broj 76 / *Anno XXXVII, number 76*



Detalj eksploatacije građevinskog pijeska i šljunka na eksploatacijskom polju „Hrastovljan“ koje se nalazi u blizini Varaždina. Koncesionar na tom polju je Colas Mineral d.o.o.

Fotografiju načinio Saša Kolar, tehničar Rudarsko-geološko-naftnog fakulteta fakulteta.

Detail of the mining of construction sand and gravel at the "Hrastovljan" mining field near Varaždin. The concessionaire of this field is Colas Mineral d.o.o.

The photograph was taken by Saša Kolar, technician at the Faculty of Mining, Geology and Petroleum Engineering.

RGNZ/MGPB

Rudarsko-geološko-naftni zbornik

The Mining-Geological-Petroleum Engineering Bulletin

Hrvatski znanstveni časopis / *Croatian scientific journal*

Godište XXXVII, broj 76 (vol. 40, sv. 5) / *Anno XXXVII, number 76 (vol. 40, issue 5)*

Referira se u / *Indexed and abstracted in:*
Chemical Abstracts, Emerging Sources Citation Index (Thomson Reuters, WoS, Core Collection), Compendex + Geo Abstracts (Geobase) + Scopus (Elsevier), GeoRef, Geotechnical abstracts, Google Scholar (via PDFs on http://hrcak.srce.hr/rgn-zbornik), Petroleum Abstracts, Norwegian register for scientific journals, series and publishers.

Akademske baze i pretraživači (otvorena pristupa) / *Academic databases and search engines (open access)*:
DOAJ (received DOAJ Seal), DOI (CrossRef), Geoscience e-journal, Electronic Journals Library, Hrčak, JournalSeek.

Komercijalne baze i pretraživači / *Commercial databases and search engines*:
EBSCO Publishing Services, ProQuest (SciTech, Natural Science, Environmental Science, Earth Science, Technology Collection, Materials Science collections).

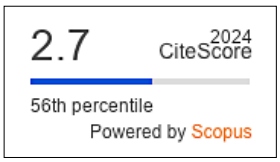
Uvjeti uporabe otvorenoga pristupa časopisu i njegovim arhivama dani su na / *Open access license and archiving is available*:
http://www.sherpa.ac.uk/romeo/search.php?id=2374&format=full&fIDnum=%7c.

UDK/*UDC* 62:66:51-56
Mrežna inačica / *Online:* ISSN 1849-0409
Tiskana inačica / *Print:* ISSN 0353-4529

Izdavač
Rudarsko-geološko-naftni fakultet Sveučilišta u Zagrebu, Pierottijeva 6, HR-10000 Zagreb

Publisher
Faculty of Mining, Geology and Petroleum Engineering, University of Zagreb, Pierottijeva 6, 10000 Zagreb, Croatia





2025.





Glavni i odgovorni urednik: Tomislav Korman, Rudarsko-geološko-naftni fakultet, Zagreb

Urednici polja:
Lidia Hrnčević (naftno rudarstvo i energetika), Rudarsko-geološko-naftni fakultet, Zagreb
Zlatko Briševac (rudarstvo), Rudarsko-geološko-naftni fakultet, Zagreb
Zoran Kovač (geologija), Rudarsko-geološko-naftni fakultet, Zagreb
Krešimir Pavlić (matematika, fizika, znanosti o svemiru), Rudarsko-geološko-naftni fakultet, Zagreb

Tehnički urednik:
Dubravko Domitrović, Rudarsko-geološko-naftni fakultet, Zagreb

Uredničkи odbor:

Članovi s Rudarsko-geološko-naftnoga fakulteta:
Duje Smirčić
Sanja Bernat Gazibara
Marija Macenić

Vanjski članovi:
Maria Alzira Pimenta Dinis, UFP Energy, Environment and Health Research Unit (FP-ENAS), Sveučilište Fernando Pessoa, Porto, Portugal
Vasilj Grygorovyč Lozynskyj, Tehnološko sveučilište u Dnjipru, Dnjipro, Ukrajina
Josip Ivšinović, Vodnikova 17, 10000 Zagreb, Hrvatska
Sara Kasmaeeyazdi, Sveučilište u Bolonji, Zavod za građevinarstvo, kemiju, te inženjerstvo okoliša i materijala, Italija
Ivica Skokić, Sveučilište u Zagrebu, Geodetski fakultet, Opservatorij Hvar, Hrvatska
Francesco Tinti, Sveučilište u Bolonji, Zavod za građevinarstvo, kemiju, te inženjerstvo okoliša i materijala, Italija
Mojtaba Yari, Sveučilište u Isfahanu, Zavod za rudarsko inženjerstvo, Iran
Satria Bijaksana, Institut Teknologi Bandung, Bandung, Indonesia
Aleksandar Mezga, Sveučilište u Zagrebu, Prirodoslovno-matematički fakultet, Geološki odsjek, Hrvatska
Manoj Khandelwal, Federation University, Australia

Lektura engleskih tekstova:
Dubravka Pleše, Rudarsko-geološko-naftni fakultet, Zagreb

Lektura hrvatskih tekstova:
Ivana Matas Ivanković, Zagreb

Izdavački savjet: Fakultetsko vijeće

Za izdavački savjet: Vladislav Brkić, dekan

Adresa na Hrčkovom OJS-u: https://hrcak.srce.hr/ojs/index.php/rgn/index

Adresa na Hrčku (arhiva): https://hrcak.srce.hr/rgn-zbornik

E-pošta glavnoga urednika: tomislav.korman@rgn.unizg.hr

Prijelom
Gredice, Horvaćanska 67, HR-10000 Zagreb

Naklada
elektroničko izdanje i 50 tiskanih primjeraka

Editor-in-Chief: *Tomislav Korman, the Faculty, HR*

Editors of scientific fields*:*
Lidia Hrnčević (Petroleum Engineering and Energetics), the Faculty, HR
Zlatko Briševac (Mining), the Faculty, HR
Zoran Kovač (Geology), the Faculty, HR
Krešimir Pavlić (Mathematics, Physics, Space Sciences), the Faculty, HR

Tehnical editor*:*
Dubravko Domitrović, University of Zagreb, Faculty of Mining, Geology and Petroleum Engineering, Croatia

Editorial board:

Members from the Faculty of Mining, Geology and Petroleum Engineering:
Duje Smirčić
Sanja Bernat Gazibara
Marija Macenić

Non-Faculty Members of the Editorial Board:
Maria Alzira Pimenta Dinis, UFP Energy, Environment and Health Research Unit (FP-ENAS), University Fernando Pessoa, Porto, Portugal
Vasyl Hryhorovych Lozynskyi, Dnipro University of Technology, Dnipro, Ukraine
Josip Ivšinović, Vodnikova 17, 10000 Zagreb, Croatia
Sara Kasmaeeyazdi, University of Bologna, Department of Civil, Chemical, Environmental, and Materials Engineering, Italy
Ivica Skokić, University of Zagreb, Faculty of Geodesy, Observatory Hvar, Croatia
Francesco Tinti, University of Bologna, Department of Civil, Chemical, Environmental, and Materials Engineering, Italy
Mojtaba Yari, Isfahan University of Technology, Department of Mining Engineering, Isfahan, Iran
Satria Bijaksana, Institut Teknologi Bandung, Bandung, Indonesia
Aleksandar Mezga, University of Zagreb, Faculty of Science, Geological Department, Croatia
Manoj Khandelwal, Federation University, Australia

English proofreading:
Dubravka Pleše, the Faculty, HR

Croatian proofreading:
Ivana Matas Ivanković, HR

Publishing council*: Faculty Council, HR*

Chairman of Council*: Vladislav Brkić, Dean, HR*

The Open Journal System web site: *https://hrcak.srce.hr/ojs/index.php/rgn/index*

The Croatian scientific and professional journals archive (Hrčak): *https://hrcak.srce.hr/rgn-zbornik*

E-mail of the Editor-in-Chief: *tomislav.korman@rgn.unizg.hr*

Layout
Gredice, Horvaćanska 67, HR-10 000 Zagreb

Edition
e-publication and 50 copies

Sadržaj/*Contents*

Radovi/*Papers*

1.	Evaluating Liquefaction Susceptibility Through HVSR and MASW Methods: A Case Study in Mamuju, West Sulawesi, Indonesia *(Andri Moh. Wahyu Laode; Muh. Altin Massinai; Muhammad Fawzy Ismullah Massinai; Erfan Syamsuddin)*	1-18
2.	Magnetic and Geochemical Studies of Iron sand Deposits around Tambora Volcano in Sumbawa, Indonesia: A proxy for search high quality iron sand *(Putu Billy Suryanata; Adella Ulyandana Jayatri; Satria Bijaksana; Silvia Jannatul Fajar; Ulvienin Harlianti)*	19-30
3.	Application of Artificial Intelligence in Reservoir Simulation for Characterizing Multi-Phase Fluid Flow through Petroleum Reservoirs *(Viswakanth Kandala; Suresh Kumar Govindarajan; Tummuri Naga Venkata Pavan; Swaminathan Ponmani; Srinivasa Reddy Devarapu)*	31-42
4.	MAETEC: An Optimized MATLAB-Based Approach for Accurate and Efficient Terrain Correction in Complete Bouguer Anomaly *(Indra Arifianto; Jun Nishijima; Rahmat Catur Wibowo)*	43-56
5.	Unveiling the dynamics of deep-focus earthquakes: Insights from the 2020 Jepara event Mw 6.7 and subduction processes beneath Java *(Tio Azhar Prakoso Setiadi; Anne Meylani Magdalena Sirait; Yehezkiel Halauwet; Andrean Vesalius Hasiholan Simanjuntak; Adi Susilo)*	57-66
6.	An investigation on the potential recovery of copper from a low-grade copper resource containing high silica content *(Milad Abbassi; Asghar Azizi)*	67-82
7.	Geology and mineralogy of Fe-Sn deposit in Batubesi, Belitung Island, Indonesia *(Aryo Dwi Handoko; Mochamad Slamet Sugiharto; Syafrizal; Alfend Rudyawan; Benyamin Sapiie)*	83-98
8.	Anthropogenic Hazards Assessment of Mining Activities in Surghar Range, Punjab, Pakistan *(Syed Sajjad Ahmad; Hafiz Muhammad Zaheer Afzal; Hafiz Zeeshan Akram; Sajjad Khan; Ihtisham Islam; Salman Ahmed Khattak)*	99-113
9.	Combining the 3D geological and geostatistical modelling of gypsum concentration, using historical borehole and blasthole information *(Stefano Merli; Sara Kasmaee; Cristina Barbalucca; Vanessa Cellini; Francesco Tinti)*	115-126
10.	Concentrating the Zn-Pb sample from Nignan ore deposit *(Maryam Abedi Moghadam; Marzieh Hosseini Nasab; Mohammad Noaparast)*	127-140
11.	Integrating ANN Prediction with Honeybee Optimisation for Flyrock Minimisation in Open-Pit Mining *(Mojtaba Rezakhah; Erfan Nemati; Amir Batarbiat; Manoj Khandelwal)*	141-152
12.	Mechanical activation and geopolymerisation of Taiwanese fly ash *(Fanni Dolgos; Roland Szabó; Wei-Ting Lin; Gábor Mucsi)*	153-165
13.	Seed-Guided, Fault-Aware Horizon Tracking via Greedy Propagation for Geological Modelling *(Ana Brcković; Marko Cvetković; Josipa Kapuralić; Ivan Medved)*	167-178
14.	A Sustainable and Practical Machine Learning Approach Using Scikit-Learn for Predicting Stope Instability: Identification of Critical Geotechnical Factors *(Amos Bemo; Deji Olatunji Shonuga; Tawanda Zvarivadza; Moshood Onifade; Manoj Khandelwal)*	179-198

RGNZ/MGPB

Evaluating Liquefaction Susceptibility Through HVSR and MASW Methods: A Case Study in Mamuju, West Sulawesi, Indonesia

Rudarsko-geološko-naftni zbornik
(The Mining-Geology-Petroleum Engineering Bulletin)
DOI: 10.17794/rgn.2025.5.1

Original scientific paper

Andri Moh. Wahyu Laode[1], Muh. Altin Massinai[1]*, Muhammad Fawzy Ismullah Massinai[1,2], Erfan Syamsuddin[1]

[1] *Department of Geophysics, Faculty of Mathematics and Natural Science, Hasanuddin University, South Sulawesi 90245, Indonesia.*

[2] *Geology Program, Department of Earth Sciences and Environment, Faculty of Science and Technology, Universiti Kebangsaan Malaysia, 43600 UKM Bangi, Selangor Darul Ehsan, Malaysia.*

Abstract

The 2021 Mamuju earthquake (Mw 6.2) highlighted the region's high vulnerability to liquefaction due to its proximity to active tectonic zones, as well as the presence of Holocene alluvial deposits, unconsolidated sedimentary formations, and water-saturated soils, all of which contribute to high susceptibility to seismic shaking. This research assesses the liquefaction potential of the Mamuju area using an integrated approach that combines the Horizontal-to-Vertical Spectral Ratio (HVSR) and Multichannel Analysis of Surface Waves (MASW) methods. This study investigates an inverse correlation between Vs30 and the seismic vulnerability index (K_g), where lower V_{s30} values correspond to higher Kg values, indicating increased liquefaction susceptibility. The HVSR analysis shows that the dominant frequency (f_0) ranges from 0.4 to 11 Hz, while the amplification factor (A_0) varies between 1.1 and 11. The results indicate that coastal zones with thick alluvial deposits exhibit the lowest f_0 values (<2.5 Hz), which correlate with V_{s30} < 175 m/s and K_g > 10, suggesting a higher likelihood of liquefaction. Conversely, areas underlain by the Mamuju Formation and Adang Volcanics, characterized by higher V_{s30} (>175 m/s), f_0 (>10 Hz), and K_g (<10), show lower susceptibility. These findings contribute to developing a detailed microzonation map for liquefaction risk, which is essential for improved urban planning and disaster mitigation in Mamuju. This study demonstrates that integrating HVSR and MASW methods is an effective approach to characterizing soil properties and enhancing liquefaction risk assessment in seismically active regions.

Keywords:
liquefaction, HVSR, MASW, Seismic Vulnerability Index, shear wave velocity, Mamuju earthquake

1. Introduction

The Mamuju region is located in a highly earthquake-active area of West Sulawesi. Based on the research of (**Hanifa et al., 2022; Meilano et al., 2023**), such conditions were due to the position near the convergence of three tectonic plates, which are the Eurasian Plate, the Indo-Australian Plate, and the Pacific Plate (**Sompotan, 2012; Supendi et al., 2021**). The movement of these plates exerts additional stress on the tectonic setting of Sulawesi, contributing to complex fault dynamics, increasing strain accumulation, and enhancing the likelihood of fault rupture, thereby affecting the seismic vulnerability of the Mamuju region. The movement of these plates may trigger subduction zones and active faults that can potentially produce high-magnitude earthquakes (**Rosid et al., 2022**). As a result of this high tectonic activity, the Mamuju region frequently experiences significant and destructive earthquakes (**Meilano et al., 2023**).

One of the destructive impacts of earthquakes is the phenomenon of soil liquefaction. Soil liquefaction is a phenomenon in which saturated, loosely packed soil temporarily loses its strength and stiffness due to a sudden increase in pore water pressure induced by cyclic loading from earthquake shaking, causing it to behave like a liquid (**Sukkarak et al., 2021; Tabrizi-Zarringhabaei et al., 2019; Zhou et al., 2020**). This condition can result in severe damage to infrastructure and buildings, such as ground subsidence, lateral spreading, and structural collapse (**Chaloulos et al., 2020**). Therefore, identifying areas vulnerable to liquefaction is crucial for earthquake disaster risk mitigation efforts (**Bao et al., 2019; Mahmoud et al., 2020**).

The 2021 Mamuju earthquake (Mw 6.2) underscored the need for a detailed assessment of soil vulnerability to liquefaction in the region (**Hanifa et al., 2022; Hossain et al., 2020**). Indications such as ground settlement and increased pore water pressure were reported in several areas (see **Figure 2A-E**), highlighting the importance of evaluating liquefaction susceptibility (**BMKG, 2021**). This study aims to analyze soil vulnerability and map liquefaction risks in Mamuju using the HVSR (Horizon-

* Corresponding author: Muh. Altin Massinai
e-mail address: altin@science.unhas.ac.id
Received: 12 January 2025. Accepted: 1 April 2025.
Available online: 21 October 2025

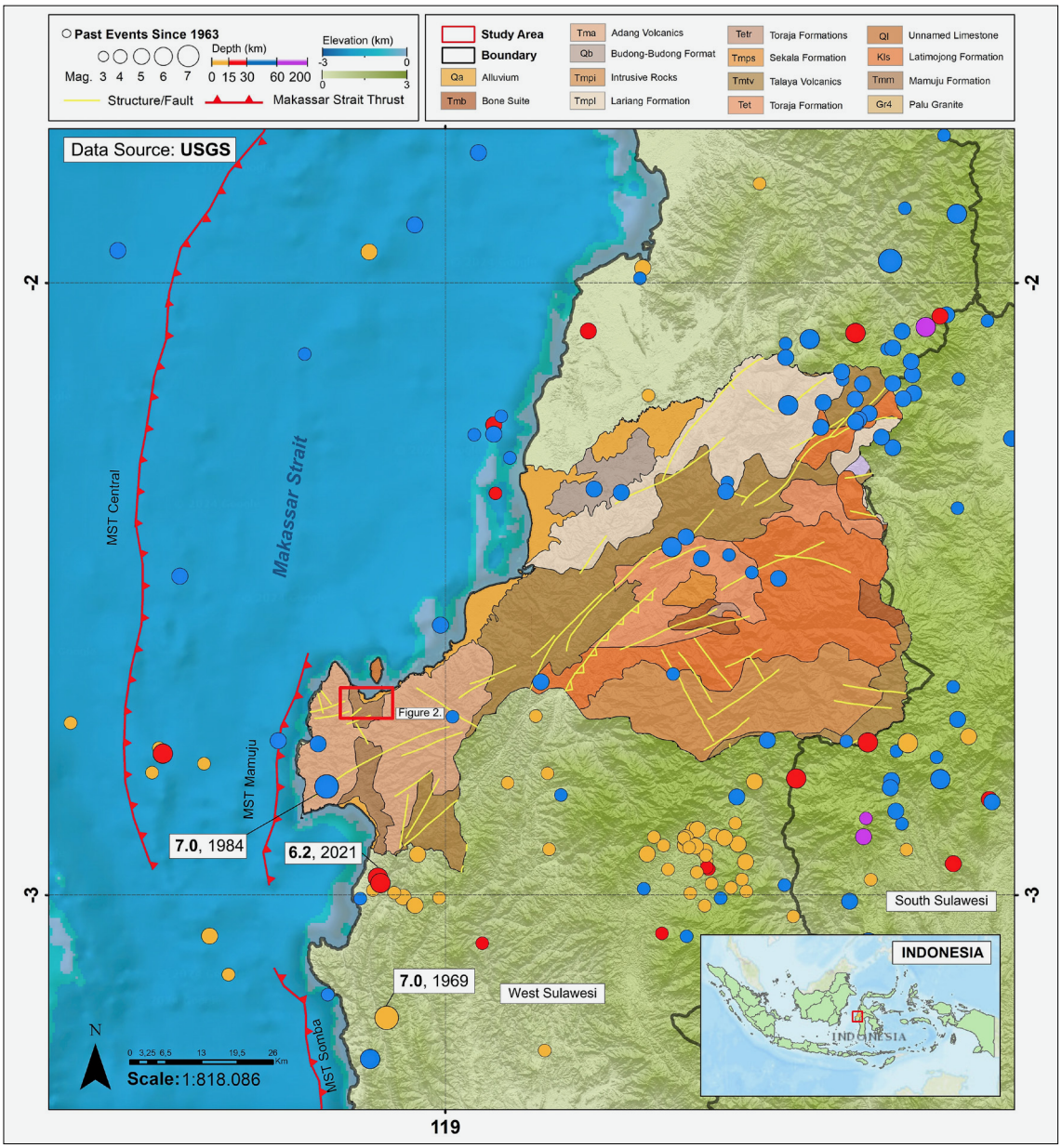


Figure 1. The geological formations and seismic activity in the study area. On January 15, 2021, a Mw 6.2 earthquake occurred near the active Makassar Strait Thrust (MST) system. Significant historical events in the region include the Mw 7.0 earthquake in 1969 and the Mw 7.0 earthquake in 1984. The colored circles represent seismic activity recorded from 1963 to 2024, based on data from the United States Geological Survey (USGS) Catalog. The colors of the circles indicate differences in earthquake depth, while the circle size represents the earthquake magnitude.

tal to Vertical Spectral Ratio) and MASW (Multichannel Analysis of Surface Waves) methods (**Quintero et al., 2023; Roy et al., 2022**). The MASW method utilizes an active seismic wave source and records the propagation of surface waves to obtain shear wave velocity (V_s) profiles (**Alan et al., 2019; Liu et al., 2020; Mohammed et al., 2020**). In contrast, the HVSR method captures ambient vibrations at the study site (**Nguyen-Tien et al., 2022; Piña-flores et al., 2020; Sedaghati et al., 2018**) to determine natural frequency, ground amplification, and the seismic vulnerability index (**Akkaya, 2020; Yaghmaei-Sabegh & Rupakhety, 2020**), which are key indicators in assessing liquefaction potential (**Kang et al., 2020**). Integrating these two methods provides a more comprehensive understanding of soil properties and seismic response, essential for accurate liquefaction risk assessments (**Alkan & Akkaya, 2023; Uyanık, 2020**).

Previous studies have demonstrated the effectiveness of combining MASW and HVSR in assessing soil vulnerability and liquefaction risk in various regions (**Chiaradonna et al., 2022; Kang et al., 2021; Mahajan et al., 2012; Mase et al., 2018; Pamuk et al., 2018; Shelley et al., 2015; Sundararajan & Seshunarayana, 2011; Syamsuddin et al., 2024**). These studies highlight

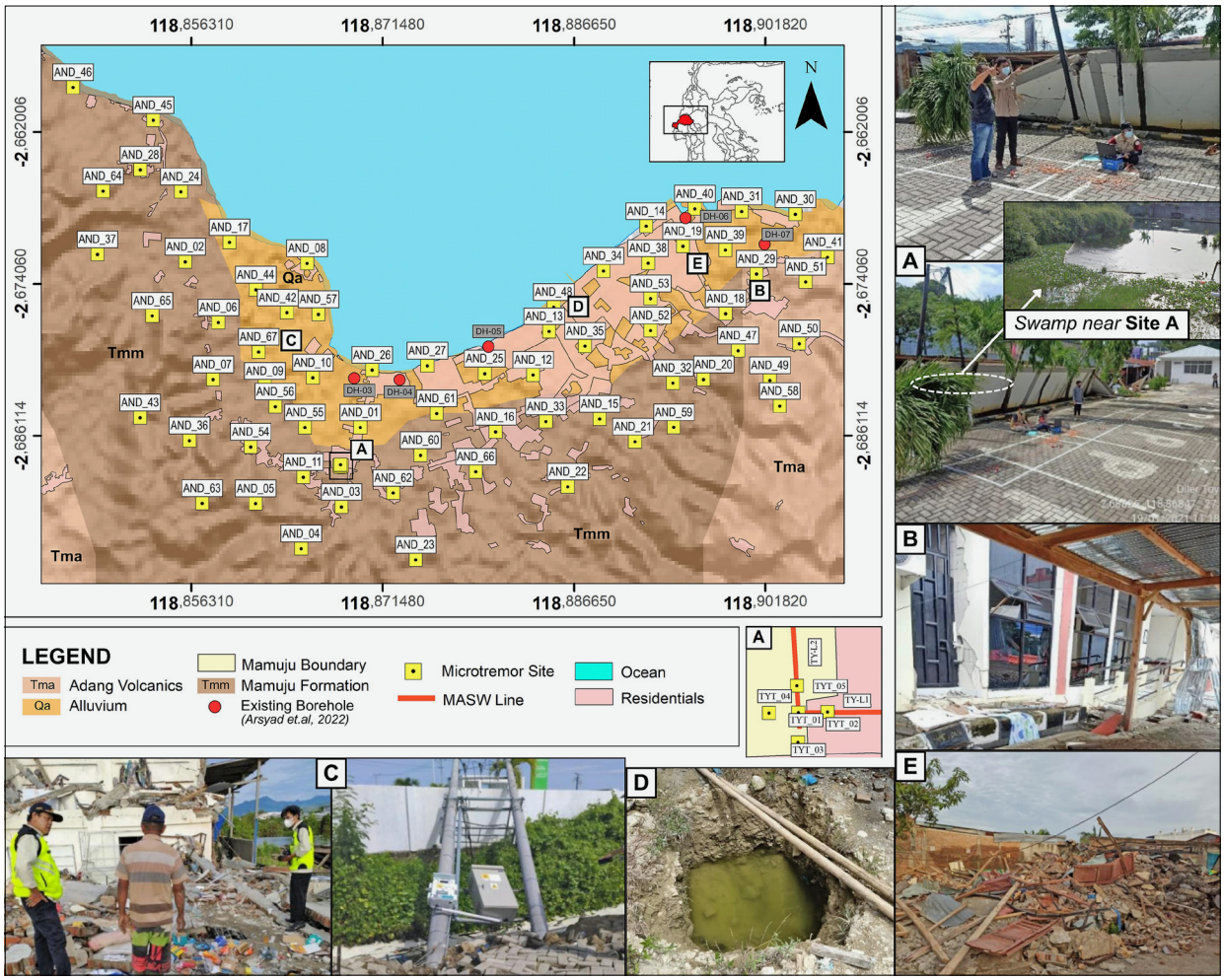


Figure 2. HVSR and MASW survey locations and geological formations of the study area. **A–D** indicate locations affected by the 2021 Mamuju earthquake, showing damage features such as sand boils, ground subsidence, collapsed buildings, and the emergence of water from previously dry holes **(BMKG, 2021)**.

the ability of MASW to delineate shear wave velocity profiles, while HVSR provides insight into site resonance frequency, amplification factors, and seismic vulnerability index, making it possible to identify subsurface conditions that contribute to the potential for liquefaction. However, most of these studies have been conducted in regions with well-documented seismic histories, whereas limited research has explored the applicability of these methods in Sulawesi, particularly in Mamuju, where recent earthquakes have caused significant damage.

Existing seismic studies in Mamuju have primarily focused on macroseismic observations and general geological assessments (**Supendi et al., 2021**), lacking detailed microzonation efforts that integrate geophysical methods to quantitatively assess liquefaction susceptibility. Furthermore, while MASW and HVSR have been used separately in other earthquake-prone regions, their combined application to analyze liquefaction susceptibility in Mamuju remains unexplored. This study fills this gap by integrating MASW and HVSR techniques to obtain high-resolution V_s profiles, seismic vulnerability index, and site amplification characteristics. The findings contribute to refining seismic hazard models, enhancing spatial planning strategies, and improving earthquake disaster mitigation efforts, particularly in Mamuju, a region with high seismic activity.

2. Tectonic Activity and Geological Setting

Due to its position at the triple junction of the Australian Plate, Sunda Plate, and Philippine Sea Plate, Sulawesi Island in eastern Indonesia experiences the relative displacement of at least four microblocks through active faulting (**Simons et al., 2007**). In West Sulawesi, the eastern boundary of the Sunda Plate is marked by the Makassar Block. The relative movement between the Makassar Block and the Sunda Plate is accommodated by the Makassar Strait Thrust (MST), which is divided into the Somba, Mamuju (MSTM), Central (MSTC), and Northern (MSTN) segments (**Meilano et al., 2023**). Although the slip rate of the MST is about one-quarter that of the Palu-Koro Fault, the MST remains a significant earthquake threat to communities along the western

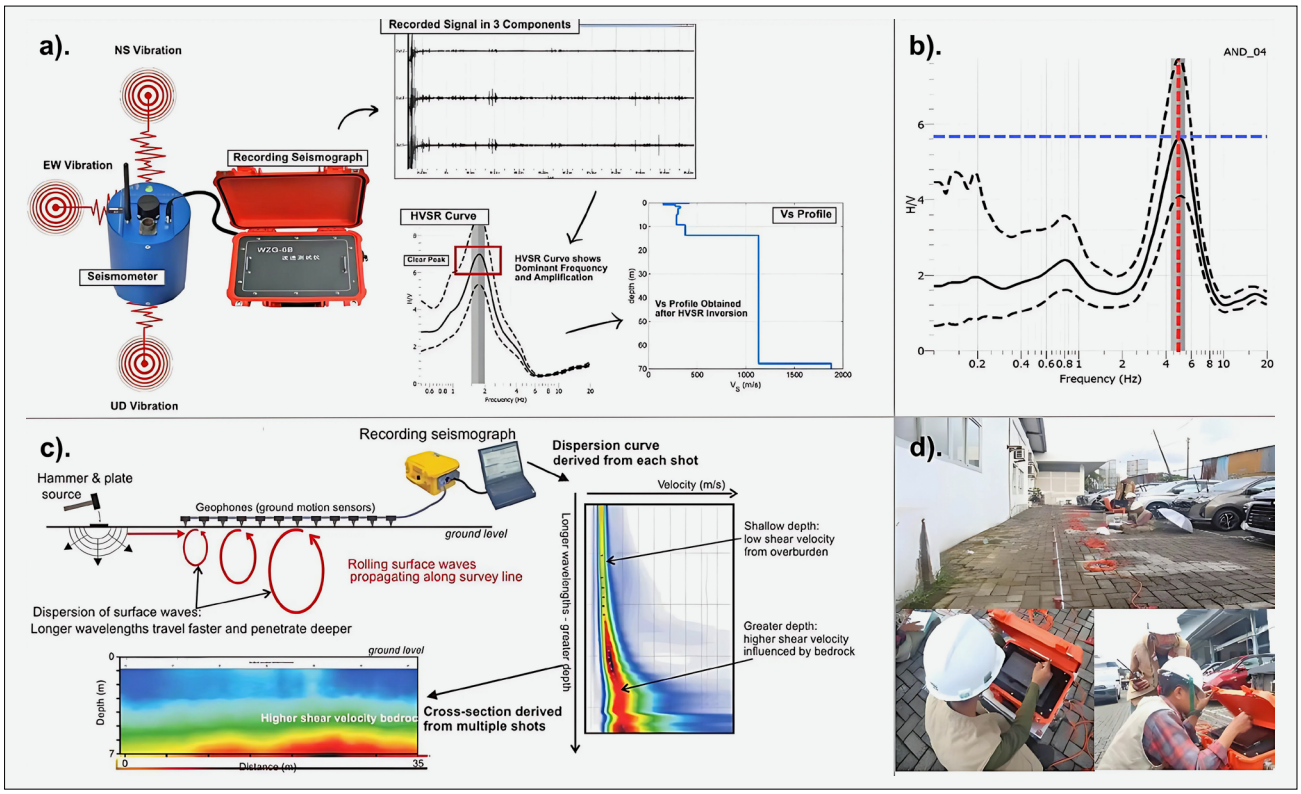


Figure 3. a) HVSR measurement procedure. **b)** Example of HVSR curve at station AND_04 (black line), maximum and minimum standard deviation (dashed black line). The dashed red vertical line shows the dominant frequency processed through GEOPSY software. The dashed blue horizontal line shows the maximum amplitude of the dominant frequency. **c)** MASW measurement procedure (**TERRADAT, 2024**). **d)** HVSR and MASW data acquisition at the research site.

Sulawesi coast, especially in Mamuju Regency (**Supendi et al., 2021**). Notable earthquakes along the MST (as seen in **Figure 1**) include the 1969 Majene earthquake (Mw 7.0), the 1984 Mamuju earthquake (Mw 7.0), and the 6.2 Mw earthquake on January 15, 2021. The 2021 earthquake occurred near the active MST system, following a Mw 5.9 earthquake 12 hours before the main shock (**Meilano et al., 2023; Supendi et al., 2021**).

The Mamuju region consists of sedimentary, metamorphic, volcanic, and intrusive rock formations ranging from the Mesozoic to the Quaternary (see **Figure 1**). The Latimojong Formation, the oldest unit, comprises metamorphic rocks such as quartzite, phyllite, and marble (**White et al., 2017**). Overlying it, the Toraja, Sekala, and Lariang Formations are composed of sandstone, shale, marl, and carbonate-rich deposits, representing marine to transitional depositional settings (**Ardianto et al., 2024**). Volcanic activity is recorded in the Talaya and Adang Volcanics, which consist of volcanic breccia, lava flows, tuff, and basaltic rocks, while Quaternary deposits, including the Budong-Budong Formation and alluvium, cover coastal and riverine areas (**Perdana & Amijaya, 2011; White et al., 2017**). The structural geology of the region is dominated by faults trending northeast-southwest and northwest-southeast, which have resulted in faulting, folding, and uplift. The highlands, primarily composed of metamorphic and volcanic rocks, contrast with the lowlands, which are covered by unconsolidated Quaternary sediments that are more susceptible to seismic amplification and liquefaction (**Rosianna et al., 2020**).

A) The research site indicated to have experienced liquefaction, marked by sand boils on the pavement blocks and collapsed walls, with a swamp located near site A (**BMKG, 2021**). **B)** Collapsed building accompanied by ground subsidence at the Mamunyu Subdistrict Office, Mamuju (**BMKG, 2021**). **C)** Ground subsidence and collapsed buildings in a residential area. **D)** Emergence of water in previously dry holes due to increased pore water pressure (**BMKG, 2021**). **E)** Collapsed buildings in a residential area near the Mamuju port (**BMKG, 2021**).

The study area comprises three geological formations: Alluvium, Mamuju Formation, and Adang Volcanics (as shown in **Figure 2**). The Alluvium Formation consists of loose sediment deposits commonly found in lowland areas near the coast and along rivers. These water-saturated alluvial layers are prone to liquefaction because they are highly susceptible to deformation due to earthquake shaking. The Mamuju Formation is composed of marl, calcareous sandstone, coral limestone, and tuffaceous sandstone, with local occurrences of conglomerate and claystone. This formation represents a shallow marine depositional environment, characterized by carbonate sedimentation interbedded with volcani-

clastic **deposits** (**Perdana & Amijaya, 2011; White et al., 2017**). The presence of poorly consolidated marl and tuffaceous sandstone indicates weak lithification, making the formation more susceptible to deformation under seismic loading (**Rosianna et al., 2023**). The Adang Volcanics consist of various volcanic rocks, primarily phonolitic leucite, containing minerals like leucite, K-feldspar, plagioclase, pyroxene, and small amounts of opaque minerals (**Shaban et al., 2016**). These rocks tend to undergo moderate to strong weathering (**Ritonga et al., 2021**). Overall, the Mamuju region and its surroundings are characterized by numerous geological formations dominated by loose sediment deposits, both in lowland areas and hills. The predominance of loose sediments increases the region's vulnerability to the destructive impacts of earthquakes (**Rosianna et al., 2020; Zaidani et al., 2023**).

2. Data and Methods

2.1. Data

The data used in this study consist of measurements from 72 microtremor sites and 2 MASW lines spread across Mamuju, West Sulawesi (see **Figure 2**). MASW data acquisition was conducted with a sampling rate of 0.5 ms and a sampling frequency of 2000 Hz, with a recording duration of 1.024 s. The survey utilized 24 geophones with a natural frequency of 4.5 Hz, arranged in a straight line, with a near-offset of 5 meters and a spacing of 1 meter between geophones. A sledgehammer was used as an active source. The roll-along configuration was employed to obtain 2D data. For line 1, the source-receiver was shifted 2 meters with a total of 12 shots, while for line 2, the source receiver was moved 1 meter with a total of 13 shots. The difference in geometry between the two profiles was due to field conditions that prevented the use of the same geometry. The documentation of microtremor HVSR and MASW acquisition is presented in **Figure 3d**.

Microtremor measurements were conducted for durations of 20-60 minutes with a sampling frequency of 100 Hz and a sampling rate of 0.01 s using a Digital Portable Seismograph type TDL-303S and a seismometer type DS-4A. The recorded data consisted of three components of the seismogram: the horizontal components (North-South and East-West) and the vertical component (Up-Down) (**Mihaylov et al., 2019**). The recorded data were then processed to obtain HVSR using the following **Equation 1 (Khalili & Mirzakurdeh, 2019; Ma et al., 2019)**:

$$\mathrm{HVSR} = \sqrt{\frac{\mathrm{H_{NS}}^2 + \mathrm{H_{EW}}^2}{\mathrm{V}^2}} \quad (1)$$

Where:

HVSR – horizontal to vertical spectral ratio,

H_{NS} – amplitude spectrum of the north-south horizontal component,

H_{EW} – amplitude spectrum of the east-west horizontal,

V – amplitude spectrum of the vertical component.

2.2. Method

The Horizontal-to-Vertical Spectral Ratio (HVSR) method is a passive geophysical technique used to evaluate the dynamic properties of soil and local site effects (**Chávez-García & Raptakis, 2017; Maghami et al., 2021; Maklad et al., 2020**). The fundamental principle of HVSR involves recording ambient vibrations using a three-component seismometer (**Bignardi, 2017; Gupta et al., 2021**). These vibrations originate from various natural and anthropogenic sources, such as wind, ocean waves, and human activities (**Ahn et al., 2021; Yang et al., 2019**). The recorded data are then analyzed to produce the HVSR curve (see **Figure 3b**), which displays the spectral amplitude ratio of the horizontal to vertical components as a function of frequency (**Fat-Helbary et al., 2019; Molnar et al., 2022**). A reliable HVSR curve must meet the criteria established by **SESAME (2004)**. These criteria include the stability of the HVSR curve across different time windows, the presence of a clear peak (as shown in **Figure 3b**), a low standard deviation within one octave of the fundamental frequency (f_0), and consistency in amplitude and shape between the three components. Data that fulfill these conditions are considered reliable and suitable for further interpretation. The HVSR measurement procedure can be seen in **Figure 3a**. Peaks in the HVSR curve indicate the dominant frequency of the soil layers (**Moon et al., 2019**), which is directly correlated with the thickness and shear wave velocity of the sediment layers above the bedrock (**Perez, 2024**). The value of the dominant frequency (f_0) for a region can be expressed by the following **Equation 2** (**Nakamura, 2000**):

$$\mathrm{f_0} = \frac{V_s}{4H} \quad (2)$$

Where:

f_0 – dominant frequency (Hz),

V_s – shear wave velocity (m/s),

H – thickness of the sediment layer (m).

Soil vulnerability to liquefaction is assessed using the seismic vulnerability index (K_g) derived from HVSR. K_g identifies the susceptibility of a soil layer to deformation due to earthquakes (**Pamuk et al., 2018**). High K_g values indicate that an area is prone to seismic effects (**Livaoğlu et al., 2019**), especially in soils with soft sedimentary rock lithology, such as coastal zones dominated by Alluvium formations (**Putti & Satyam, 2020**). These loose sediments, composed of sand, clay, and silt, have low cohesion and high water content, making them more susceptible to liquefaction during strong ground shaking (**Sana & Nath, 2016**). Liquefaction occurs when water-

saturated, loose granular soils lose their shear strength due to increased pore water pressure during seismic shaking, resulting in fluid-like behaviour of the ground (**Hanindya et al., 2023; Kusmanto et al., 2024**). This phenomenon may lead to ground subsidence, lateral spreading, and structural damage (**Kang et al., 2020**). The K_g index is particularly useful in identifying high-risk zones where seismic and liquefaction hazards are not immediately apparent from surface observations. A value of $K_g > 10$ suggests potential deformation, including liquefaction, whereas $K_g < 10$ indicates more compact and stable soils that are less prone to seismic stress-induced failure (**Akkaya, 2020; Kang et al., 2021**). Surface soil characteristics can be analyzed through the dominant frequency obtained from HVSR (**Chen et al., 2020; Rong et al., 2020**). Ground motion at a location is usually associated with a dynamic strain induced by seismic vibrations (**Trifunac, 2016**) and is often evaluated using the seismic vulnerability index (K_g) through the following **Equation 3** (**Susilo et al., 2023**):

$$K_g = \frac{A_0^{\,2}}{f_0} \tag{3}$$

Where:

A_0 – amplification,

f_0 – dominant frequency (Hz),

K_g – seismic vulnerability index.

In addition to the K_g value, V_{s30} (the average shear wave velocity at a depth of 30 meters) is derived from V_s profiles at each microtremor site through HVSR inversion (**Sivaram et al., 2018**). Soil layers with low V_s values generally indicate soft or loose soils (**Najaftomarei et al., 2020**), which are more vulnerable to changes in characteristics during strong vibrations (**Senkaya et al., 2019**). In contrast, high V_s values indicate denser and more stable soils, with a lower risk of structural changes during shaking (**Salleh et al., 2021**). To further analyze subsurface characteristics, spatial maps of dominant frequency (f_0), seismic vulnerability index (K_g), and V_{s30} were generated using interpolation techniques. Specifically, the Inverse Distance Weighting (IDW) method was applied to estimate values at unsampled locations by computing a weighted average of nearby measured points, where weights are inversely proportional to the distance (**Ghione et al., 2023; Odom & Doctor, 2023**). This method was chosen for its effectiveness in capturing local variations in geophysical parameters while maintaining computational efficiency **(Qadri et al., 2015**). In this study, V_s for shallow layers were also obtained using MASW surveys conducted at locations previously identified as areas susceptible to liquefaction. The Multichannel Analysis of Surface Waves (MASW) utilizes surface wave analysis (Rayleigh waves) to derive shear wave velocity (V_s) profiles in the soil layers (**Abudeif et al., 2019; Liu et al., 2020**). The acquired MASW data were processed using the Geopsy software, where dispersion curves were extracted and inverted using the Neighborhood Algorithm (NA) to derive the 1D shear wave velocity (V_s) profiles. These 1D profiles were then interpolated to construct a 2D V_s model to characterize subsurface conditions. The interpolation method used was kriging, which provides a statistically optimal estimation of V_s distribution by considering spatial correlations between data points, thereby ensuring a smooth and continuous representation of subsurface velocity variations (**Ismail et al., 2014**). The reliability of the V_s profile is evaluated based on the fit between the theoretical and experimental dispersion curves (**Foti et al., 2015**). The *misfit* value is a parameter that quantifies the discrepancy between experimental and theoretical dispersion curves and is calculated using the following **Equation 4** (**Wathelet et al., 2004**):

$$misfit = \sqrt{\sum_{i=0}^{n_F} \frac{(x_{di} - x_{ci})^2}{\sigma_i^{\,2} n_F}} \tag{4}$$

Where:

x_{di} – experimental Rayleigh wave phase velocity (m/s),

x_{ci} – theoretical Rayleigh wave phase velocity (m/s),

n_F – number of frequency samples,

σ_i – the uncertainty of the frequency samples considered.

The lower the value of misfit, the better the match between the experimental and theoretical dispersion curve, indicating a more reliable V_s model (**Griffiths et al., 2016**). The MASW procedure is shown in **Figure 3c**.

3. Results

In evaluating the liquefaction potential in Mamuju, West Sulawesi, the ambient noise recorded at 72 sites met the HVSR curve criteria in accordance with **SESAME (2004)**. The results are shown in **Table 1**.

3.1. Dominant Frequency

The dominant frequency, which refers to the fundamental resonance frequency of a site, is a crucial parameter in assessing site response to seismic activity (**Syamsuddin et al., 2024**). The frequency is inversely related to the thickness of the soil layer above bedrock, lower frequencies suggest deeper unconsolidated layers, while higher frequencies correspond to shallower layers (**Kang et al., 2021; Pamuk et al., 2018**). The results of the dominant frequency obtained at each site can be seen in **Figure 4**.

The dominant frequency values obtained at each site range from 0.4 to 12.6 Hz. Sites with low dominant frequencies (<2.5 Hz) are predominantly located along the coastline, indicating thick sediment layers with an alluvial rock formation. Medium dominant frequencies (2.5 – 10 Hz) are mainly found in areas with higher elevations, although some are also near the coastline. Sites

Table 1. HVSR Results at each station in Mamuju, West Sulawesi

ID	Longitude	Latitude	f_0 (Hz)	A_0	K_g	V_{s30} (m/s)
AND_01	707861	9703015	1.7	7.0	16.8	178
AND_02	706320	9704472	0.5	3.5	14.4	128
AND_03	707694	9702319	1.0	3.3	6.7	125
AND_04	707338	9701954	4.9	6.0	4.4	187
AND_05	706937	9702350	2.4	2.3	1.3	205
AND_06	706611	9703939	1.2	2.4	2.7	164
AND_07	706564	9703439	4.6	1.9	0.5	251
AND_08	707394	9704458	0.5	2.7	8.0	143
AND_09	707020	9703381	11.0	5.0	1.3	274
AND_10	707442	9703453	0.6	4.8	22.9	126
AND_11	707358	9702582	1.5	2.6	2.6	180
AND_12	709386	9703475	2.3	5.1	6.7	187
AND_13	709526	9703857	1.2	3.3	5.4	197
AND_14	710384	9704778	0.9	2.5	4.1	159
AND_15	709972	9703088	1.6	5.0	9.6	178
AND_16	709054	9702977	1.0	5.5	17.9	174
AND_17	706710	9704642	2.9	6.6	9.1	164
AND_18	711084	9704010	0.7	3.5	10.0	133
AND_19	710708	9704602	0.8	7.7	44.9	164
AND_20	710888	9703433	4.7	1.8	0.4	214
AND_21	710282	9702888	5.6	2.0	0.4	282
AND_22	709688	9702492	1.4	3.3	4.7	179
AND_23	708347	9701854	3.0	2.1	0.9	245
AND_24	706283	9705088	5.5	4.5	2.2	222
AND_25	708959	9703487	1.0	2.9	5.0	180
AND_26	707966	9703520	0.9	4.9	15.6	122
AND_27	708453	9703556	1.2	5.2	13.8	177
AND_28	705926	9705280	4.9	3.1	1.2	220
AND_29	711357	9704358	0.4	3.9	21.8	142
AND_30	711700	9704880	1.6	5.4	10.8	195
AND_31	711226	9704906	1.3	4.8	10.7	166
AND_32	710618	9703401	0.4	2.6	9.4	129
AND_33	709496	9703066	1.5	3.7	5.6	149
AND_34	710007	9704387	6.7	3.7	1.2	268
AND_35	709843	9703728	3.9	2.9	1.3	155
AND_36	706354	9702903	0.8	6.1	27.3	155
AND_37	705546	9704538	2.7	2.7	1.6	196
AND_38	710400	9704454	3.8	3.7	2.1	185
AND_39	711083	9704569	3.8	3.7	2.1	199
AND_40	710812	9704931	1.3	2.7	3.4	146
AND_41	711983	9704505	0.8	3.1	7.3	170
AND_42	707216	9704024	0.5	6.1	44.3	138
AND_43	705920	9703106	10.8	3.1	0.5	243
AND_44	706941	9704225	1.0	2.8	4.9	142
AND_45	706040	9705716	0.4	4.4	28.1	138
AND_46	705334	9706005	1.8	3.2	3.5	157
AND_47	711194	9703685	8.3	3.7	1.0	312
AND_48	709567	9704070	0.8	5.6	24.3	140
AND_49	711473	9703421	6.7	3.5	1.1	275
AND_50	711732	9703745	2.4	3.7	3.4	209
AND_51	711789	9704287	2.3	3.2	2.7	243
AND_52	710421	9703864	3.5	3.2	1.8	282
AND_53	710421	9704144	0.8	2.8	5.6	136
AND_54	706894	9702847	1.7	7.0	16.8	147
AND_55	707373	9703016	0.5	3.6	15.6	149
AND_56	707111	9703199	2.4	2.3	1.3	137
AND_57	707493	9704010	0.7	3.5	10.0	114
AND_58	711560	9703196	4.7	1.8	0.4	228
AND_59	710626	9703013	4.3	1.1	0.2	165
AND_60	708391	9702772	3.2	2.4	1.1	231
AND_61	708535	9703139	0.9	4.9	16.5	151
AND_62	708150	9702440	0.7	1.5	2.2	125
AND_63	706465	9702352	3.0	2.0	0.8	154
AND_64	705596	9705093	3.4	2.0	0.7	204
AND_65	706028	9703999	9.9	3.7	0.8	291
AND_66	708879	9702626	3.7	3.3	1.8	231
AND_67	706966	9703681	0.6	11.0	127.8	131
TYT_01	707687	9702681	0.8	1.7	2.2	114
TYT_02	707677	9702681	1.0	1.8	1.9	159
TYT_03	707687	9702671	0.6	2.1	4.4	133
TYT_04	707697	9702681	0.8	2.0	3.0	112
TYT_05	707687	9702690	0.8	2.8	5.9	105

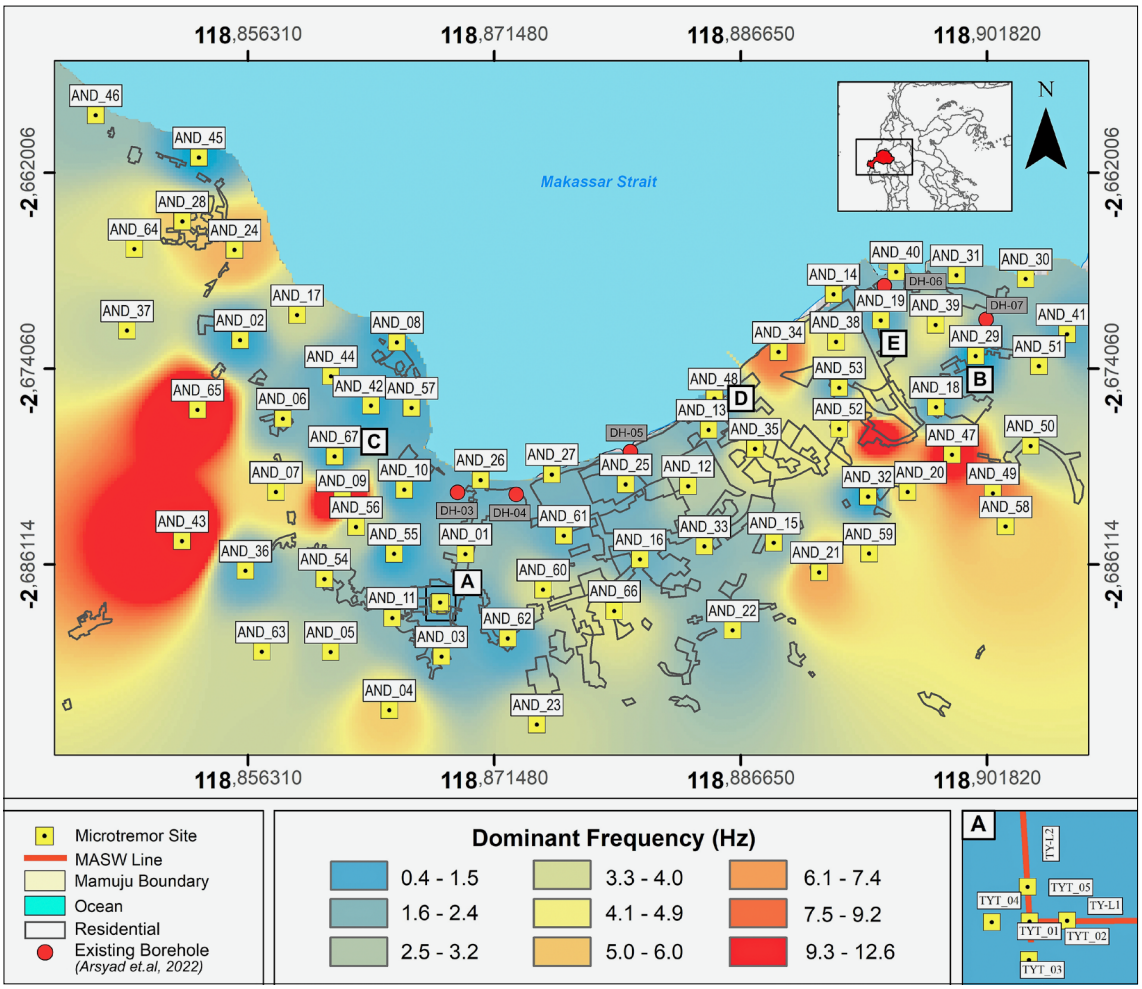


Figure 4. Distribution of dominant frequency across the study area from HVSR analysis. **A)** The research site indicated to have experienced liquefaction.

with high dominant frequencies (>10 Hz) are mostly located in the eastern and western parts of the study area, where the terrain has higher elevations compared to sites with low and medium frequencies, this frequency indicates thin sediment layers of less than 5 meters. Relating this to the geological formations in the study area (see **Figure 2**), sites with low-frequency values are found in the Alluvium Formation, while some are in the Mamuju Formation. According to (**Kang et al., 2020; Syamsuddin et al., 2024**), the Alluvium Formation consists of lithology that includes sand, gravel, silt, clay, and gravel, which is vulnerable to the destructive impacts of earthquakes, including liquefaction.

3.2. Shear Wave Velocity

Shear wave velocity (V_s) is an essential parameter for characterizing the dynamic properties of shallow subsurface materials (**Pandavenes et al., 2023**). The average shear wave velocity in the upper 30 meters (V_{s30}) is often used to classify soil types and assess their potential for amplification during an earthquake (**Alkan & Akkaya, 2023**). Lower V_{s30} values are indicative of softer, more vulnerable soils, while higher values represent stiffer, less susceptible formations (**Bajaj & Anbazhagan, 2019; Kang et al., 2021**). The distribution of V_{s30} values can be seen in **Figure 5**.

Based on the HVSR result, the V_{s30} values obtained are divided into two classifications: soft soil (<175 m/s) and stiff soil (175 – 350 m/s). Areas with V_{s30} values <175 m/s are predominantly located along the coastline, which are generally more vulnerable to ground wave amplification during an earthquake. In the study area, the Alluvium Formation mostly falls into this category. Alluvium consists of loose and unconsolidated sediments, resulting in lower shear wave velocity values. This indicates that this formation is at a higher risk of experiencing destructive earthquake impacts, such as liquefaction, especially in densely populated areas built on this soil. In contrast, the Mamuju Formation and parts of the Adang Volcanic Formation fall into the medium soil category, with V_{s30} values ranging from 175 to 350 m/s. These V_{s30} values are found in areas with higher elevations, although some are also located near the coastline. The lithology of these formations tends to be harder than the Alluvium Formation, which means the defor-

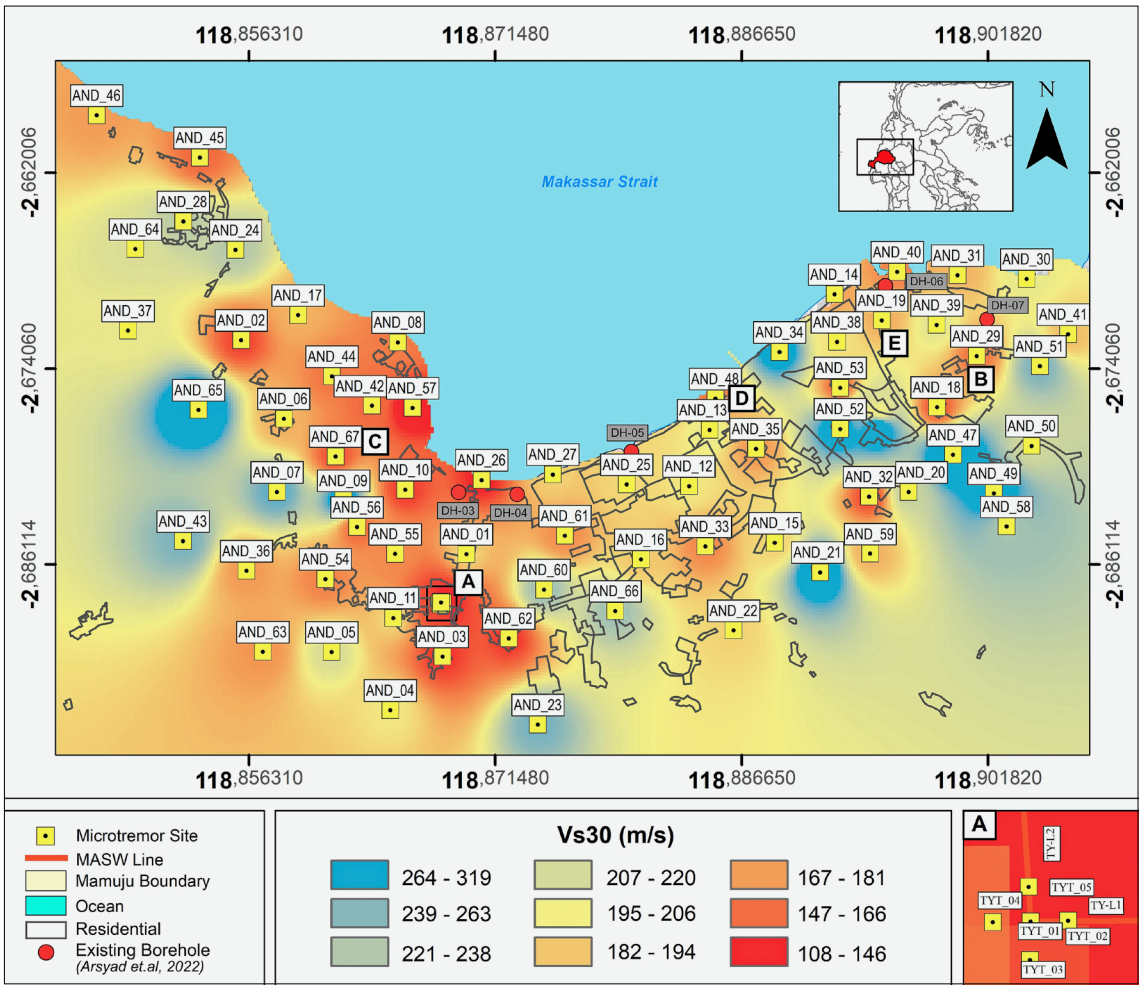


Figure 5. Distribution of Vs_{30} values across the study area from HVSR analysis. **A)** The research site indicated to have experienced liquefaction.

mation caused by earthquakes is likely to be lower. However, despite being less vulnerable to amplification, the presence of discontinuities or weathered zones within these formations can still pose local seismic risks.

In addition to the V_{s30} values obtained through HVSR inversion, MASW measurements were also conducted at locations identified as having experienced liquefaction during the 2021 earthquake. The V_s profiles from the MASW measurements are shown in **Figure 6a** and **Figure 6b**. Based on the 2D V_s profiles from both survey lines, the soil falls into the soft soil category. When compared with the 1D V_s profiles from HVSR inversion (sites TYT_01, TYT_02, TYT_03, TYT_04, and TYT_05), consistency is observed, where the V_s values at depths of less than 30 meters are low (see **Figure 7**), this indicates that the subsurface sediment layers in this area are relatively thick.

Furthermore, a comparison between V_s profiles from HVSR and N-SPT values obtained from existing borehole data by **Arsyad et al. (2022)** reveals a consistent trend across several locations, including microtremor sites AND_26 (near DH-03), AND_27 (near DH-04), AND_25 (near DH-05), AND_40 (near DH-06), and AND_29 (near DH-07). As shown in **Figure 8**, the uppermost layer (0–10 m) exhibits $V_s < 175$ m/s and N-SPT values below 10, indicating very loose to loose soil characteristics. This layer consists of very loose silty sand (0–8 m) and loose silty sand (8–18 m), which are generally associated with low bearing capacity and high susceptibility to deformation under dynamic loading.

At depths greater than 10 meters, V_s values exceed 175 m/s, while N-SPT values also increase beyond 10. This trend marks the transition from loose to more compact and consolidated soils. In the 18–44 meters depth range, classified as medium fine sand, V_s values range between 175 and 350 m/s, accompanied by a gradual increase in N-SPT values. Beyond 44 meters, the subsurface consists of dense to very dense sand, where V_s values exceed 350 m/s, and N-SPT values continue to rise, reflecting a more stable subsurface condition. The correlation between V_s and N-SPT is particularly relevant for liquefaction assessment. Previous studies suggest that soils with $V_s < 200$ m/s and N-SPT < 10 are highly susceptible to liquefaction (**Sundararajan & Seshunarayana, 2011**). In this study, such conditions are observed in the upper 10 meters, where the soil remains unconsolidated.

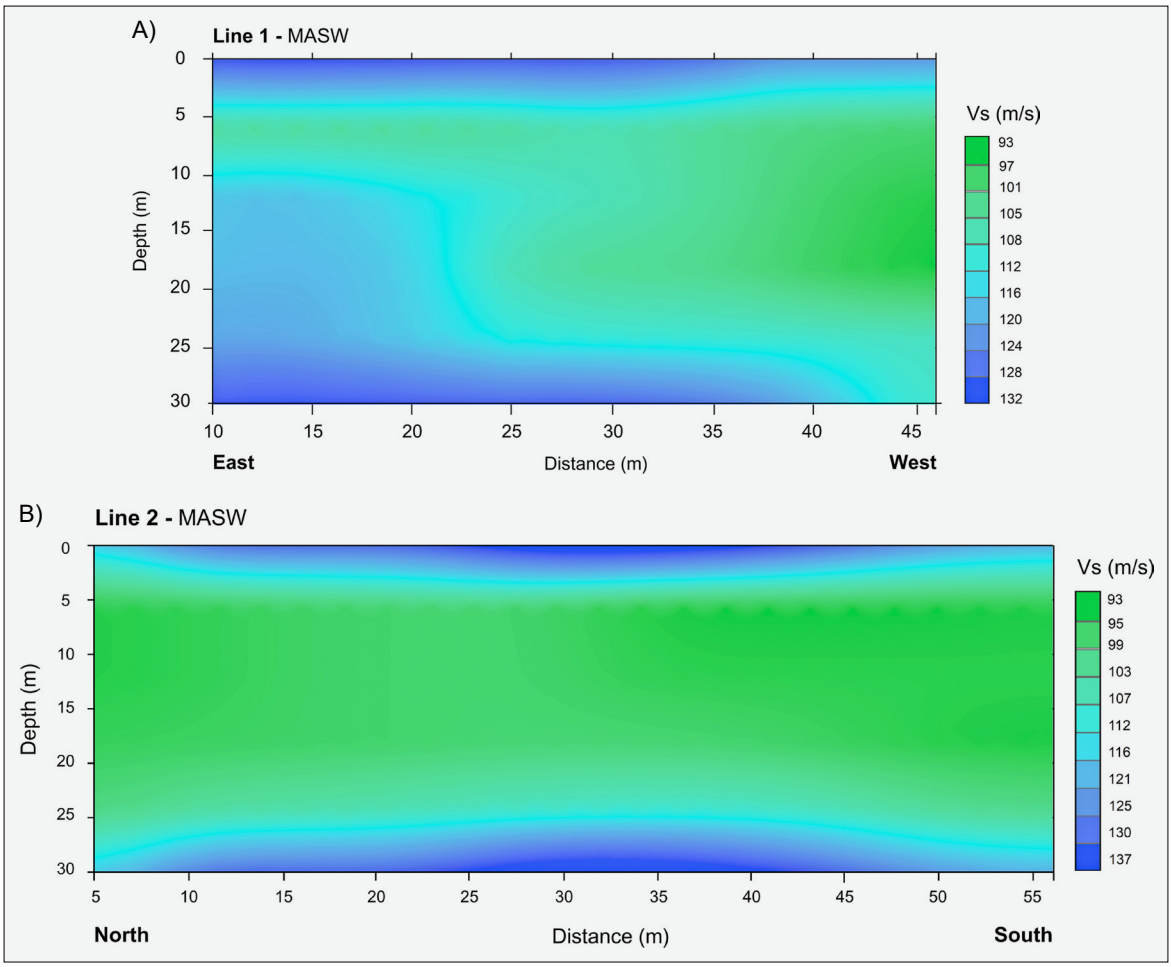


Figure 6. MASW 2D V_s profile in the area indicated to experience liquefaction.
A) 2D Profile of Line 1 MASW. **B)** 2D Profile of Line 2 MASW.

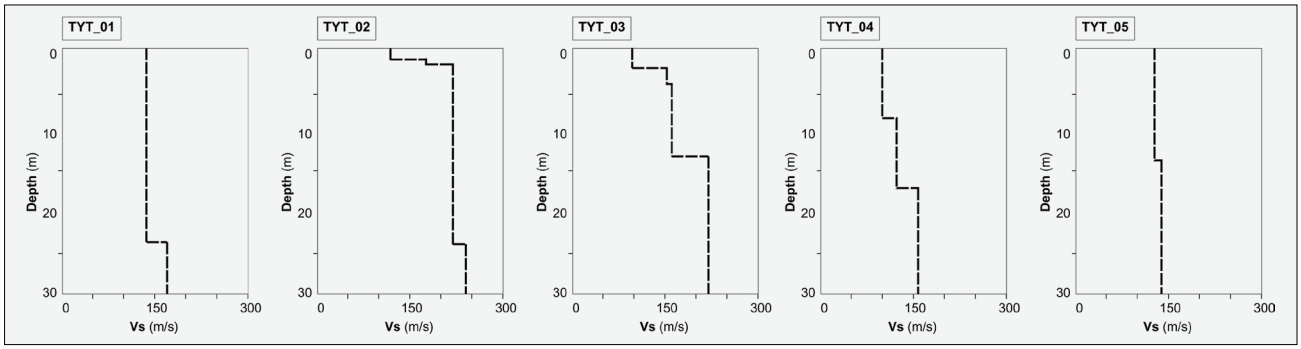


Figure 7. 1D V_s profile from HVSR inversion (station TYT_01, TYT_02, TYT_03, TYT_04, and TYT_05) in the liquefaction indicated area.

3.3. *Seismic Vulnerability Index*

The seismic vulnerability index (K_g) provides a quantitative measure of a site's susceptibility to seismic shaking, liquefaction, and potential damage (**Pamuk et al., 2018**). It is calculated by relating the amplification factor (A_0) and the dominant frequency (f_0), as seen in **Equation 2**, according to (**Akkaya, 2020; Kang et al., 2021**) higher K_g values suggest a greater likelihood of ground deformation, liquefaction, and structural damage. The distribution of K_g values in the study area can be seen in **Figure 9**. Areas dominated by the Alluvium Formation, which consists of loose sediments such as sand, clay, and silt, tend to have higher K_g values, these results are consistent with the findings of (**Kang et al., 2021; Syamsuddin et al., 2024**). This is due to the Alluvium's susceptibility to deformation and compression, increasing the liquefaction potential, especially in densely populated or infrastructurally significant zones. To further verify these findings, borehole data from previous investigations in Mamuju (**Arsyad et al., 2022**) were ana-

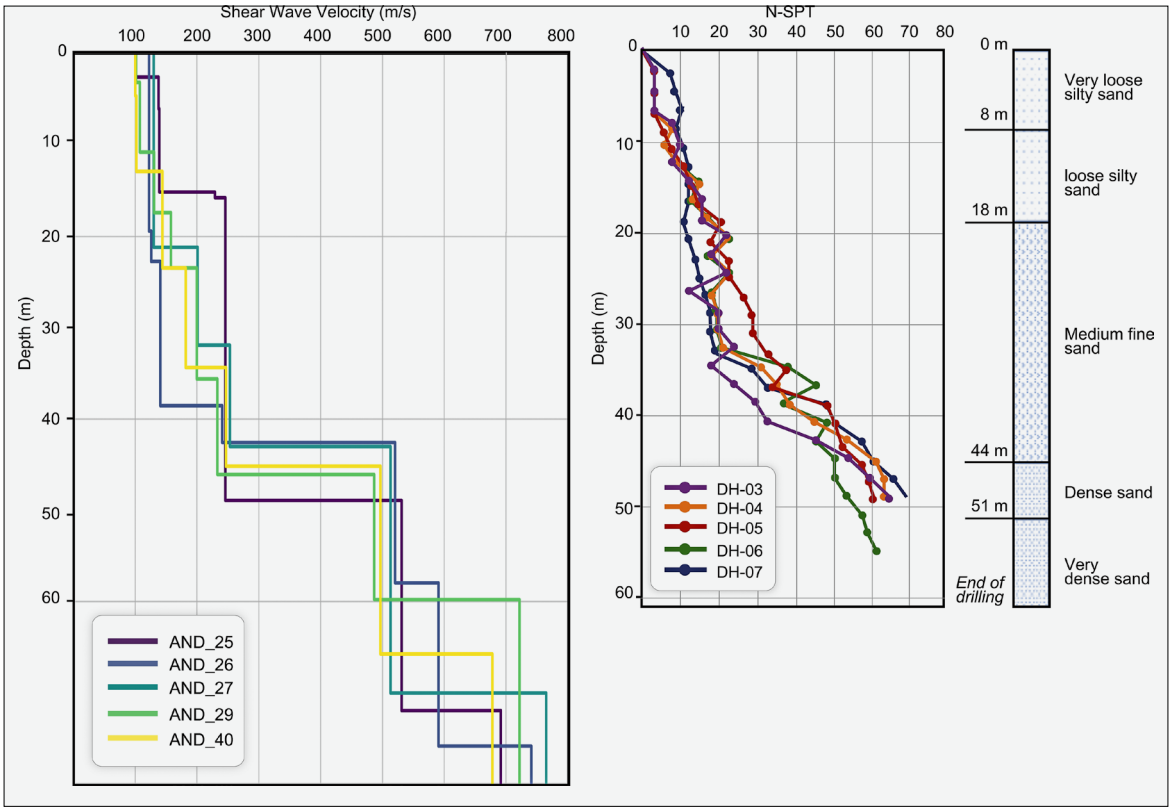


Figure 8. Comparison of the V_s profile derived from HVSR microtremor data (left) and the N-SPT profile from borehole data (right) modified from **Arsyad et al., (2022)**. The V_s profile represents the shear wave velocity variation with depth, while the N-SPT profile indicates soil resistance based on the standard penetration test. The borehole locations are correlated with nearby HVSR measurement points as follows: DH-03 corresponds to AND_26, DH-04 to AND_27, DH-05 to AND_25, DH-06 to AND_40, and DH-07 to AND_29.

lyzed. The geotechnical drillings in coastal areas revealed that the first 8 m consists of very loose silty sands, underlain by 10 m of loose silty sand, followed by 26 m of medium-dense sands and deeper dense to very dense sands. These layers coincide with the areas of high K_g values, supporting the correlation between sediment characteristics and liquefaction susceptibility. Furthermore, the borehole data indicate that liquefaction thickness could reach up to 16 m during a deterministic Mw 7.0 earthquake with a peak surface acceleration of 0.414g, consistent with the spatial distribution of K_g values. Additionally, these findings align with the locations of observed liquefaction during the 2021 Mw 6.2 earthquake, where the borehole recorded significant post-liquefaction ground settlement of up to 50 cm.

4. Discussion

The integration of HVSR and MASW methods has proven to be a robust approach for assessing liquefaction susceptibility in Mamuju, West Sulawesi. The results of this study align with existing literature, demonstrating that the combined use of f_0, V_{s30}, and K_g parameters provides a comprehensive framework for evaluating seismic vulnerability. The low f_0 values (<2.5 Hz) observed in coastal regions confirm the presence of thick, unconsolidated alluvial deposits. These findings are consistent with prior studies (**Mirzaoglu & Dýkmen, 2003; Molnar et al., 2022; Pamuk et al., 2018; Quintero et al., 2023; Syamsuddin et al., 2024**), which emphasize that low-frequency resonances are indicative of significant sediment thickness and increased susceptibility to liquefaction. The spatial distribution of low f_0 values aligns closely with areas affected by liquefaction during the 2021 earthquake, further validating the reliability of HVSR analysis in identifying high-risk zones (**Syamsuddin et al., 2024**). These affected areas correspond to the Alluvium Formation, which is characterized by loose sediments commonly found in lowland areas near the coast and along riverbanks. These water-saturated alluvial layers are highly susceptible to liquefaction due to their ability to deform under seismic loading (**Sundararajan & Seshunarayana, 2011**).

The V_{s30} results highlight the critical role of shear wave velocity in characterizing soil stiffness and seismic response (**Anbazhagan et al., 2019; Wijayanto et al., 2022**). Coastal zones with V_{s30} values below 175 m/s are dominated by loose alluvial deposits, which amplify seismic waves and significantly increase the risk of ground deformation and liquefaction. This observation corroborates the findings of **Bajaj and Anbazhagan (2019)**, who reported similar amplification effects in soft

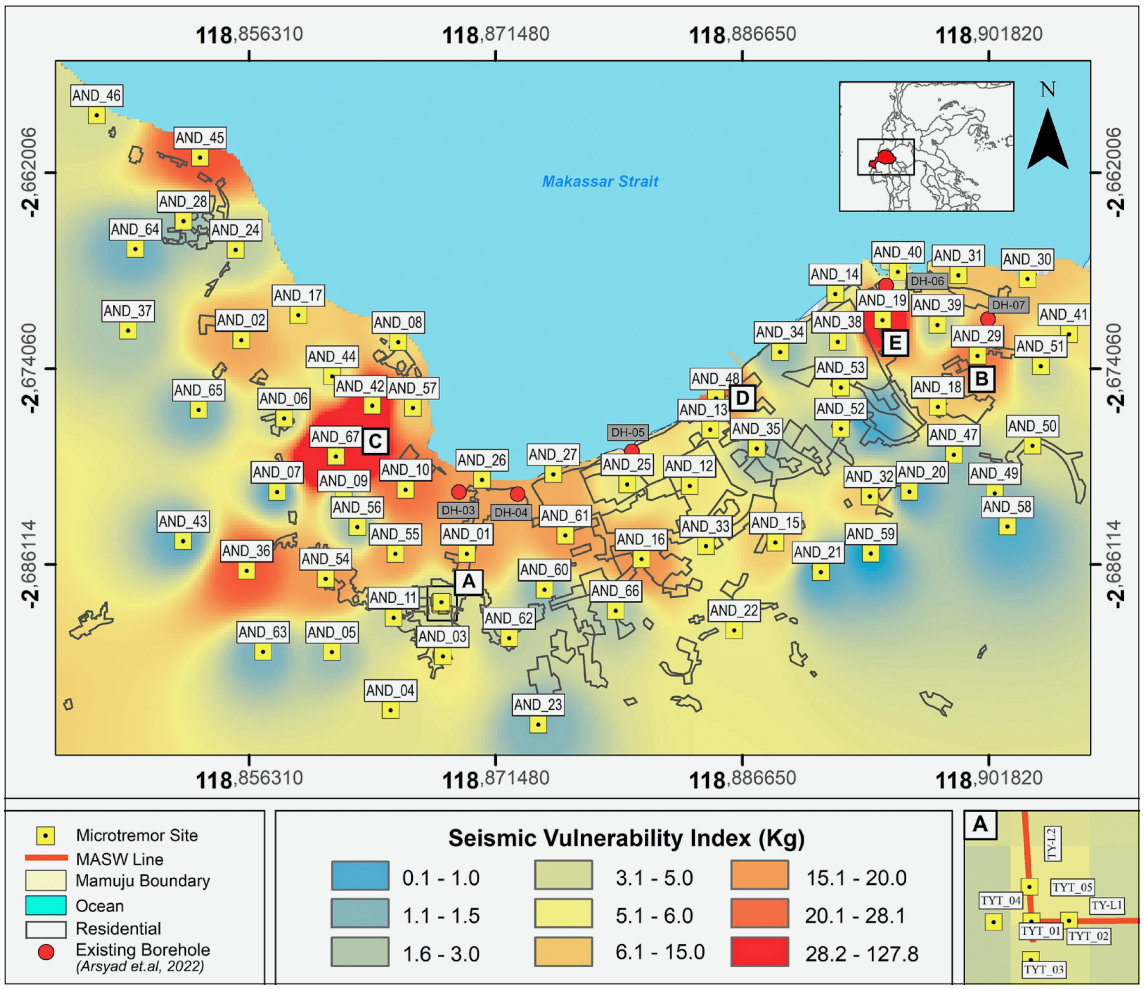


Figure 9. Distribution of seismic vulnerability index (K_g) across the study area from HVSR analysis. A) The research site indicated to have experienced liquefaction.

soils with low V_{s30} values. In contrast, the higher V_{s30} values (175–350 m/s) observed in elevated regions, corresponding to the Mamuju and Adang Volcanic formations, suggest greater soil stability. These results demonstrate that V_{s30} serves as a reliable indicator for distinguishing between areas with varying levels of seismic vulnerability. The MASW measurements in this study were conducted at locations identified as having experienced liquefaction during the 2021 earthquake. This targeted approach ensured that the most vulnerable areas were thoroughly evaluated. The two-dimensional V_s profiles derived from MASW data revealed soft soil conditions with low shear wave velocities, aligning with the one-dimensional profiles obtained from HVSR inversion. These areas are characterized by thick, unconsolidated sedimentary layers, further confirming their susceptibility to seismic wave amplification and deformation. By focusing on these high-risk zones, the MASW measurements provided critical insight into the spatial variability of subsurface properties, offering a detailed understanding of soil behaviour under seismic loading. This site-specific data not only validated the findings from HVSR but also enhanced the reliability of the microzonation map, reinforcing the importance of integrating multiple geophysical methods for seismic risk assessment.

The K_g parameter further enhances the understanding of liquefaction potential by quantifying the relationship between amplification (A_0) and dominant frequency (f_0). The high K_g values (>10) observed in coastal regions correspond to the Alluvium Formation, which consists of unconsolidated sand, silt, clay, and gravel deposits commonly found in lowland areas near the coast and along riverbanks. These loose, water-saturated sediments reinforce their susceptibility to seismic-induced deformation. Previous studies (**Alkan & Akkaya, 2023; Kang et al., 2021; Livaoğlu et al., 2019; Putti & Satyam, 2020**) have demonstrated that soils with high K_g values are prone to liquefaction due to their inability to resist dynamic stresses during earthquakes. In contrast, lower K_g values (<10) are predominantly found in the Mamuju Formation and Adang Volcanics, which consist of more compacted geological units with greater shear strength and lower amplification potential. This reinforces the reliability of the K_g index in identifying liquefaction-prone areas and underscores its role in seismic

hazard mitigation. However, while high K_g values often correlate with liquefaction occurrence, exceptions exist where liquefaction is observed in zones with moderate K_g values, highlighting the influence of additional factors beyond amplification characteristics. Moreover, not all zones with relatively high K_g values experienced liquefaction after the latest earthquake. For example, at location A, despite being within a zone classified as having moderate K_g values, liquefaction evidence in the form of sand boils on the pavement was observed. This phenomenon can be linked to the V_s profile, which indicates low V_s values extending beyond 30 meters in depth, suggesting weak soil conditions that, while generally cohesive, may still be susceptible to localized liquefaction under certain stress conditions. Additionally, the presence of a swamp near location A (see **Figure 2A**) could have influenced subsurface water distribution and pore pressure dynamics, potentially contributing to the occurrence of sand boils in the area. This highlights the importance of considering both geotechnical properties and local environmental factors in assessing liquefaction susceptibility. Given these complexities, integrating K_g with f_0 and V_{s30} offers a more comprehensive approach to microzonation and risk assessment, enabling a more detailed evaluation of site response characteristics. By combining these parameters, it becomes possible to refine liquefaction susceptibility mapping and improve the accuracy of seismic hazard assessments, ensuring a more robust framework for future mitigation efforts..

The findings of this study underscore the importance of considering geological and geotechnical factors in urban planning and disaster mitigation strategies. Coastal areas with low V_{s30}, low f_0, and high K_g values are at the greatest risk of liquefaction and require immediate attention for disaster risk reduction, consistent with the findings of **Kang et al. (2021)**. Mitigation measures such as soil stabilization, reinforcement of building foundations, and the implementation of stricter building codes are essential to reduce the potential impact of future seismic events. Additionally, the development of detailed microzonation maps based on these parameters can guide policymakers in identifying high-risk areas and prioritizing resource allocation for disaster preparedness.

While the integration of HVSR and MASW methods has yielded valuable insight, some limitations warrant further investigation. For instance, the accuracy of the f_0 values derived from HVSR is influenced by local variations in sediment properties and environmental noise conditions, as highlighted by **Molnar et al. (2022)**. Similarly, the resolution of V_{s30} profiles obtained from MASW depends on the spacing and configuration of geophones, which may introduce uncertainties in areas with complex subsurface conditions (**Liu et al., 2020**). Additionally, the presence and depth of groundwater play a crucial role in liquefaction susceptibility, as saturated loose sediments are more prone to excess pore water pressure buildup during seismic events. Areas with a high water table may exhibit stronger liquefaction effects, whereas drier soils with similar Vs characteristics may not experience the same degree of deformation. Future studies should consider incorporating groundwater measurements alongside geophysical surveys to improve liquefaction assessments. To address these limitations, future research should integrate additional geophysical methods, such as electrical resistivity tomography or borehole logging, to validate and enhance the reliability of the findings.

Moreover, the study highlights the need for further research on the dynamic behaviour of soils under cyclic loading, particularly in regions with complex geological formations like Mamuju. Laboratory testing and numerical modeling can provide deeper insight into the mechanisms of liquefaction and ground deformation, complementing the field-based findings of this study (**Abudeif et al., 2019**). Such efforts will contribute to the development of more comprehensive seismic hazard assessment frameworks, ultimately improving the resilience of communities in seismically active regions. In summary, the integration of HVSR and MASW methods has provided a detailed characterization of soil properties and seismic vulnerability in Mamuju. The findings not only align with previous research, but also offer practical implications for disaster risk reduction and urban planning. By addressing the limitations and expanding the scope of future studies, this approach can serve as a valuable model for assessing liquefaction potential in other seismically active regions worldwide.

5. Conclusions

This study provides a detailed assessment of liquefaction susceptibility in the Mamuju region, West Sulawesi, using the integrated HVSR and MASW methods to characterize subsurface conditions. The findings confirm that shear wave velocity (V_{s30}), dominant frequency (f_0), and seismic vulnerability index (K_g) are strongly correlated with underlying geological formations, significantly influencing the region's seismic response. The findings confirm that variations in shear wave velocity (V_{s30}), dominant frequency (f_0), and seismic vulnerability index (K_g) correspond closely with underlying geological formations, influencing the region's seismic response. Areas underlain by unconsolidated alluvial deposits, which exhibit low V_{s30}, low f_0, and high K_g values, are identified as highly susceptible to liquefaction due to their low shear strength and significant ground motion amplification. In contrast, the Mamuju and Adang Volcanic formations, with higher V_{s30} and f_0 values and lower K_g, indicate more stable subsurface conditions with reduced seismic amplification. The spatial distribution of these parameters aligns with ground failures observed during the 2021 Mamuju earthquake (Mw 6.2), reinforcing the reliability of geophysical methods in identifying high-risk zones. The results underscore the importance of in-

tegrating seismic microzonation approaches in earthquake-prone regions, providing critical insight for refining seismic hazard models and improving disaster mitigation strategies.

Acknowledgement

The authors would like to thank all those who have contributed to this research. This research was supported by the **Ministry of Education, Culture, Research, and Technology Indonesia (BIMA Research Program 2024)** and **LP2M Hasanuddin University**. The authors would also like to thank **BMKG and the Geophysics Department Surveyor Team** (**Muhammad Syaifullah, Hasnan Sutadi, Wirawan Saleh, and Ahmad Fauzy Arif**) for microtremor and MASW data acquisition in the field.

Funding

This research was funded by the Ministry of Education, Culture, Research, and Technology Indonesia, BIMA Research Program 2024, grant number [0459/E5/PG.02.00/2024].

6. References

Abudeif, A. M., Fat-Helbary, R. E., Mohammed, M. A., Alkhashab, H. M., & Masoud, M. M. (2019). Geotechnical engineering evaluation of soil utilizing 2D multichannel analysis of surface waves (MASW) technique in New Akhmim city, Sohag, Upper Egypt. *Journal of African Earth Sciences*, *157*, 103512. https://doi.org/10.1016/j.jafrearsci.2019.05.020

Ahn, J., Kwak, Y. D., & Kim, H. (2021). Estimating VS30 at Korean Peninsular seismic observatory stations using HVSR of event records. *Soil Dynamics and Earthquake Engineering*, *146*(106650), 1–20. https://doi.org/10.1016/j.soildyn.2021.106650

Akkaya, İ. (2020). Availability of Seismic Vulnerability Index (Kg) in The Assessment if Building Damage in Van, Eastern Turkey. *Earthquake Engineering and Engineering Vibration*, *19*(1), 189–204.

Alan, Y., Antony, M., & John, B. (2019). Precision of V S 30 values derived from noninvasive surface wave methods at 31 sites in California. *Soil Dynamics and Earthquake Engineering*, *127*, 105802. https://doi.org/10.1016/j.soildyn.2019.105802

Alkan, A., & Akkaya, İ. (2023). Investigation of site properties of the Çaldıran (Van, Eastern Turkey) settlement area using surface wave and microtremor methods. *Journal of African Earth Sciences*, *197*, 104737. https://doi.org/10.1016/j.jafrearsci.2022.104737

Anbazhagan, P., Srilakshmi, K. N., Bajaj, K., Moustafa, S. S. R., & Al-Arifi, N. S. N. (2019). Determination of seismic site classification of seismic recording stations in the Himalayan region using HVSR method. *Soil Dynamics and Earthquake Engineering*, *116*, 304–316. https://doi.org/10.1016/j.soildyn.2018.10.023

Ardianto, A., Anggayana, K., Widayat, A. H., Sasongko, D., & Fakhruddin, R. (2024). Energy Geoscience Organic geochemical, petrographic and palynological characterization of claystones of the Palaeogene Toraja Formation , and oil seeps in the Enrekang Sub-basin, south Sulawesi, Indonesia : Implications for hydrocarbon source rock poten. *Energy Geoscience*, *5*. https://doi.org/10.1016/j.engeos.2024.100287

Arsyad, A., Asti, A., Amaliyah, N., Paerong, S., & Djamaluddin, A. R. (2022). Liquefaction Potential Assessment for the City of Mamuju Sulawesi by using N-SPT based methods. *Indonesian Geotechnical Journal*, *1*(3), 37–55.

Bajaj, K., & Anbazhagan, P. (2019). Seismic site classi fi cation and correlation between V S and SPT-N for deep soil sites in Indo-Gangetic Basin. *Journal of Applied Geophysics*, *163*, 55–72. https://doi.org/10.1016/j.jappgeo.2019.02.011

Bao, X., Jin, Z., Cui, H., Chen, X., & Xie, X. (2019). Soil Liquefaction Mitigation in Geotechnical Engineering : An Overview of Recently Developed Methods. *Soil Dynamics and Earthquake Engineering*, *120*(January), 273–291. https://doi.org/10.1016/j.soildyn.2019.01.020

Bignardi, S. (2017). The uncertainty of estimating the thickness of soft sediments with the HVSR method: A computational point of view on weak lateral variations. *Journal of Applied Geophysics*, *145*, 28–38. https://doi.org/10.1016/j.jappgeo.2017.07.017

BMKG. (2021). *Preliminary report on the M6.2 earthquake survey in Mamuju-Majene, January 16–22, 2021*.

Chaloulos, Y. K., Giannakou, A., Drosos, V., Tasiopoulou, P., Chacko, J., & de Wit, S. (2020). Liquefaction-induced settlements of residential buildings subjected to induced earthquakes. *Soil Dynamics and Earthquake Engineering*, *129*, 105880. https://doi.org/10.1016/j.soildyn.2019.105880

Chávez-García, F. J., & Raptakis, D. (2017). Local amplification and subsoil structure at a difficult site: Understanding site effects from different measurements. *Soil Dynamics and Earthquake Engineering*, *92*, 334–344. https://doi.org/10.1016/j.soildyn.2016.10.008

Chiaradonna, A., Spadi, M., Monaco, P., Papasodaro, F., & Tallini, M. (2022). Seismic Soil Characterization to Estimate Site Effects Induced by Near-Fault Earthquakes : The Case Study of Pizzoli (Central Italy) during the Mw 6.7 2 February 1703, Earthquake. *Geosciences*, *12*(2), 1–33. https://doi.org/. https://doi.org/10.3390/geosciences12010002

Fat-Helbary, R. E. S., El-Faragawy, K. O., & Hamed, A. (2019). Application of HVSR technique in the site effects estimation at the south of Marsa Alam city, Egypt. *Journal of African Earth Sciences*, *154*, 89–100. https://doi.org/10.1016/j.jafrearsci.2019.03.015

Foti, S., Lai, C. G., Rix, G. J., & Strobbia, C. (2015). Surface Wave Methods for Near-Surface Site Characterization. In *CRC Press*. Surface-Wave-Methods-Near-Surface-Characterization/dp/0415678765

Ghione, F., Köhler, A., Dichiarante, A. M., Aarnes, I., & Oye, V. (2023). Vs30 and depth to bedrock estimates from integrating HVSR measurements and geology-slope approach in the Oslo area, Norway. *Frontiers in Earth Science*, *11*(1242679), 1–19. https://doi.org/10.3389/feart.2023.1242679

Griffiths, S. C., Cox, B. R., Rathje, E. M., & Teague, D. P. (2016). Mapping Dispersion Misfit and Uncertainty in Vs Profiles to Variability in Site Response Estimates. *Journal of Geotechnical and Geoenvironmental Engineering*, *142*(11), 1–12. https://doi.org/10.1061/(ASCE)GT.1943-5606.0001553.

Gupta, R. K., Agrawal, M., Pal, S. K., & Das, M. K. (2021). Seismic site characterization and site response study of Nirsa (India). *Natural Hazards*, *0123456789*. https://doi.org/10.1007/s11069-021-04767-w

Hanifa, N. R., Gunawan, E., Firmansyah, S., Faizal, L., Retnowati, D. A., Pradipta, G. C., Imran, I., & Lassa, J. A. (2022). Unmanned Aerial Vehicles for geospatial mapping of damage assessment: A study case of the 2021 Mw 6.2 Mamuju-Majene, Indonesia, earthquake during the coronavirus disease 2019 (COVID-19) pandemic. *Remote Sensing Applications: Society and Environment*, *28*(August), 100830. https://doi.org/10.1016/j.rsase.2022.100830

Hanindya, K. A., Makrup, L., Widodo, & Paulus, R. (2023). Deterministic Seismic Hazard Analysis to Determine Liquefaction Potential Due to Earthquake. *Civil Engineering Journal*, *9*(05), 1203–1216.

Hossain, M. S., Kamal, A. S. M. M., Rahman, M. Z., Farazi, A. H., Mondal, D. R., Mahmud, T., & Ferdous, N. (2020). Assessment of soil liquefaction potential: a case study for Moulvibazar town, Sylhet, Bangladesh. *SN Applied Sciences*, *2*(777), 1–12. https://doi.org/10.1007/s42452-020-2582-x

Ismail, A., Denny, F. B., & Metwaly, M. (2014). Comparing Continuous Profiles from MASW and Shear-wave Reflection Seismic Methods. *Journal of Applied Geophysics*, *105*, 67–77. https://doi.org/10.1016/j.jappgeo.2014.03.007

Kang, S. Y., Kim, K. H., Chiu, J. M., & Liu, L. (2020). MicrotremorHVSR analysis of heterogeneous shallow sedimentary structures at Pohang, South Korea. *Journal of Geophysics and Engineering*, *17*(5), 861–869. https://doi.org/10.1093/jge/gxaa035

Kang, S. Y., Kim, K. H., & Kim, B. (2021). Assessment of seismic vulnerability using the horizontal-to-vertical spectral ratio (HVSR) method in Haenam, Korea. *Geosciences Journal*, *25*(1), 71–81. https://doi.org/10.1007/s12303-020-0040-9

Khalili, M., & Mirzakurdeh, A. V. (2019). Fault detection using microtremor data (HVSR-based approach) and electrical resistivity survey. *Journal of Rock Mechanics and Geotechnical Engineering*, *11*(2), 400–408. https://doi.org/10.1016/j.jrmge.2018.12.003

Kusmanto, Ismanti, S., & Setiawan, A. F. (2024). Assessment of liquefaction risk with unidentified seismic parameters for newly-discovered faults: numerical analysis. *International Journal of GEOMATE*, *26*(114), 50–59.

Liu, H., Maghoul, P., Shalaby, A., Bahari, A., & Moradi, F. (2020). Integrated approach for the MASW dispersion analysis using the spectral element technique and trust region reflective method. *Computers and Geotechnics*, *125*, 103689. https://doi.org/10.1016/j.compgeo.2020.103689

Livaoğlu, H., Irmak, T. S., & Güven, I. T. (2019). Seismic vulnerability indices of ground for Değirmendere (Kocaeli Province, Turkey). *Bulletin of Engineering Geology and the Environment*, *78*(1), 507–517. https://doi.org/10.1007/s10064-017-1102-8

Ma, N., Wang, G., Kamai, T., Doi, I., & Chigira, M. (2019). Amplification of seismic response of a large deep-seated landslide in Tokushima, Japan. *Engineering Geology*, *249*, 218–234. https://doi.org/10.1016/j.enggeo.2019.01.002

Maghami, S., Sohrabi-bidar, A., Bignardi, S., Zarean, A., & Kamalian, M. (2021). Extracting the shear wave velocity structure of deep alluviums of " Qom " Basin (Iran) employing HVSR inversion of microtremor recordings. *Journal of Applied Geophysics*, *185*(104246), 1–19. https://doi.org/10.1016/j.jappgeo.2020.104246

Mahajan, A. K., Mundepi, A. K., Chauhan, N., Jasrotia, A. S., Rai, N., & Kumar, T. (2012). Active seismic and passive microtremor HVSR for assessing site effects in Jammu city , NW Himalaya , India - A case study. *Journal of Applied Geophysics*, *77*, 51–62. https://doi.org/10.1016/j.jappgeo.2011.11.005

Mahmoud, A. O., Hussien, M. N., Karray, M., Chekired, M., Bessette, C., & Jinga, L. (2020). Mitigation of liquefaction-induced uplift of underground structures. *Computers and Geotechnics*, *125*, 103663. https://doi.org/10.1016/j.compgeo.2020.103663

Maklad, M., Yokoi, T., Hayashida, T., ElGabry, M. N., Hassan, H. M., Hussein, H. M., Fattah, T. A., & Rashed, M. (2020). Site characterization in Ismailia, Egypt using seismic ambient vibration array. *Engineering Geology*, *279*, 105874. https://doi.org/10.1016/j.enggeo.2020.105874

Mase, L. Z., Likitlersuang, S., Tobita, T., Chaiprakaikeow, S., & Soralump, S. (2018). Local Site Investigation of Liquefied Soils Caused by Earthquake in Northern Thailand. *Journal of Earthquake Engineering*, *00*(00), 1–24. https://doi.org/10.1080/13632469.2018.1469441

Meilano, I., Salman, R., Susilo, S., Shiddiqi, H. A., Supendi, P., Lythgoe, K., Tay, C., Bradley, K., Rahmadani, S., Kristyawan, S., & Yun, S. H. (2023). The 2021 MW6.2 Mamuju, West Sulawesi, Indonesia earthquake: partial rupture of the Makassar Strait thrust. *Geophysical Journal International*, *233*(3), 1694–1707. https://doi.org/10.1093/gji/ggac512

Mihaylov, A., El Naggar, H., Mihaylov, D., & Dineva, S. (2019). Approximate analytical HVSR curve using multiple band-pass filters and potential applications. *Soil Dynamics and Earthquake Engineering*, *127*. https://doi.org/10.1016/j.soildyn.2019.105840

Mirzaoglu, M., & Dýkmen, Ü. (2003). Application of Microtremors to Seismic Microzoning Procedure. *Journal of the balkan geophysical society*, *6*(3), 143–156.

Mohammed, M. A., Abudeif, A. M., & Abd el-aal, A. K. (2020). Engineering geotechnical evaluation of soil for foundation purposes using shallow seismic refraction and MASW in 15th Mayo, Egypt. *Journal of African Earth Sciences*, *162*, 103721. https://doi.org/10.1016/j.jafrearsci.2019.103721

Molnar, S., Sirohey, A., Assaf, J., Bard, P. Y., Castellaro, S., Cornou, C., Cox, B., Guillier, B., Hassani, B., Kawase, H., Matsushima, S., Sánchez-Sesma, F. J., & Yong, A. (2022). A review of the microtremor horizontal-to-vertical spectral

ratio (MHVSR) method. *Journal of Seismology*, *26*, 653–685. https://doi.org/10.1007/s10950-021-10062-9

Moon, S. W., Subramaniam, P., Zhang, Y., Vinoth, G., & Ku, T. (2019). Bedrock depth evaluation using microtremor measurement: empirical guidelines at weathered granite formation in Singapore. *Journal of Applied Geophysics*, *171*, 103866. https://doi.org/10.1016/j.jappgeo.2019.103866

Najaftomarei, M. R., Rahimi, H., Tanircan, G., Mahani, A. B., & Shahvar, M. (2020). Site classification and probabilistic estimation of Vs30 for the Iranian strong-motion network. *Physics of the Earth and Planetary Interiors*, *308*, 106583. https://doi.org/10.1016/j.pepi.2020.106583

Nakamura, Y. (2000). Clear Identification of Fundamental Idea of Nakamura's Technique and Its Applications. *The 12th World Conference on Earthquake Engineering*, *2656*, 1–8.

Nguyen-Tien, H., Nguyen-Hong, P., Nguyen-Le, M., Che-Min, L., Tran-An, N., Pham-The, T., & Nguyen-Van, D. (2022). *Establishment of the correlation between the near-surface sedimentary thickness and the microtremor dominant frequency in the Hanoi area*. *45*(1), 49–66. https://doi.org/https://doi.org/10.15625/2615-9783/17569

Odom, W., & Doctor, D. (2023). Applied Computing and Geosciences Rapid estimation of minimum depth-to-bedrock from lidar leveraging deep-learning-derived surficial material maps. *Applied Computing and Geosciences*, *18*, 1–11. https://doi.org/10.1016/j.acags.2023.100116

Pamuk, E., Özdağ, Ö. C., Tunçel, A., Özyalın, Ş., & Akgün, M. (2018). Local site effects evaluation for Aliağa/İzmir using HVSR (Nakamura technique) and MASW methods. *Natural Hazards*, *90*(2), 887–899. https://doi.org/10.1007/s11069-017-3077-y

Pandavenes, O. A., Bernal, D., & Torrijo, F. J. (2023). A Comparative Analysis for Defining the Sliding Surface and Internal Structure in an Active Landslide Using the HVSR Passive Geophysical Technique in Pujilí (Cotopaxi), Ecuador. *Land*, *12*(961), 1–29. https://doi.org/https://doi.org/10.3390/land12050961

Perdana, M. J., & Amijaya, H. (2011). Source indication of oil seep from paniki river, kalukku, mamuju, west sulawesi based on geochemical characterization. *Proceedings JCM Makassar 2011*.

Perez, C. J. A. (2024). Reevaluating soil amplification using multi - spectral HVSR technique in La Chana Neighborhood , Granada , Spain. *Journal of Seismology*, *28*(4), 921–949. https://doi.org/10.1007/s10950-024-10227-2

Piña-flores, J., Cárdenas-soto, M., García-jerez, A., Seivane, H., Luzón, F., & Sánchez-sesma, F. J. (2020). Use of peaks and troughs in the horizontal-to-vertical spectral ratio of ambient noise for Rayleigh-wave dispersion curve picking. *Journal of Applied Geophysics*, *177*, 104024. https://doi.org/10.1016/j.jappgeo.2020.104024

Putti, S. P., & Satyam, N. (2020). Evaluation of Site Effects Using HVSR Microtremor Measurements in Vishakhapatnam (India). *Earth Systems and Environment*, *4*(2), 439–454. https://doi.org/10.1007/s41748-020-00158-6

Qadri, S. M. T., Sajjad, S. H., Sheikh, R. A., Rehman, K., Rafi, Z., Nawz, B., & Haider, W. (2015). Ambient noise measurements in Rawalpindi – Islamabad , twin cities of Pakistan: a step towards site response analysis to mitigate impact of natural hazard. *Natural Hazards*, *78*, 1111–1123. https://doi.org/10.1007/s11069-015-1760-4

Quintero, J., Gomes, R. C., Rios, S., Ferreira, C., & Viana da Fonseca, A. (2023). Liquefaction assessment based on numerical simulations and simplified methods: A deep soil deposit case study in the Greater Lisbon. *Soil Dynamics and Earthquake Engineering*, *169*, 107866. https://doi.org/10.1016/j.soildyn.2023.107866

Ritonga, R., Maulana, A., & Tonggiroh, A. (2021). Rare Earth Elements Distribution in Weathered Volcanic Rock from Mamuju Area, West Sulawesi. *IOP Conference Series: Earth and Environmental Science*, *921*(1). https://doi.org/10.1088/1755-1315/921/1/012039

Rosianna, I., Nugraha, E. D., Syaeful, H., Putra, S., Hosoda, M., Akata, N., & Tokonami, S. (2020). Natural radioactivity of laterite and volcanic rock sample for radioactive mineral exploration in mamuju, indonesia. *Geosciences (Switzerland)*, *10*(9), 1–13. https://doi.org/10.3390/geosciences10090376

Rosianna, I., Nugraha, E. D., Tazoe, H., Syaeful, H., Muhammad, A. G., Sukadana, I. G., Indrastomo, F. D., Ngadenin, Pratiwi, F., Sumaryanto, A., Sucipta, Pratama, H. A., Mustika, D., Nirwani, L., Nurokhim, Omori, Y., Hosoda, M., Akata, N., & Tokonami, S. (2023). Uranium Isotope Characterization in Volcanic Deposits in a High Natural Background Radiation Area, Mamuju, Indonesia. *Geosciences (Switzerland)*, *13*(12), 1–13. https://doi.org/10.3390/geosciences13120388

Rosid, M. S., Ali, Y. H., & Ramdhan, M. (2022). Characterization of the Mamasa Earthquake Source Based on Hypocenter Relocation and Gravity Derivative Data Analysis. *International Journal of GEOMATE*, *23*(97), 220–227. https://doi.org/10.21660/2022.97.j2375

Roy, J., Rollins, K. M., Athanasopoulos-Zekkos, A., Harper, M., Linton, N., Basham, M., Greenwood, W., & Zekkos, D. (2022). Gravel liquefaction assessment using dynamic cone penetration and shear wave velocity tests based on field performance from the 1964 Alaska earthquake. *Soil Dynamics and Earthquake Engineering*, *160*, 107357. https://doi.org/10.1016/j.soildyn.2022.107357

Salleh, A. N., Muztaza, N. M., Sa'ad, R., Zakaria, M. T., Mahmud, N., Rosli, F. N., & Samsudin, N. (2021). Application of geophysical methods to evaluate soil dynamic properties in Penang Island, Malaysia. *Journal of Asian Earth Sciences*, *207*(July 2020), 104659. https://doi.org/10.1016/j.jseaes.2020.104659

Sana, H., & Nath, S. K. (2016). Liquefaction potential analysis of the Kashmir valley alluvium, NW Himalaya. *Soil Dynamics and Earthquake Engineering*, *85*, 11–18. https://doi.org/10.1016/j.soildyn.2016.03.009

Sedaghati, F., Pezeshk, S., & Nazemi, N. (2018). Site amplification within the Mississippi embayment of the central United States : Investigation of possible di ff erences among various phases of seismic waves and presence of basin waves. *Soil Dynamics and Earthquake Engineering*, *113*, 534–544. https://doi.org/10.1016/j.soildyn.2018.04.017

Senkaya, G. V., Senkaya, M., Karsli, H., & Güney, R. (2019). Integrated Shallow Seismic Imaging of a Settlement Located in a Historical Landslide Area. *Bulletin of Engineering Geology and the Environment*.

Sesame, E. P. (2004). *Guidelines for The Implementation Of The H / V Spectral Ratio Technique on Ambient Vibrations Measurements , Processing and Interpretation*. European Commission – Research General Directorate.

Shaban, G., Fadlin, & Priadi, B. (2016). Geochemical signatures of potassic to sodic Adang Volcanics, Western Sulawesi: Implications for their tectonic setting and origin. *Indonesian Journal on Geoscience*, *3*(3), 195–216. https://doi.org/10.17014/ijog.3.3.195-214

Shelley, E. O., Mussio, V., Rodríguez, M., & Chang, J. G. A. (2015). Evaluation of soil liquefaction from surface analysis. *Geofísica Internacional*, *54*(1), 95–109. https://doi.org/10.1016/j.gi.2015.04.005

Simons, W. J. F., Socquet, A., Vigny, C., Ambrosius, B. A. C., Abu, S. H., Promthong, C., Subarya, C., Sarsito, D. A., Matheussen, S., Morgan, P., & Spakman, W. (2007). A decade of GPS in Southeast Asia: Resolving Sundaland motion and boundaries. *Journal of Geophysical Research: Solid Earth*, *112*(6). https://doi.org/10.1029/2005JB003868

Sivaram, K., Gupta, S., Kumar, S., & Prasad, B. N. V. (2018). Shear velocity structural characterization around the Lonar crater using joint inversion of ambient noise HVSR and Rayleigh wave dispersion. *Journal of Applied Geophysics*, *159*, 773–784. https://doi.org/10.1016/j.jappgeo.2018.10.022

Sompotan, A. F. (2012). *Struktur Geologi Sulawesi*. Bandung Institute of Technology.

Sukkarak, R., Tanapalungkorn, W., Likitlersuang, S., & Ueda, K. (2021). Liquefaction analysis of sandy soil during strong earthquake in Northern Thailand. *Soils and Foundations*, *61*(5), 1302–1318. https://doi.org/10.1016/j.sandf.2021.07.003

Sundararajan, N., & Seshunarayana, T. (2011). Liquefaction Hazard Assessment of Earth Quake Prone Area : a Study Based on Shear Wave Velocity by Multichannel Analysis of Surface Waves (MASW). *Geotechnical and Geological Engineering*, *29*, 267–275. https://doi.org/10.1007/s10706-010-9360-2

Supendi, P., Ramdhan, M., Priyobudi, Sianipar, D., Wibowo, A., Gunawan, M. T., Rohadi, S., Riama, N. F., Daryono, Prayitno, B. S., Murjaya, J., Karnawati, D., Meilano, I., Rawlinson, N., Widiyantoro, S., Nugraha, A. D., Marliyani, G. I., Palgunadi, K. H., & Elsera, E. M. (2021). Foreshock–mainshock–aftershock sequence analysis of the 14 January 2021 (Mw 6.2) Mamuju–Majene (West Sulawesi, Indonesia) earthquake. *Earth, Planets and Space*, *73*(1), 1–10. https://doi.org/10.1186/s40623-021-01436-x

Syamsuddin, E., Maulana, A., Hamzah, A., & Irvan, U. R. (2024). Assessing soil vulnerability in Petobo post-liquefaction zone, Palu, Central Sulawesi: A microzonation study utilizing microtremor measurements. *Journal of Degraded and Mining Lands Management*, *11*(3), 5805–5816. https://doi.org/10.15243/jdmlm.2024.113.5805

Tabrizi-Zarringhabaei, S., Ejlali, R. G., Fard, M. Y., & Sayyedfattahi, S. (2019). A new approach for particle size characterization of soil based on dynamic image analysis (Dia). *Rudarsko-Geološko-Naftni Zbornik*, *34*(4), 89–96. https://doi.org/10.17794/rgn.2019.4.9

TERRADAT. (2024). *MASW (Surface Wave Surveys)*. TerraDat.

Uyanık, O. (2020). Soil liquefaction analysis based on soil and earthquake parameters. *Journal of Applied Geophysics*, *176*, 104004. https://doi.org/10.1016/j.jappgeo.2020.104004

Wathelet, M., Jongmans, D., & Ohrnberger, M. (2004). Surface-wave inversion using a direct search algorithm and its application to ambient vibration measurements. *Near Surface Geophysics*, *2*(4), 211–221. https://doi.org/10.3997/1873-0604.2004018

White, L. T., Hall, R., Armstrong, R. A., Barber, A. J., Boudagher, M., Baxter, A., Wakita, K., Manning, C., & Soesilo, J. (2017). Journal of Asian Earth Sciences The geological history of the Latimojong region of western Sulawesi, Indonesia. *Journal of Asian Earth Sciences*, *138*, 72–91. https://doi.org/10.1016/j.jseaes.2017.02.005

Wijayanto, Mardiatno, D., Nehren, U., Marfai, M. A., & Pramono, S. (2022). Spatial Distribution of Vs30 Based on MASW and Microtremor Inversion in Gunungkidul, Yogyakarta, Indonesia. *International Journal of GEOMATE*, *22*(94), 29–38. https://doi.org/https://doi.org/10.21660/2022.94.2463

Yaghmaei-Sabegh, S., & Rupakhety, R. (2020). A new method of seismic site classification using HVSR curves: A case study of the 12 November 2017 Mw 7.3 Ezgeleh earthquake in Iran. *Engineering Geology*, *270*, 105574. https://doi.org/10.1016/j.enggeo.2020.105574

Yang, S., Mavroeidis, G. P., de la Llera, J. C., Poulos, A., Aguirre, P., Rahpeyma, S., Sonnemann, T., & Halldorsson, B. (2019). Empirical site classification of seismological stations in Chile using horizontal-to-vertical spectral ratios determined from recordings of large subduction-zone earthquakes. *Soil Dynamics and Earthquake Engineering*, *125*, 105678. https://doi.org/10.1016/j.soildyn.2019.05.017

Zaidani, M. A., Priadi, B., Sucipta, I. G. B. E., Susanto, V., & Saepuloh, A. (2023). Petrogenesis of Adang and Talaya volcanic rocks, in the Mamuju area and its surrounding, West Sulawesi. *IOP Conference Series: Earth and Environmental Science*, *1245*(1). https://doi.org/10.1088/1755-1315/1245/1/012029

Zhou, Y. G., Xia, P., Ling, D. S., & Chen, Y. M. (2020). Liquefaction case studies of gravelly soils during the 2008 Wenchuan earthquake. *Engineering Geology*, *274*, 105691. https://doi.org/10.1016/j.enggeo.2020.105691

SAŽETAK

Procjena podložnosti na pojavu likvefakcije pomoću HVSR i MASW metode: studija slučaja Mamuju, Zapadni Sulawesi, Indonezija

Potres koji je pogodio Mamuju 2021. godine (Mw 6,2) istaknuo je veliku ranjivost regije na likvefakciju zbog blizine aktivnih tektonskih zona, prisutnosti holocenskih aluvijalnih naslaga, nekonsolidiranih sedimentnih formacija i tla zasićenoga vodom, što sve pridonosi podložnosti zbog seizmičke aktivnosti. Ovo istraživanje procjenjuje podložnosti na likvefakciju područja Mamuju korištenjem integriranoga pristupa koji kombinira metodu omjera horizontalnoga i vertikalnoga spketra (HVSR) i metodu višekanalne analize površinskih valova (MASW). Ova studija istražuje inverznu korelaciju između V_{s30} i indeksa seizmičke ranjivosti (K_g), gdje niže vrijednosti V_{s30} odgovaraju višim vrijednostima K_g, što upućuje na povećanu podložnost na pojavu likvefakcije. HVSR analiza pokazala je kako se dominantna frekvencija (f_0) kreće od 0,4 do 11 Hz, dok faktor amplifikacije (A_0) varira između 1,1 i 11. Rezultati upućuju na to da obalna područja s debljim aluvijalnim naslagama pokazuju najniže vrijednosti f_0 (<2,5 Hz), koje koreliraju s V_{s30} < 175 m/s i K_g > 10, a što upućuje na veću vjerojatnost pojave likvefakcije. Nasuprot tome, područja ispod formacije Mamuju i vulkana Adang okarakterizirana su višim vrijednostima V_{s30} (>175 m/s), f_0 (>10 Hz) i K_g (<10) te upućuju na manju vjerojatnost pojave likvefakcije. Ova saznanja pridonose razvoju detaljne karte mikrozoniranja nužne za definiranje rizika od likvefakcije, što je važno ako se želi unaprijediti urbanističko planiranje i ublažavanje katastrofa u Mamujuu. Predmetno istraživanje pokazalo je kako integracija HVSR i MASW metoda predstavlja pouzdan pristup pri karakterizaciji svojstava tla, kao i unaprjeđenje procjene rizika od pojave likvefakcije u seizmički aktivnim regijama.

Ključne riječi:
likvefakcija, HVSR metoda, MASW metoda, indeks seizmičke ranjivosti, brzina posmičnih valova, potres u Mamujuu

Author's contribution

Andri Moh. Wahyu Laode (S.Si, Geophysics Master Degree Student) contributed to data collection, processing, interpretation, and drafting the original manuscript. **Muh. Altin Massinai** (Prof., Professor of Geophysics Department) supervised the research, provided critical discussions on methodology, and reviewed the manuscript. **Muh. Fawzy Imsullah Massinai** (M.T.) contributed to data interpretation, provided insight on liquefaction analysis, and assisted in manuscript preparation. **Erfan Syamsuddin** (Dr., Associate Professor of Geophysics Department) led and supervised the study, provided expertise on seismic methods, and critically reviewed the manuscript.
All authors have read and agreed to the published version of the manuscript.

RGNZ/MGPB

Magnetic and Geochemical Studies of Iron sand Deposits around Tambora Volcano in Sumbawa, Indonesia: A proxy for search high quality iron sand

Rudarsko-geološko-naftni zbornik
(The Mining-Geology-Petroleum Engineering Bulletin)
DOI: 10.17794/rgn.2025.5.2

Original scientific paper

Putu Billy Suryanata[1]*, Adella Ulyandana Jayatri[2], Satria Bijaksana[1], Silvia Jannatul Fajar[1], Ulvienin Harlianti[1]

[1] *Faculty of Mining and Petroleum Engineering, Institut Teknologi Bandung, Jalan Ganesa 10, Bandung 40132, Indonesia.*

[2] *Faculty of Mathematics and Natural Science, Universitas Mataram, Jalan Majapahit 62, Mataram 83125, Indonesia.*

Abstract

Tambora Volcano is known as a volcano that had a catastrophic eruption in 1815, with an enormous amount of material released, including pyroclastic flows and fall deposits. From these volcanic products, erosion and transportation processes acted towards the coastline and formed iron sand, which contains economically valuable minerals such as magnetite. Iron sand is one of the important elements/components for the production of steel and titanium, but its use is still limited. In Indonesia, iron sand has only been mined and used as a mixture in the production of cement and building materials because of its low iron content (45-48%). Therefore, it is important to know the characteristics and content of iron sand to maximise the results of iron sand mining. The characteristics of iron sand deposits from Mount Tambora are still unclear and have never been studied. Therefore, we conducted a study to identify the geochemical characteristics and magnetic properties of iron sand around Tambora Volcano to determine the concentration of economic elements from different volcanic products. This study uses magnetic susceptibility measurements, X-Ray Diffraction (XRD), X-Ray Fluorescence (XRF), and Inductively Coupled Plasma - Optical Emission Spectrometry (ICP-OES) measurements. Sampling was carried out at three locations in the area, namely Nanga Miro, Baringin Jaya, and Hodo. The Nanga Miro and Baringin Jaya areas are the lava flow deposit zones of the 1815 eruption and lava flows from previous eruptions, while the Hodo area is just the pyroclastic flow zone of the 1815 eruption. The results showed that the distribution of sand grain sizes in Baringin Jaya and Nanga Miro that are from the lava flow deposit zones are dominantly medium sized (MS) and fine sized (FS). Meanwhile, in Hodo, which is from the pyroclastic flow deposit zone, it is dominantly coarse sized (CS) and medium sized (MS). Areas from the lava flow zones have high susceptibility values, high Fe concentrations, and magnetic mineral content of magnetite and haematite. In addition, the REE elements (Ce, Gd, and Pr) have a high concentration in iron sand from the lava flow area and have a good Pearson correlation value. The combination of grain size distribution and magnetic and geochemical properties has shown differences in the characteristics of iron sand in the Tambora Volcano area.

Keywords:
iron sand, magnetic minerals, grain size, magnetic susceptibility, geochemistry, Tambora

1. Introduction

Iron sand is a type of sand that has a higher concentration of iron; the main compositions can be magnetite, ilmenite, and titanomagnetite, and it contains small amounts of silica, titanium, manganese, calcium, and vanadium (**McDougall, 1961**; **Templeton, 2025**). Iron sand is a type of titania-ferrous solution (TFSO), which is formed from the rapid cooling of volcanic lava and is widely distributed in coastal areas (**Wright, 1964**). Iron sand is generally found in coastal areas, rivers, and volcanic mountains with various geological settings, including magmatic arcs, volcanic islands, or continental arcs (**Wang et al., 2015**; **Nugraha et al., 2016**; **Tiwow et al., 2017**; **Satria et al., 2021**; **Zahra et al., 2023**). The formation of sand deposits is determined by several factors, including the original rock, the alteration process, the transportation media, and its deposition (**Maghfiroh et al., 2023**). Iron sand can come from volcanic eruptions or be formed from weathering of original rocks by weather and surface water, which are then transported and deposited along the coast or rivers (**Rahmi et al., 2022**). In general, iron sand deposits resulting from volcanic eruptions have a higher iron content compared to iron sand deposits resulting from weathering (**Brathwaite et al., 2017**; **Satria et al., 2021**; **Zahra et al., 2023**). Differences in iron type and composition can affect other properties of iron sand (**Leveneur et al., 2021**). According to **Rochani et al. (2007)**, Indonesia has a large potential for iron mineral resources, consist-

* Corresponding author: Putu Billy Suryanata
e-mail address: putubillysuryanata@gmail.com
Received: 18 December 2024. Accepted: 14 April 2025.
Available online: 21 October 2025

ing of iron sand (8%), iron ore (17%), and laterite iron ore (75%). Indonesia, with its unique geology, is home to iron sand deposits from Aceh, at the northern tip of Sumatra, to Sarmi, on the northern coast of Papua (**Satria et al., 2021**; **Yulianto et al., 2003**; **Zahra et al., 2023**; **Kurnio, 2007**; **Rahmi et al., 2022**). The close distance between iron sand deposits and active volcanoes indicates that most iron sand deposits originate from recent volcanic eruptions, such as on volcanic islands Sumatra, Java, Bali, the Lesser Sunda Islands, Maluku, and Papua (**Rahmi et al., 2022**; **Nugraha et al., 2016**; **Togibasa et al., 2018**), while iron sand deposits in Sulawesi and Papua originate from the destruction of much older rocks (**Kurnio, 2007**). Iron sand is one of the important elements/components for the production of steel and titanium, but its use is still limited (**Leveneur et al., 2021**). In addition, iron sand can be used to replace up to 15 mass% of magnetic materials for the production of the composite magnetic without reducing its performance, thereby reducing the cost of production materials (**Leveneur et al., 2021**). Currently, the only country in the world that makes steel from iron sand is New Zealand (**Templeton, 2025**). Unfortunately, because iron sand in Indonesia has a low iron content (45-48%), so far iron sand has only been mined and used as a mixed ingredient in the production of cement and building materials (**Yulianto et al., 2003**; **Rochani et al., 2007**). This type of utilisation has low economic value. One of the iron sand deposit locations in Indonesia is on the coast around Mount Tambora, Sumbawa Island. Sumbawa Island is located in the Lesser Sunda Arc, which is a transition zone from oceanic subduction to continent-island arc collision (**Darman, 2012**; **Minarwan, 2012**). The source of iron sand in this area is likely from eruption products and from the weathering of the eruption products of Mount Tambora, which is famous for its devastating eruption in 1815 (**Rampino, 1982**). The eruption produced pyroclastic flows and fall deposits with a volume of more than 50 km³ (Dense-Rock Equivalent (DRE), 1.4 x 10^{14} kg) (**Self et al., 1984; Sigurdsson and Carey, 1989**; **Kandlbauer and Sparks, 2014**). The pyroclastic flow deposits from this eruption spread around Mount Tambora (**Self et al., 1984; Abrams and Sigurdsson, 2007**; **Suhendro et al., 2021**). In addition, the eruption products of Mount Tambora also spread to the Bengkulu region (Sumatra Island), Banda Island, and Brunei Darussalam (**Kandlbauer and Sparks, 2014**). The eruption of Mount Tambora is included in the category of the largest and most powerful eruptions in history on Earth with a Volcanic Explosivity Index (VEI) of 7 (**Newhall and Self, 1982**; **Sigurdsson and Carey, 1989**; **Kandlbauer and Sparks, 2014**). This eruption also created a caldera with a diameter of 7 km with a depth of 1.4 km (**Sutawidjaja et al., 2006**) (see **Figure 1**). There has never been any research done on the physical and chemical characteristics of iron sand deposits from Mount Tambora. Therefore, it is important to conduct studies related to this at Tambora Volcano. The purpose of this study is to evaluate the geochemical, magnetic, and physical characteristics of iron sand in the Mount Tambora area. In order to accomplish this, iron sand samples were subjected to a number of measurements, such as identification of grain size distribution, magnetic susceptibility measurements, geochemical analysis (major elements and rare earth elements), and mineralogical analysis. Thus, it is expected that the results of the combination of magnetic and geochemical characteristics are used to determine the distribution of economic elements (i.e. REE) and increase the value of iron sand around Mount Tambora. By knowing the geochemical and magnetic characteristics, grain size, and sources of iron sand, it can be used as a magnetic material, and not just as a mixture in building materials.

2. Material and Methods

Field sampling was carried out in December 2018 at three locations, i.e. Nanga Miro (8° 9' 19.36" S; 117° 44' 4.45" E), Baringin Jaya (8° 17' 10.54" S; 117° 45' 32.51" E), and Hodo (8° 27' 1.44" S; 118° 4' 52.75" (see **Figure 1**). These sampling sites are located within the Pekat District in the Regency of Dompu, which is one of the ten regencies in the Nusa Tenggara Barat Province of Indonesia. Three samples were taken from each location so that a total of 9 samples were analysed in this study. The iron sand samples were measured in conditions without pretreatment (no grain size separation), also called bulk samples. In addition to measurements on bulk samples, a grain size sorting process was also carried out from the iron sand that was previously selected. Each sample was taken as a representative for each area. The collected samples were then prepared, and their magnetic susceptibility was measured at the Laboratory of Characterisation and Modelling of Physical Properties of Rocks, Institut Teknologi Bandung, West Java, Indonesia. Preparation began by washing the samples using running water and drying at room temperature. Furthermore, the samples were divided into 2 groups, namely the bulk sample group and the sample group for grain size analysis.

First, magnetic susceptibility measurements were carried out for all bulk samples (see **Table 1**). About 1 kg of three bulk samples from each location were set aside as bulk samples. The magnetic susceptibility is measured in a Bartington MS2 magnetic susceptibility system (Bartington Instruments Ltd., Witney, UK) with a dual frequency (470 Hz and 4.7 kHz) MS2B sensor. For this measurement, a portion of bulk was then placed inside a standard cylindrical holder (2.54 cm in diameter and 2.2 cm in height) and weighed using an Ohaus precision balance. Three holders were prepared for bulk from each location. The results of magnetic susceptibility measurements are expressed as mass-specific low and high frequency magnetic susceptibility (χ_{LF} and χ_{HF}). From the

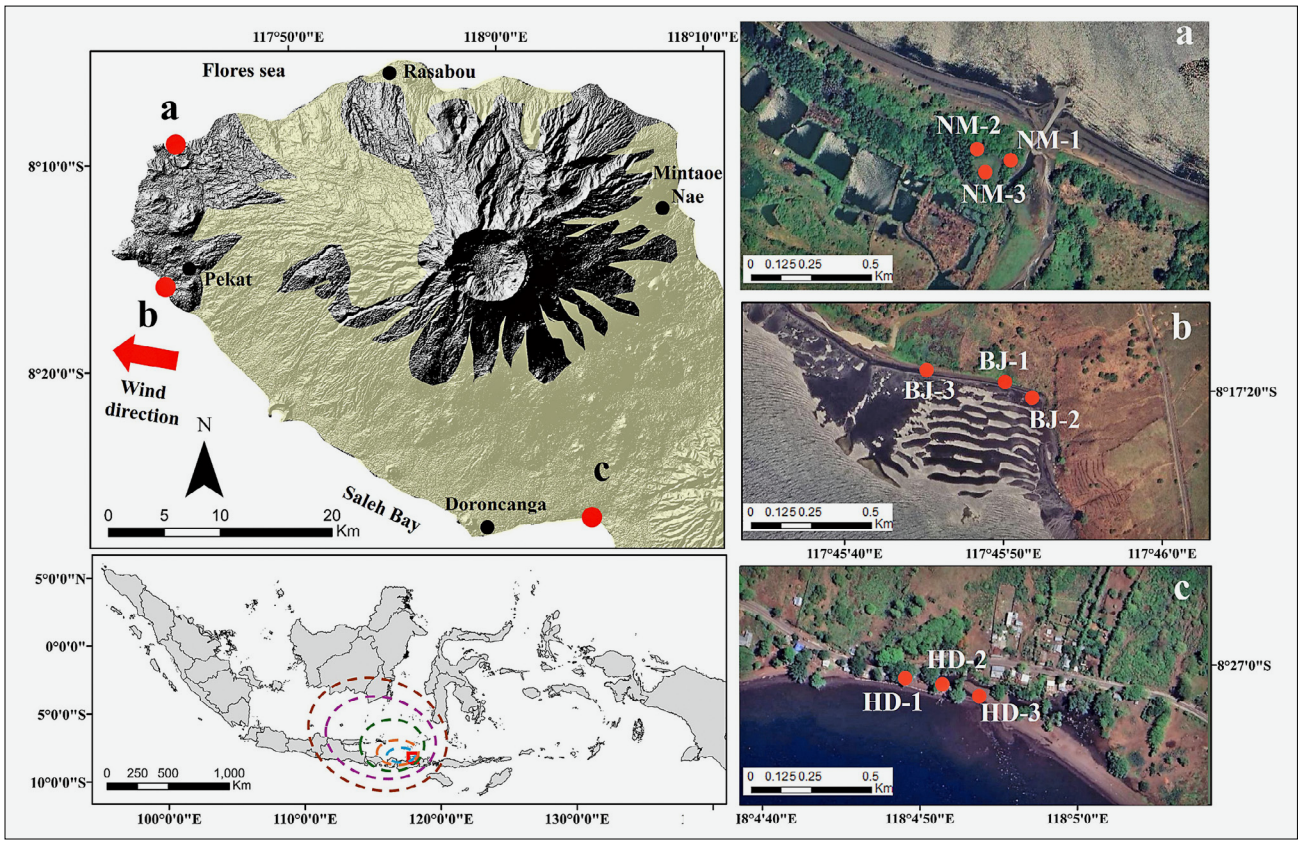


Figure 1. Sampling sites around Tambora Volcano, West Nusa Tenggara, Indonesia. Based on **Sigurdsson and Carey (1989)**, the yellow colour shows the distribution area of pyroclastic flow around Tambora Volcano. Wind direction is indicated by the red arrow, and administrative locations are marked by the black circle. Isopach of tephra fallout (pyroclastic fall) during the 1815 eruption of Tambora based on **Sigurdsson and Carey (1989)** and **Self et al. (1984)**. The isopach is symbolized by a dashed line with colour variations that indicate differences in layer thickness: blue (50 cm), orange (25 cm), green (20 cm), purple (5 cm), and brown (1 cm). There are three iron sand sampling locations shown with earth surface imagery from Google Earth (https://earth.google.com/): a) Nanga Miro, b) Baringin Jaya, and c) Hodo.

two high and low frequency values, the frequency-dependent susceptibility ($\chi_{FD\%}$) value is calculated according to **Suryanata et al. (2023)**. Second, about 3 kg of the selected bulk samples from each location were then subjected to grain-size analyses following the **Wentworth (1992)** scale. The highest magnetic susceptibility value is used to determine one sample to be selected to represent each location for grain size distribution analysis. This selection was made because it was assumed that the sample with the highest susceptibility value in the same area would have a higher magnetic mineral content, and further analysis would be carried out. Samples were sieved using ASTM (American Society for Testing and Materials) standard sieves. A 10-mesh sieve was first used to eliminate particles larger than sand size. Subsequently, the samples were sieved through a series of mesh sieves. Furthermore, each result of grain size separation for different sizes will be called sub-samples. There were five sub-samples based on their grain size, i.e. very coarse sand (VCS), which has a grain size > 18 mesh; coarse sand (CS), which has a grain size between 18 and 35 mesh; medium sand (MS), which has a grain size between 35 and 60 mesh; fine sand (FS), which has a grain size between 60 and 120 mesh; and very fine sand (VFS), which has a grain size < 120 mesh. This sub-sample division refers to previous research conducted by **Satria et al. (2021)**. The sub-samples were weighed using a digital scale. Their weight percentages (mass%) were then determined by dividing their weights by the total weight before sieving. The values of mass% for the sub-samples will be referred to as grain size distribution (GSD) (see **Figure 2a**). After the grain size separation of iron sand was carried out, magnetic susceptibility measurements were carried out for all sub-samples.

Figure 2b shows the particle size distribution for selected samples. The coefficient of uniformity (CU) and the coefficient of curvature (CC) of each sub-sample could easily be calculated from the curves in **Figure 2b**. These two coefficients are defined respectively as $CU = D_{60}/D_{10}$ and $CC = (D_{30} \times D_{30})/(D_{60} \times D_{10})$, where 10% of the particles are finer and 90% of the particles are coarser than D_{10} size, 30% of the particles are finer and 70% of the particles are coarser than D_{30} size, and 60% of the particles are finer and 40% of the particles are coarser than D_{60} size as indicated by D_{10}, D_{30}, and D_{60}, respec-

Table 1. List of measurements on Bulk samples and sub-samples of iron sand in this study

Sampling Code			Magnetic Susceptibility	XRF	XRD	REE
Baringin Jaya	BJ-1	Bulk	v			
	BJ-2	Bulk	v	v	v	v
		VCS	v	v	v	
		CS	v	v	v	
		MS	v	v	v	
		FS	v	v	v	
		VFS	v	v	v	
	BJ-3	Bulk	v			
Nanga Miro	NM-1	Bulk	v	v	v	v
		VCS	v	v	v	
		CS	v	v	v	
		MS	v	v	v	
		FS	v	v	v	
		VFS	v	v	v	
	NM-2	Bulk	v			
	NM-3	Bulk	v			
Hodo	HD-1	Bulk	v	v	v	v
		VCS	v	v	v	
		CS	v	v	v	
		MS	v	v	v	
		FS	v	v	v	
		VFS	v	v	v	
	HD-2	Bulk	v			
	HD-3	Bulk	v			

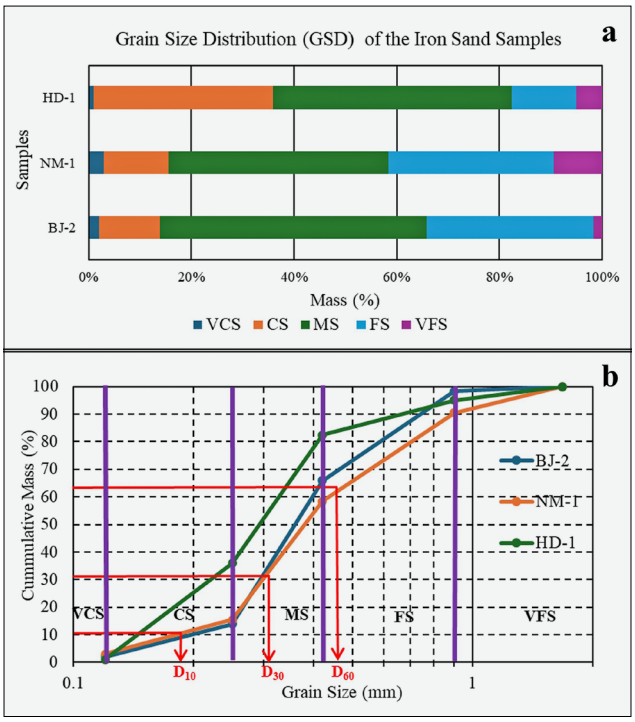


Figure 2. a) The percentage mass of iron sand grain size distribution sub-samples and b) The graph of cumulative mass of particle size distribution for selected samples. Red lines and red texts illustrate how D_{10}, D_{30}, and D_{60} were determined for samples NM-1. See text for further explanation.

tively (**Chapuis, 2021**). The values of CU for Nanga Miro, Baringin Jaya and Hodo samples are 2.32, 2.00, and 2.13, respectively, while the values of CC are 0.44, 0.40 and 0.32, respectively. Despite slight differences in their values of CU and CC, all samples could be classified as poorly graded, as expected for beach sand.

Based on the results of magnetic susceptibility measurements, we selected samples with the highest magnetic susceptibility values for the same location (NM-1, BJ-2, and HD-1) to conduct geochemical measurements (XRF and XRD) for bulk samples and all sub-samples and previous studies. We selected these samples to enable correlation with the amount of magnetic minerals. XRD analyses were carried out using a SmartLab X-Ray Diffractometer (Rigaku Corporation, Tokyo, Japan) equipped with Cu and Rigaku PDXL software (version 2.0) to identify crystal structures, lattice parameters, and perform mineral quantification. XRF analyses were carried out using a Supermini 200 X-ray fluorescence (Rigaku Corporation, Tokyo, Japan) that identifies major, minor, and trace elements contained. In this study, only the following elements were presented: Fe, Si, Ca, Al, Mg, Ti, Na, and K. The XRD and XRF measurements are conducted at the Laboratory of the Centre for Mineral and Coal Resources in Bandung, Indonesia. Furthermore, we also use the ICP-OES (Inductively Coupled Plasma Atomic-Optical Emission Spectrometry) measurement method to determine the rare earth element content contained in iron sand. In this measurement, we only use the same bulk samples as the XRF and XRD measurements. This is done to determine the REE content in the selected sample as a whole, not just at a certain grain size. This measurement used the Agilent type 700/725 (Agilent Technologies, Santa Clara, CA, USA). REE analyses were conducted at the Laboratory of the Centre for Mineral and Coal Resources in Bandung, Indonesia, that used Bushveld granite from Transvaal, South Africa, as reference material (see **Yunginger et al., 2018**). In this study, only the following elements were presented: Ce, Lu, Nd, Pr, and Gd.

3. Results

Table 2 shows the magnetic susceptibility values (χ_{LF} and $\chi_{FD\%}$) of iron sand samples from around Tambora Volcano. From **Table 2,** we can see that in general samples from the Baringin Jaya area have χ_{LF} values that are much larger than samples from Nanga Miro and Hodo, where samples from Hodo have the smallest values.

As shown in **Figure 2**, the GSD results for the BJ-2 and NM-1 samples are rather similar, while those of HD-1 are rather different. The predominant grain sizes in BJ-2 and HD-1 are MS and FS, while those in Hodo are MS and CS. In all locations, the mass% values for VCS are rather small (1 to 3%). In **Table 3**, the χ_{LF} val-

Table 2. Magnetic susceptibility of all bulk samples in three sampling locations. Bulk samples selected for grain size separation are marked in bold

Sampling Code	Bulk samples								
	BJ-1	**BJ-2**	**BJ-3**	**NM-1**	**NM-2**	**NM-3**	**HD-1**	**HD-2**	**HD-3**
χ_{LF} (10^{-8} m^3/kg)	5219.0	**7253.2**	3690.4	**2670.9**	2483.7	1217.9	**1267.5**	1037.0	1144.5
χ_{FD}%	7.8	**0.8**	0.7	**3.1**	7.9	8.7	**2.0**	4.0	3.0

Table 3. Magnetic susceptibility of sub-samples from selected bulk samples subjected to grain size separation.

Sampling Code	Sub-samples									
	VCS		CS		MS		FS		VFS	
	χ_{LF}	χ_{FD}%	χ_{LF}	χ_{FD}%	χ_{LF}	χ_{FD}%	χ_{LF}	χ_{FD}%	χ_{LF}	χ_{FD}%
BJ-2	1148.9	4.3	1459.9	0.8	5471.4	0.9	1844.4	7.5	25188.0	0.8
NM-1	1970.8	2.3	1983.7	0.9	4766.0	0.7	1923.8	10.0	4224.6	9.7
HD-1	1319.6	1.9	1419.6	1.5	1331.3	1.7	1054.3	3.8	1328.8	4.9

Table 4. Results of XRF measurements of the major elements

Sample Location	Grain Size	Elements (%)								
		Fe	**Si**	**Ca**	**Al**	**Mg**	**Ti**	**Na**	**K**	**Total**
Baringin Jaya	BJ-2 Bulk	20.7	34.1	15.1	14.7	2.2	1.9	2.5	4.7	95.9
	BJ-2 VCS	5.4	54.4	5.2	15.9	2.4	0.6	7.3	8.5	99.6
	BJ-2 CS	2.7	58.2	5.7	21.0	2.1	0.4	7.5	2.2	99.8
	BJ-2 MS	17.9	36.7	16.3	14.9	3.2	1.7	2.8	4.2	97.7
	BJ-2 FS	30.4	29.8	15.0	11.9	3.6	2.5	2.1	2.3	97.6
	BJ-2 VFS	41.5	25.1	7.6	12.2	2.0	3.6	2.3	2.7	97.0
	Average	19.8	39.7	10.8	15.1	2.6	1.8	4.1	4.1	97.9
	Standard Dev.	13.5	12.3	4.7	3.0	0.6	1.1	2.4	2.2	-
Nanga Miro	NM-1 Bulk	40.8	26.4	10.3	12.4	1.2	3.5	0.8	2.9	98.3
	NM-1 VCS	3.4	59.4	4.4	19.7	2.4	0.5	7.6	2.3	99.8
	NM-1 CS	1.7	58.3	6.2	26.1	1.5	0.2	4.8	1.1	99.9
	NM-1 MS	25.7	33.5	17.8	12.9	1.9	2.0	1.1	3.5	98.4
	NM-1 FS	58.4	17.4	6.5	8.6	1.6	4.7	0.5	1.1	98.8
	NM-1 VFS	65.3	14.0	2.5	9.1	0.8	5.2	0.4	1.3	98.5
	Average	32.6	34.8	8.0	14.8	1.6	2.7	2.5	2.0	99.0
	Standard Dev.	24.7	18.1	5.0	6.2	0.5	1.9	2.7	0.9	-
Hodo	HD-1 Bulk	13.5	39.3	15.9	16.1	1.2	1.1	2.3	8.0	97.4
	HD-1 VCS	4.9	57.0	4.6	15.5	1.9	0.6	8.0	7.2	99.6
	HD-1 CS	5.1	54.3	9.8	15.5	9.8	0.5	4.0	0.8	99.8
	HD-1 MS	11.6	40.6	17.6	16.5	1.5	1.0	2.6	6.7	98.0
	HD-1 FS	14.6	37.8	17.0	14.2	0.7	1.4	1.4	9.6	96.7
	HD-1 VFS	11.8	42.1	12.3	15.8	0.9	1.1	2.8	9.8	96.6
	Average	10.2	45.2	12.9	15.6	2.6	1.0	3.5	7.0	98.0
	Standard Dev.	3.9	7.5	4.6	0.7	3.2	0.3	2.1	3.0	-

ues representing the magnetic susceptibility of the sub-samples are listed. For BJ-2 sub-samples, the VFS has the highest χ_{LF} value, while the NM-1 sub-sample has the highest χ_{LF} value in the MS sub-sample. In all locations, finer grain sizes do not necessarily have higher χ_{LF} values and vice versa. Each location has its own pattern of the χ_{LF} values and GSD. The bulk samples as well as the VCS, CS, and MS samples from the three locations have relatively low values of $\chi_{FD\%}$ (0.7 to 4.9%), inferring the absence of SP (superparamagnetic) grains. The $\chi_{FD\%}$ values tend to be higher in finer grain sizes of FS and VFS, inferring the presence of SP grains. However, there is no clear pattern on $\chi_{FD\%}$ values with GSD. The VFS sample from BJ-2 has the highest χ_{LF} value with a very small $\chi_{FD\%}$ value.

Geochemical test results consist of XRF, XRD, and REE measurement results. The XRF analysis for the bulk samples as well as the VCS, CS, MS, FS, and VFS sub-samples is listed in **Table 4**. The Fe content varies in bulk samples, ranging from 13.5% for HD-1 to 40.8% for NM-1. Likewise for Ti element content, NM-1 bulk samples generally have the highest Ti element content, and HD-1 samples have the lowest Ti element content (see **Figure 3**; **Table 4**). Looking into sub-samples, Fe content tends to be higher in finer grain sizes, with the exception of that in HD-1 sub-samples. The FS sub-sam-

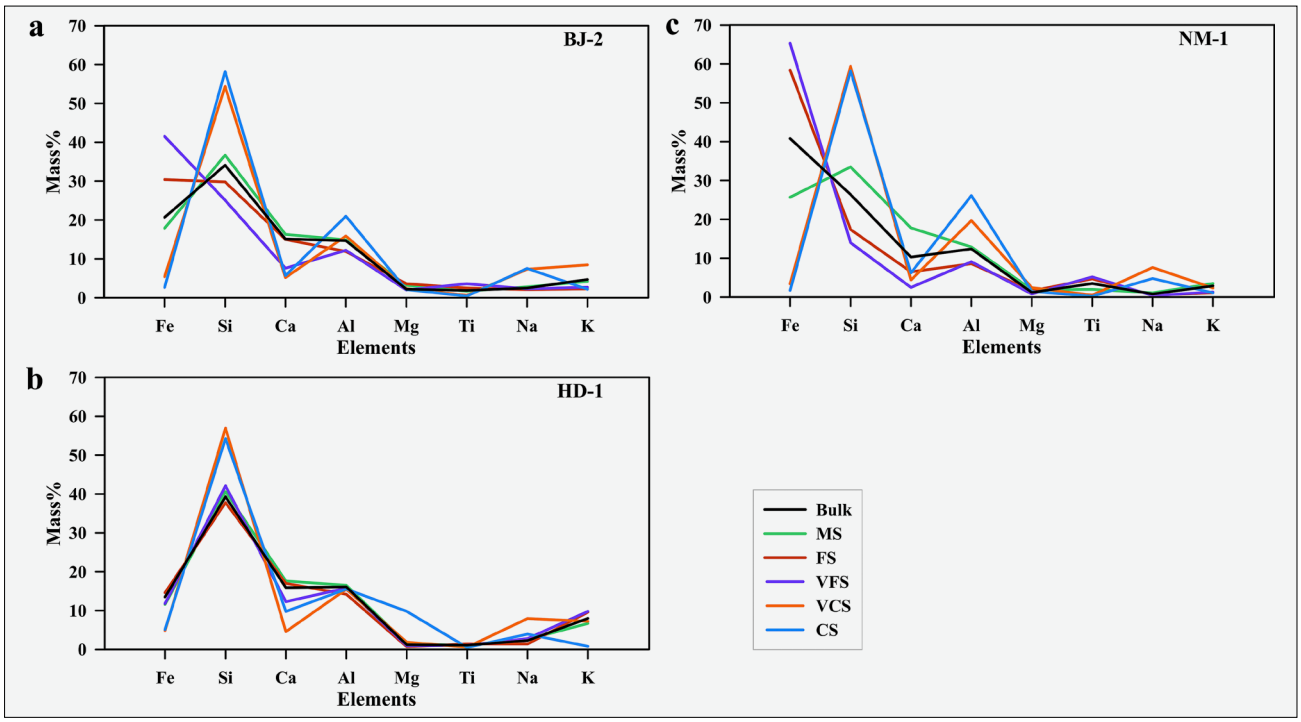


Figure 3. Element concentrations trends for bulk samples and sub-samples in three sampling locations

ple from HD-1 has higher Fe content compared to that of the VFS sub-sample. The Ti content follows the same trend as that of Fe content. However, Si content tends to be smaller in finer grain sizes, with again the exception of that in HD-1 samples. Meanwhile, Ca content consistently tends to be smaller in finer grain sizes.

The results of XRD measurements are shown in **Figure 4** in the form of diffractogram patterns on bulk iron sand samples, VCS, CS, MS, FS, and VFS grain sizes. In the diffractogram of sample NM-1, it can be seen that there are magnetic minerals of the magnetite and haematite types found in bulk iron sand samples and all sub-samples. Unlike sample NM-1, in sample BJ-2 only magnetite minerals are found in all sub-samples. In the sample HD-1, there is a magnetic mineral, namely magnetite, which has a very small content. The highest magnetic mineral content is in the CS sub-sample, seen from the larger diffractogram spike (see **Figure 4**). All samples, bulk and sub-samples, contain labradorite and augite. Only in sample HD-1 is there analcime, and only in sample BJ-2 is there a bixbyite mineral. Overall, the results show differences in the characteristics of the three locations.

The measurement results using the ICP-OES method to test the presence of REE are listed in **Table 5**. REE concentrations are presented in the form of element concentrations in ppm. The overall results show that the concentrations of Light Rare Earth Elements (LREE) such as Ce, Gd, Nd, and Pr at all three locations are higher than the concentrations of Heavy Rare Earth Elements (HREE) such as Lu. The REE content in the NM-1 sample tends to be higher than the other two locations, where sample from the HD-1 area have the lowest REE content.

4. Discussion

The presented results show that iron sand in the Tambora Volcano area has distinctive characteristics depending on the location. These differences are observed in the distribution of grain size, magnetic susceptibility values, XRF analysis results, XRD analysis, and REE content. Magnetic susceptibility measurements for each location in the study area show a range of different χ_{LF} values. On average, the χ_{LF} values in the Baringin Jaya and Nanga Miro areas are higher than in the Hodo area (see **Table 3**). Variations in magnetic susceptibility values depend on the constituent minerals (**Hunt et al., 1995**). Based on **Kartadinata et al. (2008)**, the rock units located around the Baringin Jaya and Nanga Miro areas are rocks from lava flows. The lava flows are products of monogenetic volcanoes that are grouped as the product of the Young Tambora Volcano (YTV) IV stage, which are predominantly lava. Another example of a group type of monogenetic volcano that is close to the Tambora Volcano is Mount Satonda. (**Takada et al., 2000; Suhendro et al., 2025**). Meanwhile, in the Hodo area the dominant volcanic product is the 1815 pyroclastic flow deposit consisting of a mixture of pumices, scoria, or lavas. The difference in the rocks that are the main source of eroded products that produce iron sand in the Baringin Jaya, Nanga Miro and Hodo areas causes differences in the characteristics of the minerals contained, especially magnetic minerals. The difference in magnetic minerals causes iron sand in the Baringin Jaya and Nanga Miro area to have higher susceptibility magnetic value and concentration of magnetic minerals compared

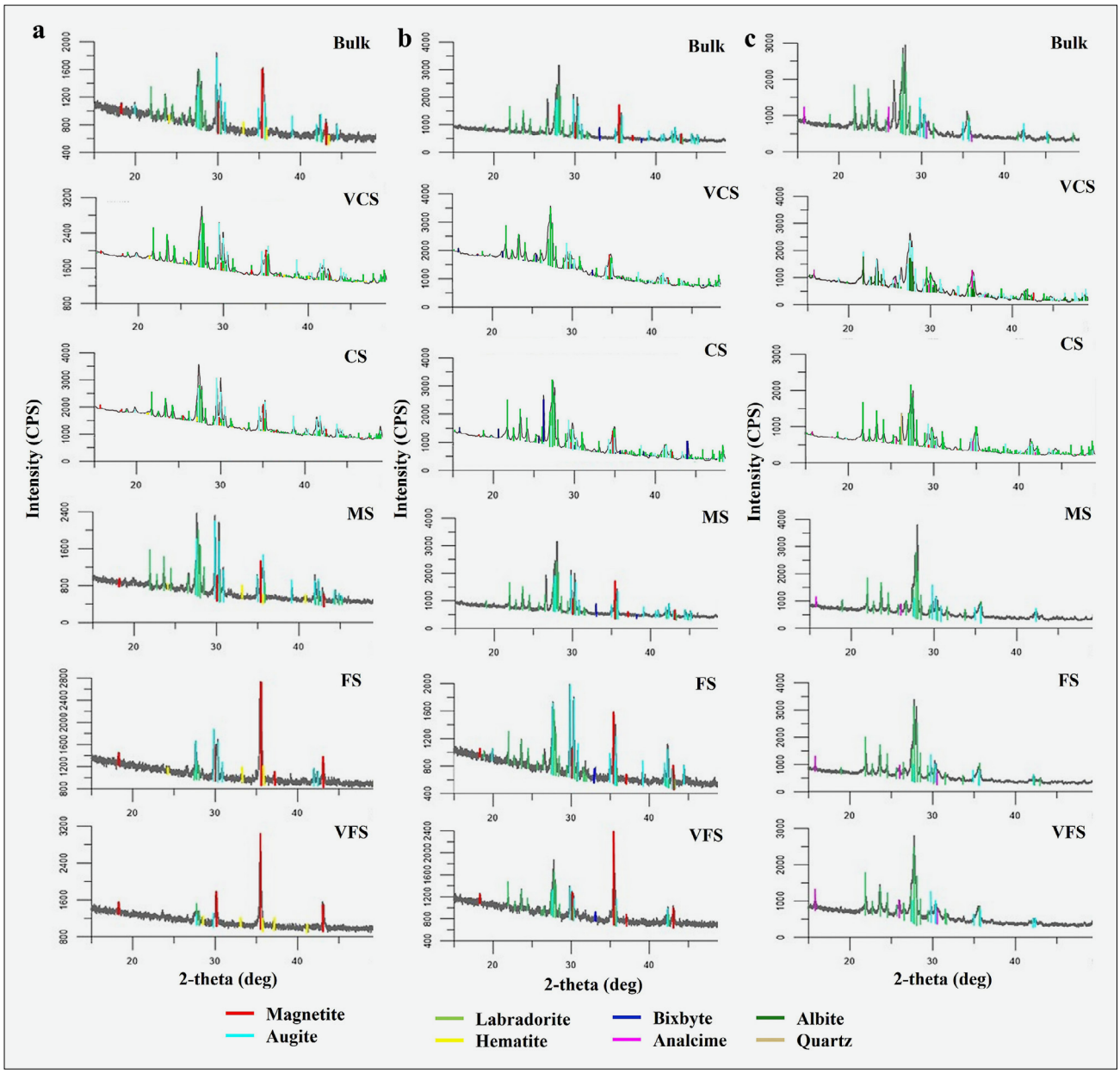


Figure 4. X-ray diffractograms of iron sand samples and sub-samples from a) NM-1, b) BJ-2, and c) HD-1.

to iron sand in the Hodo area. One of the main compositions of the 1815 Tambora pyroclastic flows is pumice, which has a fairly high SiO_2 content of around 56.5–58 mass% (**Gertisser et al., 2011; Suhendro et al., 2021**). Meanwhile, the lava products produced from monogenetic volcanoes are classified as basaltic and basaltic-andesite types (**Takada et al. 2000; Kartadinata et al. 2008; Suhendro et al., 2025**). Lava is usually mafic or has a low SiO_2 content, forming more magnetic minerals than pyroclastic flow, resulting in a higher magnetic susceptibility value (**Pratama et al., 2018; Suhendro et al., 2021; Suryanata et al., 2023**).

Samples from Nanga Miro and Baringin Jaya, which are iron sands originating from the area around the Tambora lava flow deposit, are dominated by MS and FS grain sizes. Meanwhile, the samples from the Hodo area

Table 5: The concentration of REE in bulk iron sand samples from studied locations

REE	BJ-2	NM-1	HD-1
	(ppm)	(ppm)	(ppm)
Ce	82	140	68
Gd	25	47	17
Lu	3	9	6
Nd	25	21	25
Pr	20	44	14

are iron sands originating from the area around the Tambora 1815 pyroclastic flow deposit (see **Figure 5**) and are dominated by CS and MS grain sizes. The characteristics of the grain size distribution in the Nanga Miro and

Baringin Jaya areas have the same distribution pattern as the volcanic iron sand on Lampanah Beach, Aceh (**Satria et al., 2021**). Genetically, the grain size distribution is closely related to wave energy in the process of washing sand grains by waves, which are then deposited (**Tamuntuan et al., 2019**). In addition, other elements that impact grain size distribution include terrain, transport mechanism, source material, distance from the shoreline, distance from the source (river), and transport time (**Abuodha, 2003**; **Arens et al., 2002**). From the magnetic susceptibility values of each sub-sample for each region, differences in characteristics can be seen. The VFS sub-sample has a much higher magnetic susceptibility value compared to the other sub-samples, except for the Hodo sample, which has a high magnetic susceptibility value in the CS sub-sample.

The results of the analysis of the major element content of each selected sample for the three areas show different characteristics and tend to support what is indicated by magnetic susceptibility, both for bulk samples and each sub-sample (see **Tables 2, 3, and 4**). Based on the concentration of Fe, the Nanga Miro and Baringin Jaya areas are those that have high concentrations compared to the Hodo area. Similar concentrations of Fe in the Nanga Miro and Baringin Jaya areas indicate that the iron sand in these areas come from the same source. This assumption is supported with geological information around the Tambora Volcano (see **Figure 5**). Meanwhile, the Pearson correlation value of magnetic susceptibility (χ_{LF} and $\chi_{FD\%}$) with major elements shows that correlation of Fe, Ti and χ_{LF} of the Baringin Jaya sample is greater than that of the other locations, while correlation of Fe, Ti and $\chi_{FD\%}$ is greater than that of the other two locations (see **Table 6**). The positive correlation of Fe, Ti and $\chi_{FD\%}$ and the negative correlation of Fe, Ti and χ_{LF} in the Nanga Miro sample are likely influenced by the location of the Nanga Miro iron sand sampling which is far from the rock source and vice versa for the Baringin Jaya iron sand sample, which is close to the rock source. However, the Pearson correlation for the Hodo sample does not exceed 0.75 (see **Table 6**). This indicates a different rock source of the Hodo iron sand compared to Baringin Jaya and Nanga Miro. The geochemical components of the elements and minerals contained in iron sand can be related to the Tambora eruption in 1815 and previous eruptions. The measurement results also show that iron sand in the Tambora Monogenetic lava flow (Nanga Miro and Baringin Jaya areas) has a high Fe concentration compared to iron sand in the pyroclastic flow zone, which is more felsic (higher SiO_2 content).

Based on the relationship between XRD analysis and magnetic values from the three locations, each area containing magnetic minerals has a high χ_{LF} value (Nanga Miro and Baringin Jaya). The samples from the Nanga Miro area contain a mixture of magnetite and haematite mineral content that distinguishes it from the other two locations. Magnetite is an iron oxide mineral that is highly magnetic and sticks to magnets. Meanwhile, hematite is an iron oxide occurring in trace amounts in many natural environments with concentrations below the detection limit of many bulks' analytical techniques. The magnetic properties of hematite make it suitable for magnetic quantification, although its weak spontaneous magnetisation at room temperature ($Ms = \sim 0.4$ $Am^2 kg^{-1}$) compared to magnetite ($Ms = 92$ $Am^2 kg^{-1}$) (**Tanii et al., 2014**; **Roberts et al., 2020**). The presence of hematite mineral content can be one of the factors that causes the lower χ_{LF} value in iron sand from Nanga Miro area compared to Baringin Jaya area. Other characteristic minerals that are always present in all localities are labradorite and augite minerals. Both minerals are the main minerals associated with gabbro rocks (**Moghaddam et al., 2019**). This shows that the type of rock in the area is mafic.

Other minerals that distinguish each region are the presence of bixbyite minerals in the Baringin Jaya area and analcime minerals in the Hodo area. Bixbyite minerals are iron-manganese oxide minerals (**Rayaprol and Kaushik, 2015**). They are ferrimagnetic at 300 K and antiferromagnetic at 36 K (**Rayaprol et al., 2013**). The magnetic properties of these minerals can contribute to the high χ_{LF} values in the Baringin Jaya area. Meanwhile, analcime minerals are a type of natural zeolite (**Vereshchagina et al., 2018**), which can be formed as a late-stage interstitial magmatic mineral (**Piper et al., 2013**). This mineral consists of hydrated sodium, aluminium, and silicate. Other than magmatic, S-type (sedimentary) analcimes are authigenic minerals replacing early formed zeolites, glass of tuffs, and tuffaceous rocks (**Varol, 2020**). This analcime mineral is a mineral that usually characterises a deposit from pyroclastic flows (**Naitza et al., 2003**). It tends to have a low magnetic susceptibility value or even no magnetic properties at all. Apart from the low Fe content, this analcime content causes the susceptibility value of iron sand around the Hodo area to have a small value.

Furthermore, the REE content can be related to several other minerals from rock erosion in the area around the sample. The REE elements can come from the eruption product or weathering of rocks in the area. The concentration of LREEs such as Gd, Nd, and Pr is also found in iron sand in the Tambora Volcano area. High concentrations of LREE usually occur in sediments eroded from pyroclastic and bedrock rocks, mostly igneous rocks with alkaline types of basalt to trachyandesite (**Yunginger, 2018**; **Gertisser et al., 2011**). In placer deposits, beach sand, or heavy mineral placer deposits, REE is usually found in monazite and xenotime minerals (**Gupta and Krishnamurthy, 2005**; **Balaram, 2019**). Monazite (Ce) and monazite (Nd) minerals have paramagnetic magnetic properties (**Jordens et al., 2013**). The results of this study indicate that the monogenetic volcanoes lava flow has high concentrations of Ce, Gd, and Pr elements.

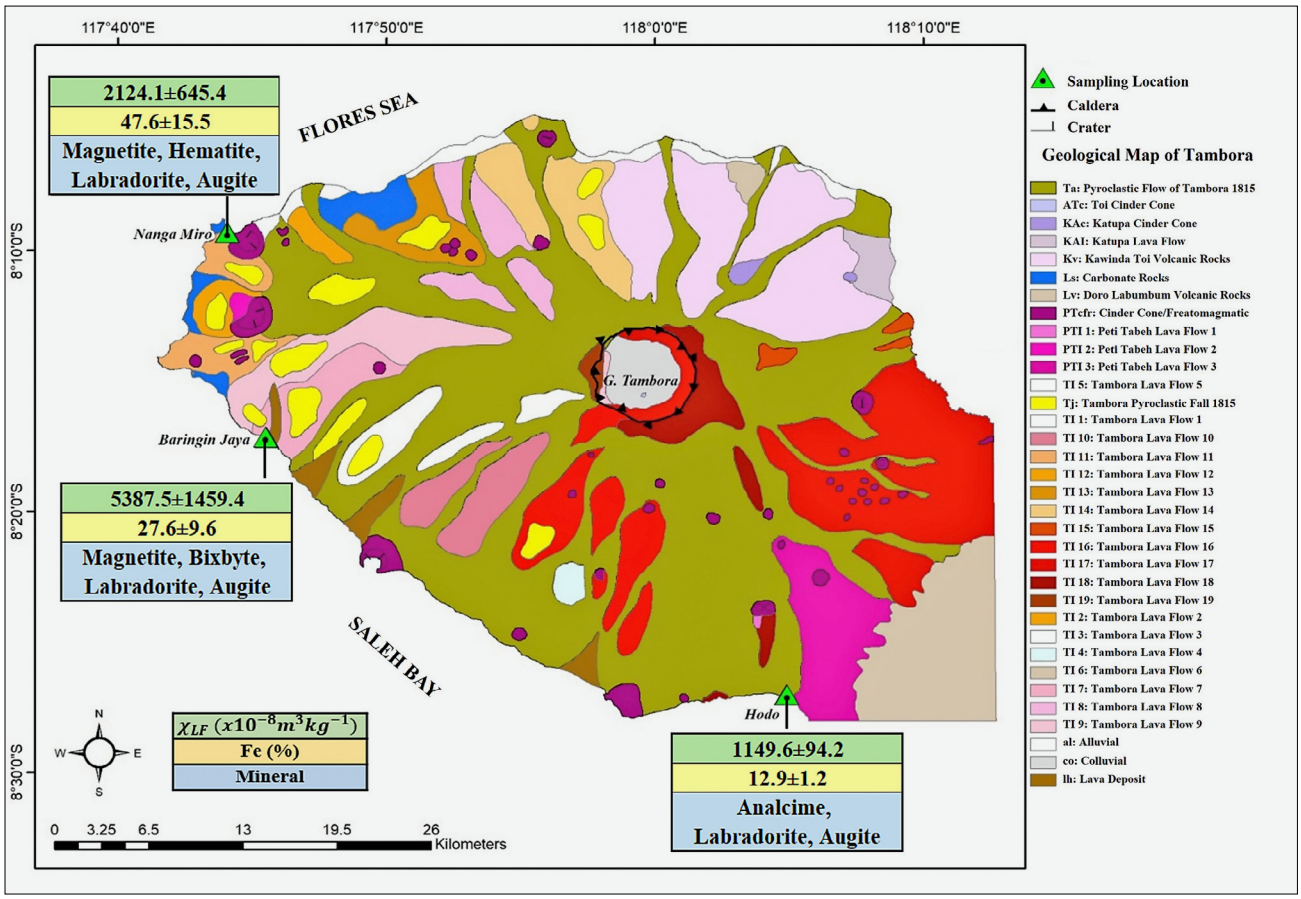


Figure 5. Geological map of the research area with research results (Modified from **Kartadinata et al., 2008**)

Table 6. Pearson correlation between magnetic susceptibility (χ_{LF} and $\chi_{FD\%}$) major elements for bulk samples, VCS, CS, MS, FS, and VFS sub samples for each region. Correlation value with bold format indicates positive correlation with value ≥ 0.75.

Baringin Jaya Samples	**χ_{FD}%**	**Fe**	**Si**	**Ca**	**Al**	**Mg**	**Ti**	**Na**	**K**
χ_{LF}	-0.43	**0.77**	-0.64	-0.11	-0.48	-0.40	**0.81**	-0.49	-0.29
χ_{FD}%		0.10	-0.08	0.12	-0.40	0.66	0.03	-0.06	0.10
Nanga Miro Samples	**χ_{FD}%**	**Fe**	**Si**	**Ca**	**Al**	**Mg**	**Ti**	**Na**	**K**
χ_{LF}	-0.02	0.36	-0.47	0.52	-0.48	-0.35	0.34	-0.56	0.50
χ_{FD}%		**0.85**	-0.75	-0.54	-0.70	-0.48	**0.85**	-0.51	-0.60
Hodo Samples	**χ_{FD}%**	**Fe**	**Si**	**Ca**	**Al**	**Mg**	**Ti**	**Na**	**K**
χ_{LF}	-0.30	-0.17	0.16	0.00	-0.68	0.53	-0.06	-0.17	-0.40
χ_{FD}%		0.18	-0.18	-0.08	0.20	-0.31	0.21	-0.10	0.46

We also conducted Pearson correlation between magnetic susceptibility (χ_{LF} and $\chi_{FD\%}$) and major elements with REE for bulk samples for the entire area (see **Table 7**). From **Table 7**, we can see that there is a correlation between major element concentrations and several REE elements. The element of Lu is positively correlated with $\chi_{FD\%}$ and Nd, positively correlated with Si, Ca, Al, Na, and K elements. From this, it can be seen that the erosion products of Tambora pyroclastic flow or lava flow contain fairly high REEs (Ce, Gd, and Pr) that can be associated with Fe and Ti elements. As we know, Fe and Ti are elements that form magnetic minerals, although they do not have a good correlation with the magnetic susceptibility values. Further studies may be needed on the relationship between magnetic mineral characteristics from other magnetic measurements such as hysteresis parameter or remanent magnetic with geochemical analysis in iron sand.

5. Conclusions

Magnetic susceptibility and geochemical measurements combined with grain size distribution analysis resulted in a better understanding of the characteristics of

Table 7. Pearson correlation between magnetic susceptibility (χ_{LF} and $\chi_{FD\%}$) and major elements with REE for bulk samples for the entire area. Correlation value with bold format indicates positive correlation with value ≥ 0.75.

Bulk Samples	Ce	Gd	Lu	Nd	Pr
χ_{LF}	-0.05	0.03	-0.69	0.23	-0.04
χ_{FD}%	0.62	0.56	**0.98**	-0.76	0.62
Fe	**1.00**	**1.00**	0.71	-0.97	**1.00**
Si	-0.97	-0.99	-0.59	**0.92**	-0.98
Ca	-1.00	-0.99	-0.79	**0.99**	-1.00
Al	-0.98	-0.99	-0.62	**0.93**	-0.98
Mg	-0.28	-0.21	-0.84	0.45	-0.28
Ti	**0.99**	**1.00**	0.67	-0.95	**0.99**
Na	-0.96	-0.94	-0.91	**1.00**	-0.96
K	-0.88	-0.91	-0.35	**0.77**	-0.88

iron sand along the coast around the Tambora Volcano. From three sample locations, 2 groups of different iron sand characteristics were obtained even though all three were in the Tambora Volcano area. Nanga Miro and Baringin Jaya have high magnetic susceptibility in line with high Fe element concentrations, magnetite and hematite minerals were found, higher LREE (Ce, Gd, and Pr) concentrations, and dominant grain sizes of MS and FS, while Hodo has characteristics that are the opposite of the other two areas and has grain sizes of CS and MS. Based on the concentration of Fe and magnetic minerals (iron content), it can be said that the iron sand in Hodo comes from a different source than the other samples, namely from pyroclastic flow deposit. While samples from Baringin Jaya and Nanga Miro come from lava products produced from monogenetic volcanoes of the Young Tambora Volcano (YTV) IV stage. This study also shows that the iron sand of Tambora Volcano has the potential of hosting economically valuable REEs.

Acknowledgment

The permission to conduct field research at Tambora Volcano, Dompu Regency, West Nusa Tenggara was given by the *Badan Kesatuan Bangsa dan Politik Dalam Negeri* (*BAKESBANGPOLDAGRI*) West Nusa Tenggara, Indonesia. Financial support for this research was provided by Education Fund Management Institution (LPDP) Indonesia through the master's degree Research Scheme to Adella Ulyandana Jayatri.

6. References

Abrams, L.J., Sigurdsson, H. (2007). Characterization of pyroclastic fall and flow deposits from the 1815 eruption of Tambora volcano, Indonesia using ground-penetrating radar. Journal of Volcanology and Geothermal Research, 161, 352–361.

Abuodha, J.O.Z. (2003). Grain size distribution and composition of modern dune and beach sediments, Malindi Bay coast, Kenya. Journal of African Earth Sciences, 36, 41–54

Arens, S.M., Van Boxel, J.H., Abuodha, J.O.Z. (2002):. Changes in Grain Size of Sand in Transport Over a Foredune, Earth Surface Processes and Landforms, 27, 1163 – 1175.

Arsyad, M., Tiwow, V.A., Rampe, M.J. (2018). Analysis of Magnetic Minerals of Iron Sand Deposit in Sampulungan Beach Takalakar Regency South Sulawesi Using the X-Ray Diffraction Method, Journal of Physic: Conference Series, 1120, 012060.

Balaram, V. (2019). Rare earth elements: A review of applications, occurrence, exploration, analysis, recycling, and environmental impact, Geoscience Frontiers, 10, 1285-1303.

Brathwaite, R.L., Gazley, M.F., Christie, A.B. (2017). Provenance of Titanomagnetite in iron sand on the west coast of the North Island New Zealand, Journal of Geochemical Exploration, 178, 23-34.

Chapuis, R.P., (2021). Analyzing grain size distributions with the modal decomposition method: literature review and procedures. Bulletin Engineering Geological Environment, 80, 6649–6666.

Darman, H. (2012). Seismic Expression of Tectonic Features in the Lesser Sunda Islands, Indonesia. Indonesian journal of sedimentary geology, 25 (1). https://doi.org/10.51835/bsed.2012.25.1.171

Gertisser, R., Self, S., Thomas, L.E., Handley, H.K., Calsteren, P.V., Wolf, J.A. (2011). Processes and Timescales of Magma Genesis and Differentiation Leading to the Great Tambora Eruption 1815, Journal of Petrology, 53, 271-297.

Gupta, C.K., Krishnamurthy, N. (2005). Extractive Metallurgy of Rare Earths. CRC Press, Boca Raton, Florida

Hunt, C.P., Moskowitz, B.M., Banerjee, S.K. (1995). Magnetic Properties of Rock Minerals. American Geophysical Union ,189-204.

Jordens, A., Cheng, Y.P., Waters, K.E. (2013). A review of the beneficiation of rare earth element bearing minerals. Minerals Engineering, 41, 97-114

Kandlbauer, J., Sparks, R.S.J. (2014). New estimates of the 1815 Tambora eruption volume. Journal of Volcanology and Geothermal Research, 286, 93-100.

Kartadinata, M.N., Mulyana, A.R., Kriswati, C., Haerani, N. (2008). Peta Geologi Gunungapi Tambora Sumbawa Provinsi Nusa Tenggara Barat, Pusat Vulkanologi dan Mitigasi Bencana Geology, Bandung. (In Indonesian Language).

Kurnio, H., (2007). Coastal characteristics of iron sand deposits in Indonesia. Indonesia Mining Journal, 10, 27–38.

Leveneur, J., Trompetter, W.J., Chong, S.V., Rumsey, B., Jovic, V., Kim, S., McCurdy, M., Anquillare, E., Smith, K.E., Long, N., Kennedy, J., Covic, G., Boys, J. (2021). Ironsand (Titanomagnetite- Titanohematite): Chemistry, Magnetic Properties and Direct Applications for Wireless Power Transfer. Materials, 14, 5455.

Maghfiroh, L., Susilo, A., Wiyono, Faris, A.N. (2023). Magnetic mineral characterization of iron sand deposits in Bambang Beach Lumajang, East Java, Indonesia. International Conference on Science, Mathematics, Environment, and Education AIP Conference Proceedings, 2540.

McDougall, J. C. (1961). Ironsand deposits offshore from the west coast North Island, New Zealand. New Zealand journal of geology and geophysics, 4, 283-300.

Minarwan, M. (2012). Tectonic Models of the Lesser Sunda Islands. Indonesian journal of sedimentary geology, 25 (1).

Moghaddam, M.J., Karimpour, M.H., Shafaroudi, A.M., Santos, J.F., Mendes, M.H. (2019). Geochemistry Sr-Nd isotopes and zircon U-Pb Geochronology of Intrusive Rocks: Constraint on the genesis of the Cheshmeh Khuri Cu Mineralization and its link with granitoids in the Lut Block Eastern Iran. Journal of Geochemical Exploration, 202, 59 -76.

Naitza, S., Padalino, G., Rizzo, R. (2003). Distribution and genesis of zeolite mineralization in Cenozoic pyroclastic flows from Central Sardinia (Italy): guidelines for mineral exploration. Mineral Exploration and Sustainable Development, Milpress, Rotterdam, 915-198.

Newhall, C. G., Self, S. (1982). The Volcanic Explosivity Index (VEI): An Estimate of Explosive Magnitude for Historical Volcanism. Journal of Geophysical Research, 87, C2, 1231-123.

Nugraha, P.A., Sari, S.P., Hidayati, W.N., Dewi, C.R., Kusuma, D.Y. (2016). The origin and composition of iron sand deposit in the southern coast of Yogyakarta. AIP Conference Proceedings, 1746, 020028

Piper, D. Z., Bau, M. (2013). Normalized Rare Earth Elements in Water, Sediments, and Wine: Identifying Sources and Environmental Redox Conditions, 4, 69–83.

Pratama, A., Bijaksana, S., Abdurrachman, M., Santoso, N.A. (2018). Rock Magnetic, Petrography, and Geochemistry Studies of Lava at the Ijen Volcanic Complex (IVC), Banyuwangi, East Java, Indonesia. Geosciences, 8, 183.

Rahmi, A., Rifai, H., Rahmayuni, R., Yuwanda, A.N., Visgun, D.A., Dwiridal, L. (2022). Irregular Magnetic Susceptibility Pattern of Iron Sand from Pasia Jambak Beach, Pasia Nan Tigo, Padang, Indonesia. Journal of Physics: Conference Series, 2309, 012027.

Rampino, M.R. (1982). Historic Eruptions of Tambora (1815) Krakatau (1883) and Agung (1963) Their Stratospheric Aerosols and Climatic Impact, Quaternary Research, 18, 127-143.

Rayaprol, S., Kaushik, S.D. (2015). Magnetic and Magnetocaloric Properties of $FeMnO_3$. Ceramics International, 8, 9567 – 9571.

Rayaprol, S., Kaushik, S.D., Babu, P.D., Siguri, V. (2013). Structure and Magnetism of $FeMnO_3$. AIP Conference Proceeding, 1512,1132-1133.

Roberts, A. P., Zhao, X., Hu, P., Abrajevitch, A., Chen, Y.-H., Harrison, R. J., et al. (2021). Magnetic domain state and anisotropy in hematite (α-Fe2O3) from first-order reversal curve diagrams. Journal of Geophysical Research: Solid Earth, 126, e2021JB023027.

Rochani, S., Pramusanto, Sariman, Anugrah, R.I. (2008). The Current Status of Iron Minerals in Indonesia. Indonesian Mining Journal, 11 (11): 1-17.

Satria, B., Masrurah, Z., Fajar, S.J. (2021). Magnetic susceptibility and grain size distribution as prospective tools for selective exploration and provenance study of iron sand deposits: A case study from Aceh, Indonesia. Heliyon 7, e08584.

Self, S., M.R. Rampino, M.S. Newton, and J.A. Wolff, (1984). Volcanological study of the great Tambora eruption of 1815. Geology, 12, 659-663.

Sigurdsson, H., Carey, S. (1989). Plinian and co-ignimbrite tephra fall from the 1815 eruption of Tambora volcano. Bulletin of Volcanology. 51: 243-270.

Suhendro, I., Toramaru, A., Miyamoto, T., Miyabuchi, Y., Yamamoto, T. (2021). Magma chamber stratification of the 1815 Tambora caldera-forming eruption. Bulletin of Volcanology, 83: 63.

Suhendro, I., Harijoko, A., Wibowo, H.E., Naen, G.N.R.B., Agroli, G., Nurfiani, D., Mutaqin, B.W., Sobaruddin, D.P. (2025). Timing, process, and origin of the alkaline magmas beneath Satonda volcano (Lesser Sunda Arc, Indonesia): evidence of magma mush disruption and mobilization. Bulletin of Volcanology, 87, 25.

Suryanata, P. B., Bijaksana, S., Abdurrachman, M., Pratama, A., Desi Wulan Ndari, N. R., Fajar, S. J. (2023). Preliminary Petromagnetic Study of 1849, 1926, 1963, 1968 and 1974 Surface Lavas from Batur Volcano, Bali, Indonesia: Insight on the Magmatic Process of Source and Rock Magnetic Nature. Rudarsko-Geološko-Naftni Zbornik. 38:31–40. https://doi.org/10.17794/rgn.2023.1.3

Sutawidjaja, I.S., Sigurdsson, H., Abrams, L. (2006). Characterization of Volcanic Deposits and Geoarchaeological Studies from the 1815 Eruption of Tambora Volcano. Jurnal Geologi Indonesia, 1, 49 – 57.

Takada, A., Yamamoto, T., Kartadinata, N., Budianto, A., Munandar, A., Matsumoto, A., Suto, S., Venuti, M. C. (2000). Eruptive history and magma plumbing system of Tambora volcano, Indonesia. Report of International Research and Development Cooperation ITIT Project, Geological Survey of Japan, Philippine Institute of Volcanology and Seismology and Volcanology survey of Indonesia.

Tamuntuan, G.H., Tanauma, A., Pasau, G., Sangian, H. (2019). Grain Size Distribution, Morphology, and Elemental Composition of Iron Sand from North Sulawesi. IOP Conference Series: Materials Science and Engineering. 567.

Tanii, H., Inazumi, T., Terashima, K. (2014). Mineralogical Study of Iron Sand with Different Metallurgical Characteristic to Smelting with Use of Japanese Classic Iron-making Furnace Tatara, ISIJ International, 54, 1044 – 1050.

Templeton, F. Iron and steel - The steel industry, Te Ara - the Encyclopedia of New Zealand, http://www.TeAra.govt.nz/en/graph/5892/chemical-composition-of-ironsands (accessed 6 March 2025 and published 12 Jun 2006)

Tiwow, V.A., Arsyad, M., Palloan, P., Rampe, M.J. (2017). Analysis of mineral content of iron sand deposit in Bontokanang Village and Tanjung Bayang Beach, South Sulawesi, Indonesia. IOP Conf. Series: Journal of Physics: Conf. Series, 997, 012010.

Togibasa, O., Bijaksana., S dan Novala, G.C. (2018). Magnetic Properties of Iron Sand from the Tor River Estuary, Sarmi, Papua. Geoscience, 8,113.

Varol, E. (2020). Interpretation of the origin of analcimes with mineralogical, microtextural, and geochemical investigations: a case study from Aktepe region (NE of Kalecik, Ankara, Central Anatolia, Turkey). Arabian Journal of Geoscience, 13, 343.

Vereshchagina, T.A., Kutikhina, E.A., Solovyov, L.A., Vereshchagina, S.N., Mazurova, E.V., Chernykh Y.Y., Anshits A.G. (2018). Synthesis and Structure of Analcime and Analcime Zircon Composite Derived from Coal fly ash cenospheres. Microporous and Mesoporous Materials, 258, 228-235.

Wang, Z., Pinson, D., Chew, S., Rogers, H., Monaghan, B.J., Pownceby, M.I., Webster, N.A.S., Zhang, G. (2016). Behavior of New Zealand Ironsand During Iron Ore Sintering. Metallurgical And Materials Transactions B, 47, 330-343.

Wentworth, C.K. (1922). A Scale of Grade and Class Terms for Clastic Sediments. The Journal of Geology, 30, 377-392.

Wright, J.B. (1964). Iron-titanium oxides in Some New Zealand ironsands. New Zealand Journal of Geology and Geophysics, 7 (3), 424-444.

Yulianto, A., Bijaksana, S., Loeksmanto, W. (2003). Comparative Study on Magnetic Characterization of Iron Sand from Several Locations in Central Java. Indonesian Journal of Physics, 14(2), 63.

Yunginger, R. Bijaksana, S., Dahrin, D., Zulaikha, S., Hafidz, A., Kirana, K.H., Sudarningsih., S., Mariyanto, M., Fajar, S.J. (2018). Lithogenic and Anthropogenic Components in Surface Sediments from Lake Limboto as Shown by Magnetic Mineral Characteristics Trace Metals and REE Geochemistry, Geosciences, 8, 116.

Zahra, H., Idrus, A., Handayani, T., Ernowo, Suwahyadi, Nugroho, D., Sunuhadi. (2023). Mineralogy and Provenance of Iron Sand Deposits from Cipatujah and Cikalong, Tasikmalaya, West Java, Indonesia. Iraqi Geological Journal, 56 (2D), 187-200.

SAŽETAK

Magnetna i geokemijska istraživanja naslaga željezovitoga pijeska oko vulkana Tambora u Sumbawi, Indonezija: alternativni pristup istraživanju visokokvalitetnoga željezovitog pijeska

Vulkan Tambora poznat je po katastrofalnoj erupciji iz 1815. godine te enormnoj količini erumpiranoga materijala – piroklastičnih tokova i taloga. Procesima erozije i transporta ovi vulkanski materijali transportirani su prema obali te su formirali željezoviti pijesak koji sadržava ekonomski vrijedne minerale poput magnetita. Željezoviti pijesak jedan je od važnih elemenata/komponenti za proizvodnju čelika i titana, ali je njegova upotreba još uvijek ograničena. U Indoneziji se željezoviti pijesak vadio samo u rudnicima i koristio kao mješavina u proizvodnji cementa i građevinskih materijala zbog niskoga sadržaja željeza (Fe = 45 – 48 %). S obzirom na navedeno, važno je poznavati karakteristike i sadržaj željezovitoga pijeska kako bi se maksimizirali rezultati njegova rudarenja. Karakteristike naslaga željezovitoga pijeska s planine Tambora još uvijek su nejasne i nikada nisu proučavane. U okviru ovoga istraživanja određena su geokemijska i magnetna svojstva željezovitoga pijeska oko vulkana Tambora kako bi se dobile koncentracije ekonomskih elemenata iz različitih vulkanskih materijala. Pritom su korištena mjerenja magnetne susceptibilnosti, rendgenska difrakcijska analiza (XRD), rendgenska fluorescencijska analiza (XRF) te mjerenja spektrometrije optičke emisije u induktivno spregnutoj plazmi (ICP-OES). Uzorkovanje je obavljeno na trima lokacijama, a to su Nanga Miro, Baringin Jaya i Hodo. Nanga Miro i Baringin Jaya zone su tokova lave iz erupcije 1815. godine te tokova lave iz prethodnih erupcija, dok područje Hodo predstavlja zonu piroklastičnoga toka erupcije iz 1815. godine. Rezultati su pokazali da je raspodjela veličina zrna pijeska u Baringin Jayi i Nanga Mirou koja su iz zona tokova lave dominantno srednjih (MS) i sitnih veličina (FS). S druge strane, u području Hodo, koje je iz zone piroklastičnoga toka, zrna pijeska dominantno su krupne (CS) i srednje veličine (MS). Područja iz zona tokova lave imaju visoke vrijednosti magnetne susceptibilnosti, visoke koncentracije Fe te sadržaj magnetnih minerala magnetita i hematita. Osim toga, elementi rijetkih zemalja (Ce, Gd i Pr) imaju visoku koncentraciju u željezovitome pijesku iz područja tokova lave te upućuju na srednje vrijednosti Pearsonova koeficijenta korelacije. Kombinacija raspodjele veličine čestica te magnetnih i geokemijskih karakteristika pokazala je razlike u karakteristikama željezovitoga pijeska u području vulkana Tambora.

Ključne riječi:
željezoviti pijesak, magnetni minerali, veličina zrna, magnetni susceptibilitet, geokemija, Tambora

Author's contribution

Putu Billy Suryanata (PhD, Geophysical Engineering with expertise in rock magnetism for volcanoes) performed the field work and rock sample data collection, magnetic data measurements and processing, provided the data interpretation, composed the original draft, edited and performed project administration. **Adella Ulyandana Jayatri** (M.Eng., Geophysical Engineering with expertise in rock magnetism) performed the field work and rock sample data collection, magnetic data measurements and processing, provided the data interpretation, and edited the original paper. **Satria Bijaksana** (PhD, Professor, expert on rock magnetism) provided the rock magnetism data interpretation, edited the draft, supervision, and project administration. **Silvia Jannatul Fajar** (PhD, Assistant Professor, expert on rock magnetism for lakes) performed magnetic data measurements, provided rock magnetic data interpretation and proofreading. **Ulvienin Harlianti** (M.Eng., Geophysical Engineering with expertise on rock magnetism in lakes and palaeomagnetism) provided interpretation in rock magnetic data, wrote the original paper and proofread.
All authors have read and agreed to the published version of the manuscript.

RGNZ/MGPB

Application of Artificial Intelligence in Reservoir Simulation for Characterizing Multi-Phase Fluid Flow through Petroleum Reservoirs

Rudarsko-geološko-naftni zbornik
(The Mining-Geology-Petroleum Engineering Bulletin)
DOI: 10.17794/rgn.2025.5.3

Review scientific paper

Viswakanth Kandala[1], Suresh Kumar Govindarajan[1], Tummuri Naga Venkata Pavan[1]*, Swaminathan Ponmani[2], Srinivasa Reddy Devarapu[3]

[1] *Reservoir Simulation Laboratory, Petroleum Engineering Division, Department of Ocean Engineering, Indian Institute of Technology, Madras, India.*

[2] *Department of Petroleum Engineering, Academy of Maritime Education and Training, Kanathur, Chennai, India.*

[3] *Department of Petroleum Engineering and Earth Sciences, UPES, Dehradun, India.*

Abstract

Artificial intelligence (AI) has rapidly advanced and influenced all scientific fields, including the petroleum industry, where it is no longer a novel concept. This article explores the evolving role of AI and its integration with traditional reservoir simulation approaches. The first section highlights the diminishing emphasis on conceptual and mathematical modelling in reservoir simulation, with a growing focus on sophisticated numerical solution techniques. This shift often neglects fundamental reservoir physics and mathematics, leading to the superficial characterization of multi-phase fluid flow in petroleum reservoirs. The second section examines the prevalent use of petroleum software packages, which heavily rely on input data without accounting for variations in data scales. These tools treat underlying programming as a black box, often bypassing critical basic sciences, such as reservoir conceptualization, applied mathematics, and numerical techniques, resulting in incomplete reservoir characterization. The third section discusses the role of machine learning (ML) and AI in reservoir applications. While data science plays a pivotal role, the lack of integration with fundamental reservoir physics reduces fluid flow analysis to an art devoid of scientific rigour. The final section proposes a hybrid approach that couples AI/ML with traditional reservoir simulation. This integration bridges the gap between science-based reservoir simulation and AI-driven fluid flow characterization, enabling the petroleum industry to achieve a new paradigm for multi-phase fluid flow analysis. By combining fundamental science with advanced AI techniques, this approach offers a comprehensive framework for accurate reservoir characterization and improved hydrocarbon production.

Keywords:
artificial intelligence, machine learning, reservoir simulation, conceptual model, mathematical model, numerical model

1. Introduction

Post-pandemic, the world is gradually returning to pre-pandemic normalcy in terms of hydrocarbon consumption, despite ongoing geopolitical challenges. Studies project an average global GDP growth rate of 3% until 2030, with emerging economies playing a crucial role. As hydrocarbons continue to be a key driver of this growth, their exploration and utilisation must be optimised for maximum efficiency. In this evolving landscape, advanced technologies such as Artificial Intelligence (AI) and Machine Learning (ML) are rapidly progressing, facilitating the integration of the physical and digital domains on an unprecedented scale, with far-reaching impact.

The adoption of AI and ML in the upstream industry is steadily increasing, with numerous applications showcasing their potential. The AI market in the upstream sector is expected to grow from $2.8 billion in 2023 to $5.1 billion by 2028. AI primarily focuses on creating machines that mimic human intelligence, encompassing a broad range of technologies. Within AI, ML represents a subset that builds models on pre-trained data, identifying patterns to predict outcomes (**Bhattacharya**, **2021**). Deep Learning (DL), a further specialized subset of ML, processes large volumes of data using complex algorithms to make decisions. Data Science (DS), which intersects with AI, ML, and DL, combines statistics, programming, and domain expertise to extract meaningful insight and knowledge from both structured and unstructured data.

In a producing hydrocarbon reservoir, vast amounts of real-time data are generated from various sources such as sensors, gauges, and meters. This data is characterized by its volume, velocity, variety, veracity, and

* Corresponding author: Tummuri Naga Venkata Pavan
e-mail address: pavantummuri@gmail.com
Received: 5 December 2024. Accepted: 24 April 2025.
Available online: 21 October 2025

Table 1. Applications of AI/ML in Reservoir Simulation Available in Literature

Application	ML Methods	References
Hydraulic fracture design	ANN, Deep learning	**Mohaghegh et al., 1999; Liu et al., 2021; Jia et al., 2024**
Uncertainty analysis	ANN	**Mohaghegh, 2011**
Waterflooding design	ANN, Multi objective optimizations	**Farahi et al., 2021; Zhong et al., 2020**
Phase stability calculations	ANN, SVM	**Li et al., 2019; Zhang et al., 2020**
Shale gas simulations	ANN, XGBoost, CatBoost	**Kalantari-Dahaghi and Mohaghegh, 2011; Wang et al., 2023**
History Matching	ANN, GAN	**Jo et al., 2021; Ramgulam et al., 2007; Srinivasan et al., 2021**
Oil production prediction	NN	**Muradkhanli, 2018; Zhang et al., 2022; Li et al., 2022**

ANN (Artificial Neural Network), NN (Neural Network), GAN (Generative Adversarial Network), SVM (Support Vector Machine), XGBoost (Extreme Gradient Boosting), CatBoost (Categorical Boosting).

value – attributes that classify it as 'big data.' Such big data plays a critical role in subsurface characterization, reservoir performance analysis, and optimization.

In the context of reservoir management, AI facilitates critical decision-making and the characterization of multi-phase fluid flow within petroleum reservoirs. Some of these applications, as reported in the literature, are summarized in **Table 1**. While a strong foundation in mathematics is essential, particularly in areas related to reservoir simulation, domain expertise is less critical when using AI compared to traditional reservoir simulation methods. Building on the foundation of a single-layer perceptron, or a machine capable of independent thinking, we have now reached a stage where AI/ML approaches driven by pattern recognition and creativity, including those in the petroleum industry, have become indispensable. At the same time, the practice of scientific-based reservoir simulation remains crucial for effective reservoir characterization. Thus, the current article attempts to discuss these two distinct approaches, science-based and AI-based reservoir simulation, individually and proposes leveraging their combined effects to successfully characterize multi-phase fluid flow in petroleum reservoirs with minimal uncertainty.

In the petroleum industry, three main types of models are commonly used: physical models, empirical models, and mathematical models (**Noshi and Schubert, 2018**). Physical models involve scaled-down versions of actual field-scale reservoirs (**Pavan et al., 2024; Reddya and Kumarb, 2014**). However, the extent to which the laboratory setup accurately mimics real field conditions is often questionable. This approach is not only costly and time-consuming but also presents significant challenges in upscaling, as the fundamental physics and the reservoir geometry at the laboratory scale differ substantially from those in field conditions. Empirical models, on the other hand, are based on insight derived from experimental observations, such as Darcy's law. While useful, these models are prone to human error or measurement inaccuracies, which can affect their reliability. Furthermore, they cannot be generalized, as they are not directly deduced from fundamental physical principles. Mathematical models address some of these limitations by deriving non-linearly coupled partial differential equations (PDEs) from classical physical principles (**Ansari and Govindarajan, 2022, 2024; Kandala and Govindarajan, 2023**). However, this approach typically involves numerous assumptions and simplifications to manage the mathematical complexity, which may compromise the model's fidelity. Despite these limitations, reservoir simulation continues to play a critical role in petroleum reservoir management. AI is now transforming the industry by addressing many challenges associated with these traditional models, including reservoir simulation. With its ability to analyse and derive insight from vast datasets, capturing complex relationships between rock, fluid, and rock-fluid properties it is increasingly being recognized as a powerful tool. It enhances decision-making, enables deeper understanding, and provides timely insight required by field reservoir engineers, thereby complementing and potentially surpassing traditional modelling approaches.

With the petroleum industry rapidly transitioning to oil-field digitization through the application of data-driven modelling, the role of AI has become critical (**Solomatine and Ostfeld, 2008**). The key question is no longer whether to adopt AI, but how to maximize its potential within the petroleum industry to achieve continuous improvements in operational performance (**Al-Rbeawi, 2023; Kronberger et al., 2020**). In this context, this article proposes coupling reservoir simulation with AI to harness the strengths of both approaches, ensuring maximum benefits with minimal uncertainty. This methodology assigns equal weight to reservoir simulation and AI, leveraging their complementary capabilities. Moreover, the integration of AI/ML within the framework of the big data revolution is expected to significantly reduce reservoir operation costs without compromising safety standards.

This work will significantly benefit the new generation of petroleum engineers pursuing careers in reservoir engineering and simulation, particularly at the intersection of AI and ML. It provides valuable insight into the critical aspects that must be considered on the reservoir side before embarking on model development and apply ML models. This includes understanding the intricacies of reservoir properties, data acquisition, and preprocessing, all of which are essential for building accurate and reliable models. Moreover, thought-provoking questions have been put forward for the readers, which can inspire further research in this field.

2. Reservoir Simulation

The fundamental aspect of reservoir simulation essentially involves four basic stages (see **Figure 1**) a) conceptual modelling, b) mathematical modelling, c) numerical modelling and d) simulation using packages, through which multi-dimensional, multi-phase compressible fluid flow in a petroleum reservoir is characterized. However, even after meticulously following these four stages, the simulation can only partially reflect the reality of the actual reservoir. The degree to which the simulation replicates the real field conditions whether it approaches 95% accuracy or not depends significantly on an individual's in-depth knowledge of reservoir geology, petro-physics, fluid dynamics, thermodynamics, geo-mechanics, differential calculus, along with a strong understanding of the fundamental drainage principles of a hydrocarbon reservoir below and above the bubble point pressure.

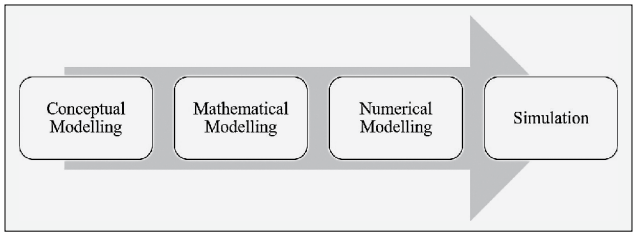


Figure 1. Key steps in reservoir simulation

2.1. Conceptual Modelling

The first stage of reservoir simulation involves the formulation of a conceptual model, as illustrated in **Figure 2**. Unfortunately, this crucial aspect is often undervalued due to the significant conceptual understanding it demands about a reservoir. This stage involves visualising the actual, complex three-dimensional petroleum reservoir within a conceptual framework, highlighting intricate details such as delineation of reservoir boundaries, conformities, and heterogeneities; well patterns and the locations of injection and production wells; the feasibility of pseudo-steady-state and transient fluid flow; phase change aspects; the restructuring of the three-dimensional solid grain network; variations in Reynolds number as a function of distance from injection or production wells; and the maintenance of laminar flow streamlines, including identifying the location and time where inertial effects, if any, may arise. Additionally, the transport of oil, water, and gas through complex pore networks, the interplay of capillary, viscous, and gravity forces, and their collective influence on fluid flow and oil-water contacts within this three-dimensional domain need to be considered. All these aspects must be conceptually (virtually) brought to life for further analysis.

Once this conceptualisation is achieved, the next step is to identify and list the (a) physical processes, (b) chemical processes (**Devarapu et al., 2023; Dinesh et al., 2024; Govindarajan et al., 2022**), and (c) biological processes (**Chakraborty et al., 2020**) individually associated with the reservoir. Following this, the feasibility of coupled processes – (a) between physical and chemical processes, (b) between chemical and biological processes, and (c) between biological and physical processes must be assessed. From these lists, the dominant and sensitive individual processes, as well as their associated coupled processes, must be identified and documented. This detailed understanding forms the output of the conceptual modelling stage.

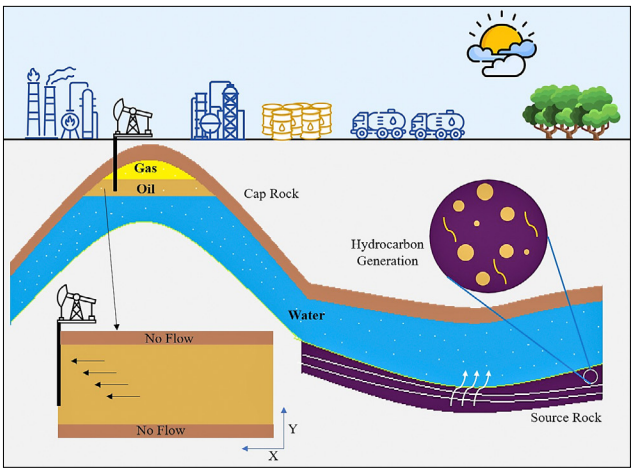


Figure 2. Typical petroleum reservoir schematic illustrating the deduction of a 2D conceptual model, showcasing the no-flow boundaries, wells, and flow dynamics.

2.2. Mathematical Modelling

The second step, mathematical modelling requires a strong understanding of mathematics, especially differential calculus. In this stage, the results from conceptual modelling must be translated into mathematical equations. A solid mathematical foundation is necessary to proceed, as it's important to know when to use linear or non-linear algebraic equations, ordinary differential equations (ODEs), or partial differential equations (PDEs). Basic knowledge of elliptic, parabolic, and hyperbolic PDEs is essential (as shown in **Table 1**). For instance, elliptic PDEs are not relevant for transient-

Table 2. Overview of PDE properties, highlighting the nature of solutions, time dependence, and equilibrium behaviour.

Property	Elliptic PDE	Parabolic PDE	Hyperbolic PDE
Form	$au_{xx} + bu_{xy} + cu_{yy} + du_x + eu_y + fu = g(x,y)$	$u_t = au_{xx} + bu_x + cu + f(x,t)$	$u_{tt} = au_{xx} + bu_x + cu + f(x,t)$
Time Dependence	Time Independent	Evolves over time in single direction	Evolves over time like waves in both directions
Nature of Solutions	Smooth and bounded	Gradual varies with time	Propagates as waves with finite speed
Stability	Unstable to perturbations (no growth of solutions)	Dissipates over time	Sensitive to initial conditions (can lead to shock waves)
Propagation of Information	Global (affects entire domain)	Parabolic diffusion-like propagation	Local (finite speed, well-defined regions of influence)
Equilibrium Behaviour	Steady-state	Diffusion to equilibrium	Oscillatory or wave-like
Examples	Steady-state flow	Transient pressure diffusion	Seismic wave propagation

state fluid flow problems. In contrast, parabolic and hyperbolic PDEs are important in transient reservoir physics. A system where pressure changes over time and eventually reaches a steady state can be modelled with a parabolic diffusivity equation (**Ansari and Govindarajan, 2023; Devarapu et al., 2023; Pavan et al., 2023; Pavan and Govindarajan, 2023; Sivasankar and Suresh Kumar, 2018**). However, if the system shows waves or heterogeneities, hyperbolic PDEs may also be needed. Once the conceptual model is converted into a set of coupled PDEs, it is crucial to determine the correct initial and boundary conditions for the equations. The solution should be well-posed, meaning numerical solutions should be unique and stable when solving them computationally.

2.3. Numerical Modelling

Numerical modelling involves solving mathematical models that are comprised of PDEs or ODEs, using computer algorithms when exact solutions are difficult to obtain. This requires a good understanding of various numerical methods, especially for non-linear and coupled PDEs.

For example, if the model is a simple parabolic diffusivity equation, finding a numerical solution is easier. In such cases, errors from initial or boundary conditions usually disappear over time as the system reaches a steady state. However, for models with hyperbolic equations, like wave equations, finding a stable solution is harder. This is because hyperbolic PDEs amplify any errors at the start, leading to significant convergence problems.

In petroleum reservoir modelling, we often deal with both parabolic and hyperbolic PDEs. For instance, when modelling fluid flow in a reservoir, we use mass and momentum conservation equations, which result in a mix of parabolic PDEs and additional hyperbolic terms. These hyperbolic terms are sometimes ignored, assuming a simple, homogeneous reservoir, which is rarely the case in reality.

To solve the mathematical models, it's important to understand: (a) the number of equations, (b) dependent and independent variables, (c) constants and variable coefficients, (d) knowns and (e) unknowns. This understanding is crucial when linearizing non-linear PDEs for numerical solutions. Linear systems can be solved using direct methods (giving exact solutions) or iterative methods (giving approximate solutions). Direct methods compute exact answers in a finite number of steps, while iterative methods start with an initial guess and refine it over time. Examples of iterative methods include Jacobi's, Gauss-Seidel, and Relaxation methods, which converge to the solution after a few iterations, as shown in **Figure 3** (**Srinivasa Reddy and Suresh Kumar, 2015**). Having figured out an appropriate and efficient numerical solution technique, a clear flow chart indicating the details of input variables, initial unknowns, initial guesses, and the equation to be solved is prepared. If convergence is achieved, it means it will go to the next step; otherwise, it will go back to the same old step until convergence is achieved. Common numerical methods include finite difference (FDM), finite element (FEM), and finite volume (FVM) techniques. The FDM approximates solutions using Taylor's series but cannot capture reservoir heterogeneities between nodes. Larger cell widths can miss crucial details, making it less effective for complex reservoirs. The FEM improves this by introducing elements between nodes, giving better control over variable variations. However, FEM struggles with fluid mass conservation, making it less ideal for petroleum reservoir simulations. The FVM is based on fluid mass conservation and better suited for handling steep gradients and shocks, like flow in fractured reservoirs or shale gas systems (**Kudapa et al., 2017**).

To ensure accurate results, the numerical model must achieve both numerical convergence and mathematical convergence. Programming, often in Fortran or C or Python, begins with simple PDEs and known initial and boundary conditions to verify the code before tackling real complex equations. The results are validated against existing solutions, experimental data, and field data to ensure reliability. In practice, many skip the foundational steps of conceptual and mathematical modelling, directly

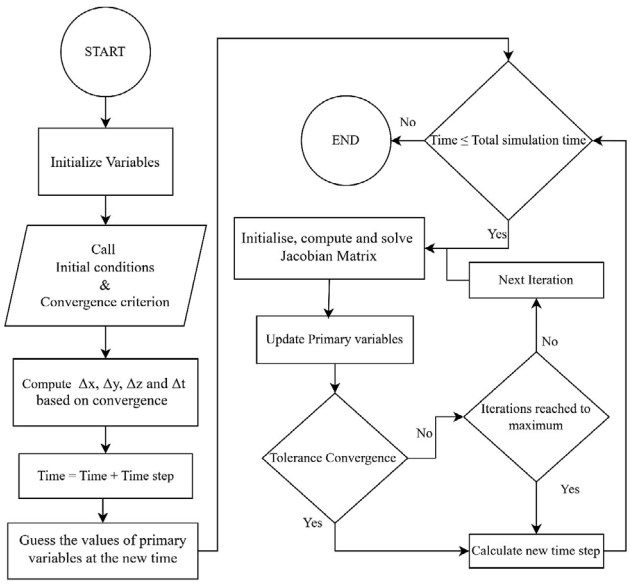


Figure 3. Algorithm describing an iterative approach for solving a system of non-linear PDE

using pre-existing equations from literature with minor modifications. This approach often neglects reservoir physics and mass conservation, leading to poor characterization of multi-phase fluid flow in heterogeneous reservoirs. A reservoir simulation engineer must possess a strong foundation in reservoir physics, computational fluid dynamics, and geology to interpret numerical results confidently and make accurate decisions in the field.

2.4. Reservoir Simulation using Packages

The concept of reservoir fluid flow characterization using existing petroleum software packages remains highly useful for field engineers in the petroleum industry as they may not be able to spend time on the fundamental stages of modelling discussed in previous sections. Thus, in this approach, most of the energy is spent only on gathering the required data from various sources. In this approach, even the data gathering remains not justified completely because of some of the following reasons: (a) the data towards rock property, fluid property, and rock-fluid interaction property do not generally tend to be uniform in nature with reference to the amount of data gathered; (b) most of the rock property, fluid property and rock-fluid interaction property data pertain to a core-scale (done at lab; or from PVT cell data), while, only very few data pertain to a field-scale; (c) some of the fluid property and rock-fluid interaction property data pertain to a much smaller scale (like contact angle and interfacial curvature data) than from the required Representative Elementary Volume (REV); (d) incorporating data at different scales with extreme variations on the same input platform, such as interfacial tension data at the sub-pore scale alongside permeability data at the large field scale, thereby deviating from the continuum hypothesis-based Darcian approach. (**Venkata Pavan et al., 2024**); (e) feeding more data pertaining to reservoir statics rather than feeding the required reservoir dynamics data; (f) securing laboratory-scale capillary pressure data with ease, while the concept of equilibrium capillary pressure may take a very long time at the field scale; (g) obtaining relative permeability data at the laboratory scale based solely on water saturation may not reflect real field conditions, where hysteresis plays a significant role, and fluid flow is often characterized by partial drainage and partial imbibition. Thus, data gathering alone is insufficient; a thorough understanding of data scales, uniformity, and the number of data points for each rock, fluid, and rock-fluid interaction property is crucial. Many engineers may lack a strong foundation in reservoir physics (conceptual model), applied reservoir mathematics (mathematical model), and numerical solution techniques (numerical model) used in petroleum software. Without a clear idea of initial and boundary conditions and their stability criteria, simply inputting cell width and time step may not produce meaningful results, leading to misinterpretation. Therefore, relying solely on input data without formulating conceptual, mathematical, and numerical models is unsuitable for academic purposes. However, industry professionals, having undergone these modelling stages, can interpret results effectively while considering limitations. Unlike fresh graduates, they have the expertise to critically analyse simulations, ensuring informed decision-making. This approach, in most cases, lacks a strong foundation in fundamental reservoir sciences.

3. AI in Petroleum Industry

AI is advancing towards mimicking human decision-making processes. ML, a subset of AI, enables computers to respond beyond their programmed behaviour by utilizing external data. It primarily helps in the extraction of actionable insight from big data. ML can be categorized into distinct types, as illustrated in **Figure 4**. The reliability and generalization of a model largely depend on the quantity and diversity of data used during its development. Various statistical and graphical approaches are employed to analyse the performance of predictive models in the petroleum industry. For example, in reservoir simulation, data from multiple sources are integrated without extensive preprocessing. In contrast, ML-based approaches emphasize data preprocessing, refining datasets before applying graphical and statistical analyses. This refinement process involves eliminating unreliable data points, such as outliers or incorrect entries, to enhance the accuracy and reliability of predictive tools. Error analysis is a critical component in this approach, as it evaluates the performance and accuracy of predictive models. The core of error analysis involves quantifying deviations between predicted and actual data points using mathematical formulations. In AI applications, unlike in reservoir simulations, data preprocessing is pivotal, with several essential steps undertaken before using the data for modelling purposes.

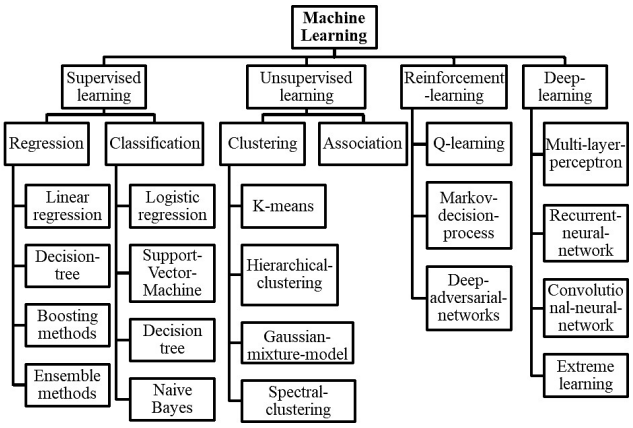


Figure 4. Classification of Machine Learning Techniques

Data preprocessing, as shown in **Figure 5**, primarily involves the following steps: (a) 'Data cleaning', which comprises eliminating inconsistencies, smoothing noisy data, and imputation of missing data points; (b) 'Data integration', where diverse data representations are combined to deduce a unique and consistent representation; (c) 'Data transformation', which includes normalisation, generalisation, and aggregation of data; (d) 'Data reduction', involving the reduction of data representation within a database; (e) 'Data discretisation', where data points within the same interval are averaged; and (f) 'Data statistics', covering metrics such as Skewness (indicating the asymmetry of the probability distribution of a random variable about its mean) and Kurtosis (indicating the degree of tailed-ness in a probability distribution).

Once preprocessing is complete, data processing begins, comprising (i) **'**Data training', where approximately three-fourths of the dataset is used to train the model, and (ii) 'Data validation and testing', aimed at evaluating the model's ability to predict new data points. Post-processing of data involves evaluating the model using either 'statistical error analysis' – which assesses performance through metrics such as average percent relative error, average absolute percent relative error, root mean square error, standard deviation, or the coefficient of determination – or 'graphical error analysis', which visualises performance through tools like error distribution curves or cross plots. The applicability domain of the model is then finalised by identifying outliers within the dataset.

Finally, 'sensitivity analysis' is conducted to determine how uncertainties in the model's inputs influence the uncertainties in its outputs. This involves performing relevancy factor analysis before the model is deemed ready for application in the petroleum industry, where intelligent models are increasingly employed.

The development of intelligent models began with the introduction of artificial neural networks (ANNs), inspired by biological neurons and the human brain. Key ANN architectures come in different types based on their structure and purpose. Feedforward neural networks (FNN) are the basic, where data transfers in uni direction from input to output. Convolutional neural networks (CNN) are used for image and spatial data processing, recognizing patterns through filter layers. Recurrent neural networks (RNN) are for sequential data, where past information influences the current output, making them useful in forecasting and language processing. Long short-term memory (LSTM) networks, a type of RNN, help retain information for longer periods. Generative adversarial networks (GAN) consist of two networks, one for data generation and the other for evaluation, commonly used in image creation. Radial basis function (RBF) networks use mathematical functions to improve classification and pattern recognition. Transformer networks, used in modern language models, process information efficiently by focusing on critical parts of the input. Building on these, fuzzy logic systems were introduced to enhance higher-level reasoning and inference, leading to the emergence of adaptive neuro-fuzzy inference systems (ANFIS), which integrate ANN capabilities with fuzzy logic principles.

In reservoir simulation, data-driven neural networks apply these intelligent modelling techniques to learn from historical reservoir and production data for predicting reservoir behaviour. However, their accuracy depends on data availability, and limited datasets can lead to unreliable predictions. To overcome this limitation, physics-informed neural networks (PINNs) incorporate fundamental physical laws, such as conservation of mass and Darcy's law, ensuring that predictions align with real reservoir flow behaviour even in data-scarce conditions. This integration of data-driven and physics-informed approaches enhances the reliability and applicability of intelligent models in reservoir analysis and decision-making (**de la Mata et al., 2023**).

The concept of decision trees, particularly in the forms of random forests and extra trees (extremely randomized trees), has become a cornerstone of intelligent models due to their simplicity, interpretability, graphical representation, and low computational cost. More recently, genetic programming, an evolutionary algorithm exploring both program and solution spaces, and gene expression programming, which seeks optimal expression models through chromosome-based encoding and solution reporting, have gained traction. These methods have surpassed the group method of data handling (GMDH) in various applications (**Hemmati-Sarapardeh et al., 2020**).

Towards the development of training and optimization algorithms, numerous techniques have been introduced in recent years. These span a broad spectrum of optimization approaches, ranging from nature-inspired heuristics to gradient-based deterministic methods, and offer solutions for diverse problem domains. These include: (a) Genetic Algorithm;(b) Differential Evolution; (c) Particle Swarm Optimization; (d) Ant Colony Optimization; (e) Artificial Bee Colony; (f) Firefly Algorithm; (g) Imperialist Competitive Algorithm; (h) Simu-

Table 3. Advantages and disadvantages of application of various ML algorithms in reservoir simulation (**Zhou et al., 2024**)

Algorithm	Advantages	Disadvantages
Linear Regression	Interpretable and suitable for variable data.	Cannot model nonlinear relationships.
Fuzzy Logic	Handles uncertainty and reduces noise.	Requires domain expertise and algorithm knowledge.
Decision Trees	Easy to interpret using root-to-leaf rules.	Prone to overfitting; pruning is challenging.
Random Forest	Accurate; handles high-dimensional, noisy data.	Limited effectiveness in low-dimensional scenarios.
XGBoost	Efficient, handles missing data, and controls overfitting well.	Poor fit for petroleum scenarios; prone to overfitting.
AdaBoost	Low error, simple coding, no tuning.	Ineffective in scenarios with many outliers.
Support Vector Machine	Accurate; robust to noise and outliers; handles nonlinear data.	Kernel selection is challenging for specific problems.
Evolutionary Algorithms	Few parameters; minimal background knowledge needed.	Easily falls into local optima; requires scenario-specific objectives.
ANN	Handles complex relationships and noisy data effectively.	Difficult to design; requires complex training and many parameters.
RNN	Processes sequential data with memory capabilities.	Struggles with historical data; prone to gradient issues.
LSTM and variants	Manages long dependencies and gradient issues effectively.	Long training, parameter-heavy, and computationally intensive.

lated Annealing; (i) Coupled Simulated Annealing; (j) Gravitational Search Algorithm; (k) Cuckoo Optimization Algorithm; (l) Gray Wolf Optimization; (m) Whale Optimization Algorithm; (n) Levenberg-Marquardt Algorithm; (o) Bayesian Regularization Algorithm; (p) Scaled Conjugate Gradient Algorithm; and (q) Resilient Backpropagation Algorithm.

AI has been extensively used in the upstream industry for various applications, including well testing, production prediction, history matching (**Costa et al., 2014**), hydrocarbon property estimation, oil field development (**Sircar et al., 2021; Ren et al., 2024**), and fracture parameter predictions (**Ahmed et al., 2019; Nande, 2018**). While AI-driven intelligent models have brought significant improvements, their effectiveness needs to be carefully studied. A key challenge lies in selecting appropriate algorithms for reservoir fluid flow analysis, particularly in assessing reservoir rock, fluid, and rock-fluid interaction properties to determine the fraction of enhanced oil recovery. Additionally, well-test analysis and formation damage analysis still require more advanced specialized algorithms. It is crucial to evaluate how accurately AI can deduce rock parameters, fluid parameters, and rock-fluid interaction parameters, ensuring that these deductions align with real field conditions. Even if AI can accurately predict all reservoir properties using advanced algorithms, we still need to check how close these predictions are to actual field scenarios. A key question is the role of detailed mathematical formulations in fluid flow analysis of petroleum reservoirs and how much AI-based models – using pattern recognition, system identification, and cognitive processes – have been able to replicate real-world fluid flow behaviour. Another important area is understanding how AI performs cross-validation during training and selects the most suitable reservoir model. The process of dividing datasets into training and validation sets, choosing data for learning versus validation, and deciding when to stop training needs further exploration. It is important to consider whether achieving low errors in training and validation sets is sufficient to stop learning or if additional "blind" data is necessary for better evaluation. AI plays a crucial role in addressing disparities in data during the training phase of model development. These intelligent models learn by recognizing hidden patterns between input reservoir properties and output responses, using optimization algorithms to improve performance. While AI is highly effective in handling large datasets, identifying patterns, and detecting trends, a key question remains: can AI fully capture all aspects of reservoir heterogeneity? Another critical consideration is the extent to which AI reduces uncertainty in reservoir performance. Ultimately, the reliability of an AI model depends significantly on the quality and quantity of reservoir data used. For instance, insufficient permeability data can challenge the model's ability to make accurate predictions. Moreover, in cases where data is limited, dividing the dataset into training, validation, and test subsets may not be feasible, further impacting the robustness and reliability of the intelligent model. These limitations highlight the need for quality data and careful handling during model development.

In essence, introducing AI has essentially translated the reservoir scientific basis into an art form as it essentially hangs around pattern recognition. This particular approach by any user, in the absence of acquiring the actual

reservoir drainage physical principles, while mostly playing with the data set alone, may not help the engineer in the long run, and this approach survives with art as a basis while science seems to be missing completely.

4. Coupled Effect of AI and Reservoir Simulation

As far as the reservoir engineering discipline is concerned, the concept of AI/ML remains widely used in reservoir characterization, in particular, reservoir pressure, temperature and volume estimations, including bubble point pressure, formation volume factor, isothermal compressibility and brine salinity. In addition, ML has also been used in a compositional oil simulator towards phase-equilibrium estimations that include phase-stability tests and phase-splitting calculations (**Mirzaei and Das, 2007**). Reservoir rock properties, including porosity and permeability, have also been estimated using fuzzy logic and SVM (**Koray et al., 2024; Lim, 2005**). An attempt has already been made to forecast the time-lapse saturation profiles at well locations using injection/production data (**Balza and Li, 2020**). In fact, extreme learning machines (ELM) have helped to forecast multiple reservoir parameters, namely lithofacies, shale content, saturation and reservoir porosity (**Lawal et al., 2024; Liu et al., 2021**). Further, ANNs not only helped to forecast bottom hole pressure in vertical wells but also have aided multi-dimensional interpolation of relative permeability to overcome the influences of various parameters during hybrid recovery processes.

Now, considering three possible approaches for implementing ML algorithms: (a) developing surrogate models for relatively homogeneous and isotropic reservoirs to reduce computational resources and costs; (b) creating ML models for reservoirs where human expertise is crucial, particularly for reservoir planning and field management decisions during hydrocarbon production; and (c) developing ML models for highly heterogeneous and anisotropic reservoirs, which are more complex to understand and model. The first two options can be managed with reservoir simulation, while the third option may still require the help of AI/ML along with reservoir simulation. However, it should be clearly noted that in petroleum reservoir fluid flow analysis, the reservoir environment is mostly heterogeneous, with every decision becoming extremely expensive, while the available data remains highly sporadic in nature. However, the petroleum production period being longer, efficient use of AI/ML could be expected to offer long-term gains when it merges hands with the scientific-based reservoir simulation. And, AI/ML algorithms are expected to play a crucial role in addressing the challenges associated with (a) large amounts of biased data (not all the rock, fluid, rock-fluid data uniformly); (b) various data associated with various scales; (c) a significant amount of inconsistent and inaccurate data; and (d) high rate of biased data influx (again, not, all the rock, fluid, rock-fluid data influx uniformly) (**Koroteev and Tekic, 2021**). On top of it, now, AI/ML would be able to scrutinize, filter and select the daily produced data from downhole as well as from surface sensors effectively as against the conventional structured and unstructured data used in the petroleum industry to keep track of production, maintenance and safety. Of course, in the petroleum industry, securing accurate data either becomes nearly impossible or extremely expensive and eventually, whether we will be able to provide a sufficient quantity and quality data for training, verification and validation remains a crucial task. The other drawback associated with the AI/ML approach is the time delay associated with the data processing because a significant amount of data is associated with high uncertainty.

In general, conventional scientific engineering analysis using reservoir simulators often faces challenges due to the extensive data requirements for reservoir rock properties, fluid properties, and rock-fluid interactions. Introducing AI techniques can help identify and model the complex non-linear relationships between these parameters, improving our understanding of their interactions. However, the success of AI depends heavily on collecting and filtering credible data from reservoir sites. While AI techniques offer potential, relying solely on them without incorporating reservoir simulation can lead to inaccurate correlations, unrealistic clustering, and biases due to missing data or unstable oil-water fronts (**Ertekin and Sun, 2019**). This highlights the need for a balanced approach. Advanced methods like transfer learning can address this gap by starting with a reservoir simulation model and refining it using AI/ML with specific training data. Combining AI/ML with reservoir simulation can reduce the computational challenges of solving complex coupled PDEs and provide deeper insight into petroleum reservoirs. This hybrid approach offers a more reliable and efficient way to model and analyze reservoirs.

It is now clearly known that reservoir simulation has a very strong scientific basis, while AI has a very strong art basis. If the petroleum industry makes an attempt to couple these two approaches in the best possible way, then the characterization of fluid flow through petroleum reservoirs will end up with minimal uncertainty while gaining the maximum benefit. The concept of reservoir simulation remains well known in the petroleum industry, while the application of AI in the petroleum industry is not in full swing. The way various data needs to be trained and the appropriate selection of algorithms meant for the successful estimation of reservoir rock and fluid parameters require a special skill. In essence, merging science and art elevates multi-phase fluid flow analysis to the next level. By integrating AI with reservoir simulation, we preserve traditional reservoir simulation practices while embracing advancements in AI. This approach enables the petroleum industry to leverage the

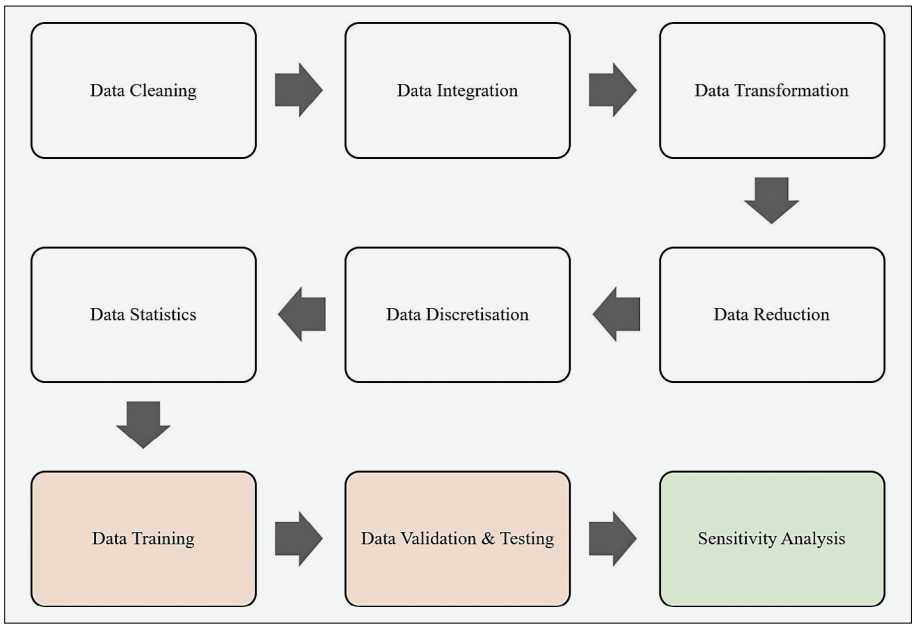


Figure 5. Key steps in data preprocessing, processing, training and testing

strengths of both methods, leading to more effective characterization of multi-phase fluid flow in petroleum reservoirs.

5. Conclusions

This article highlights the limitations of the current approach to reservoir simulation, particularly the reliance on petroleum software packages without a solid understanding of reservoir physics and mathematical principles. It also critiques the use of machine learning and artificial intelligence in reservoir characterization, viewing it more as an art than a rigorous science. Finally, the study explores the integration of reservoir simulation and AI, discussing its potential to transform the petroleum industry by enabling more advanced and accurate fluid flow analysis.

The following conclusions have been deduced from the present study.

1. The current approach to reservoir simulation through numerical modelling often ignores the fundamental physics of reservoir behaviour and the formulation of conceptual and mathematical models using applied reservoir mathematics. Instead, the focus is mainly on developing advanced numerical solution techniques, many of which do not follow the basic principle of fluid mass conservation.
2. Using petroleum reservoir simulation software without developing conceptual, mathematical, or numerical models – and relying on input data that is often not justified in terms of scale and uniformity – is not suitable for academic purposes. This method is more appropriate for industry professionals who have the expertise to understand different aspects of modelling. In an academic setting, fresh graduates may lack the necessary knowledge to correctly interpret simulation results. Industry experts, on the other hand, can carefully analyze results while considering the limitations and challenges at each stage, leading to better interpretations.
3. In AI applications, unlike traditional reservoir simulation, pre-processing of data is a very important step where proper measures are taken before using the data for processing. The introduction of AI has made reservoir science more dependent on pattern recognition, turning it into an art rather than pure science. However, depending only on data manipulation without understanding the actual physical principles of reservoir drainage may not be a sustainable approach in the long run, as it moves away from the scientific foundation.
4. By combining "art-based AI" with "science-based reservoir simulation," we can continue the traditional practice of reservoir simulation while adopting AI advancements. This hybrid approach allows the petroleum industry to benefit from the strengths of both methods, leading to better characterization of multiphase fluid flow in reservoirs. It prevents a complete shift from knowledge-based models to only data-driven AI/ML techniques, ensuring that AI supports rather than replaces traditional reservoir simulation.
5. Finally, this study highlights the importance of fundamental physics in reservoir simulation and its role in developing AI-based models. It also provides guidance for entry-level reservoir engineers on how to approach reservoir simulation problems, explaining the essential steps required for effectively simulating subsurface processes. Additionally, thought-provoking questions have been included to encourage further research in this field.

Acknowledgement

The authors greatly acknowledge the support of the research from the Indian Institute of Technology, Madras.

Conflict of interest

The authors declare that there is no financial or personal interest to research work associated with this paper.

6. References

Ahmed S, A., Elkatatny, S., Ali, A. Z., Abdulraheem, A., & Mahmoud, M. (2019). Artificial Neural Network ANN Approach to Predict Fracture Pressure. *Presented at the SPE Middle East Oil and Gas Show and Conference*. https://doi.org/10.2118/194852-ms

Al-Rbeawi, S. (2023). A Review of Modern Approaches of Digitalization in Oil and Gas Industry. *Upstream Oil and Gas Technology*, *11*, 100098. https://doi.org/10.1016/j.upstre.2023.100098

Ansari, M. I., and Govindarajan, S. K. (2022). One-dimensional heat distribution simulation in heavy oil reservoirs during steam flooding methods. *OCEANS 2022 - Chennai*, 1–8. https://doi.org/10.1109/OCEANSChennai45887.2022.9775245

Ansari, M. I., and Govindarajan, S. K. (2023). Numerical investigation on the impact of initial water saturation distribution on hot water flooding performance under non-isothermal conditions. *Rudarsko-Geološko-Naftni Zbornik*, *38*(2), 143–155. https://doi.org/10.17794/rgn.2023.2.11

Ansari, M. I., and Govindarajan, S. K. (2024). Numerical Simulation Study to Analyze the Cold Thermal Front Growth in Discrete Fracture Geothermal Reservoir. *Fifth EAGE Global Energy Transition Conference and Exhibition (GET 2024)*, 1–5. https://doi.org/10.3997/2214-4609.202421318

Balza, A., and Li, Y. (2020). Integrating time-lapse gravity, production, and geologic structure data in a gas reservoir study. *Interpretation*, *8*(4), SS129–SS143. https://doi.org/10.1190/INT-2019-0272.1

Bhattacharya, S. (2021). *A Primer on Machine Learning in Subsurface Geosciences*. Springer International Publishing. https://doi.org/10.1007/978-3-030-71768-1

Chakraborty, S., Govindarajan, S. K., and Gummadi, S. N. (2020). Numerical Modeling on the Influence of Effective Porosity, Microbial Kinetics, and Operational Parameters on Enhanced Oil Recovery by Microbial Flooding Within a Sandstone Formation. *SPE Journal*, *25*(06), 2932–2961. https://doi.org/10.2118/200639-PA

Costa, L. A. N., Maschio, C., & Schiozer, D. J. (2014). Application of artificial neural networks in a history matching process. *Journal of Petroleum Science and Engineering*, *123*, 30-45. https://doi.org/10.1016/j.petrol.2014.06.004

de la Mata, F. F., Gijón, A., Molina-Solana, M., & Gómez-Romero, J. (2023). Physics-informed neural networks for data-driven simulation: Advantages, limitations, and opportunities. *Physica A: Statistical Mechanics and its Applications*, *610*, 128415. https://doi.org/10.1016/j.physa.2022.128415

Devarapu, S. R., Dau, T. K. D., Kudapa, V. K., and Govindarajan, S. K. (2023). Compositional numerical analysis of multiphase flow of crude oil in porous media under non-isothermal conditions. *International Journal of Chemical Reactor Engineering*, *21*(12), 1465–1476. https://doi.org/10.1515/ijcre-2023-0019

Dinesh, N. S. V., Pavan, P. S., and Sivasankar, P. (2024). Decarbonization of Alkali–Surfactant–Polymer Flooding Enhanced Oil Recovery Process with Hydrogen under Uncertainty. *Energy and Fuels*, *38*(12), 11093–11106. https://doi.org/10.1021/acs.energyfuels.4c01872

Ertekin, T., & Sun, Q. (2019). Artificial intelligence applications in reservoir engineering: a status check. *energies*, *12*(15), 2897. https://doi.org/10.3390/en12152897

Farahi, M. M., Ahmadi, M., & Dabir, B. (2021). Model-based water-flooding optimization using multi-objective approach for efficient reservoir management. *Journal of Petroleum Science and Engineering*, *196*, 107988. https://doi.org/10.1016/j.petrol.2020.107988

Govindarajan, S. K., Kumar, A., Mishra, A., and Pavan, T. N. V. (2022). Conceptual Modelling of Low Salinity Water Flooding in a Fractured Reservoir. *Petroleum and Coal*, *62*(4), 1435–1448. https://www.researchgate.net/publication/333133950_STORAGE_TANK_PROTECTION_USING_ASPEN_HYSYS

Hemmati-Sarapardeh, A., Larestani, A., Amar, M. N., and Hajirezaie, S. (2020). *Applications of Artificial Intelligence Techniques in the Petroleum Industry*. Elsevier. https://doi.org/10.1016/C2018-0-04421-7

Jia, J., Fan, Q., Jing, J., Lei, K., & Wang, L. (2024). Intelligent hydraulic fracturing under industry 4.0 – a survey and future directions. *Journal of Petroleum Exploration and Production Technology*, *14*(12), 3161-3181. https://doi.org/10.1007/s13202-024-01877-6

Jo, H., Pan, W., Santos, J. E., Jung, H., & Pyrcz, M. J. (2021). Machine learning assisted history matching for a deepwater lobe system. *Journal of Petroleum Science and Engineering*, *207*, 109086. https://doi.org/10.1016/j.petrol.2021.109086

Kalantari-Dahaghi, A., & Mohaghegh, S. D. (2011, March). Numerical simulation and multiple realizations for sensitivity study of shale gas reservoir. In *SPE Oklahoma City Oil and Gas Symposium/Production and Operations Symposium* (pp. SPE-141058). SPE. https://doi.org/10.2118/141058-ms

Kandala, V., and Govindarajan, S. K. (2023). Numerical Investigations of Low-Salinity Water Flooding in a Saline Sandstone Reservoir. *Journal of Energy Engineering*, *149*(5). https://doi.org/10.1061/JLEED9.EYENG-4893

Koray, A.-M., Bui, D., Kubi, E. A., Ampomah, W., and Amosu, A. (2024). Machine learning based reservoir characterization and numerical modeling from integrated well log and core data. *Geoenergy Science and Engineering*, *243*, 213296. https://doi.org/10.1016/j.geoen.2024.213296

Koroteev, D., and Tekic, Z. (2021). Artificial intelligence in oil and gas upstream: Trends, challenges, and scenarios for

the future. *Energy and AI*, *3*, 100041. https://doi.org/10.1016/j.egyai.2020.100041

Kronberger, P., Dabrowski, P., Chacon, J., and Bangert, P. (2020, November 2). The Digitalization Journey of the Brage Digital Twin. *Day 2 Tue, November 03, 2020*. https://doi.org/10.2118/200728-MS

Kudapa, V. K., Sharma, P., Kunal, V., and Gupta, D. K. (2017). Modeling and simulation of gas flow behavior in shale reservoirs. *Journal of Petroleum Exploration and Production Technology*, *7*(4), 1095–1112. https://doi.org/10.1007/s13202-017-0324-4

Lawal, A., Yang, Y., He, H., and Baisa, N. L. (2024). Machine Learning in Oil and Gas Exploration: A Review. *IEEE Access*, *12*, 19035–19058. https://doi.org/10.1109/ACCESS.2023.3349216

Li, W., Wang, L., Dong, Z., Wang, R., & Qu, B. (2022). Reservoir production prediction with optimized artificial neural network and time series approaches. *Journal of Petroleum Science and Engineering*, *215*, 110586. https://doi.org/10.1016/j.petrol.2022.110586

Li, W., Zhang, T., Liu, X., Dong, Z., Dong, G., Qian, S., ... & Zhang, T. (2024). Machine learning-based fracturing parameter optimization for horizontal wells in Panke field shale oil. *Scientific Reports*, *14*(1), 6046. https://doi.org/10.1038/s41598-024-56660-8

Li, Y., Zhang, T., & Sun, S. (2019). Acceleration of the NVT flash calculation for multicomponent mixtures using deep neural network models. *Industrial & Engineering Chemistry Research*, *58*(27), 12312-12322. https://doi.org/10.1021/acs.iecr.9b00527

Lim, J.-S. (2005). Reservoir properties determination using fuzzy logic and neural networks from well data in offshore Korea. *Journal of Petroleum Science and Engineering*, *49*(3–4), 182–192. https://doi.org/10.1016/j.petrol.2005.05.005

Liu, X., Ge, Q., Chen, X., Li, J., and Chen, Y. (2021). Extreme learning machine for multivariate reservoir characterization. *Journal of Petroleum Science and Engineering*, *205*, 108869. https://doi.org/10.1016/j.petrol.2021.108869

Mirzaei, M., and Das, D. B. (2007). Dynamic effects in capillary pressure–saturations relationships for two-phase flow in 3D porous media: Implications of micro-heterogeneities. *Chemical Engineering Science*, *62*(7), 1927–1947. https://doi.org/10.1016/j.ces.2006.12.039

Mohaghegh, S. D. (2011). Reservoir simulation and modeling based on artificial intelligence and data mining (AI&DM). *Journal of Natural Gas Science and Engineering*, *3*(6), 697-705. https://doi.org/10.1016/j.jngse.2011.08.003

Mohaghegh, S., Popa, A., & Ameri, S. (1999, October). Intelligent systems can design optimum fracturing jobs. In *SPE Eastern Regional Meeting* (pp. SPE-57433). SPE. https://doi.org/10.2118/57433-ms

Muradkhanli, L. (2018). Neural networks for prediction of oil production. *IFAC-PapersOnLine*, *51*(30), 415-417. https://doi.org/10.1016/j.ifacol.2018.11.339

Nande, S. (2018, September). Application of machine learning for closure pressure determination. In *SPE Annual Technical Conference and Exhibition*. SPE. https://doi.org/10.2118/194042-stu

Noshi, C. I., and Schubert, J. J. (2018, October 7). The Role of Machine Learning in Drilling Operations; A Review. *Day 4 Wed, October 10, 2018*. https://doi.org/10.2118/191823-18ERM-MS

Pavan, T. N. V., Devarapu, S. R., and Govindarajan, S. K. (2024). Characterization of Leaky Deep Saline Aquifer for Storing sc-CO_2. *Energy and Fuels*, *38*(12), 11051–11063. https://doi.org/10.1021/acs.energyfuels.4c01599

Pavan, T. N. V., Devarapu, S. R., Kudapa, V. K., and Govindarajan, S. K. (2023). Numerical investigations on sc-CO_2 gas sequestration in layered heterogeneous deep saline aquifers. *International Journal of Chemical Reactor Engineering*, *21*(12), 1477–1485. https://doi.org/10.1515/ijcre-2023-0041

Pavan, T. N. V., and Govindarajan, S. K. (2023). Numerical investigations on performance of sc-CO_2 sequestration associated with the evolution of porosity and permeability in low permeable saline aquifers. *Geoenergy Science and Engineering*, *225*, 211681. https://doi.org/10.1016/j.geoen.2023.211681

Ramgulam, A., Ertekin, T., & Flemings, P. B. (2007). Utilization of artificial neural networks in the optimization of history matching. In *SPE Latin America and Caribbean Petroleum Engineering Conference*. SPE. https://doi.org/10.2118/107468-ms

Reddya, D. S., and Kumarb, G. S. (2014). A Numerical Investigation on the role of Oil Saturations on Performance of In-Situ Combustion in Porous Media. *International Journal of Scientific T Engineering Research*, *5*(5), 531–538.

Ren, Y., Cai, H., Hou, Y., Bao, H., & Zhang, L. (2024). Oilfield Production Prediction Method Based on PCA and Deep LSTM Neural Network. In *2024 International Conference on New Trends in Computational Intelligence (NTCI)*. IEEE.

Sircar, A., Yadav, K., Rayavarapu, K., Bist, N., & Oza, H. (2021). Application of machine learning and artificial intelligence in oil and gas industry. *Petroleum Research*, *6*(4), 379-391.

Sivasankar, P., and Suresh Kumar, G. (2018). Modelling the influence of interaction between injection and formation brine salinities on in-situ microbial enhanced oil recovery processes by coupling of multiple-ion exchange transport model with multiphase fluid flow and multi-species reactive transport. *Journal of Petroleum Science and Engineering*, *163*(August 2017), 435–452. https://doi.org/10.1016/j.petrol.2018.01.004

Solomatine, D. P., and Ostfeld, A. (2008). Data-driven modelling: some past experiences and new approaches. *Journal of Hydroinformatics*, *10*(1), 3–22. https://doi.org/10.2166/hydro.2008.015

Srinivasa Reddy, D., and Suresh Kumar, G. (2015). Numerical simulation of heavy crude oil combustion in porous combustion tube. *Combustion Science and Technology*, *187*(12), 1905–1921.

Srinivasan, S., O'Malley, D., Mudunuru, M. K., Sweeney, M. R., Hyman, J. D., Karra, S., Frash, L., Carey, J. W., Gross, M. R., Guthrie, G. D., Carr, T., Li, L., & Viswanathan, H. S. (2021). A machine learning framework for rapid forecasting and history matching in unconventional reservoirs.

Scientific Reports, *11*(1), 21730. https://doi.org/10.1038/s41598-021-01023-w

Venkata Pavan, T. N., Devarapu, S. R., and Suresh Kumar, G. (2024). Role of capillary pressure on carbon dioxide sequestration : mathematical analysis. *International Journal of Coal Preparation and Utilization*, *00*(00), 1–15. https://doi.org/10.1080/19392699.2024.2411549

Wang, M., Hui, G., Pang, Y., Wang, S., & Chen, S. (2023). Optimization of machine learning approaches for shale gas production forecast. *Geoenergy Science and Engineering*, *226*, 211719.

Zhang, K., Wang, X., Ma, X., Wang, J., Yang, Y., Zhang, L., & Yao, J. (2022). The prediction of reservoir production based proxy model considering spatial data and vector data. *Journal of Petroleum Science and Engineering*, *208*, 109694.https://doi.org/10.1016/j.geoen.2023.211719

Zhang, T., Li, Y., Li, Y., Sun, S., & Gao, X. (2020). A self-adaptive deep learning algorithm for accelerating multi-component flash calculation. *Computer Methods in Applied Mechanics and Engineering*, *369*, 113207.

Zhong, Z., Sun, A. Y., Wang, Y., & Ren, B. (2020). Predicting field production rates for waterflooding using a machine learning-based proxy model. *Journal of Petroleum Science and Engineering*, *194*, 107574.

Zhou, W., Liu, C., Liu, Y., Zhang, Z., Chen, P., and Jiang, L. (2024). Machine Learning in Reservoir Engineering: A Review. *Processes*, *12*(6), 1219. https://doi.org/10.3390/pr12061219

SAŽETAK

Primjena umjetne inteligencije u simulaciji ležišta za karakterizaciju protoka višefaznoga fluida kroz naftna ležišta

Umjetna inteligencija (AI) brzo napreduje i utječe na sva znanstvena područja, uključujući i naftnu industriju, gdje ona više nije novost. Ovaj članak istražuje razvoj umjetne inteligencija i njezinu integraciju s tradicionalnim pristupima simulacije ležišta. Prvi dio rada ističe sve manji naglasak na konceptualno i matematičko modeliranje u simulaciji ležišta, uz rastući fokus na sofisticirane tehnike numeričkoga rješenja. Ovaj pristup često zanemaruje temeljnu fiziku i matematiku ležišta, što dovodi do površne karakterizacije višefaznoga protoka fluida u naftnim ležištima. U drugome dijelu rada analizirano je često korištenje softverskih paketa u naftnoj industriji, koji se u velikoj mjeri oslanjaju na ulazne podatke, a da pritom ne uzimaju u obzir varijacije u skalama podataka. Ti alati tretiraju temeljno programiranje kao „crnu kutiju", često zaobilazeći ključne temeljne znanstvene discipline poput konceptualizacije ležišta, primijenjene matematike i numeričkih tehnika, što rezultira nepotpunom karakterizacijom ležišta. U trećemu dijelu rada razmatrana je uloga strojnoga učenja (ML) i umjetne inteligencije u primjenama na ležištima. Dok znanost o podatcima igra ključnu ulogu, nedostatak integracije s temeljnim fizičkim zakonitostima ležišta svodi analizu protoka fluida na „umjetnost" bez znanstvene strogosti. U zadnjemu dijelu rada predložen je hibridni pristup koji povezuje AI/ML s tradicionalnom simulacijom ležišta. Ova integracija premošćuje jaz između znanstveno utemeljene simulacije ležišta i analize protoka fluida vođene umjetnom inteligencijom, omogućujući naftnoj industriji da postigne novu paradigmu za analizu višefaznoga protoka fluida. Kombinirajući temeljnu znanost s naprednim tehnikama umjetne inteligencije, ovaj pristup nudi sveobuhvatni okvir za preciznu karakterizaciju ležišta i poboljšanu proizvodnju ugljikovodika.

Ključne riječi:
umjetna inteligencija, strojno učenje, simulacija ležišta, konceptualni model, matematički model, numerički model

Author's Contribution

Viswakanth Kandala (Research Scholar): conceptualization, writing, tables and figures. **Suresh Kumar Govindarajan** (Full Professor): conceptualization, writing the original draft, and supervision. **Tummuri Naga Venkata Pavan** (Research Scholar): writing, figures, editing, and formatting. **Swaminathan Ponamani** (Assistant Professor): tables and editing. **Srinivasa Reddy Devarapu** (Associate Professor): conceptualization, editing.
All authors have read and agreed to the published version of the manuscript.

RGNZ/MGPB

Rudarsko-geološko-naftni zbornik
(The Mining-Geology-Petroleum Engineering Bulletin)
DOI: 10.17794/rgn.2025.5.4

Original scientific paper

MAETEC: An Optimized MATLAB-Based Approach for Accurate and Efficient Terrain Correction in Complete Bouguer Anomaly

Indra Arifianto[1,2]*, Jun Nishijima[1], Rahmat Catur Wibowo[3]

[1] *Earth Resources Engineering Department, Faculty of Engineering, Kyushu University, Fukuoka, 819-0395, Japan.*

[2] *Geological Engineering Department, Faculty of Engineering, Universitas Gadjah Mada, Jl. Grafika No 2., Sleman, D.I. Yogyakarta, 55281, Indonesia.*

[3] *Geophysical Engineering, Universitas Lampung, Sumantri Brojonegoro No.1, Lampung, 35145, Indonesia.*

Abstract

Terrain correction is important in generating accurate Complete Bouguer Anomaly (CBA) maps and is essential for gravity studies. Traditional methods for terrain correction can be time-consuming, and many computerized programs are computationally intensive. To address these challenges, we introduce MAETEC, an optimized algorithm MATLAB-based approach designed to enhance the efficiency and accuracy of terrain correction in CBA computations. MAETEC uses an effective algorithm and MATLAB's parallel computing capabilities to speed up the terrain correction process. Our approach integrates simple gravity equations, e.g. Nagy prism and its simplification techniques, zonation strategy, and parallel processing to significantly reduce computation time without compromising accuracy. Validation of MAETEC against other terrain correction software and methods demonstrates its effectiveness in producing precise CBA maps with reduced processing times. We illustrate the application of MAETEC through a case study in a geothermal exploration area and also for a regional gravity study. The results show a marked improvement in the efficiency of terrain correction compared to existing available software, e.g. GTeC, Oasis, and TCDEMF, making MAETEC a valuable gravity processing tool. Overall, MAETEC offers a fast, accurate, and user-friendly solution for terrain correction, facilitating the generation of high-quality CBA maps and advancing our understanding of subsurface geological structures.

Keywords:

Terrain correction, gravity method, complete Bouguer anomaly, flat-top square prism, efficient algorithm

1. Introduction

The Complete Bouguer Anomaly (CBA) map is one of the geophysical tools for illustrating subsurface rock density anomalies. Derived from the free-air gravity anomaly, the CBA map is created through a series of topographic reductions, including Bouguer correction (Bullard A), spherical correction (Bullard B), and terrain correction (Bullard C) (**Nowell, 1999; Cella, 2015**). Bullard A, addressing the Bouguer plate effect, and Bullard B, accounting for the Earth's curvature, can be calculated using straightforward equations and approximations for each observation gravity station, as demonstrated by **LaFehr (1991)** and **Whitman (1991)**. Bullard A and B corrections are relatively simple to compute manually or with basic software. However, terrain correction (Bullard C) is time-consuming, especially when traditionally performed by the hammer chart method (**Telford et al., 1990**).

In response to this challenge, with the advancement of computer technology, earth scientists have developed software or code in Fortran, Python, Matlab, etc., that automates terrain correction. By inputting a digital elevation model (DEM) along with the coordinates and elevation of the gravity stations, software like TCDEMF (**Nishijima, 2009**), FA2BOUG (**Fullea et al., 2008**), GTeC (**Cella, 2015**), GIS-Matlab (**Almeida et al., 2018**), TGF (**Yang et al., 2020**), and Oasis Montaj (Commercial Geosoft Software) simplifies terrain correction processing. Some of these tools can be complex and challenging for non-expert geologists or geophysicists unfamiliar with certain input parameters, like setting up the optimum input to acquire an accurate result. Therefore, we present a simple and efficient algorithm for performing terrain correction utilizing MATLAB's parallel computing toolbox. Our algorithm is designed to enhance the terrain correction computational process, making it more effective, efficient, and user-friendly for non-expert geologists and geophysicists. We also compare our algorithm's results and computational times with accessible software such as TCDEMF, GTeC, Oasis Montaj, and FA2BOUG (indirectly) to validate the accuracy and compare our approach's efficiency.

* Corresponding author: Indra Arifianto
e-mail address: indra.arifianto@mail.ugm.ac.id

Received: 17 March 2025. Accepted: 24 April 2025.
Available online: 21 October 2025

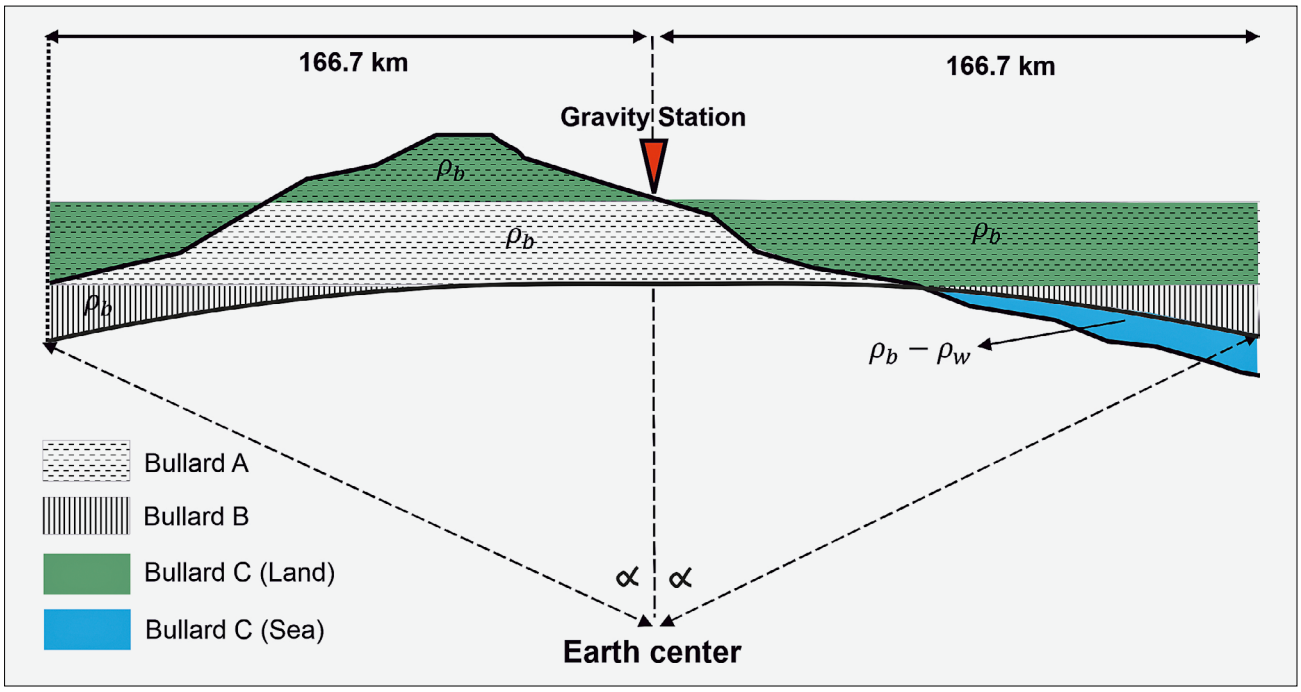


Figure 1. Illustration of corrections of topographic components to obtain the complete Bouguer anomaly from the free-air gravity anomaly. Firstly, the free air gravity anomaly is subtracted from Bouguer correction (Bullard A) with a particular density value (ρ_b) at a certain elevation to account for the gravitational effect of the topographic mass below the gravity station. Then, the free air gravity anomaly should be added with spherical correction for the Earth's curvature, known as the Bullard B correction, and it is applied to a distance of approximately 166.7 km as suggested by **LaFehr (1991)** to account for the earth's curvature effect with the same density value (ρ_b). Lastly, the terrain correction (Bullard C) is added to the free air gravity anomaly to acquire a complete Bouguer anomaly. This terrain correction cancels out the gravitational effect of the Bouguer plate in valleys while adding to the gravity value on hilltops (light blue color). For the ocean areas, the Bouguer density value is adjusted by subtracting it with the density of the seawater ($\rho_b - \rho_w$) (blue color).

The standard gravity data correction, including tides, instrumental drift, latitude, free air, and topography, should be performed to get a CBA map. The free air anomaly map shows gravity anomaly measured at a reference level, usually sea level or geoid. After free air anomaly, the anomaly due to the topography effect should be removed to get the CBA map. **Bullard (1936)** who first categorized topographic correction into three types, later known as Bullard A, B, and C. The Bullard A, also known as the Bouguer correction, treats the topography as an infinite horizontal thick slab (see **Figure 1**). As the Earth is not an infinite slab, the curvature of the Earth needs to be accounted for by the Bullard B correction with a spherical cap of a surface radius of 166.7 km (**LaFehr, 1991**). Lastly, the undulation of the topography around the gravity station must be handled by the terrain correction (Bullard C).

In the past, terrain corrections (Bullard C) were performed using the Hammer method, where the area around the gravity station was subdivided into circular zones and compartments (**Hammer, 1939**). The correction was calculated by averaging the value of the topographic elevation of each compartment and subtracting it from the gravity station's elevation. The correction value then can be calculated by assuming that the zone is a cylindrical ring divided by several sectors (**Hammer, 1939**). Nowadays, advanced computer techniques help compute terrain correction by utilizing DEM data, making it less time-consuming and more accurate. Moreover, many methods developed are more accurate than the hammer method, e.g. triangular tessellation, Nagy prism or flat top squared prisms, Fourier method, and optimally selecting sector (modification of hammer method) (**Parker, 1995; Cella, 2015; Jahanjooy et al., 2020**).

The computerization of terrain correction programs have been developed since the 1960s. **Bott (1959)** and **Kane (1962)** were among the earliest developed gridded elevation data for computing gravitational effects that is accurate for the close inner and far outer zone area. **Nagy (1966)** and **Plouff (1976)** introduced the prism method for calculating terrain correction using DEM data, which is accurate in high-resolution DEM. Better resolution will have higher accuracy but requires higher computational costs (time and computer memory). **Blais and Ferland (1984)** found that for great distances, the formula for a prism can be simplified as a vertical line mass centered at a grid point, reducing computational time for the far zone.

Another approach for terrain correction uses a Gaussian function, which offers faster computation but may not accurately capture sharp topographic variations, as proposed by **Herrera-Barrientos and Fernandez (1991)**. Additionally, a Fourier-based method separates the terrain

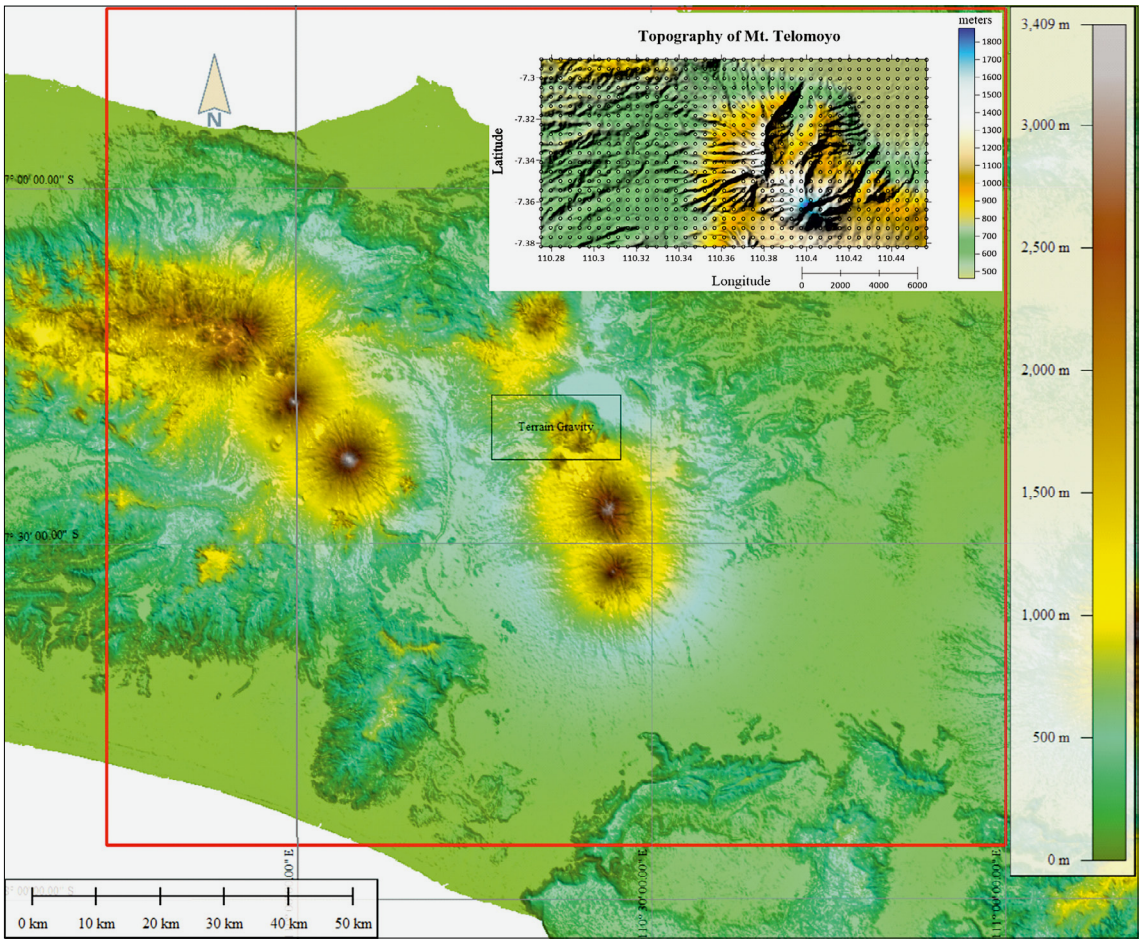


Figure 2. Available digital elevation model (DEM) data covers an area of 18,200 km² acquired from SRTM USGS Earth Explorer with a square gridded resolution of 50 meters on the Central of Java Island, Indonesia, which results in 7,280,000 pixels (red rectangle). The inset map shows the location of the 861 synthetic gravity station (black circle) for terrain correction around Mt. Telomoyo geothermal exploration area that covers an area of 200 km² (black rectangle).

correction into local and distant components, with the distant contribution transformed into a convolution series through Chebyshev economization to further improve computational efficiency (**Parker, 1995**). However, **Tsoulis (1998; 2003)** and **Gomes et al. (2013)** reported that when the topographic grid is very dense and steep, there will be divergence in the terrain calculation and significant overestimated values in high-elevation terrain due to classical integration. Some authors (**Ballina Lopez, 1990; Hwang et al., 2003; Fullea et al., 2008**) set up the digital terrain models and the input data under restrictive conditions, limiting their application (**Cella, 2015**).

Researchers have been developing programs that combine several techniques and strategies to achieve high accuracy and less computational time. The strategy commonly used in the terrain correction program is zone division, which is choosing a method to compute the terrain effect in each zonation area (i.e. Nagy prism, triangular tessellation, and triangular prism) and implementing parallel computing (**Cella, 2015; Murillo, 2017**). In this study, the terrain correction algorithm strategy implements three terrain correction methods, as suggested by **Nowel (1999)** (simplified flat-top squared prism and the quarter segment of a uniform slope wedge) and Nagy prism (flat-top squared prism) method (**Nagy, 1966; Plouff, 1976; Nagy et al., 2000**) in four adjustable zonations to maximize accuracy and a MATLAB parallel computing toolbox to minimize computational time. This paper demonstrates that combining flat-top squared prism and simplified flat-top squared prism methods with right radius zonation resulted in terrain correction with one microgal accuracy, considering the DEM resolution.

2. Methods

2.1. Data and Tools

This study uses the global Digital Elevation Model (DEM) data from SRTM (Shuttle Radar Topography Mission) USGS Earth Explorer with a resolution of 1 arc second or about 30 meters (**OpenTopography, 2013**). The study case area is around Telomoyo Mountain, part

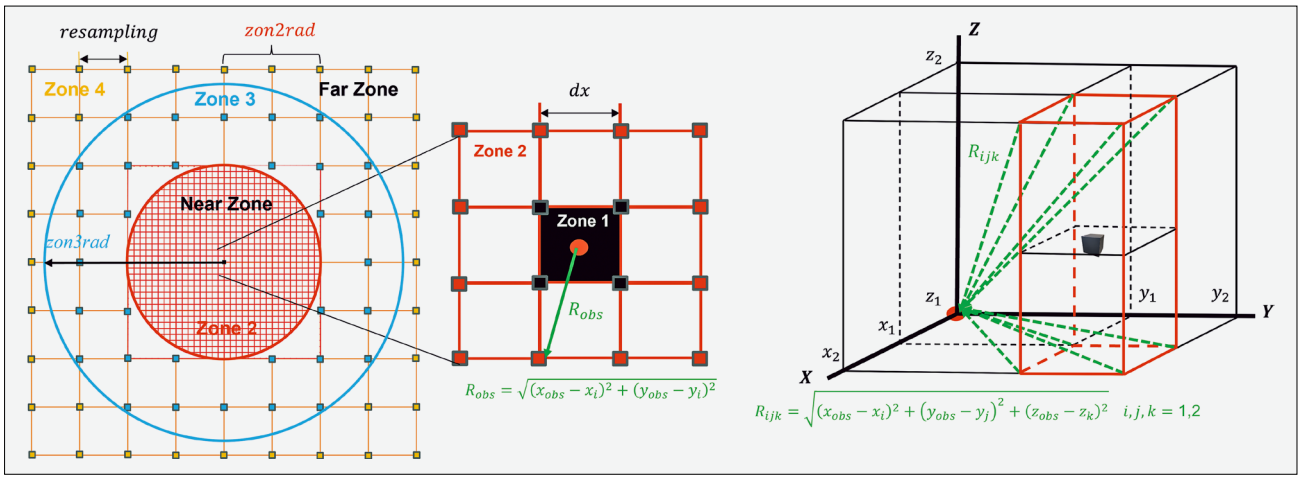


Figure 3. The left figure shows DEM zonation determination for calculating the terrain effect in each gravity station. DEM is divided into two main zones for each observation point: the near zone (red grid inside the red circle) and the far zone (yellow grid outside of the red circle). The near zone consists of Zones 1 (DEM point in black square) and 2 (DEM point in red square). The far zone consists of Zone 3, located between the red and blue circle (DEM point in blue square), and Zone 4, located outside of the blue circle, up to *maxTCrange* distance (DEM point in yellow square). The right figure illustrates how to calculate terrain correction in a gravity station for each DEM point (red rectangular prism with eight corner) in Zone 2 and Zone 3, which applies the flat top squared prism.

of the geothermal exploration area in the middle of Java Island, Indonesia (**Abdillah et al., 2024**), where the DEM covers about 120 by 120 km, and the synthetic gravity station is located in the middle of the study area (see **Figure 2**). According to the geological map of the Magelang and Semarang (**Thanden et al., 1996**), the Telomoyo area's lithological unit mainly consists of Quaternary volcanic breccia and lava, surrounded by Tertiary sedimentary rocks overlaid by Quaternary volcaniclastic products. According to **Saibi et al. (2012)**, the average rock density value in the Ungaran area is 2470 kg/m^3 or 2.47 gram/cm^3, and this value is used as the terrain density (ρ) input for terrain correction in the Telomoyo area due to their similar geological settings and volcanic history.

The code is written in MATLAB software, and all the computational processes performed using 11th Gen Intel® Core (TM) i7-1160G7@1.20GHz (8 CPUs) running on a 64-bit Windows 11 operating system with a memory of 16 GB of RAM. Using these computer specs, the code can run up to about 7.3 million points of DEM data, and it takes about 1-5 minutes to calculate the terrain correction of 861 gravity stations.

This research uses GTeC (Gravity Terrain Correction), the same MATLAB-based software, for benchmarking because GTeC provides a reliable and flexible solution for accurately calculating terrain corrections. GTeC's ability to integrate multiple DEM with progressively finer resolutions improves accuracy, especially in areas with steep slopes or near coastlines. Additionally, its use of tessellation-based algorithms for inner zones allows precise modelling of terrain effects, even in complex and rugged regions. GTeC software has been validated using synthetic topographic data and applied to a microgravity survey real-case (**Cella, 2015**). The validation results demonstrated excellent agreement of GTeC results with those obtained from commercial software, showcasing its reliability and accuracy.

2.2. Input Data and Setting Parameter

The input data is DEM data with a horizontal resolution of 50 meters for detailed geology prospecting depending on computer specs where the finer resolution will result in better accuracy. Still, it demands more memory and computational time. The DEM input data file should be in the **.xyz* format consisting of coordinates X and Y (in meters), UTM Zone (e.g. WGS 1984) format, and the Z-elevation unit (in meters). This code also accepts bathymetric DEM data (if available) in the negative elevation values. We only use positive values in the Mt. Telomoyo terrain correction test case because TCDEMF does not accept bathymetric data. However, we include negative DEM values (bathymetric) for the regional terrain correction test in the Atlas Mountain regional case. In general, DEM for terrain correction should cover a minimum of 50 km in all directions from the terrain gravity study area (see **Figure 2**). The data input format is in **.txt* format, with the information of gravity station name, longitude (can be in UTM or decimal degrees), latitude (can be in UTM or decimal degrees), and elevation of the gravity stations (in meters).

The parameter setting in MAETEC needs to be set as the input, including the average terrain density values of the study area (in gram/cm^3). The maximum terrain correction radius search (*maxTCrange*) should be defined in meters. An input of 50,000 meters for a maximum terrain correction radius should be sufficient; beyond this range, the effect will not be significant to the measured

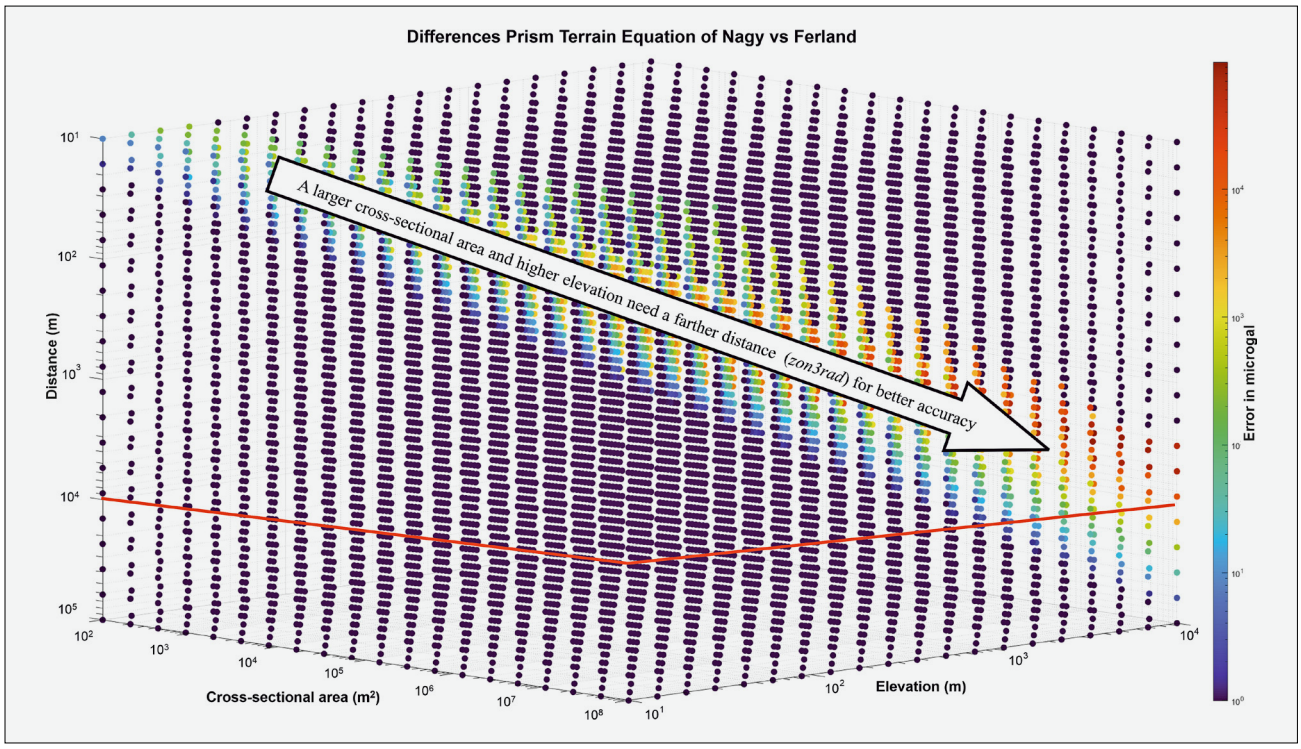


Figure 4. A plot of the difference gravity effect of a single DEM point calculated using the simplified squared prism (**Equation 3**) and Flat-top squared prism (**Equation 2**) considering the distance of the gravity station with the DEM point (*R*), the elevation of the DEM point (*H*), and the DEM resolution or the cross-sectional area (*A*) (*R, H,* and *A* referring to **Equation 3**). The red line is distance (*R*) = 10 km.

point. For the zonation, MAETEC divides zonation into two main zones: the near and far zones. Each zone consists of two sub-zones, Zones 1 and 2 in the near zone and Zones 3 and 4 in the far zone (see **Figure 3**).

To control the radius of each zone in the setting, we need to determine the DEM resolution (*dx*) as the input (unit in meters). Zone 1 is the closest area when the gravity station is not located exactly on the DEM point, and Zone 1 is fixed as four nodes closest to the gravity stations (see **Figure 3**). Zone 2 (*zone2rad*) and Zone 3 (*zone3rad*) can be set based on resolution and the number of desired grids as the input where the far zone (Zone 3 and 4) DEM resolution is resampled to a lower resolution as input *resampling* to save the computer memory. For example, if the *dx* input is 50 meters and the *resampling* input is 4 then the new DEM resolution for Zone 3 and 4 will be 200 meters (see **Figure 3**). The maximum radius of Zone 4 is taken from the parameter of *maxTCrange*. The variation of grid size or resolution of the DEM and the zonation radius significantly impacts the accuracy of the terrain correction and computational time.

2.3. *Algorithm Implementation*

2.3.1 Near-zone (R_{obs} < zon2rad)

The near *zone* uses DEM input at the actual resolution. Reducing the number of DEM arrays for the near zone is essential to optimize the computational process. This is performed only by employing the DEM coordinates inside Zone 1 and 2. Using this DEM input, MAETEC calculates the radius of each gravity station point (R_{obs}) (see **Figure 3**). According to **Nowel (1999)**, the gravity terrain effect of the closest four points to the gravity station in zone 1 (g_{zone1}) can be calculated using the assumption of the quarter segment of a uniform slope wedge derived from **Kane (1962)**.

$$g_{zone1} = \frac{1}{2}\pi G\rho R\left(1-\frac{R}{\sqrt{R^2+H^2}}\right) \quad (1)$$

G is the gravitational constant (6.672×10^{-11} Nm^2/kg^2), ρ is the density of the terrain, R is the distance from the gravity station to the DEM elevation points, and H is the DEM elevation height.

For Zone 2, when the distance (R_{obs}) exceeds the grid size or the DEM resolution and less than the Zone 2 radius (*zon2rad*), we apply the Nagy prism or flat-top squared prism because the DEM data is set as a square grid. **Nagy (1966)** and **Plouff (1976)** explained the equation to calculate the gravity terrain effects of the flat top square prism (g_{zone2}) expressed as:

$$g_{zone2\&\ zone3} = G\rho\mu_{ijk}\left[x\ln\ln\left(y+R_{ijk}\right)+\right.$$

$$\left.+\,y\ln\ln\left(x+R_{ijk}\right)-z\arctan\arctan\left(\frac{xy}{zR_{ijk}}\right)\right]\Bigg|_{x_1}^{x_2}\Bigg|_{y_1}^{y_2} \quad (2)$$

Table 1. The comparison of the computational time average and root mean square error (RMSE) of different available terrain correction software with different scenarios, including zonation ranges, terrain correction methods, and DEM resolution. GTeC, TCDEMF, and Oasis Montaj zone radius and DEM grid size have been adjusted to the MAETEC zonation setting for simplification. Each color represents the terrain equation methods used in each zone: Uniform sloped wedge (**Kane, 1962**); Flat top squared prism (**Nagy, 1966**); Simplified squared prism (**Blais and Ferland, 1984**); Sloped triangle prism (**Götze and Lahmeyer, 1988**); Squared segment ring (**Kane, 1962**).

Zonation		MAETEC				GTEC (Cella, 2015)	TCDEMF (Nishijima, 2009)	Oasis Montaj (Geosoft)
		Scene - 1	Scene - 2	Scene- 3	Scene- 4			
Zone radius	Zone 1 (Nearest)	50 m	50 m	50 m	50 m	100 m	50 m	50 m
	Zone 2	1600 m	800 m	800 m	1600 m	1000 m	50000 m	400 m
	Zone 3	14000 m	10000 m	10000 m	14000 m	1600 m	-	800 m
	Zone 4	50000 m	50000 m	50000 m	50000 m	14000 m	-	1600 m
	Zone 5	-	-	-	-	50000 m	-	50000 m
DEM grid size / resolution	Zone 1 (Nearest)	50 m	50 m	50 m	50 m	10 m	50 m	50 m
	Zone 2	50 m	50 m	50 m	50 m	50 m	50 m	50 m
	Zone 3	200 m	200 m	400 m	400 m	100 m	-	100 m
	Zone 4	200 m	200 m	400 m	400 m	200 m	-	200 m
	Zone 5	-	-	-	-	400 m	-	400 m
Computational Time (avg.)		330 sec	100 sec	35 sec	63 sec	330 sec	820 sec	180 sec
RMSE		65 µgal	74 µgal	136 µgal	78 µgal	0	468 µgal	1050 µgal

R_{ijk} is the distance from the gravity station to each corner of the prism (see **Figure 3**). x, y and z are the distances of the coordinates of the gravity station with each corner point of the prism. The term μ_{ijk} indicates the sign (positive or negative) associated with each corner point of the prism is defined as $\mu_{ijk} = (-1)^i(-1)^j(-1)^k$ where $i,j,k = 1,2$, corresponding to the prism's eight corner combinations along the x, y, and z directions (see **Figure 3**). For the DEM point located in the sea, MAETEC will automatically use density value from density terrain (ρ) subtracted with the density of seawater used 1.027 gram/cm^3 (see **Figure 1**).

2.3.2 Far-zone (zon2rad < R_{obs} < maxTCrange)

For the far zone, the DEM needs to be resampled (by *resampling* parameter) with a larger grid size (see **Figure 3**) to reduce the computational time. However, it is important to note that decreasing the DEM resolution (increasing grid size or cross-sectional area) may lead to lower terrain correction accuracy. Many terrain correction programs, such as FA2BOUG, GTeC, and Oasis Montaj, use this resampling strategy for different zone radius (**Fullea et al., 2008; Cella, 2015**). In Zone 3, MAETEC implements the same flat-top square prism as Zone 2 (see **Equation 2**) but with a larger grid size or resolution to calculate the terrain effect (g_{zone3}).

Since the flat-top squared prism can be simplified to a simple equation for a large distance (**Blais and Ferland, 1984**), we employ Ferland's equation to calculate terrain correction (g_{zone4}) for Zone 4:

$$g_{zone4} = G\rho A\left(\frac{1}{R} - \frac{1}{\sqrt{R^2 + H^2}}\right) \quad (3)$$

A represents the cross-sectional area, grid size, or resolution of the resampled DEM. R and H are the same as the distance and DEM elevation in **Equation 1**. Setting the minimum distance for Zone 4 is important to optimize the algorithm's computational time since the computational cost for the flat-top square prism is more expensive than **Equation 3**. The minimum distance for Zone 4 (*zone3rad*) is suggested at 10000 meters regardless of the height of the prism for the DEM resolution less than 2000 meters or less than 4×10^6 square meters cross-sectional area (A). However, increasing the DEM resolution or cross-sectional area (A) requires further radius or distance (R) to reach a high accuracy (lower error), where the best distance for Zone 4 (*zone3rad*) is selected when less than 10 microgal accuracies are achieved by considering the elevation difference (H) and DEM resolution or cross-sectional area (A) (see **Figure 4**).

3. Results

3.1. MAETEC optimum setting

Mount Telomoyo geothermal exploration area is selected to test the accuracy and optimum setting of the MAETEC software. 861 synthetic gravity stations were calculated using 50-meter grid size resolution DEM from SRTM (**OpenTopography, 2013**) (see **Figure 2**). Utilizing the same DEM resolution input, GTeC is considered the reference for other terrain correction software because it enables triangular tessellation to mesh the DEM. The triangular tessellation to mesh calculates the terrain effect using sloped triangular prisms, ensuring greater precision (**Götze and Lahmeyer, 1988**).

Theoretically, triangular tessellation is closer to the real topographic condition, where it reduces the "staircase effect" due to the flat top squared prism (**Cella, 2015**). The GTeC settings to get good accuracy for radius zones 1, 2, 3, 4, and 5 are 100 meters, 1000 meters, 1600 meters, 14000 meters, and 50000 meters with the step or grid resolution of 10 meters, 50 meters, 100 meters, 200 meters, and 400 meters, respectively (see **Table 1**).

To optimize the settings for MAETEC and ensure computational accuracy, we tested four zonation radius and grid size scenarios (see **Table 1**). Scenarios 1, 2, and 3 progressively decrease terrain correction accuracy by altering zonation parameters and DEM resolution, whereas Scenario 4 aims to balance accuracy with computational time. We assessed accuracy by comparing the terrain corrections from each scenario with the reference GTeC at each gravity station location and computing its root mean square error (RMSE).

In Scenario 1, Zone 2 (*zon2rad*) is set to 1,600 meters. The DEM resampling for the far zones (Zones 3 and 4) is performed at four times the original grid spacing, resulting in a 200-meter grid resolution. The radius of Zone 3 (*zon3rad*) is set at 14,000 meters to enhance accuracy, and the radius of Zone 4 is set at 50,000 meters (see **Table 1**).

In Scenarios 2 and 3, Zone 2 (*zon2rad*) is reduced to 800 meters to evaluate the improvement in computational time and its effect on near-zone (Zones 1 and 2) accuracy. Additionally, the radius of Zone 3 (*zon3rad*) is decreased to 10,000 meters in both scenarios to further improve computational efficiency (see **Table 1**). The primary difference between Scenarios 2 and 3 lies in the DEM resampling of the far zones: Scenario 2 uses a *resampling* factor of four times the original resolution (*4*dx*), while Scenario 3 uses a factor of eight times (*8*dx*) to assess the impact on accuracy.

Finally, Scenario 4 maintains the near zone (Zones 1 and 2) radius at 1,600 meters (*zon2rad*), as in Scenario 1. However, the DEM resampling for the far zones (Zones 3 and 4) is increased to eight times the DEM resolution (*dx*), resulting in a 400-meter grid resolution (see **Table 1**). In Scenario 4, the radius of Zone 3 (*zon3rad*) is set to 10,000 meters to reduce computational time while maintaining accuracy since the far zones (particularly Zone 4) usually have less influence on terrain gravity.

3.2. Analysis of MAETEC Scenarios

The result of terrain correction from scenario 1, where the larger Zone 2 radius of 1600 meters (*zon2rad*) results in better accuracy in the near zone (Zone 1 and 2) while minimizing the *resampling* factor at 4 times, leading to better accuracy in the far zone (Zone 3 and 4). Determining the radius of Zone-3 (*zon3rad*) at 14000 meters will also increase the accuracy in the far zone (Zone 3 and 4), where the accuracy test of Eq. 3 in Zone 4 suggests that the distance is more than 14000 meters at a cross-sectional area of less than 10^6 square meters (or grid resolution of 1000 meters) at any height will have the error less than 1 microgal per DEM point (see **Figure 4**). Therefore, this scenario results in the highest where the root means square error (RMSE) of terrain correction compared to the GTeC as the reference is only 65 μgal (see **Table 1**). However, scenario 1 spent around 330 seconds, the longest time compared to other MAETEC scenarios.

The MAETEC algorithm shows that the near zone is the most important zone for acquiring good accuracy, which can be seen by comparing scenarios from the radius of Zone 2 of scenarios 1 and 2 with scenarios 3 and 4. Thus, the computational time is spent mostly in Zone 2, where the flat-top squared prism is implemented. As the flat-top squared prism is also applied in Zone 3, the computational time will increase if the radius of Zone 3 (*zon3rad)* gets larger. However, accuracy will also increase as the Zone 3 radius increases, as shown by the RMSE and computational time in scenarios 3 and 4. Thus, Scenario 4 is the optimum setting for MAETEC, which gives accuracy similar to scenarios 1 and 2 but faster (2-5 times faster) due to the DEM resampling in the far zone (Zone 3 and 4) (see **Table 1**).

3.3. Comparison with Available Software

The accuracy of the MAETEC needs to be verified by other terrain correction software. This study compares three software with different methods and strategies to evaluate MAETEC accuracy and computational time. The first software is TCDEMF (**Nishijima, 2009**), which separates zonation into two zones and implements a single slope octant for the closest zone (**Kane, 1962**) and a flat-top squared prism for the rest of the DEM data (see **Table 1**). The second software is GTeC (**Cella, 2015**), which separates the zone into five zones that implement flat-top squared prism in Zones 3, 4, and 5 and triangular tessellation in Zones 1 and 2 (see **Table 1**). To optimize the GTeC accuracy, the zonation distance setting, different input DEM resolutions (steps), selection of terrain correction method in zones 4 and 5 (near zone), and parallel computing are available in the input setting. The last software is the commercial Geosoft Oasis Montaj, which implements algorithm methods described by **Kane** (**1962**) and Nagy (**Nagy, 1966; Plouff, 1976; Nagy et al., 2000**), which apply advanced grid-mesh interpolation, zonation, and resampling techniques (see **Table 1**).

In the GTeC, the terrain correction value ranges from 1.049 mgal to 24.032 mgal where the maximum value terrain effect is at the peak of Telomoyo Mountain (see **Figure 5a**). MAETEC uses scenario 4 to compare with other software by plotting and visualizing the result, which results in a range of terrain correction from 1.056 mgal to 24.052 mgal (see **Figure 5b**). As shown in **Table**

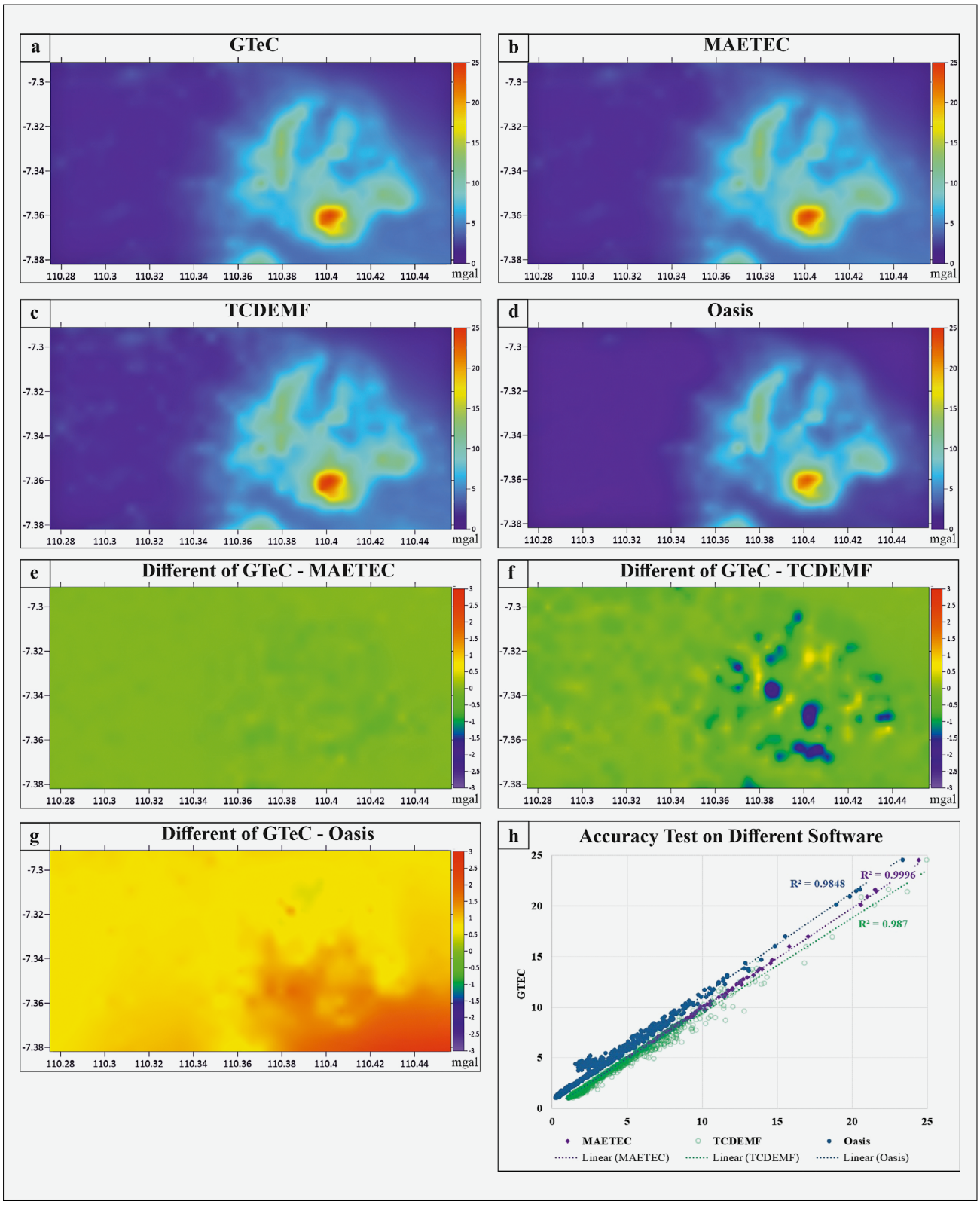


Figure 5. Maps of the terrain correction calculated at the points stations are shown in **Figure 2** using different software: GTeC (a), MAETEC (b), TCDEMF (c), and Oasis Montaj (d). The error of each software is compared with GTeC software as a reference. The MAETEC error is relatively low, with a maximum error of less than 0.5 mgal (e). The TCDEMF error is up to ± 2.5 mgal at high terrain areas (f). The Oasis Montaj error appears highest compared to other software, up to + 3 mgal (g). The plot showing the accuracy comparison between MAETEC and other terrain correction software, using GTeC as the reference. All software demonstrates high correlation coefficients above 0.980, indicating comparable accuracy, with MAETEC achieving the highest correlation of up to 0.999(h).

1, the RMSE of MAETEC with the reference software (GTeC) is less than 0.1 mgal, but some areas still have a difference of about 0.2 mgal (see **Figure 5e**). TCDEMF ranges from 1.086 mgal to 24.721 mgal (see **Figure 5c**), which differs with reference software at some locations from -2.592 mgal to 0.693 mgal (see **Figure 5f**). Oasis Montaj terrain correction result ranges from 0.247 mgal to 22.883 mgal (see **Figure 5d**); this results in about 0.483 mgal to 2.773 mgal lower value of terrain correction than the reference software (see **Figure 5g**).

Overall, MAETEC can produce an accurate terrain calculation with an average coefficient correlation of 0.999 with GTeC, 0.987 with TCDEMF, and about 0.985 with Oasis Montaj software (see **Figure 5h**), despite using a different method and algorithm than other software (see **Table 1**). The significant difference in the calculation of MAETEC with TCDEMF might be due to the resampling or gridding system of the DEM data during the conversion of the coordinate from decimal degree to UTM, whereas in the MAETEC and GTeC input can be directly in meters coordinate and the TCDEMF input is in decimal degrees. The significant difference in the Oasis Montaj is due to the resampling and zonation technique where, according to the explanation of the software to improve processing efficiency, the far zones are sequentially resampled by a factor of two then set to the average of the grid values they cover (see **Table 1**). Zone 2 averages every four initial neighboring DEM cells, while Zone 3 averages every sixteen initial cells and applies to the next zones.

3.4. Regional Terrain Correction

MAETEC is also tested for regional data with topography or DEM data resolution of the 1' x 1' ETOPO Global database, gridded at about 2000 meters resolution, taken from supplementary data in **Cella** (**2015**). The study case uses the same area as the one investigated by **Fullea et al.** (**2008**) and **Cella** (**2015**) from the Atlas Mountain, Morocco (see **Figure 6**). This terrain correction can be used for regional studies such as crustal thickness or tectonic studies. As mentioned by **Cella** (**2015**), the error of gravity data by FA2BOUG software for the regional data is up to ± 20 mgal in the higher slope gradient, which is very big considering the gravity anomaly in the subsurface. Therefore, it is important to create the best scenarios to ensure the accuracy of the computational cost of the regional terrain correction by MAETEC (see **Table 2**).

To evaluate the regional gravity correction in Atlas Mountain, GTeC parameter was set for a density of 2.67 g/cm^3 (**Cella, 2015**) with search radius zones 1, 2, 3, 4, and 5, which are 2000 m, 6000 m, 38000 m, 86000 m, and 167000 m with the grid size of 250 m, 500 m, 1000 m, 2000 m, and 4000 m, respectively (see **Table 2**). With this parameter, the GTeC produces gravity values ranging from 1.137 mgal to 164.194 mgal (see **Figure 7a**), where most of the contributors to gravity terrain correction come from Zone 1 and 2, which apply a sloped triangle prism method.

Table 2. The comparison of input parameters of MAETEC with GTeC for the regional terrain correction test, the computational time, and the accuracy (RMSE). GTeC is the reference for calculating RMSE.

Zonation		**MAETEC**	**GTEC**
Radius	**Zone 1 (Nearest)**	250 m	2000 m
	Zone 2	4000 m	6000 m
	Zone 3	20000 m	38000 m
	Zone 4	167000 m	86000 m
	Max radius	-	167000 m
DEM grid size / resolution	**Zone 1 (Nearest)**	250 m	250 m
	Zone 2	250 m	500 m
	Zone 3	2000 m	1000 m
	Zone 4	2000 m	2000 m
	Max zone	-	4000 m
Computational Time		80 sec	390 sec
RMSE		1.009 mgal	

For the MAETEC setting, the grid size of the near zone (Zones 1 and 2) is resampled to 250 meters (*dx*), with the radius of Zone 2 being 4000 meters (*zon2rad*), to which the MAETEC applies a linear gridding algorithm. The far zone (Zone 3 and 4) grid size is resampled 8 (*resampling*) times of the near zone, corresponding to a 2000-meter grid size with the *zon3rad* and *maxTCrange* set to 20000 meters and 167000 meters as the radius for the Zone 3 and 4, respectively (see **Table 2**). Compared to GTeC, the MAETEC terrain calculation produces an RMSE of 1.009 mgal and needs only 80 seconds to compute all 4716 survey points (see **Table 2**). MAETEC code produces gravity terrain correction values ranging from 0.787 mgal to 165.039 mgal (see **Figure 7b**). The difference of this terrain correction with GTeC code is considered low with a maximum error of not more than ± 3.15 milligal (see **Figure 7c**).

MAETEC code can calculate the terrain correction accurately and efficiently for regional gravity terrain correction purposes. The plot of GTeC versus MAETEC correlation coefficient is 0.999, which is considered a very good result (see **Figure 7d**). The high error from the plot is between 0 and 20 mgal value, corresponding to the shallow marine area (see **Figure 7c**). This high error is affected by the topography of the DEM in the near zone due to the continental slope of the African continent.

In the regional test, DEM resampling must be performed to produce a smoother topography that leads to more accurate terrain correction. Resampling becomes crucial for regional terrain gravity correction when the input DEM resolution exceeds 100 meters. According to **Cella** (**2015**), down-sampling DEM resolution will increase the accuracy of the terrain correction. Thus, it is

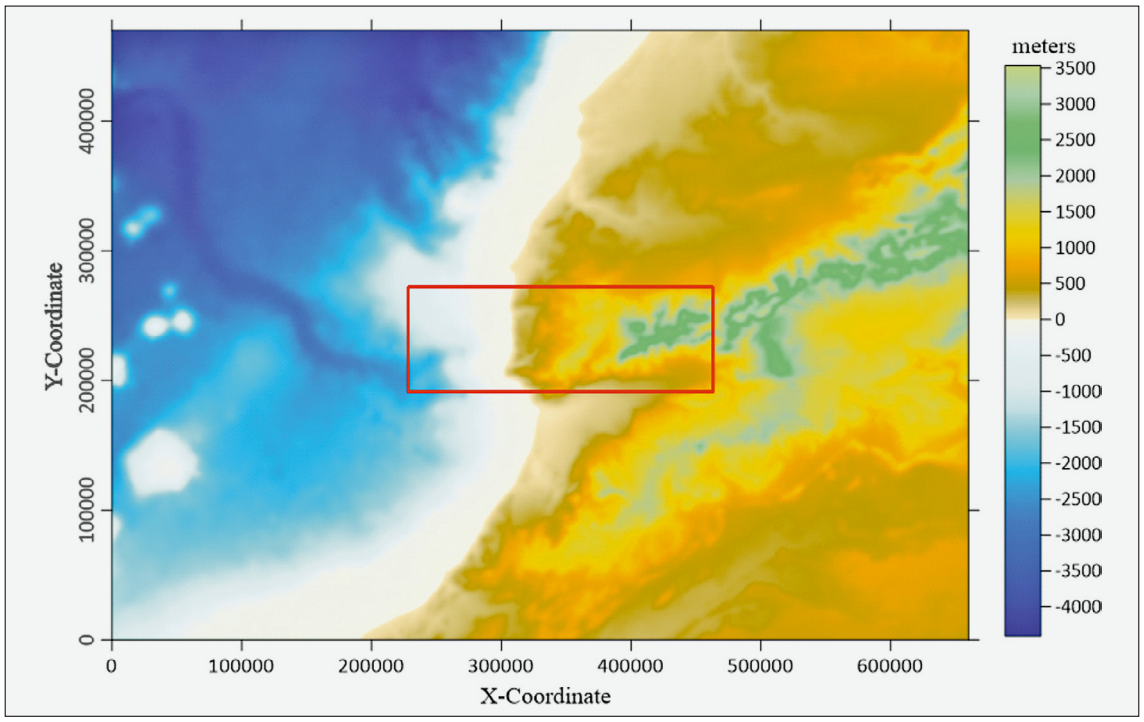


Figure 6. Regional case terrain correction in North Western Africa with DEM resolution of 2000 meters, data taken from ETOPO Global Database (**NOAA National Geophysical Data Center, 2009**). A total of 4717 synthetic gravity stations are located onshore (Atlas Mountain) and offshore (at sea level), covering an area of 18200 km² (inside red rectangle).

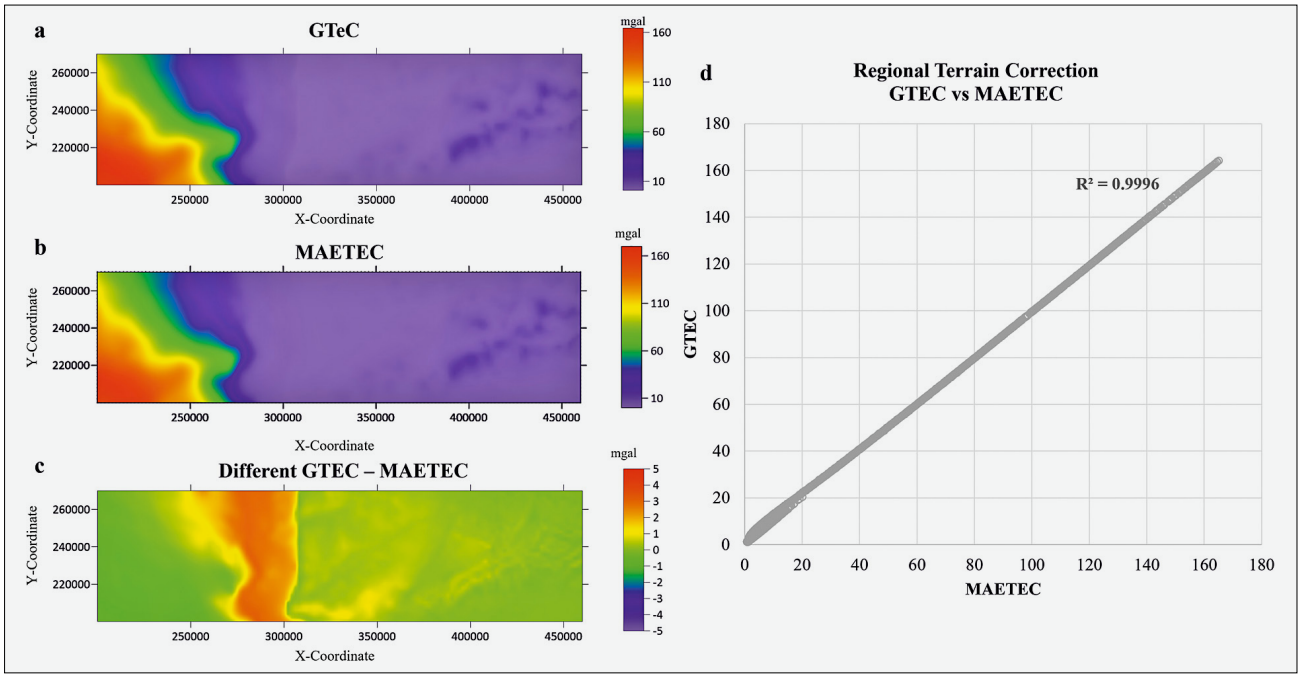


Figure 7. Maps of the regional terrain correction calculated at the points stations that are shown in Figure 6 of GTeC (a), MAETEC (b), and the difference (error) of the MAETEC compared with GTeC as the reference software (c). The plot for each gravity station regional terrain correction of GTeC and MAETEC shows a very good correlation (d).

recommended to perform a down-sampling of the original DEM to 1/8 of its original size for large DEM cases (from 2000 meters to 250 meters) to balance accuracy and computational time. Meanwhile, the near zone radius (*zon2rad*) suggested a maximum of 32 times the resolution down-sampled DEM, which is 4000 meters (see **Table 2**). For the far zone, *zon3rad* was set at 20000 meters to get an accuracy of less than 0.1 microgal for the 2000-meter grid size DEM input (4×10^6 m^2 cross-sectional area) (see **Figure 4**).

4. Discussion

The development and implementation of MAETEC showcase significant improvements in the computational efficiency and accuracy of terrain corrections for Complete Bouguer Anomaly (CBA) maps. Several key points arise from the comparative analysis and the application of MAETEC in different geological settings.

4.1. Computational Efficiency

One of the most notable achievements of MAETEC is its ability to significantly reduce computation times without compromising accuracy. This is primarily due to the utilization of MATLAB's parallel computing capabilities and an optimized zonation strategy. The parallel computing toolbox allows the distribution of computational tasks across multiple CPU cores, effectively speeding up the processing of large DEM datasets.

The comparison of different zonation scenarios (see **Table 1**) indicates that MAETEC's Scenario 4, which combines a larger near-zone radius with effective DEM resampling in the far zone, offers the best balance between accuracy and computational time. This scenario achieves an RMSE of 65 μgal compared to GTeC, the reference terrain correction software, while completing the calculations five times faster than Scenario 1. This setting strategy can also be applied to the down-sampling case of the low-resolution DEM input for a regional case study, which results in an RMSE of only 1 mgal for the study case but five times faster than the GTeC code.

MAETEC also shows better efficiency than Oasis, TCDEMF, and GTeC by choosing the right terrain correction equation for each zonation. In this case, the most important part is that implementing the simplified flat-top prism in **Equation 3** (**Blais and Ferland, 1984**) on the right distance radius of the far zone will save much computational time yet maintain high accuracy compared to resampling the DEM grid size and calculating all data by the flat-top prism which is applied in many terrain correction software.

4.2. Accuracy and Validation

The accuracy of MAETEC was validated against other terrain correction software, such as GTeC, TCDEMF, and Oasis Montaj. The results demonstrate a high correlation between MAETEC and GTeC, with a coefficient of 0.999. Minor discrepancies up to 0.2 mgal are within acceptable limits for most geological applications. For regional practice, MAETEC also shows great accuracy with a maximum error of around 3 mgal compared to software such as FA2BOUG, which has errors up to 20 mgal in the steep slope area, referring to **Cella (2015)**.

The differences between TCDEMF and Oasis Montaj are attributed to their distinct resampling and zonation techniques. TCDEMF shows a variation due to the conversion of coordinates and potential interpolation errors during DEM gridding. Oasis Montaj, on the other hand, employs more aggressive resampling strategies to enhance processing efficiency, which can lead to underestimation of value in some areas. Meanwhile, the higher FA2BOUG error (**Cella, 2015**) might be caused by using only two zonation techniques without applying a down-sampling technique, which produces big errors in the higher slope gradient.

4.3. Practical Applications

MAETEC's ability to handle high-resolution DEM data efficiently makes it particularly useful for detailed geological and geophysical surveys, such as geothermal exploration with higher terrain complexity, as demonstrated in the Telomoyo Mountain case study. The algorithm's flexibility in setting zonation parameters and DEM resolutions allows users to adapt the processing according to their specific requirements and available computational resources. For regional studies, such as the Moroccan region case, MAETEC proved to be capable of processing lower-resolution DEM data while maintaining acceptable accuracy levels.

The input process for MAETEC is straightforward and similar to the settings used in Oasis Montaj, FA-2BOUG, and TCDEMF. It requires a DEM input that uses the same UTM reference as the coordinate location of the gravity survey. Additionally, MAETEC can accept gravity survey data in latitude and longitude (decimal degrees) and provide outputs in UTM coordinates (**Palacios, 2006**). MAETEC can also generate UTM references for the gravity stations, which can then be used to determine the appropriate UTM reference for exporting the input DEM topography data. The zoning strategy is easy to use, with simple zonation in both near and far zones. As the input setting, it only needs the DEM size resolution (*dx*) for the near zone and the DEM resampling for the far zone and simple radius determination techniques, that are *zon2rad, zon3rad*, and *maxTCrange* for Zone 2, 3, and 4, respectively. This simplicity suggests that MAETEC is effective for both local and regional scale gravity studies and also easy to use, making it a versatile geophysical tool.

5. Conclusions

MAETEC represents a substantial step forward in the efficient and accurate computation of terrain corrections for Complete Bouguer Anomaly maps. Conclusions can be drawn from this study:

- MAETEC significantly reduces computation times by leveraging MATLAB's parallel computing capabilities and optimized zonation strategies. Scenario 4, in particular, offers a balanced approach, achieving high accuracy with minimal computational cost.
- Validation against other terrain correction software demonstrates that MAETEC provides accurate re-

sults. The high correlation with GTeC confirms its reliability, while minor discrepancies with TCDEMF, Oasis Montaj, and FA2BOUG are attributed to differences in resampling and zonation methods.

- The flexibility of MAETEC in handling different DEM resolutions and zonation settings makes it a practical tool for both detailed local surveys and broader regional studies.
- MAETEC offers a robust, efficient, and user-friendly solution for terrain correction in gravity studies, facilitating the generation of high-quality CBA maps and advancing our understanding of subsurface geological structures.

Acknowledgement

This research was supported by the Japan International Cooperation Agency (JICA) through the provision of a scholarship and research funding, for which we are deeply grateful. We sincerely thank all our colleagues in the Geothermic Laboratory at the Department of Earth Resource Engineering, Kyushu University, for their invaluable discussions and input throughout this research. We also want to thank Federico Cella in Scuola di Scienze e Tecnologie, University of Camerino, for sharing GTeC code to benchmark our work. Finally, we appreciate the editor and the anonymous reviewer's comments and suggestions on improving the manuscript.

Data Availability Statement

To help readers understand how to run MAETEC or configure its parameters, we provide a demonstration dataset and the corresponding MAETEC.par file. These materials allow users to perform terrain corrections and review sample output results generated by the MAETEC software. All supplementary files can be accessed at http://bit.ly/3VycXUj.

Declarations

Financial Interests: The authors have no financial or proprietary interests in any material discussed in this article.

Conflict of interest: The authors declare that they have no competing interests

6. References

Abdillah, Y.Z., Sidik, R.P., Putra, Z.M.D.C.W., Wibowo, D.A., Darmawan, A., Mulyana R.S., Kristianto, B.A. (2024). Geochemistry of Cold Springs in Geothermal Exploration Stage – Case Study of Candi Umbul Telomoyo, Central Java. *IOP Conf Ser: Earth Environ Sci 1293(1)*:012004. https://doi.org/10.1088/1755-1315/1293/1/012004

Almeida, F., Matias, M., Lourenço, M., Martins, A., (2018). A MatLab Script to Perform Gravity Terrain Corrections Using DEM-EU Digital Elevation Model in a Teaching Lab. In: 24th European Meeting of Environmental and Engineering Geophysics. European Association of Geoscientists & Engineers, Porto, Portugal, pp 1–5

Ballina, L. H.R., (1990). FORTRAN program for automatic terrain correction of gravity measurements. *Computers & Geosciences 16(2):*237–244. https://doi.org/10.1016/0098-3004(90)90130-L

Blais, J.A.R., Ferland, R. (1984). Optimization in Gravimetric Terrain Corrections. *Canadian Journal of Earth Sciences 21(5):*505–515. https://doi.org/10.1139/e84-055

Bott, M.H.P. (1959). The Use of Electronic Digital Computers for The Evaluation of Gravimetric Terrain Corrections. *Geophysical Prospecting 7(1):*45–54. https://doi.org/10.1111/j.1365-2478.1959.tb01452.x

Bullard, E.C. (1936). Gravity measurements in East Africa. Philosophical Transactions of the Royal Society of London Series A, *Mathematical and Physical Sciences, 235 (757):*445–531

Cella, F. (2015). GTeC – A versatile MATLAB® Tool for a Detailed Computation of The Terrain Correction and Bouguer Gravity Anomalies. *Computers & Geosciences 84:72–85.* https://doi.org/10.1016/j.cageo.2015.07.015

Fullea, J., Fernàndez, M., Zeyen, H. (2008). FA2BOUG – A FORTRAN 90 Code to Compute Bouguer Gravity Anomalies from Gridded Free-air Anomalies: Application to the Atlantic-Mediterranean Transition Zone. *Computers & Geosciences 34(12):*1665–1681. https://doi.org/10.1016/j.cageo.2008.02.018

Gomez, M.E., Bagu, D.R., Del Cogliano, D., Perdomo, R.A. (2013). Evaluation of Terrain Corrections Through FFT and Classical Integration in Two Selected Areas of The Andes and Their Impact on Geoidal Heights. *Bol Ciênc Geod 19(3):*407–419. https://doi.org/10.1590/S1982-21702013000300004

Götze, H. -J., Lahmeyer, B. (1988). Application of Three-Dimensional Interactive Modeling in Gravity and Magnetics. *Geophysics 53(8):*1096–1108. https://doi.org/10.1190/1.1442546

Hammer, S. (1939). Terrain Corrections for Gravimeter Stations. *Geophysics 4(3):*184–194. https://doi.org/10.1190/1.1440495

Herrera-Barrientos, J., Fernandez, R. (1991). Gravity terrain corrections using Gaussian surfaces. *Geophysics 56(5):* 724–730. https://doi.org/10.1190/1.1443091

Hwang, C., Wang, C.G, Hsiao, Y.S. (2003). Terrain correction computation using Gaussian quadrature. *Computers & Geosciences 29(10):*1259–1268. https://doi.org/10.1016/j.cageo.2003.08.003

Jahanjooy, S., Pirouei, M., Kolo, K. (2020). High accuracy gravity terrain correction by Optimally Selecting Sectors algorithm based on Hammer charts method. *Studia Geophysica et Geodaetica 64(2):*172–185. https://doi.org/10.1007/s11200-019-0273-0

Kane, M.F. (1962). A Comprehensive System of Terrain Corrections Using a Digital Computer. *Geophysics 27(4):*455–462. https://doi.org/10.1190/1.1439044

LaFehr, T.R. (1991). An Exact Solution for The Gravity Curvature (Bullard B) Correction. *Geophysics 56(8):*1179–1184. https://doi.org/10.1190/1.1443138

Murillo, N.E.P. (2017). A Matlab Code to Compute Gravity Measurements' Terrain Corrections In Puracé (Cauca), Colombia. Geosciences Department - Science Faculty - Universidad de Los Andes

Nagy, D. (1966). The Prism Method for Terrain Corrections Using Digital Computers. *Pure and Applied Geophysics 63(1):31–39*. https://doi.org/10.1007/BF00875156

Nagy, D., Papp, G., Benedek, J. (2000). The Gravitational Potential and Its Derivatives for The Prism. *Journal of Geodesy* 74(7–8):552–560. https://doi.org/10.1007/s001900000116

Nishijima, J., (2009). A Terrain Correction Program Using 50m Mesh Digital Elevation Data. Kyushu University

NOAA National Geophysical Data Center (2009). ETOPO1 1 Arc-Minute Global Relief Model

Nowell, D.A.G. (1999). Gravity Terrain Corrections an Overview. *Journal of Applied Geophysics 42(2)*:117–134. https://doi.org/10.1016/S0926-9851(99)00028-2

OpenTopography (2013). Shuttle Radar Topography Mission (SRTM) Global

Palacios, R. (2006). deg2utm https://www.mathworks.com/matlabcentral/fileexchange/10915-deg2utm. Accessed 26 May 2023

Parker, R.L. (1995). Improved Fourier Terrain Correction, Part I. *Geophysics 60(4):*1007–1017. https://doi.org/10.1190/1.1443829

Plouff, D. (1976). Gravity and Magnetic Fields of Polygonal Prisms and Application to Magnetic Terrain Corrections. *Geophysics 41(4):*727–741. https://doi.org/10.1190/1.1440645

Saibi, H., Aboud, E., Setyawan, A., Ehara, S., Nishijima, J. (2012). Gravity Data Analysis of Ungaran Volcano, Indonesia. *Arabian Journal of Geosciences 5(5)*:1047–1054. https://doi.org/10.1007/s12517-011-0303-x

Telford, W.M., Geldart, L.P., Sheriff, R.E. (1990). Applied Geophysics, 2nd edn. Cambridge University Press

Thanden, R.E., Sumadirja, H., Richard, P.W., Sutisna, K., Amin, T.C. (1996). Geological Map of the magelang and semarang sheets, Jawa, Geological Research and Development Centre, Bandung, Indonesia.

Tsoulis, D. (2003). Terrain Modeling in Forward Gravimetric Problems: a Case Study on Local Terrain Effects. *Journal of Applied Geophysics 54(1–2):*145–160. https://doi.org/10.1016/j.jappgeo.2003.09.001

Tsoulis, D. (1998). A combination method for computing terrain corrections. *Physics and Chemistry of the Earth 23(1)*:53–58. https://doi.org/10.1016/S0079-1946(97)00241-3

Whitman, W.W. (1991). A Microgal Approximation for the Bullard B Earth's Curvature Gravity Correction. *Geophysics 56(12)*:1980–1985. https://doi.org/10.1190/1.1443009

Yang, M., Hirt, C., Pail, R. (2020). TGF: A New MATLAB-based Software for Terrain-related Gravity Field Calculations. *Remote Sensing 12(7)*:1063. https://doi.org/10.3390/rs12071063

SAŽETAK

Optimizirani pristup temeljen na MATLAB-u za točnu i učinkovitu korekciju terena u potpunoj Bouguerovoj anomaliji

Korekcija terena važna je u generiranju točnih karata potpune Bouguerove anomalije (CBA) i nužna je za gravitacijska istraživanja. Tradicionalne metode za korekciju terena mogu biti dugotrajne, a mnogi računalni programi računski su zahtjevni. Kako bismo odgovorili na ove izazove, predstavljamo MAETEC, optimizirani algoritam zasnovan na MATLAB-u, dizajniran za poboljšanje učinkovitosti i točnosti korekcije terena u CBA izračunima. MAETEC primjenjuje učinkovit algoritam i MATLAB-ove mogućnosti paralelnoga računanja za ubrzavanje procesa korekcije terena. Naš pristup integrira jednostavne gravitacijske jednadžbe, npr. Nagyevu prizmu i njezine tehnike pojednostavnjenja, strategiju zoniranja i paralelnu obradu kako bi se znatno smanjilo vrijeme izračuna bez ugrožavanja točnosti. Validacija MAETEC-a u odnosu na drugi softver i metode za korekciju terena pokazuje njegovu učinkovitost u proizvodnji preciznih CBA karata sa smanjenim vremenom obrade. Prikazujemo primjenu MAETEC-a kroz studiju slučaja u području geotermalne eksploatacije, kao i za regionalno gravitacijsko istraživanje. Rezultati pokazuju znatno poboljšanje učinkovitosti korekcije terena u usporedbi s postojećim dostupnim softverom, npr. GTeC, Oasis i TCDEMF, što MAETEC čini vrijednim alatom za obradu gravitacijskih mjerenja. Općenito, MAETEC nudi brzo, točno i korisniku prilagođeno rješenje za korekciju terena, olakšavajući generiranje visokokvalitetnih CBA karata i unapređujući naše razumijevanje podzemnih geoloških struktura.

Ključne riječi:
korekcija terena, gravitacijska metoda, potpuna Bouguerova anomalija, ravna kvadratna prizma, učinkovit algoritam

Author's contribution

Indra Arifianto: conceptualization, methodology, software, data curation, formal analysis, investigation, writing - original draft, visualization. **Jun Nishijima**: methodology, supervision, project administration, resources, writing - review & editing, funding acquisition. **Rahmat Catur Wibowo**: validation, data curation, formal analysis, writing - review & editing.
All authors have read and agreed to the published version of the manuscript.

RGNZ/MGPB

Unveiling the dynamics of deep-focus earthquakes: Insights from the 2020 Jepara event Mw 6.7 and subduction processes beneath Java

Rudarsko-geološko-naftni zbornik
(The Mining-Geology-Petroleum Engineering Bulletin)
DOI: 10.17794/rgn.2025.5.5

Original scientific paper

Tio Azhar Prakoso Setiadi[1]*, Anne Meylani Magdalena Sirait[2], Yehezkiel Halauwet[3], Andrean Vesalius Hasiholan Simanjuntak[3,4], Adi Susilo[5,6]

[1] *National Research and Innovation Agency, Bogor, 16911, Indonesia.*
[2] *Geophysics Program, Faculty of Mathematics and Natural Sciences, Universitas Indonesia, Depok, 16424, Indonesia.*
[3] *Meteorological, Climatological, and Geophysical Agency (BMKG), Central Jakarta, Kemayoran, 10610, Indonesia.*
[4] *Tsunami Disaster and Mitigation Research Center (TDMRC), University of Syiah Kuala, Banda Aceh, 231111, Indonesia.*
[5] *Department of Physic, Faculty of Mathematics and Natural Sciences, Brawijaya University, Malang, 65145, Indonesia.*
[6] *Research Study of Geosciences and Hazard Mitigation, Universitas Brawijaya, Malang, 65145, Indonesia.*

Abstract

The 2020 Jepara earthquake (Mw 6.7) represents a significant deep-focus seismic event within the subducting Indo-Australian Plate beneath Java Island. This study investigates its characteristics using automatic moment tensor inversion and double-difference relocation based on seismic data from the Meteorology, Climatology, and Geophysics Agency (BMKG). A total of 1,899 earthquakes recorded between 2010 and 2022 were analyzed, focusing on events with a depth of up to 600 km. Moment tensor analysis revealed a normal faulting mechanism with two nodal planes: the first with a strike of 310º, dip of 59º, and rake of -68º, and the second with a strike of 92º, dip of 37º, and rake of -121º. The centroid depth was refined to 544 km, and the variance reduction (VR) exceeded 60%, which classifies the results as high-quality (Category A). Approximately 85% of the hypocenters were successfully relocated, improving root mean square (RMS) travel times to less than 1 second. The earthquake is associated with slab dehydration and the polymorphic phase transition of olivine to spinel under high pressure and temperature. These processes contribute to changes in fault mechanisms and the structural variation of the mantle transition zone. The findings enhance understanding of the deep-focus earthquakes beneath Java and can significantly contribute to future earthquake mitigation in Indonesia.

Keywords:
Java Island, deep-focus earthquakes, moment tensor inversion, double-difference relocation, slab dehydration

1. Introduction

Java Island experiences significant seismic activity due to active tectonic processes (**Gunawan and Widiyantoro, 2021; Widiyantoro et al., 2020**). These processes are primarily driven by the subduction of the Indo-Australian oceanic plate beneath the Eurasian continental plate at a rate of 5–6 cm/year. Additionally, active onshore faults with slip rates of 1–2 cm/year contribute to frequent and sometimes destructive earthquakes (**Argus and Gordon, 1991; DeMets et al., 2010; Pasari et al., 2021a**). Historically significant events include the 1994 Banyuwangi earthquake (Mw 7.8) (**Abercrombie et al., 2001; Polet and Kanamori, 2000**), the 2006 Pangandaran earthquake (Mw 7.8) (**Kato et al., 2007; Ammon et al., 2006; Fujii and Satake, 2006**), the 2006 Yogyakarta earthquake (Mw 6.0) (**Saputra et al., 2021; Walter et al., 2008**), and the recent 2020 Jepara earthquake (Mw 6.0). The Jepara earthquake, occurring at a depth of 560 km, ranks as one of the largest deep earthquakes in the past decade, with its effects felt across Java (MMI IV–V) and extending to Sumatra, South Bali, and Lombok (MMI II–IV).

Deep earthquakes represent a complex geophysical phenomenon requiring detailed investigation. According to BMKG records, only 3% of earthquakes in the last decade were categorized as deep-focus events (see **Figure 1**). Tectonically, these earthquakes occur within subducting slabs, resembling shallow earthquakes superficially but differing significantly in their mechanisms (**Li et al., 2018; Zhan, 2020**). The deep hypocenters amplify seismic wave propagation, leading to pronounced shaking at distant locations, as observed in the 1998 Mexico earthquake (Mw 7.8) (**Ramírez-Herrera and Orozco, 2002; Tibi et al., 2003**). Deep earthquakes originate in dense, old oceanic slabs, which slow wave attenuation while enhancing wave propagation (**Tibi et al., 2003; Wu and Takeo, 2004**). These events can cause signifi-

* Corresponding author: Tio Azhar Prakoso Setiadi
e-mail address: tio.prakoso08@gmail.com
Received: 23 December 2024. Accepted: 24 April 2025.
Available online: 21 October 2025

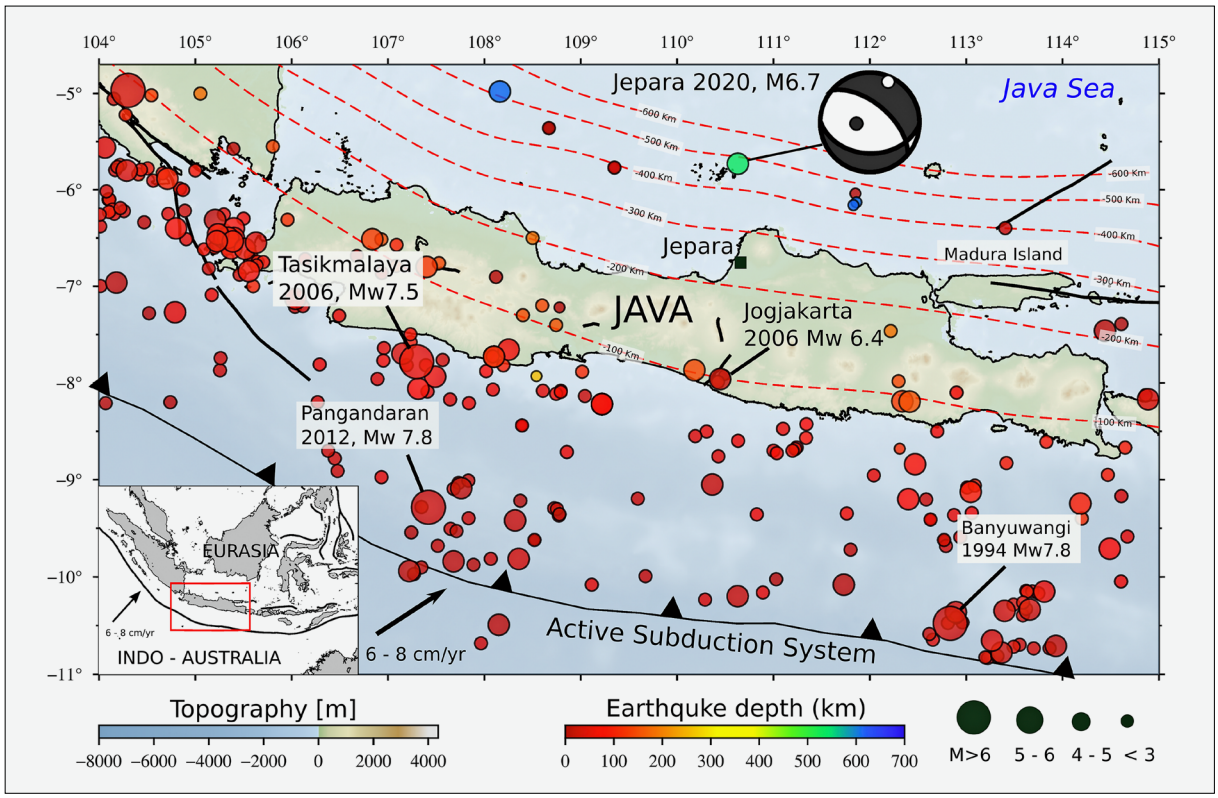


Figure 1. The seismicity and tectonic map of Java Island shows the distribution of felt earthquakes over the last 50 years. Notable strong and destructive earthquakes that occurred in the Java region include the Bantul 2006 M 5.9, Pangandaran 2006 M 7.7, Tasikmalaya 2009 M 7.0 and 2017 M 6.9, Lebak 2018 M 6.1, Banten 2019 M 6.9, Jepara 2020 M 6.7, and Malang 2021 M 6.1 earthquakes. The tectonics of Java Island are controlled by the subduction activity of the Indo-Australian Plate, subducting the Eurasian Plate at 6-8 cm/yr. Several active faults on Java Island, such as the Cimandiri, Lembang, Baribis, Kendeng, and Opak faults, also influence the island's seismicity. (Source: Fault data obtained from Pusgen 2017, Bathymetry from BATNAS BIG, and seismicity from the International Seismic Centre).

cant damage in distant regions, particularly in alluvial sediment areas, as exemplified by the 2007 Indramayu earthquake, which caused damage in Sukabumi.

Several studies have been published using full waveform to highlight an unknown active fault in Indonesia such as Tobelo Fault (Simanjuntak et al., 2023), Balantak Fault (**Simanjuntak et al., 2024**), onshore Sumatra backthrust (**Muksin et al., 2023**) and Cianjur Fault (**Supendi et al., 2023**). However, there is lack of studies concerning subduction activities, especially for intermediate and deep-focus earthquakes. **Adi et al. (2024)** studied the possible backthrust system in south-central Java at an intermediate depth while the 2020 Jepara earthquake occured in deep-focus in the northern part of Java. Several destructive earthquakes have produced a significant nowcasting earthquake score for most major cities in Indonesia especially in Java Island (**Pasari et al., 2021b; Pasari et al., 2021c**). Therefore, the 2020 Jepara earthquake raise an important question about the mechanism of deep-focus earthquake and its geodynamic process.

The 2020 Jepara earthquake was accompanied by subsequent events in Rangkasbitung, Enggano, and Pangandaran on the same day. The deep nature of the Jepara earthquake likely triggered these follow-up earthquakes, which were widely felt by residents. This study aims to investigate the characteristics of the 2020 Jepara earthquake through analysis of earthquake catalogs and seismic records. Source mechanism analysis was conducted using automatic moment tensor inversion based on seismic data from stations across Java Island. Additionally, hypocenter relocation, employing travel-time data, was utilized to refine the earthquake locations and delineate the tectonic structure beneath Java. The findings from this study will contribute to understanding deep-focus earthquakes in Java, providing insight for both scientific research and disaster mitigation efforts.

2. Methods

The earthquake data utilized in this study was obtained from analyses conducted by the Meteorology, Climatology, and Geophysics Agency (BMKG). The dataset includes the travel times of seismic phases (P and S) recorded by all seismic stations within a range of 0º–5º latitude and longitude. A total of 1,899 earthquakes spanning a 13-year period (2010–2022) were analyzed. Data selection was based on specific criteria: an azi-

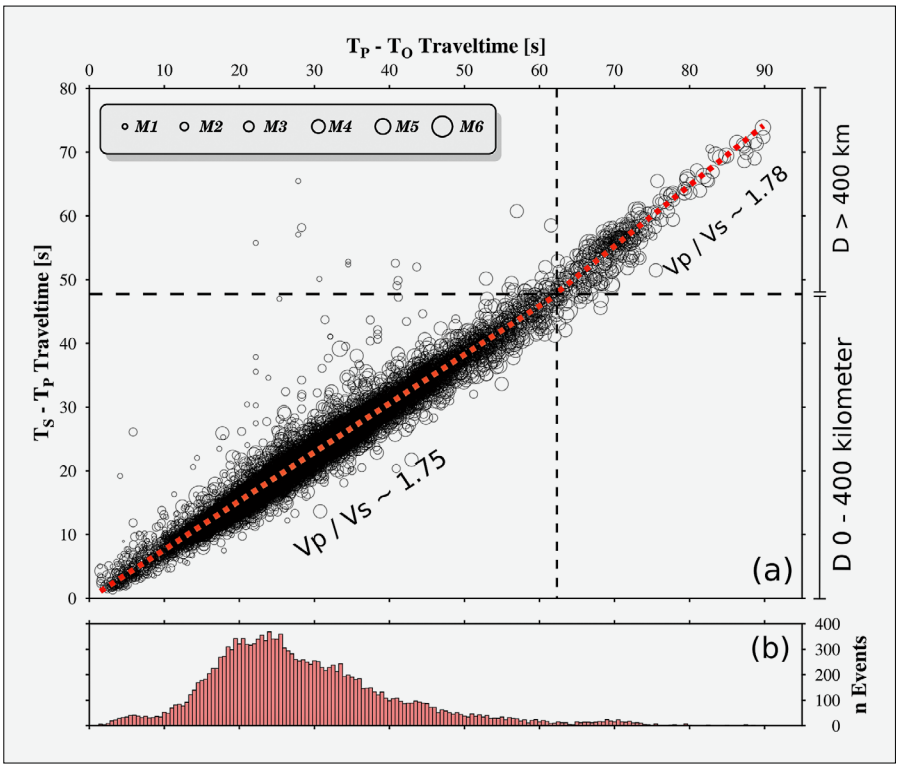


Figure 2. Wadati diagram showing the travel time distribution with two Vp/Vs ratios of 1.75 and 1.78. The highest number of phases is in the travel time range of Tp – To about 20 – 30 seconds with a total of 300 – 400 phases.

muthal gap of less than 200º, a minimum of 5 P-phase observations, 3 S-phase observations, and a depth range of 0–600 km. The travel time distribution revealed a Vp/Vs ratio of 1.75 for distances of 0–400 km and 1.78 for distances exceeding 400 km, as illustrated in **Figure 2**.

The earthquake mechanism was investigated using seismic wave recordings from BMKG stations. Hypocenter information for the Jepara earthquake, which occurred on July 7, 2020, at 05:54:44 WIB, was obtained from the BMKG catalog. The earthquake had an epicenter located at 6.12º S, 110.55º E, with a depth of 578 km and a magnitude of Mw 6.7. Seismic recordings were collected within a time window spanning 10 minutes before and 60 minutes after the event's origin time. These waveform data underwent several preprocessing corrections, including baseline correction to eliminate offsets, removal of instrument response to obtain true ground motion, and the application of a bandpass filter (0.02–0.08 Hz) to suppress low-frequency drift and high-frequency noise. After these corrections, the velocity signals were integrated into displacement for further analysis. To optimize processing time and maintain data quality, waveform data containing significant gaps or low signal-to-noise ratios were excluded from the analysis.

2.1. Moment Tensor Inversion

In this study, we performed an automatic moment tensor inversion on the observed seismic waveforms. These waveforms represent a combination of the earthquake source mechanism and the propagation characteristics of the medium. The moment tensor solution was derived using a weighted least-squares inversion approach, which minimizes the discrepancy between observed and synthetic waveforms (**Tarantola, 2005**).

The inversion process employed full-waveform data to analyze the characteristics of both body and surface waves. Signals with low signal-to-noise ratios (SNR) were excluded using a tapering technique. This technique was applied to a time window twice the duration of the difference in arrival times between the P and S waves (**Sokos and Zahradnik, 2008; Vackář et al., 2017**). An example of this signal tapering process at one of the seismic stations can be seen in **Figure 3**. Moment tensor inversion was performed over a spatial and temporal grid to determine the centroid location and time parameters of the earthquake. The grid model extended within a radius of 10–15 km from the initial hypocenter location, with depth intervals of 5–10 km and a time deviation of ±5 seconds from the origin time. Synthetic signals were generated using a one-dimensional seismic velocity model that integrated the CRUST1.0 model for the crustal layer (**Laske et al., 2013**) and the AK135 model for the mantle layer (**Kennett et al., 1995**).

The quality of the moment tensor solutions was assessed using variance reduction (VR), a metric that quantifies the agreement between observed and synthetic waveforms. Based on VR values, the solutions were categorized into four quality classes: A, B, C, and D. Solutions with VR values of 20% or higher were considered acceptable, while those below 20% (Quality D) were deemed poor and excluded from further analysis. Quality A represented the most reliable centroid moment tensor (CMT) solutions, involving at least four stations

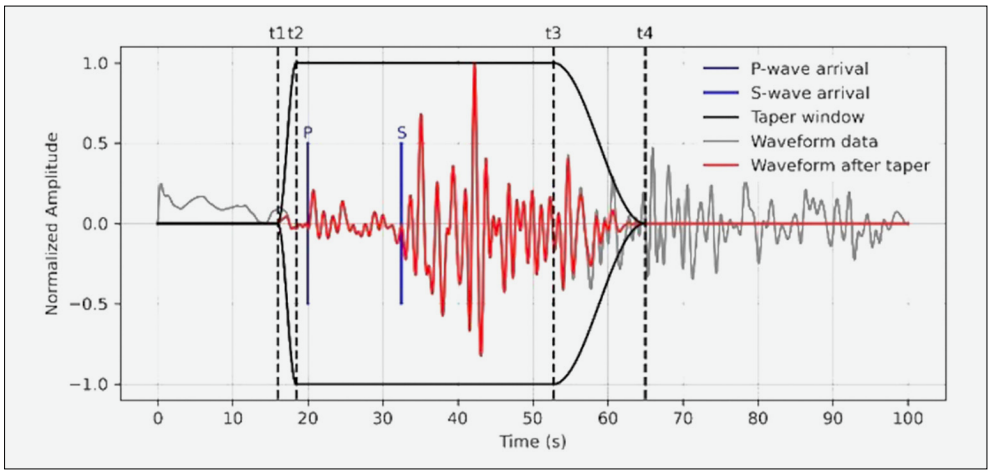


Figure 3. Illustration of signal tapering at one of the stations. The P phase (blue line) arrives at 20 seconds and the difference in S-P time is 12.5 seconds, both within the tapering window used in the moment tensor inversion process.

with a VR of approximately 60%. Quality B included solutions with three stations achieving a VR of 60% or four stations with a VR ranging from 40% to 60%. Quality C encompassed solutions with VR values between 20% and 40%, which were acceptable but less robust compared to Quality A and B.

2.2 Double Difference Relocation

The HypoDD program (**Waldhauser, 2001**) was employed in this study to perform double-difference relocation (**Waldhauser and Ellsworth, 2000**) for determining earthquake hypocenters. This method assumes that when the distance between two earthquake hypocenters is smaller than their distance to the recording station, their ray paths traverse a similar medium. HypoDD minimizes residuals between observed and calculated travel-time differences through an iterative process, refining earthquake locations and updating partial derivatives with each iteration as shown in the schematic cartoon in **Figure 4**.

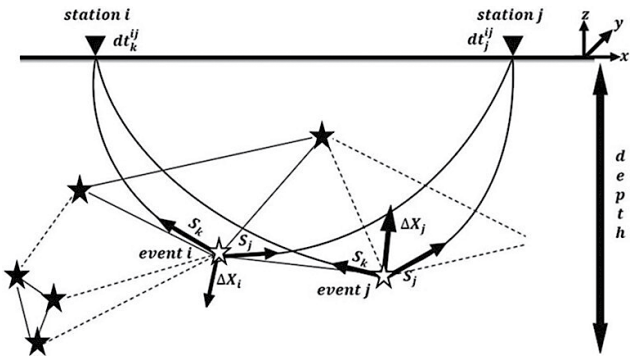


Figure 4. The schematic cartoon of relative relocation using HypoDD shows residuals between observed and calculated travel-time differences through an iterative process, refining earthquake locations and updating partial derivatives with each iteration (modified from **Waldhauser and Ellsworth, 2000**).

This method has been effectively utilized to relocate earthquakes in Indonesia using BMKG data, contributing to more precise earthquake locations and improved tectonic interpretations. Notable applications include studies in Indonesia (**Nugraha et al. 2018; Setiadi et al. 2022**). The relocation results from these studies have significantly advanced the understanding of tectonic structures in the region.

3. Results and Discussions

The automatic moment tensor inversion was successfully conducted using nine seismic sensors out of a total of fifteen. The inversion utilized data from three seismic wave components: vertical (Z), north-south (N), and east-west (E). Seven sensors were excluded from the analysis due to low variance reduction (VR) quality and insufficient signal-to-noise ratio (SNR), which would have resulted in unsatisfactory solutions. Stations SNJI, TPI, and NKBI produced the most reliable solutions, with high VR values and minimal discrepancies between observed and synthetic waveforms. We applied the bandpass filter with range 0.02 – 0.08 Hz that is suitable with most seismic stations used. Example result from SNJI stations shows a good fitting between observation and synthetic waveform as shown in **Figure 5**. The SNJI seismic stations SNJI performs best fitting results than other stations. It can be stated that the synthetic model from Green's function model used are suitable with the geological condition as well as the bandpass frequency range.

Other stations, such as PRJI, BKJI, and BBJI, exhibited overlapping solutions between observations and synthetics, which were attributed to minor mismatches in the Green's function model. Despite this, these three stations provided reasonably good solutions, with VR values exceeding 20%. The moment tensor results yielded two nodal planes with the following parameters: the first nodal plane has a strike of 310º, a dip of 59º, and a rake of -68º, while the second nodal plane has a strike of 92º, a dip of 37º, and a rake of -121º.

The centroid depth was refined to 544 km from the initial estimate of 536 km. The earthquake magnitude derived from the moment tensor inversion was recalculated as Mw 6.7, slightly lower than the previously re-

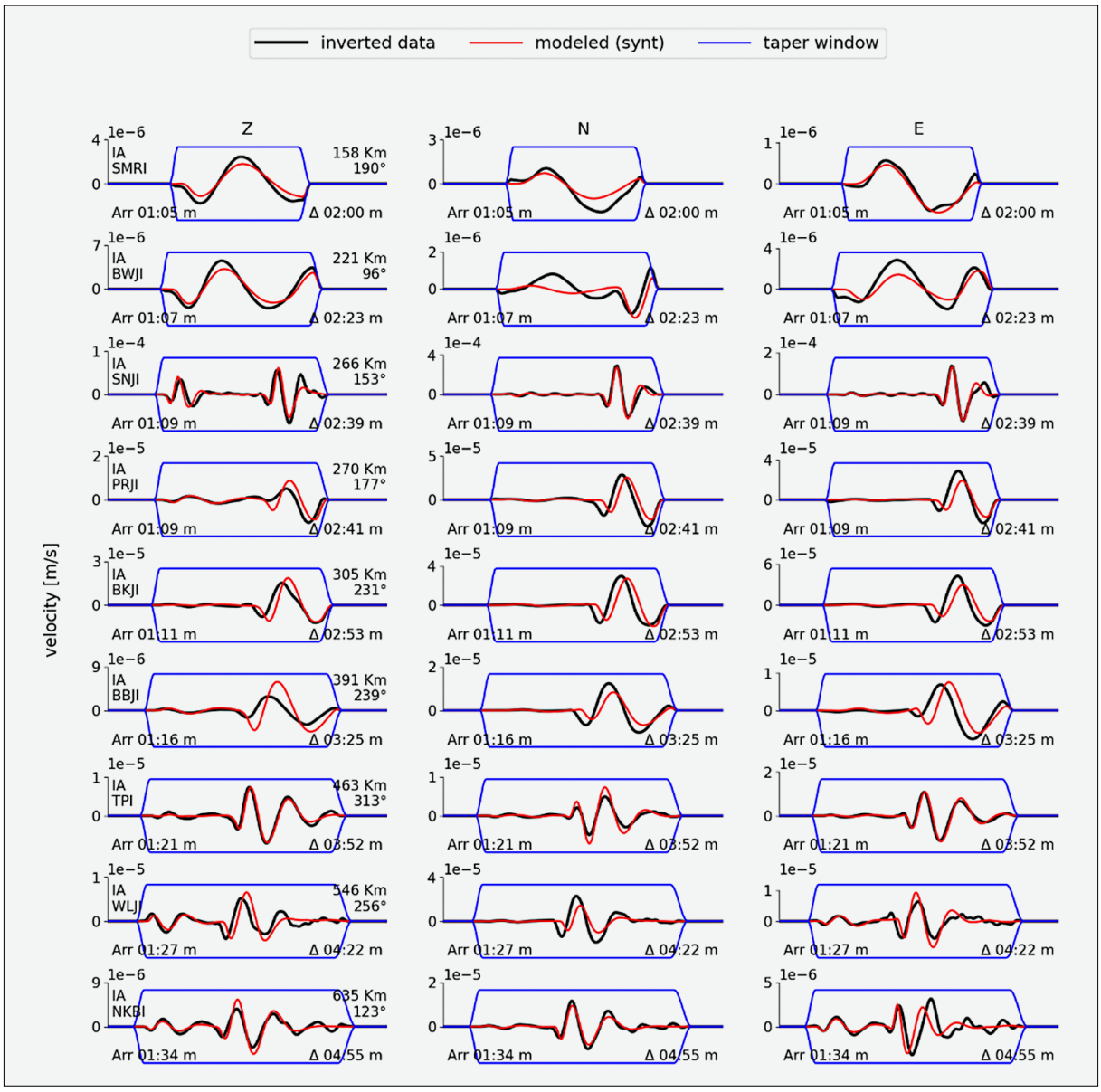


Figure 5. Results of the moment tensor inversion at 9 seismic stations used in this study. The inversion was carried out on the displacement signals on three components (Z, N, E). The black line represents the observed signal while the red line represents the synthetic signal generated through the Green's function model.

ported Mw 6.8. This magnitude was determined using longer wave periods, yielding stable and reliable results. The centroid time was adjusted by 4 seconds, changing from 07:54:46 to 07:54:50, due to the inclusion of all seismic waves from the available sensors. Statistically, the variance reduction (VR) quality of the moment tensor inversion results falls within category A, indicating a reliable centroid moment tensor (CMT) solution. This classification was based on a minimum of four stations achieving a VR value of approximately 60%. The results are consistent with those from other agencies, as shown in **Table 1**. However, the results from this study are considered more accurate due to the utilization of local seismic stations, which provided higher resolution data as shown in **Figure 6**.

The relocation results reveal significant changes in the root mean square (RMS) travel times of hypocenters, as illustrated in **Figure 7**. These adjustments indicate that the new hypocenter locations are more accurate and form distinct clusters that align well with the derived source mechanism solutions. Approximately 85% of the earthquakes were successfully relocated with consistent centroidal nodal depth (CND) solution values ranging from 40 to 80 during each iteration (**Waldhauser and Ellsworth, 2000**).

The relocated hypocenters were integrated with the source mechanism solutions, as shown in **Figure 8a**. To further analyze the distribution, a vertical cross-section was created to illustrate the spatial relationship between the relocated hypocenters and the source mechanisms,

providing insight into the characteristics of the 2020 Jepara earthquake. The vertical section along line A–A' (see **Figure 8b**) highlights the complex tectonic structure of Java Island, including features such as trenches, seamounts, and ocean basins formed by subduction processes. Additionally, the relocation results delineate earthquake clusters within the outer-rise, interface, intraslab, and deep-focus zones (see **Figure 8c**).

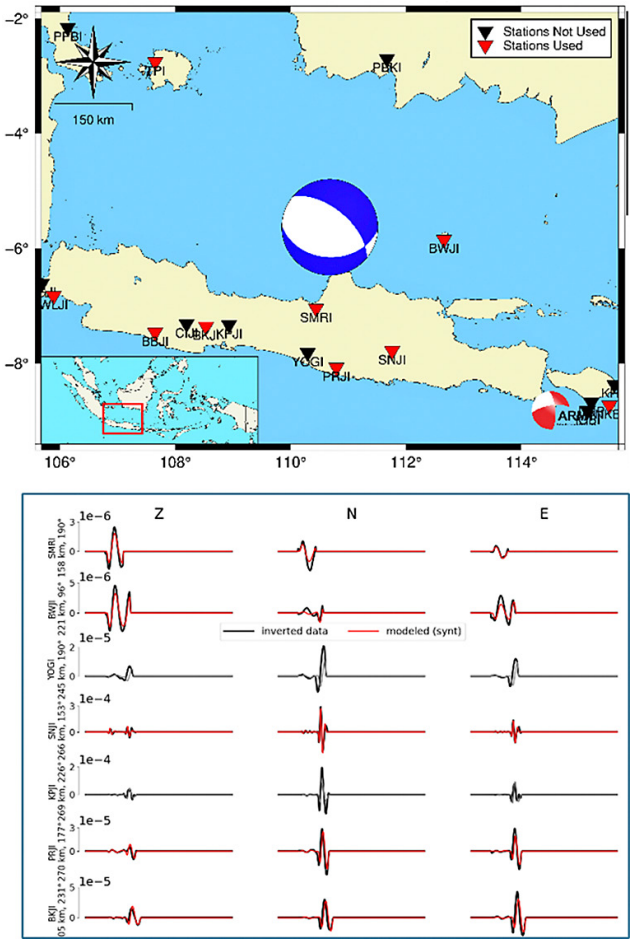


Figure 6. Map of seismic stations used (red triangles) and not used (black triangles), as well as the results of the source mechanism with normal faulting in the east-west strike direction (top panel). An example of waveform inversion results used, with stations showing the comparison of synthetic signals (red lines) used in the inversion, while others are not used due to having low VR (Variance Reduction) (bottom panel).

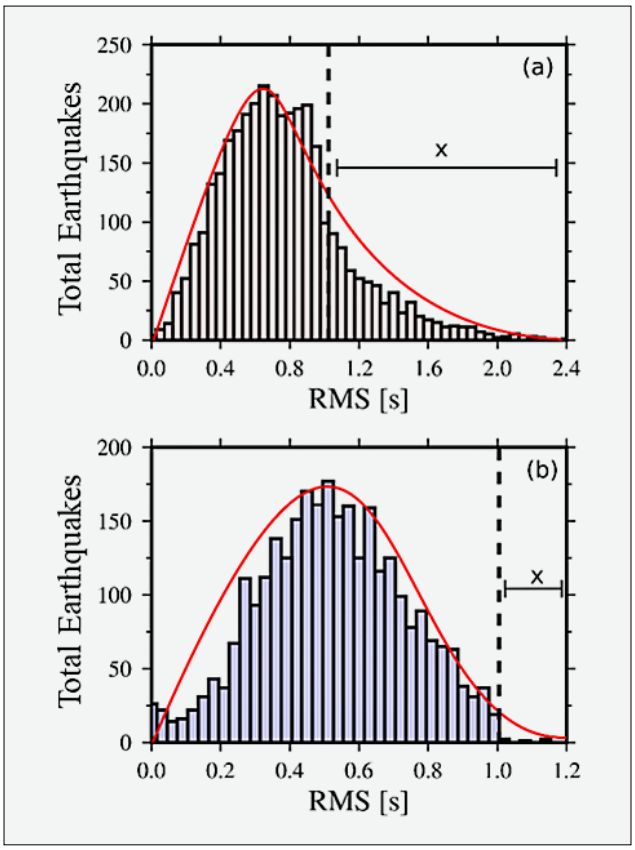


Figure 7. HypoDD relocation results shows the graph before relocation with RMS 0 – 2.4 s (a) and after relocation with most hypocenters with an improved RMS < 1.0 s(b).

Vertical slice profiles reveal key seismic phenomena in Java Island, including locking at the interface zone and low seismicity at depths of 200–500 km. These features are associated with high coupling in the asperities of the Java subduction zone (**Widiyantoro et al., 2020;**

Table 1. Comparison of source mechanism results of the 2022 Malang earthquake between this study and other institutions (seismic moment (Mo) in the table is in units of 10^{19} Nm).

Result from	Nodal Plane	Longitude	Latitude	Magnitude (Mw)	Depth (km)	Seismic Moment (Mo)
USGS	301, 56, -72	110.68	-5.6	6.6	533	1.2
	91, 38, -114					
GFZ	316, 61, -61	110.64	-5.65	6.6	536	1
	86, 39, -131					
IPGP	310, 59, -69	110.67	-5.36	6.8	536	1.7
	97, 37, -121					
GCMT	313, 60, -67	110.69	-5.6	6.7	533	1.3
	92, 37, -124					
This study	310, 59, -68	121.45	-6.1	6.7	536	1.6
	97, 37, -121					

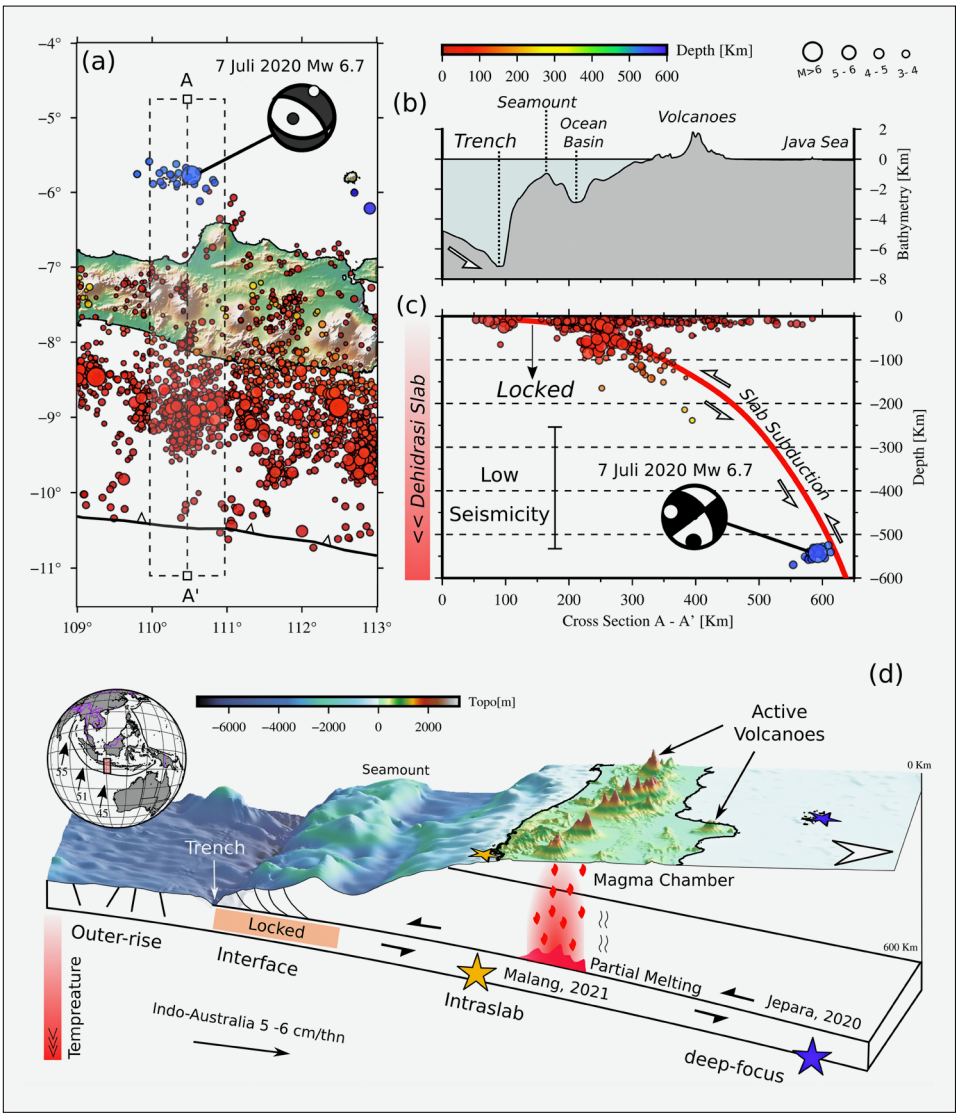


Figure 8. (a) Map showing the relocation results and source mechanisms of the 2020 Jepara earthquake. (b) Geological structures and formations resulting from the subduction process, with the vertical profile section A–A' illustrating the hypocenter distribution at depths of 0–600 km. (c) Low seismicity observed at depths of 200–500 km is associated with increased temperature and pressure leading to slab dehydration. (d) The schematic diagram explains the subduction tectonics of Java Island, highlighting seismic activity in the outer-rise, interface, intraslab, and deep-focus zones. Geological formations such as trenches, seamounts, and accretionary prisms, along with the distribution of volcanoes across Java Island, are shown. Examples of significant earthquakes include the 2021 Malang Mw 6.4 earthquake in the intraslab zone and the 2020 Jepara Mw 6.7 deep-focus earthquake occurring above the mantle.

Zhan, 2020). Geodetic strain rate analysis further confirms high coupling in southern Java (**Hanifa et al., 2014**). The Jepara earthquake occurred within the interior of the oceanic slab, driven by processes such as dehydration and serpentinization, which are linked to a decrease in slab density (**Widiyantoro et al., 2020; Ribeiro, 2022**). Slab dehydration in the Java subduction zone may facilitate seawater infiltration into the oceanic plate, creating conditions favourable for deep-focus earthquakes. From a seismic perspective, nearly all deep-focus earthquakes exhibit a significant compensated linear vector dipole (CLVD) component (**Sandanbata et al, 2021**). This characteristic is often associated with brittle deformation within the slab, despite the high-pressure and high-temperature environment (**Widiyantoro et al., 2020**).

The change in fault mechanisms reflects instability in shear forces (**Chen and Wen, 2015**). This phenomenon is attributed to the polymorphic phase transition of olivine to spinel under deviatoric pressure within the interior of the oceanic plate. This mineralogical transformation marks the transition from the upper mantle (dominated by olivine) to the mantle transition zone (characterized by spinel), occurring at depths of 410–660 km (**Zhan, 2020; Ishii et al., 2021**). As a result, fault mechanisms can transform from a thrust faulting mechanism to normal or strike-slip faulting within the mantle transition zone (**Chen and Wen, 2015; Zhou et al, 2022**). This fault transformation generates structural variations in the mantle transition zone beneath Java Island, leading to distinct seismic source mechanisms at different depths.

4. Conclusions

We successfully highlighted and characterized the July 07, 2020 Jepara earthquake with analyses using moment tensor inversion and hypocenter double-difference relocation. The full-waveform inversion provides an adequate result for all seismic stations used with an error of ~0.5s and a variance reduction of ~60%. The inversion results provide a final magnitude moment at Mw 6.7 at

centroid depth of 544 km and focal mechanism parameter with two nodal planes, the first one with a strike of 310º, a dip of 59º, and a rake of -68º, while the second one has a strike of 92º, a dip of 37º, and a rake of -121º. Furthermore, approximately 85% of the hypocenters were successfully relocated, forming distinct spatial clusters that align with the source mechanism and slab structure of the 2020 Jepara earthquake. Combined analysis of the moment tensor inversion and hypocenter relocation successfully reveals the geometry of the subducting slab and clarifies the position and mechanism of the 2020 Jepara deep-focus earthquake beneath Java Island. The observed normal faulting is likely related to the transition zone, indicating a change in rupture mechanism at depth. These findings enrich tectonic understanding and provide insight for future seismic hazard mitigation in northern Java.

Acknowledgement

We extend our deepest gratitude to the Indonesian Agency for Meteorology, Climatology, and Geophysics (BMKG) for the seismic waveform and hypocentre data and the National Research and Innovation Agency (BRIN) for their outstanding support and contributions to this research. Without the support and facilities provided by BMKG and BRIN, this research would not have been possible. We thank Geophysical Station Office of Karang Panjang, Ambon for letting us to use a well-established program called Automatic Regional Moment Tensor (ARMT). All figures were generated by Generic Mapping Tools (GMT) v.6 (Wessel et al., 2019) and some figures were illustrated with Inkscape v.10.

5. References

Adi, S.P.; Simanjuntak, A.V.H.; Supendi, P.; et al. (2024). Different faulting of the 2023 (Mw 5.7 and 5.9) South-Central Java earthquakes in the backthrust fault system. Geotechnical and Geological Engineering, 42: 3123–3135. 10.1007/s10706-023-02720-1

Argus, D.F.; Gordon, R.G. (1991). No-net-rotation model of current plate velocities incorporating plate motion model NUVEL-1. Geophysical Research Letters, 18: 2039–2042. 10.1029/91GL01532

Asnawi, Y.; Simanjuntak, A.; Muksin, U.; Okubo, M.; Putri, S.I.; Rizal, S.; Syukri, M. (2022). Soil classification in a seismically active environment based on shear wave velocity and HVSR data. Global Journal of Environmental Science and Management, 8(3): 297–314. 10.22034/gjesm.2022.03.01

Chen, Y.; Wen, L. (2015). Global large deep-focus earthquakes: Source process and cascading failure of shear instability as a unified physical mechanism. Earth and Planetary Science Letters, 423: 134–144. 10.1016/j.epsl.2015.04.031

DeMets, C.; Gordon, R.G.; Argus, D.F. (2010). Geologically current plate motions. Geophysical Journal International, 181: 1–80. 10.1111/j.1365-246X.2009.04491.x

Gunawan, E.; Widiyantoro, S. (2019). Active tectonic deformation in Java, Indonesia inferred from a GPS-derived strain rate. Journal of Geodynamics, 123: 49–54. 10.1016/j.jog.2019.01.004

Halauwet, Y.; Afnimar; Triyoso, W.; Vackář, J.; Daryono, D.; Supendi, P.; Hakim, M.L. (2024). A new automated procedure to obtain reliable moment tensor solutions of small to moderate earthquakes ($3.0 \leq M \leq 5.5$) in the Bayesian framework. Geophysical Journal International, 239(2): 1000–1020. 10.1093/gji/ggae309

Hanifa, N.R.; Sagiya, T.; Kimata, F.; Efendi, J.; Abidin, H.Z.; Meilano, I. (2014). Interplate coupling model off the southwestern coast of Java, Indonesia, based on continuous GPS data in 2008–2010. Earth and Planetary Science Letters, 401: 159–171. 10.1016/j.epsl.2014.06.010

Ishii, T.; Ohtani, E. (2021). Dry metastable olivine and slab deformation in a wet subducting slab. Nature Geoscience, 14: 526–530. 10.1038/s41561-021-00756-7

Kennett, B.L.; Engdahl, E.R.; Buland, R. (1995). Constraints on seismic velocities in the Earth from traveltimes. Geophysical Journal International, 122: 108–124. 10.1111/j.1365-246X.1995.tb03540.x

Laske, G.; Masters, G.; Ma, Z.; Pasyanos, M. (2013). Update on Crust 1.0: A 1-degree global model of Earth's crust. Geophysical Research. 10.17611/DP/17992676

Li, J.; Zheng, Y.; Thomsen, L.; Lapen, T.J.; Fang, X. (2018). Deep earthquakes in subducting slabs hosted in highly anisotropic rock fabric. Nature Geoscience, 11: 696–700. 10.1038/s41561-018-0188-3

Muksin, U.; Arifullah, A.; Simanjuntak, A.V.; Asra, N.; Muzli, M.; Wei, S.; Okubo, M. (2023). Secondary fault system in Northern Sumatra, evidenced by recent seismicity and geomorphic structure. Journal of Asian Earth Sciences, 245: 105557. 10.1016/j.jseaes.2023.105557

Nugraha, A.D.; Shiddiqi, H.A.; Widiyantoro, S.; Thurber, C.H.; Pesicek, J.D.; Zhang, H.; Wiyono, S.H.; Ramadhan, M.; Wandano; Irsyam, M. (2017). Hypocenter relocation along the Sunda arc in Indonesia, using a 3D seismic velocity model. Seismological Research Letters. 10.1785/0220170107

Pasari, S.; Simanjuntak, A.V.H.; Mehta, A.; et al. (2021a). A synoptic view of the natural time distribution and contemporary earthquake hazards in Sumatra, Indonesia. Natural Hazards, 108: 309–321. 10.1007/s11069-021-04682-0

Pasari, S.; Simanjuntak, A.V.; Mehta, A.; Sharma, Y. (2021b). The current state of earthquake potential on Java Island, Indonesia. Pure and Applied Geophysics, 178: 2789–2806. 10.1007/s00024-021-02781-4

Pasari, S.; Simanjuntak, A.V.H.; Neha; et al. (2021c). Nowcasting earthquakes in Sulawesi Island, Indonesia. Geoscience Letters, 8: 27. 10.1186/s40562-021-00197-5

Polet, J.; Kanamori, H. (2000). Shallow subduction zone earthquakes and their tsunamigenic potential. Geophysical Journal International, 142: 684–702. 10.1046/j.1365-246x.2000.00205.x

Ramírez-Herrera, M.T.; Orozco, J.J.Z. (2002). Coastal uplift and mortality of coralline algae caused by a 6.3 Mw earthquake, Oaxaca, Mexico. Journal of Coastal Research, 18: 75–81.

Ribeiro, J.M. (2022). Slab dehydration beneath forearcs: Insights from the southern Mariana and Matthew-Hunter rifts. Geochemical Perspectives Letters, 20: 22–26. 10.7185/geochemlet.2203

Sandanbata, O.; Kanamori, H.; Rivera, L.; Zhan, Z.; Watada, S.; Satake, K. (2021). Moment tensors of ring-faulting at active volcanoes: Insights into vertical-CLVD earthquakes at the Sierra Negra Caldera, Galápagos Islands. Journal of Geophysical Research: Solid Earth, 126(6). 10.1029/2021JB021693

Saputra, H.; Wahyudi, W.; Suardi, I.; Anggraini, A.; Suryanto, W. (2021). The waveform inversion of mainshock and aftershock data of the 2006 M6.3 Yogyakarta earthquake. Geoscience Letters, 8(1): 9. 10.1186/s40562-021-00176-w

Setiadi, T.A.P.; Daud, Y.; Martha, A.A.; Rohadi, S. (2022). Earthquake relocation using the double difference teleseismic method in the Java region. Jurnal Meteorologi dan Geofisika, 23(1): 23–27. 10.31172/jmg.v23i1.842

Simanjuntak, A.V.; Palgunadi, K.H.; Supendi, P.; Daryono, D.; Prakoso, T.A.; Muksin, U. (2023). New insight on the active fault system in the Halmahera volcanic arc, Indonesia, derived from the 2022 Tobelo earthquakes. Seismological Research Letters, 94(6): 2586–2594. 10.1785/0220230006

Simanjuntak, A.V.H.; Ansari, K. (2024). Multivariate hypocenter clustering and source mechanism of 2017 Mw 6.2 and 2019 Mw 6.5 in the South Seram Subduction System. Geotechnical and Geological Engineering, 42: 4303–4316. 10.1007/s10706-024-02780-x

Simanjuntak, A.V.H.; Palgunadi, K.H.; Supendi, P.; et al. (2024). The western extension of the Balantak Fault revealed by the 2021 earthquake cascade in the central arm of Sulawesi, Indonesia. Geoscience Letters, 11: 35. 10.1186/s40562-024-00353-7

Supendi, P.; Winder, T.; Rawlinson, N.; Bacon, C.A.; Palgunadi, K.H.; Simanjuntak, A.; Jatnika, J. (2023). A conjugate fault revealed by the destructive Mw 5.6 (November 21, 2022) Cianjur earthquake, West Java, Indonesia. Journal of Asian Earth Sciences, 257: 105830. 10.1016/j.jseaes.2023.105830

Tarantola, A. (2005). Inverse problem theory and methods for model parameter estimation. Society for Industrial and Applied Mathematics. 10.1137/1.9780898717921

Tibi, R.; Wiens, D.A.; Inoue, H. (2003). Remote triggering of deep earthquakes in the 2002 Tonga sequences. Nature, 424: 921–925. 10.1038/nature01903

Vackář, J.; Burjánek, J.; Gallovič, F.; Zahradník, J.; Clinton, J. (2017). Bayesian ISOLA: New tool for automated centroid moment tensor inversion. Geophysical Journal International, 210: 693–705. 10.1093/gji/ggx158

Waldhauser, F.; Ellsworth, W.L. (2000). A double-difference earthquake location algorithm: Method and application to the Northern Hayward Fault, California. Bulletin of the Seismological Society of America, 90: 1353–1368. 10.1785/0120000006

Waldhauser, F. (2001). HypoDD – A program to compute double-difference hypocenter locations. US Geological Survey.

Walter, T.R.; Wang, R.; Luehr, B.-G.; Wassermann, J.; Behr, Y.; Parolai, S.; Anggraini, A.; Günther, E.; Sobiesiak, M.; Grosser, H.; Wetzel, H.-U.; Milkereit, C.; Sri Brotopuspito, P.J.K.; Harjadi, P.; Zschau, J. (2008). The 26 May 2006 magnitude 6.4 Yogyakarta earthquake south of Mt. Merapi volcano: Did lahar deposits amplify ground shaking and thus lead to the disaster? Geochemistry, Geophysics, Geosystems, 9(5): Q05006. 10.1029/2007GC001810

Wessel, P.; Luis, J.F.; Uieda, L.A.; Scharroo, R.; Wobbe, F.; Smith, W.H.; Tian, D. (2019). The generic mapping tools version 6. Geochemistry, Geophysics, Geosystems, 20(11): 5556–5564. 10.1029/2019GC008515

Widiyantoro, S.; Gunawan, E.; Muhari, A.; Rawlinson, N.; Mori, J.; Hanifa, N.R.; et al. (2020). Implications for megathrust earthquakes and tsunamis from seismic gaps south of Java, Indonesia. Scientific Reports, 10: 1–11. 10.1038/s41598-020-72142-z

Wu, C.; Takeo, M. (2004). An intermediate deep earthquake rupturing on a dip-bending fault: Waveform analysis of the 2003 Miyagi-ken Oki earthquake. Geophysical Research Letters, 31. 10.1029/2004GL021228

Zhan, Z. (2020). Mechanisms and implications of deep earthquakes. Annual Review of Earth and Planetary Sciences, 48: 147–174. 10.1146/annurev-earth-053018-060314

Zhou, W.-Y.; Hao, M.; Zhang, J.S.; Chen, B.; Wang, R.; Schmandt, B. (2022). Constraining composition and temperature variations in the mantle transition zone. Nature Communications, 13: Article 1094. 10.1038/s41467-022-28795-7

SAŽETAK

Otkrivanje dinamike dubokih potresa: opažanja događaja Mw 6,7 u Jepari 2020. i procesa subdukcije ispod Jave

Potres koji se dogodio u Jepari 2020. godine (Mw 6,7) važan je duboki seizmički događaj zbog subdukcije indijsko-australske ploče ispod otoka Jave. Ova studija istražuje njegove karakteristike korištenjem automatske inverzije momenta tenzora i relokacija metodom dvostrukih razlika na temelju seizmičkih podataka Agencije za meteorologiju, klimatologiju i geofiziku (BMKG). Analizirano je ukupno 1899 potresa zabilježenih između 2010. i 2022. godine, s fokusom na događaje koji su se dogodili na dubini do 600 km. Analiza tenzora momenta otkrila je normalno rasjedanje s dvjema nodalnim ravninama: prva s pružanjem od 310º, nagibom od 59º i kutom otklona od –68º, a druga s pružanjem od 92º, nagibom od 37º i kutom otklona od –121º. Dubina centroida određena je na 544 km, dok je smanjenje varijance (VR) premašilo 60 %, što rezultate klasificira kao visokokvalitetne (kategorija A). Otprilike 85 % hipocentara uspješno je relocirano, te je srednja kvadratna vrijednost (RMS) vremena putovanja vala poboljšana na manje od 1 sekunde. Potres je povezan s dehidratacijom tektonske ploče i polimorfnim faznim prijelazom olivina u spinel pod visokim tlakom i temperaturom. Ti procesi doprinose promjenama u žarišnim mehanizmima potresa i strukturnim varijacijama prijelazne zone plašta. Rezultati poboljšavaju razumijevanje dinamike dubokih potresa ispod Jave i mogu znatno doprinijeti ublažavanju učinaka budućih potresa u Indoneziji.

Ključne riječi:
otok Java, duboki potresi, inverzija momenta tenzora, relokacija metodom dvostruke razlike, dehidratacija tektonske ploče

Author's contribution

Tio Azhar Prakoso Setiadi (Lead researcher, MSc, Geophysicist) designed the study, lead the research, conducted hypocenter analysis, and prepared the initial manuscript draft. **Anne Maria Magdalena Sirait** (Principal investigator, PhD, Geophysicist) provided methodological guidance, finalized all results, visualization and reviewed the final manuscript. **Yehezkiel Halauwet** (Research associate, MSc, Geophysicist) performed the moment tensor analysis and assisted in refining the discussion. **Andrean V. H. Simanjuntak** (Principal investigator, PhD, Geophysicist) collected the data, performed the preliminary analysis, visualization and ensured the accuracy and scientific rigor of the manuscript. **Adi Susilo** (Principal investigator, Prof, Geophysicist) supervised and funded the research, reviewed the final manuscript, and ensured the accuracy and scientific rigor of the manuscript.
All authors have read and agreed to the published version of the manuscript.

RGNZ/MGPB

An investigation on the potential recovery of copper from a low-grade copper resource containing high silica content

Rudarsko-geološko-naftni zbornik
(The Mining-Geology-Petroleum Engineering Bulletin)
DOI: 10.17794/rgn.2025.5.6

Original scientific paper

Milad Abbassi[1], Asghar Azizi[1]*
[1] *Faculty of Mining, Petroleum & Geophysics Engineering, Shahrood University of Technology, Postal code: 3619995161, Shahrood, Iran.*

Abstract
The present research aimed to experimentally peruse the tank leaching of copper from a low-grade ore containing 0.57% Cu, 24.69% Si, and 10.367% Fe. To this end, firstly, the behaviour of important variables influencing the dissolution process was examined using the one factor at a time (OFAT) method and response surface modelling (RSM), and then the leaching kinetics was scrutinized to obtain further recognition of the leaching operations. The findings derived from the OFAT technique demonstrated that the particle size of 0-2 mm was a better choice for the tank leaching relative to other fractions. The presence of clay compounds in the ore led to a high increase in acid consumption. The leaching rate improved with an increase in the solid percentage from 20 to 40% and then decreased with a further increase due to lack of proper mixing. Additionally, the pulp stirring speed had a little effect on the dissolution of copper, confirming that the mixing rate of pulp should be at a level that suspends the particles and prevents them from settling. Then, the RSM was utilized to model and optimize the process and determine the possible interaction between operating parameters. The results showed that copper leaching was significantly dependent on the interaction between the factors. The optimized amounts of parameters were found to be 90 kg/t acid concentration, 35% solid content, 150 rpm pulp mixing rate, 2.5 h leaching time, and 0-2 mm size range. The kinetic analysis showed that the diffusion model through the production layer with an activation energy of 14.15 kJ/mol was the rate-controlling stage of the reaction, and based on that, a new model describing the dissolution kinetics of copper was proposed.

Keywords:
copper oxide, tank leaching, extraction efficiency, optimization, dissolution kinetics

1. Introduction

Copper is one of the most important and widely used industrial metals worldwide after iron and aluminum. Many industries have direct or indirect dependence on this strategic metal due to its unique features, like high thermal and electrical conductivity, alloying ability, ductility, malleability, and resistance to corrosion (**Nozari and Azizi, 2020; Hosseinzadeh et al., 2021**). The widespread use of copper means that it is directly affected by global economic conditions, and any minor changes in the economic statistics can lead to fluctuations in its price. In nature, copper can combine with almost every element in the periodic table, forming various minerals such as oxides, sulfides, carbonates, silicates, hydroxides, chlorides, sulfates, and phosphates. Copper resources are mainly detected in the form of sulfides and oxides, such as chalcopyrite ($CuFeS_2$), bornite ($CuFeS_4$), chalcocite (Cu_2S), covellite ($Cu(OH)_2$), malachite ($Cu(OH)_2$), and azurite ($Cu_3(CO_3)_2(OH)_2$) (**Habashi, 1999; Azizi et al., 2018; Nozhati and Azizi, 2020**). More than 80% of the world's primary copper resources exist in the form of sulfides, which are treated by the flotation process and then concentrated by conventional pyrometallurgical methods (**Davenport and King, 2002; Hosseinzadeh et al., 2021**). Whereas, the oxide resources are mostly processed by hydrometallurgical techniques, including acid leaching followed by solvent extraction and electrowinning (SX-EW) methods. It is accepted that approximately 20% of copper produced worldwide is processed by hydrometallurgical methods (**Hosseinzadeh et al., 2021**). Recent surveys show that the trend of the copper production industry is increasingly moving towards hydrometallurgical methods and low-grade reserve processing. **Ahmed et al. (2016)** reported that zinc (95%) and copper (99%) could be efficiently leached from brass slag by H_2SO_4. Additionally, the leaching kinetics followed a shrinking core model with surface chemical reaction as the rate-controlling step. **Tanda et al. (2017)** investigated the leaching behaviour of copper oxide minerals in an alkaline glycine liquor and reported that under optimal conditions after 24 hours, nearly 95.0%, 91.0%, 83.8%, and 17.4% of

* Corresponding author: Asghar Azizi
e-mail address: azizi.asghar22@yahoo.com, aazizi@shahroodut.ac.ir
Received: 5 March 2025. Accepted: 7 May 2025.
Available online: 21 October 2025

copper were recovered from azurite, malachite, cuprite, and chrysocolla, respectively. **Bai et al. (2018)** perused the optimization and the kinetics of copper leaching from a low-grade cuprite ore. Their findings indicated that approximately 92.5% copper was extracted using 150 g/dm³ sulfuric acid at the particle size of 0.125-0.074 mm, reaction temperature of 353 K, and 180 min leaching time. **Nozari and Azizi (2020)** experimentally examined the dissolution kinetics of copper from a mixed oxide-sulfide copper ore in Iran. The results showed that above 88% copper was recovered at optimal values of operating parameters: 17% H_2SO_4 dosage, 11.3 ml/g solid/liquid ratio, 390 rpm pulp mixing rate, 50°C temperature, and 60 minutes dissolution time. **Apua and Madiba (2021)** investigated the leaching kinetics for the extraction of different elements (copper, cobalt, and iron) from a copper oxide ore in H_2SO_4 solution. Their results demonstrated that approximately over 97% copper could be recovered by sulfuric acid at 70°C, pH 1 after 60 min. Also, the mechanism controlling the leaching kinetics was a mixed model including diffusion and chemical reaction. **Tanaydin et al. (2022)** surveyed the leaching behaviour of malachite in HNO_3 solution in two stages. Optimal leaching conditions were determined using 0.5 M nitric acid concentration, 50°C temperature, a solid-to-liquid ratio of 0.004 g/ml, and an agitation speed of 500 rpm. Under optimal conditions, the leaching rate was 99% after 120 minutes of reaction time. **Mohanraj et al. (2022)** studied the characteristics and recovery of copper from a low-grade copper ore using the hydrometallurgy method, reporting that approximately 95% of copper could be recovered using 0.5 M sulfuric acid and 30% H_2O_2 under conditions of 300 rpm stirring speed, 53-63 microns particle size, a liquid-to-solid ratio of 20:2, and a leaching time of 30 minutes (**Mohanraj et al., 2022**). **Yang et al. (2023)** investigated cuprite leaching with ozone as an oxidant in H_2SO_4 solution and its oxidation dissolution process. Leaching test results showed that the leaching efficiency of cuprite promoted by 43.24% with increasing ozone when temperature, H_2SO_4 concentration, and stirring rate were kept constant at 50°C, 0.014 M, and 800 rpm, respectively. **Sun et al. (2023)** examined the improvement of the leaching operations of copper in sulfuric acid solution using oxygen and ultrasound, showing that with ultrasonic application, the copper dissolution rate increased to 7.52 g/h/L, 1.83 times more than without ultrasound (4.109 g/h/L). Following this, **Pan et al. (2024)** studied the process mineralogy and the leaching of Yulong copper oxide ore in Tibet with sulfuric acid and calcium fluoride. Their findings revealed that the dissolution rate of copper promoted to 60.57% (7.34% more than atmospheric pressure leaching) using 50 g/L H_2SO_4 and CaF_2 with the magnitude of 1% of the ore mass at 0.074 mm (85%) particle size, 1:4 liquid/solid ratio, 30°C temperature, and 4 h dissolution time. Recently, **Hu et al. (2025)** investigated the copper extraction from a low-grade copper oxide ore containing high silicon and proposed an alkali-dissolving desilication method, followed by ammonia leaching for efficient recovery of copper.

In general, the literature shows that sulfuric acid is the most commonly used leaching reagent due to its economic efficiency and higher dissolution rate compared to other leaching agents. Although numerous studies have been conducted on copper recovery from oxide resources, few studies have focused on the leaching of low-grade ores, espicially resources containing high silica and their kinetic modelling. The presence of silicate minerals makes the copper ore relatively resistant to the leaching process. **Toro et al. (2021)** reviewed the role of silicates and clay minerals in a copper heap leaching process and demonstrated that these minerals are a rate-limiting parameter in the leaching processes. The effect of silicate and clay minerals on the overall leaching agent consumption may be even greater than the presence of carbonates in ore. Additionally, the presence of silicate and clay compounds in fine particle size may result in the risk of silica gel formation due to the reaction between leaching lixiviant (sulfuric acid) and silicate owing to the easy polymerization of silica in solution. Thus this study was aimed to assess the facility of dissolving a low-grade copper oxide source with high silica content. On the other hand, given that the optimal conditions for copper recovery vary significantly from one ore to another due to the complexity of mineralogy, the important parameters affecting the leaching process of copper are assessed and optimized. Additionally, the leaching kinetics as a powerful tool and one of the significant aspects of separation techniques was scrutinized to deepen understanding of the dissolution process.

2. Material and methods

2.1. Materials

The studied sample (about 150 kg) was collected from the Kuh Khairy mine, Iran. The received sample was then subjected to preparation operations. The sample was firstly crushed using a jaw crusher (Fritsch 01.703, Fritsch, Idar-Oberstein, Germany), and then by a cone crusher to attain particles smaller than 4 mm in diameter. After mixing and dividing the sample into four parts, half of the sample was coded, packaged, and archived, and then the other half was homogenized and ground in a ball mill so that above 90% of particles were smaller than 2 mm in diameter. After that, the sample was remixed and homogenized and then split by means of cones and riffles to obtain a representative sample. Finally, the chemical composition of the representative sample was identified using x-ray fluorescence spectrometer (Philips PW1480 x-ray spectrometer, Netherlands) as shown in **Table 1**. As can be seen in **Table 1**, the studied sample contains high levels of silicate and

clay components, and the copper content in the sample is about 0.57%. The content of Si (0.467×52.88= 24.69) and Fe (0.7×14.81= 10.367) is also found to be 26.69, and 10.367%, respectively. In addition, the representative sample (less than 2 mm in diameter) was analyzed by an atomic absorption spectrometer (Thermo Elemental's SOLAAR S Series, Waltham, MA, USA), and the copper content was found to be ~0.54%.

Table 1. Chemical compositions of the studied representative sample

Component	Content (%)	Component	Content (%)
Si	24.69	Mn	0.18
Fe	10.37	Zn	0.03
Al	6.80	Na	0.59
Cu	0.57	K	0.66
Ca	2.65	Cr	0.03
Mg	2.56	Ba	0.02
Ti	0.42	Sr	0.02

2.2. Leaching experiments

Leaching tests were conducted on the prepared representative sample in 1 L beakers using a mechanical stirrer with adjustable stirring speeds. For each leaching test, initially, a sulfuric acid solution was prepared at a predetermined concentration. Then, 200 g of the representative sample along with a specified volume of the sulfuric acid solution based on the desired solid percentage was transferred into the beaker. After adjusting the

Table 2. The experimental conditions for performing the leaching tests using RSM-CCD strategy and the determined values of recovery and the content of copper leached

Factor	Factorial levels			Star point α = 2.0		
	Low (-)	Center (0)	High (+)	-2	+2	
(A) Acid concentration (kg/t)	70	80	90	60	100	
(B) Solid percent (%)	25	30	35	20	40	
(C) Leaching time (h)	1.5	2	2.5	1	3	
(D) Stirring rate (rpm)	150	250	350	50	450	
Run	A	B	C	D	Copper content leached (mg/L)	Cu leaching efficiency (%)
1	70	25	1.5	150	1050.5	55.29
2	70	25	2.5	350	1205.78	63.46
3	90	35	1.5	150	2113.58	68.86
4	90	35	1.5	350	1973.84	64.31
5	60	30	2	250	1456.86	59.64
6	90	25	2.5	350	1278.9	67.31
7	90	35	2.5	350	2062.71	67.21
8	90	25	1.5	350	1144.33	60.23
9	70	25	2.5	150	1212.54	63.82
10	80	30	1	250	1480.16	60.59
11	80	30	3	250	1676	68.61
12	70	35	2.5	150	2041.85	66.53
13	80	30	2	250	1614.4	66.09
14	80	30	2	70	1581.5	64.74
15	80	40	2	250	2740.77	72.13
16	80	30	2	250	1651.5	67.61
17	70	35	2.5	350	2004.92	65.32
18	70	25	1.5	350	1111.67	58.51
19	100	30	2	250	1671.96	68.44
20	90	25	2.5	150	1262.25	66.43
21	90	35	2.5	150	2165.02	70.54
22	90	25	1.5	150	1169.04	61.53
23	70	35	1.5	150	1890.1	61.58
24	80	30	2	450	1599.61	65.48
25	80	30	2	250	1624.43	66.50
26	70	35	1.5	350	1957.7	63.78
27	80	20	2	250	895.28	62.83

stirring speed, the solution was stirred for a specific duration. After finishing leaching time, the resulting pulp was filtered, and the leach liquor was analyzed by atomic absorption spectrometer to specify the copper concentration. Ultimately, the leaching efficiency of copper (R) for each experiment was calculated utilizing the following formula:

$$R = \frac{C_f \times V}{C_i \times m} \times 100 \quad (1)$$

in which C_f describes the concentration of copper in the leach liquor or PLS (Pregnant Leach Solution) (g/L), V denotes the volume of the leach solution (L), C_i represents the copper content in the solid sample (%, i.e. here C_i was 0.54/100 based on atomic absorption spectrometer (AAS)), and m is the weight of the sample (g).

2.3. Experimental design based on RSM-CCD

Modelling and process optimization were accomplished utilizing response surface methodology (RSM) combined with central composite design (CCD) to obtain more accurate information about the influence of effective parameters on the dissolution process, especially interactive effects between the parameters. RSM-CCD is one of the most important and efficient DOE (design of experiments) techniques used to develop, improve, model, and optimize the processes and assess the relative importance of the operating parameters (**Montgomery, 2001; Myers and Montgomery, 2002; Bezerra et al., 2008; Motamedizadeh et al., 2021**). Thus, according to the RSM-CCD model and **Equation 2**, a set of 27 experiments ($N=2^{(5-1)}+2\times4+3=27$) consisting of 16 partial factorial runs, 8 axial runs ($\alpha = 2$) and 3 repeated experiments at the middle point was designed and conducted. **Table 2** shows the opted factors and the operating conditions for performing leaching tests.

$$N = 2^{(n-p)} + 2n + n_c \quad (2)$$

where N is the total number of experiments, n depicts the number of parameters, nc exhibits the number of central experiments, and P is a fraction of the number of parameters (here P= 1) (**Motamedizadeh et al., 2021**).

2.4. Kinetic study

The reaction kinetics was investigated to identify and understand the mechanism of copper leaching process. The reactions occurring between the ore particles and leach liquor during the leaching process are typically heterogeneous and, in such a system, the expression of the overall reaction rate is complicated by the interactions between physical and chemical processes (**Habbache et al., 2009; Ghasemi and Azizi, 2018**). Based on previous studies, the reaction rate between mineral particles and acidic leach solution mainly follows the shrinking core models (SCMs). SCM models are preferred for the kinetic modelling due to their accurate representation for the actual leaching process (especially closer approximation of real particles in the different situations) compared to other models (**Levenspiel, 1999; Nozari and Azizi, 2020; Apua and Madiba, 2021; Houshmand et al., 2024**). In heterogeneous SCM models, the reactant particles are assumed to be nonporous, spherical shape, and their size does not change during reaction. Also, the reaction between the mineral particles and the leaching Lixiviant occurs on the outer surface of the particles (**Ekmekyapar et al., 2015; Bai et al., 2018**). However, these assumptions may not exactly match with the reality. Therefore, SCM models were utilized for kinetic modelling of copper leaching process. In this regard, the diverse SCM models were applied to the experimental data as shown in **Equations 7-9**.

Surface chemical reaction

$$1-(1-X)^{\frac{1}{3}} = k_{sc} \times t \quad (3)$$

Liquid film diffusion

$$1-(1-X)^{\frac{2}{3}} = k_{lf} \times t \quad (4)$$

Diffusion through a product layer

$$1-3(1-X)^{\frac{2}{3}} + 2(1-X) = k_{pl} \times t \quad (5)$$

In the aforementioned equations, k_{sc}, k_{lf}, and k_{pl} are the kinetic rate constants, individually, for surface chemical reaction, diffusion through liquid film, and product layer diffusion model (min^{-1}), X is the conversion fraction of copper recovered and t implies the dissolution time (min). Meanwhile, the process kinetics is commonly controlled by the slowest stage.

3. Results and Discussion

To realize the possibility of copper recovery from the low-grade source with high silica, the present research was conducted in three operational phases. In the first stage, the behaviour and impact of operating variables such as particle size, sulfuric acid concentration, solid percentage (pulp density), pulp stirring speed, leaching temperature, and leaching time were investigated under fixed conditions with OFAT (one factor at a time) method. In the second phase, the possible interactive effects between operating parameters were evaluated, and the process optimization was performed using statistical experimental design and response surface methodology. In the third step, the leaching kinetics was studied to identify the dissolution mechanism and gain further insight of the copper leaching process.

3.1. Impact of major parameters on copper leaching

Figures 1, and 4-7 display the impact of operating parameters including particle size, sulfuric acid dose,

solid percentage (pulp density), stirring rate, and leaching time on the leaching efficiency and the content of copper in PLS solution. These factors were assessed on the basis of OFAT method when one parameter was changed and the other parameters were fixed at a constant value. The following observations can be made on the impact of the parameters on the leaching yield of copper.

The optimal and desirable particle size has a great impact on the dissolution amount of copper. As can be seen in **Figure 1**, the 0-500 µm particle size has a higher copper content and extraction efficiency. Interestingly, contrary to the expectation that copper dissolution should reduce with increasing particle size, it is observed that for particle sizes of 0–2 mm the dissolution rate increases. It is generally accepted that the leaching rate increases with decreasing particle size due to an improved liberation degree of the mineral, increased contact surface area, and enhanced permeability of the leaching agent (**Janyasuthiwong et al. 2016; Hao et al. 2022; Tanaydin et al. 2022**). However, this behaviour may vary among the size fractions of a given ore, depending on the mineralogy, mineral associations, and the dissemination of various species (**Hansen et al., 2005**).

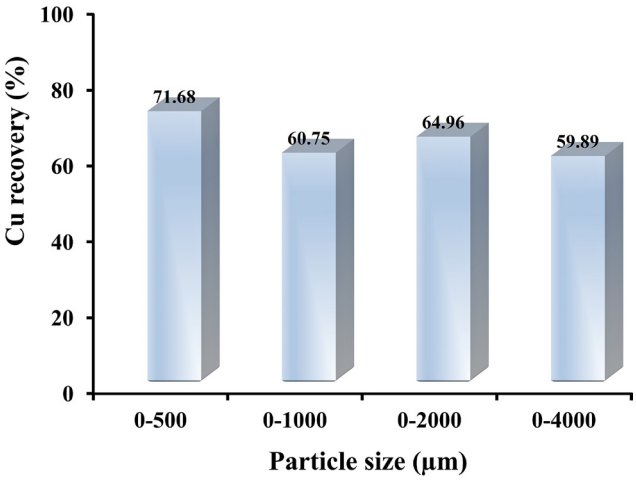
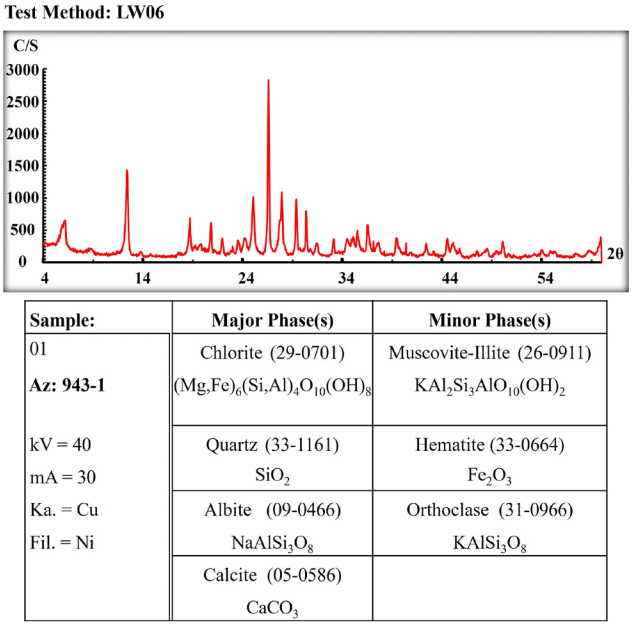


Figure 1. The impact of particle size on the leaching efficiency under conditions: 25°C temperature, 70 kg/t acid concentration, 30% solid percentage, 150 rpm stirring speed, and 90 min leaching time

According to XRF and XRD analyses (see **Figure 2**), the studied sample significantly contains silicate and clay minerals, which affect the copper dissolution performance due to their different and complex structures. The presence of clay and silicate compounds in the sample can influence the consumption of acid (leaching agent), and this is more severe in the fine particles. For instance, some silicate minerals (like mica, and clay) can consume acid generated by the oxidation phenomenon, and/or can quickly adsorb acid (such as kaolinite, and montmorillonite) (**Toro et al., 2021**). In addition, clays and silicates have negative effects on most mineral processing units owing to their adverse impacts on the pulp rheology and cause many problems in the filtration stage (**Luo et al., 2024**). Thus, regarding the presence of clay and silicate compounds in the sample, as well as the high fines (which creates filtration problems) produced in the smaller size fraction, the fraction of 0-2000 µm was selected for further study. The particle size analysis for the fraction of 0-2000 µm is given in **Figure 3**.



Sample:	Major Phase(s)	Minor Phase(s)
01 **Az: 943-1** kV = 40 mA = 30 Ka. = Cu Fil. = Ni	Chlorite (29-0701) $(Mg,Fe)_6(Si,Al)_4O_{10}(OH)_8$	Muscovite-Illite (26-0911) $KAl_2Si_3AlO_{10}(OH)_2$
	Quartz (33-1161) SiO_2	Hematite (33-0664) Fe_2O_3
	Albite (09-0466) $NaAlSi_3O_8$	Orthoclase (31-0966) $KAlSi_3O_8$
	Calcite (05-0586) $CaCO_3$	

Figure 2. X-ray diffraction (XRD) spectra of the studied sample

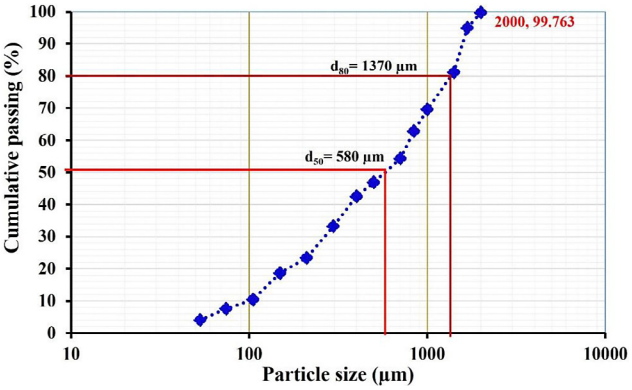


Figure 3. Particle size distribution for the investigated 0-2 mm sample

The nature of the leaching operations is based on the penetration of the lixiviant into the very small pores in the ore. Theoretically, an increasing concentration of lixiviant will increase the reaction rate. However, in leaching operations, especially acid leaching, an excessive increase in the concentration of the leaching agent, in addition to the non-optimal consumption of acid, leads to the dissolution of gangue compounds into the PLS solution. **Figure 4** indicates the impact of acid dosage ranging from 50 to 130 kg/t on the leaching performance. It can be seen that the recovery rate and the value

of leached copper increase with an increasing acid concentration from 50 to 80 kg/t, but a further increase in acid concentration has little effect on copper extraction efficiency and remains almost constant. This trend can be attributed to the change in leaching mechanism due to the change in acid concentration, and more importantly, due to the mineralogical composition of the studied sample (presence of silicate and clay compounds in the sample) which increases acid consumption. Thus, considering the copper content of about 1650 ppm in PLS liquor and also from an economic point of view, a concentration of 80 kg/t of acid was selected to continue the investigation.

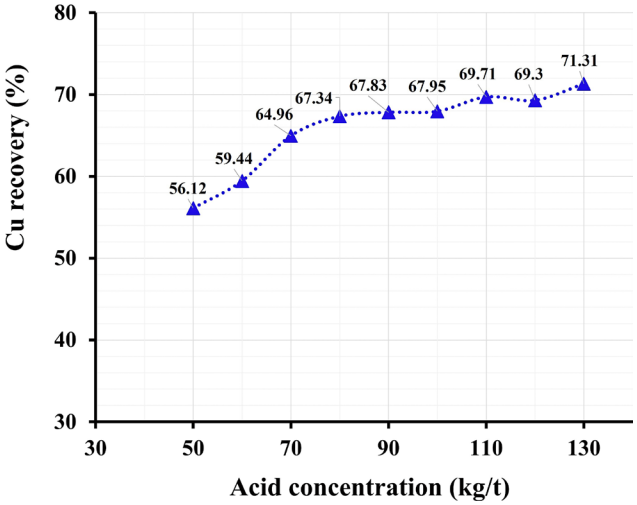


Figure 4. The impact of acid consumption on the leaching efficiency under conditions: 25°C temperature, 0-2000 µm particle size, 30% solid percentage, 150 rpm stirring speed, and 90 min leaching time

The pulp density (solid percentage) depends on the leaching system and its role in the tank leaching is very important. Therefore, six leaching tests were conducted to determine the effect of pulp solids percentage at the values of 20, 25, 30, 35, 40, and 45% under constant operating conditions including ambient temperature, 0-2 mm particle size, pulp mixing rate of 150 rpm, sulfuric acid concentration of 80 kg/t, and leaching time of 90 min. The behaviour of solid percentage on the extraction rate from the studied sample is shown in **Figure 5**. It is observed that as the solid percentage increases from 20 to 40%, the amount of leached copper increases sharply, and with further increase, the leaching efficiency decreases due to lack of proper mixing. The reason for the increase in recovery with increasing solid percentage can be attributed to the better performance of the agitation process due to more and more effective collision of particles in the solution. Therefore, low solid percentages reduce the dissolution efficiency and require a large amount of acid for a small amount of the sample and, on the other hand an excessive increase in the solid percent creates problems for slurry mixing, pumping, and filtration operations. Hence, a solid percentage of 35 (given

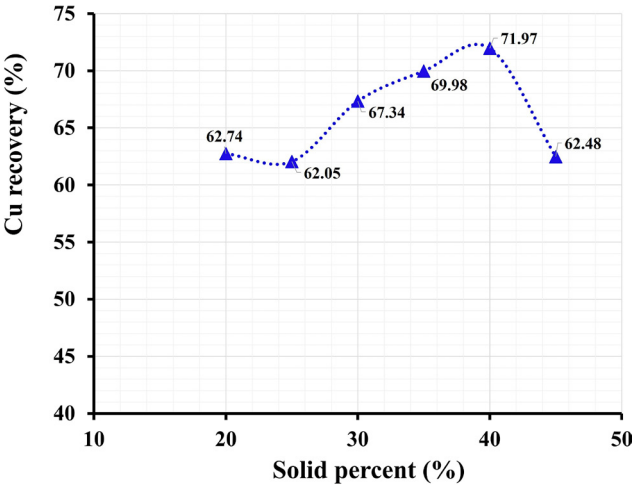


Figure 5. The impact of solid content on the leaching efficiency under conditions: 25°C temperature, 80 kg/t acid concentration, 0-2000 µm particle size, 150 rpm stirring speed, and 90 min leaching time

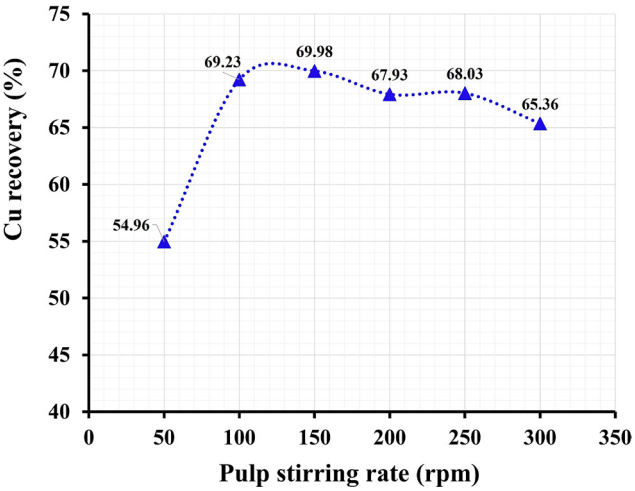


Figure 6. The impact of pulp stirring rate on the leaching efficiency under conditions: 25°C temperature, 80 kg/t acid concentration, 0-2000 mm particle size, 35% solid percentage, and 90 min leaching time

the recovery rate of about 70% and the copper content of about 2.15 g/L in PLS) was selected for further studies.

Figure 6 shows the leaching recovery as a function of pulp agitation rate. As can be considered, the highest amount of copper is leached in a stirring rate of 150 rpm, and high mixing speeds have a negative impact on the dissolution efficiency. In general, the pulp agitation increases the dissolution rate at the beginning of the operation, but has little effect as the operation continues. In many systems, it is sufficient to have an agitation speed that suspends the solid particles and prevents them from settling. Therefore, based on the results received and observations, a stirring speed of 150 rpm was used to continue the study.

Each leaching project has an economic time depending on the concentration of the dissolving agent, particle size, and leaching method, and if the leaching time is

longer than this desired time, the project tends to become uneconomical. Thus, the effect of contact time of the received sample with the leaching agent (sulfuric acid) was studied from 15 to 180 minutes as shown in **Figure 7**. As expected, the extraction efficiency (copper recovery and copper content in the PLS solution) increased with leaching time rising and reached its maximum value (about 71% with a concentration of 2192 mg/L) after 2 h. Thereafter, the copper dissolution rate increased slightly with increasing time, and the changes in the copper leaching rate were very small.

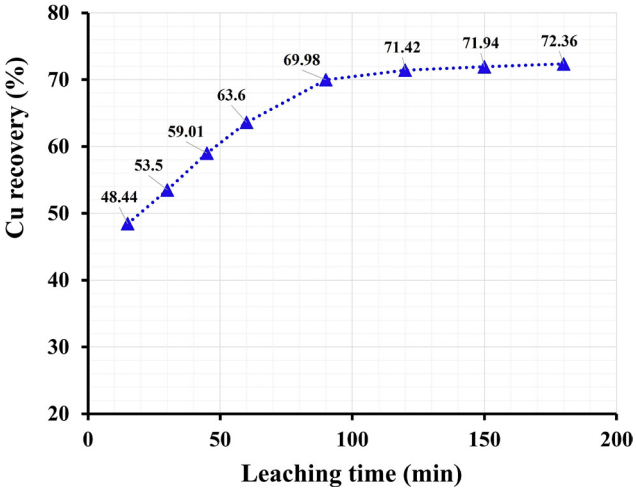


Figure 7. The impact of leaching time on the leaching efficiency under conditions: 25°C temperature, 80 kg/t acid concentration, 0-2000 µm particle size, 35% solid percentage, and 150 rpm pulp stirring rate

3.2. *Modelling and process optimization*

3.2.1. Modelling and interactive effects between the operating parameters

After designing and carrying out the tests based on RSM-CCD strategy (see **Table 2**), the experimental data was statistically analyzed in the Design Expert software environment. In this regards, a quadratic polynomial model based on **Equation (6)** (**Bezerra et al., 2008**) was fitted to the data.

$$Y = \theta_0 + \sum_{i=1}^{k} \theta_i x_i + \sum_{i=1}^{k} \theta_{ii} x_i^2 + \sum_{1 \le i \le j}^{k} \theta_{ij} x_i x_j + \varepsilon \quad (6)$$

where Y denotes the process responses (leaching recovery of copper (%) or copper concentration leached (mg/L), k is the number of parameters, θ_0 depicts a constant term, θ_i is the coefficients of the linear terms, x_i and x_j display the parameters, θ_{ii}, represents the coefficients of the quadratic terms, α_{ij} is the coefficients of the interactive terms among the parameters, and ε implies the residual error (the difference between the measured and the predicted values).

Ultimately, after removing the very negligible terms (p-value > 0.05), the final regression models developed to approximate the leaching rate (R_{Cu}) and the content of copper leached were obtained according to **Equations 7** and **8**, respectively.

$$R_{Cu} = +66.69 + 1.91 \times A + 2.09 \times B + \\ + 2.19 \times C - 0.12 \times D - 0.76 \times A \times D - \\ - 0.9 \times B \times C - 0.58 \times B \times D - 0.88 \times A^2 - \\ - 0.74 \times C^2 - 0.61 \times D^2 \quad (7)$$

$$C_{Cu} = +1569.52 + 46.87 \times A + 436.07 \times B + \\ + 50.62 \times C - 5.37 \times D + 52.51 \times B^2 \quad (8)$$

In the above **Equations**, A, B, C, and D represent the sulfuric acid concentration, solid percentage, leaching time, and pulp agitation rate, respectively. Also, all parameters are based on the coded units. The coded amounts were used for simplifying the calculations and uniform comparison and determined according to the following formula (**Motamedizadeh et al., 2021**).

$$X_i = \frac{x_i - x_0}{\Delta x}, \ i = 1, 2, 3, \ldots \quad (9)$$

in which X_i is the value of coded parameter, x_i is the value of real parameter, x_0 is the magnitude of real parameter at the centre point, and (rx) is the step change in the actual parameter.

The final quadratic polynomial models developed were statistically evaluated employing analysis of variance (ANOVA) at a 95% confidence level (p-values less than 0.05) as presented in **Tables 3** and **4**.

The high F-values and low probability levels ($p < 0.05$) in the ANOVA tables indicate the model proposed and the parameter is statistically significant. As can be seen, the developed models show an excellent relationship between the operational parameters and the process responses with p-values less than 0.0001, and so they can be used to predict the response variable. Meanwhile, the difference between (R^2) and adjusted (R^2) of 0.0379 (The leaching efficiency) and 0.0026 (the copper content leached) indicate a very good correlation between experimental data and the fitted model. Additionally, the larger F-values and smaller p-values indicate which the parameter has a greater influence than the other parameters. It is observed from **Table 3** that the leaching time, solid percentage and acid concentration have the greatest impact on the copper leaching recovery, respectively, while pulp mixing rate does not have much effect on the efficiency of process. It is also seen that the leaching efficiency of copper highly depends on the interactive impacts among the parameters. The significance degree of the parameters on the copper concentration leached is found to be in the order of the quadratic effect of solid percent (B^2) > the linear effect of solid percent (B) > the linear effect of leaching time (C) > the linear effect of acid concentration (A) > the linear effect of stirring rate (D). The perturbation graph (see **Figure 8**) showing the effect of all operating parameters on the process re-

Table 3. The results of ANOVA of the model proposed to approximate the leaching rates of copper and determine the relative importance of the influential operating parameters

Source	Sum of squares	Degree of freedom (DF)	Mean Square	F Value	p value	Remark
Model	362.49	10	35.25	24.77	< 0.0001	significant
Acid concentration (A)	87.13	1	87.13	59.54	< 0.0001	
Solid percentage (B)	104.79	1	104.79	71.61	< 0.0001	
Leaching time (C)	115.15	1	115.15	78.69	< 0.0001	
Stirring speed (D)	0.37	1	0.37	0.25	0.6231	
AD	9.23	1	9.23	6.3	0.0232	
BC	12.94	1	12.94	8.84	0.009	
BD	5.44	1	5.44	3.72	0.0718	
A2	18.41	1	18.41	12.58	0.0027	
C2	13	1	13	8.88	0.0088	
D2	8.88	1	8.88	6.07	0.0255	
Residual	23.41	16	1.46			
Lack of Fit	22.18	14	1.58	2.56	0.3161	not significant
Pure Error	1.24	2	0.62			
Cor. Total	385.9	26				
Summary of statistical analysis of model						
R^2	0.9393					
Adjusted R^2	0.9014					
Adeq Precision	19.4989					

Table 4. The results of ANOVA of the model proposed to approximate the copper concentration leached and determine the relative importance of the influential operating parameters

Source	Sum of squares	Degree of freedom (DF)	Mean Square	F Value	p value	Remark
Model	4.75×106	5	9.5×105	376.91	< 0.0001	significant
Acid concentration (A)	52716.56	1	52716.56	20.91	< 0.0002	
Solid percentage (B)	4.56×106	1	4.56×106	1809.81	< 0.0001	
Leaching time (C)	61498.24	1	61498.24	24.39	< 0.0001	
Stirring speed (D)	691.33	1	691.33	0.27	0.606	
B2	73532.32	1	73532.32	29016	< 0.0001	
Residual	52955.46	21	2521.69			
Lack of Fit	52218.86	19	2748.36	7.46	0.1246	not significant
Pure Error	736.6	2	368.3			
Cor. Total	4.81×106	26				
Summary of statistical analysis of model						
R^2	0.989					
Adjusted R^2	0.9864					
Adeq Precision	73.685					

sponses (the leaching rate and the content of copper leached) also confirms these results. This graph displays the impacts of all the parameters at a special point in the design space. The sharp slope or curve in graph implies the sensitivity of the leaching rate and the content of copper leached to that parameter. As observed in **Figure 3**, all parameters except pulp stirring rate significantly affect the process responses, confirming the results derived from ANOVA tables.

In addition to the above, the three-dimensional (3D) response surface plots were utilized to attain a better understanding of the main and synergistic effects of parameters on the leaching recovery and content of copper leached, as shown in **Figures 7-10**. These graphs are obtained based on the change in two variables when other variables are fixed at their middle level, and display the nature and magnitude of possible interactions between various parameters.

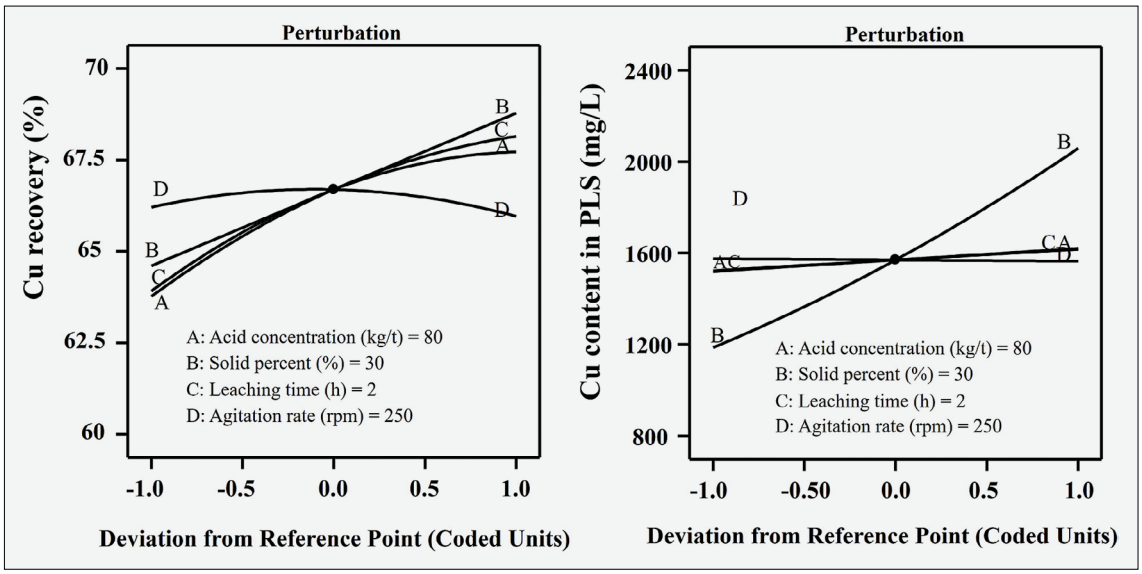


Figure 8. Perturbation plot showing the impact of all operating parameters on the leaching recovery and the concentration of copper leached

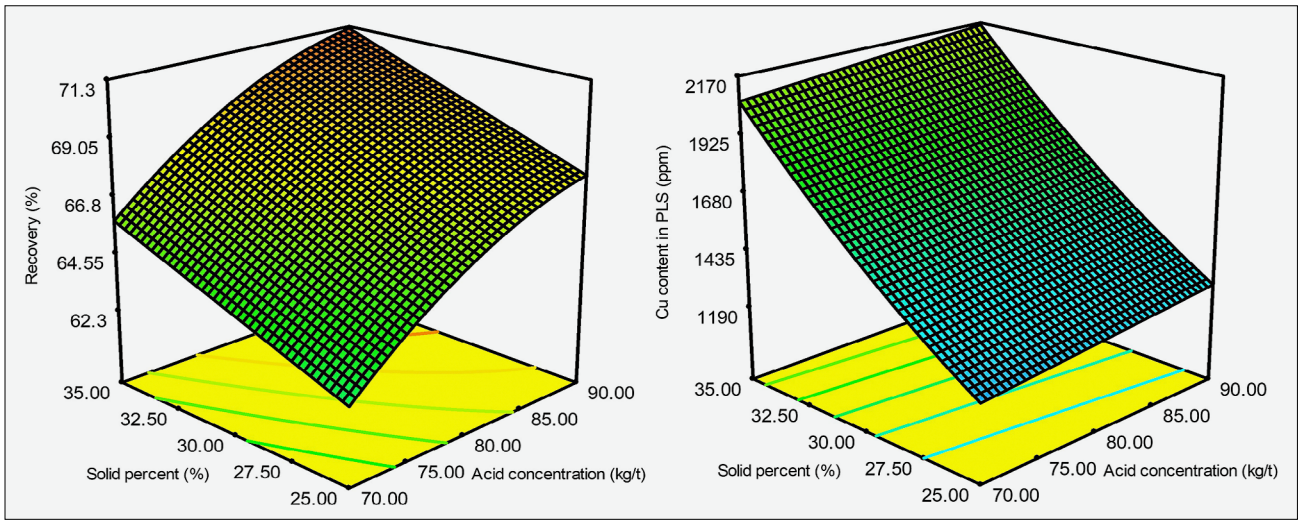


Figure 9. 3D graphs displaying the combined impact of acid concentration and solid percentage on the recovery and concentration of copper leached

Figure 9 shows the simultaneous effect of acid concentration and solid percentage on the recovery and concentration of copper in the PLS solution. As can be seen, copper recovery is a quadratic function of acid concentration and has a linear relationship with solid percentage. It is obvious that at low and high solids percentages, copper recovery enhances with an increase in the acid concentration, and this increase is more intense at lower solid percentages. The highest copper recovery is observed at a solid percentage of 35 and an acid concentration of 90 kg/t, which, under these conditions, reaches more than 71% with a copper concentration of ~2170 mg/L in PLS solution. It is noteworthy that under these conditions, the mixing rate was 150 rpm and the leaching time was 2.5 hours. Additionally, it was found that the effect of acid concentration on copper recovery is greater and the effect of solid percentage on the leached copper concentration is higher. At the lower solid percentage, the acid has more surface area and effective contact to react with copper-bearing minerals, leading to higher leaching rate, but only if the acid is not overly concentrated, as it may cause excessive dissolution of other unwanted elements. While, at high solid percentages, the leaching pulp becomes denser, reducing the effectiveness of acid due to less surface area exposure. In this case, the higher acid concentrations may be required to compensate for the reduced contact, though this can increase costs and side reactions. **Wang et al. (2019)** attributed the increase in copper dissolution with increasing acid concentration to the enhanced activity of hydrogen ions (H^+). They also reported that the upward trend in copper dissolution rate decreases with a further increase.

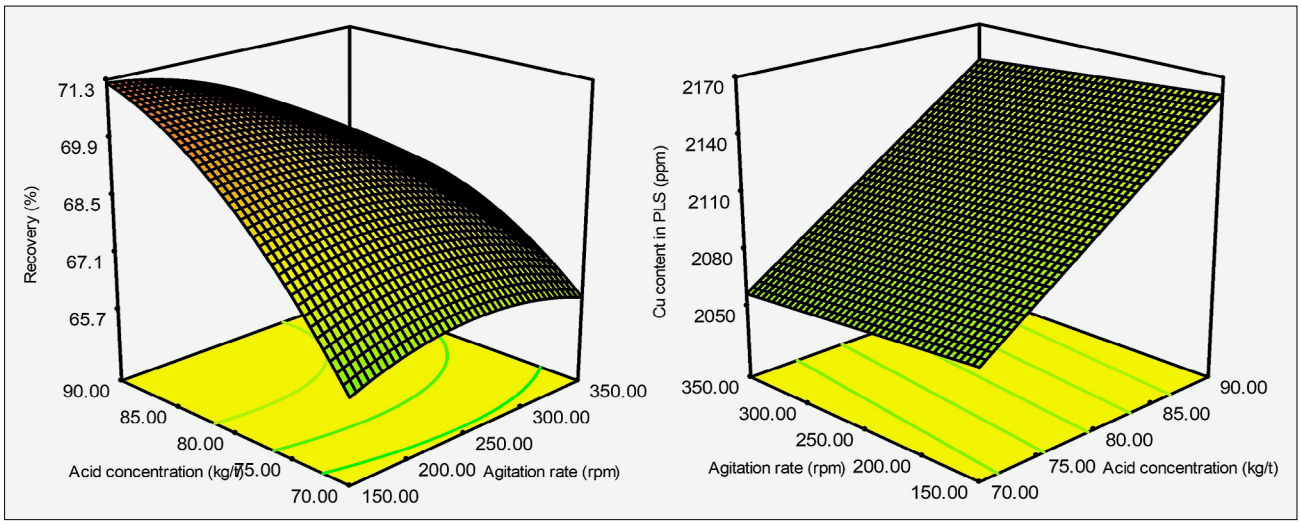


Figure 10. 3D graphs displaying the combined impact of acid concentration and pulp mixing rate on the recovery and concentration of copper leached

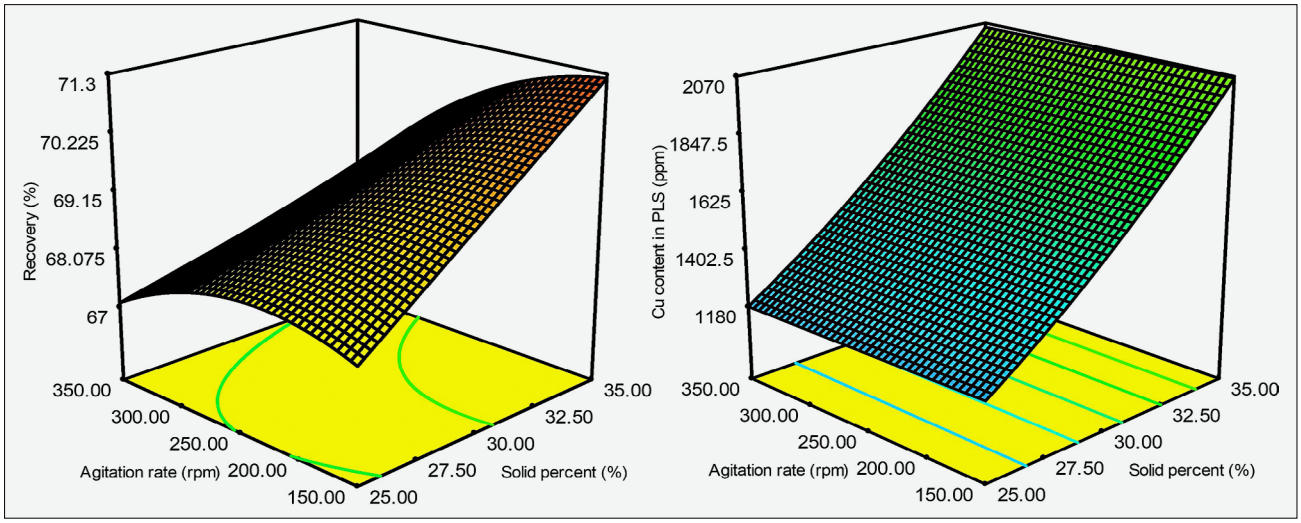


Figure 11. 3D graphs displaying the combined impact of solid percentage and pulp mixing rate on the recovery and concentration of copper leached

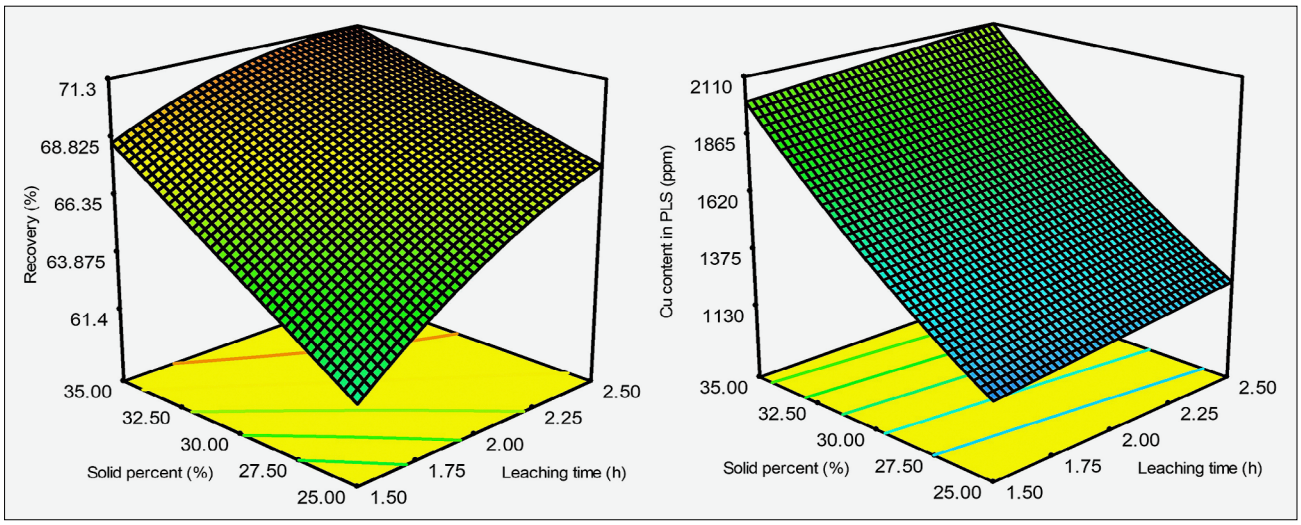


Figure 12. 3D graphs displaying the combined impact of solid percentage and leaching time on the recovery and concentration of copper leached

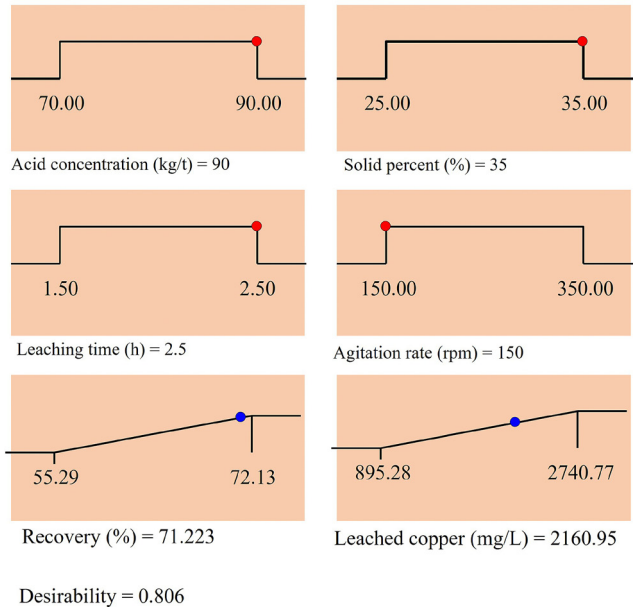


Figure 13. The optimized values of operating parameters to achieve maximum copper dissolution efficiency (recovery and content of copper in PLS solution)

The combined effect of acid concentration and solid percentage with pulp mixing rate are shown in **Figures 10** and **11**, individually. It can be seen that the dissolution rate of copper increases with the pulp mixing speed at the beginning of the operations, and generally the pulp stirring speed had a smaller effect on the dissolution performance compared to the other two parameters, showing that the copper dissolution process is affected by a certain value of pulp mixing rate. Additionally, according to **Figures 10** and **11**, the dissolution efficiency increases greatly by increasing the acid concentration and solid percentage at a lower mixing rate within 2.5 h. At lower mixing rates, high acid concentration compensates for slower mass transfer by offering strong chemical reactivity, leading to increased leaching efficiency. A high solids percentage provides more material for the acid, and increases overall dissolution at low stirring rates. However, an excessive solid percentage will cause the leaching pulp to be denser and reduce the copper recovery. Nevertheless, the combination of these factors can still significantly improve efficiency, even if stirring is not optimal. It is also observed that when the acid concentration and stirring speed are simultaneously low, the recovery decreases. Similar results were found in the work reported by **Maleki et al. (2023)**.

Figure 12 exhibits the interaction between the solid percentage (pulp density) and the contact time of leaching agent with the sample. As can be seen, these two parameters have a synergistic effect in increasing copper leaching efficiency, and this synergistic effect is greater at lower solid percentages, although it reaches its maximum value at 35% solids and a contact time of 2.5 hours. In general, increasing the leaching rate with a decrease in solid/liquid ratio can be due to the greater amount of acid per unit amount of solid sample and the decrease in mass transfer resistance (**Hosseinzadeh et al., 2021**).

3.2.2. Process optimization

The numerical optimization of leaching process was conducted using Design Expert (DX) software and employing the desirability function procedure. The optimal operating conditions proposed by RSM modelling for achieving the highest leaching efficiency and the leached copper content are illustrated in ramp plots in **Figure 13**. As observed, the optimized values of leaching parameters for -2 mm size fraction as follow: 90 kg/t sulfuric acid concentration, 35% solid content, 150 rpm agitation rate, and leaching time of 2.5 hours. It is found that under these optimal conditions, a PLS solution with a copper concentration of ~2160 mg/L and an efficiency of more than 71% can be achieved. It is noteworthy that in the confirmation experiment conducted under the proposed optimum conditions similar to Run 21 (see **Table 2**), a recovery of about 70.5% with a copper content of 2165 mg/L in PLS was achieved.

3.3. Leaching kinetic modelling

To model, the left side of **Equations 3-5** was plotted as a function of leaching time for each operational variable, including the concentration of leaching agent, solid percentage (solid/liquid ratio), pulp agitation speed, and leaching temperature. For instance, the results obtained from the temperature parameter are shown in **Figure 14**, in which the slope of the straight lines represents the kinetic rate constant for copper leaching. The values of kinetic constants and correlation coefficients for each parameter are provided in **Table 5**. According to **Figure 14** and **Table 5**, the diffusion equation through a product layer exhibits the best correlation relative to other kinetic equations, demonstrating that this model is the controlling step of the reaction rate.

To better distinguish the reaction mechanism, the activation energy was determined by analyzing the data and applying the Arrhenius equation according to the following equation (**Levenspiel, 1999; Adebayo and Olasehinde, 2015**):

$$k = A \times e^{\frac{-E_a}{R \times T}} \Rightarrow Ln(k) = Ln(A) - \frac{E_a}{R}.\frac{1}{T} \qquad (10)$$

where k implies the reaction rate constant (min^{-1}), A illustrates the frequency factor (min^{-1}), E_a denotes the activation energy (J/mol), R depicts the universal gas constant (8.314 $J \cdot K^{-1} \cdot mol^{-1}$), and T is for the leaching temperature (K).

To measure the activation energy, Ln(k) versus (1/T) for each temperature was plotted, as shown in **Figure 15**. The slope of the straight line in this graph represents $-\frac{E_a}{R}$. Thus, the activation energy of the diffusion model

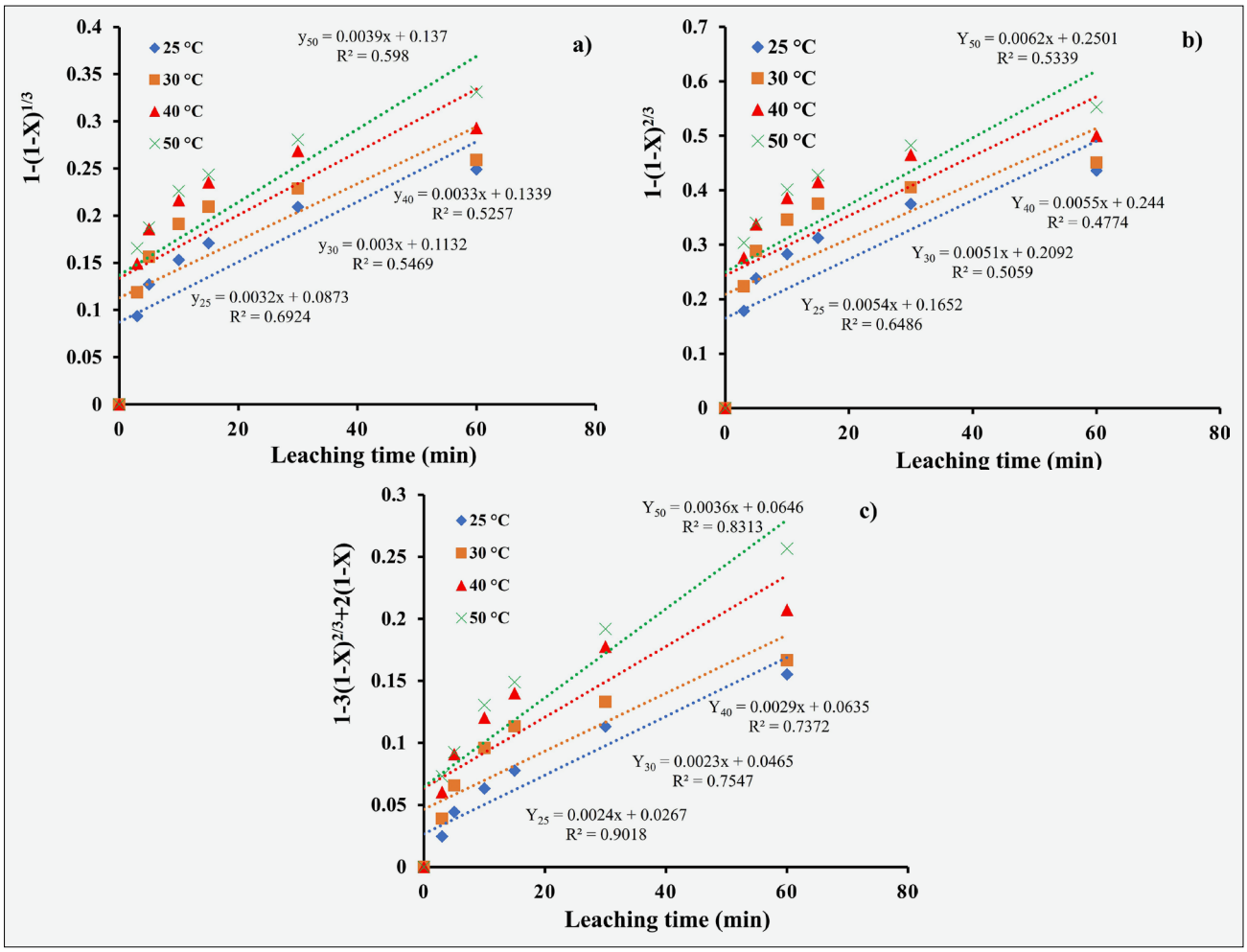


Figure 14. The graph of the SCMs models versus leaching time at different temperatures (25, 30, 40, and 50)

Table 5. The kinetic analysis of the shrinking core models fitted to the experimental data

	Surface chemical reaction		Liquid film diffusion		Diffusion through a product layer	
Factors	**k_{sc} (min^{-1})**	**R^2**	**k_{lf} (min^{-1})**	**R^2**	**k_{pl} (min^{-1})**	**R^2**
Temperature (°C)						
25	0.0032	0.6924	0.0054	0.6486	0.0024	0.9018
30	0.0030	0.5469	0.0051	0.5059	0.0023	0.7547
40	0.0033	0.5257	0.0055	0.4774	0.0029	0.7372
50	0.0039	0.5980	0.0062	0.5339	0.0026	0.7313
Acid concentration (kg/t)						
70	0.0030	0.5574	0.0051	0.5182	0.0023	0.7501
80	0.0031	0.5607	0.0052	0.5168	0.0024	0.7777
90	0.0033	0.5161	0.0054	0.4726	0.0028	0.7060
100	0.0034	0.5320	0.0055	0.4847	0.0027	0.7345
Stirring speed (rpm)						
100	0.0033	0.5655	0.0054	0.5214	0.0027	0.7655
150	0.0031	0.4923	0.0052	0.4515	0.0026	0.6802
250	0.0036	0.5540	0.0059	0.5031	0.0032	0.7541
350	0.0032	0.4980	0.0053	0.4540	0.0027	0.6984
Solid percentage (%)						
25	0.0035	0.6767	0.0059	0.6387	0.0027	0.8441
30	0.0032	0.5538	0.0054	0.5160	0.0025	0.7306
35	0.0036	0.5247	0.0058	0.4814	0.0031	0.6945
40	0.0041	0.5647	0.0065	0.5081	0.0039	0.7508

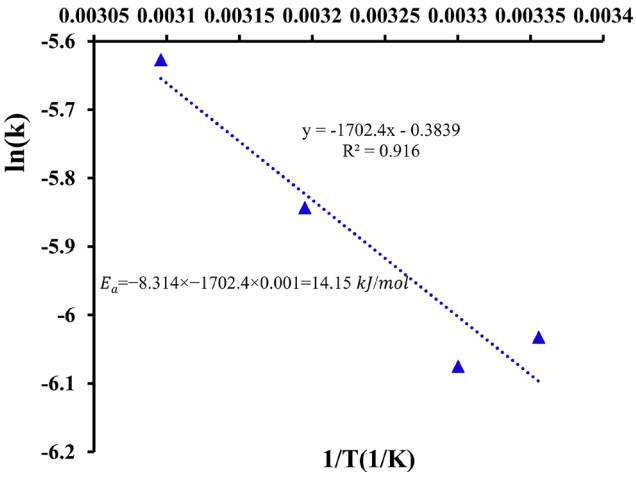


Figure 15. Arrhenius graph for product layer diffusion model to approximate the activation energy

through a product layer was calculated 14.15 kJ/mol ($-\frac{E_a}{R} = -1702.4 \rightarrow E_a = -8.314 \times -1702.4 = 14154J = 14.15kJ$). According to **Espiari et al. (2006)** and **Ekmekyapar et al. (2012)**, the values of E_a less than 40 kJ/mol demonstrate that the leaching process is controlled by diffusion phenomena. **Ekmekyapar et al. (2015)** investigated the leaching kinetics of malachite ore in ammonium sulfate solutions and reprotted the diffusion model through the product layer was the rate-controlling step of the dissolution kinetics. **Hosseinzadeh et al. (2021)** performed a similar kinetic study on copper leaching from a low-grade copper oxide source, and reported that the predominant mechanism was a difusion process with the activation energy of 11.72 kJ/mol. Therefore, by combining **Equations 5** and **10** and ascertaining the influence of parameters on the apparent rate constant given in **Table 5**, the mathematical equation showing the kinetics of copper leaching can be described as follows:

$$1-3(1-x)^{\frac{2}{3}}+2(1-x) = A \times (SA)^{s} \times (SP)^{p} \times (SR)^{r} \times e^{\frac{-Ea}{R \times T}} \times t \quad (11)$$

in which A, SA, SP, and SR represent frequency factor, sulfuric acid concentration, solid percentage, and pulp stirring rate, individually, and the constants s, p, and r depict the reaction order for each the corresponding parameter. The reaction orders (constants) were determined by plotting Ln(SA), Ln(SP), and Ln(SR) against Ln(kpd) and approximating the slope of straight line each curve. The constants s, p, and r were estimated to be 1.3021, 2.1337, and 0.8689, respectively. Ultimately, the ultimate model describing the leaching kinetics of copper was understood as **Equation 12**:

$$1-3(1-x)^{\frac{2}{3}}+2(1-x) = A \times (SA)^{1.3021} \times (SP)^{2.1337} \times (SR)^{0.8689} \times e^{\frac{-14.15 \times 10^{3}}{8.314 \times T}} \times t \quad (12)$$

4. Conclusions

The presence of silicates and clays in ores creates various problems in the mineral processing industry, such as the formation of gel during sulfuric acid leaching, filtration problems, high consumption of leaching lixiviant (acid), and reduced leaching efficiency, all of which lead to high costs. Thus, the major aim of the present paper was to scrutinize the potential recovery of copper from a low-grade ore consisting of high silica content using tank leaching method. To this end, this study was conducted in three working phases. In the first phase, the behaviour of major parameters consisting of particle size, sulfuric acid concentration, solid percentage (pulp density), stirring rate, and leaching time was assessed with the one factor at a time method. The findings demonstrated that the amount of extracted copper augmented with increasing the acid concentration, leaching time and the solid percent. Meanwhile, 0-2 mm size fraction was a better choice for the tank leaching than other fractions including 0-500 µm, 0-1 mm and 0-4 mm. Also, the amount of acid used for the studied sample was very high, and this was due to the presence of silicate and clay compounds in the sample. Additionally, the stirring speed of pulp had little effect on the leaching process of copper compared to other factors. In the next step, modelling and optimizing the leaching process, and evaluating the interactive effects between the operating parameters were conducted using the statistical design of experiments based on response surface methodology (RSM). The results showed that the effect of leaching time, solid percent, and acid dosage had the greatest efficacy on the dissolution efficiency of copper. In addition, the leaching recovery of copper was remarkably dependent on the interactive impacts among the solid percent and leaching time, and the acid concentration and agitation speed. The influence degree of the operating variables on the copper content leached was distinguished in the order of the quadratic effect of solid percent > the linear effect of solid percent > the linear effect of leaching time > the linear effect of acid concentration > the linear effect of stirring rate. The optimization of leaching process was performed with the desirability function technique and the maximum leaching efficiency (71%) with a PLS solution containing 2160 g/L of copper was obtained at the acid concentration of 90 kg/t, solid percentage of 35, pulp mixing rate of 150 rpm, leaching time of 2.5 h, and size fraction of 0-2 mm. Eventually, the kinetics of copper leaching was analyzed using the shrinking core (SCMs) equations to recognize the mechanism of the process and the controlling step of the reaction rate. It was found that the leaching process was controlled by diffusion model through the product layer with the activation energy of 14.15 kJ/mol. Finally, a kinetic mathematical equation depicting the leaching process of copper from the desired copper oxide ore was proposed.

Acknowledgement

The authors gratefully acknowledge the support of the Shahrood University of Technology during this research.

5. References

Adebayo, A. O., and Olasehinde, E. F. (2015). Leaching kinetics of lead from galena with acidified hydrogen peroxide and sodium chloride solution. Mineral Processing and Extractive Metallurgy, 124(3), 137-142. https://doi.org/10.1179/1743285515Y.0000000001

Ahmed, I. M., Nayl, A. A., and Daoud, J. A. (2016). Leaching and recovery of zinc and copper from brass slag by sulfuric acid. Journal of Saudi Chemical Society, 20, S280–S285. https://doi.org/10.1016/j.jscs.2012.11.003

Apua, M. C., and Madiba, M. S. (2021). Leaching kinetics and predictive models for elements extraction from copper oxide ore in sulphuric acid. Journal of the Taiwan Institute of Chemical Engineers, 121, 313-320. https://doi.org/10.1016/j.jtice.2021.04.005

Azizi, A., Bayati, B., and Karamoozian, M. (2018). A comprehensive study of the leaching behavior and dissolution kinetics of copper oxide ore in sulfuric acid lixiviant. Scientia Iranica, 25(3), 1412-1422. https://doi.org/10.24200/sci.2018.5226.1154

Bai, S., Fu, X., Li, C., and Wen, S. (2018). Process improvement and kinetic study on copper leaching from low-grade cuprite ores. Physicochemical Problems of Mineral Processing, 54(2), 300-310. http://dx.doi.org/10.5277/ppmp1818

Bezerra, M. A., Santelli, R. E., Oliveira, E. P., Villar, L. S., and Escaleira, L. A. (2008). Response surface methodology (RSM) as a tool for optimization in analytical chemistry. Talanta, 76(5), 965-977. https://doi.org/10.1016/j.talanta.2008.05.019

Davenport, W. G., King, M., Schlesinger, M., and Biswas, A. K. (2002). Extractive metallurgy of copper, Pergamon, New York.

Ekmekyapar, A., Aktaş, E., Künkül, A., and Demirkiran, N. (2012). Investigation of leaching kinetics of copper from malachite ore in ammonium nitrate solutions. Metallurgical and Materials Transactions B, 43, 764-772. https://doi.org/10.1007/s11663-012-9670-2

Ekmekyapar, A., Demirkıran, N., Künkül, A. S. I. M., and Aktaş, E. (2015). Leaching of malachite ore in ammonium sulfate solutions and production of copper oxide. Brazilian Journal of Chemical Engineering, 32(1), 155-165. https://doi.org/10.1590/0104-6632.20150321s00003211

Espiari, S., Rashchi, F., and Sadrnezhaad, S. K. (2006). Hydrometallurgical treatment of tailings with high zinc content. Hydrometallurgy, 82, 54-62. https://doi.org/10.1016/j.hydromet.2006.01.005

Ghasemi, S. M. S., and Azizi, A. (2018). Alkaline leaching of lead and zinc by sodium hydroxide: kinetics modeling. Journal of materials research and technology, 7(2), 118-125. https://doi.org/10.1016/j.jmrt.2017.03.005

Habashi, F. (1999). A Textbook of Hydrometallurgy, (second ed.), Métallurgie Extractive, Qúebec City, Canada.

Habbache, N., Alane, N., Djerad, S., and Tifouti, L. (2009). Leaching of copper oxide with different acid solutions. Chemical Engineering Journal, 152(2-3), 503-508. https://doi.org/10.1016/j.cej.2009.05.020

Hansen, H. K., Yianatos, J. B., and Ottosen, L. M. (2005). Speciation and leachability of copper in mine tailings from porphyry copper mining: influence of particle size. Chemosphere, 60(10), 1497-1503. https://doi.org/10.1016/j.chemosphere.2005.01.086

Hao, J., Wang, X., Wang, Y., Wu, Y., and Guo, F. (2022). Optimizing the leaching parameters and studying the kinetics of copper recovery from waste printed circuit boards. ACS omega, 7(4), 3689-3699. https://doi.org/10.1021/acsomega.1c06173

Hosseinzadeh, M., Entezari Zarandi, A., Pasquier, L. C., and Azizi, A. (2021). Kinetic investigation on leaching of copper from a Low-grade copper oxide deposit in sulfuric acid solution: A case study of the crushing circuit reject of a copper heap leaching plant. Journal of Sustainable Metallurgy, 7, 1154-1168. https://doi.org/10.1007/s40831-021-00408-5

Houshmand, A. R., Azizi, A., and Bahri, Z. (2024). Recovery of lead from the leaching residue derived from zinc production plant: process optimization and kinetic modeling. Geosystem Engineering, 27(1), 14-26. https://doi.org/10.1080/12269328.2023.2292984

Janyasuthiwong, S., Ugas, R., Rene, E. R., Alessandra, C., Esposito, G., and Lens, P. N. (2016). Effect of operational parameters on the leaching efficiency and recovery of heavy metals from computer printed circuit boards. Journal of Chemical Technology & Biotechnology, 91(7), 2038-2046. https://doi.org/10.1002/jctb.4798

Levenspiel, O. (1999). Chemical Reaction Engineering, Third Edition, John Wiley & Sons, Inc., p. 27. https://www.bau.edu.jo/UserPortal/UserProfile/PostsAttach/57412_6499_1.pdf

Luo, Y., Ekanayake, N. I., Amini, N., Moon, E., Hapgood, K., Scales, P. J., and Stickland, A. D. (2024). Quantifying the effects of clays on mineral tailings filtration. Minerals Engineering, 216, 108830. https://doi.org/10.1016/j.mineng.2024.108830

Maleki, H., Chehreghani, S., Noaparast, M., Mirmohammadi, M. S., and Ghanbarzad, M. (2023). Dissolution kinetics of a copper oxide ore sample and optimizing the effective parameters, using response surface methodology. Rudarsko-geološko-naftni zbornik, 38(2), 75-85. https://doi.org/10.17794/rgn.2023.2.5

Mohanraj, G. T., Rahman, M. R., Arya, S. B., Barman, R., Krishnendu, P., and Meena, S. S. (2022). Characterization study and recovery of copper from low grade copper ore through hydrometallurgical route. Advanced Powder Technology, 33(1), 103382. https://doi.org/10.1016/j.apt.2021.12.001

Montgomery, D. C. (2001). Design and analysis of experiments, New York: John Wiley & Sons.

Motamedizadeh, M., Azizi, A., and Bahri, Z. (2021). Recycling lead from a zinc plant residue (ZPR) using brine leaching and cementation with aluminum powder. Envi-

ronmental Science and Pollution Research, 28(31), 42121-42134. https://doi.org/10.1007/s11356-021-13643-w

Myers, R. H., and Montgomery, D. C. (2002). Response surface methodology: process and product optimization using designed experiments, 2nd Ed. John Wiley & Sons, New York.

Nozari, I., and Azizi, A. (2020). Experimental and kinetic modeling investigation of copper dissolution process from an Iranian mixed oxide/sulfide copper ore. Journal of Sustainable Metallurgy, 6, 437-450. https://doi.org/10.1007/s40831-020-00291-6

Nozhati, R. A., and Azizi, A. (2020). Leaching of copper and zinc from the tailings sample obtained from a porcelain stone mine: feasibility, modeling, and optimization. Environmental Science and Pollution Research, 27(6), 6239-6252. https://doi.org/10.1007/s11356-019-07199-z

Pan, Z., Jian, C., Peng, Z., Fu, X., He, R., Yue, T., and Sun, W. (2024). Study on process mineralogy of the combined copper oxide ore in Tibet and acid leaching behavior with calcium fluoride. Minerals, 14(4), 352. https://doi.org/10.3390/min14040352

Sun, G., Jiang, M., Wang, S., Fu, L., Zuo, Y., Zhang, G., and Zhang, L. (2023). Enhancement of copper metal dissolution in sulfuric acid solution with oxygen and ultrasound. Journal of Materials Research and Technology, 26, 5016-5027. https://doi.org/10.1016/j.jmrt.2023.08.266

Tanaydin, M. K., Tanaydin, Z. B., and Demirkiran, N. (2022). Optimization of process parameters and kinetic modelling for leaching of copper from oxidized copper ore in nitric acid solutions. Transactions of Nonferrous Metals Society of China, 32(4), 1301-1313. https://doi.org/10.1016/S1003-6326(22)65875-8

Tanda, B. C., Eksteen, J. J., and Oraby, E. A. (2017). An investigation into the leaching behaviour of copper oxide minerals in aqueous alkaline glycine solutions. Hydrometallurgy, 167, 153-162. https://doi.org/10.1016/j.hydromet.2016.11.011

Toro, N., Ghorbani, Y., Turan, M. D., Robles, P., and Gálvez, E. (2021). Gangues and clays minerals as rate-limiting factors in copper heap leaching: a review. Metals, 11(10), 1539. https://doi.org/10.3390/met11101539

Wang, G. R., Liu, Y. Y., Tong, L. L., Jin, Z. N., Chen, G. B., and Yang, H. Y. (2019). Effect of temperature on leaching behavior of copper minerals with different occurrence states in complex copper oxide ores. Transactions of Nonferrous Metals Society of China, 29(10), 2192-2201. https://doi.org/10.1016/S1003-6326(19)65125-3

Yang, J., Chen, L., Wu, D., Cao, J., and Guo, J. (2023). Leaching of cuprite with ozone as an oxidant in sulfuric acid solution and its oxidation leaching mechanism. Arabian Journal of Chemistry, 16(10), 105159. https://doi.org/10.1016/j.arabjc.2023.105159

SAŽETAK

Istraživanje potencijalne oporabe bakra iz niskokvalitetnih izvora koji sadržavaju visok sadržaj silicijeva dioksida

Cilj ovoga istraživanja bio je eksperimentalno ispitati izluživanje bakra iz rude niske kvalitete koja sadržava 0,57 % bakra, 24,69 % silicija i 10,367 % željeza. Prvo je ispitano ponašanje važnih varijabli koje utječu na proces otapanja korištenjem metode jedan faktor u vremenu (OFAT) i modeliranja odzivne površine (RSM), zatim je detaljno ispitana kinetika izluživanja kako bi se identificiralo naredno djelovanje izluživanja. Rezultati dobiveni OFAT metodom pokazali su da je veličina čestica od 0 do 2 mm bolja opcija za izluživanje u spremniku u odnosu na druge frakcije. Prisutnost glinenih spojeva u rudi dovela je do velikoga povećanja potrošnje kiseline. Brzina izluživanja poboljšala se s povećanjem postotka krutih tvari s 20 na 40 %, a zatim se smanjila s daljnjim povećanjem zbog nedostatka pravilnoga miješanja. Osim toga, brzina miješanja pulpe imala je mali utjecaj na otapanje bakra potvrđujući da brzina miješanja pulpe treba biti na razini koja suspendira čestice i sprječava njihovo taloženje. Zatim je s RSM-om obavljeno modeliranje i optimizacija procesa te određivanje moguće interakcije između radnih parametara. Rezultati su pokazali da je izluživanje bakra znatno ovisilo o interakciji između radnih parametara. Optimizirani parametri bili su koncentracija kiseline od 90 kg/t, sadržaj krutih tvari od 35 %, brzina miješanja pulpe od 150 o/min, vrijeme izluživanja od 2,5 h i raspon veličine čestica od 0 do 2 mm. Kinetička analiza pokazala je da je difuzijski model u proizvodnome nizu s energijom aktivacije od 14,15 kJ/mol mjera koja kontrolira brzinu reakcije, te je na temelju toga predložen novi model koji opisuje kinetiku otapanja bakra.

Ključne riječi:
bakrov oksid, izluživanje u spremniku, učinkovitost ekstrakcije, optimizacija, kinetika otapanja

Author's contribution

Milad Abbassi (M.Sc. student): conceptualization, investigation, data curation, formal analysis, methodology, software, and writing – original draft. **Asghar Azizi** (Associate professor): conceptualization, funding acquisition, investigation, methodology, project administration, software, supervision, validation, visualization, writing – original draft and writing – review & editing.
All authors have read and agreed to the published version of the manuscript.

RGNZ/MGPB

Geology and mineralogy of Fe-Sn deposit in Batubesi, Belitung Island, Indonesia

Rudarsko-geološko-naftni zbornik
(The Mining-Geology-Petroleum Engineering Bulletin)
DOI: 10.17794/rgn.2025.5.7

Original scientific paper

Aryo Dwi Handoko[1,2]*, Mochamad Slamet Sugiharto[3], Syafrizal[4], Alfend Rudyawan[1], Benyamin Sapiie[1]

[1] *Department of Geological Engineering, Faculty of Earth Sciences and Technology, Institut Teknologi Bandung, Indonesia.*
[2] *Research Center for Geological Resources, National Research and Innovation Agency, Indonesia.*
[3] *PT TIMAH, Indonesia.*
[4] *Department of Mining Engineering, Faculty of Mining and Petroleum Engineering, Institut Teknologi Bandung, Indonesia.*

Abstract

Batubesi deposit is a primary Fe-Sn deposit located in the eastern part of Belitung, Indonesia. Previously, mineralisation was known as greisen, but recent studies show that the region has developed skarn-type deposits. Despite that, skarn-type mineralisation has not been well studied. This research aims to study Fe-Sn mineralisation in Batubesi with a geological and mineralogical approach, primarily from field observation and diamond drill core logs and samples. The laboratory methods used are petrology, SEM-EDX, micro-XRF, and XRD analysis to determine mineralogical assemblage, as well as fused bead XRF to determine the geochemical composition of the deposit. The results show that the Batubesi deposit is dominated by skarn-type mineralisation with minor greisen. Two skarn stages have been observed: prograde and retrograde. Prograde stages are characterised by the precipitation of calc-silicate minerals and magnetite then often fractured or brecciated. The fractures and breccia are then altered by the retrograde stage, composed of amphibole, muscovite, and biotite. Sometimes, the alteration is so intense that the previous prograde stage is completely altered. Furthermore, the retrograde stage consists of sulfide minerals as veins such as pyrite, chalcopyrite, and arsenopyrite. Magnetite is the common ore mineral, followed by cassiterite, scheelite, ferberite, pyrite, chalcopyrite, arsenopyrite, glaucocerinite, and sphalerite.

Keywords:
Batubesi, iron-tin, skarn, ore deposit, mineralogy

1. Introduction

Tin is a critical metal for low-carbon technology (**Moss et al., 2013**) and other purposes, such as chemicals, tinplate, solder, and alloys (**U.S. Geological Survey, 2022**). Tin consumption has risen in the last two decades, primarily by increased consumption in China. The consumption increases also led to a shift in world tin consumption that changed the biggest tin consumers from Europe and North America to China (**Li et al., 2021**).

Historically, there are several critical tin-producing regions in the world, namely the Southeast Asian Tin Belt, South China Tin Province, the Central Andean Tin Belt, and Cornwall Tin Province (**Lehmann, 2020**). The Southeast Asia Tin Belt stretches from Myanmar to Indonesia through Thailand and Malaysia. This region is currently one of the significant tin mine areas that hosted one-third of the estimated annual tin production in 2021 (**U.S. Geological Survey, 2022**).

Tin deposits can be classified into several categories, such as pegmatite, greisen, porphyry, skarn, vein, and placer, with cassiterite as the main ore mineral (**Dill, 2010**). Ionic radius of tin (Sn^{4+}, 0.71 Å) is similar with iron (Fe^{3+}, 0.64 Å), titanium (Ti^{4+}, 0.68 Å), niobium (Nb^{5+}, 0.70 Å), tantalum (Ta^{5+}, 0.73 Å), and scandium (Sc^{3+}, 0.81 Å) (**Railsback, 2003**). Thus, it can be substituted by those ions in earth-forming or other minerals. Garnet, an abundant mineral in skarn, can contain up to 1% tin, while magnetite in skarn deposits can incorporate up to 0.4% tin (**Chen et al., 2022**). Tin mineralisation source is believed from the breakdown of tin-bearing minerals such as muscovite or biotite caused by melting or alteration (**Chen et al., 2022; Kunz et al., 2022; Wolf et al., 2018; Zhao et al., 2022**). Additionally, tin may be preserved in magma and deposited in granite, increasing its content in granite (**Neymark et al., 2021**).

Skarn here is defined as mineralisation that contains an abundant amount of calc-silicate minerals, such as

* Corresponding author: Aryo Dwi Handoko
e-mail address: 32020004@mahasiswa.itb.ac.id; aryodwihandoko@gmail.com
Received: 5 March 2025. Accepted: 14 May 2025.
Available online: 21 October 2025

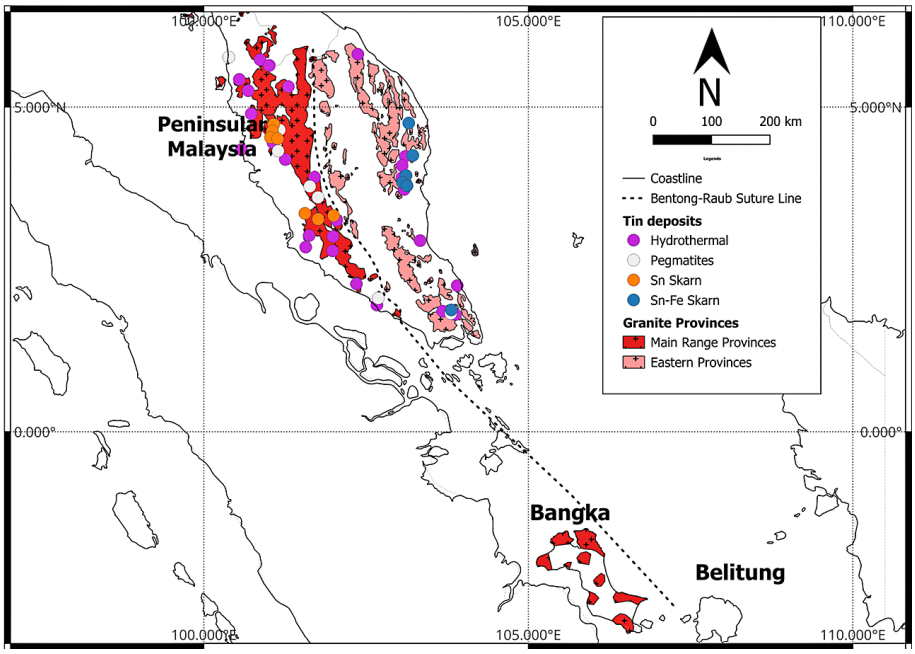


Figure 1. Maps of Peninsular Malaysia including Bangka and Belitung Islands, that show the spatial difference between Sn skarn (orange dot) and Sn-Fe skarn (blue dot). Tin deposits, Peninsular Malaysia granite provinces and Bentong-Raub Suture line from previous published data (**Yang et al., 2020**). Similarly, Bentong-Raub Suture line in oceans and Bangka granite provinces from published data (**Ng et al., 2017**).

garnet, pyroxene, and or wollastonite (**Einaudi et al., 1981; Meinert, 1992; Meinert et al., 2005**), hence its protolith may be other than carbonate rocks such as siliciclastic, igneous, or metamorphic rocks (**Chang et al., 2019**). Skarn can be subclassified based on their dominant metallic content, such as Cu-, Au-, W-, Sn-, and Fe-skarn (**Meinert et al., 2005**). Those skarns share similar compositional characteristics, such as Au, Mo, and W skarns commonly hosted in reduced skarn, meanwhile Cu skarns hosted in oxidised skarns (**Meinert, 2020; Meinert et al., 2005**). Besides that, skarn is also commonly zoned both temporally and spatially caused by variations of temperature and composition that also affect mineralisation patterns in skarn (**Meinert, 1997**). This zonation also affects garnet and pyroxene, common minerals in skarns. Furthermore, their ratio is controlled by redox conditions, which are regulated by magma and wall rocks, i.e. garnet is more abundant in more oxidised parts of the system (near intrusions), whereas pyroxene is more abundant in more reduced parts of the system (near wallrock) (**Chang et al., 2019**).

Primary tin mining in Belitung has been done in several deposits, such as Kelapa Kampit, Nam Salu, Tikus, Tebrong, and Selumar, with several other known tin mineral deposits (**Adam, 1960; Crow & Van Leeuwen, 2005; Schwartz et al., 1995; Schwartz & Surjono, 1990**). Batubesi is one of the known tin mineral deposits in Belitung, which was mined for its iron content and is currently being explored for tin mining. Historically, tin mineralisation types in Batubesi were known as vein and greisen (**Schwartz et al., 1995; Sujitno et al., 1981**). However, recent studies suggest that Batubesi tin mineralisation type is a skarn deposit (**Bargawa et al., 2023; Sugiharto et al., 2024**). Those studies mainly cover ore potency evaluation and tungsten occurrence with minimal detailed geological and mineralogical condition related to Fe-Sn skarn mineralisation in Batubesi explained. This study wants to emphasize and determine the geological and mineralogical characteristics of Batubesi skarn tin mineralisation. Additionally, this study wanted to present how skarn deposit can develop in Belitung Island where carbonate is not known to exist.

1.1. Geology of Belitung Island

Southeast Asia Tin Belt granite provinces can be divided into Main Range Province, Eastern Province, Western Province, and North Thailand Migmatitic Province (**Cobbing et al., 1986**) with different tin mineralisation type and metal association (**Hutchison, 1978**). Main Range Province and Eastern Province are divided by Bentong-Raub Suture, which also occurs as a boundary in tin skarn characteristics (**Searle et al., 2012**). It can be seen clearly in the Malay Peninsula, where tin skarn is mostly located in Main Range Province (western part of Bentong-Raub Suture), while tin-iron skarn is mostly located in Eastern Province (eastern part of Bentong-Raub Suture) (**Yang et al., 2020**) (see **Figure 1**).

Belitung Island is in the southern part of the Southeast Asian Tin Belt, located around the Bentong-Raub Suture zone, but the suture itself remains unclear. Some researchers argue that the suture developed from Malay Peninsula and extended to Belitung Island (**Hutchison, 2014; Ng et al., 2017**), while others claim that the suture is located in the southern Bangka and Belitung (**Metcalfe, 2017; Searle et al., 2012**). It is believed that Belitung is a peneplain area with resistive quartz standing as hills (**Johari, 1987**) with elevation commonly below 100m, with the highest point around 500m. Belitung is composed of siliciclastic sediments in which some of them undergone metamorphism, chert, basaltic lava, flysch sediments, and volcanic breccia intruded by grani-

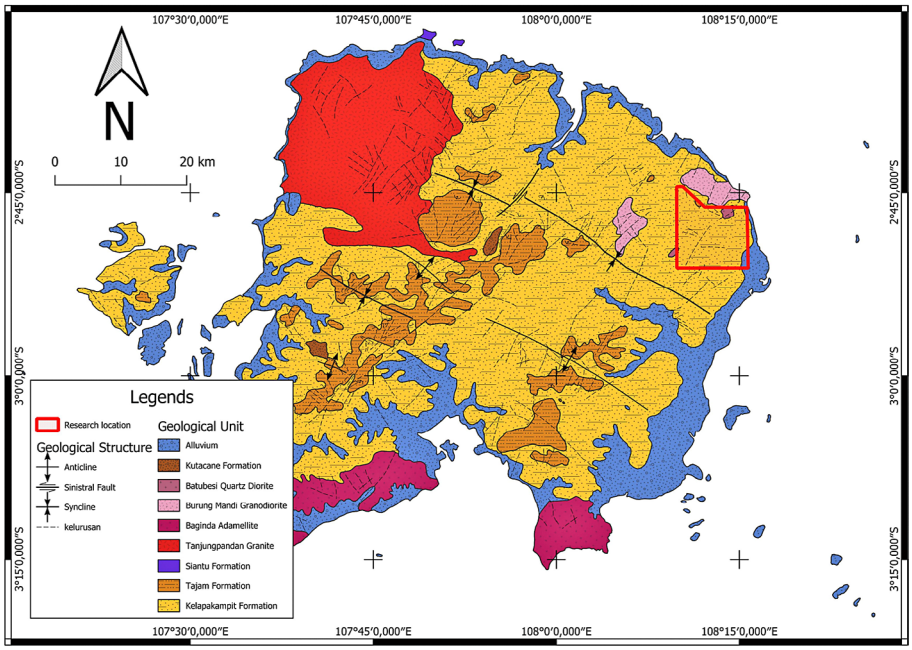


Figure 2. Belitung geological map with research location (red box) (modified after **Baharuddin & Sidarto, 1995**)

toid and diorite (**Baharuddin & Sidarto, 1995**). Flysch sediment fossils suggest that the rocks formed at the Permo-Carboniferous age in marine environments, similar to interfingering basaltic lava and volcanic breccia. Meanwhile, siliciclastic sediments probably interfingers flysch sediments but with unknown depositional environments. The sediments were then intruded by Tanjungpandan granite at 208-245 Ma, followed by Baginda Adamellite (160-208 Ma), Burungmandi Granodiorite (115-160 Ma) and Batubesi Quartz Diorite (115-160Ma) (**Priem et al., 1975**). Plutonic igneous rocks in Belitung can be divided into four types, namely gabbroic, granodioritic, adamellitic, and granitic rocks (**Aleva, 1960**). However, later studies suggest that no gabbroic igneous rocks are present; only basaltic lava can be found (**Baharuddin & Sidarto, 1995**).

1.2. Deposit geology

Batubesi Fe-Sn skarn deposit is one of the primary tin deposits located in Belitung Island, Indonesia. It is currently being explored for its tin mining potential, in continuation of previous iron mines. It is in the island's eastern part, approximately 20 km southwest of Open Pit Nam Salu Geosite. The elevation is around 12 to 25 meters with plain relief, close to Mang Mountain (406 m) and Bolong Mountain (305 m). The Batubesi Fe-Sn deposit is located at the contact between Kelapa Kampit flysch sediments (mostly siliciclastic) and granitic intrusions with a width of several hundred meters (see **Figure 2**).

2. Materials and methods

Three diamond drill cores and outcrop analysis have been performed to understand the rock, minerals, and alteration characteristics from the study area. Furthermore, seventy-eight rock samples from diamond drill cores have been collected to be analyzed for their mineral assemblage, geochemistry, and sequence in the laboratory. Most of the samples are taken from oriented drill cores, and their orientation is preserved in the samples. Handheld XRF was used in screening process to identify tin and metal rich samples but not displayed here as it only shows semi-quantitative results from the samples not reflecting their whole rock geochemistry. Several methods are used for analysis, such as petrography, SEM-EDX, micro-XRF, and X-ray diffraction. Some samples have undergone several analyses to ensure their mineral, texture, and structure identification process.

2.1. Petrography

Seventy-eight thin sections and eighteen polished samples have been analysed for their mineral, texture, and structure identification. One oriented diamond drill core sample may have several thin sections with different orientations. This method is best suited to determine mineral texture and structure that can determine mineral paragenetic sequences. Moreover, this method can be used to complement other mineral identification techniques. Polished sections were made when samples had substantial amounts of opaque minerals, some of which were also used for SEM-EDX and micro-XRF analyses. Polished samples taken from diamond drill cores were then mounted in resin and polished with diamond paste. The analysis was done at Faculty of Earth and Science and Technology, Institut Teknologi Bandung and National Research and Innovation Agency, Indonesia.

2.2. SEM-EDX

Four polished samples were analyzed for SEM Jeol JSM IT300 equipped with EDX Oxford XMAX at Ad-

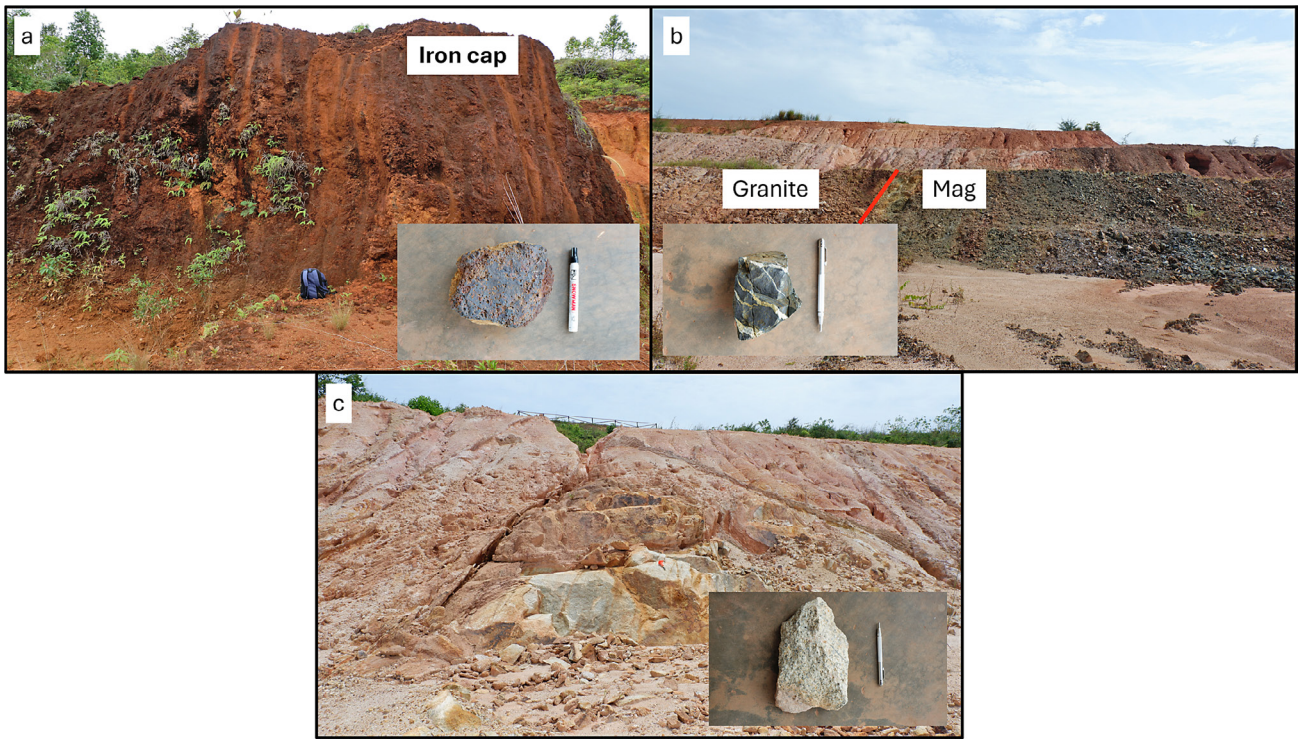


Figure 3. (a) Iron cap with vesicular structure (inset), commonly found near surface. (b) Contact between granite and magnetite-rich rocks (Mag) from pit bench. Magnetite commonly intruded by quartz vein (inset). (c) Granite outcrop in Batubesi with its hand specimen (inset). Abbreviations: Mag: magnetite

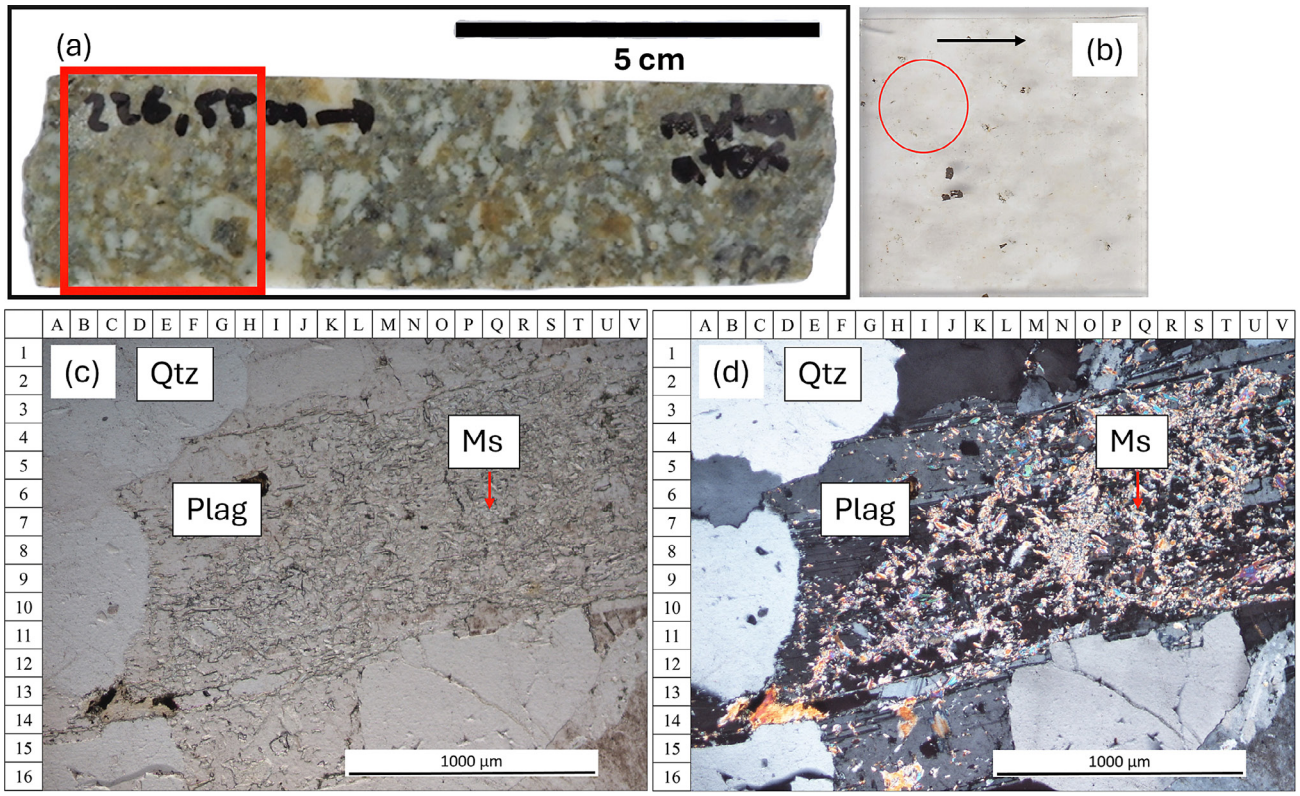


Figure 4. Photomicrograph of slightly greisenized granite shows plagioclase altered to muscovite from sample AB01020_A. Sample taken from drill cores marked with thin section region (red rectangle) (a), thin section marked with observation zone by optical microscope (red circle) (b), photomicrograph of observation zone in parallel nicol (c) as well as cross nicol (d). Abbreviations: Plag: plagioclase, Ms: muscovite

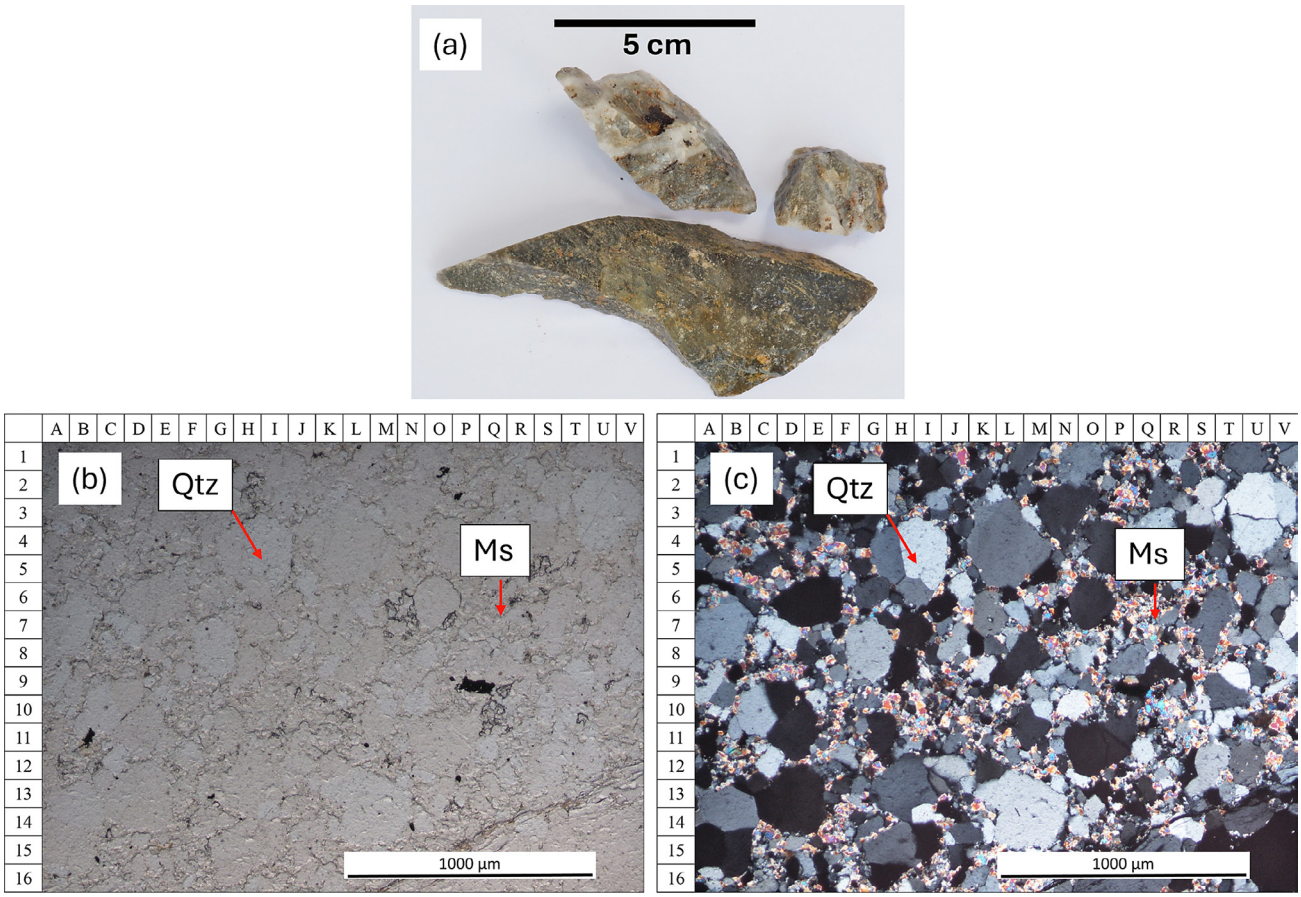


Figure 5. Sample taken from drill cores (a) with photomicrograph of greisen alteration in Batubesi in parallel nicol (b) as well as cross nicol (c) from sample AB01018_A. Greisen alteration near granitic rock marked by quartz (white-grey, H5) (c) and muscovite (high birefringence, I11) (c) rich rocks. Abbreviations: Qtz: quartz, Ms: muscovite

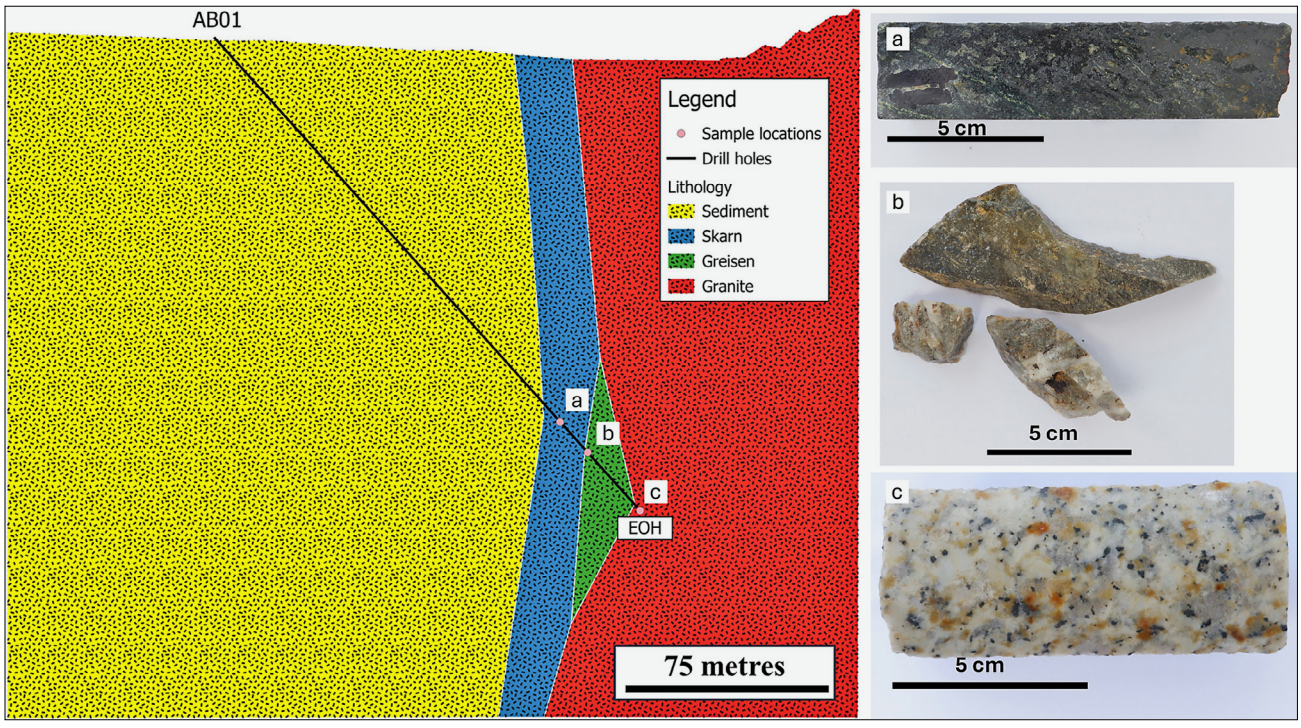


Figure 6. A cross-section of AB01 from Batubesi Fe-Sn deposit shows the relative position of granite, greisen, skarn, and sedimentary rocks. Greisen (green) is located between granite (red) and skarn (blue)

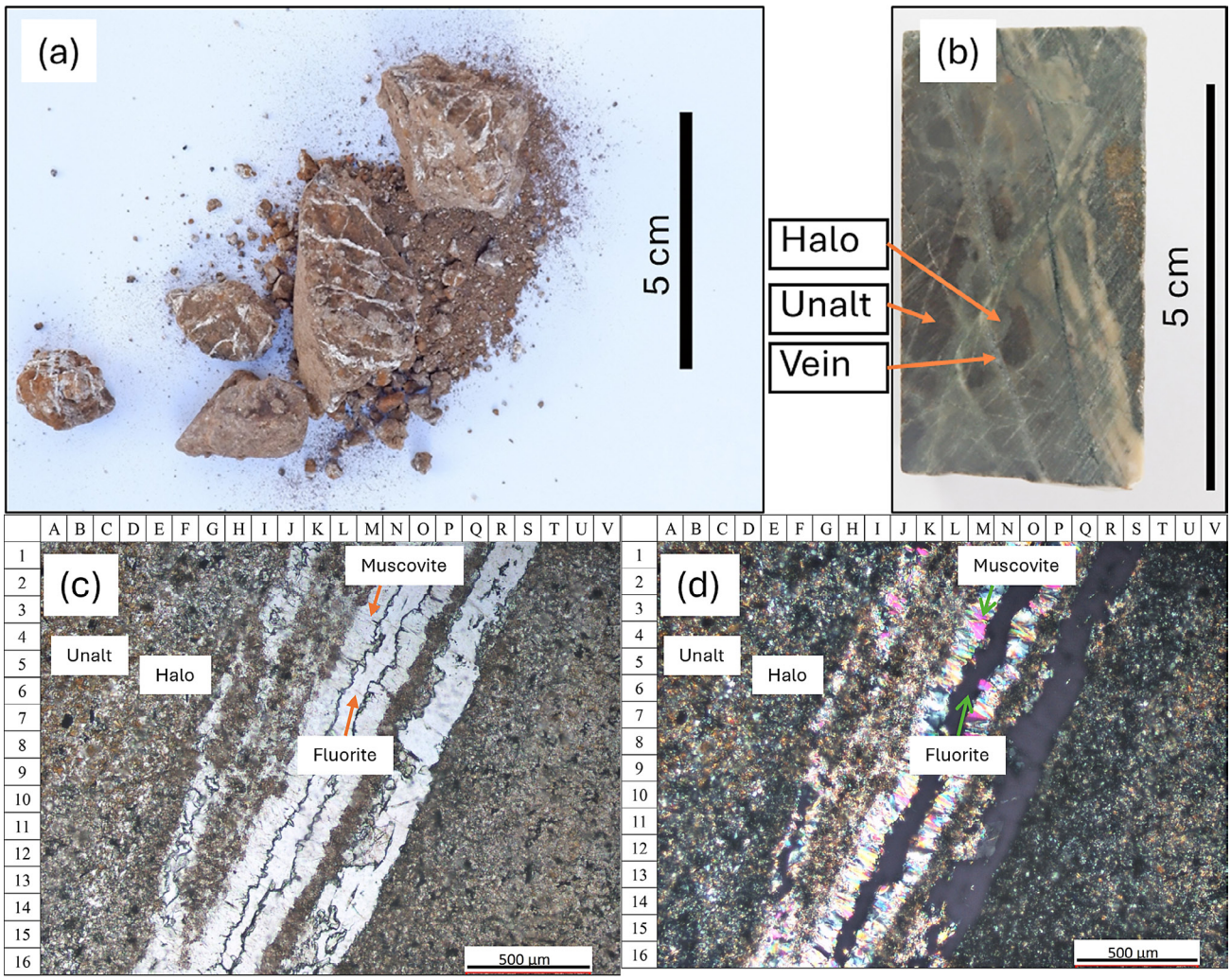


Figure 7. Clastic sedimentary rocks (AB01003) from Batubesi deposit retrieved from drill cores (a) with meta-siltstone (AB03006_B) (b) samples displaying unaltered meta-siltstone (Unalt), veins (Vein), and alteration halo around veins (Halo). Photomicrograph of meta-siltstone samples in parallel nicol (c) and cross nicol (d) shows the unaltered meta-siltstone, alteration halo, with fluorite-muscovite veins

vanced Characterization Laboratories Bandung, National Research and Innovation Agency, Indonesia. This method is used to determine minerals that contain light elements (e.g. fluorite). Samples are taken from petrographic polished sections that contain various types of opaque minerals as well as a high amount of tin. The sample numbers were then reduced that amount for various types of rocks and mineralisation. The samples are polished with diamond paste. Thus, some carbon contamination is expected during analysis. Samples were coated with gold before elemental mapping and elemental point analysis.

2.3. Micro-XRF

Five diamond drill samples were analyzed using Bruker M4 Tornado Plus micro-XRF analysis and AMICS to determine the mineral types based on their chemical composition. The samples were chosen based on their mineral characteristics as well as initial geochemical properties based on handheld XRF to describe important mineralogical and geochemical characteristics of the deposit. The samples were analysed at Mineral Testing Laboratory Jakarta, National Research and Innovation Agency, Indonesia. Samples were analyzed with a pixel size of around 25-40 µm and pixel time between 15-25 ms/pixel.

2.4. XRD

Sixteen diamond drill samples were analyzed with powder X-ray diffraction at National Research and Innovation Agency, Indonesia. The samples have been chosen to analyse minerals that contain small minerals or texture that are hard to observe by optical microscopy. This method also serves as secondary analytical procedures to confirm petrographic and micro-geochemical analysis such as micro-XRF and SEM-EDX. Samples were grounded manually to size below 200 mesh with agate mortar and pestle to retain their mineral structure. They were analyzed by CuKα X-ray source with 5°-90° 2-theta angles. The spectra are then compared with an open X-ray spectra database (e.g. **Lafuente et al., 2016**).

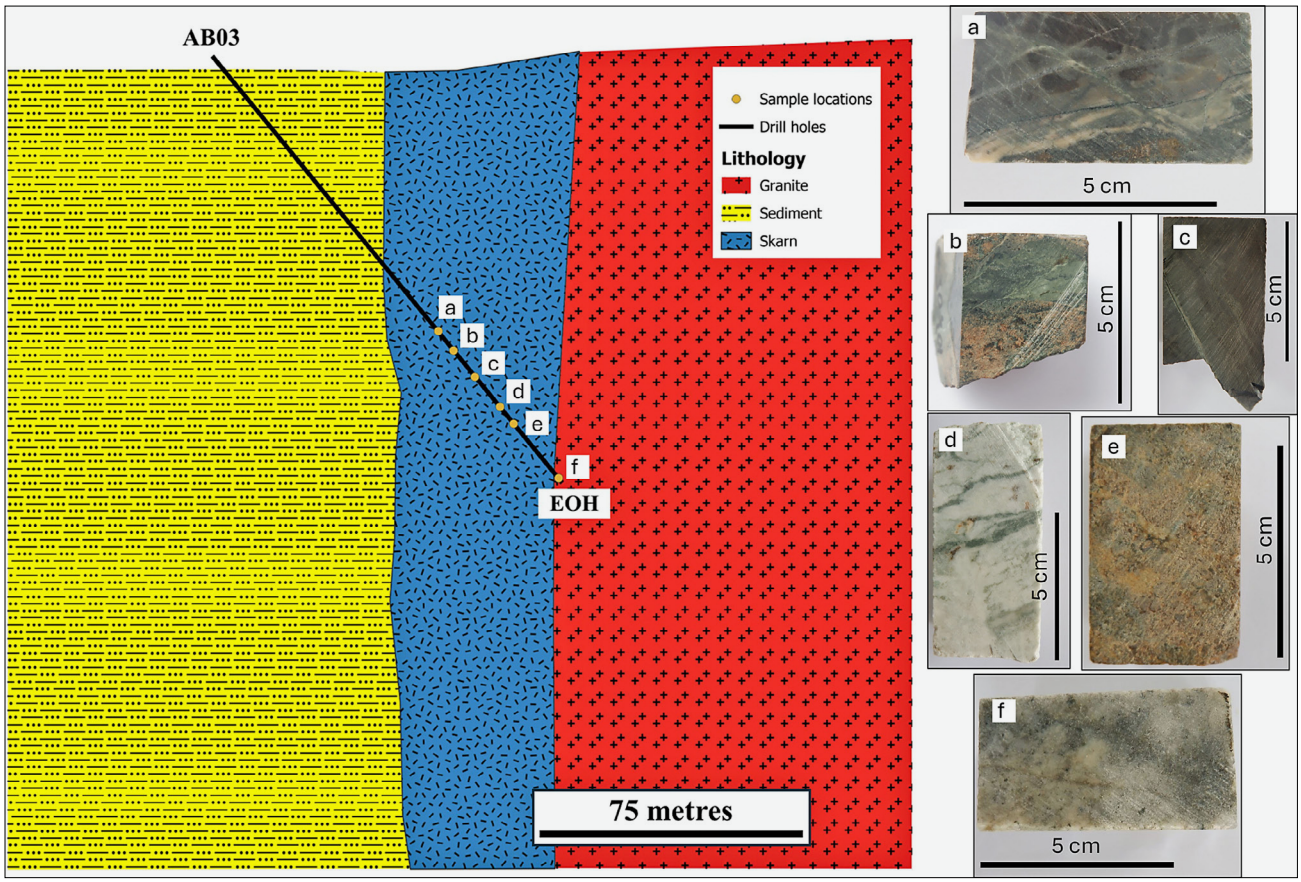


Figure 8. A cross-section of AB03 from Batubesi Fe-Sn deposit shows the relative position of skarn mineralisation with granite and sedimentary rocks. Siltstone (a, c) are located between garnet mineralisation, whereas wollastonite-rich rocks (d) are located within the skarn mineralisation

3. Results

Batubesi Fe-Sn deposit is located in a flat area and has been mined with open pit methods, resulting in tens of meters deep holes and some of them submerged below the water surface. Besides that, near Batubesi mines, there are several abandoned small holes from artisanal tin mining filled with water. At the top part of the deposit, iron caps composed of vesicular magnetite are observed (see **Figure 3a**). These vesicular rocks are also commonly found as boulders around the deposit with various sizes around tens of centimetres.

Fresh rock outcrops are scarce outside the open pit, and the surrounding ground is mixed with materials from previous mining, which hinders rock identification based on weathered materials. Skarn mineralisation was identified as black magnetite-rich rock intruded by quartz veins that can be found around open pit floor and bench (see **Figure 3b**). Besides that, granitic rocks are also found in the open pit bench with fractures commonly developed on it (see **Figure 3c**).

Three-stage skarn mineralisation has been observed in the study area: isochemical metamorphism, prograde and retrograde. Isochemical metamorphism is characterised by the occurrence of meta-siltstone in Batubesi deposit. The prograde stage is dominated by magnetite and



Figure 9. Wrigglite textures with black and white bands cut by veins in the shallower part of the deposit. SEM-EDX and petrographic analysis show that the black bands are magnetite with small amounts of cassiterite and wolfram-bearing minerals, while the white bands are fluorite.

calc-silicate mineralisation, e.g. garnet, pyroxene, vesuvianite, and wollastonite. Magnetite-garnet are the main minerals in highly altered regions, where almost all host rocks are altered, and their texture is not visible. Magnetite can be found in massive, banded, or veins and sometimes have rhythmically altered bands with arsenopyrite. Magnetite was observed being cut by carbonate and quartz veins. Conversely, garnet commonly occurs in massive texture along with fluorite and is often brecciated or fractured and then filled with biotite, muscovite, and amphibole minerals from the retrograde stage. It is also cut by other minerals from retrograde stage such as quartz, Fe-oxides (hematite), and carbonate

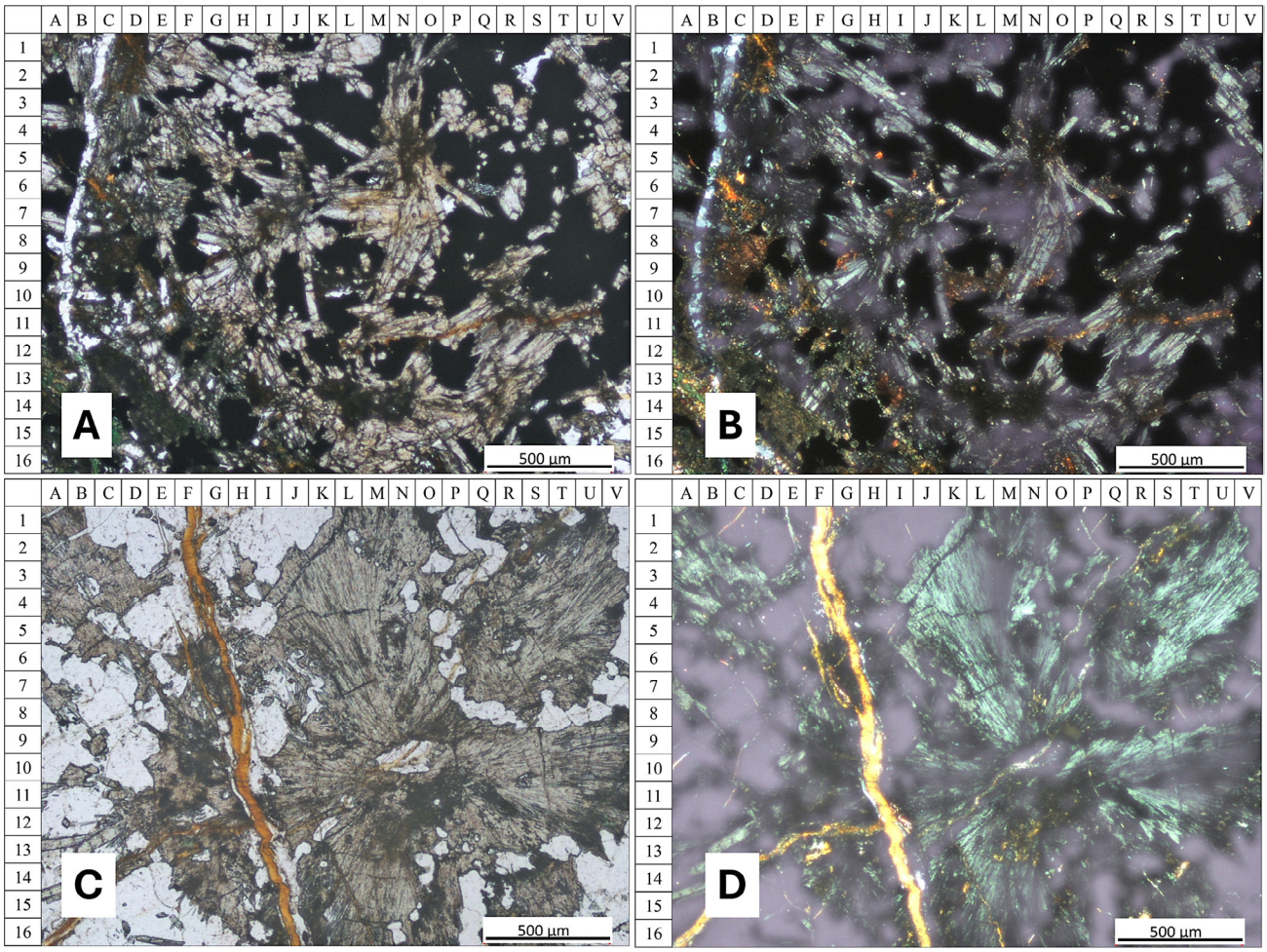


Figure 10. Photomicrograph of skarn sample from AB02015_A shows magnetite and garnet infill and cut host rock minerals with parallel nicol (a, c) and cross nicol (b, d) polarization, respectively. Magnetite (black, J10) (a) infills the space between chalcedony (white-grey, H10) (a) and cuts by quartz vein (white, C1) (a). Cross nicol (b) shows magnetite as black (J10), while chalcedony as greenish grey (H10) with biotite as reddish brown (B6). Moreover, in cross nicol (d), garnet (black, P5) cut radial chalcedony (green-grey, S5), then both cut by later vein (yellow, F1). Parallel nicol (c) show garnet as white-grey (P5) and chalcedony as grey (S5).

veins with or without an alteration envelope. Additionally, the retrograde stage also consists of sulfide minerals such as pyrite, chalcopyrite, and arsenopyrite

3.1. Petrology and mineralogy

Granitic rocks in the area are fine-grained, equigranular to porphyritic rocks mainly composed of quartz and feldspar, minor biotite and trace amounts of zircon. Many of them are greisenized from slightly altered (see **Figure 4**) to moderately altered (see **Figure 5**). Greisen alteration occurs near the contact between granitic rock and host rock, marked by quartz and muscovite-rich rocks, sometimes with chlorite-muscovite veins cutting through it (see **Figure 6**) or replacing plagioclase (see **Figure 4**). Muscovite is usually found between quartz minerals with a size of around 40 µm. Alteration intensity is reduced when moving away from the magnetite-garnet zone and is characterised by the absence of magnetite; only garnet exists, and the more unmineralised host rock is present. Wollastonite mineralisation occurs in these lower-intensity alteration zones that are several meters thick. Additionally, Fe-oxide minerals are dominated by hematite near the surface.

The host rocks in the Batubesi deposit contain friable clastic sedimentary rocks that can be observed from drill cores, and it does not contain carbonate (see **Figure 7a**). Near the granite-host rock contact, the host rock has undergone metamorphism and is mainly observed as meta-siltstone. It has a black appearance with a gritty texture that can absorb water. Mineral size in meta-siltstone is small (around 12-34 µm) and difficult to distinguish by petrography analysis. However, X-ray diffraction analysis suggests that it comprises quartz, muscovite, and kaolinite. Meta-siltstones are commonly fractured, and veins of quartz, carbonate, muscovite, fluorite, and or chlorite are commonly found with or without an alteration halo (see **Figure 7b**). The metamorphosed rocks are also commonly found around minerals formed by the skarn process (e.g. calc-silicate and magnetite) (see **Figure 8**).

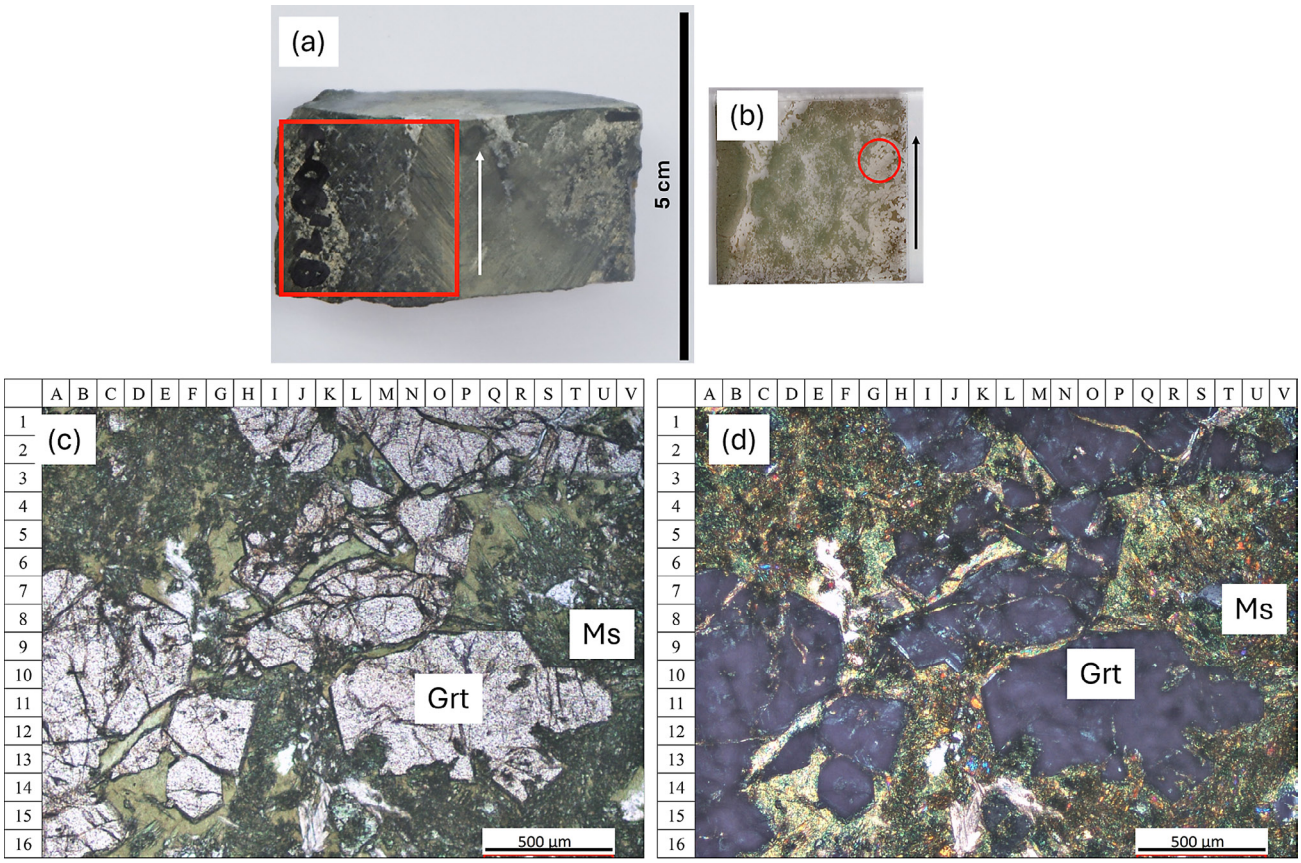


Figure 11. Altered garnet hand specimen marked with red box that locate thin section samples (a). Thin section samples from a hand specimen with a red circle that marks the microscope analysis (b). Photomicrograph of skarn mineralisation in Batubesi altered by late-stage mineralisation in parallel nicol (c) and cross nicol (d) from sample AB03002_A. Garnet is brecciated and altered to muscovite (G10). Abbreviations: Grt: garnet, Ms: muscovite

Skarn mineralisation in Batubesi is characterised by abundant magnetite, calc-silicate minerals, fluorite, muscovite, pyroxene, biotite, and amphibole. Magnetite is the most common skarn mineral found in the Batubesi deposit, with a black appearance and magnetic properties, commonly seen as a massive body, and layers found in wrigglite (see **Figure 9**) and alternating layers between magnetite and arsenopyrite. It becomes the main iron-bearing mineral in the Batubesi deposit. Magnetite is found to infill chalcedony in the deposit, then cut by a quartz vein, indicating their relative ages (see **Figure 10a**).

Calc-silicate minerals are typical minerals for skarn deposits. In the Batubesi deposit, calc-silicate minerals are commonly found as garnet, followed by wollastonite, vesuvianite, and actinolite. Garnet has a dull luster and different colours, such as red, green, and white, and is often found together with fluorite. Petrography analysis shows that garnet cut chalcedony mineral, indicating that garnet is younger than chalcedony (see **Figure 10c**). Garnet shows typical hexagonal structures with oscillatory zoning between isotropic and anisotropic parts. Many garnets were fractured and then underwent retrograde stage mineralisation, precipitating minerals such as biotite, amphibole, and muscovite (see **Figure 11**). The alteration sometimes is so intense that garnet is completely altered, retaining its oscillatory zoning features.

Wollastonite, actinolite, and vesuvianite are rarely found in the Batubesi deposit. Wollastonite can be found in an area with scarce calc-silicate or magnetite mineralisation, mostly unmineralized meta-siltstone (see **Figure 8**). It is primarily found in wollastonite-rich carbonate white layers with several metres thick, with cm to mm thick greenish pyroxene and fluorite-calcite veins (see **Figure 12**). Mineral sizes and habits are hard to determine by hand specimen observation as the sample has a uniform white colour. Petrography analysis suggests that the mineral habits are elongated parallel with a grey colour in parallel nicol and a grey to red-orange colour in cross nicol. On the other hand, actinolite and vesuvianite are rare and can be observed with garnet-rich rocks. Actinolite commonly occurs as an acicular mineral that has a pale green-green colour in parallel nicol and a greenish colour in cross nicol. Meanwhile, vesuvianite occurs as prismatic minerals in a thin section with high relief (similar with garnet), transparent in parallel nicol and grey (low birefringence) in cross nicol.

Ore minerals observed in the Batubesi area from petrographic analysis are cassiterite, magnetite, arsenopyrite, pyrite, and chalcopyrite that occur in skarn and as veins in meta-siltstone. Cassiterite mostly occurred in garnet-rich skarn mineralisation that have colourless to

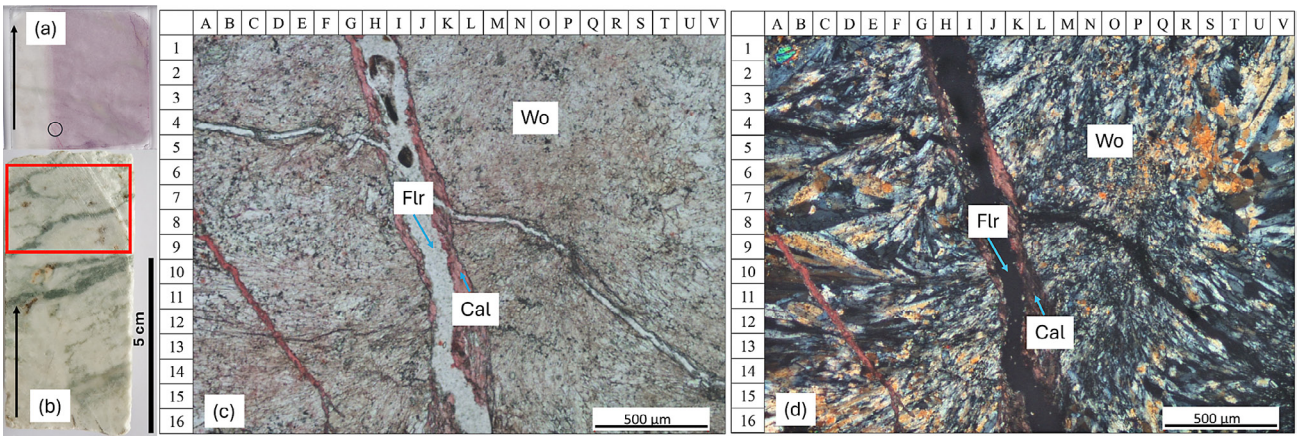


Figure 12. Wollastonite-rich rocks from AB03014_B samples with red alizarin stain cut by calcite-fluorite veins with a black circle that shows the observation zone by optical microscope (a). Sample from drill core marked with a thin section region (b). Parallel nicol (c) and cross nicol (d) photomicrograph that shows wollastonite mineral cut by fluorite and calcite veins. Abbreviations: Wo: wollastonite, Cal: calcite, Flr: fluorite

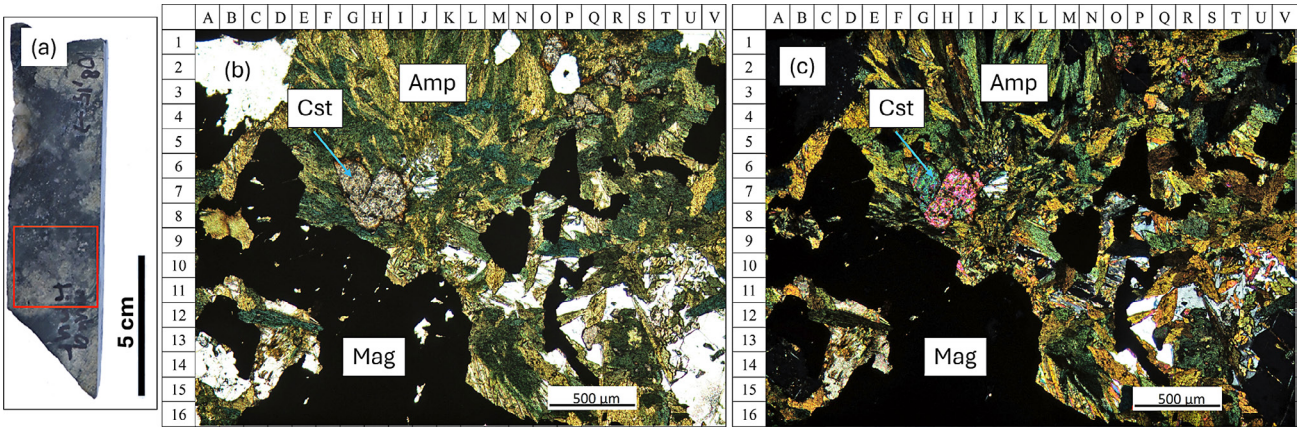


Figure 13. Location of thin section (red box) in core samples (a). Photomicrograph of cassiterite mineral in parallel nicol (brownish green, H7) (b) and cross nicol (green-pink, H7) (c) in Batubesi from sample AB02032_B. Abbreviations: Cst: cassiterite, Amp: amphibole, Mag: magnetite

brown colour in thin sections, with sizes from 160 µm to around 400 µm (see **Figure 13**). Some of them were found in altered garnets, while others were found in unaltered garnets. Magnetite can be seen as massive and layered mineral often shows wrigglite and fluid-like banded structure. Petrographic analysis in the wrigglite zone show that it comprises opaque minerals (mostly magnetite) and fluorite. On the other hand, in fluid-like banded structures opaque minerals mostly magnetite, with a minor amount of arsenopyrite, pyrite, and chalcopyrite.

3.2. XRD

X-ray diffraction analysis is usually coupled with petrographic analysis to determine mineral type in the study area. It is the primary mineral determination analysis for rocks that contain smaller minerals, such as meta-siltstone. Based on XRD data coupled with petrographic analysis, meta-siltstone is composed of quartz, muscovite, and kaolinite (see **Figure 14**). Phlogopite, microcline, albite, fluorite, magnetite, annite, pargasite, hastingsite, chamosite, andradite, uvarovite, vesuvianite, ferro-actinolite, cassiterite, and hedenbergite were also detected in XRD analysis.

3.3. SEM-EDX

SEM-EDX is useful to analyse minerals by their chemical composition. Despite its small area of analysis compared to micro-XRF, SEM-EDX successfully analyses light elements such as fluor and heavy elements such as wolfram. It is used for the identification of minerals that contain light elements (e.g. fluorite) as well as minerals that are too small to be identified by optical microscopes and their abundance is too small to be detected by bulk XRD analyses. Carbon contamination can be seen throughout the samples, because it can be found in magnetite and all other samples. It is caused by diamond paste during the polished sample preparation before the SEM-EDX analysis. This method analyses magnetite and fluorite bands in wrigglite, as well as other minerals such as

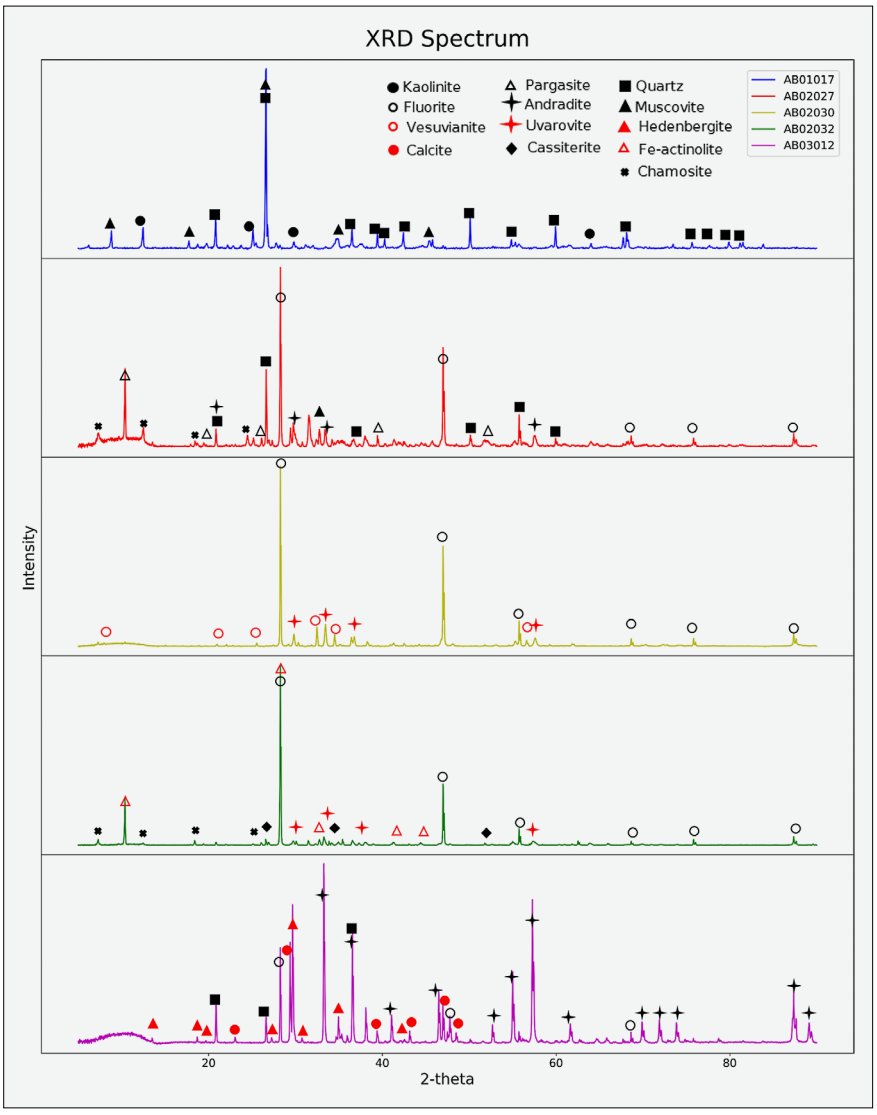


Figure 14. Bulk sample XRD spectrum of samples from Batubesi Fe-Sn deposit that shows various minerals from skarn and meta-siltstone

glaucocerinite, cassiterite, and scheelite by chemical mapping (see **Figure 15**). Additionally, point analysis shows that wolfram-bearing minerals in Batubesi are composed of ferberite and scheelite (see **Figure 16**). Scheelite are often found with a minor amount of ferberite, suggesting alteration occurs between W-bearing minerals.

3.4. Micro-XRF

Micro-XRF analysis shows that ore minerals detected in Batubesi region are magnetite, cassiterite, ferberite, scheelite, arsenopyrite, pyrite, chalcopyrite, and sphalerite. Cassiterite, ferberite, and scheelite mainly occur as fine minerals, ranging from 25 μm (one pixel) to 700 μm (see **Figure 17** and **Figure 18**). In addition, arsenopyrite, pyrite, and chalcopyrite can be seen in larger minerals, up to several millimetres. Arsenopyrite, pyrite, and chalcopyrite are commonly found as mineral assemblages (see **Figure 17**).

Hematite and pyrite veins are also present and detected by micro-XRF analysis. Hematite vein cut andradite mineral, with a small amount of Sn-bearing mineral. The analysis suggests that the Sn-bearing mineral is malayaite, but other possibilities (e.g. fine cassiterite) may be possible because of silica contamination from andradite during micro-XRF spot analysis. Conversely, pyrite veins are frequently shown with other sulphide minerals such as arsenopyrite and chalcopyrite. Later point analysis in garnet mineral shows that it contains a large amount of Fe, suggesting that it can be classified as andradite.

4. Discussion

4.1. Host rock characteristics

The characteristics of host rock play an important part in skarn mineralisation, as they can affect the redox and chemical characteristics of ore mineralisation, including skarn systems. The host rock in the Batubesi deposit is composed of sedimentary rocks, mainly siliciclastic rocks, with no carbonate present. Although not as common as its carbonate-hosted counterparts, siliciclastic skarn has been recorded previously (e.g. **Chang et al., 2019**).

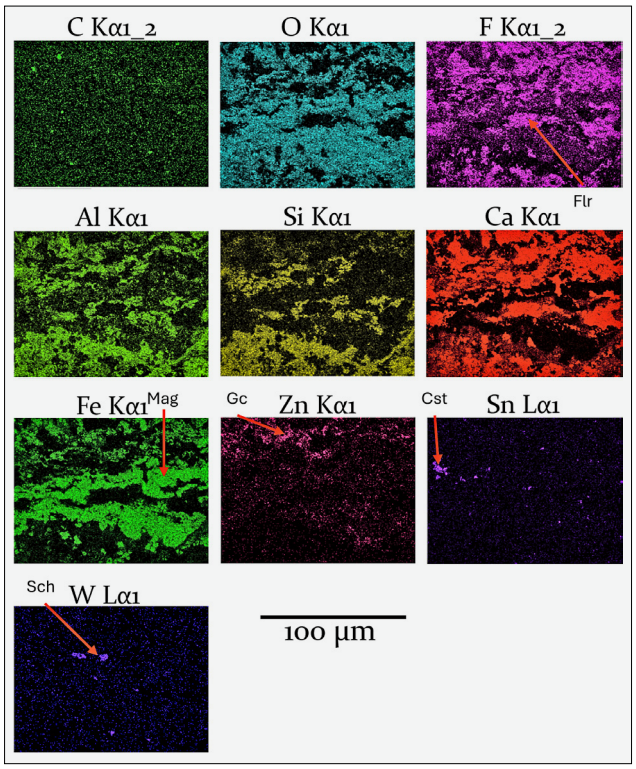


Figure 15. SEM-EDX analysis on wrigglite from skarn (AB02013) shows magnetite and fluorite bands with small amounts of glaucocerinite, cassiterite, and scheelite (Fe, Sn, and W modified after **Sugiharto et al., 2024**). Abbreviations: Gc: glaucocerinite, Flr: fluorite, Mag: magnetite, Cst: cassoterite, Sch: scheelite

Meta-siltstone is observed near the sediment-granite contact, probably due to metamorphism caused by granitic intrusions, which is common in skarn-related mineralisation (**Pirajno, 2008**). It can also be seen in zones of highly mineralised skarn zones, and the amounts tend to increase outwards to the low mineralised skarn zones. Besides that, evidence of another type of rock is also present in the area. Indications of another type of host rock are garnet and magnetite seen to be intruded and filled spaces between early minerals (chalcedony) in petrographic analysis (see **Figure 10**). Both minerals are commonly related to early skarn mineralisation (**Chen et al., 2023; Lu et al., 2003; Mei et al., 2015**), chalcedony probably comes from earlier rocks and does not correlate with Batubesi's meta-siltstone known characteristics. Despite that, the rock types and characteristics of chalcedony-bearing rocks remain unclear because it is largely replaced during skarn mineralisation.

4.2. Granitic rock

Plutonic igneous rocks in Belitung can be divided into four types, namely gabbroic, granodioritic, adamellitic, and granitic rocks (**Aleva, 1960**). However, later studies suggest that no gabbroic igneous rocks are present; only basaltic lava can be found (**Baharuddin & Sidarto, 1995**). Igneous rocks in the study area mainly comprise quartz and feldspar, with a small amount of biotite and zircon. It can be classified as felsic rocks and has a granitic composition. The granite is fine-grained and has equigranular to porphyry textures. Feldspar in granite commonly has a perthite structure. No vein is observed in granitic rocks, but fractures develop. Some of them have greisen alteration with plagioclase and feldspar are often altered to muscovite. Greisen alteration that occurs in granite related to skarn deposits is observed in other deposits that are products of the same mineralisation system as skarn (**Meyer et al., 2024**).

4.3. Alteration and mineralisation

Skarn mineralisation dominates the study area, with smaller amounts of greisen mineralisation near the granitic rocks. Skarn is characterised by calc-silicate and magnetite mineralisation that is several hundred meters wide and tens of meters deep. In contrast, greisen is characterised by quartz and muscovite-dominated rocks sev-

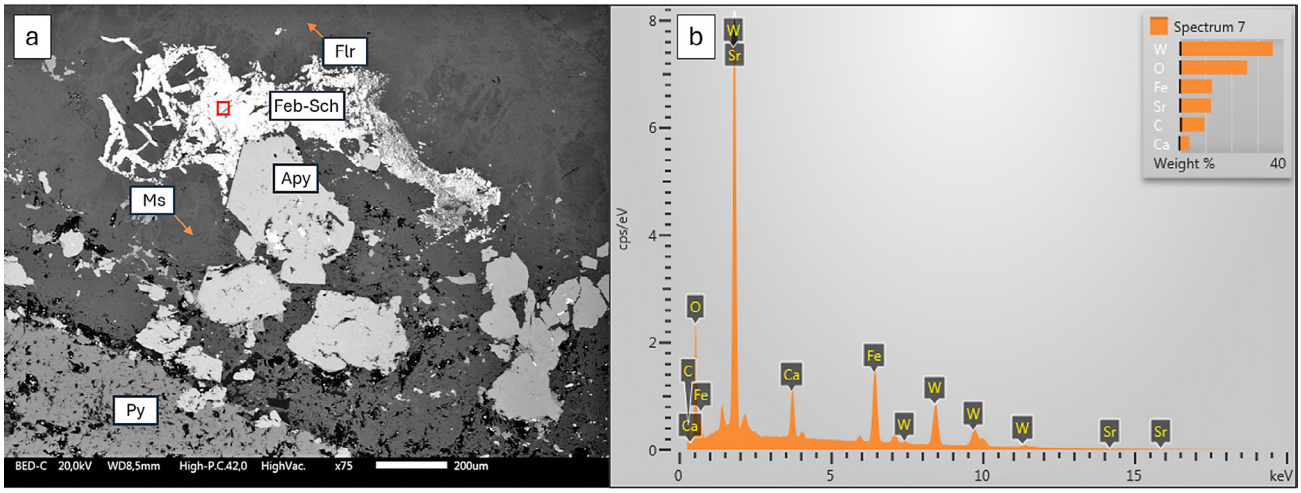


Figure 16. BSE image of skarn AB02037 (a) that shows ferberite and scheelite minerals (red box). Red box EDX analysis from (a) shows that the composition is C, O, Ca, Fe, Sr, and W (b). Abbreviations: Apy: arsenopyrite, Py: pyrite, Feb: ferberite, Sch: scheelite, Ms: muscovite, Flr: fluorite

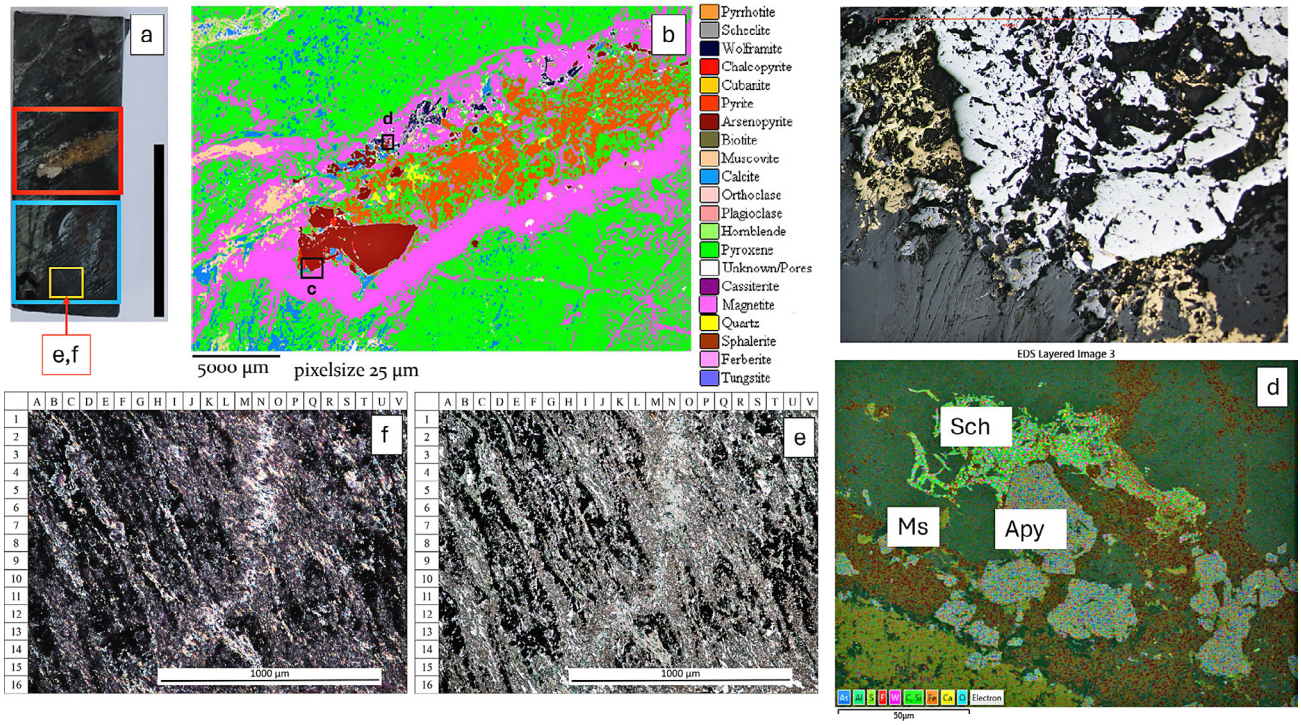


Figure 17. Multiple microanalysis to determine mineral assemblages in Batubesi skarn sample AB02037A. Quarter diamond drill samples with annotation for polished section (red box), thin section (blue box), and photomicrograph (yellow box) (a). Micro-XRF analysis shows mineral assemblage in polished section with green is pyroxene, pink is magnetite, dark red is arsenopyrite, orange is pyroxene, and blue is wolframite (b). Petrographic analysis from the polished section shows arsenopyrite (grey) and chalcopyrite (dark yellow) (c). SEM-EDX analysis that shows scheelite (Sch), arsenopyrite (Apy), and muscovite (Ms) minerals (d). Parallel nicol (e) with cross nicol (f) photomicrograph from thin section that show layers of opaque (magnetite?) and translucent (muscovite?) minerals that are cut by a late muscovite vein

eral meters deep and wide. This is different from the previous study that stated mineralisation in the Batubesi area is greisen (**Schwartz et al., 1995; Sujitno et al., 1981**)

Skarn mineralisation in the Batubesi deposit is formed in meta-siltstone and chalcedony-bearing host rock, dominated by magnetite and garnet with minimal pyroxene present. The skarn mineralisation has three stages, similar to the skarn formation model from which is isochemical metamorphism, prograde skarn, and retrograde skarn (**Pirajno, 2008**). The retrograde skarn occurred in the brecciated (see **Figure 11**) or fractured lithology (see **Figure 17**). This is related to fluid flow and permeability of retrograde mineralising fluid in skarn.

Garnet is abundant in the Batubesi deposit compared to pyroxene. This ratio can inform us about the redox state during skarn mineralisation. Garnet is precipitated in an oxidised state, whereas pyroxene is precipitated in a reduced which is mainly controlled by element supply of ferric/ferrous element from skarn system (**Chang & Meinert, 2008**). Thus, skarn mineralisation in the Batubesi Fe-Sn deposit is in an oxidised state.

4.4. Mineral zonation

Skarn commonly shows mineral zonation patterns, both spatial and temporal, that can help in deposit exploration (**Meinert, 1997**). For example, one model suggests that mineral zonation in skarn reaction from pluton to wall rock is garnet>pyroxene, pyroxene<garnet, wollastonite, and marble (**Meinert et al., 2005**). This zonation is applicable in skarn systems that have oxidising magma and reducing wall rock (**Chang & Meinert, 2008**). However, the Batubesi deposit is in an oxidised state, thus, the zonation is not applicable. For example, the wollastonite zone in the Batubesi deposit is not situated near host rock, it is rather located inside garnet mineralisation. Observable mineral zonation in Batubesi deposit is caused by the degree of alteration from retrograde stage. Highly altered zones are present in the alteration center that is located in the middle of the magnetite-garnet rich zone, and then the alteration degree gradually weakens outside. This is probably caused by the supply of fluids gradually lessen by proportional to the distance from the source.

4.5. Ore mineral assemblage

Ore minerals found in Batubesi region are oxide minerals (e.g. magnetite, cassiterite and ferberite), sulfate minerals (scheelite), and sulfides (pyrite, chalcopyrite, and arsenopyrite). Magnetite is the most abundant ore mineral in the Batubesi region that commonly has a massive structure; sometimes, it shows alternating layers with arsenopyrite. Magnetite cut by later carbonate, quartz, and sulfide veins shows that it precipitated early in the mineralisation process. Sulfide minerals in the Batubesi area are

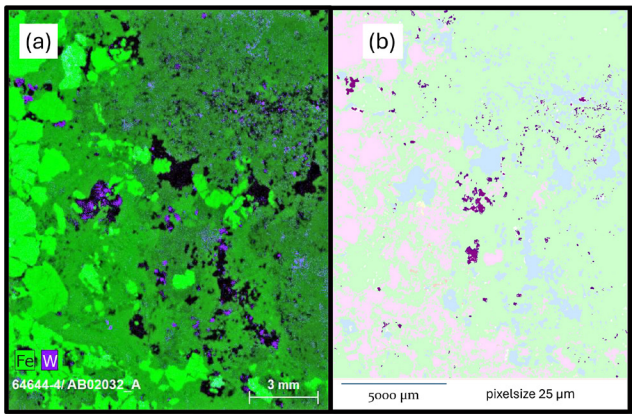


Figure 18. Wolfram element distribution from skarn sample AB02032_A (a) and Cassiterite mineral distribution (solid purple) in skarn sample AB02032_A (b). Other minerals in (b) are magnetite/ferberite (pink), pyroxene (green), and calcite (blue)

sometimes found as fine-grain minerals in magnetite. Still, they are commonly seen as sulfide veins in the latter skarn stage, ranging from several mm to several cm in widths composed of pyrite, chalcopyrite, and arsenopyrite. W-bearing minerals are only detected in SEM-EDX and micro-XRF as fine minerals. They are commonly found in similar grains, indicating that the minerals are altered. The alteration from scheelite to ferberite, and vice versa, is possible and controlled by several factors, such as the Ca/Fe ratio (**Baumer et al., 1985**).

5. Conclusions

Batubesi Fe-Sn deposit is one of the primary tin mineralisation in Belitung, known to have greisen-type mineralisation. Recently, skarn-type mineralisation has been known to develop in the region, but there is minimal information about it. This research has been done to study mineralisation in Batubesi, including the skarn-type mineralisation.

Host rock in Batubesi is composed of meta-siltstone and chalcedony-bearing rock, with no carbonate rocks present. Despite that, meta-siltstone is the one that is commonly found as a host rock in Batubesi. Minerals in the host rocks is around 12-23 µm consisting of quartz, muscovite, and kaolinite. Characteristics and composition of chalcedony-bearing rocks is not understood because the rocks are completely replaced with skarn-bearing rocks.

The Batubesi Fe-Sn deposit mineralisation type can be divided into skarn-type mineralisation and greisen-type mineralisation. Greisen mineralisation occurs near granite intrusion with several meters thick, underlain skarn. Greisen is characterised by mineralisation of muscovite. Some of the muscovite can be found as the product of plagioclase and feldspar alteration.

Skarn mineralisation is several hundred meters thick and is characterised by calc-silicate and magnetite mineralisation. It can be divided into three stages: isochemical metamorphism, prograde and retrograde. Isochemical metamorphism is characterised by the development of meta-siltstone. Prograde skarn was identified as having calc-silicate and magnetite mineralisation. Magnetite is only present in the highly altered part of the skarn. Conversely, garnet commonly occurs in massive texture along with fluorite and is often brecciated or fractured and then filled with biotite, muscovite, and amphibole minerals from the retrograde stage. It is also cut by other minerals from the retrograde stage such as quartz, Fe-oxides (hematite), and carbonate veins with or without an alteration envelope. Additionally, the retrograde stage also consists of sulfide minerals, such as pyrite, chalcopyrite, and arsenopyrite.

Acknowledgement

We thank PT TIMAH for its permission and accommodations during sample collection and field observations, the National Research and Innovation Agency, Indonesia, for laboratory analysis, and the Faculty of Earth and Science and Technology, Institut Teknologi Bandung, for laboratory analysis. ADH would like to thank the Saintek Scholarship from the Ministry of Research and Technology National Research and Innovation Agency, which was continued by the National Research and Innovation Agency Continuing Scholarship during its doctoral study in Institut Teknologi Bandung.

Funding

This research was funded by the Saintek Scholarship from the Ministry of Research and Technology, National Research and Innovation Agency, followed by Continuing Scholarship from the National Research and Innovation Agency, Indonesia.

6. References

Adam, J. (1960). On the geology of the primary tin-ore deposits in the sedimentary formation of Billiton. *Geologie en Mijnbouw, 39*(10), 405-426.

Aleva, G. J. J. (1960). The plutonic rocks from Billiton. *Geologie en Mijnbouw, 39*(10), 427-436.

Baharuddin, & Sidarto (Cartographer). (1995). Peta Geologi Lembar Belitung, Sumatera

Bargawa, W. S., Sidiq, H., Dovena, A., & Supandi, S. (2023). Skarn and Greisen Model for Tin Depositin Batubesi Area, East Belitung, Indonesia. *The Iraqi Geological Journal*, 77-88.

Baumer, A., Caruba, R., & Guy, B. (1985). Experimental study of hydrothermal transformations scheelite⇌ ferberite: preliminary results. *Bulletin de minéralogie, 108*(1), 15-20. doi:10.3406/bulmi.1985.7854

Chang, Z., & Meinert, L. D. (2008). Zonation in skarns - Complexities and controlling factors. In *Proceedings of PACRIM Congress 2008*. Goldcoast, Queensland, Australia.

Chang, Z., Shu, Q., & Meinert, L. (2019). Skarn Deposits of China. In *Mineral Deposits of China: Society of Economic Geologists Special Publication* (Vol. 22, pp. 189).

Chen, S.-C., Yu, J.-J., Bi, M.-F., & Lehmann, B. (2022). Tin-bearing minerals at the Furong tin deposit, South China: Implications for tin mineralization. *Geochemistry, 82*(1), 125856. doi:https://doi.org/10.1016/j.chemer.2021.125856

Chen, Y.-K., Ni, P., Pan, J.-Y., Cui, J.-M., Li, W.-S., Fang, G.-J., . . . Han, L. (2023). Fluid evolution and metallogenic mechanism of the Xianghualing skarn-type Sn deposit, South China: Evidence from petrography, fluid inclusions and trace-element composition of cassiterite. *Ore Geology Reviews, 154*, 105351. doi:https://doi.org/10.1016/j.oregeorev.2023.105351

Cobbing, E. J., Mallick, D. I. J., Pitfield, P. E. J., & Teoh, L. H. (1986). The granites of the Southeast Asian Tin Belt. *Journal of the Geological Society, 143*(3), 537-550. doi:10.1144/gsjgs.143.3.0537

Crow, M., & Van Leeuwen, T. (2005). Metallic mineral deposits. *Geological Society, London, Memoirs, 31*(1), 147-174.

Dill, H. G. (2010). The "chessboard" classification scheme of mineral deposits: Mineralogy and geology from aluminum to zirconium. *Earth Science Reviews, 100*(1), 1-420. doi:10.1016/j.earscirev.2009.10.011

Einaudi, M. T., Meinert, L. D., Newberry, R. J., & Skinner, B. J. (1981). Skarn Deposits. In *Seventy-Fifth Anniversary Volume* (pp. 0): Society of Economic Geologists.

Hutchison, C. S. (1978). Southeast Asian tin granitoids of contrasting tectonic setting. *Journal of Physics of the Earth, 26*(Supplement), S221-S232.

Hutchison, C. S. (2014). Tectonic evolution of Southeast Asia. *Bulletin of the Geological Society of Malaysia, 60*, 1-18.

Johari, S. (1987). Relationship between Sn mineralization and geochemical anomalies in non-residual overburden at Tebrong area, Belitung, Indonesia. *Journal of Geochemical Exploration, 28*(1-3), 219-234.

Kunz, B. E., Warren, C. J., Jenner, F. E., Harris, N. B. W., & Argles, T. W. (2022). Critical metal enrichment in crustal melts: The role of metamorphic mica. *Geology, 50*(11), 1219-1223. doi:10.1130/g50284.1

Lafuente, B., Downs, R. T., Yang, H., & Stone, N. (2016). The power of databases: the RRUFF project. In *Highlights in mineralogical crystallography* (pp. 1-29): Walter de Gruyter GmbH.

Lehmann, B. (2020). Formation of tin ore deposits: A reassessment. *LITHOS*, 105756. doi:https://doi.org/10.1016/j.lithos.2020.105756

Li, H., Qin, W., Li, J., Tian, Z., Jiao, F., & Yang, C. (2021). Tracing the global tin flow network: highly concentrated production and consumption. *Resources, Conservation and Recycling, 169*, 105495. doi:https://doi.org/10.1016/j.resconrec.2021.105495

Lu, H.-Z., Liu, Y., Wang, C., Xu, Y., & Li, H. (2003). Mineralization and Fluid Inclusion Study of the Shizhuyuan W-Sn-Bi-Mo-F Skarn Deposit, Hunan Province, China. *Economic Geology, 98*(5), 955-974. doi:10.2113/gsecongeo.98.5.955

Mei, W., Lü, X., Cao, X., Liu, Z., Zhao, Y., Ai, Z., . . . Abfaua, M. M. (2015). Ore genesis and hydrothermal evolution of the Huanggang skarn iron–tin polymetallic deposit, southern Great Xing'an Range: Evidence from fluid inclusions and isotope analyses. *Ore Geology Reviews, 64*, 239-252. doi:https://doi.org/10.1016/j.oregeorev.2014.07.015

Meinert, L. D. (1992). Skarns and Skarn Deposits. *Geoscience Canada, 19*. doi:10.12789/gs.v19i4.3773

Meinert, L. D. (1997). Application of skarn deposit zonation models to mineral exploration. *Exploration and Mining Geology, 6*, 185-208.

Meinert, L. D. (2020). 3. The genesis and exploration of skarn deposits. *Geochemical Perspectives, 9*(1), 17-41.

Meinert, L. D., Dipple, G. M., Nicolescu, S., Hedenquist, J. W., Thompson, J. F. H., Goldfarb, R. J., & Richards, J. P. (2005). World Skarn Deposits. In *One Hundredth Anniversary Volume* (pp. 0): Society of Economic Geologists.

Metcalfe, I. (2017). Tectonic evolution of Sundaland. *Bulletin of the Geological Society of Malaysia, 63*, 27-60. doi:10.7186/bgsm63201702

Meyer, N., Markl, G., Gerdes, A., Gutzmer, J., & Burisch, M. (2024). Timing and origin of skarn-, greisen-, and vein-hosted tin mineralization at Geyer, Erzgebirge (Germany). *Mineralium Deposita, 59*(1), 1-22. doi:10.1007/s00126-023-01194-8

Moss, R., Tzimas, E., Willis, P., Arendorf, J., Thompson, P., Chapman, A., . . . Peason, J. (2013). Critical Metals in the Path towards the Decarbonisation of the EU Energy Sector. *Assessing rare metals as supply-chain bottlenecks in low-carbon energy technologies. JRC Report EUR, 25994*.

Neymark, L. A., Holm-Denoma, C. S., Larin, A. M., Moscati, R. J., & Plotkina, Y. V. (2021). LA-ICPMS U-Pb dating reveals cassiterite inheritance in the Yazov granite, Eastern Siberia: Implications for tin mineralization. *Mineralium Deposita*. doi:10.1007/s00126-020-01038-9

Ng, S. W.-P., Whitehouse, M. J., Roselee, M. H., Teschner, C., Murtadha, S., Oliver, G. J. H., . . . Chang, S.-C. (2017). Late Triassic granites from Bangka, Indonesia: A continuation of the Main Range granite province of the South-East Asian Tin Belt. *Journal of Asian Earth Sciences, 138*, 548-561. doi:10.1016/j.jseaes.2017.03.002

Pirajno, F. (2008). *Hydrothermal processes and mineral systems*: Springer Science & Business Media.

Priem, H., Boelrijk, N., Hebeda, E., Verdurmen, E., Verschure, R., & Bon, E. (1975). Isotope geochronology in the Indonesian tin belt. *Geology Mijnbouw, 54*(1), 61-70.

Railsback, L. B. (2003). An earth scientist's periodic table of the elements and their ions. *Geology, 31*(9), 737-740. doi:10.1130/g19542.1

Schwartz, M., Rajah, S., Askury, A., Putthapiban, P., & Djaswadi, S. (1995). The southeast Asian tin belt. *Earth-Science Reviews, 38*(2-4), 95-293. doi:10.1016/0012-8252(95)00004-T

Schwartz, M., & Surjono. (1990). Greisenization and albitization at the Tikus tin-tungsten deposit, Belitung, Indonesia. *Economic Geology, 85*, 691-713. doi:10.2113/gsecongeo.85.4.691

Searle, M., Whitehouse, M., Robb, L., Ghani, A., Hutchison, C., Sone, M., . . . Oliver, G. J. H. (2012). Tectonic evolution of the Sibumasu–Indochina terrane collision zone in Thailand and Malaysia: constraints from new U–Pb zircon chronology of SE Asian tin granitoids. *Journal of the Geological Society, 169*(4), 489-500.

Sugiharto, M. S., Artyanto, A., Pratama, W. V., & Basuki, N. I. (2024). Tungsten-bearing mineral occurrences of Batubesi tin skarn deposits. *Bulletin of Geology 8*(2). Retrieved from https://www.buletingeologi.com/index.php/buletin-geologi/article/view/395

Sujitno, S., Ronojudo, A., & Timak, M. (1981). The occurrence of complex tin-iron ores in Belitung, Indonesia. *Hasan, AH, Bin, H., van Wees. H.(Eds), Complex Tin Ores and Related Problems*, 107-123.

U.S. Geological Survey. (2022). *Mineral commodity summaries 2022* (2022). Retrieved from Reston, VA: http://pubs.er.usgs.gov/publication/mcs2022

Wolf, M., Romer, R. L., Franz, L., & López-Moro, F. J. (2018). Tin in granitic melts: The role of melting temperature and protolith composition. *LITHOS, 310-311*, 20-30. doi: https://doi.org/10.1016/j.lithos.2018.04.004

Yang, J.-H., Zhou, M.-F., Hu, R.-Z., Zhong, H., Williams-Jones, A. E., Liu, L., . . . Mao, W. (2020). Granite-Related Tin Metallogenic Events and Key Controlling Factors in Peninsular Malaysia, Southeast Asia: New Insights from Cassiterite U-Pb Dating and Zircon Geochemistry. *Economic Geology, 115*(3), 581-601. doi:10.5382/econgeo.4736

Zhao, P., Yuan, S., Williams-Jones, A. E., Romer, R. L., Yan, C., Song, S., & Mao, J. (2022). Temporal Separation of W and Sn Mineralization by Temperature-Controlled Incongruent Melting of a Single Protolith: Evidence from the Wangxianling Area, Nanling Region, South China. *Economic Geology, 117*(3), 667-682. doi:10.5382/econgeo.4902

SAŽETAK

Geologija i mineralogija Fe-Sn ležišta u Batubesiju, otok Belitung, Indonezija

Ležište Batubesi primarno je Fe-Sn ležište koje se nalazi u istočnome dijelu Belitunga u Indoneziji. Prvotno je mineralizacija bila poznata kao grajzen, ali nedavne studije pokazale su da se u regiji razvio tip ležišta skarn. Unatoč tome, mineralizacija skarna nije dobro istražena. Cilj je ovoga istraživanja proučiti Fe-Sn mineralizaciju u Batubesiju geološkim i mineraloškim metodama, primarno iz terenskih opažanja, nabušenih jezgara iz bušotina i uzoraka. Pritom su korištene petrološke analize, SEM-EDX, mikro-XRF i XRD analize u svrhu određivanja mineraloškoga sastava, kao i XRF na principu fuzije za određivanje geokemijskoga sastava ležišta. Rezultati pokazuju da u ležištu Batubesi dominira mineralizacija skarnskoga tipa s manjim udjelom grajzena. Uočene su dvije faze skarna: prograđna i retrograđna. Prograđne faze karakterizira taloženje kalcitno-silikatnih minerala i magnetita koji su često frakturirani ili brečirani. Pukotine i breče zatim se mijenjaju u okviru retrograđne faze te su sastavljene od amfibola, muskovita i biotita. Ponekad je promjena toliko intenzivna da je prethodna prograđna faza potpuno izmijenjena. Nadalje, retrograđna faza sastoji se od sulfidnih minerala u obliku žila poput pirita, halkopirita i arsenopirita. Magnetit je uobičajeni rudni mineral, a slijede ga kasiterit, šelit, ferberit, pirit, halkopirit, arsenopirit, glaukokerinit i sfalerit.

Ključne riječi:
Batubesi, željezo-kositar, skarn, rudno ležište, mineralogija

Author's contribution

Aryo Dwi Handoko (Doctoral Candidate) conceptualization, data curation, formal analysis, investigation, methodology, project administration, resources, validation, visualization, writing – original draft and writing – review & editing. **Mochamad Slamet Sugiharto** (Geologist) resources, and validation. **Syafrizal** (Professor) supervision and writing – review & editing. **Alfend Rudyawan** (Lecturer) supervision and writing – review & editing. **Benyamin Sapiie** (Professor) supervision and writing – review & editing.
All authors have read and agreed to the published version of the manuscript.

RGNZ/MGPB

Anthropogenic Hazards Assessment of Mining Activities in Surghar Range, Punjab, Pakistan

Rudarsko-geološko-naftni zbornik
(The Mining-Geology-Petroleum Engineering Bulletin)
DOI: 10.17794/rgn.2025.5.8

Original scientific paper

CC BY

Syed Sajjad Ahmad[1], Hafiz Muhammad Zaheer Afzal[1], Hafiz Zeeshan Akram[1], Sajjad Khan[2], Ihtisham Islam[3]*, Salman Ahmed Khattak[4,5,6]*

[1] *Geological Survey of Pakistan, Trade Centre Phase II M.A. Jauhar Town, Lahore.*

[2] *Geosciences Advance Research Laboratories, Geological Survey of Pakistan, Shahzad Town, 1461 Islamabad, Pakistan.*

[3] *Department of Geology, Shaheed Benazir Bhutto University Sheringal, Upper Dir 18030, Pakistan*

[4] *State Key Laboratory for Critical Mineral Research and Exploration, Institute of Geochemistry, Chinese Academy of Sciences, Guiyang 550081, China.*

[5] *University of Chinese Academy of Sciences, Beijing, 100049, China.*

[6] *Department of Earth Sciences, The University of Haripur, 22620, Khyber Pakhtunkhwa, Pakistan.*

Abstract

This study investigates the environmental impacts of coal mining in the Surghar Range, Punjab, Pakistan, with a focus on the contamination of soil and groundwater by potentially toxic elements (PTEs). To evaluate the extent and sources of contamination, 22 soil and 134 water samples were collected and analyzed using standard physicochemical and geochemical methods. This study identified iron (Fe), zinc (Zn), and lead (Pb) as the primary anthropogenic PTEs, while chromium (Cr) and arsenic (As) also appear at elevated levels in some locations. Soil PTE concentrations followed the order: Fe > Zn > Pb > Cr > As. Pollution indices revealed moderate to high levels of contamination, with a pollution load index (PLI) of 1.20 indicating overall moderate pollution. Although the potential ecological risk index (PERI) was relatively low at 18, the concentration levels of certain PTEs exceed internationally recognized thresholds, necessitating environmental remediation. Principal Component Analysis (PCA) identified Fe and Zn as dominant contributors to pollution. Groundwater analysis showed a spatial gradient in water quality: samples near the Indus River were of freshwater quality, while salinity levels increased westward toward the mining zone, with brine-level salinity detected in Tehsil Isa Khel. Water near mining areas exhibited lower pH and higher electrical conductivity (EC), indicative of acid mine drainage and sulfur-rich coal influence. Comparative analysis with global mining regions revealed that mean PTE concentrations in the Surghar Range are significantly higher, emphasizing the need for sustainable mining practices and targeted environmental management strategies to protect soil and water resources.

Keywords:
coal mining, environmental hazards, Potentially Toxic Elements (PTEs), water quality, soil contamination

1. Introduction

Coal remains a vital energy source, accounting for approximately 29% of global energy production, 41% of the world's electricity generation, and serving as a critical input for 44% of global industrial production (**Wu and Chen, 2018**). Both subsurface and open-pit coal mining operations involve a phased development in mine construction and the disposal of adjacent rocks, which often contain low content and iron sulfide minerals (**Acharya and Kharel, 2020**). These activities expose various rock types to atmospheric conditions and accelerate subsurface weathering processes. Consequently, acid mine drainage can arise during and continue long after coal mining operations as a result of the oxidation of pyrite and other sulphide minerals exposed to air and water, and subsequent leaching of acidic oxidation products. Oxidation and hydrolysis processes and thus the formation of acid mine drainage is accelerated at low pH values of mine water, which enhances mineral dissolution and the release of toxic elements (**Acharya and Kharel, 2020**). The water quality degradation, irrigation water degradation, biodiversity and soil quality issues are the impacts of mining activities which directly impact agricultural productivity and human health (**Tiwary, 2001; Mossa and James, 2013; Mensah et al., 2015**).

Mining activities are recognized for introducing substantial levels of heavy metals into agricultural soils, resulting in the degradation of soil fertility, reduction in biodiversity and loss of crop productivity. For example, **Mileusnić et al. (2014)** assessed contamination from

* Corresponding author: Salman Ahmed Khattak, Ihtisham Islam
e-mail address: salman@mail.gyig.ac.cn, ihtisham.islam@sbbu.edu.pk
Received: 14 February 2025. Accepted: 3 June 2025.
Available online: 21 October 2025

improperly disposed tailings at the Kombat mine in Namibia, revealing a significant accumulation of toxic metals that pose serious risks to soil health. Studies show that mining residues, through leaching, contribute to soil acidification and mobilization of metals, which further compromise soil quality and may have adverse impacts on surrounding ecosystems and human health (**Koptsik, 2014; Zhang et al., 2015**). Furthermore, the physical disturbances from mining operations lead to soil compaction, reduced permeability and a decline in organic matter, each of which diminishes the agricultural productivity of affected soils (**Tordoff et al., 2000; Zhao et al., 2007**).

Mining anthropogenic effects have always been serious concern for the ecological resources of the leased area. The consequences of mining activities affect almost every segment of the environment (**Mossa and James, 2013)** (see **Figure 1**). In South Africa, extensive gold mining operations have led to the release of toxic metals into surrounding environments, affecting both ecosystems and human health (**Ochieng et al., 2010**). Similarly, the coal mining regions in Appalachia, USA, have experienced severe water contamination due to acid mine drainage, resulting in elevated levels of heavy metals such as iron and aluminium (**Palmer et al., 2010**). In Australia, bauxite mining in the Darling Range has led to soil erosion and loss of biodiversity, posing long-term ecological challenges. In all these regions, to validate the findings, the concentrations of PTEs were compared with WHO drinking water quality standards, following the approach used in earlier studies (**Ochieng et al., 2010; Palmer et al., 2010**). Therefore, mining activities worldwide have led to significant environmental degradation, with detrimental effects on biodiversity, air, soil and water quality.

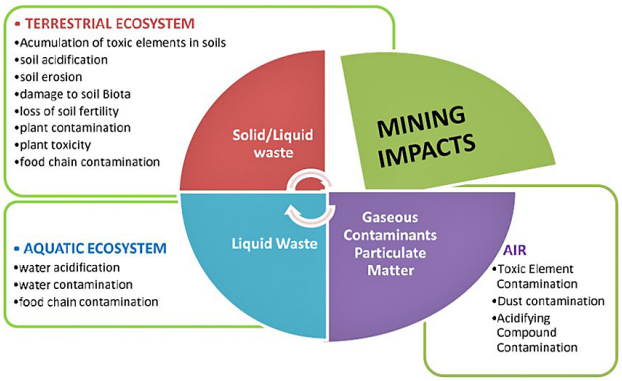


Figure 1. Potential environmental impacts of the mining industry (modified after **Khan et al., 2020**)

The Surghar Range, part of the Trans-Indus region of Pakistan, is geologically diverse, hosting significant mineral resources including coal in Paleocene–Eocene strata, iron ore in Cretaceous formations, and silica sand in Jurassic rocks. In the study area, coal is primarily extracted from the Hangu Formation (Paleocene), while silica sand is mined from the Datta Formation (Jurassic). The Makarwal region, in particular, has a long history of coal mining, with approximately 140 active and abandoned mines. However, these operations have evolved with minimal adherence to modern environmental regulations and virtually no post-mining land reclamation, leading to severe degradation of local ecosystems. Despite the economic importance of these environmental resources, previous investigations in the area have focused predominantly on stratigraphy, lithology and resource assessments (**Khan, 1949; Fatmi, 1972; Faruqi, 1983; Danilchik and Shah, 1987; Warwick and Javed, 1990; Shah, 2009; Umair et al., 2022**), with little attention given to environmental consequences.

Over the past several decades, extensive coal and silica sand mining in the Surghar Range has proceeded largely unchecked, contributing to soil degradation, groundwater contamination, and loss of biodiversity. Despite clear evidence of ecological damage, there remains a critical gap in scientific literature that systematically examines the environmental implications of mining activities in this region. While numerous global studies have assessed the environmental impacts of mining, the localized effects within this geologically and ecologically sensitive region of Pakistan remain poorly understood. Most prior studies have focused solely on geological mapping or resource quantification, leaving the ecological and hydrochemical dimensions of mining-related degradation underexplored.

This study fills that gap by conducting the first thorough evaluation of the spatial distribution, concentration and ecological risk of potentially toxic elements (PTEs) in both soil and groundwater over the Surghar Range. This study uses an integrated methodological framework that includes in-situ field sampling, laboratory studies, multivariate statistical approaches and geographic modelling to provide a quantitative assessment of environmental deterioration. Key developments include the use of pollution indices and hydrochemical signatures to document acid mine drainage and heavy metal contamination, as well as a regional comparison of PTE concentrations and global mining standards to contextualize the data.

This work fills an essential scientific need by providing actual findings from a poorly controlled mining zone, while also establishing baseline environmental data for the region. The findings emphasize the importance of early policy interventions, land restoration measures, and the adoption of sustainable mining techniques. More broadly, the study provides a transferable analytical framework for other developing countries experiencing similar environmental hazards from mining activity.

2. Tectono-geological context

The Western Himalayas of Pakistan reveal a complex geological history shaped by the collision of the Indian and Eurasian plates, which initiated the Himalayan

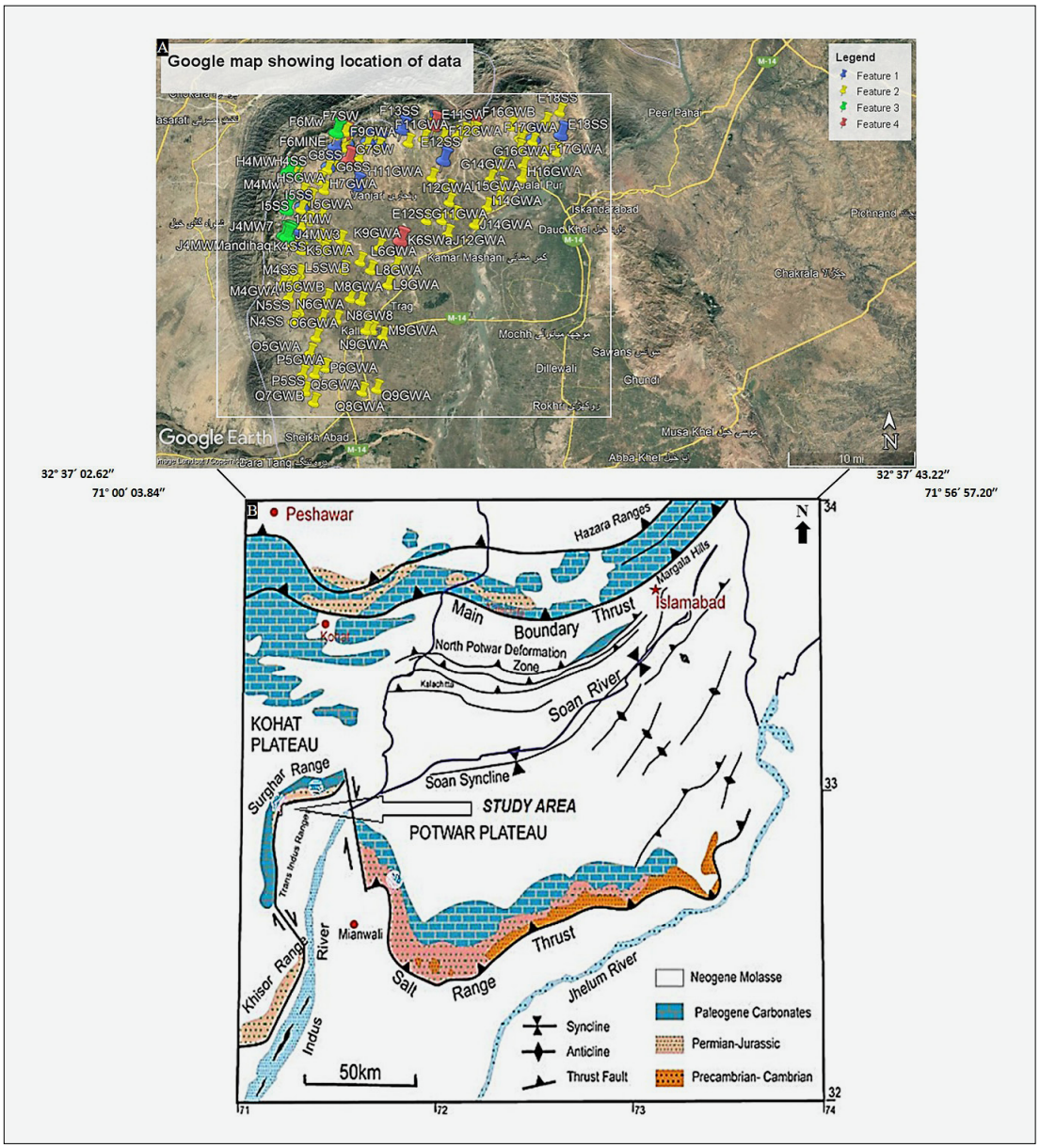


Figure 2. A) Google Earth map showing the locations of the studied samples, with the study area boundaries outlined in a white square. Symbols of various samples collection are as follows: blue arrows indicate soil samples, yellow arrows represent groundwater, green arrows denote mine water release from mine, and red arrows indicate surface water. The sample codes are defined as follows: GW stands for groundwater, SS for soil samples, MW for mine water (water released from mines), and SW for surface water/river water. B) Regional geological map illustrating the study area (modified from **Shah, 2009; Umair et al., 2022**)

orogeny and created significant suture zones, such as the Main Karakoram Thrust (MKT) and Main Mantle Thrust (MMT) (**DiPietro and Pogue, 2004**). This tectonic interaction also produced thrust systems, including the Main Boundary Thrust (MBT) and Salt Range Thrust (SRT). The MBT separates the Himalayan fold-and-thrust belt into two distinct zones: the northern hinterland and the southern foreland, encompassing features like the Hazara-Kashmir syntaxis, Kohat-Potwar fold belt and Salt Range (**DiPietro and Pogue, 2004**). Continuous thrusting of the Indian Plate beneath the Eurasian Plate since the Eocene has led to the formation of the Himalayan ranges and associated fold-and-thrust belts by stacking sedimentary rocks over the Indian Craton (**DiPietro and Pogue, 2004**).

The study area, part of the Surghar Range southwest of Islamabad (see **Figure 2**), marks the easternmost extension of the sub-Himalayan fold-and-thrust belt (**Khattak et al., 2017**), separated from the western Salt Range by the Kalabagh fault (**DiPietro and Pogue, 2004**). The Surghar Range displays a stratigraphic sequence of sedimentary rocks from the Triassic to recent periods, oriented east-west and dipping northward (**Shah, 2009**) (see **Figure 3**). The stratigraphy includes

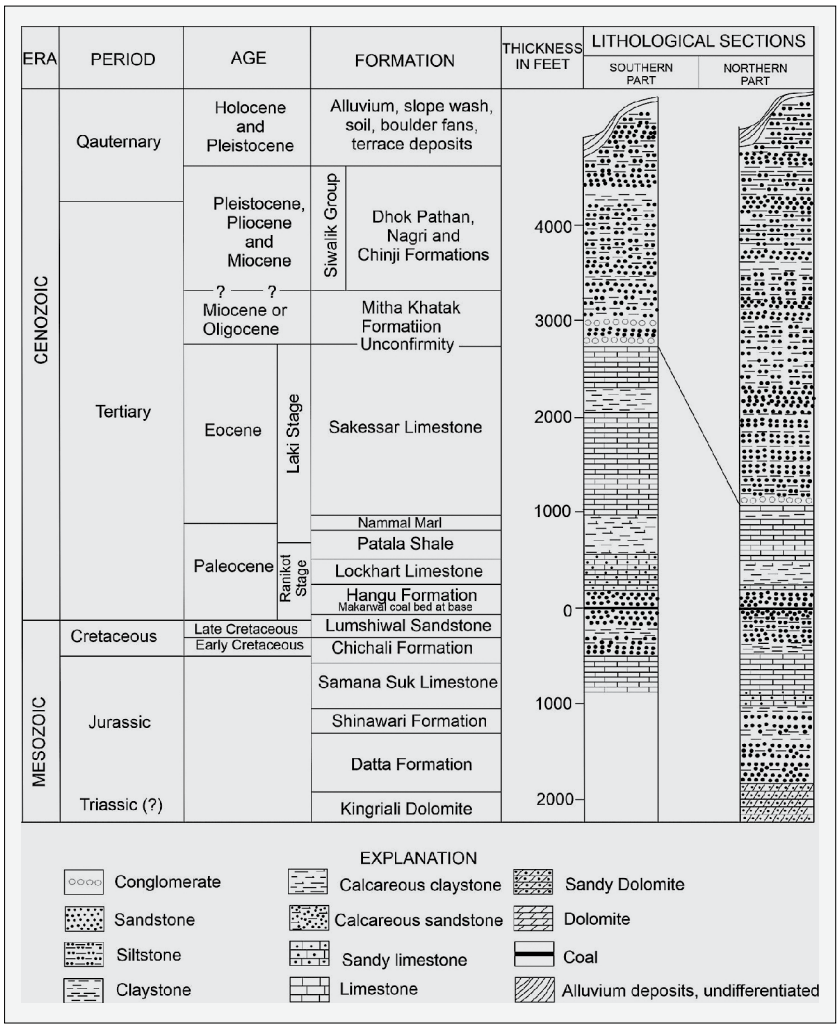


Figure 3. Stratigraphy of the study area and surrounding (modified after **Fatmi, 1972; Shah, 2009**)

formations from the Triassic Mianwali to the Eocene Sakessar Limestone, with notable formations like the Jurassic Datta (sandstone, shale, ferruginous silica sands) and Cretaceous Lumshiwal (iron-stained, coal-bearing sandstone) (**Shah, 2009**).

Mining of coal, silica sand and other resources in the Surghar Range, Punjab, Pakistan, has resulted in significant environmental impacts, particularly affecting soil quality, surface water and groundwater, raising concerns about the sustainability of these activities. Studies have shown that coal mining in the nearby Makarwal and Cherat areas has led to elevated concentrations of toxic trace elements in soil, exceeding safe thresholds (**Shah et al., 2019; Ali et al., 2023**). Similarly, groundwater contamination caused by the leaching of heavy metals from coal deposits has been reported, impacting water quality and posing health risks. While **Malkani (2017)** identified extensive silica sand deposits in the Mianwali District, including the Surghar Range, studies on the environmental consequences of silica sand extraction remain limited. This research addresses these gaps by assessing the combined impacts of coal and silica sand mining on soil, surface water and groundwater through field sampling, laboratory analysis and geospatial techniques.

3. Methodology

The area is part of the Surghar Range and is situated southwest of Islamabad. The study area, where extensive mining of coal, salt, silica sand and iron ore take place, was systematically divided for investigation into multiple grids, each covering a 3-square-kilometer area (see **Figure 2**). A systematic sampling approach was employed to collect soil and water samples from the study area to assess environmental impacts associated with mining activities. Specifically, 22 soil samples were extracted from designated tailing (dumping) sites at an approximate depth of 30.48 cm (1 foot) to analyze the potential contamination and alteration in soil properties due to disposal practices. Furthermore, a total of 134 water samples, representing both surface water (5 samples), mine related water sources (6 samples) and groundwater sources (123 samples), were collected across various strategically selected locations to evaluate the spatial distribution of potential pollutants and ascertain their impact on local water quality. This comprehensive sampling approach was designed to provide a robust dataset for environmental impact assessment and to support subsequent data analysis on contamination levels

and patterns. In the study, river (surface water) samples were collected from various points along the river, especially near mining sites, using clean containers submerged at different depths to ensure representative sampling. Groundwater samples were taken from wells or boreholes, using clean sampling devices to extract water from different depths. These methods allowed for a comprehensive analysis of contamination levels and their distribution in both surface and groundwater sources across the study area.

The analysis of potentially toxic elements (PTEs), including Pb, Zn, Cr, Fe and As, was conducted at the Geosciences Advanced Research Laboratory in Islamabad, Pakistan, using inductively coupled plasma mass spectrometry (ICP-MS; PerkinElmer ELAN 6100). To prepare the soil samples for analysis, a multi-acid digestion was performed using a combination of nitric acid (HNO_3) and hydrochloric acid (HCl) in a closed-vessel microwave-assisted digestion system. This method effectively extracts trace elements from complex soil matrices, enabling the accurate detection of low-concentration PTEs. Rigorous quality control protocols were followed to ensure analytical accuracy and reliability. Certified reference materials (CRMs) were used to validate the accuracy of results, while method blanks and duplicate samples were included to assess precision. Additionally, regular calibration of the ICP-MS instrument and the use of control charts ensured consistent performance throughout the analytical process. The analysis procedure involved digesting 250 mg of calcinated powdered samples with a standard multi-acid solution to produce 25 cc of a 2M HCl solution with a 1:100 dilution for subsequent analysis using ICP-MS (HORIBA Jobin-Yvon Activa). This approach enabled the identification of PTEs contents within the same solution. The method provided a relative uncertainty of approximately 5% for the most sensitive elements and about 10% for others, with detection limits ranging from 5 to 20 ppb (equivalent to 0.5–2 ppm based on the dilution factor).

Regarding water quality analysis, several physicochemical parameters were evaluated to characterize the sample profiles, such as pH, electrical conductivity (EC), total dissolved solids (TDS), calcium and magnesium concentrations, hardness and alkalinity. In-situ measurements of pH, electrical conductivity (EC), total dissolved solids (TDS) and temperature were conducted using portable meters. pH was measured using a calibrated pH meter (model pH-08107 of HANNA) by immersing the probe in each sample to ensure precise assessment of hydrogen ion concentration, reflecting the acidity or alkalinity of the water. The TDS were quantified with a TDS meter (model TDS Low of ECO Testr), providing a measure of the ionic content, which is crucial for assessing salinity and water purity. The EC was determined with a conductivity meter (model CM-1k of COND Meter), which measures the ability of water to conduct electricity, an indicator directly related to the total ionic strength and salinity levels. Calcium and magnesium analysis was performed by complexometric titration with EDTA (ethylene diamine tetra-acetic acid), using specific indicators to ascertain the endpoint for each ion separately, which allowed for accurate individual quantification. Total hardness as $CaCO_3$ was determined also by titrating the sample with EDTA and calculating based on the required titrant volume to reach the endpoint, indicative of the water's scaling potential and its suitability for various uses. Sulphate concentrations were determined using a turbidimetric method, where barium chloride was added to form a barium sulfate precipitate and turbidity was measured spectrophotometrically, providing insight into sulfate levels which can affect taste and corrosiveness. Chlorides were analyzed using argentometric titration, where silver nitrate was added in the presence of potassium chromate as an indicator; the endpoint was marked by a distinct colour change. Total hardness (TH) was calculated by summing the measured concentrations of calcium and magnesium, giving a comprehensive measure of the water's mineral content. Total alkalinity (TA) was measured by titrating with a standard acid to determine bicarbonate and carbonate content, offering an indication of the water's buffering capacity, crucial for understanding its resistance to pH fluctuations. These standardized procedures were rigorously applied to ensure consistency and reliability in evaluating the quality and suitability of the water samples for different applications.

The contamination levels in soil were assessed through the following indices: the geo-accumulation index (I_{geo}), enrichment factor (EF), contamination factor (Cf) and degree of contamination (CD), following established methods (**Buat-Menard and Chesselet, 1979; Jeffery, 1981**). For the background values of the different element in earth surface, **Truekian and Wedephol (1961)** method was used. The I_{geo} was computed using the equation $I_{geo} = \log_2 (C_n/1.5B_n)$, where C_n is the measured concentration of a metal in soil, and B_n is its background concentration, with 1.5 as a factor to account for potential natural variability (**Lokeshwari and Chandrappa, 2006; Fagbote and Olanipekun, 2010**). The values of I_{geo} less than 1 indicates unpolluted soil, values between 1 to 5 indicates moderate to highly polluted soil and values greater than 5 indicates very high polluted soil (**Nimick and Moore, 1991**) (see **Table 1**). The EF was determined as $EF = (C_n/C_{ref}) (B_n/B_{ref})$, where C_{ref} and B_{ref} represent concentrations of a reference element (often iron or aluminium) in soil and its background, respectively, to assess anthropogenic influence (**Lăcătuşu, 1998; Atgn et al., 2000; Huu et al., 2010**). The Cf was calculated by the ratio $Cf = C_n/B_n$, indicating the level of metal contamination relative to background levels (**Harikumar et al., 2009**). A value of Cf less than 1 is a low contamination factor while greater than 6 is a very high contamination factor (see **Table 2**). Finally, the CD was obtained by summing the Cf values for each metal,

expressed as CD = ∑Cfi, representing the cumulative contamination level across multiple metals. These indices provide a multi-faceted approach to understanding the extent and source of soil contamination.

Table 1. The seven classes of geo-accumulation index (I_{geo}) by **Nimick and Moore (1991)**

Classes	I_{geo} class	Value of soil quality
1	< 0	Unpolluted
2	0-1	Unpolluted to moderately polluted
3	1-2	Moderately polluted
4	2-3	Moderately to highly polluted
5	3-4	Highly polluted
6	4-5	Highly polluted to very highly polluted
7	> 5	Very highly polluted

Table 2. Classification of contamination factor (Cf) by **Muller (1969)**

Class	Contamination Factor	Description of contamination factor
1	< 1	Low
2	1-3	Moderate
3	3-6	Considerable
4	> 6	Very high

The pollution load index (PLI) is calculated using the formula: $PLI = (CF1 \times CF2 \times \cdots \times CFn)^{1/n}$ where CF represents the contamination factor for each element, and n is the total number of elements (**Tomlinson et al., 1996; Yang et al., 2011**). For this study, assuming the contamination factor (CF) values are provided, the CFs for Fe, Zn, Pb, Cr and As are multiplied together, and the fifth root (n = 5) is taken. A PLI value greater than 1 indicates pollution in the area (**Córdoba-Tovar et al., 2023**), with the index reflecting pollution levels ranging from moderate to very high. The potential ecological risk index (PERI) for this study is calculated by summing the ecological risk factors (Eri) for each potentially toxic element (PTE) using the formula: $PERI = \sum(Tr_i \times CF_i)$, where Tr is the toxic response factor and CF is the contamination factor for each element. The PERI highlights the overall ecological risk, with significant contributions from elements such as lead (Pb) and arsenic (As) due to their higher contamination factors.

Principal component analysis (PCA) was employed to reduce the dimensionality of contamination indices and identify key contributors to variance in the dataset, following established protocols for environmental data analysis (**Jolliffe and Cadima, 2016**). The principal component analysis (PCA) was performed on contamination indices derived from both soil and water data, specifically the geoaccumulation index (I_{geo}), enrich-

Table 3. Original data on determined concentrations of potentially toxic elements in mg/kg in soil samples. "BDL" indicates values below the detection limit

Sample Id	Fe (mg/kg)	Cd (mg/kg)	Cr (mg/kg)	Zn (mg/kg)	Pb (mg/kg)	As (mg/kg)
K4 S.S	1526	BDL	2.793	0.622	2.024	90.9
L4 S.S	2048	BDL	1.464	0.734	BDL	40.6
M4 S.S	2110	BDL	1.64	1.119	0.547	54.4
N5 S.S	6990	BDL	2.426	2.497	BDL	137.3
N4 S.S	2256	BDL	0.723	1.266	0.553	272.7
O5 S.S	3072	BDL	1.148	1.32	0.732	255
P5 S.S	1586.2	BDL	1.183	1.566	2.641	25.4
I5 S.S	884.8	BDL	1.097	0.964	3.41	15.4
H4 S.S	4774	BDL	2.128	4.826	BDL	295
G6 S.S	1070.2	BDL	1.737	1.215	2.808	30.37
G6 S.Sb	1664.2	BDL	0.949	1.427	2.015	135
G8 S.S	1639.6	BDL	0.739	1.461	2.04	BDL
F8 S.S	1474.4	BDL	0.886	1.543	0.864	75.7
F7 S.Sa	1573.2	BDL	1.173	1.722	1.982	BDL
F9 S.Sa	1319.4	BDL	1.013	1.6	1.053	BDL
F10 S.Sa	1349	BDL	1.197	1.688	1.157	BDL
E11 S.S	1880	BDL	1.17	1.088	1.936	57.7
F16 S.Sa	2992	BDL	1.167	1.598	2.408	29.8
F17 S.Sa	1609.8	BDL	1.28	0.868	1.326	167
E18 S.S	1409.8	BDL	0.599	1.086	0.673	BDL
F13 S.S	2206	BDL	BDL	1.133	2.822	BDL
L5 S.S	1662.6	BDL	BDL	0.98	2.044	202.4

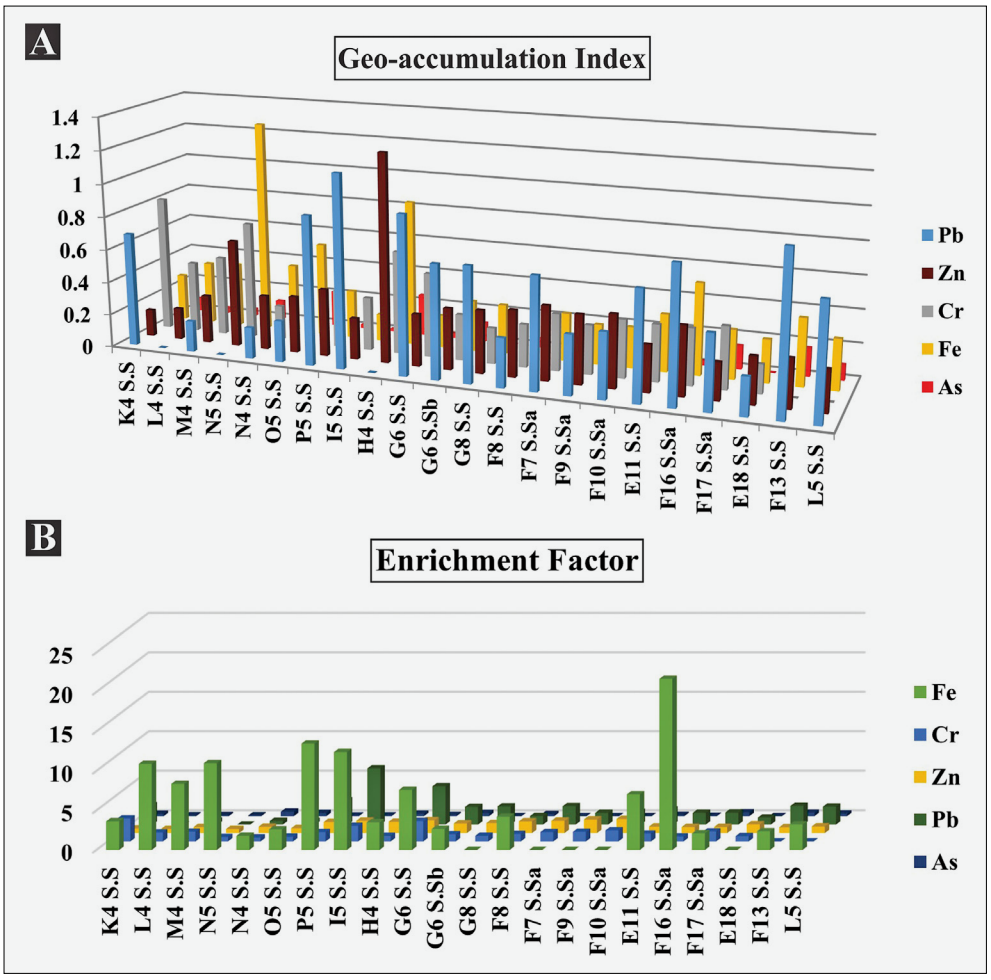


Figure 4. Results of the analyzed field data: (A) bar chart illustrating the I_{geo} values and (B) bar chart illustrating the EF values for Pb, Zn, Cr, Fe and As based on their concentration in soil samples

ment factor (EF) and contamination factor (Cf). These indices were calculated for both soil and water samples and subsequently used in the PCA to identify the primary contributors to variance in the dataset. The aim of the analysis was to capture and interpret the relationships between these indices across both environmental media. First, all variables for soil data, including the I_{geo}, EF and Cf, were standardized to a mean of zero and standard deviation of one. For the water data, similar indices were applied to assess water quality and contamination levels. Both datasets were standardized prior to PCA to ensure comparability, and the analysis was conducted to offer a comprehensive overview of contamination across the two media. This standardization ensured that variables with different scales contributed equally to the analysis. A covariance matrix was calculated to assess inter-variable relationships and reveal linear dependencies. Eigenvalues and eigenvectors of this matrix were then computed; eigenvalues indicate the amount of variance each principal component (PC) captures, while eigenvectors define the direction of each PC in relation to the original variables. The PCs were ordered by eigenvalue magnitude, with those capturing the highest variance retained for interpretation. This study selected PCs explaining over 80% of the total variance. To interpret PCA results, loadings derived from eigenvectors were examined to identify high-loading variables, indicating significant contributors to each PC. This was complemented by plotting PCA scores to visualize clustering patterns and contamination profiles. These steps allowed identification of elements most influential in contamination, guiding targeted remediation recommendations based on key contributors to variance (**Jolliffe and Cadima, 2016**). SPSS software was used for PCA analysis. The procedure for carrying out PCA is given in **supplementary materials**.

4. Results and Discussion

The results of the study indicate significant contamination of soil and water in the mining-affected area. Assessment of soil using indices, the I_{geo}, EF, Cf and CD, confirmed widespread pollution attributed to mining activities (see **Figures 4A, 4B, 5A, 5B** and **Table 3**). Based on the I_{geo} values (see **Figure 4A**), the highest pollution

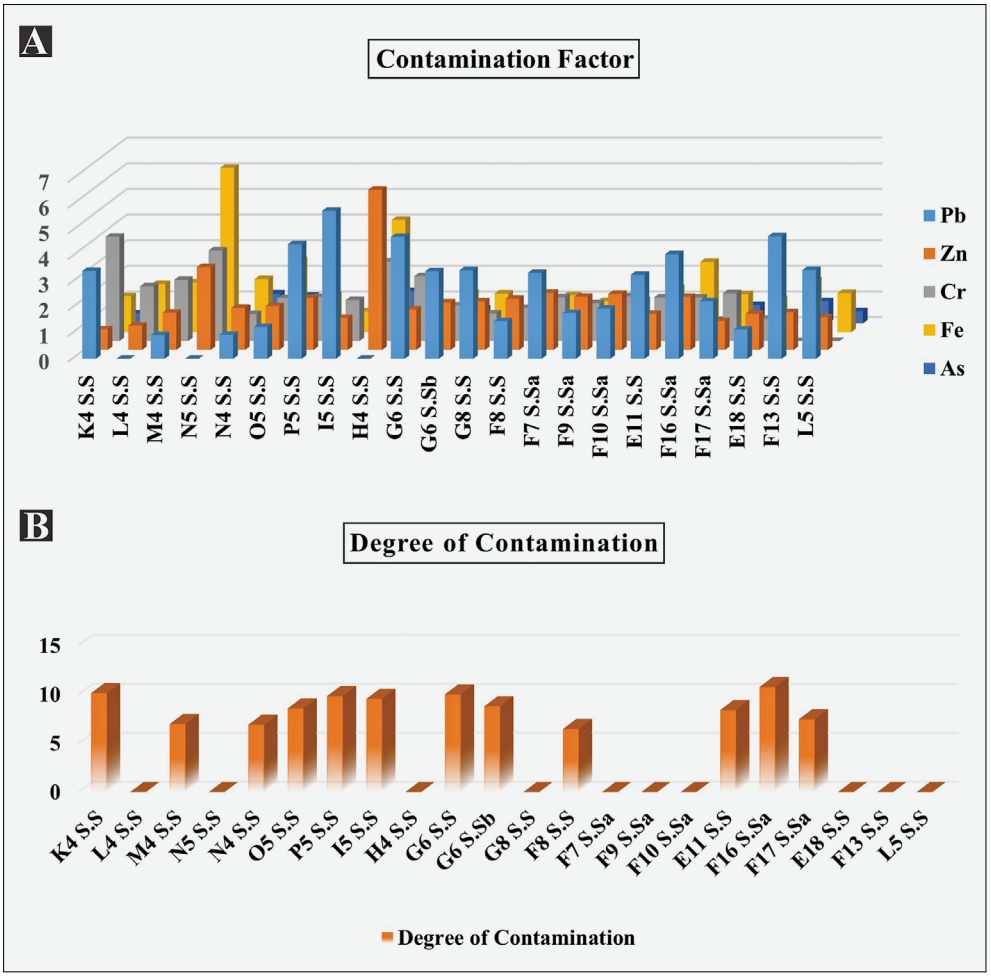


Figure 5. Results of the analyzed field data: (A) bar chart illustrating the Cf index values and (B) bar chart illustrating the CD values for Pb, Zn, Cr, Fe and As based on their cumulative contamination level in soil samples

is attributed to iron (Fe) with a value of 1.3, followed by zinc (Zn), lead (Pb), chromium (Cr) and arsenic (As), which has the lowest value at 0.3. This indicates a contamination order of Fe > Zn > Pb > Cr > As, suggesting moderate to strong pollution by Fe and low to moderate levels for the remaining elements. Similarly, EF values (see **Figure 4B**) show significant enrichment of Fe (maximum EF = 21.6), while Pb, Cr, Zn and As exhibit lower enrichment, with As recording the minimum EF of 0.4. These results also classify the area as moderately to highly contaminated. The Cf values (see **Figure 5A**) further support this trend, with Fe presenting the highest contamination factor of 6, followed by Zn, Pb, Cr and As which again shows a minimum Cf of 0.4. CD values of samples ranging between 8 and 11 (see **Figure 5B**) place the area under the moderate contamination category.

Soil samples analysis reveals that concentrations of Fe, Zn, Pb, Cr and As exceed acceptable limits according to standard PTE indices i.e., I_{geo} and Cf (see **Tables 1** and **2**), further confirming the impact of mining activities.

The PLI calculated for the study area is approximately 1.20, also indicating moderate contamination by PTEs, as this value is slightly above the baseline (baseline PLI = 1.0). The potential ecological risk index (PERI), incorporating Cf values and toxic response factors, yields a value of 18. When compared to the value range (PERI < 50) defined for low potential ecological risk in standard ecological risk classification (e.g. **Hakanson, 1980**), this calculated value of PERI indicates a low ecological risk. Therefore, although the area is affected by PTEs from mining, the overall threat to ecosystem health remains limited. Nevertheless, the presence of elevated PTEs underscores the need for mitigation and management strategies to prevent further environmental degradation.

Principal Component Analysis (PCA) of the soil contamination data shows that Principal Component 1 (PC1) accounts for the majority of the variance, with high loadings from iron (Fe) and zinc (Zn), indicating that these elements are the primary contributors to soil contamination in the study area (see **Figure 6**). Principal Component 2 (PC2) explains additional variance, with significant contributions from lead (Pb) and chromium (Cr), suggesting their roles in soil pollution, though to a lesser

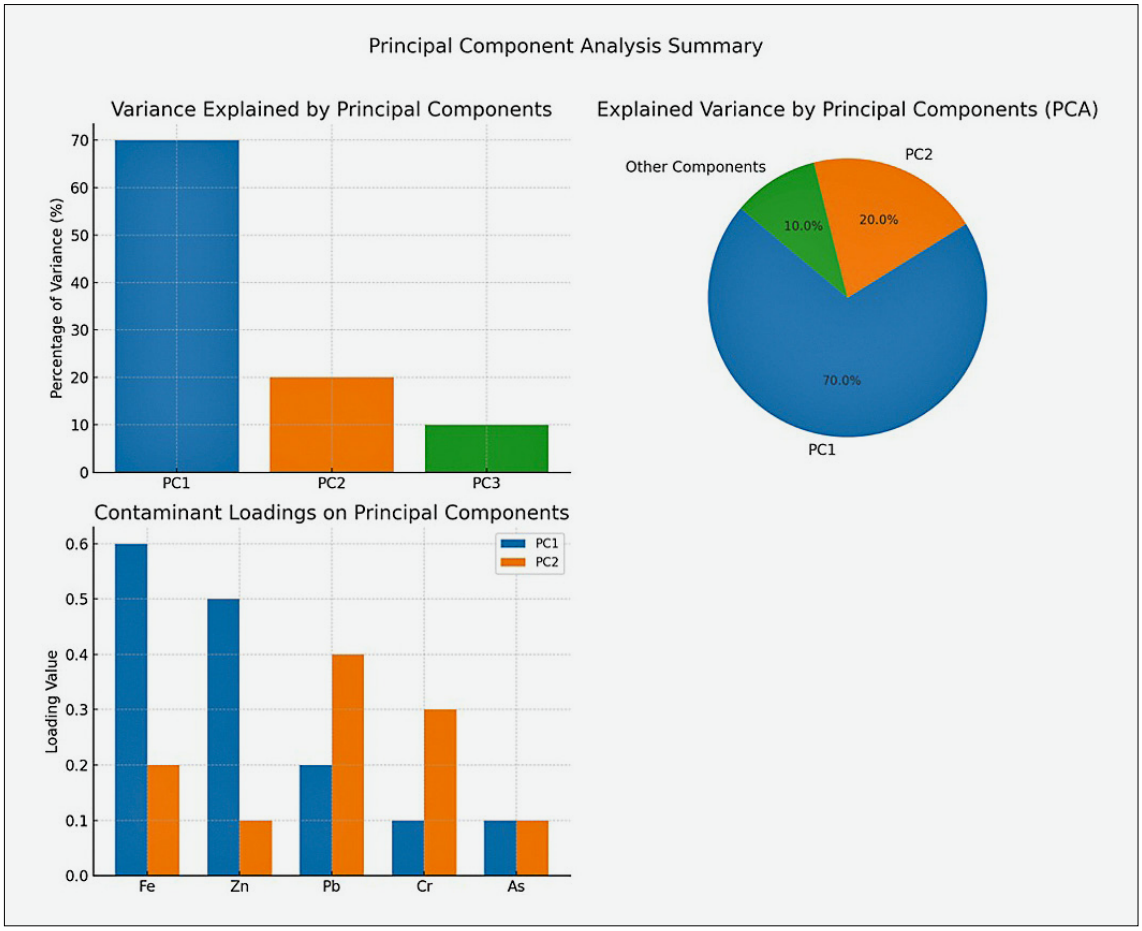


Figure 6. Results of the PCA analysis

Table 4. Comparison of water quality parameters from the present study with WHO recommendations

Parameters	WHO recommendations		Results of the present study (Average of 134 samples)		
	Desirable level	Maximum permissible level	Maximum	Minimum	Average
pH	7.5-8.5	9.2	8.7	3.1	7.4
TDS	Up to 500 mg/l	1500 mg/l	6150 mg/l	117 mg/l	1312.8 mg/l
EC	-	2500 µs/cm	10000 µs/cm	239 µs/cm	3539.7 µs/cm
Calcium	Up to 75 mg/l	200 mg/l	1362.5 mg/l	16 mg/l	214.4 mg/l
Magnesium	Up to 50 ppm	150 ppm	2690 ppm	1 ppm	451 ppm
Hardness as $CaCO_3$	Up to 100 mg/l	500 mg/l	1680 mg/l	8 mg/l	438.4 mg/l
Sulphates	Up to 200 mg/l	400 mg/l	807.27 mg/l	33.9 mg/l	79.07 mg/l
Chlorides	Up to 200 mg/l	600 mg/l	2117.2 mg/l	16 mg/l	132.0 mg/l
Total hardness	Soft: < 75 mg/l	Hard: 150-300 mg/l Very hard: > 300 mg/l	3625 mg/l	31.74 mg/l	666.2 mg/l
TA	-	200 mg/l	2200 mg/l	40 mg/l	537 mg/l

extent. This analysis highlights Fe and Zn as the most critical contaminants, which should be prioritized in remediation efforts. The findings align with global studies, such as those by **Al-Soudany et al. (2024)** and **Jawjit et al. (2024)**, which also examined soil contamination from industrial activities and urban waste. The contamination in the Surghar Range is notably higher in Fe and Zn compared to regions like India and China, yet lower in Pb and Cr, aligning with reports from less polluted mining regions (**Hakanson, 1980**).

In terms of water quality, both laboratory and field-tested parameters exhibit considerable variability. Labo-

Table 5. Mean concentrations of PTEs in the soil based on present results and their comparison with the results of other's studies in the world

Mean Concentrations of PTEs in the soil (mg/kg)						
Region	**Fe (mg/kg)**	**Cd (mg/kg)**	**Cr (mg/kg)**	**Zn (mg/kg)**	**Pb (mg/kg)**	**As (mg/kg)**
This Study (Pakistan)	2140.78	BDL	1.32	1.46	1.73	117.79
Spain (Hudson-Edwards et al., 1999; Alvarez et al., 2003)	294	6.59	-	465.8	881.8	-
India (Prasad et al., 2014; Reza et al., 2015)	166.2	3.82	-	338.8	304.7	-
Iran (Pirsaheb et al., 2013; Ghaderpoori, 2018)	50	1.49	-	363.4	1002	-
China (Yuan et al., 2013; Duan and Tan, 2013)	198	11	-	1163	641.3	-
South Korea (Kim et al., 2001; Lee et al., 2005)	22.1	1.99	-	183.2	111.1	-
Vietnam (Thuy et al., 2000; Tra Ho and Egashira, 2000)	3.7	1.35	-	41.09	30635	-
PEC (Caeiro et al., 2005)	-	4.98	-	459	128	-
TEC (MacDonald et al., 2000)	-	0.99	-	121	35.8	

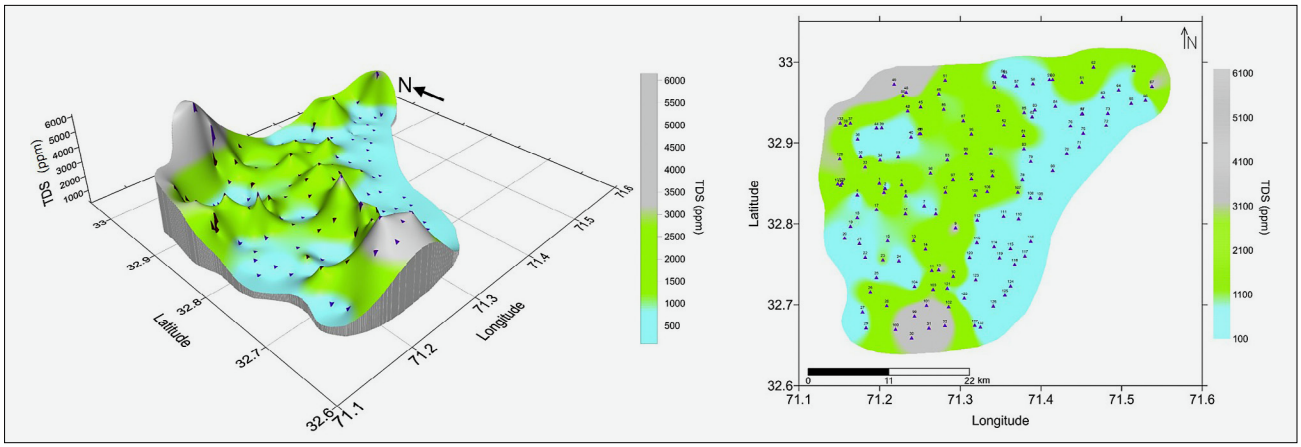


Figure 7. Depicting TDS from the collected field data: 3D surface plot (left) and 2D heatmap (right) representations of TDS results

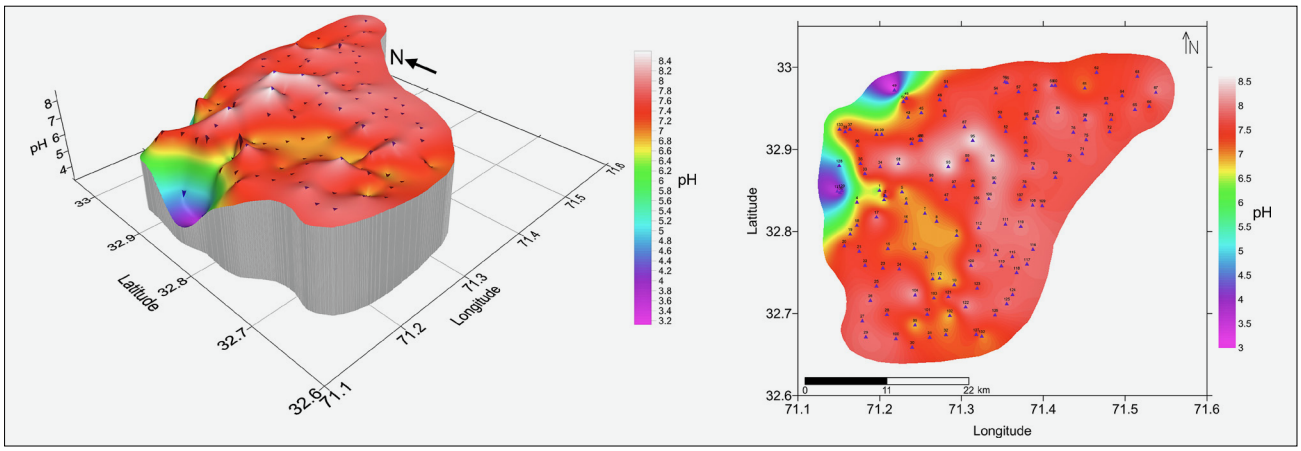


Figure 8. Depicting pH from the collected field data: 3D surface plot (left) and 2D heatmap (right) representations of pH results

ratory results show chloride concentrations ranging from 16 to 2117.22 mg/l (average 132 mg/l), total hardness (TH) from 31.74 to 3625 mg/l (average 666.2 mg/l), and total alkalinity (TA) from 40 to 2200 mg/l (average 537 mg/l). Calcium hardness ranges from 8 to 1680 mg/l (average 438.4 mg/l) and magnesium hardness from 0 to 2262.5 mg/l (average 443.95 mg/l), with calcium ions averaging 14.63 mg/l and magnesium ions averaging 106.55 mg/l. Carbonate concentrations range from 0 to 520 mg/l (average 104 mg/l) and bicarbonate concentrations from 0

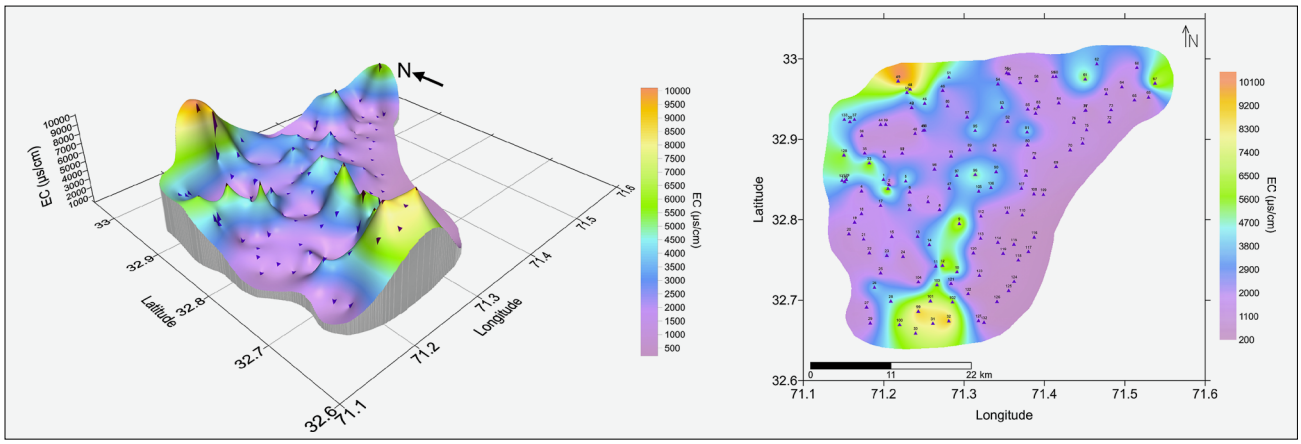


Figure 9. Depicting EC from the collected field data: 3D surface plot (left) and 2D heatmap (right) representations of EC results

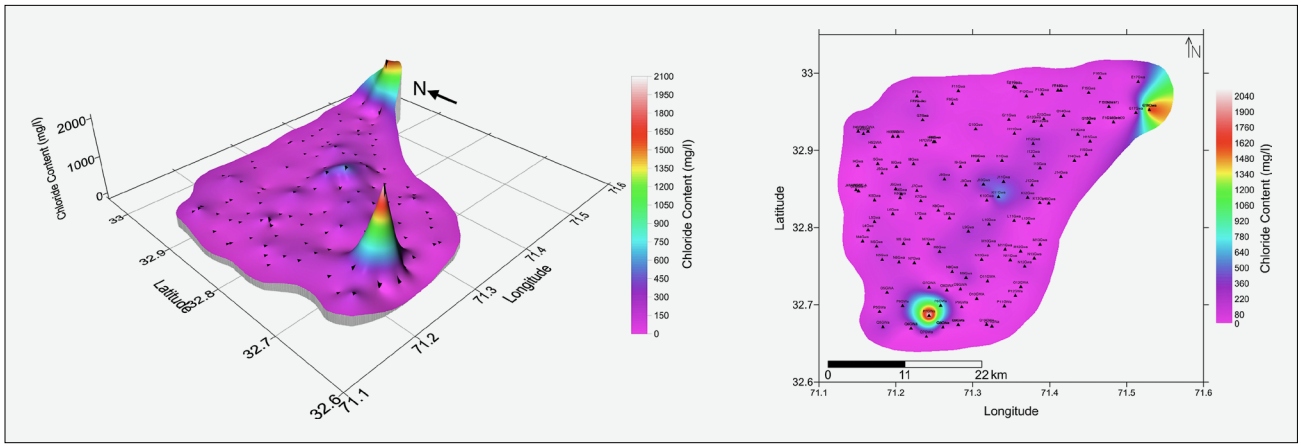


Figure 10. 3D surface plot (left) and 2D heatmap (right) representations of chloride concentrations for the collected samples

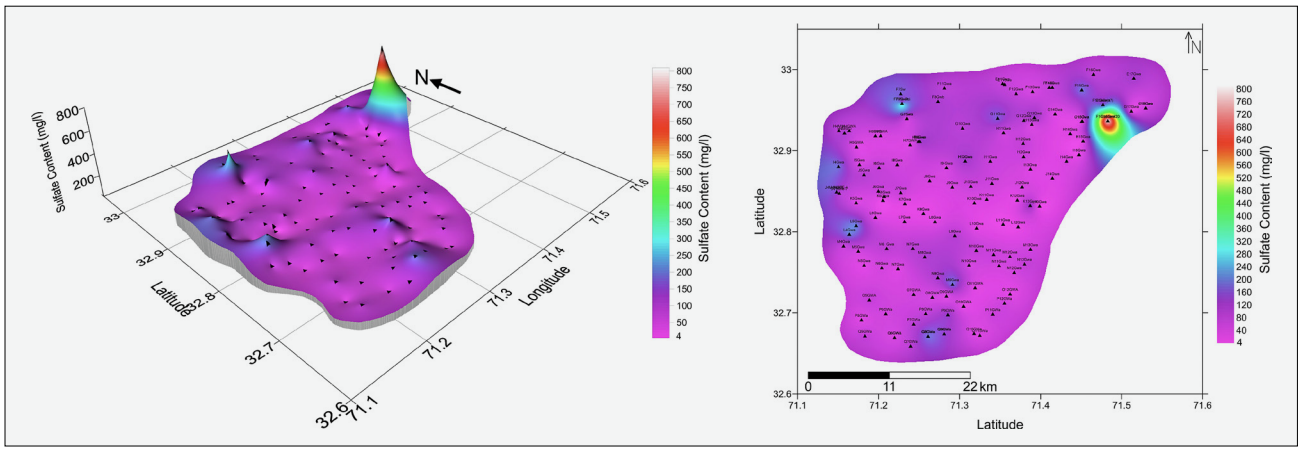


Figure 11. 3D surface plot (left) and 2D heatmap (right) representation of sulphate concentrations for collected samples

to 1680 mg/l (average 417.72 mg/l). Sulfate levels vary from 33.9 to 807.27 mg/l (average 79.07 mg/l), while hydroxide ions are absent. Field data show total dissolved solids (TDS) ranging from 117 to 6150 mg/l (average 1312.8 mg/l), electrical conductivity (EC) from 239 to 10,000 µS/cm (average 3539.7 µS/cm), and pH from 3.1 to 8.7 (average 7.4), indicating generally neutral to slightly alkaline conditions. These results demonstrate considerable heterogeneity in water quality across the sampling locations (see **Table 4**). The deterioration of water quality,

marked by variations in parameters like TDS and pH, mirrors trends observed in other mining regions globally, including Spain and the United States (**McLemore, 2017**). Furthermore, the absence of cadmium (Cd) contamination of water contrasts with higher levels reported in other industrial areas (**Zhang et al., 2011**).

A comparison of the mean concentrations of PTEs in the soil of present study with the reported results worldwide is shown in **Table 5**. The significantly higher iron (Fe) levels in this study, compared to other regions shown, suggest either natural geochemical enrichment or anthropogenic contributions, warranting further investigation into local geological and industrial activities. Cadmium (Cd) being below detection limits highlights the absence of significant industrial or agricultural contamination, unlike the higher levels reported in Spain, China, PEC and India. The low concentrations of chromium (Cr), zinc (Zn) and lead (Pb) indicate minimal contamination relative to countries like Iran, India, China and Spain. However, the elevated arsenic (As) levels are concerning and could be linked to natural geochemical processes, such as arsenic-bearing minerals in the study area's lithology or localized human activities like mining or the use of arsenic-containing pesticides. These results suggest that mining activities have significantly elevated the levels of PTEs in the soil near the mining areas compared to the plains. Previous studies by **Al-Soudany et al. (2024)**, **Jawjit et al. (2024)** and **Saeed et al. (2024)** have focused on enhancing expansive soils with water treatment sludge ash (WTSA), assessing urban hazardous waste risks, and stabilizing cadmium-contaminated soil using silica-rich alkaline activators. These studies highlight innovative waste reuse approaches for environmental protection and soil improvement.

Mining activities not only impact soil quality but also degrade water quality, as evidenced by the analysis of 134 water samples from the study area. Parameters such as TDS, EC, pH and temperature were measured on-site (see **Table 4**).

Comparison with WHO recommendations showed that water quality often exceeds permissible limits, with high levels of hardness (an average of about 666 mg/l), alkalinity, calcium and magnesium (**WHO, 2020**) (see **Table 4**). The water quality classification based on TDS 3D map indicates that the study area can be divided into different zones depending on fresh, slightly saline, moderately saline, very saline and brine water. The area near the Indus River has freshwater quality while as we move westward toward the Surghar Range, the TDS value increases and water quality changes from slightly saline to brine water. The southern part of the area which is tehsil Isa Khel of the Mianwali District also has very saline to brine water quality (see **Figure 7**, **Table 4**). The water quality classification based on pH 3D map shows that most areas had pH levels within WHO limits, but areas near mining activities exhibited acidic water due to high sulfur content associated with coal mining (see **Figure 8**, **Table 4**). The water quality classification based on EC 3D map indicates that values were high in areas with extensive mining activities and in the southern part of the study area, indicating poor water quality due to high dissolved ion content (see **Figure 9**, **Table 4**). In addition to these, high concentrations of chlorides and sulphates in water are also determined in the study area (see **Figures 10** & **11**, **Table 4**).

5. Conclusions

1. Analysis of soil samples revealed elevated levels of PTEs, including Pb, Zn, Cr, Fe and As surpassing acceptable limits in the order of iron (Fe) > zinc (Zn) > lead (Pb) > chromium (Cr) > arsenic (As).
2. The pollution load index (PLI) was calculated using the contamination factors (CFs) of Fe, Zn, Pb, Cr and As to assess the pollution level in the study area. A PLI value of 1.20 suggests moderate contamination by PTEs, implying that the region is slightly contaminated and therefore there is a need for environmental remediation.
3. The potential ecological risk index (PERI) was also determined set to assess the ecological threat these PTEs present. A PERI value of 18 indicates a minimal environmental risk; thus, contamination by PTEs is not expected to cause major ecological harm.
4. Principal component analysis (PCA) identified key sources of contamination, with the first principal component (PC1) showing that Fe and Zn are the primary contributors to soil pollution of the study area, while PC2 highlighted the roles of Pb and Cr, but to a lesser degree. This analysis underscores the importance of Fe and Zn as the most critical contaminants, informing the direction of remediation efforts.
5. Comparison of water quality results with WHO recommendations showed that the observed water quality parameters often exceed permissible limits, with high levels of hardness, alkalinity, TDS, calcium and magnesium concentrations. Similarly, regional comparison of mean concentration of PTEs of present study indicates elevated levels compared to other regions.
6. Three-dimensional models constructed based on total dissolved solids (TDS), pH, electrical conductivity (EC), chlorides and sulphates concentrations of water samples are a reliable way to demarcate the hazardous areas efficiently. The results show that areas near the extreme western side of study area where various mining activities occur, have higher levels of PTEs compared to the plains farther from these areas.

In summary, the present study highlights the significant environmental impact of anthropogenic activities, including mining operations, industrial discharges and

urbanization emerging as key contributors to the contamination of soil and water by potentially toxic elements (PTEs), particularly Fe, Zn and Pb. These elements were identified as the primary pollutants of concern, while Cr and As also warrant proactive monitoring and management. Elevated concentrations of PTEs were consistently observed in proximity to mining sites, highlighting the localized yet intense influence of such activities. Furthermore, acid mine drainage (AMD) exacerbates the situation by degrading environmental quality and increasing the mobility and bioavailability of PTEs, thereby posing further risks to ecosystem and human health.

Acknowledgements

The authors extend sincere gratitude to the Geosciences Advanced Research Laboratories, Geological Survey of Pakistan for their invaluable assistance in analysing soil and water samples. We also thank the Director General of the Geological Survey of Pakistan for logistical support during fieldwork. Our appreciation goes to the local authorities and residents of the Surghar Range area, district Mianwali, Punjab, and Pakistan, for their cooperation and hospitality during our field work.

Funding

This research was done under R&D project Grant No. R & D 1801/GSP of Geological Survey of Pakistan.

6. References

Acharya, B. S., Kharel, G. (2020). Acid mine drainage from coal mining in the United States – An overview. Journal of Hydrology, 588, 125061.

Al-Soudany, K. Y. H., Fattah, M. Y., Rahil, F. H. (2024). Enhancement of expansive soil properties by water treatment sludge ash in landfill liners. Civil Engineering Journal, 10(11), 3508–3530.

Ali, L., Ali, S., Khattak, S., Janjuhah, H. T., Kontakiotis, G., Hussain, R., Rukh, S., Shah, M. T., Bathrellos, G. D., Skilodimou, H. D. (2023). Distribution, Risk Assessment and Source Identification of Potentially Toxic Elements in Coal Mining Contaminated Soils of Makarwal, Pakistan: Environmental and Human Health Outcomes. Land, 12(4), 821.

Alvarez, E., Marcos, M. F., Vaamonde, C. Fernández-Sanjurjo, M. J. (2003). Heavy metals in the dump of an abandoned mine in Galicia (NW Spain) and in the spontaneously occurring vegetation. Science of Total Environment. 313, 185–197.

Atgn, R. S., El-Agha, O., Zararsiz, A., Kocatas, A., Parlak, H., Tuncel, G. (2000). Investigation of the sediment pollution in Izmir Bay: trace elements. Spectrochimica Acta Part B, 55, 1151–1164.

Buat-Menard, P., Chesselet, R. (1979). Variable influence of the atmospheric flux on the trace metal chemistry of oceanic suspended matter. Earth and Planetary Science Letters, 42(3), 399–411.

Caeiro, S., Costa, M. H., Ramos, T. B., Fernandes, F., Silveira, N., Coimbra, A., Medeiros, G., Painho, M. (2005). Assessing heavy metal contamination in Sado Estuary sediment: An index analysis approach. Ecological Indicators, 5, 151–169.

Córdoba-Tovar, L., Marrugo-Negrete, J., Ramos Barón, P. A., Díez, S. (2023). Ecological and human health risk from exposure to contaminated sediments in a tropical river impacted by gold mining in Colombia. Environmental Research, 233, 116759.

Danilchik, W., Shah, S. I. (1987). Stratigraphy and coal resources of the Makarwal area, Trans-Indus mountains, Mianwali district, Pakistan. USGS, Professional Paper; (USA), 75, 13–41.

DiPietro, J. A., Pogue, K. R. (2004). Tectonostratigraphic subdivisions of the Himalaya: A view from the west. Tectonics, 23(5).

Duan, J., Tan, J. (2013). Atmospheric heavy metals and arsenic in China: Situation, sources and control policies. Atmospheric Environment, 74, 93–101.

Fagbote, E. O., Olanipekun, E. O. (2010). Evaluation of the status of heavy metal pollution of soil and plant (Chromolaena odorata) of Agbabu Bitumen Deposit Area, Nigeria. European Journal of Scientific Research, 5(4), 241–248.

Faruqi, S. H. (1983). Special features of the geology of Makarwal coal fields. Proceedings of the National Seminar on Development of Mineral Resources, 2d, May 21–24, 1983, Peshawar, Pakistan, 21–24.

Fatmi, A. N. (1972). Stratigraphy of the Jurassic and Lower Cretaceous rocks and Jurassic ammonites from northern areas of West Pakistan. Bulletin of the British Museum (Natural History) Geology, 20(7), 297–380.

Ghaderpoori, M. (2018). Heavy metals analysis and quality assessment in drinking water–Khorramabad city, Iran. Data Brief, 16, 685.

Hakanson, L. (1980). An ecological risk index for aquatic pollution control: a sedimentological approach. Water Research, 14(8), 9751001.

Harikumar, P. S, Nasir, U. P, Rahman, M. P. (2009). Distribution of heavy metals in the core sediments of a tropical wetland system. International Journal of Environmental Science and Technology, 6(2), 225–232.

Hudson-Edwards, K. A., Schell, C., Macklin, M. G. (1999). Mineralogy and geochemistry of alluvium contaminated by metal mining in the Rio Tinto area, southwest Spain. Applied Geochemistry, 14, 1015–1030.

Huu, H. H., Rudy, S., Damme, A. V. (2010). Distribution and contamination status of heavy metals in estuarine sediments near CauOng HarborHa long Bay, Vietnam. Geologica Belgica, 13(1–2), 37–47.

Jawjit, S., Narom, N., Thongkaow, P. (2024). Evaluating household hazardous waste generation, composition, and health risks in an urban municipality. Journal of Human Earth and Future, 5(3), 1–12.

Jeffery, D. W. 1981: Chemical methods for assessing bioavailable metals in sludges and soils. Technical Report, Water Research Centre, Stevenage Laboratory.

Jolliffe, I. T., Cadima, J. (2016). Principal component analysis: A review and recent developments. Philosophical Transactions of the Royal Society A: Mathematical, Physical and Engineering Sciences, 374(2065), 20150202.

Kim, K. K., Kim, K. W., Kim, J. Y., Kim, I. S., Cheong, Y. W., Min, J. S. (2001). Characteristics of tailings from the closed metal mines as potential contamination source in South Korea. Environmental Geology, 41, 358–364.

Khan, S., Waqas, M., Ding, F., Shamshad, I., Arp, H. P. H., Li, G. (2020). The influence of various organic amendments on the bioavailability and uptake of trace metals in maize. Journal of Environmental Management, 256, 109950.

Khan, N. M. (1949). A survey of coal resources of Pakistan. Geological Survey of Pakistan Records, 2(2), 1–11.

Khattak, S. A., Rehman, G., Ahmad, S., Jan, M. F., Khurshid, S., Ghani, A. (2017). Deformational style and hydrocarbons trapping mechanism of the sub-Himalayan frontal ranges near Fateh Jhang, Punjab, Pakistan. Journal of Himalayan Earth Sciences, 50(2), 1–13.

Koptsik, G. (2014). Problems and prospects concerning the phytoremediation of heavy metal polluted soils: A review. Eurasian Soil Science, 47(9), 923–939.

Lăcătuşu, R. 1998: Appraising levels of soil contamination or pollution with heavy metals. European Soil Bureau Research Report Nr.4

Lee, J. Y., Choi, J. C., Lee, K. K. (2005). Variations in heavy metal contamination of stream water and groundwater affected by an abandoned lead–zinc mine in Korea. Environmental Geochemistry and Health, 27, 237–257.

Lokeshwari, H., Chandrappa, GT. (2006). Heavy metals content in water; hyacinth water and sediments of Lalbagh Tank, Bangalore, India. Journal of Environmental Engineering and Science, 48(3),183–188.

MacDonald, D. D., Ingersoll, C. G., Berger, T. A. (2000). Development and evaluation of consensus-based sediment quality guidelines for freshwater ecosystems. Archives of Environmental Contamination and Toxicology, 39, 20–31.

Malkani, M. S. (2017). Mineral Resources of North and South Punjab, Pakistan. Geological Survey of Pakistan. GSP Information Release No. 995: 42.

McLemore, V. T. (2017). Mining districts and prospect areas of New Mexico: New Mexico bureau of geology and mineral resources, Resource Map, 24, 65, scale 1:1,000,000.

Mensah, A. K., Mahiri, I. O., Owusu, O., Mireku, O. D., Wireko, I., Kissi, E. A. (2015). Environmental impacts of mining: A study of mining communities in Ghana. Applied Ecology and Environmental Sciences, 3(3), 81–94.

Mileusnić, M., Mapani, B. S., Kamona, F. A., Ružičić, S., Mapaure, I., Chimwamurombe, P. M. (2014). Assessment of agricultural soil contamination by potentially toxic metals dispersed from improperly disposed tailings, Kombat mine, Namibia. Journal of Geochemical Exploration, 144 (c), 409–420.

Mossa, J., James, L. A. (2013). Impacts of mining on geomorphic systems. Treatise on Geomorphology, 13, 74–95.

Muller, G. (1969). Index of geoaccumulation in sediments of the Rhine River. GeoJournal, 2, 108–118.

Nimick, D. A., Moore, J. M. (1991). Prediction of water-soluble metal concentrations in fluvially deposited tailings sediments, upper Clark Fork Valley, Montana, U.S.A. Applied Geochemistry, 6(6), 635–646. https://doi.org/10.1016/0883-2927(91)90074-Y.

Ochieng, G. M., Ephrahim S. S., Onyeka, I. N. (2010). Impacts of mining on water resources in South Africa: A review. Scientific Research and Essays, 5(22), 3351–3357.

Palmer, M. A., Bernhardt, E. S., Schlesinger, W. H., Eshleman, K. N., Foufoula-Georgiou, E., Hendryx, M. S., Lemly, A. D., Likens, G. E., Loucks, O. L., Power, M. E., White, P. S., Wilcock. P. R. (2010). Mountaintop mining consequences. Science, 327(5962), 148–149.

Pirsaheb, M., Khosravi, T., Sharafi, K., Babajani, L., Rezaei, M. (2013). Measurement of heavy metals concentration in drinking water from source to consumption site in Kermanshah – Iran. World Applied Sciences Journal, 21, 416–423.

Prasad, B., Kumari, P., Bano, S., Kumari, S. (2014). Ground water quality evaluation near mining area and development of heavy metal pollution index. Applied Water Science, 4, 11–17.

Reza, S. K., Baruah, U., Singh, S. K., Das, T. H. (2015). Geostatistical and multivariate analysis of soil heavy metal contamination near coal mining area, Northeastern India. Environmental Earth Sciences, 73, 5425–5433.

Saeed, K., Al-Khyat, S., Hacheem, Z., Fartosy, S. H. (2024). Evaluating the efficiency of alkaline activator with silica-rich wastes in stabilizing cadmium-contaminated soil. Civil Engineering Journal, 10(7), 2123–2143.

Shah, S. M. I. (2009). Stratigraphy of Pakistan. Memoirs of the Geological Survey of Pakistan, 12, 355.

Shah, K. S., Rahman, A., Khan, S. (2019). Socio-Environmental Impacts of Coal Mining: A Case Study of Cherat Coal Mines Pakistan. Int. J. Econ. Environ. Geol.10(3), 129–133.

Thuy, H. T., Tobschall, H. J., An, P. V. (2000). Distribution of heavy metals in urban soils–a case study of Danang-Hoian Area (Vietnam). Environmental Geology, 39, 603–610.

Tiwary, R. K. (2001). Environmental impact of coal mining on water regime and its management. Water, Air, and Soil Pollution, 132(1-2), 185–199.

Tordoff, G. M., Baker, A. J. M., Willis, A. J. (2000). Current Approaches to the Revegetation and Reclamation of Metalliferous Mine Wastes. Chemosphere, 41, 219–228.

Tra Ho, T. L., Egashira, K. (2000). Heavy metal characterization of river sediment in Hanoi, Vietnam. Communication in Soil Science and Plant Analysis, 31, 2901–2916.

Turekian, K. K., Wedepohl, K. H. (1961). Distribution of the elements in some major units of the earth's crust. Bulletin Geological Society of America, 72, 175–192.

Umair, M., Yang, R. D., Cheng, W., Khattak, S. A. (2022). Geochemistry and mineralogy of Paleocene coal from the Padhrar and Darra Adam Khel coalfields of Pakistan. Acta Geologica Sinica (English Edition), 96(6), 2056–2073.

Warwick, P. D., Javed, S. (1990). Quality and character of Pakistan coal. In Kazmi, A.H., Siddiqi, R.A. eds., Significance of the coal resources of Pakistan: Geological Survey of Pakistan, Quetta, 127–135.

Wu, X. F., Chen, G. Q. (2018). Coal use embodied in globalized world economy: From source to sink through supply chain. Renewable and Sustainable Energy Reviews, 81, 978–993.

World Health Organization (WHO) (2020). Guidelines for drinking-water quality, 4th edition incorporating the 1st addendum. World Health Organization.

Yang, Q., Xu, Y., Liu, S., He, J., Long, F. (2011). Concentration and potential health risk of heavy metals in market vegetables in Chongqing, China. Ecotoxicology and Environmental Safety, 74(6), 1664–1669.

Yuan, G. L., Sun, T. H., Han, P., Li, J. (2013). Environmental geochemical mapping and multivariate geostatistical analysis of heavy metals in topsoils of a closed steel smelter: Capital Iron & Steel Factory, Beijing, China. Journal of Geochemical Exploration, 130, 15–21.

Zhang, X., Zhong, T., Liu, L., Ouyang, X. (2015). Impact of Soil Heavy Metal Pollution on Food Safety in China. PLoS ONE, 10(8), e0135182.

Zhang, J., Deng, H. G., Chen, S. Y., Sun, W. B., Li, X. G., (2011). Eco-environment health risk assessment of Dongping lake water-resources. Journal of Safety and Environment, 11(6), 111–115.

Zhao, Y. F., Shi, X. Z., Huang, B., Yu, D. S., Wang, H. J., Sun, W. X., Öboern, I., Blombäck, K. (2007). Spatial Distribution of Heavy Metals in Agricultural Soils of an Industry-Based Peri-Urban Area in Wuxi, China. Pedosphere, 17(1), 44–51.

SAŽETAK

Procjena opasnosti od rudarskih aktivnosti u području Surghar, Punjab, Pakistan

Ova studija istražuje utjecaj eksploatacije ugljena na okoliš na lokaciji Surghar Range, Punjab, Pakistan, s naglaskom na onečišćenje tla i podzemne vode potencijalno toksičnim elementima (PTE). Kako bi se procijenio opseg i definirali izvori onečišćenja, prikupljena su i analizirana 22 uzorka tla i 134 uzorka vode korištenjem standardnih fizičko-kemijskih i geokemijskih metoda. Ova studija identificirala je željezo (Fe), cink (Zn) i olovo (Pb) kao primarne PTE-e koji su posljedica antropogenoga utjecaja, dok se krom (Cr) i arsen (As) također pojavljuju u povišenim koncentracijama na određenim lokacijama. Prema iznosima koncentracija u tlu utvrđen je redoslijed PTE-a: Fe > Zn > Pb > Cr > As. Indeksi onečišćenja otkrili su umjerene do visoke razine onečišćenja, s indeksom opterećenja onečišćenjem (PLI) od 1,20, što upućuje na ukupno umjereno onečišćenje. Iako je indeks potencijalnoga ekološkog rizika (PERI) bio relativno nizak, odnosno 18, koncentracije određenih PTE-a premašile su međunarodno definirane granične vrijednosti upućujući na potrebu sanacije okoliša. Analiza glavnih komponenti (PCA) identificirala je Fe i Zn kao dominantne uzročnike onečišćenja. Analiza podzemne vode pokazala je prostornu promjenu kvalitete vode: uzorci u blizini rijeke Ind bili su kvalitete slatke vode, dok su se razine saliniteta povećavale prema zapadu, prema zoni eksploatacije, tako da je u Tehsil Isa Khelu utvrđen salinitet koji odgovara salinitetu slane vode. Voda u blizini rudarskih područja pokazala je niži pH i višu električnu vodljivost (EC), što upućuje na kisele rudničke vode, odnosno utjecaj ugljena bogatoga sumporom. Komparativna analiza s globalnim rudarskim regijama otkrila je kako su prosječne koncentracije PTE-a u Surghar Rangeu znatno više, što naglašava potrebu za provedbom održivih rudarskih praksi i ciljanim strategijama upravljanja okolišem kako bi se zaštitili tlo i vodni resursi.

Ključne riječi:
eksploatacija ugljena, opasnosti za okoliš, potencijalno toksični elementi (PTE), kvaliteta vode, onečišćenje tla

Authors' Contribution

Syed Sajjad Ahmad (MS, Deputy Director) has done formal analysis and investigation; and wrote the original draft. **Hafiz Muhammad Zaheer Afzal** (MS, Assistant Director) has done writing and reviewing. **Hafiz Zeeshan Akram** (MS, Assistant Director) has done writing and reviewing. **Sajjad Khan** (PhD, Deputy Director) has done the interpretation; writing and reviewing. **Ihtisham Islam** (PhD, Lecturer) has done writing and reviewing. **Salman Ahmed Khattak** (MS, Lecturer/Researcher) has done formal analysis and investigation, writing, reviewing and wrote the original draft. All co-authors made substantial contributions, read and commented on several versions of the manuscript, and agreed with the contents of the manuscript.

RGNZ/MGPB

Combining the 3D geological and geostatistical modelling of gypsum concentration, using historical borehole and blasthole information

Rudarsko-geološko-naftni zbornik
(The Mining-Geology-Petroleum Engineering Bulletin)
DOI: 10.17794/rgn.2025.5.9

Original scientific paper

Stefano Merli[1], Sara Kasmaee[1], Cristina Barbalucca[2], Vanessa Cellini[2], Francesco Tinti[1]*

[1] Department of Civil, Chemical, Environmental and Materials Engineering, University of Bologna, via Terracini 28, 40121, Bologna, Italy.
[2] Saint-Gobain Italia S.p.A., via del Senio 90, 48032 Casola Valsenio (RA), Italy.

Abstract

Geostatistics is used for estimating grade content in an ore deposit, thus enhancing the 3 Dimensional (3D) geological model precision, lowering the geological risk and boosting the performances of the mining industry. Despite the advantages, for decades the commercial application of the geostatistical tools has been mainly restricted to large metal mines. Except for a few notable cases, the majority of small-scale operations (quarries and industrial minerals) had hardly adopted geostatistical methods, due to the perceived complications compared to the advantages. Nowadays, things are changing, thanks to: the reduction of artisanal mining, the spread of informatization in all sectors, the necessity to improve the quarrying efficiency, the path towards sustainable mining and the challenges to obtain the social license to operate. This paper presents the recent digitalization and modelling work conducted at the "Monte Tondo" gypsum quarry (Italy), located in Northern Italy, besides the UNESCO natural heritage site named "karst and evaporite caves of the northern Apennines". The geostatistical techniques were used to estimate the concentration block model using blastholes while a 3D geological model was realised using historical boreholes. Combining two models could help for a better understanding and interpreting of the extracted gypsum and could make an important improvement to detect the future areas of interventions, subjected to strict authorization rules by the local environmental authority.

Keywords:
gypsum quarry, ordinary kriging, geological model, geostatistical block model

1. Introduction

The extraction of gypsum mineral ($CaSO_4 \cdot 2H_2O$) from the Bologna and Romagna Apennines dates centuries (**Fabbri et al., 2021**). Its use as a construction material can be appreciated in the basements of many historical buildings of the area, among which the iconical "*two towers*": Asinelli and Garisenda, the Bologna city symbol (**Pesci et al., 2011**; **Carpinteri et al., 2016**; **Dallavalle et al., 2022**). The specific gypsum type of the area is selenite, with the peculiarity of depositing in layers, and with transparent translucent crystals. The term "selenite" dates back centuries, and it refers to the ancient Greek name of the moon, for its property to reflect moonlight (**Del Monte, 2005**). Some recent studies proved the resistance of selenite to urban air quality deterioration, with respect to other natural stones (**Del Monte et al., 2001**).

The use of gypsum at the industrial level in the area dates back to the 1950s: the opening of the "Monte Tondo" quarry between the municipalities of Riolo Terme and Casola Valsenio began in 1958 by ANIC S.p.A., a state company based in Ravenna. The first industrial use of gypsum was dedicated to the production of ammonium sulphate, used in agriculture as fertilizer. Later in the 1970s, a second use as an additive for cement production was found, too. This new application became predominant in the 1980s. Meanwhile, a factory dedicated to the production of premixed plasters, owned by VIC Italiana S.p.A., was realized nearby and notable amounts of the gypsum from the Monte Tondo quarry were sent to the plant. The use of gypsum in the building sector grew rapidly in the 1990s, and the factory, which changed the ownership and passed to the English group BPB, started to produce plasterboards. In 2005, the plant and the quarry were both acquired by the French Group Saint-Gobain. From that moment onwards, all the gypsum extracted from the "Monte Tondo" quarry has been processed internally by Saint-Gobain in the nearby plant, for a variety of building applications: plasterboards, plasters, tiles, sealants, adhesives. All these final products are sold with the commercial brand Gyproc®. The attention on environment and sustainability has posed new challenges to the gypsum valorisation process, and so the life

* Corresponding author: Francesco Tinti
e-mail address: francesco.tinti@unibo.it
Received: 15 April 2025. Accepted: 9 June 2025.
Available online: 21 October 2025

cycle assessment has become a standard in the sector (**Pedreno-Rojas et al., 2020**; **Weimann et al., 2021**; **Morsali et al., 2024**).

With such premises, Saint-Gobain Italia nowadays has the possibility and duty to control all the purity requirements of the raw material, on both the extraction and processing sides. Currently, the excavation method is drill-and-blast, applied over several benches composing the mid-mountain quarry (**Casertano et al., 2024**). In order to be selected for the plant, the gypsum concentration must be comprised of between 83% and 87% blasted rock. Excavated materials with lower and higher concentration values are stocked in low-grade and high-grade stockpiles, for subsequent mixing. The aim is to provide enough feed for the processing plant at a stable concentration (**Merli, 2024**).

In this context, it is evident how the interest shifted from merely separating the gypsum from clay levels (which was the common practice) to instead estimating, with the highest degree of accuracy possible, the gypsum concentrations in the different quarry benches and authorized areas for extraction, in order to better control the feed of the plant.

This paper presents the work performed to respond to this need. All the historical borehole data and the recent blasthole data were collected, and the relevant information was extracted and digitalized. The topographic surveys and the authorization limits were integrated to define the intervention area and to create proper boundaries at the stage of 3D modelling. The geostatistical tools of variogram and kriging were then employed to estimate the concentration variabilities within the mining area, together with their accuracy and precision of the estimation, defined by the estimation variance (**Matheron, 1971**). Such geostatistical tools are commonly applied by the mining industry to natural deposits, but can also support the characterization of stockpiles of excavated raw materials (**Kasmaee et al., 2018**; **Kasmaee et al., 2019**).

The methods, even though traditionally applied to large metal mines, have been started to be tested on quarries, for improving the production efficiency (**Ozdemir et al., 2018**; **Busuyi Afeni et al., 2021**; **Joshi et al., 2022**). Moreover, geostatistics can be also applied in other fields, such as to estimate rock properties (**Pakdaman & Moosavi, 2023**), to map pollutants (**Salvi et al., 2023**) or to predict natural phenomena (**Kasmaee & Tinti, 2018**). By applying such geostatistical knowledge, the geological 3D model of the gypsum deposit was then realised using the historical boreholes; it was later combined with the concentration block model, obtained by the information from the blastholes. Geological interpretations and grade variability analyses were subsequentely performed. The final result was the variability assessment of the gypsum concentration in the authorized area, for a better and more efficient planning of the excavations in the upcoming years.

2. Methods

The local geological and geomorphological setting are characterised by over 350 m thick evaporite sequence cut by the Senio stream. The original sedimentary sequence is strongly fractured and has undergone stacking as a consequence of ancient submarine landslides. The geological formation is made of 16 gypsum layers separated by clayey interlayers and deposited during the Messinian salinity crisis, around 6 millions year ago (**Lugli et al., 2008**). The quarry has a typical geometry of halfway benches and extends from 220 m a.s.l. (base square) to approximately 340 m on the N-E side, intercepting some of the gypsum layers, among which four



Figure 1. Eastern view of the quarry, with evidenced the four gypsum layers currently under excavation (**Marabini & Poli, 2021**)

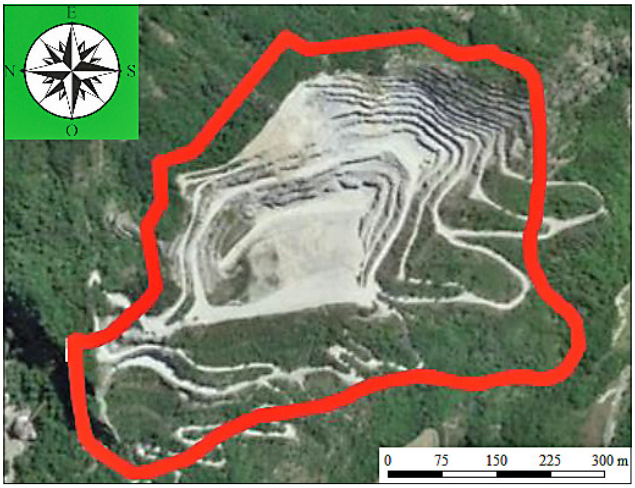


Figure 2. Satellite image of the quarry (Google Earth - Date: November 2024), encircled by the authorization limits for extraction activities

are currently under excavation by drill-and-blast techniques (see **Figure 1**). The quarry is composed of fifteen benches of variable height, from 10 to 15 m, and one bench of 20 m height, located at the base square. It is worth noticing that below the base square an abandoned tunnel system is present, heritage of the previous underground mining methods, where bat colonies of various types have settled during the years (**Clavel, 2024**). It

confirms that plants and animal species may thrive in post-mining habitats (**Salgueiro et al., 2020**). Moreover, besides and below the quarry, some karst cavities of natural importance exist all around the authorized area, for a total length of 6 km, among which the most famous and important is the "Re Tiberio" cave (**Sevil-Aguareles et al., 2025**). Furthermore, the presence of gypsum in the area favors the natural creation of around sixty sulphur springs, a geological phenomenon occurring in other similar contexts (**Vlahovic & Skopljak, 2019**). Renowned baths, located a few kilometres down from the "*Monte Tondo*" extraction site, have been exploiting such waters since 1877. Finally, the quarry is located beside the UNESCO natural heritage site named "*karst and evaporite caves of the northern Apennines*". Due to the above-mentioned conditions, the mining activity is strongly conditioned by environmental and nature preservation constraints; therefore, the ongoing exploitation activity, and its expansion, must be managed with extreme caution (see **Figure 2**).

2.1. Data collection

Various boreholes were drilled throughout the years (1967, 1986, 1994, 1996, 2004) for different purposes, mainly to identify the geological layers and the presence of groundwater. The boreholes of 1967 and 1994 refer to the area of investigation and included the measurement of gypsum concentration; for such reasons, they were used for the present work. Each borehole reported a log with gypsum concentration in the various layers (see **Figure 3**).

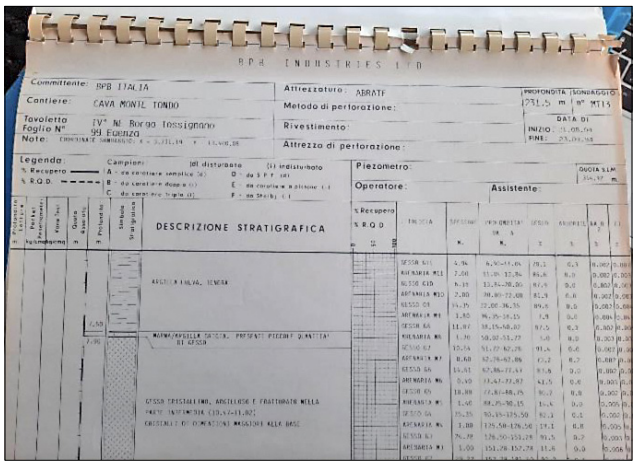


Figure 3. Extract of a borehole sheet from 1994

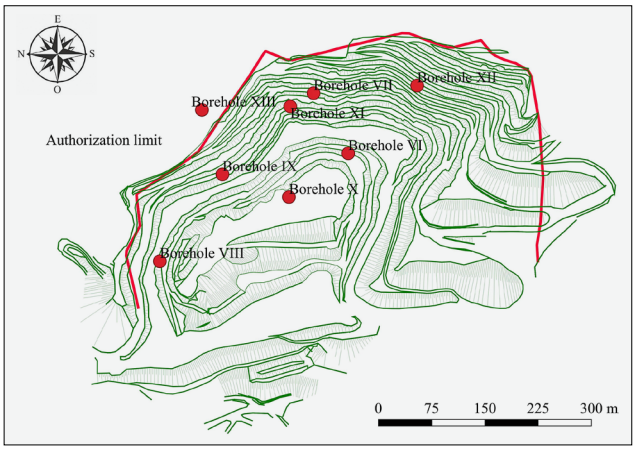


Figure 4. Localization of the boreholes in the quarry

gyproc	CONTROLLO QUALITÀ - LABORATORIO DI CAVA				
	CAVA MONTE TONDO				
Gradone:	300	Data perforazioni:			28-31/08/23
Sezione:	19-20	Data analisi:			31/08/2023
Attenzione:		Data volata:			01/09/2023
Volumi Estratti [m3]:	2700	Volumi Estratti [ton]:			5400
	N FORO	H FORO m	CRISTALLI D'ACQUA (%)	COEFF	Purezza [%]
	1	18	17.27	4.778	82.52
	2	18	18.39	4.778	87.87
	3	18	15.29	4.778	73.06
	4	18	16.87	4.778	80.60
	5	18	16.66	4.778	79.60
	6	18	18.04	4.778	86.20
	7	18	18.48	4.778	88.30
	8	18	16.73	4.778	79.94
	9	18	15.02	4.778	71.77
	10	18	16.02	4.778	76.54
	11	18	17.65	4.778	84.33
	12	18	15.73	4.778	75.16
		Av. Purity			80.49
		St. Dev.			5.59

Figure 5. Sample of results of lab analysis for one blasthole

Lithological data (geological zones) were available within the borehole sheet which were extracted as an input for geological modelling. Based on the input data, four main lithological units were detected: clay, gypsum with small crystals, gypsum with large crystals and sandstone.

Table 1. General data of the boreholes drilled in the area for sampling, with average gypsum concentration

N°	Year	Altitude (m)	Depth (m)	Longitude (WGS84-UTM32)	Latitude (WGS84-UTM32)	Average gypsum concentration (%)
XI	1994	346	238	713300.502	4903370.808	88.68
XII	1994	383	219	713329.892	4903191.668	83.59
XIII	1994	315	220	713295.602	4903495.598	86.33
VI	1967	380	180	713234.252	4903289.028	90.56
VII	1967	355	188	713319.112	4903337.978	90.98
VIII	1967	335	192	713081.902	4903555.088	90.90
IX	1967	340	193	713204.582	4903466.678	91.57
X	1967	355	194	713172.532	4903372.728	89.55

Table 2. A sample of 10 records of recent blasts in the area with average gypsum concentration taken from blastholes

N°	Date	Bench altitude (m)	N° of boreholes	Borehole length (m)	Bench angle	Longitude (WGS84-UTM32)	Latitude (WGS84-UTM32)	Average gypsum concentration (%)
1	14/04/23	300	7	16	53	713271.10	4903159.75	94.80
2	05/05/23	300	11	16	50	713288.64	4903197.44	93.04
3	01/06/23	290	12	13	43	713257.33	4903173.51	94.08
4	09/09/23	240	19	7 < H < 24	97	713212.14	4903287.62	93.85
5	23/06/23	280	14	14	92	713282.57	4903332.40	92.44
6	30/06/23	250	11	16	20	713198.09	4903252.83	91.12
7	12/07/23	325	5	5	146	713343.70	4903419.34	85.87
8	21/07/23	240	11	16	96	713216.24	4903325.31	90.23
9	28/07/23	240	13	9 < H < 26	105	713218.70	4903302.04	94.30
10	04/08/23	280	8	12	52	713257.17	4903196.29	90.42

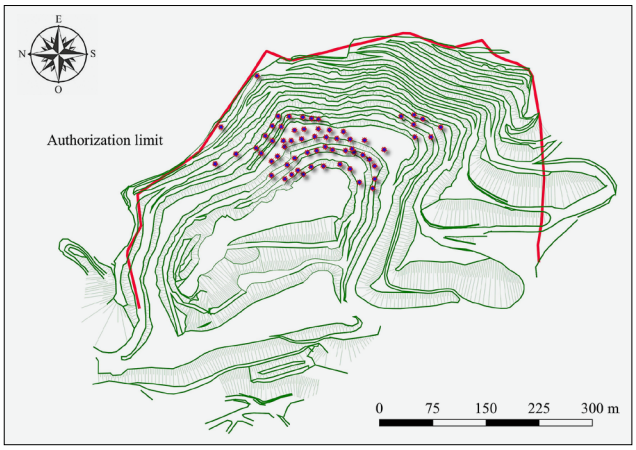


Figure 6. Localization of the blastholes (years 2021-2023) in the quarry

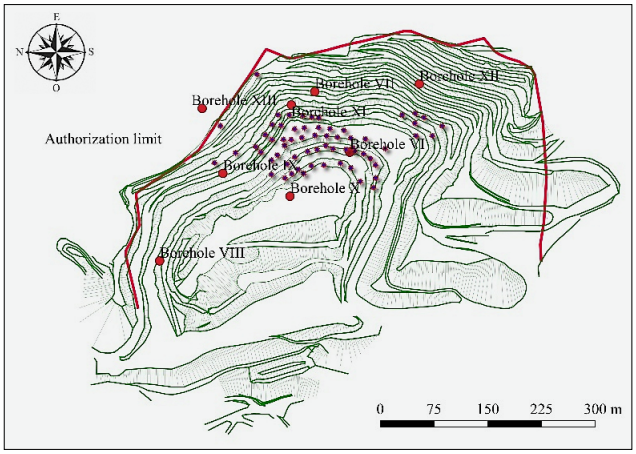


Figure 7. Localization of both blastholes and boreholes used for the analysis

Statistical mean was performed to calculate the average gypsum concentration. The boreholes data (altitude, depth, coordinates and calculated average gypsum concentration) are reported in **Table 1**.

The localization of the boreholes in the quarry is displayed in **Figure 4**.

Added to this, starting in 2021, the average concentration of gypsum has been measured on site for each blasthole. During each drilling, a bag of extracted material has been filled directly through the machine. Each bag has then been brought to the quality lab for proper analyses of the properties of interest (see **Figure 5**).

A sample of the data for the period 2021-2023 is reported in **Table 2.**

The localization of all blastholes in the years 2021-2023 in the quarry is displayed in **Figure 6.**

All the information used for the present work were then obtained by combining blastholes and boreholes (see **Figure 7**).

2.2. *Data analysis*

As the first step, fundamental for geostatistical analysis, the input data were statistically studied. The statistics parameters of the blastholes are reported in **Table 3**.

Focusing on gypsum concentration, the percentile analysis is reported in **Table 4.**

The frequency analysis is reported for gypsum concentration and blastholes length in **Figure 8**.

As **Figure 8** shows, the most representative class of blastholes length is the 16 m class, followed by the 12 m class, and, detached, the 24 m class. The blastholes were therefore divided into three groups, depending on the

Table 3. Statistics of gypsum concentration and length for all the analysed blastholes

Statistics	N° of measurements	Min	Max	Average	Variance	Standard deviation
Gypsum concentration (%)	724	71.77	97.47	90.50	16.24	4.03
Length (m)	687	5.00	26.00	15.03	8.23	2.87

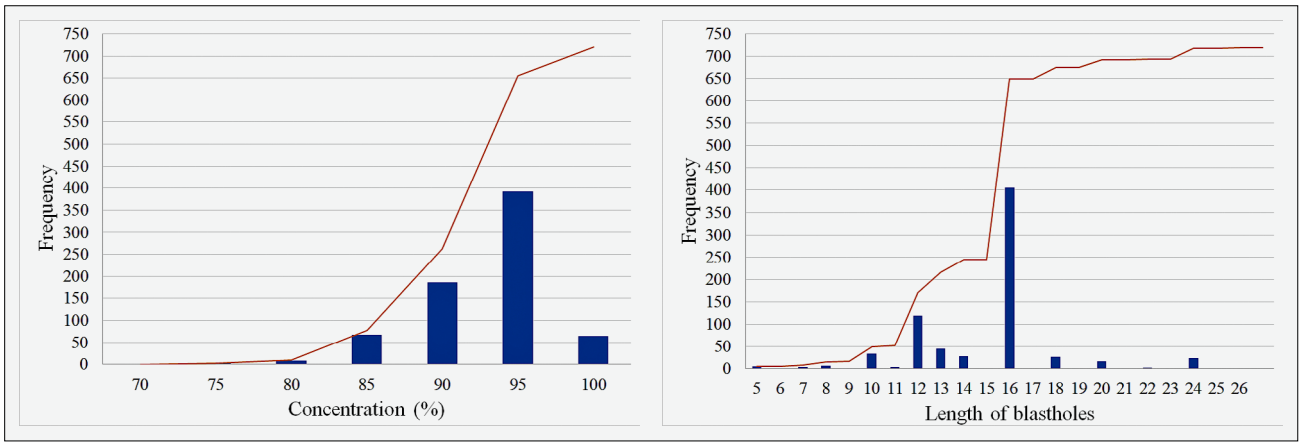


Figure 8. Frequency distribution of gypsum concentration in blastholes (left) and their length (right)

Table 4. Percentile analysis of gypsum concentration in the blastholes

Percentile	P5	P10	P25	P50	P75	P90	P95
Gypsum concentration (%)	82.74	84.52	88.25	91.58	93.51	94.94	95.56

Table 5. Statistics of blastholes divided by classes of length

Classes of length	N° of measurements	Tolerance	Range	Gypsum concentration (%)			
				Min	Max	Average	Variance
L = 12 m	212	2 m	10-14 m	78.69	97.47	89.17	20.49
L = 16 m	431	2 m	14-18 m	71.77	96.70	91.01	13.68
L = 24 m	27	2 m	22-26 m	87.39	97.23	92.84	6.54

Table 6. Absolute and relative frequency of the gypsum concentration for the class L=12 m

Class of length L=12 m		
Gypsum concentration (bins %)	Frequency	Relative frequency
≤70	0	0.00
70-75	0	0.00
75-80	8	3.77
80-85	53	25.00
85-90	60	28.30
90-95	88	41.51
95-100	3	1.42

Table 7. Absolute and relative frequency of gypsum concentration for the class L=16 m

Class of length L=16 m		
Gypsum concentration (bins %)	Frequency	Relative frequency
≤70	0	0.00
70-75	3	0.70
75-80	5	1.16
80-85	34	7.89
85-90	126	29.23
90-95	258	59.86
95-100	5	1.16

predominant lengths of the holes: 12 m, 16 m and 24 m. The statistics relating to these groups are reported in the following tables: **Table 5**, **Table 6**, **Table 7** and **Table 8**.

As shown in **Table 5**, there are only 27 samples with 24 m length, which can be divided into two 12 m samples and include them in the 12 m class. Therefore, two classes of 12 m and 16 m were considered for the next step analysis.

Table 8. Absolute and relative frequency of gypsum concentration for the class L=24 m

Class of length L=24 m		
Gypsum concentration (bins %)	Frequency	Relative frequency
≤70	0	0.00
70-75	0	0.00
75-80	0	0.00
80-85	0	0.00
85-90	5	18.52
90-95	18	66.67
95-100	4	14.81

2.3. Geological modelling

3D geological modelling was constructed using lithological zones, extracted from borehole data in RockWorks® (**Rockware, 2024**) software. The RockWorks®

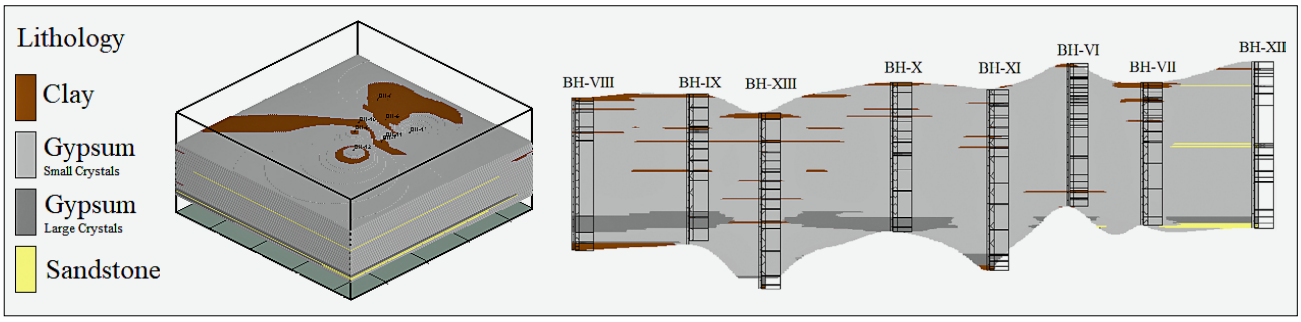


Figure 9. 3D geological representation (left) and vertical cross-section passing through all boreholes (right) showing the geological model of the gypsum quarry

software was selected being a widespread and robust tool for such types of analyses. The simple method of inverse distance weighting – IWD (power 2) was used for the geological modelling since the lithology was quite homogenous (see **Figure 9**). The neighbourhood parameters for performing IWD were selected equally to the parameters used for the geostatistical analysis (see **Section 2.4**).

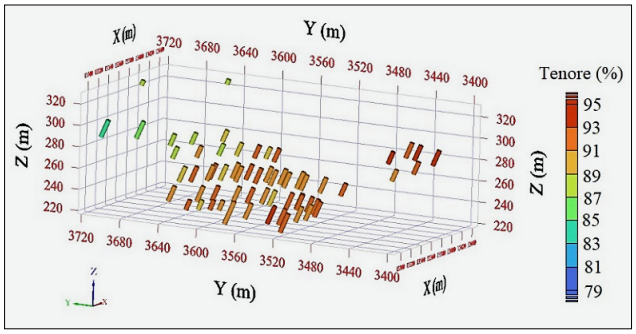


Figure 10. Grades of cylindrical support representing the blasthole groups in the quarry area. The coordinate reference system is local.

The 3D geological model included the four main geological zones as:

- Sandstone;
- Clay;
- Gypsum with small crystals;
- Gypsum with large crystals.

A unique grid with 5×5×5 m^3 dimension was used for both geological modelling and gypsum concentration model. Constructing the geological model is an important step which can help interpreting the concentration

Table 9. Statistics over the cylindrical support

Statistics over cylindrical support	Min	Max	Mean	Variance	Standard deviation
Grade (%)	80.49	94.87	90.40	9.75	3.12
Thickness (m)	5.00	24.00	14.95	7.94	2.82

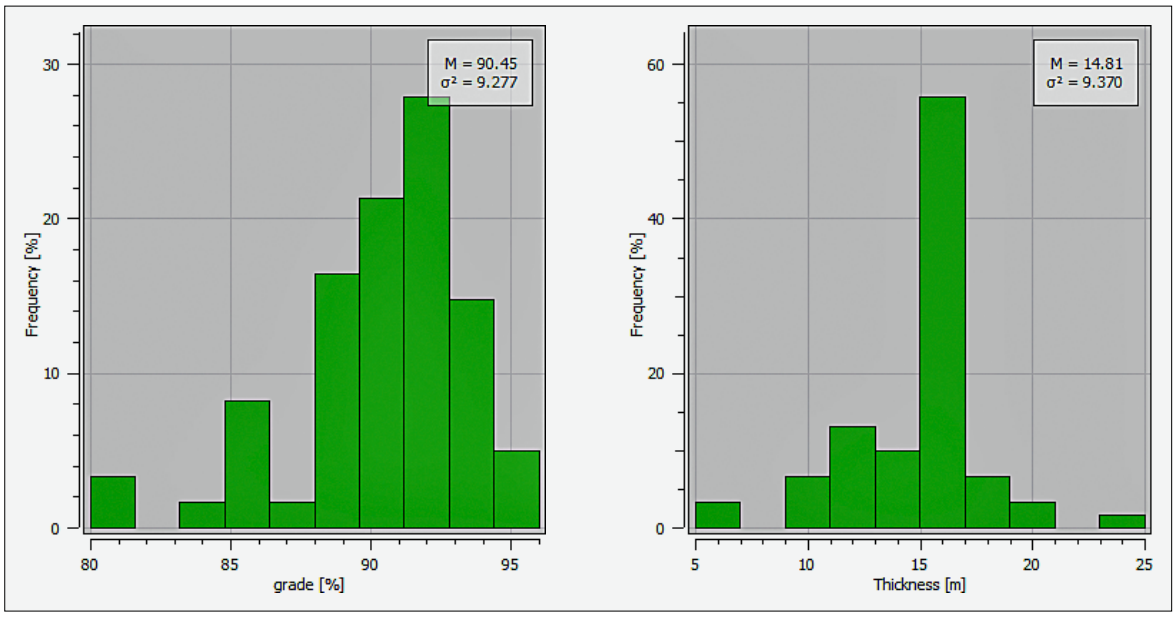


Figure 11. Histogram of the sixty-three-gypsum grade and thickness data

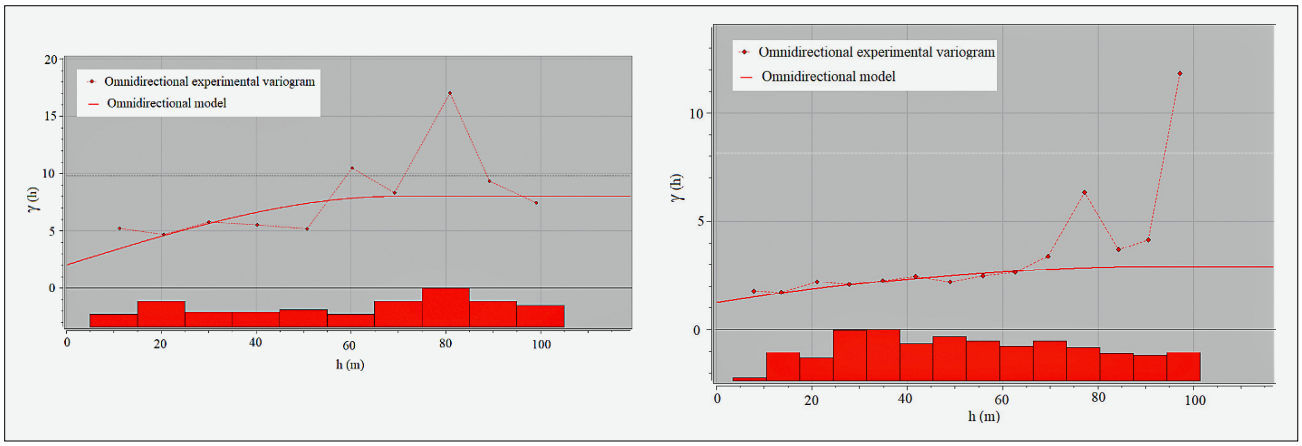


Figure 12. Experimental variogram, model and number of pairs over the two set of data, those with thickness 12 m (left) and those with thickness 16 m (right).

block modelling and variation of gypsum concentration based on geological zones' variation.

2.4. Geostatistical analysis

To use the blastholes, at the center of each blast, two parameters were assigned:

- the average gypsum concentration, which is representative of the blastholes grade;
- the support (thickness), calculated as the average length of the blastholes, in case they differ from each other; regularization was used to put all blasts as the length of 16 m. The 16-m length was selected based on statistical analysis shown in **Figure 8** and from **Table 5** to **Table 8**, and since the highest frequency of data was 16 m. Therefore, few data have been changed (smoothed) by regularization.

In this way, gypsum blast data, each one with cylindrical support, were obtained for the quarry (see **Figure 10**).

The statistics over the cylindrical support are reported in **Table 9** and **Figure 11.**

Variographic analysis was performed over the data. The samples were divided in two groups, those of length 12 m and those of length of 16 m. The corresponding variograms were calculated (see **Figure 12**).

Table 10. Type and parameters of the variogram models selected

	Data with thickness 12 m	Data with thickness 16 m
Model type	Spherical	Spherical
Nugget	2.1	1.3
Sill	7.34	2.96
Range	65	85

Table 11. Detail of the grid used in the block model

	X	Y	Z
Number of nodes	90	120	100
Grid dimension	5 m	5 m	5 m
Grid origin	13080 m	3260 m	100 m

Due to the data behaviour, number of pairs and field dimension, the same spherical model was chosen to approximate both spatial structures, but using different pa-

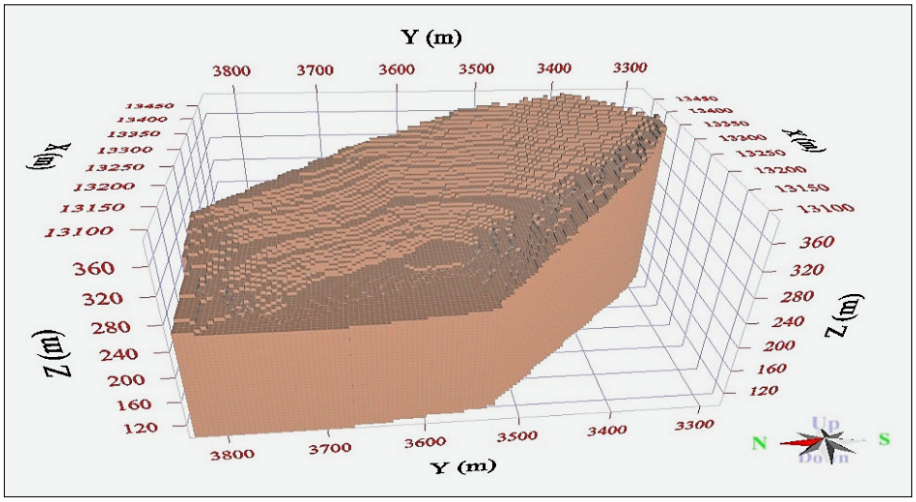


Figure 13. Block model for the gypsum quarry

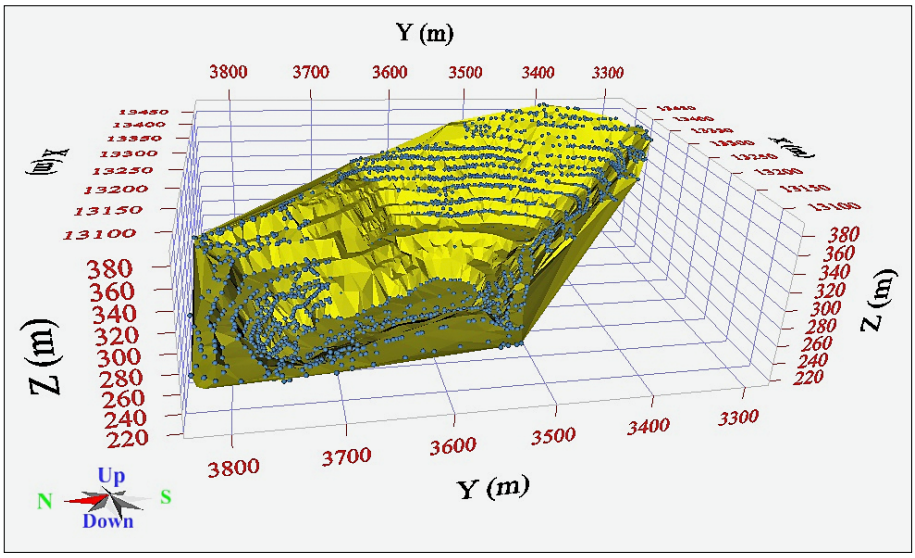


Figure 14. Block model representing the DEM-2023

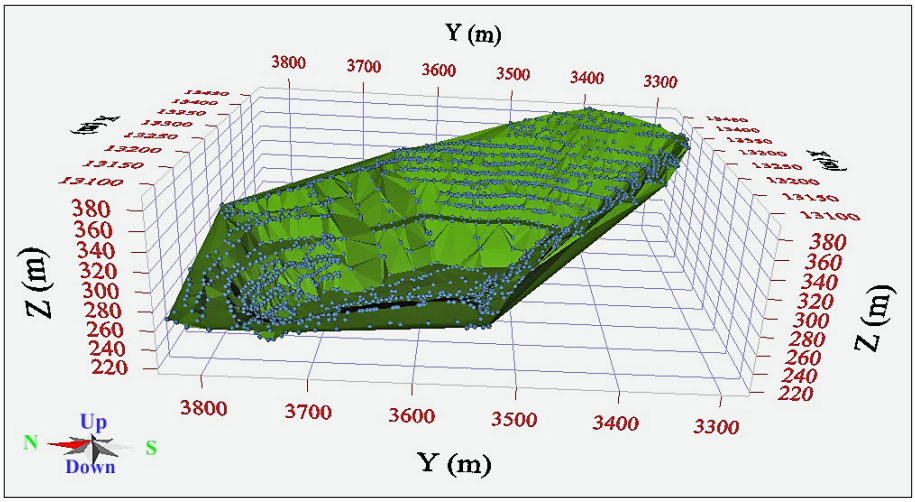


Figure 15. Block model representing the DEM-final-design

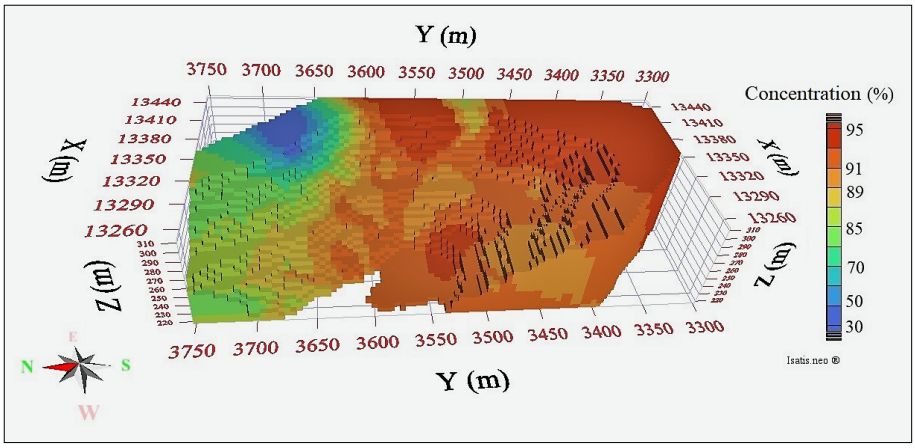


Figure 16. 3D model of the estimation of gypsum concentration

rameters. The specific parameters used are reported in **Table 10**.

The 16-m variogram corresponds to the spatial structure of the data mode (see **Figure 12**). Therefore, the corresponding model was chosen for further analysis.

The volumes chosen for the geostatistical analysis were the ones delimited by the Digital Elevation Model (DEM) of the quarry for the years 2022 (DEM2022) and 2023 (DEM2023), and also the final quarry morphology (DEM-final-design). The topography of the quarry is yearly updated, since the company must report every year the excavated volumes to the regional geological and environmental authority.

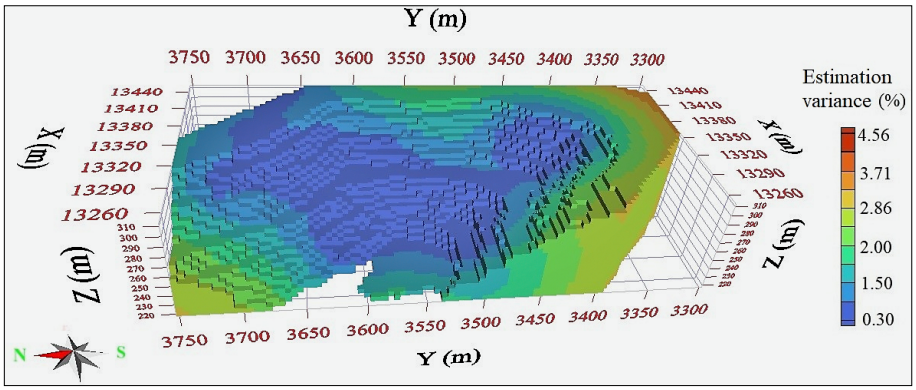


Figure 17. 3D model of the estimation variance

Ordinary Kriging was performed, using the software ISATIS.NEO® (**Geovariances, 2024**), to reconstruct the gypsum estimation in two following quarry fields:

1. The volume comprised between the DEM2022 and the DEM2023, of which the gypsum grade is known. This was used as reference to validate the correctness of the variogram model and the estimation procedure adopted.
2. The volume comprised between the DEM2023 and DEM-final-design, in order to obtain the final estimation of gypsum concentration in the remaining area to be exploited.

The block model used for the estimation of gypsum concentration has dimension 5×5×5 m^3. The details are reported in **Table 11**, while **Figure 13** shows its assonometry.

3. Results

After proper cutting, the block model for the two quarry limits (DEM-2023 and DEM-final-design) are presented in **Figure 14** and **Figure 15.** The cut between the two is the final block model where performing the estimation.

The estimation of gypsum concentration, together with the associated estimation variance, for the cut block model DEM-final-design – DEM-2023 are reported in **Figure 16** and **Figure 17**.

4. Discussion

Geostatistical 3D modelling is not a common step in small-scale quarries in Italy. Nowadays, based on the trend towards digitalization and the sensitive environmental monitoring, this work was a good opportunity to transform old data and maps into digital versions, which is helpful not only for reporting and social acceptance strategies, but also for re-evaluating the concentration variability in a more precise way. Therefore, the Monte Tondo gypsum quarry is at the forefront in such a context. Within this work, all old data and maps were digitalized and re-evaluated to create a 3D model. There were many challenges to create such 3D models, since most of quarry process did not consider important points for estimation, such as support of sampling, spread borehole grid, etc.

The estimation map of the quarry (see **Figure 16**) shows a major gypsum concentration in the South West benches, which is coherent with the four gypsum layers represented in **Figure 1**. On the other hand, less concentration values of gypsum are predicted on the North East benches, where large volume of clay at levels 290-310 m have been effectively found. Such a presence of clay is coherent with the geological model of **Figure 9**, where clay was defined at the top layers of the model. The estimation variance map presented a low value in the middle of the block model, while higher values can be found at the model borders. It highlights a decrease of precision of the estimation from the centre to the borders.

By comparing the model of the estimation variance (see **Figure 17**) with the 3D view of samples (see **Figure 10**), it is clear the precision is greater near the samples and where information is available, i.e. mainly where the blasts were carried out between 2021 and 2023. The high density of the data has made it possible to reconstruct a reliable representation of the gypsum content in the exploitation areas of the quarries.

Concerning the volume still to be excavated (corresponding to 372,100 m^3, comprised between DEM-final-design and DEM-2023), based on the carried out estimation, it is expected to get an average gypsum concentration around 87.2%, with an average estimation standard deviation around 0.7%. Such results indicate high theoretical precision of estimation. The gypsum concentration, in average, is at the upper border of the correct range for feeding the processing plant. The highest values are expected in the southern area of the quarry and at greater depths, while the lowest values can be found in the northern area and at higher elevations. This means that almost all gypsum benches can be proficiently exploited, in order to realize a correct and stable concentration mix to the processing plant. The result is highly beneficial, since it provides evidence to the regional authority of the potential and the goodness of the quarrying activity, with minimum stock of mining residues in the environment. The details of gypsum concentration forecast for the different benches are reported in **Table 12**.

Table 12. Average values of the estimation, for each quarry bench

Bench n.	Elevation H (m)	Height (m)	Estimated gypsum concentration (%)	Estimation standard deviation (%)
1	220≤H<240	20	91.17	0.56
2	240≤H<250	10	90.60	0.53
3	250≤H<265	15	90.38	0.62
4	265≤H<280	15	88.59	0.68
5	280≤H<290	10	84.53	0.74
6	290≤H<300	10	81.11	0.81
7	300≤H<310	10	78.75	1.05

The comparison between the geological model and the concentration block model was helpful to interpret the variation of gypsum concentration in the different zones and benches of the quarry. The low concentration zones of gypsum (evidenced by the estimated block model) are linked to the clay zones (represented in the geological model). This comparison confirms the variability of gypsum concentration, which is consistent with the geological changes.

Thanks to the estimated block model, the company has the possibility to further develop the production schedule of the quarry, and to subsquentely optimize the excavation and crushing process, in order to get the correct and stable gypsum concentrations, with minimum loss of raw materials. Such activities are an international mining standard, and it is worthy and promising they start to be applied in quarry operations, too.

5. Conclusions

Digitalization is a fundamental stage for all mines and quarries in Europe and one of the strategical steps that can help even small-scale quarries to have a better understanding of their geology and concentration models. This is possible by inserting all historical data (boreholes) and active data (blastholes) in consistent softwares, in order to create robust geological and concentration models. The quarry operations in the "Monte Tondo" case study benefited from digitalization and geostatistical modelling to construct both geological and gypsum concentration models. The realization of a detailed 3D model representing the estimation of the gypsum content in the target exploitation area allowed for the improvement of the quarry management. This model is obtained by blastholes, while boreholes contributed to creating the geological setting, which helped in interpreting the lithological changes. Specifically, clearly distinguishing the low concentration areas from the high ones allowed for the efficient management of the raw materials mix, as to keep the inlet of the processing plant always inside the admissible concentration range.

Moreover, the 3D visualization allowed for better monitoring of the progress of the excavation, how the morphology of the quarry evolved over time and then to tackle, sufficiently in advance, any type of geological situation different from what was originally expected.

6. References

Busuyi Afeni, T., Oluwatosin Akeju, V., & Aladejare, A. (2021). A comparative study of geometric and geostatistical methods for qualitative reserve estimation of limestone deposit. *Geoscience Frontiers, 12*, 243-253. doi:10.1016/j.gsf.2020.02.019

Carpinteri, A., Lacidogna, G., Manuello, A., & Niccolini, G. (2016). A study on the structural stability of the Asinelli tower in Bologna. *Structural control and health monitoring, 23*, 659-667. doi:10.1002/stc.1804

Casertano, D., Tinti, F., Kasmaeeyazdi, S., Cellini, V., & Bruno, R. (2024). Drill and Blast in Gypsum Quarries: Optimization of Technical, Economic, and Safety Aspects in "Monte Tondo" Mid-mountain Case Study. *Mining, Metallurgy & Exploration, 42*, 99-113. doi:10.1007/s42461-024-01133-9

Clavel, J.-P. (2024). *Biodiversity Stewardship in Gypsum Quarrying: our Best Practices.* Brussels, Belgium: Eurogypsum.

Dallavalle, G., Di Tommaso, A., Gottardi, G., Trombetti, A., Lancellotta, R., & Lugli, S. (2022). The Garisenda Tower in Bologna: Effects of degradation of selenite. In V. F. Lancellotta (A cura di), *Geotechnical Engineering for the Preservation of Monuments and* (p. 1088-1100). Naples: CRC Press. doi:10.1201/9781003308867

Del Monte, M. (2005). L'epoca d'oro della selenite a Bologna. *Il Geologo dell'Emilia Romagna*, 5-24.

Del Monte, M., Ausset, P., Forti, P., Lèfevre, R., & Tolomelli, M. (2001). Air pollution records on selenite in the urban environment. *Atmospheric Environment, 35*, 3885–3896. doi:10.1016/S1352-2310(01)00143-1

Fabbri, S., Chiarini, V., Ercolani, M., Sansavini G., Santagata, T., & De Waele, J. (2021). Terrestrial laser scanning, geomorphology and archaeology of a Roman gypsum quarry (Vena del Gesso Romagnola area, Northern Apennines, Italy). *Journal of Archaelogical Science: Reports, 36*, 102810.

Geovariances. (2024). Tratto da https://www.geovariances.com/en/software/isatis-neo-geostatistics-software/

Joshi, D., Chithaluru, P., Singh, A., Yadav, A., Elkamchouchi, D., Brenosa, J., & Anand, D. (2022). An Optimized Open Pit Mine Application for Limestone Quarry Production Scheduling to Maximize Net Present Value. *Mathematics, 10*, 4140. doi:10.3390/math10214140

Kasmaee, S., & Tinti, F. (2018). A method to evaluate the impact of urbanization on ground temperature evolution at a regional scale. *Rudarsko-geolosko-Naftni-Zbornik, 33*(5), 1-12. doi:10.17794/rgn.2018.5.1

Kasmaee, S., Raspa, G., Tinti, F., Bonduà, S., & Bruno, R. (2019). Geostatistical Estimation of Multi-Domain Deposits with Transitional Boundaries: A Sensitivity Study for the Sechahun Iron Mine. *Minerals, 9*(115), 1-22. doi:doi.org/10.3390/min9020115

Kasmaee, S., Tinti, F., & Bruno, R. (2018). Characterization of metal grades in a stockpile of an Iron Mine (Case study - Choghart iron mine, Iran). *Rudarsko-Geolosko-Naftni-Zbornik, 33*(2), 51-59. doi:10.17794/rgn.2018.2.5

Lugli, S., Manzi, V., & Roveri, M. (2008). New facies interpretations of the Messinian evaporites in the Mediterranean. *CIESM Workshops monographs*, *33*, p. 67-72. Almeria.

Marabini, S., & Poli, P. (2021). *Servizio di attività tecnica di valutazione delle componenti ambientali, paesaggistiche e socio-economiche in relazione al possibile proseguimento dell'attività estrattiva del Polo Unico Regionale del Gesso in località Monte Tondo.* Riolo Terme.

Matheron, G. (1971). *The Theory of Regionalized Variables and its Application* (1 ed.). Paris: École Nationale Supérieure des Mines de Paris.

Merli, S. (2024). *Digitalizzazione e modellazione 3D della cava di gesso di Monte Tondo.* Bologna: Master Thesis in Environmental Engineering, University of Bologna.

Morsali, S., Rakhshanbabanari, K., Osmani, M., Cavalaro, S., Gutai, M., Castro-Diaz, M., . . . Massey, A. (2024). Life Cycle Assessment of Plasterboard Production: A UK Case Study. *Sustainability, 16*, 3564. doi:10.3390/su16093564

Ozdemir, A., Dag, A., & T., I. (2018). A Comparative Assessment on Cement Raw Material Quarry Quality Distribution via 3-D Identification. *Journal of Mining Science, 54*(4), 609-616. doi:10.1134/S1062739118044075

Pakdaman, A., & Moosavi, M. (2023). Surface Roughness Assessment of Natural Rock Joints Based on an Unsupervised Pattern Recognition Technique Using 2D Profiles. *Rudarsko-Geološko-Naftni Zbornik, 38*(2), 185-198. doi:10.17794/rgn.2023.2.14

Pedreno-Rojas, M., Fort, J., Cerny, R., & Rubio-de-Hita, P. (2020). Life cycle assessment of natural and recycled gypsum production in the Spanish context. *Journal of Cleaner Production, 253*,120056.doi:10.1016/j.jclepro.2020.120056

Pesci, A., Casula, G., & Boschi, E. (2011). Laser scanning the Garisenda and Asinelli towers in Bologna (Italy):. *Journal of Cultural Heritage, 12*(12), 117-127. doi:10.1016/j.culher.2011.01.002

Rockware. (2024). Tratto da https://www.rockware.com/product/rockworks/

Salgueiro, P., Prach, K., Branquinho, C., & Mira, A. (2020). Enhancing biodiversity and ecosystem services in quarry restoration – challenges, strategies, and practice. *Restoration Ecology, 28*(3), 655-660. doi:10.1111/rec.13160/suppinfo

Salvi, F., Raspa, G., & Torri, G. (2023). Parametrization identification and characterization of the radon priority areas for indoor radon risk management. *Journal of Environmental Radioactivity, 261*, 107120. doi:10.1016/j.jenvrad.2023.107120.

Sevil-Aguareles, J., Pisani, L., Chiarini, V., Santagata, T., & De Waele, J. (2025). Gypsum cave notches and their palaeoenvironmental significance: A combined morphometric study using terrestrial laser scanning, traditional cave mapping, and geomorphological observations. *Geomorphology, 471*, 109576. doi:10.1016/j.geomorph.2024.109576

Vlahovic, T., & Skopljak, F. (2019). Genesis of the thermal-mineral waters of Ilidža, Bosnia and Herzegovina. *Rudarsko-geološko-naftni zbornik, 34*(1), 127-138. doi: 10.17794/rgn.2019.1.11

Weimann, K., Adam, C., Buchert, M., & Sutter, J. (2021). Environmental Evaluation of Gypsum Plasterboard Recycling. *Minerals, 11*(101), 1-13. doi:10.3390/min11020101

SAŽETAK

Kombiniranje 3D geološkoga i geostatističkoga modeliranja koncentracije gipsa uz korištenje informacija iz starih istražnih bušotina i minskih bušotina

Geostatistika se koristi za procjenu sadržaja rude u ležištu, čime se poboljšava preciznost 3D geološkoga modela, smanjuje geološki rizik i poboljšava izvedba rudarskih radova. Unatoč prednostima desetljećima je komercijalna primjena geostatističkih alata uglavnom bila usmjerena na velike rudnike metala. Osim nekoliko iznimnih slučajeva većina malih rudarskih kopova (kamenolomi i kopovi industrijskih minerala) gotovo da nije primjenjivala geostatističke metode zbog uočenih većih komplikacija u odnosu na prednosti. Danas su stvari drugačije zahvaljujući smanjenju zanatskoga rudarstva, širenju informatizacije u svim sektorima, potrebi za poboljšanjem učinkovitosti vađenja kamena, putu prema održivome rudarstvu i izazovima u dobivanju društvene dozvole za rad. Ovaj rad predstavlja nedavni rad na digitalizaciji i modeliranju proveden u kamenolomu gipsa „Monte Tondo", koji se nalazi u sjevernoj Italiji, uz UNESCO-ovo zaštićeno mjesto prirodne baštine koje se zove Krške i evaporitne špilje Sjevernih Apenina. Geostatističke tehnike korištene su za procjenu koncentracije u blok-modelu pomoću podataka iz minskih bušotina, dok je 3D geološki model realiziran korištenjem podataka iz starih istražnih bušotina. Kombiniranje dvaju modela moglo bi pomoći u boljemu razumijevanju i interpretaciji kvalitete eksploatiranoga gipsa te bi moglo znatno poboljšati otkrivanje budućih područja eksploatacije podložnih strogim pravilima odobrenja lokalnih tijela za zaštitu okoliša.

Ključne riječi:
kamenolom gipsa, obični kriging, geološki model, geostatistički blok-model

Author's contribution

Stefano Merli (MSc): data curation, investigation and visualization. **Sara Kasmaee** (PhD): conceptualization, data curation, formal analysis, methodology, validation, visualization, writing – original draft and writing – review & editing. **Cristina Barbalucca** (MSc): data curation, formal analysis, resources and supervision. **Vanessa Cellini** (MSc): data curation and project administration. **Francesco Tinti** (PhD) conceptualization, methodology, project administration, writing – original draft and writing – review & editing.
All authors have read and agreed to the published version of the manuscript.

RGNZ/MGPB

Concentrating the Zn-Pb sample from Nignan ore deposit

Rudarsko-geološko-naftni zbornik
(The Mining-Geology-Petroleum Engineering Bulletin)
DOI: 10.17794/rgn.2025.5.10

Preliminary communication

CC BY

Maryam Abedi Moghadam[1], Marzieh Hosseini Nasab[2]*, Mohammad Noaparast[1]
[1] *School of Mining Engineering, College of Engineering, University of Tehran, Tehran, Iran.*
[2] *Department of Mining Engineering, University of Sistan and Baluchestan, Zahedan, Iran.*

Abstract
The aim of the present study is to increase the grade of zinc from lead and zinc ore from the Noahang (Chah-Ahan) area of the Nignan deposit to more than 40% Zn, using the flotation method. The experiments were conducted on a low-grade sample with average grades of 3% zinc and 0.05% lead. The main zinc minerals in this sample were sphalerite and smithsonite in the carbonate field, and galena was rarely observed. The results of mineralogical studies and polished thin sections showed that the degree of liberation of zinc ores in the size fraction -106+75 µm was 90-95%. Different parameters such as size, solid mass percentage, type and dosage of collector were investigated, and under optimal conditions, a concentrate with a grade of 5% Zn and 70.4% recovery was obtained. In addition, kinetic experiments were conducted to achieve the highest Zn recovery in the rougher stage, which reached up to 58.6% of recovery. The results indicated that the best grade and recovery of zinc were achieved when the sample was crushed with a wet rod mill for 8 minutes to reach to the desired degree of liberation. The final grade and recovery of flotation method were obtained as 42.19 and 40.08% for zinc concentrate, respectively.

Keywords:
Noahang mineral area, flotation, degree of liberation, grade, recovery

1. Introduction

Metals have many applications in industries (**Hosseini Nasab and Rezazadeh, 2022; Hosseini Nasab, 2024**), and lead and zinc are among the most widely used non-ferrous metals in various industries. Oxidized ores of these two metals are the most important source of production of these metals after their sulfide types. Despite the problems and complexities in this field (due to the nature of these types of ores), the flotation method is the most common method for their processing (**Moradi, 2005**). Nowadays, due to the reduction of high-grade mineral reserves and the economic exploitation and processing of low-grade minerals, low-grade metal ores have become of particular importance (**Moradi, 2005; Maleki et al., 2023; Faramarz et al., 2024**). Therefore, the low-grade lead and zinc-oxidized ores are also considered among these reserves (**Moradi, 2005**).

Due to the similarity of genesis and formation of lead and zinc minerals, despite their different physical and chemical properties, they are mostly found together in mines (**Ghorbani, 2008**). The main use of lead metal is in transportation and electrical, and zinc is mainly used as part of battery tanks, in foundry molds and in the automotive industry. Zinc is also used in galvanizing steel products and prevents the corrosion of steel (**Goodwin, 2008**). Most zinc oxides and carbonate minerals have very fine crystal sizes (3-10 µm), and are available in carbonate, oxide and silicate forms (**Boni, 2003**). Lead is found in nature as sulfide, sulfate, carbonate and lead salts (**Black and Allen, 1999**). The most common methods for increasing the grade of lead and zinc ores include flotation and gravity methods in which gravity separation is less commonly used than flotation (**Karimpour and Saadat, 2006**). Mainly, process optimization can be pursued more effectively and with a lower percentage of error by correcting the type and amount of chemical materials used. In this regard, by conducting targeted experiments, more suitable chemicals that are employed on a commercial scale in the world would normally be used which yield the appropriate results, as well (**King, 2001**).

In the present study, the feasibility of flotation of lead and zinc ores from the Nignan deposit, which is located in South Khorasan Province, Iran, was investigated, and the process was optimized in terms of the type and amount of chemical materials used, including collectors, *depressants,* and activators. This research, using case studies and statistical analyses, seeks to find the optimal flotation conditions for zinc ore from the Nignan deposit

* Corresponding author: Marzieh Hosseini Nasab
e-mail address: hosseininasab@eng.usb.ac.ir
Received: 5 May 2025. Accepted: 12 June 2025.
Available online: 21 October 2025

that would lead to achieving the best possible grade and recovery.

1.1. Research objectives

Most of the extracted mineral soils containing lead and zinc are of the sulfide and oxide type, and therefore the technical processing approach which is accordingly employed is usually the flotation method. The objectives of the present research can be briefly stated in the following:

- study on the concentrating of lead and zinc ore sample from the Nignan deposit, using flotation.
- achieving a grade of more than 40% zinc, in zinc concentrate with acceptable recovery.

To achieve these objectives, it is necessary to organize and implement the appropriate flotation experiments on a laboratory scale for the ore sample of the Nignan mine. Flotation experiments were conducted using potassium amyl xanthate (PAX), coco alkyl amine acetate (Armac C) and their combination as collectors, zinc sulfate and copper sulfate as zinc *depressant* and activator, and polypropylene glycol (A65) as a frother.

Before conducting flotation experiments, sampling was performed and the samples were crushed. Then, a sample was subjected to sieve analysis and the distribution of lead and zinc metals in different size fractions were determined. The work index of the sample was also experimentally calculated. To determine the degree of liberation of the ore, thin polished sections were prepared to run the mineralogical and microscopic studies to use its results in the flotation process.

1.2. Introduction to the Nignan Complex

Due to the proximity of the Nignan lead and zinc exploration area to two important crustal blocks of Iran (the Lut and Tabas blocks), and the proximity to the Nayband fundamental fault, this part of central Iran has been affected by the geodynamic processes governing both crustal blocks, and numerous lead and zinc deposits have formed there. According to field observations and studies of polished sections, the mineralogy in this area is simple and consists of primary minerals sphalerite, pyrite and hematite, as well as secondary minerals cerussite, hemimorphite, smithsonite, goethite and limonite. Galena, calcite and dolomite are the main tailings, and quartz and barite are present in smaller amounts (**Gholami and Ebrahimi, 2010**).

1.3. Research background

In this section, while reviewing previous research on the related topic, the working method and chemicals used will be discussed.

Moradkhani et al. (2010) conducted a study on the effect of Armac-C collector on the flotation of non-sulfide ores in the presence of a KAX collector. In this study, the effect of cationic collector concentration (co-co-alkyl-amine-acetate) on the optimization of zinc grade and recovery in flotation using combined collectors (KAX-Armac C) was investigated. The orthogonal array design L18 (21×37) was selected according to the Taguchi method, which includes one parameter with two levels and seven parameters with three levels. The parameters included the concentration of sodium silicate, starch, sodium sulfide, xanthate (in two stages) and Armac-C concentration, pH and flotation time. To determine the relationship between experimental conditions and recovery levels, statistical analysis and S/N evaluation methods were used. According to the obtained results, the Armac-C concentration had the greatest effect on zinc recovery in the process.

Mahdilou et al. (2013) conducted a study on the flotation of zinc oxide ore using cationic and cationic-anionic composite collectors. In this research, the flotation of smithsonite was investigated, using the cationic collectors Armac-C and Armac-T, and their mixture with potassium amyl xanthate (KAX) as an anionic collector. The results showed that the Armac-T collector was slightly more selective than Armac-C, but their combination with KAX acted in the opposite way. The KAX-Armac C composite collector improved the zinc grade and recovery of the flotation concentrate, while KAX-Armac T did not show any positive effect. At a KAX-Armac C mixture ratio of 1:2, the amine collector consumption was reduced, and an optimal concentrate with 94% recovery and 43% zinc grade was obtained without any depressing agent.

Mehrabani et al. (2010) conducted a study on the optimization and modelling of the flotation process of a low-grade lead and zinc ore (3% zinc and 1% lead). In this study, three parameters, activator (copper sulfate), collector (potassium amyl xanthate), and pH, were investigated at five levels. The RSM method was used to analyze the experiments and accordingly model the process. Analysis of variance indicated that the most important factor affecting the recovery and separation efficiency of zinc was the collector, and in the optimization of the process, the maximum recovery and separation efficiency values were 79.12% and 64.59%, respectively, using a concentration of 150 g/t of activator, 120 g/t of collector at a pH of 10.4. However, in optimization studies, a case was reported in which using the same reagents, the recovery and separation efficiency of zinc were improved by 9 and 5%, respectively.

Seke (2005) optimized the selective flotation of galena and sphalerite from the Pinah mine. This study was conducted to determine the flotation capability of galena and sphalerite when the sulfide sample was a mixture of lead, zinc, and copper. Since sphalerite recovery increased with galena recovery and increased concentrate volume, xanthate collector could not be used. However, by activating sphalerite with copper (II) ions, sphalerite recovery increased but galena recovery decreased. Due to the texture of the ore, cyanide alone was not capable

of depressing sphalerite. The simultaneous use of cyanide and zinc sulfate improved sphalerite depressant compared to cyanide alone. To improve the selection of galena and sphalerite, the rougher lead concentrate must be re-ground because prior to this step, the separation of lead and zinc was poor.

Dehghani and Shahbazi (2017) conducted a study entitled "Depression of pyrite and sphalerite in the rougher flotation of galena from Gushfeel lead and zinc ore". The lead and zinc rich-pyrite ore of the Gushfeel underground mine in Irankooh has a complex mineralogical composition. The lead concentrate obtained from the flotation of this ore contains amounts of iron and zinc exceeding the permissible limits. In this study, the effect of zinc sulfate, sodium cyanide, and iron sulfate on the depressant of sphalerite and pyrite in the flotation of galena from the Gushfeel ore was investigated. Experiments were conducted on samples finer than 75 and 90 μm, and it was observed that during galena flotation in 75 μm samples and at normal pH, with increasing zinc sulfate consumption from 300 to 1000 g/t, the lead grade in the lead concentrate increased from 4.5 to 7.1%, while its recovery remained unchanged. On the other hand, the iron grade of the concentrate decreased from 13 to 10% and the recovery of iron and zinc decreased by about 6.5 and 7%, respectively. In flotation of 90 μm samples, with increasing zinc sulfate from 500 to 1000 g/t, the iron and lead grades increased slightly, but the zinc grade decreased. In this case, the recovery of lead, zinc and iron in the lead concentrate decreased by about 7, 4 and 2% respectively, and with a further increase in zinc sulfate, the recovery of zinc and iron in the lead concentrate increased. With an increase in sodium cyanide consumption from 100 to 200 g/t, the iron content in the lead concentrate did not change, but its lead and zinc content decreased by 2 and 0.4%. Factorial experiments conducted, at two levels of zinc sulfate, sodium cyanide and pH parameters, also showed that the effect of the parameters depends on the pH of the environment. In addition, the maximum recovery of lead in these conditions was about 30%, while the recovery of zinc and iron in the lead concentrate in this case was about 7.9% and 5.2%, respectively.

Mahdavi Amin et al. (2019) conducted a study entitled "Evaluation of the role of particle size in the performance of the lead and zinc flotation circuit of the Bama-Irankooh mining complex". In this research, the effect of particle size on flotation was investigated on two industrial and laboratory scales by dividing particles into three size ranges: coarse, medium, and fine. To increase recovery, the amount and distribution of chemicals changed. For this purpose, first, on a laboratory scale using the Taguchi 9L design, the effect of the amount and type of chemicals on recovery was investigated, and the results showed that using 30 g/t of Aero 3477 collector in the rougher cells along with 15 g/t of potassium amyl xanthate collector, and 7 g of MIBC frother in the scavenger cells increased the recovery of coarse particles by 5.4%. In addition, using 15 g/t of Aero 3477 in the rougher cells along with 7 g/t of potassium amyl xanthate and 30 g/t of MIBC frother in the scavenger cells would increase the recovery of fines by 5.3%. Finally, the best distributions obtained from the experiments were implemented in the plant and it was found that using 30 g/t of Aero 3477 collector in the rougher cells along with 15 g/t of potassium amyl xanthate collector and 7 g/t of MIBC frother in the scavenger cells increased the recovery of fines and coarse particles by 2.5% and 3.9%, respectively, and increased the grade of zinc concentrate by 4.1%.

The flotation of oxide minerals of lead and zinc, especially zinc oxides, is much more difficult than the flotation of sulfide minerals. Lead, zinc, and copper oxides are much more difficult to be floated due to their higher solubility and greater surface hydration compared to sulfides (**Fuerstenau et al., 1987, Irannejad et al., 2011**). Prior to the flotation of lead and zinc ores at the Irankooh (Bama) mines, the ore is pre-processed by the heavy medium gravity (HMS) method. The centrifugal separator in this unit is a Dyna Whirlpool (DWP) type, and this operation was performed after secondary crushing. The lead flotation process of the plant was as follows: the pulp overflowing from the cyclone was fed to two preparation units with sizes of <150 μm, which are placed in series. Sodium sulfide is added to the first preparation unit and potassium amyl xanthate is added to the second, and the frother is added to the pulp as it enters the first flotation cell. The chemicals used in lead flotation include sodium silicate (500 g/t), sodium sulfide (25.3 kg/t), potassium amyl xanthate (300 g/t), and a frother (250-400 g/t) (**Moradi, 2001**). The zinc flotation process is as follows: the fines were removed from the tailings of the lead circuit by two cyclones installed in series and then tailings were fed to the zinc preparation units. For the zinc circuit, sodium sulfide and sodium silicate were added in the first preparation, and Armac TD was added in the second *preparation*. The zinc circuit consists of 12 cells of 2 m^3; so that the product of the first 6 cells was removed as concentrate and the product of the second 6 cells was returned to the preparation stage (**Karam Soltani, 1999**).

2. Methods

2.1. Sample preparation

For the purpose of preliminary studies and feasibility study of the enrichment of the sample from the Nignan lead and zinc deposit, approximately 40 kg of crushed sample was sent to the Mineral Processing Laboratory of the University of Tehran. For laboratory studies, after homogenization and preparation of a representative sample, it was forwarded to the assay laboratory for feed chemical analysis, XRF, XRD, ICP analyses, and micro-

scopic studies. After identifying the characteristics of the sample and determining the degree of liberation of valuable minerals, initial flotation experiments were designed to find the optimal grade and recovery.

Table 1. Feed analysis results

Sample Code	Zn_T (%)	Zn_O (%)	Pb_T (%)	Pb_O (%)	Cu_T (%)	Cu_O (%)	Ag (ppm)
Feed	3.01	1.66	0.05	0.02	nd*	nd*	5

*nd: Not Detected

Table 2. XRF Analysis Results

Sample	SiO_2	Al_2O_3	CaO	Fe_2O_3	ZnO
	%	%	%	%	%
	14.5	3.6	36.8	3.5	4
	SO_3	Na_2O	K_2O	TiO_2	La&Lu
	%	%	%	%	%
	2.5	0.5	0.5	0.2	<0.1
	PbO	L.O.I	MgO	Cl	P_2O_5
	%	%	%	%	%
	<0.1	31.3	2.6	<0.1	<0.1

2.2. *Analyses of the feed*

In order to check the lead and zinc content and analyze XRD, XRF and ICP, a representative sample was prepared as feed and sent to the desired laboratories. The results of the feed analysis are in **Table 1**.

As can be seen in **Table 1**, the prepared sample contains about 3% zinc, and has a low lead content, and

Table 3. XRD analysis results

Sample XRD		
Lamp type: Cu	Voltage: 40KV	Current: 30mA
Nsteps: 200	Step Size: 0/01	2θ: 5-90
Name	**Formula**	
Calcite	$CaCO_3$	
Quartz	SiO_2	
Ankerite	$Ca_{0.997}(Mg_{0.273}Fe_{0.676}Mn_{0.054})(CO_3)_2$	
Smithsonite	$ZnCO_3$	
Kaolinite	$Al_2Si_2O_5(OH)_4$	
Glaucophane	$Na_2(Mg,Fe,Al)_5Si_8O_{22}(OH)_2$	
Sphalerite	ZnS	
Gypsum	$CaSO_4.2H_2O$	
Illite	$KAl_2Si_3AlO_{10}(OH)_2$	

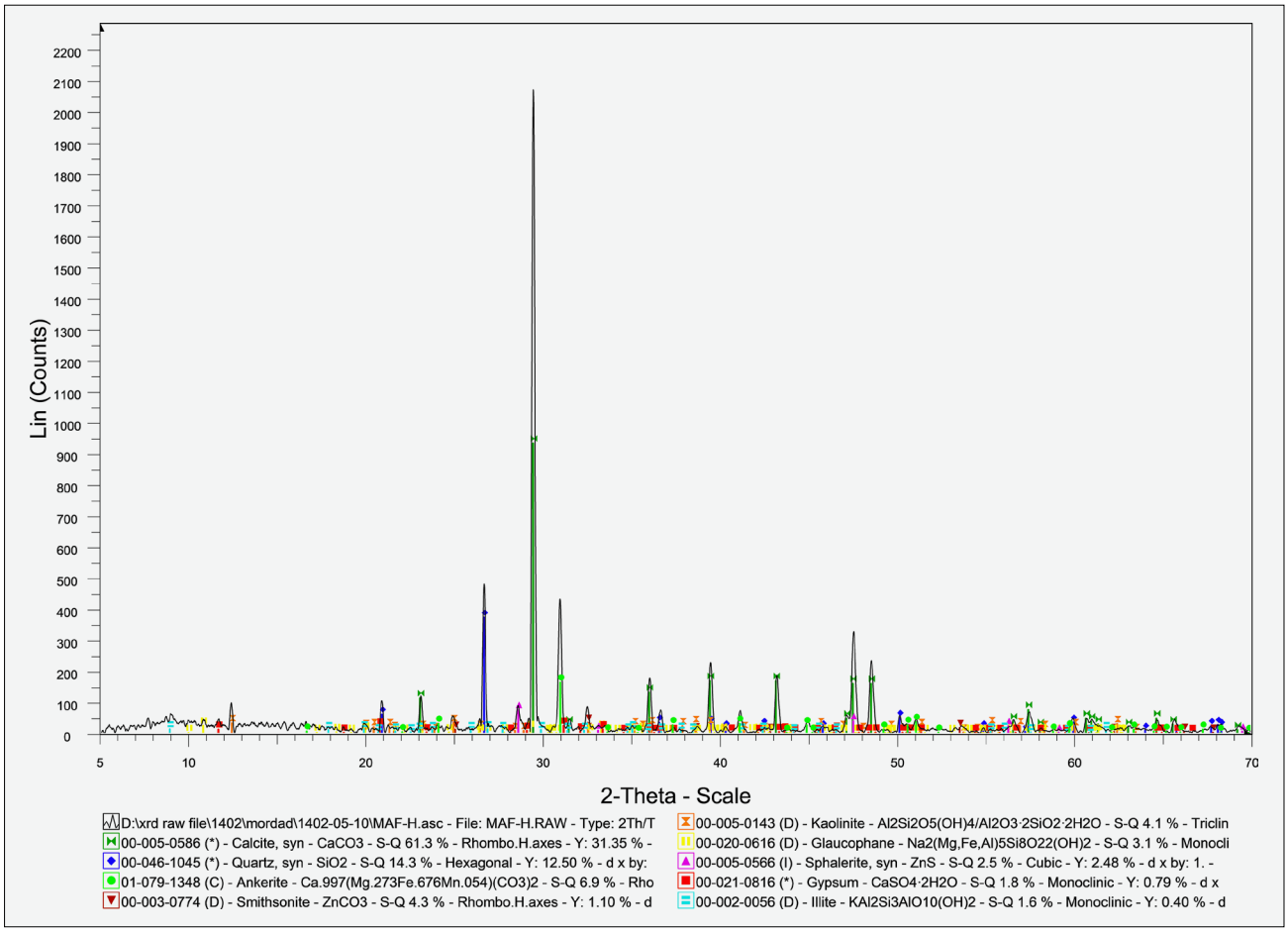


Figure 1. XRD analysis graph

Table 4. Results of ICP-OES analysis

Sample								
	Ag	Al	As	B	Ba	Bi	Ca	Cd
	ppm	ppm	ppm	ppm	ppm	ppm	ppm	Ppm
	<2	19282	43.6	<10	232	<5	262961	1.4
	Cu	Fe	Ga	K	La	Li	Mg	Mn
	ppm	ppm	ppm	ppm	ppm	ppm	ppm	Ppm
	267	24574	4.3	4016	12.2	12.2	15721	342
	P	Pb	Sb	Sn	Sr	Ti	Tl	V
	ppm	ppm	ppm	ppm	ppm	ppm	ppm	Ppm
	21.95	777.4	<5	<5	482	1018	<5	30.7
	Ce	Co	Cr	Mo	Na	Ni	Zn	S
	ppm	ppm	ppm	ppm	ppm	ppm	ppm	ppm
	23	3.6	88.8	<5	4117	27.4	32263	9826

albeit its effect should be investigated in the experiments. In addition, this sample does not contain copper and silver elements.

2.2.1 XRF analysis

In order to identify the elements present in the prepared samples, a representative sample was forwarded for XRF analysis, and its results are reported in **Table 2**.

2.2.2. XRD analysis

In order to identify the minerals present in the prepared sample, the XRD analysis was performed and its results are presented in the form of a graph in **Figure 1** and in **Table 3**.

2.2.3. ICP-OES analysis

To identify the elements present in the prepared sample, the ICP-OES analysis was carried out and its results are shown in **Table 4**.

As can be seen in the XRD, XRF, and ICP analysis tables, the zinc grade is quite clear and zinc minerals including smithsonite and sphalerite have been reported.

2.3. Microscopic studies

In order to prepare polished thin sections, 1 kg of the sample was sieved and samples of different size fractions were sent for the preparation of polished sections. The results of microscopic studies for the size fraction of -106+75 µm are as follows.

In this size fraction, zinc oxide and sulfide minerals (sphalerite and smithsonite) comprise a total of about 2-3% by volume of the fragments, and are often observed in the form of free and separate fragments. Rarely, fragments involving sphalerite and smithsonite can be found. The degree of liberation of zinc minerals in this size fraction (-106+75 µm) was determined to be about 90-95% (see **Figure 2**).

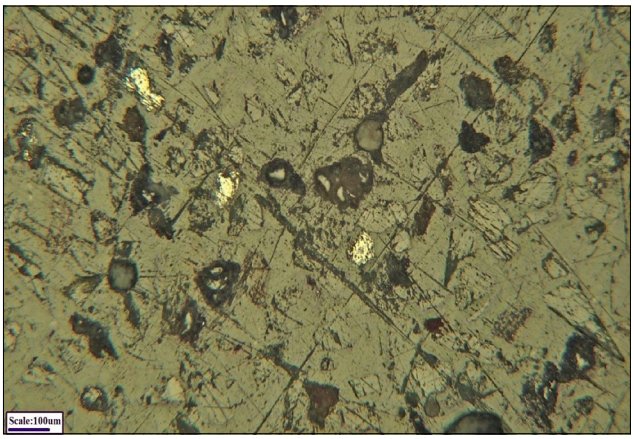


Figure 2. Free fragments of sphalerite, reflected light, PPL condition

Pyrite is present in the range of 0.5-1% by volume, iron oxide-hydroxides in the range of 1-2% by volume, and rarely galena and iron-titanium oxides are mentioned.

2.4. Optimal grinding time

In order to calculate the grinding time, 5 1-kilogram samples were prepared and each was ground by a wet rod mill for specific times of 8, 13, 18, 23, and 28 minutes and with a solids percentage of 50% (one kilogram of sample plus one liter of water). After filtration of the ground samples, 250 g were taken for wet sieve analysis for each time.

Figure 3 presents the graphs of the grinding times versus the crushed d80s. The optimal value of d80 after 8 minutes of grinding was determined. With a grinding time of 8 minutes, the sieve size through which 80% of the material passes was 98 µm.

The bond index of the sample was experimentally estimated, using standard Bond Ball mill and the obtained value was 8.55 kWh/st and/or 9.40 kWh/t, which defines the sample as soft to medium (based on **Table 5**).

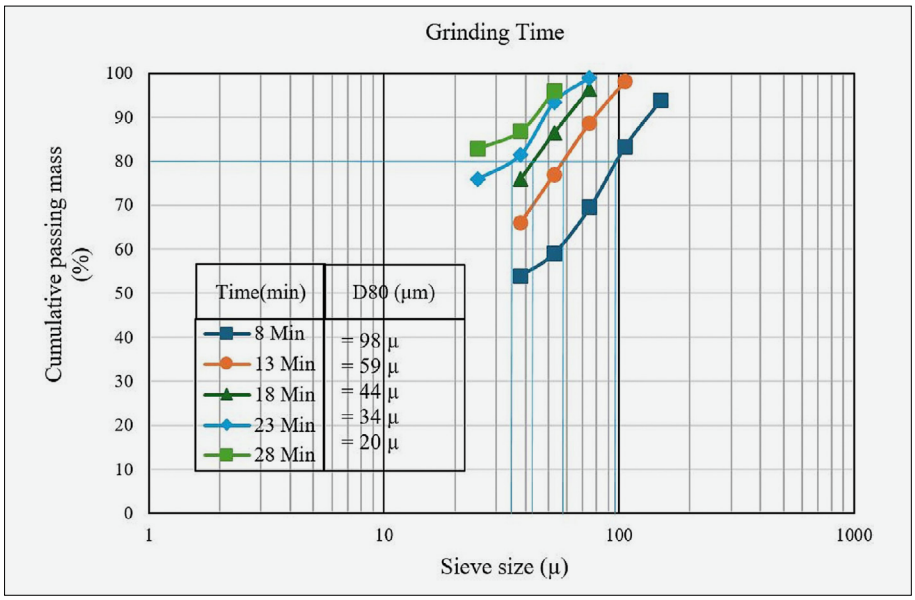


Figure 3. Changes in d80 of crushing curves at different times

Table 5. Classification of rock properties based on bond index value

Property	Soft	Medium	Hard	Very hard
Band index (kWh/st)	7-9	9-14	14-20	>20

2.5. *Flotation tests*

The flotation process is a dynamic process which is established based on the feed and tailings physico-chemical characteristics (**Kazemi et al., 2023),** and operating parameters such as collector concentration, frother concentration, pH, retention time, etc., and the grade of product and recovery could be dramatically changed. Therefore, it is essential to run experiments under different conditions, in order to achieve the optimum values of various parameters.

2.5.1. Initial tests

According to the results of microscopic studies and the desired degree of liberation, which is 80% at a size of 100 µm, 10 flotation tests were defined to obtain the amount of chemical consumption, and the behavior of the feed in the presence of different chemicals. The conditions of these tests are as follows.

In the **1st experiment**, one kilogram of the sample along with one liter of water was ground in a rod mill for 8 minutes to reach the desired size of particles and degree of freedom. In all ten of these experiments, two skimming stages are performed, the first skimming stage is designed for lead flotation, and the second one is for zinc flotation. In the second stage, a certain amount of chemicals was added to the sample. In this experiment, a 2 liter Denver flotation cell (model D12) with a stirring speed of 1200 rpm and also ethyl xanthate and amyl xanthate collector along with an IRO A65 frother were employed. The conditions of first experiment are given in **Table 6**.

Table 6. First experiment conditions

Conditions	Amount
First stage	
pH of the feed	7.75
ethyl xanthate collector (Z4) with 1% concentration	50 g/t
retention time of the collector	3 minutes
A65 frother	100 g/t
retention time of the frother	1 minute
first skimming stage	5 minutes
Second stage	
amyl xanthate collector (Z6) with 5% concentration	200 g/t
retention time of the collector	3 minutes
A65 frother	60 g/t
retention time of the frother	1 minute
second skimming stage	5 minutes

The **2nd experiment** was performed similar to the first experiment, but in the first stage, 500 g/t of zinc sulfate was added to depress zinc, and 300 g/t of copper sulfate was added to activate zinc. After each step of addition, the pH was measured, as well. The **3rd experiment** was in accordance with the conditions of the first experiment, with the difference that sulfidation was also carried out using sodium sulfide with a rate of 1000 g/t. The **4th experiment** was the same as the second one, but sulfidation was also carried out, using sodium sulfide. In addition, the **5th experiment** was carried out by eliminating the lead flotation process due to its low grade. The **6th experiment** was designed from the beginning by eliminating the lead process, due to its low grade and adding the

Table 7. 9th experiment conditions

Conditions	Amount
First stage	
pH of the feed	7.99
Copper sulfate (5% concentration)	250 g/t
retention time of the activator	5 minutes
pH after adding copper sulfate	7.8
amyl xanthate collector (Z6) with 5% concentration	200 g/t
Armax C collector (5% concentration)	250 g/t
retention time of the collector	3 minutes
first skimming stage	10 minutes
Second stage	
copper sulfate (5% concentration)	500 g/t
retention time of the activator	5 minutes
pH after adding copper sulfate	7.8
Armax C collector (5% concentration)	250 g/t
retention time of the collector	3 minutes
second skimming stage	10 minutes

sulfidation step. As the best results were achieved in 5th experiment, so the **7th experiment** was considered identical to the fifth experiment, and after 18 minutes of grinding the feed reached to 40-50 µm, which was finer than other experiments. In the **8th experiment** in accordance with the 5th experiment and with the same amount of grinding time (18 minutes) and by examining the Armax C collector in the second stage, and due to the frothing property of this type of collector, the frother in the second stage was not used. In the **9th experiment**, all the conditions of the previous experiment were maintained and the only change was the addition of the Armax C collector in the first stage. The condition of this test is given in **Table 7**. Finally in the **10th experiment**, it was attempted to use the collector aid which was supplied from South Africa D22-B3 (5% concentration) as a collector aid, for zinc oxide minerals. However, experiment 9 was selected as the experiment with the optimal conditions, in which the zinc grade and recovery were 5 and 70.4%, respectively.

2.6. Flotation kinetics experiment

The flotation kinetic test was conducted to obtain the flotation retention time for maximum recovery in the rougher stage. This test was conducted with the conditions of the 9th flotation test as the optimal test by using 4 kg of the sample with a grinding time of 8 minutes, in 6 skimming stages with specific times. In the first part, after adding chemicals, 4 skimming stages were performed in two periods of 1 minute, one period of 2 minutes and one period of 4 minutes. In the second part, after adding chemicals in a specific amount, 2 skimming stages were performed in periods of 8 minutes and 16 minutes. The results are presented in **Table 8**.

Table 8. Kinetic Test Conditions (4 kg of sample)

Conditions	Amount
First stage	
rotor speed	1200 rpm
pH of the feed	7.99
Copper sulfate	250 g/t
retention time of the activator	5 minutes
amyl xanthate collector (Z6) with 5% concentration	200 g/t
Armax C collector (5% concentration)	250 g/t
retention time of the collectors	3 minutes
Oil	1.2 g/t
Opening of the aeration valve	50%
first skimming stage (0-1)	1 minute
second skimming stage (1-2)	1 minute
third skimming stage (2-4)	2 minute
fourth skimming stage (4-8)	4 minute
Second stage	
amyl xanthate collector (Z6) with 5% concentration	100 g/t
Armax C collector (5% concentration)	125 g/t
Oil	1.2 g/t
The residence time of the above items	1 minute
fifth skimming stage (8-16)	8 minute
Sixth skimming stage (16-32)	16 minute

As the cumulative recovery of the kinetic test was lower than the cumulative recovery of test 9, the kinetic test was repeated for one kilogram of the sample. The conditions are given in **Table 9**.

The results of this test were close to test 9, in terms of cumulative recovery. Therefore, the design of the rougher-cleaner circuit was carried out in accordance with this test, which is accordingly discussed below.

2.6.1. Rougher-Cleaner test

According to the second kinetic test, which was carried out in a one-kilogram sample, 4 kilograms of the sample were prepared. After grinding, each sample was prepared in a one-liter cell so that all tests were similar to the kinetic test. In this test, taking into account the best grade and recovery obtained in the kinetic test, 4 minutes of skimming was carried out, its product was separated as a rougher concentrate, and then, the second stage concentrate was considered as feed of the scavenger stage. The conditions and relevant results are given in **Table 10**.

2.6.2. Closed-cycle Rougher-Scavenger-Cleaner test

The results obtained from the Rougher-Cleaner test were the same with kinetic test in terms of final recovery.

Table 9. Conditions of the second kinetic test (1 kg of sample)

Conditions	Amount
First stage	
rotor speed	1200 rpm
Copper sulfate	250 g/t
retention time of the activator	5 minutes
amyl xanthate collector (Z6) with 5% concentration	200 g/t
retention time of the amyl xanthate collector	3 minute
Armax C collector (5% concentration)	250 g/t
retention time of the collectors	3 minute
Oil	1.2 g/t
first skimming stage (0-1)	1 minute
second skimming stage (1-2)	1 minute
third skimming stage (2-4)	2 minute
fourth skimming stage (4-8)	4 minute
Second stage	
Copper sulfate	500 g/t
retention time of the activator	5 minute
Armax C collector (5% concentration)	250 g/t
retention time of the collectors	3 minute
Oil	1.2 g/t
fifth skimming stage (8-20)	12 minute

Thus, in order to achieve the highest grade and recovery that can represent the plant circuit, the Rougher-Scavenger-Cleaner test was designed in a closed circuit in accordance with the previous test. The discrepancy was that in the first stage, exactly in accordance with the Rougher-Cleaner test, and in the subsequent stages, in addition to the dry feed added in an amount of 3 kg to the Rougher cell, scavenger concentrate and the first cleaner tailings were also added to the 8-liter Rougher cell, as well. The consumed chemicals were used in a ratio of 75% of the initial chemicals. In addition, in the first cleaner in the subsequent stages, in addition to the Rougher concentrate, the second cleaner tailings were also added to it. **Figure 4** presents the block diagram of the Rougher-Scavenger-Cleaner closed circuit.

Table 10. Rougher-Cleaner test conditions

Conditions	Amount
First stage	
rotor speed	1200 rpm
Copper sulfate	250 g/t
retention time of the activator	5 minutes
amyl xanthate collector (Z6) with 5% concentration	200 g/t
retention time of the amyl xanthate collector	3 minutes
Armax C collector (5% concentration)	250 g/t
retention time of the collectors	3 minutes
Oil	1.2 g/t
first skimming stage	4 minutes
Second stage	
second skimming stage	4 minutes
Copper sulfate	500 g/t
retention time of the activator	5 minutes
Armax C collector (5% concentration)	250 g/t
retention time of the collectors	3 minutes
Oil	1.2 g/t
Continuation of the second skimming stage	12 minutes

3. Results and Discussions

Since the main objective of this research was to investigate on the zinc concentration, a number of initial ex-

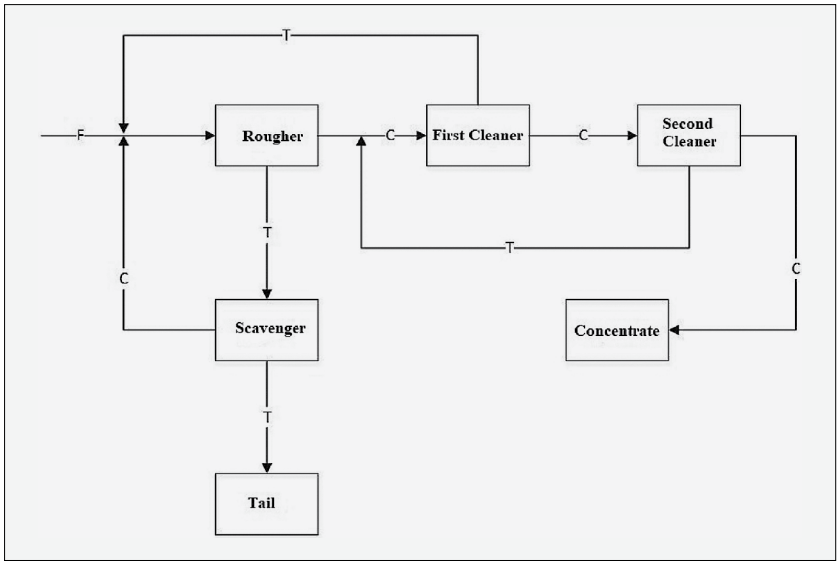


Figure 4. Block diagram of the closed circuit of the Rafter-Scavenger-Cleaner

periments were designed to achieve the best grade and recovery, and to find the optimal flotation conditions. Consequently, after finding the best results, kinetic experiments, rougher-cleaner experiments, and closed-cycle experiments were conducted. The conditions and descriptions of the experiments are presented in the previous section.

3.1. Results of Initial Experiments

In order to find the optimal grade and recovery, 10 initial flotation experiments with changing conditions were performed. The results of these experiments are presented as following.

1st Experiment: After the experiment, the obtained samples including the first and second stage concentrate and tailings were forwarded to the chemical analysis laboratory. The first experiment was designed to determine the behavior of the sample by adding a collector and a frother. Ethyl xanthate collector (Z4) was used for lead flotation and amyl xanthate collector (Z6) was used for zinc flotation. In this experiment, the lead and zinc grades were measured as 0.18 and 6.27%, respectively, and the lead and zinc recoveries were measured as 46.7 and 29.6%, respectively. The results indicated that the test performance in the zinc extraction section was not convienient, and in the lead section, due to the low feed grade, no significant product was obtained, as well.

2nd Experiment: With the conditions of the 1st experiment and adding zinc sulfate in the first stage and copper sulfate in the second stage, the 2nd experiment was designed. In the 2nd experiment, the lead and zinc grades were calculated as 0.29 and 18.32%, respectively, and their recoveries were also calculated as 31.8 and 41.9%, respectively. The results showed that by using zinc sulfate depressant and copper sulfate activator, the grades of both lead and zinc metals increased and also by activating the surface, the recovery of zinc increased, but the recovery of lead was still not significant due to its low grade in the feed.

3rd Experiment: In this experiment, by maintaining the conditions of the 1st experiment and adding sodium sulfide in both stages, the sulfidation process was applied to sulfide the surface of oxide minerals. In general, the process of combining or saturating with sulfur or its compounds is called sulfidization. Initially, only the sulfite hydrate ion was used as an activator of oxide minerals until Schwartz published the results of his studies on the sulfidization of the surface of oxide minerals in 1905 (**Moradi, 2005**). In this experiment, the lead and zinc grades were calculated to be 0.27 and 2.78%, respectively, and the lead and zinc recoveries were calculated to be 30.6 and 6.8%, respectively. According to the results, the sulfidation process for the lead increased the concentrate grade and decreased the recovery compared to the first experiment, which cannot be justified, but it had a negative effect for the zinc, so that the grade and recovery dropped sharply, which could indicate the depression of zinc that was not flotated and activation did not take place in this section.

4th Experiment: By combining the conditions of the 2nd and 3rd experiments, namely the use of sodium sulfide, zinc sulfate and copper sulfate, the 4th experiment was conducted in two stages. In this experiment, the lead and zinc grades were calculated as 0.42 and 3.03%, respectively, and the lead and zinc recoveries were calculated as 37.9 and 5.1%, respectively. The results showed that the lead grade and recovery were better than the previous experiments, and it would therefore be postulated that the zinc retention and sulfidation process in the lead section had better results, but it is still not justified due to the low lead product grade. Of course, the zinc activation and sulfidation process in the second section was not desirable, and it can be concluded from the conditions of the 2nd and 4th experiments that the depression and activation process in the zinc section was not effective. The sulfidation operation also had a negative effect on this section, and the zinc grade and recovery dropped sharply.

5th Experiment: As the results of the experiments show, the lead grade was very low and the enrichment of this metal for the project will not be economically viable. Therefore, the analysis of lead metal has been omitted in the following and the experiments have been focused on the zinc. According to the comparison of the 1st and 2nd experiments to investigate on the zinc activation operation, and its positive effect on zinc concentration, the first stage of this experiment was carried out by using copper sulfate as a zinc activator in the amount of 250 g/t and using twice the amount of A65 frother compared to the 1st experiment in the amount of 200 g/t, as well as the amyl xanthate collector in the amount of 200 g/t. In the second stage, in addition to the mentioned chemicals, the sulfidation process was also applied. The amount of copper sulfate was twice the amount in the first stage and the frother was used in the amount of 140 g/t. By applying these conditions, the grade and recovery of zinc were obtained as 12.82 and 40.2%, respectively. The results show that increasing the skimming time to 10 minutes, and using the above chemicals increased the zinc content by almost two times compared to the 1st experiment. Zinc recovery also increased significantly.

6th Experiment: In this experiment, the conditions of 5th experiment were constant and in addition to the second stage, the sulfidation process was also carried out in the first stage. In this experiment, the zinc grade and recovery were 4.7 and 18.5%, respectively, which were significantly lower than the zinc grade and recovery in the previous experiment. Therefore, according to the results of several experiments with different conditions, the use of sodium sulfide as a sulfidation agent for this sample is not recommended, as it decreased zinc grade and recovery.

Table 11. Zinc results in the 9th experiment

Sample	Mass (gr)	Mass (%)	Grade and Recovery (%)				
			Oxide		Total		Oxide to Total Ratio (%)
			grade	Recovery	grade	Recovery	
First stage concentrate	280.2	28.3	1.48	22.6	6.52	55.1	22.7
Second stage concentrate	185.3	18.7	2.41	24.3	2.72	15.2	88.6
Tailing	525	53	1.86	53.1	1.87	29.6	99.5
Feed	990.5	100	1.86	100	3.34	100	55.5

Table 12. Results of the kinetic test

Steps	Sample	Skimming time (min)	Mass (gr)	Mass (%)	Total grade (%)	Recovery (%)	Cumulative mass (%)	Average grade (%)	Cumulative recovery (%)	Enrichment Ratio
First stage	First concentrate	1	96.1	2.4	3.95	3.12	2.4	3.95	3.12	1.28
	Second concentrate	1	109.4	2.8	4.36	3.92	5.2	4.17	7.05	1.35
	Third concentrate	2	189.7	4.8	7.59	11.85	10	5.81	18.9	1.89
	Fourth concentrate	4	205	5.2	5.82	9.82	15.2	5.81	28.71	1.89
Second stage	Fifth concentrate	8	84.8	2.1	6.55	4.57	17.4	5.91	33.28	1.92
	Sixth concentrate	16	534	13.5	3.79	16.65	30.9	4.98	49.94	1.62
-	Total tailing	-	2728.5	69.1	2.23	50.06	100	-	-	-
-	Feed	-	3947.5	100	3.08	-	-	-	-	-

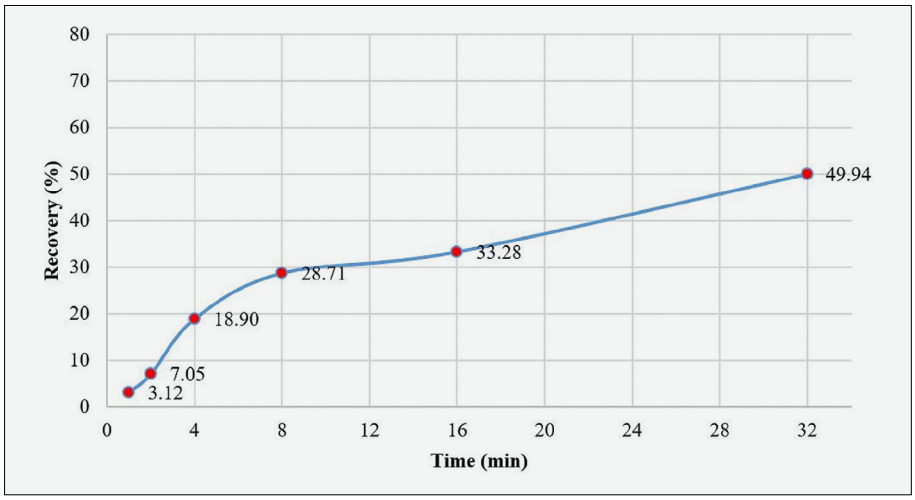


Figure 5. Recovery variation curve of the first kinetic test versus the grinding time

7th Experiment: According to the results of the 5th experiment as an experiment with desirable grade and recovery, the 7th experiment was designed with the conditions of the 5th experiment. In order to investigate the effect of particle size on grade and zinc recovery, the materials were re-ground with a grinding time of 18 minutes until they reached to size of 40-50 µm. The grade and zinc recovery of this test, were calculated as 7 and 52.3%, respectively. The results show that reducing the particle size causes a decrease in grade and an acceptable increase in zinc recovery; this result could stem from the phenomenon of zinc *entrainment* in fines sizes that has caused this issue.

8th Experiment: By removing sodium sulfide from the conditions of 5th experiment, and adding the Armac-C collector in the second stage, 8th experiment was conducted. It should be noted that due to the frothing property of the Armac-C collector, the addition of the A65 frother in the second stage was avoided. With these conditions, the zinc grade and recovery were 3.9 and 66.1%,

Table 13. Results of the second kinetic test (one kilogram)

Steps	Sample	Skimming time (min)	Mass (gr)	Mass (%)	Total grade (%)	Recovery (%)	Cumulative mass (%)	Average grade (%)	Cumulative recovery (%)	Enrichment Ratio
First stage	First concentrate	1	24.2	2.4	34.36	26.66	2.4	34.36	26.66	11.16
	Second concentrate	1	21.4	2.2	10.24	7.03	4.6	23.04	33.68	7.48
	Third concentrate	2	37	3.7	4.72	5.6	8.4	14.83	39.28	4.82
	Fourth concentrate	4	53.8	5.4	2.85	4.92	13.8	10.11	44.2	3.28
Second stage	Fifth concentrate	12	187.4	18.9	2.4	14.42	32.7	5.65	58.62	1.83
-	Total tailing	-	665.3	67.3	1.94	41.38	100	-	-	-
-	Feed	-	989.1	100	3.15	100	-	-	-	-

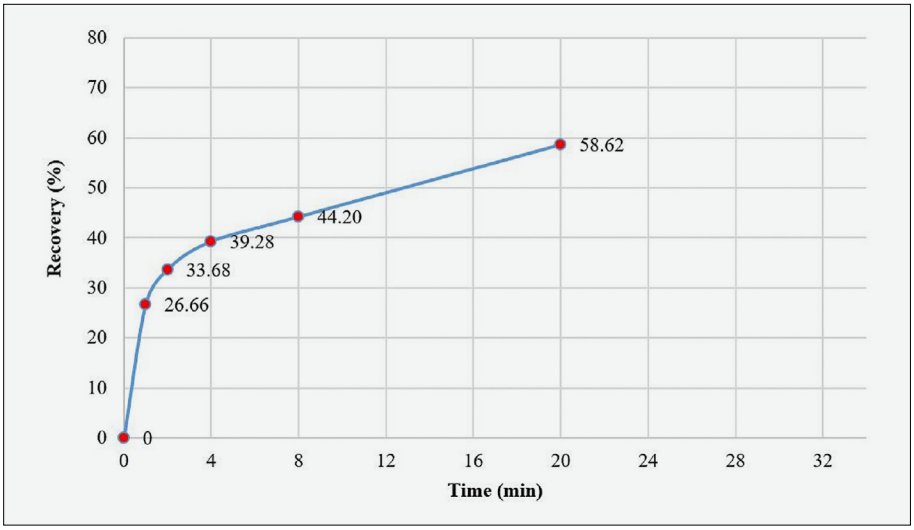


Figure 6. Recovery variation curve of the second kinetic test versus grinding time

respectively, which significantly reduced the grade and increased recovery compared to the results of 5th experiment. This experiment had a higher recovery compared to 7th experiment which had a reduction in grain size, and the purpose of the rougher experiments was to increase recovery. As mentioned above, the reason for the reduction in grade was the zinc *entrainment*, but in this experiment, the reason for the reduction in grade was the increase in recovery in the second section, which could be considered the effect of the Armac-C collector in collecting as much zinc as possible in the second stage.

9th Experiment: In this experiment, by eliminating the sulfidation agent due to its negative effect and using chemicals that had positive results in previous experiments, such as Armac-C collector and copper sulfate, it was attempted to achieve the highest zinc grade and recovery. The results of the 9th experiment are shown in **Table 11**.

According to the calculations, the zinc grade and recovery in this experiment were calculated as 5 and 70.4%, respectively. Due to the proper performance of the Armac-C collector, this collector was also used in the first section, and the frother was removed due to the frothing property of the collector in both stages. This experiment was determined as an experiment with optimal conditions with the methods and chemicals mentioned.

10th Experiment: In this experiment, along with the amyl xanthate collector, the D22-B3 collector aid was supplied and used. The zinc grade and recovery in this experiment were 13.94 and 37.1%, respectively. Compared to the previous experiment, the zinc grade increased, but the recovery did not decrease. Therefore, the collector aid used in this experiment was not suitable. The purpose of designing and conducting the initial experiments was to achieve the highest recovery percentage and with a view to the grade. Since the 9th experiment has a higher recovery than the other experiments, the conditions of this experiment are selected as the optimal experiment.

3.2. Results of the kinetic test

According to the conditions of the 9th experiment as the test with optimal conditions, the kinetic test was car-

Table 14. Results of the Rougher-Cleaner Test

Sample (duration minutes)	Mass (g)	Mass (%)	Cumulative mass (%)	Total Zinc		Oxide Zinc		Ratio
				Grade (%)	Recovery (%)	Grade (%)	Recovery (%)	
Concentrate of Cleaner II (0-1)	32.8	0.8	0.8	52.81	14.5	0.17	0.1	0.3
Concentrate of Cleaner II (1-2)	5.8	0.1	1	41.8	2	0.37	0.03	0.9
Concentrate of Cleaner II (2-3)	3.7	0.1	1.1	26.13	0.8	0.71	0.04	2.7
Concentrate of Cleaner II (3-4)	3.1	0.1	1.2	17.34	0.4	0.82	0.04	4.7
Tailing of Cleaner II (0-4)	46.2	1.2	2.3	4.3	1.7	1.48	1	34.4
Tailing of Cleaner I (0-4)	244.5	6.2	8.5	3.59	7.3	1.48	5.1	41.2
Scavenger Concentrate (4-20)	1100	27.9	36.4	3.35	30.8	1.78	27.8	53.1
Scavenger Tailing (4-20)	2510	63.6	100	2.02	42.4	1.85	65.9	91.6
Computational feed	3946.1	100	-	3.03	100	1.79	100	58.9

Table 15. Results of the Rougher-Scavenger-Cleaner test

Sample	Mass (g)	Mass (%)	Cumulative mass (%)	Total Zinc		Oxide Zinc		Ratio
				Grade (%)	Recovery (%)	Grade (%)	Recovery (%)	
Concentrate of Cleaner II	252	1.7	1.7	42.19	23.05	0.4	0.53	0.95
Tailing of Cleaner II	90	0.6	2.3	9.56	1.87	1.15	0.54	12.03
Tailing of Cleaner I	1940	13	15.3	2.78	11.69	1.56	15.82	56.12
Scavenger Concentrate	2769	18.5	33.8	3.75	22.51	1.53	22.14	40.8
Scavenger Tailing	9912	66.2	100	1.9	40.89	1.18	60.97	61.83
Feed	14963	100	-	3.08	100	1.28	100	41.47

Table 16. Final Grade and Recovery Results

Feed grade (%)	Concentrate grade (%)	Tailing grade (%)	Total recovery (%)
3.08	42.19	1.9	40.08

ried out, using 4 kg of the sample, and the relevant results are shown in **Table 12**, and in **Figure 5**.

Given that the cumulative recovery of the kinetic test was calculated to be less than the cumulative recovery of the 9th experiment, which was considered the optimal test, the kinetic test was repeated for one kilogram of the sample. The results of the second kinetic test are as described in **Table 13**, and **Figure 6**.

The second kinetic test had a higher recovery than the first test and reached a recovery closer to the 9th experiment. The purpose of the kinetic test was to achieve the retention time in the rougher section, which should have the highest recovery in this section. Therefore, according to the above results, an approximate recovery of 59% could be achieved in this kinetic test.

3.3. Results of the Rougher-Cleaner Test

The results of the Rougher-Cleaner test with the conditions mentioned in section (2.6.1) are shown in **Table 14**.

After achieving the maximum recovery according to the retention time of the kinetic test, the cleaner operation was also carried out on the rougher stage concentrate, and in each stage, the concentration was carried out for 1 minute, so that the kinetics of the cleaner stage could reach the maximum recovery, and the appropriate grade in this section, accordingly. The results show that after four stages of concentration for 4 minutes, a grade of 46.8% was obtained. Considering the grade of the first cleaner tailings and the scavenger concentrate, which was close to the grade of the input feed, a closed-circuit test was designed to calculate the grade and final recovery, which can be representative of industrial conditions, during several closed-circuit flotation stages.

3.4. Results of the Rougher-Scavenger-Cleaner test

The results of the Rougher-Scavenger-Cleaner test with the conditions mentioned in section (2.6.2) are shown in **Table 15**.

The results in **Table 15** were obtained with 15 kg of feed prepared according to the optimal conditions, and after 5 stages of closed-circuit flotation test to achieve a steady state, which shows that the zinc concentrate grade was desirable, but the zinc grade in the tailings was high, which was also the reason for the reduced recovery. Therefore, according to the designed test, the flotation process was completed, and in order to reduce the zinc grade in the tailings, which was mostly in the oxide phase, a leaching test should be designed. Thus, the final

grade and recovery of the flotation section are as follows in **Table 16**.

As can be seen in **Table 16**, the feed grade and concentrate of zinc is 3% and 42.19%, respectively, and the overall recovery is 40.08%.

4. Conclusions

1) The results of XRD and XRF analyses showed that the lead and zinc ore sample from the Nignan deposit has a zinc grade of 3.01% and lead between 0.04 and 0.05%, and carbonate minerals (calcite, less dolomite and iron carbonates) are the main non-metallic phase.
2) The results of microscopic and degree of liberation studies showed that this sample contains zinc sulfide and oxide minerals, including sphalerite and smithsonite, and has 90 to 95% of liberation in size fraction of 90-100 µm.
3) The results of the grinding time tests indicated that the sample reached a degree of liberation of about 98 µm in 8 minutes of grinding by a wet rod mill.
6) According to the sieve analysis of the feed and product of the Bond ball mill, the Bond work index was obtained as 9.40 kWh/t (8.55 kWh/st), which defines that the sample was in the soft to medium category.
7) Initial flotation tests were designed in 10 experiments, and the best result in terms of grade and recovery was considered from the 9th experiment, in which 250 g/t of copper sulfate, 200 g/t of 5% amyl xanthate collector and 250 g/t of Armac-C collector aid were employed in the first stage. In the second stage of this test, 500 g/t of copper sulfate and 250 g/t of Armac-C collector were used.
8) The zinc grade and recovery in the 9th experiment were obtained as the best experiment, 5 and 70.4%, respectively.
9) Due to the low lead content in the feed, the lead section was omitted from the flotation tests.
10) Kinetic tests were designed and run to calculate the highest recovery in the rougher section.
11) According to the results of the kinetic tests and the rougher-cleaner test, the closed-circuit flotation test was designed which represents the industrial process.
12) The final grade and recovery of flotation were obtained as 42.19 and 40.08% for zinc concentrate, respectively.

5. References

Black, L., & Allen, G. C. (1999). Nature of lead patination. *British Corrosion Journal*, 34(3), 192-197. https://doi.org/10.1179/000705999101500833

Boni, M. (2003). Non-Sulfide Zinc Deposits: a new-(old) type of economic mineralization, SGA News, N.15.

Dehghani, A., and Shahbazi, M. (2017). Depression of pyrite and sphalerite in the rougher flotation of galena from Gushfeel lead and zinc ore. *Journal of Mining Engineering*, 12(35), 35-51. doi:20.1001.1.17357616.1396.12.35.4.7

Faramaz, A., Maleki, H., Noaparast, M., Jozanikohan, G., & Noeparast, H. (2024). Implementation of flotation to recover lead and barite from Komsheche Mine jig tailings. *Rudarsko-geološko-naftni zbornik*, 39(1), 11-20. https://doi.org/10.17794/rgn.2024.1.2

Fuerstenau, M.C., Olivas, S.A., Herrera-Urbina, R., & Han, K.N. (1987). The Surface Characteristics and Flotation Behavior of Anglesite and Cerussite. *International Journal of Mineral Processing*, 20, 73-85. https://doi.org/10.1016/0301-7516(87)90018-4

Gholami, S., and Ebrahimi, Kh. (2010). Mineralogy of Nignan Lead- Zinc deposit- North West of Boshroieh, Central Iran. Abstract in 4th National Geology Conference of Payame Noor University, Mashhad, November, 636-643. doi: 10.1016/B978-0-08-095975-7

Ghorbani, R. (2008). Investigation and feasibility study of processing lead oxide ore from *Koohbanan* area of Kerman. Bachelor's thesis, Kashan University. (in Persian)

Goodwin, F. E. (2008). Zinc and lead uses: Technical and market trends. *47th Annual Conference of Metallurgists, Canadian Institute of Mining, Metallurgy and Petroleum, At: Winnipeg, MB*.

Hosseini Nasab, M. (2024). Ash Reduction of the Tailings of Agh-Darband Coal Washing Plant by Flotation Method. *International Journal of Engineering, TRANSACTIONS A: Basics*, 37(4), 739-752. doi:10.5829/IJE.2024.37.04A.13

Hosseini Nasab, M., and Rezazadeh, R. (2022). Optimization of line of magnetite recovery from wet tailings by creating second medium intensity magnetic field (case study: Processing plant of Gol-e-Gohar Hematite). *International Journal of Engineering, TRANSACTIONS B: Applications*, 35(8), 1608-1618. doi: 10.5829/IJE.2022.35.08B.17

Irannejad, M., Ejtemaei, M., & Gharabaghi, M. (2011). The effect of reagents on selective flotation of smithsonite-calcite-quartz. *Minerals Engineering*, 22(13), 1402-1408. https://doi.org/10.1016/j.mineng.2009.01.012

Karam Soltani, K. (1999). Determining the extraction and mineralization strategy of the Angouran lead and zinc mine, Master's thesis, Faculty of Engineering, University of Tehran, 1999. (in Persian)

Karimpour, M. H., and Saadat S. (2006). Applied Economic geology. University of Ferdowsi Mashhad. (in Persian)

Kazemi, F., Bahrami, A., Ghorbani, Y., Danesh, A., Abdollahi, M., Falah, H., & Salehi, M. (2023). The interaction and synergic effect of particle size on flotation efficiency: A comparison study of recovery by size, and by liberation between lab and industrial scale data. *Rudarsko-geološko-naftni zbornik*, 38(1), 1-12. https://orcid.org/0000-0002-9564-1016

King, R.P. (2001). Modeling and simulation in mineral processing systems. Department of Metallurgical Engineering, University of Utah, USA. https://doi.org/10.1016/C2009-0-26303-3

Mahdavi Amin, M., Parsapour, Gh., & Forutan, A. (2019). Increasing the zinc recovery in the flotation circuit of the Bama plant using improvement in the reagent distribution regimen. *Journal of Mineral Resources Engineering*, 3(4), 93-106. doi:10.30479/JMRE.2019.1585

Maleki, H., Noparast, M., Chehreghani, S., Mirmohammadi, M. S., & Rezaei, A. (2023). Optimization of flotation of the Qaleh Zari mine oxidized copper ore sample by the sequential sulfidation approach using the response surface method technique. *Rudarsko-geološko-naftni zbornik*, 38(1), 59-68. https://doi.org/10.17794/rgn.2023.1.6

Mehdilo, A., Irannajad, M., & Zarei, H. (2013). Flotation of zinc oxide ore using cationic and cationic-anionic mixed collectors. *Physicochemical Problems of Mineral Processing*, 49(1), 145-156. doi:10.5277/ppmp130114

Mehrabani, J., Noaparast, M., Mousavi, S. M., Dehghan, R., & Ghorbani, A. (2010). Process optimization and modelling of sphalerite flotation from a low-grade Zn-Pb ore using response surface methodology. *Separation and Purification Technology*, 72(3), 242-249. https://doi.org/10.1016/j.seppur.2010.02.005

Moradi, S. (2001). Investigation of zinc metal recovery from 0-2 mm line tailings of Angouran flotation plant using hydrometallurgical method. Master's thesis, Tarbiat Modares University. (in Persian)

Moradi, S. (2005). Zn, University of Science and Technology Publications, Second edition, 666 pages. (in Persian)

Moradkhani, M., Hajisoleymani, B., & Noaparast, M. (2010). The effect of C.A.A.A. (Armac C) collector concentration on the flotation of zinc non-sulfide ore in the presence of kax collector, Pb Zn 2010 - Lead-Zinc 2010 Symposium, Held in Conjunction with COM 2010, January, 1037-1045.

Seke, M.D. (2005). Optimisation of the selective flotation of galena and sphalerite at Rosh Pinah mine. University of Pretoria. http://hdl.handle.net/2263/24718

SAŽETAK

Koncentriranje uzorka olova i cinka iz rudnoga ležišta Nignan

Cilj je ovoga istraživanja flotacijom povećati udio cinka na više od 40 % iz olovne i cinkove rude iz područja Noahang (Chah-Ahan) ležišta Nignan. Eksperimenti su provedeni na uzorku s prosječnim udjelom od 3 % cinka i 0,05 % olova. Glavni minerali cinka u ovome uzorku bili su karbonati sfalerit i smitsonit, a galenit je rijetko uočen. Rezultati mineraloških istraživanja na poliranim tankim izbruscima pokazali su da je mogući stupanj raščina cinkovih ruda 90 – 95 % u frakciji veličine –106+75 μm. Istraženi su različiti parametri poput veličine, postotka čvrste mase, vrste i doziranja kolektora te je pod optimalnim uvjetima dobiven koncentrat s udjelom od 5 % cinka i iskorištenjem od 70,4 %. Također, provedeni su kinetički eksperimenti kako bi se postiglo najveće iskorištenje cinka u grubljoj fazi, koje je dosegnulo 58,6 %. Rezultati su pokazali da su najbolji stupanj i iskorištenje cinka postignuti kada je uzorak drobljen mokrim štapnim mlinom 8 minuta kako bi se postigao željeni stupanj raščina. Flotacijom je postignuta konačna kvaliteta koncentrata od 42,19 % i iskorištenje od 40,08 % za ispitivani koncentrat cinka.

Ključne riječi:
mineralno područje Noahang, flotacija, stupanj raščina, kvaliteta koncentrata, iskorištenje

Author's contribution

Maryam Abedi Moghadam (Master's degree) gathered samples, characterized the samples, and contributed to the crushing, grinding, separation and flotation processes and described the characterization and evaluation of the final products. **Marzieh Hosseini Nasab** (Associate Professor) also contributed to the crushing, grinding, separation and flotation processes. Supervision, validation, visualization, writing – original draft and writing – review & editing were her other responsibilities for this research. **Mohammad Noaparast** (Professor of Mineral Processing) evaluated the results, reviewed the draft manuscript, and provided technical suggestions.
All authors have read and agreed to the published version of the manuscript.

RGNZ/MGPB

Integrating ANN Prediction with Honeybee Optimisation for Flyrock Minimisation in Open-Pit Mining

Rudarsko-geološko-naftni zbornik
(The Mining-Geology-Petroleum Engineering Bulletin)
DOI: 10.17794/rgn.2025.5.11

Original scientific paper

Mojtaba Rezakhah[1], Erfan Nemati[1], Amir Batarbiat[1], Manoj Khandelwal[2]*
[1] *Department of Mining Engineering, Faculty of Engineering, Tarbiat Modares University, Tehran, Iran.*
[2] *Institute of Innovation, Science and Sustainability, Federation University Australia, Ballarat, VIC.*

Abstract
Flyrock is an undesirable phenomenon resulting from blasting in open-pit mines, posing significant risks to both environmental and human safety. Given these risks, a comprehensive study of flyrock is essential to mitigate its adverse effects. This study presents a novel hybrid intelligent model designed to predict and minimize flyrock distance by integrating an Artificial Neural Network (ANN) with a Honeybee Optimization Algorithm. Utilizing a dataset of 334 blast records collected from the Sungun copper mine, various ANN models were developed and evaluated. After assessing multiple models through a formal scoring system, the most effective one was selected for optimization. The chosen ANN model demonstrated strong predictive performance, achieving coefficients of determination (R^2) of 0.8930 and 0.8874, as well as root mean square error (RMSE) values of 0.2486 and 0.2512 for the training and testing phases, respectively, outperforming conventional empirical models. To further refine the blast pattern for safety, the Honeybee Optimization Algorithm was employed to minimize the predicted flyrock distance. The optimal flyrock distance was determined to be 7.25 meters, reflecting a 27.5% reduction compared to the lowest observed value in the collected data. This demonstrates the superiority of the proposed hybrid approach in enhancing blasting safety and efficiency.

Keywords:
Flyrock prediction, Optimisation algorithm, Blasting pattern, Honeybee algorithm, Metaheuristic algorithms

1. Introduction

Optimising mining operations from blast pattern design to fragmentation prediction and equipment performance enhancement is crucial for increasing productivity, reducing operational costs, and minimising environmental impacts. Recent research demonstrates that integrating mathematical modelling with artificial intelligence (AI) techniques, such as neural networks and metaheuristic algorithms, significantly improves the accuracy and effectiveness of mining process predictions and control strategies (**Khajevand et al., 2025; Mirzehi Kalateh Kazemi et al., 2023; Mirzehi et al., 2023; Monjezi et al., 2007; Moreno et al., 2015; Rezakhah & Moreno, 2019**).

Blasting is a fundamental operation in mining, critical for rock fragmentation and material handling. However, only about 15–20% of the explosive energy contributes to effective fragmentation and displacement. The remaining energy is often wasted due to various factors, leading to undesirable outcomes such as flyrock (Raina, 2023). Flyrock presents serious safety hazards, can damage equipment, escalate operational costs, and ultimately lower overall productivity. Its occurrence is influenced by both uncontrollable factors (e.g. rock strength) and controllable factors (e.g. explosive energy, blast design). A mismatch between these variables can result in hazardous flyrock incidents.

Several studies have sought to understand and predict flyrock behaviour. For example, **Adhikari et al. (1999)** investigated the influence of blast design parameters on flyrock and offered strategies for mitigating its risks. Artificial neural networks (ANNs) have been shown to effectively forecast flyrock distance and fragmentation (**Monjezi et al., 2010**), while a Mamdani fuzzy inference system demonstrated superiority over traditional statistical models in predicting flyrock distances (**Rezaei et al., 2011**).

Recent studies show that combining optimization techniques with machine-learning algorithms significantly improves flyrock distance prediction accuracy. The ACWNNsR model, integrating ANN, fuzzy cognitive maps, and Z-number theory, demonstrated strong predictive capability (**Hosseini et al., 2022**). Embedding particle swarm optimization and jellyfish search into ANN training highlighted charge weight, powder factor, and hole angle as key inputs (**Wang et al., 2023**). The

* Corresponding author: Manoj Khandelwal
e-mail address: m.khandelwal@federation.edu.au
Received: 15 May 2025. Accepted: 17 July 2025.
Available online: 21 October 2025

LSSVM-WOA hybrid ensured robust and stable forecasts (**Ding et al., 2023**). ANFIS models coupled with variable selection procedures identified burden as the most critical parameter (Hudaverdi, 2022). Among tree-based learners, AdaBoost delivered the best performance and singled out powder factor as the dominant influence (Yari, et al., 2023). The equilibrium-optimizer–extreme learning machine (EO-ELM) approach also pinpointed the most sensitive variables (Bhatawdekar, et al., 2023). Finally, the Harris Hawks optimization–enhanced multilayer perceptron (HHO-MLP) achieved the highest overall modeling accuracy (Murlidhar, et al., 2021).

Similarly, an empirical equation for flyrock prediction was proposed based on dimensional analysis and validated using Monte Carlo simulations, confirming its reliability in modelling blast parameter variability (**Ghasemi et al., 2012**). More recent research has also shown that incorporating geomechanical factors, such as elastic wave velocity, into blast fragmentation models can enhance prediction accuracy and support better blast designs in open-pit mining (**Tajik et al., 2023**).

In related work, a hybrid approach was applied, combining the artificial bee colony (ABC) algorithm with ANN to optimise the safety factor in retaining walls, demonstrating the robustness and precision of such hybrid methods (**Noroozi Ghaleini, et al., 2019**). Building on this foundation, the present study employs neural networks to predict flyrock based on various blast pattern configurations. A scoring system was developed to assess multiple models and identify the best-performing one. Subsequently, the bee colony optimisation algorithm was applied to determine the optimal blast pattern parameters to effectively reduce flyrock and improve blasting efficiency. This research, therefore, aims to optimise and control flyrock using neural networks and metaheuristic algorithms and compares these AI-driven models with conventional flyrock prediction approaches to evaluate their practical viability and performance.

Flyrock is the leading safety risk in open-pit blasting, yet most AI models merely predict throw distance without offering design corrections and rely on small, unvalidated datasets. This study fills that gap with the first closed-loop ANN + Honey-Bee Optimizer: a high-accuracy neural network models flyrock behaviour, while the optimizer adjusts charge, spacing and angle until the predicted distance meets legal limits. Validation on 334 real blasts from the Sungun copper mine confirms both higher accuracy and direct, actionable control, delivering a practical tool for reducing flyrock in day-to-day operations.



Figure 1. Drilling and Blasting Area in Sungun Copper Mine

2. Field Investigation and Data Collection

To develop a predictive and optimization model for blast parameters aimed at minimizing flyrock, a total of 334 new datasets were collected from the Sungun copper mine, located in northwest Iran, approximately 35 km from Varzaghan in East Azerbaijan province. This mine is characterised by a hydrothermal ore deposit with mineralisation associated with the Cenozoic Sahand-Bazman orogenic belt, hosted within altered quartz-monzonite rocks. The primary ore minerals include chalcopyrite, pyrite, chalcocite, cuprite, and malachite, with copper being the principal extracted resource. Additionally, the deposit contains economically significant amounts of gold, silver, and molybdenite. **Figure 1** illustrates the operational area of the Sungun copper mine.

Each dataset comprises key blasting parameters, including stemming, burden and spacing, blast hole diameter, blast hole length, sub-drilling length, specific charge, and flyrock distance. A descriptive statistical analysis was conducted on the collected datasets, with the results summarised in **Table 1**.

Table 1. Statistical Characteristics of the Data Used in the Network

Parameter	Minimum	Maximum	Mean	Standard Deviation	Data Type
Blast Hole Diameter (in)	3	6	5	0.79	Input
Blast Hole Length (m)	3	12.5	10.81	6.98	Input
Spacing (m)	2	6.5	4.76	0.87	Input
Burden (m)	2	5	3.96	0.68	Input
Stemming Length (m)	1.8	4.5	3.78	0.67	Input
Specific Charge (kg/m³)	0.1	1	0.42	0.12	Input
Sub-drilling Depth (m)	0	5.4	0.27	0.55	Input
Flyrock Distance (m)	10	100	67	21.5	Output

The selected input variables include both fundamental blast design parameters and a derived parameter known as Specific Charge. Although Specific Charge is mathematically related to other inputs, its inclusion as a distinct variable is justified because it represents the overall concentration of explosive energy a critical factor in flyrock generation that geometric parameters alone do not fully capture. It is important to note that while uncontrollable geological factors can also contribute to flyrock, this study focuses on optimizing the controllable design parameters to minimize risk. The minimum recorded flyrock distance of 10 meters, although relatively short, was classified as a flyrock event according to site-specific safety protocols, as it landed beyond the designated safety perimeter, thereby necessitating its inclusion in the dataset.

3. Artificial Neural Network

Artificial neural networks (ANNs) are designed to mimic the structure and functionality of the human brain. Essentially, an ANN consists of interconnected neurons arranged in multiple layers, where each neuron acts as a simple processing unit that transmits information to others within the network. A large collection of these neurons forms a neural network. One of the most widely used learning algorithms in perceptron neural networks is the feedforward learning algorithm (**Laguna & Martí, 2002**), which operates based on the error correction learning law, a generalisation of the least-means algorithm.

Feedforward neural networks consist of three main layers: an input layer, a hidden (middle) layer, and an output layer. While the number of hidden layers is not restricted, a single hidden layer is often sufficient for solving complex nonlinear problems. The feedforward learning process is divided into two stages: the feedforward stage and the backward (error correction) stage. In the feedforward stage, inputs are passed sequentially through each layer, ultimately producing an output as the responses of the network. During the forward phase, synaptic weights are initialised. In the backward phase, these weights are adjusted based on error correction rules. The difference between the predicted response of the network and the desired (expected) response, known as the error signal, is propagated backward through the network, refining the synaptic weights to improve prediction accuracy.

To evaluate the network's performance, the coefficient of determination (R^2) and root mean square error (RMSE) were used to measure the correlation between predicted and actual flyrocks. In this study, the neural network was implemented using the Lüneburg-Marquette learning algorithm, one of the most widely used optimisation techniques in ANN training. Based on prior research, the network structure was selected with three layers, an input layer with 7 input variables, a hidden layer and an output layer with a single output. A single hidden layer is sufficient to approximate any nonlinear function. Various studies have explored optimal methods for determining the number of neurons in the hidden layer, offering mathematical approaches to avoid the trial-and-error method. **Equations 1 to 6** outline the established methodologies for selecting the appropriate number of hidden neurons (**Hecht-Nielsen, 1987; Hornik et al., 1989; Masters, 1993; Paola, 1994; Ripley, 1993; Wang, 1994**).

$$H \leq 2N_i + 1 \tag{1}$$

$$H = \frac{N_i + N_o}{2} \tag{2}$$

$$H = \frac{2 + N_0 \times N_i + 0.5N_0 \times \left(N_0^2 + N_i\right) - 3}{N_i + N_0} \tag{3}$$

$$H = \frac{2N_i}{3} \tag{4}$$

$$H = \sqrt{N_i \times N_0} \tag{5}$$

$$H = 2N_i \tag{6}$$

In this study, the neural network was implemented using the Levenberg-Marquardt learning algorithm. This algorithm was chosen due to its high efficiency and fast convergence rates for training small to medium-sized feedforward neural networks, making it well-suited for the dataset size in this research (Ampazis & Perantonis, 2000).

In this study, N_i represents the number of inputs, while N_o denotes the number of outputs in the model. Based on recommended parameter values, the Levenberg-Marquardt learning algorithm was implemented using a neural network with a hidden layer containing 2 to 15 neurons. To determine the most effective model, the coefficient of determination (R^2) and root mean square error (RMSE) were evaluated for both the training and testing phases. A comparative analysis was conducted by assigning scores to each model configuration. The scoring process involved awarding the highest score to models with the largest R^2 values, while lower scores were assigned as R^2 decreased. Conversely, models with the lowest RMSE values received the highest scores, with scores decreasing as RMSE increased. At the end of the evaluation, the scores for each model configuration were summed to determine the overall performance ranking (Kaastra & Boyd, 1996).

The scoring process involved four criteria: R^2 for training, RMSE for training, R^2 for testing, and RMSE for testing. For each criterion, the 14 models were ranked from best (rank 14) to worst (rank 1). For R^2, a higher value received a higher rank, while for RMSE, a lower value received a higher rank. The final score for each

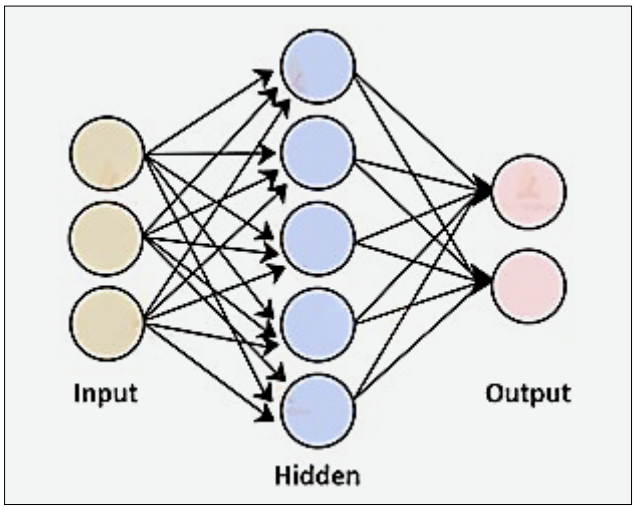


Figure 2. Schematic of a Basic Artificial Neural Network (ANN) with Input, Hidden, and Output Layers

model was the sum of its four ranks, allowing for a balanced assessment of both accuracy and generalisation ability.

Figure 2 presents a schematic diagram of how the neural network works.

4. Honeybee Optimisation Algorithm

The Honeybee Optimisation Algorithm is inspired by the collective behaviour of bee colonies, where individual bees, though simple on their own, work together to form a highly organised and efficient system for discovering and exploiting nectar resources. Within a colony, bees are divided into three main groups, each assigned a specific task in foraging.

The first group consists of scout bees, responsible for exploring the environment and new food resources. Once a scout bee finds a suitable resource, it returns to the hive and communicates its location through a movement known as the circular dance. The second group, the worker bees, focuses on exploiting these discovered food resources, ensuring efficient nectar collection. The third group, the onlooker bees, remains in the hive, observing the circular dance of the scout bees. Based on the quality of the reported resources, onlooker bees select the most promising sites for further extraction. The Honeybee Optimisation Algorithm was first introduced by Karaboga in 2005 (**Karaboga, 2005**). Since then, extensive research has been conducted on bee behaviour in nature, leading to the development of optimisation algorithms inspired by their social structure. While this algorithm has been applied in various fields, one of its notable implementations in mining is the prediction and optimisation of the backbreak caused by blasting operations (**Ebrahimi et al., 2016; Kanellopoulos & Wilkinson, 1997; Rezaei et al., 2011; Sayadi et al., 2013; Zorlu et al., 2008)**. The algorithm follows a structured process consisting of four key stages. As illustrated in **Figure 3**, the workflow of the Bee Algorithm is structured into

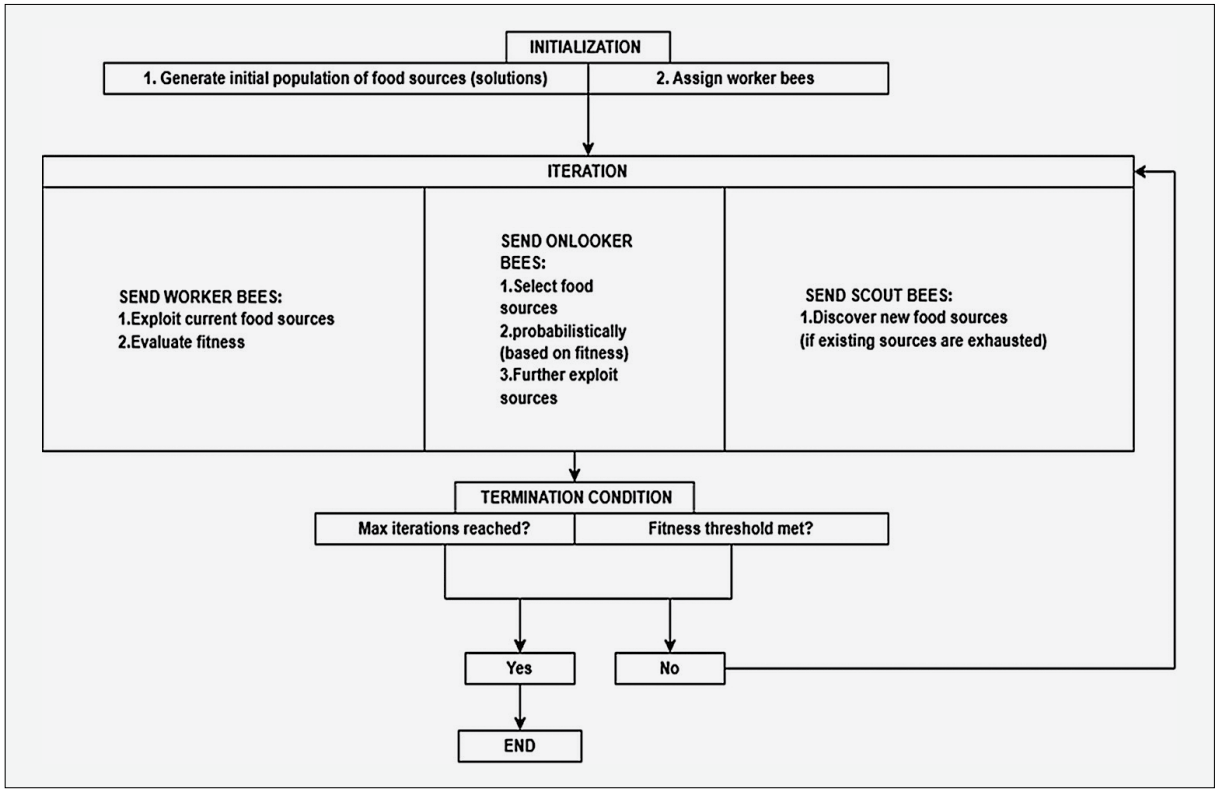


Figure 3. Flowchart of the Bee Algorithm illustrating its three primary phases: Initialisation, Iteration, and Termination Condition evaluation.

three core phases: Initialization, Iteration, and Termination Condition Evaluation, ensuring a systematic optimization process. The main steps of the Bee Algorithm are outlined in **Karaboga & Basturk (2007)**:

Step 1: In the initial phase of the algorithm, the bee population is equally divided into worker bees and non-worker bees. Each food source is assigned a single worker bee, which means the number of worker bees corresponds directly to the number of food sources around the hive. Consequently, within the defined solution space, the initial solution is generated based on the number of food sources. Once these initial solutions are established, their respective values are compared using problem-specific evaluation functions.

Step 2: In this step, for each of the answers to the problem, a new answer is created using the relationship:

$$v_{i.j} = x_{i.j} + \varphi_{i.j}(x_{i.j} - x_{k.j}) \tag{7}$$

$$i \in \{1.2...BN\}$$

$$j \in \{1.2...D\}$$

$$k \in \{1.2...BN\} \wedge k \neq i$$

$$\varphi \in [-1.1]$$

Where x_{ij} is the j^{th} parameter of the i^{th} solution of the problem, v_{ij} is the j^{th} parameter of the new solution, i is a number from one to the number of solutions to the problem, φ is a random number in the range of -1 to 1, k is a random number from one to the number of solutions to the problem, BN is the number of initial solutions to the problem, and D is the number of optimization parameters.

After creating a new solution, if the value of this solution is greater than the value of the previous solution, it will be replaced; otherwise, this solution will be forgotten.

Step 3: In this step, the probability of receiving a bee from each source is calculated using the following formula:

$$p_i = \frac{fit_i}{\sum_{n=1}^{SN} fit_n} \tag{8}$$

Where fit_i is the fitness of source i (varies depending on the type and size of the problem and must be determined by the user) and p_i is the probability of selecting source i by observer bees. According to the fitness, a number of bees are assigned to each source. After calculating the value of each source using **Equation 7**, a new answer is created for the selected answers. If this answer has a higher value than the previous answer, this answer replaces the previous answer, and otherwise, a penalty is imposed. The purpose of the penalty is to create a counter for the number of non-improvement answers, and if the answer does not improve, one unit is added to its value.

Step 4: In this step, if the counter of the number of non-improvement answers reaches a predetermined limit (C_{max}), this answer will be replaced with a random answer. Also, in this step, the conditions for the end of the iterations are checked. If the termination conditions of the algorithm are met, the iterations will end, otherwise, it will return to step two.

The implementation of the Honeybee algorithm in this study involved setting several key parameters to ensure robust optimisation. The algorithm was run with a population size of 50 bees for 100 iterations. The fitness function was defined as the inverse of the flyrock distance predicted by the optimised ANN model, aiming to minimise this output. The termination condition was set to the maximum number of iterations. The search space for each blast parameter was constrained within the observed minimum and maximum values from the collected dataset presented in **Table 1**.

5. Conventional Predictor

Conventional empirical methods are used as a basis for predicting flyrock distance in surface blasting operations. These models are developed based on field data and simplified mathematical relationships, each considering specific parameters. Some of the most important conventional models are:

5.1. Lundborg et al. Equation (1981)

This model provides the following relationship based on the diameter of the blast hole (*d*) and specific charge (*q*):

$$l_{max} = 143d\left(q - 0.2\right) \tag{9}$$

Where:

l_{max} = Maximum throw (m),
d = Hole diameter (inch),
q = Specific charge (kg/m^3).

6. Results and Discussion

6.1 Prediction by ANN

The artificial neural network (ANN) model demonstrated robust predictive performance for flyrock distance. A total of 14 neural network configurations were evaluated, varying the number of neurons in the hidden layer (2 to 15). The best-performing model (Model 7) achieved a coefficient of determination (R^2) of 0.8930 and 0.8874 for the training and testing phases, respectively, with root mean square error (RMSE) values of 0.2486 and 0.2512. These results highlight the model's ability to generalise well to unseen data, indicating strong nonlinear approximation capabilities. The selected ANN structure consisted of 7 input parameters (blast hole diameter, length, spacing, burden, stemming, specific

Table 2. Predicted Values for Flyrock

No. Model	No. Neuron	Train		Test		Train		Test		Total Score
		R^2	RMSE	R^2	RMSE	rank R^2	rank RMSE	rank R^2	rank RMSE	
1	2	0.8082	0.3399	0.7726	0.3391	1	1	2	4	8
2	3	0.8354	0.3035	0.7957	0.3302	3	3	5	5	16
3	4	0.8299	0.3058	0.8154	0.3122	2	2	6	6	16
4	5	0.8593	0.2784	0.8612	0.2532	4	4	8	12	28
5	6	0.8761	0.2676	0.8742	0.2638	10	10	10	10	40
6	7	0.8742	0.2689	0.8705	0.2728	9	9	9	8	26
7	8	0.8930	0.2486	0.8874	0.2512	14	13	13	14	54
8	9	0.8780	0.2655	0.8742	0.2668	11	11	10	9	41
9	10	0.8668	0.2782	0.8949	0.2530	6	5	14	13	38
10	11	0.8686	0.2726	0.8761	0.2536	7	8	12	11	38
11	12	0.8892	0.2486	0.7832	0.3633	13	13	4	3	33
12	13	0.8686	0.2729	0.8354	0.3068	7	7	7	7	28
13	14	0.8780	0.2648	0.7140	0.4025	11	12	1	1	25
14	15	0.8630	0.2757	0.7762	0.3755	5	6	3	2	16

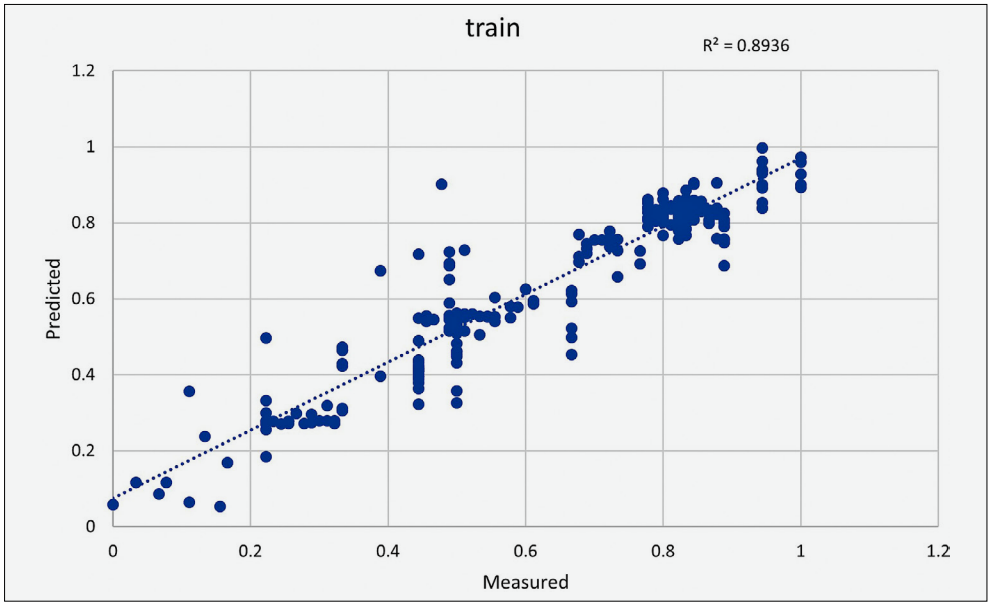


Figure 4. Predicted values of Flyrocks for training Model No. 7

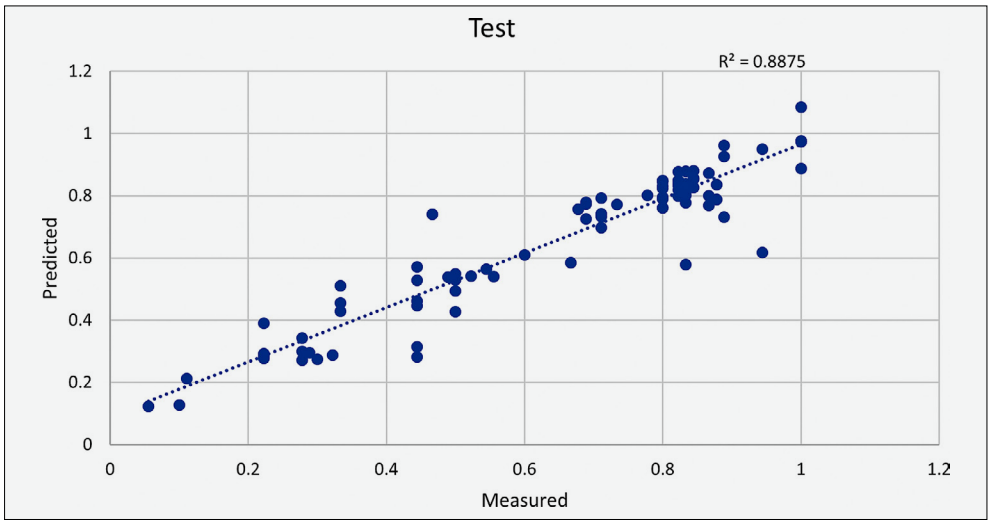


Figure 5. Predicted values of Flyrocks for testing Model No. 7

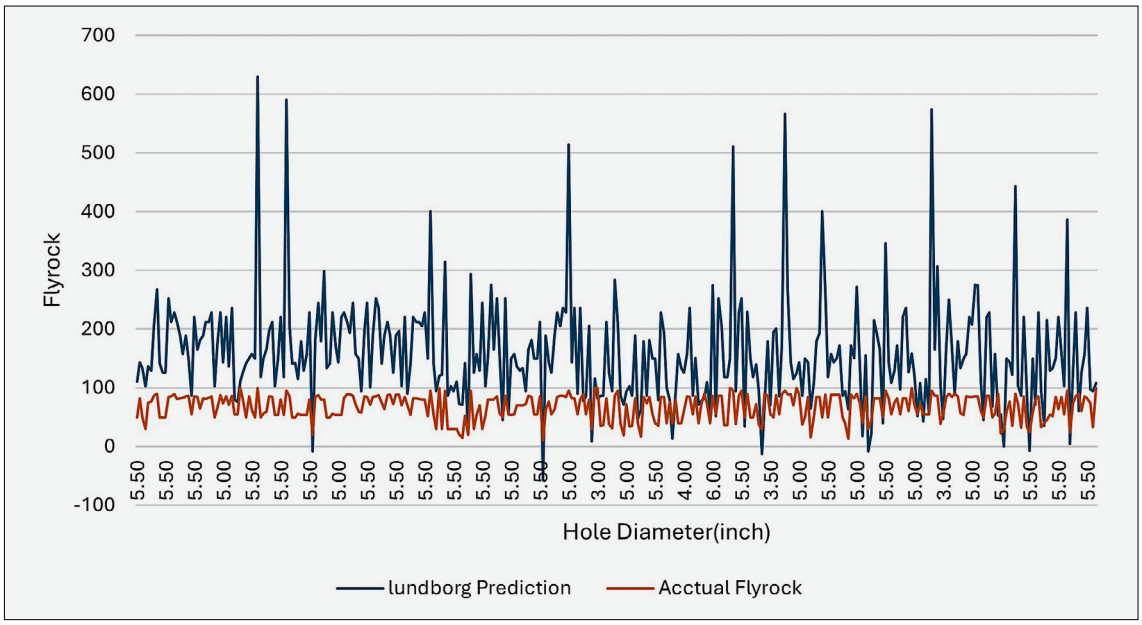


Figure 6. Comparison graph between the Lundborg method and actual flyrock

charge, and sub-drilling depth), a single hidden layer with 8 neurons, and one output (flyrock distance). Sensitivity analysis revealed that burden (B) and stemming length were the most influential parameters, contributing to 70.8% of the variance in flyrock predictions. **Table 2** shows the results of this neural network analysis.

6.2. Prediction by Conventional Predictor

The evaluation of traditional flyrock prediction methods, by **Lundborg (1981)**, revealed significant limitations in their accuracy. For the Lundborg model, the root mean square error (RMSE) was calculated as 121.1 meters, with a coefficient of determination (R^2) of 0.52. This indicates that the model explains only 52% of the variance in flyrock distances and suffers from oversimplification, as it ignores critical parameters like rock strength and explosive energy. For example, in sample predictions, the model estimated a flyrock distance of 110.1 meters for an actual value of 50 meters, highlighting its unreliability. **Figure 6** presents a comparative analysis of the Lundborg method versus actual flyrock measurements.

6.3. Flyrock Minimization using the Honeybee Algorithm

As previously mentioned, the search process continues until the minimum flyrock value is identified. Multiple iterations of the Honeybee algorithm were executed using different population sizes of bees. **Figure 7** shows the execution of the algorithm in minimizing flyrock distance.

Based on the results, the minimized flyrock distance was determined to be 7.25 meters. As indicated in **Table 1**, the initial minimum flyrock distance was approxi-

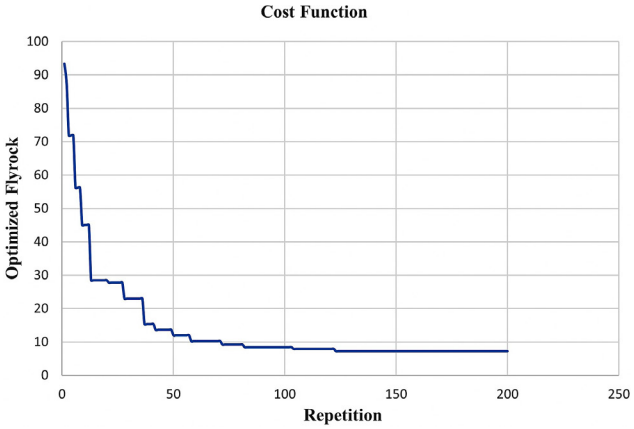


Figure 7. Minimization of the amount of Flyrocks throw in meters

mately 10 meters. By implementing the Honeybee optimisation algorithm, this value was reduced by 27.5%, demonstrating a significant improvement. Additionally, optimal values were obtained for key blasting parameters, including blast hole diameter and length, sub-drilling depth, burden, spacing, and stemming, as presented in **Table 3**.

6.4. Comparative Analysis

This paper compares flyrock prediction in mining blasting operations using two intelligent methods: Artificial Neural Networks (ANN) and Honeybee Optimization Algorithm, with traditional models. The ANN model demonstrated better performance compared to conventional models. Specifically, the ANN model achieved R^2 values of 0.8930 for training and 0.8874 for testing, indicating high predictive accuracy and effective simulation of flyrock behaviour. In contrast, the traditional

Table 3. Blasting pattern optimisation values

Parameter	Optimal Value
Diameter(in)	4
Holes length(m)	6
Sub-drilling (m)	0
Burden (m)	3
Spacing (m)	3.5
Stemming (m)	2

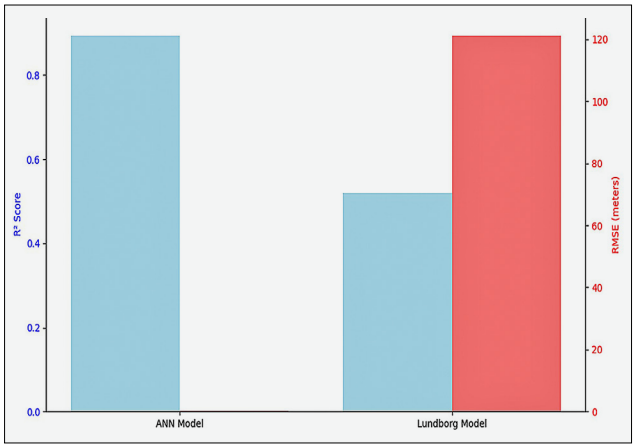


Figure 8. Comparative Analysis of Flyrock Prediction Models

Lundborg model, based on simplified mathematical relationships, only explained 52% of the variance in flyrock distance and showed poor prediction performance.

Furthermore, a statistical t-test on the prediction errors confirmed that the lower RMSE of the ANN model compared to the Lundborg model is statistically significant ($p < 0.05$), validating its superior performance.

Moreover, this model overlooks important parameters such as rock strength and explosive energy, which can lead to inaccurate results. The Honeybee Optimization Algorithm was then applied to optimize blast parameters and reduce flyrock. The algorithm optimized parameters like blast hole diameter, length, sub-drilling depth, spacing, and stemming length, reducing the flyrock distance from 10 meters to 7.25 meters, which represents a 27.5% improvement. This demonstrates that the Honeybee algorithm, using modern optimization methods, can significantly reduce flyrock distance. Sensitivity analysis in the study revealed that the burden parameter has the greatest impact on reducing flyrock, while stemming and specific charge have the most influence on increasing it.

Compared to traditional models, which rely on simplified empirical relationships, intelligent methods like ANN and Honeybee can provide more accurate predictions and more effective optimization of the blasting process in mines. These results show that intelligent techniques can significantly help in controlling flyrock and improving safety and productivity in mining operations.

7. Evaluating the Influence of Blasting Parameters on Flyrock

Several advanced analytical methods, namely, Pearson correlation analysis, multiple regression modelling, random forest regression, and permutation importance analysis, were applied to evaluate the impact of various blasting parameters on flyrock. The key findings from these analyses are as follows:

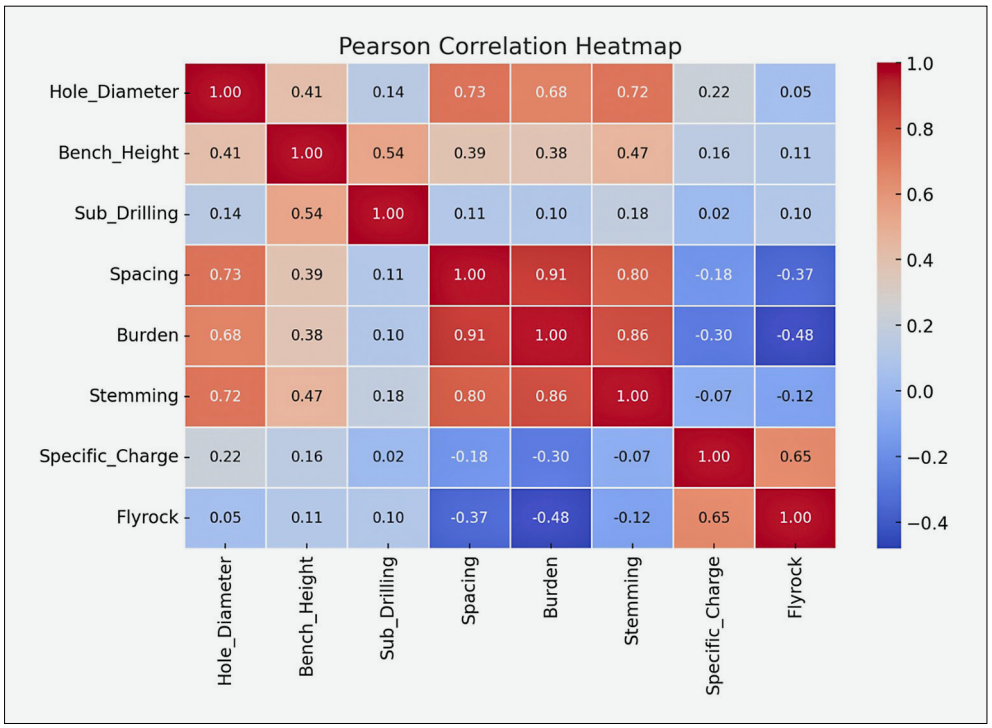


Figure 9. Pearson Correlation Heatmap

7.1. Analysis with Pearson correlation

Figure 9 shows a heatmap illustrating the Pearson correlation between input parameters and flyrock distance. Among these parameters, burden (B) exhibits the most significant negative correlation with flyrock, indicating that an increase in burden leads to a considerable reduction in flyrock distance. Conversely, stemming length and specific charge show the strongest positive correlation, suggesting that an increase in these parameters results in a greater flyrock distance.

7.2. Multiple Regression Model

To quantify the contribution of each parameter, a multiple regression model was established (see **Figure 10**). The model achieved an R^2 value of 0.708, indicating that approximately 70.8% of the variations in flyrock can be explained by the selected variables. Among these parameters, burden exhibited the strongest negative correlation with flyrock, meaning an increase in burden leads to reduced flyrock distance. Conversely, stemming length and specific charge demonstrated a significant positive correlation, indicating that higher values of these parameters contribute to increased flyrock distance.

7.3. Feature Importance Analysis (Random Forest Model)

To validate these results, a feature importance analysis was conducted using the Random Forest model (see **Figure 11**). The analysis confirmed that burden, stemming, and specific charge are indeed the most influential factors affecting flyrock behaviour. The results suggest that optimising Burden can significantly reduce excessive flyrock, while proper adjustments of stemming length and specific charge ensure a more controlled energy distribution.

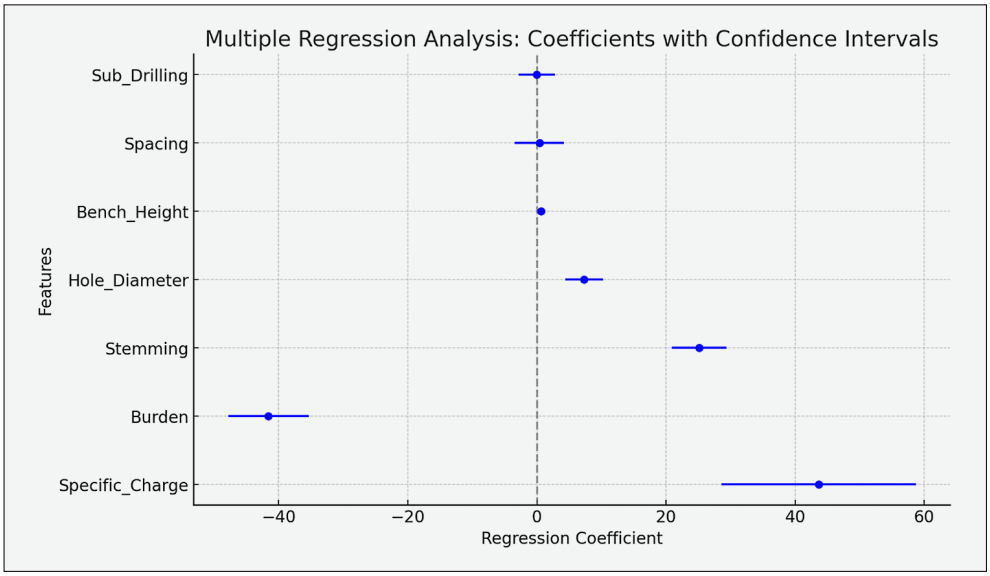


Figure 10. Multiple Regression Analysis: Coefficients with Confidence Intervals

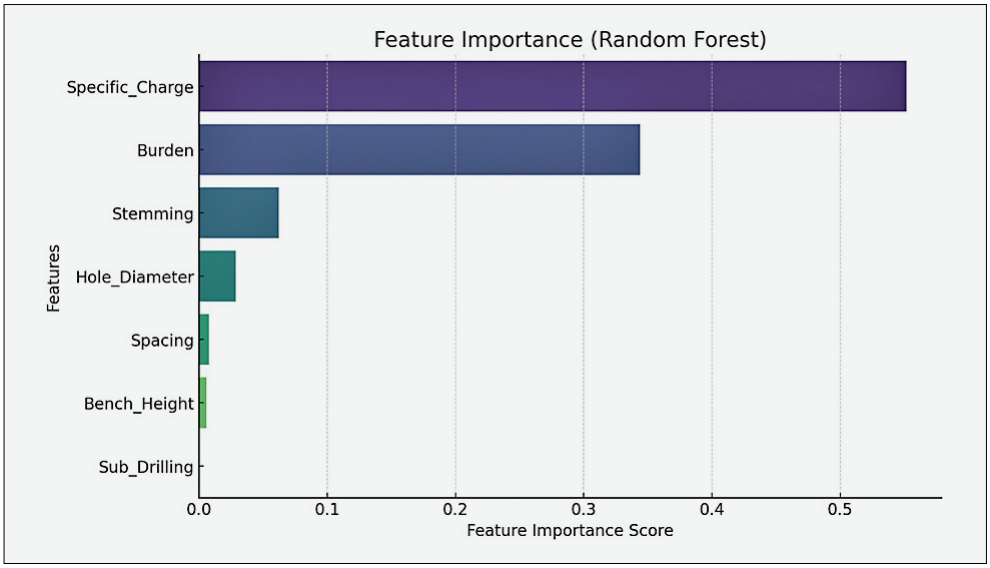


Figure 11. Feature Importance (Random Forest)

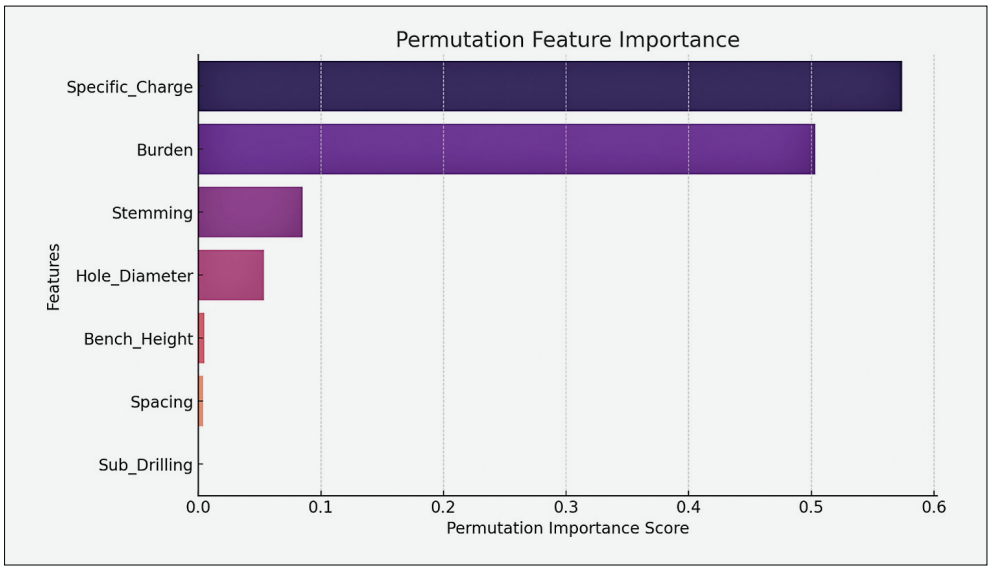


Figure 12. Permutation Feature Importance

Table 4. Consolidated Summary of Sensitivity Analysis Results

Feature	Pearson Correlation (Rank)	Regression Coeff. (Rank)	Random Forest Imp. (Rank)	Permutation Imp. (Rank)	Overall Influence
Specific Charge	1 (Positive)	1 (Positive)	1	1	Very High
Burden	2 (Negative)	2 (Negative)	2	2	Very High
Stemming	3 (Positive)	3 (Positive)	3	3	High
Hole Diameter	4	4	4	4	Medium
Spacing	5	5	5	6	Low
Bench Height	6	6	6	5	Low
Sub-drilling	7	7	7	7	Very Low

7.4. Permutation Importance Analysis

In order to improve the sensitivity analysis, a permutation importance method was used (see **Figure 12**). Such a method systematically changes each variable with its value to see its significance on flyrock prediction. The findings are consistent with burden as the most impactful variable in reducing flyrock, with stemming and specific charge causing the distance of flyrock, respectively.

The results of the various sensitivity analyses consistently show that burden, stemming, and specific charge are the three most crucial parameters influencing flyrock. However, although burden as a major factor helps fight the rock throw, stemming and specific charge increase flyrock and therefore require key optimisation.

These results have been statistically confirmed using a multiple regression model and correlation analysis, while Random Forest and Permutation Importance validated this systematic and well-established finding as machine-learning-based. The congruence of these methods further validates the results and allows for confirmation that changes to burden, stemming, and specific charge in the blast design can greatly enhance flyrock control.

To consolidate the findings from the different analytical techniques, **Table 4** provides a summary of the parameter importance rankings. The consistency across all four methods strongly validates the identification of burden, stemming, and specific charge as the most critical parameters governing flyrock.

8. Conclusions

This study successfully demonstrated the development and application of a hybrid intelligent system, combining an Artificial Neural Network (ANN) with a Honeybee Optimisation Algorithm, for the prediction and minimisation of flyrock in surface mining. The key novelty of this research lies in its integrated approach, moving beyond simple prediction to provide optimised, actionable blast design parameters for enhanced safety.

The developed ANN model, selected through a systematic scoring method, showed excellent predictive capabilities with high R^2 values (0.8930 for training, 0.8874 for testing) and low RMSE values, significantly outperforming traditional empirical methods. A comprehensive sensitivity analysis consistently identified burden, stemming, and specific charge as the most influential parameters affecting flyrock distance. The practical implication of this work is significant. By applying the Honeybee algorithm to the validated ANN model, blast

parameters were optimised to achieve a minimum flyrock distance of 7.25 meters, representing a 27.5% reduction from the safest observed blasts in the field data. This result confirms that data-driven optimisation can lead to considerable improvements in operational safety and efficiency.

For future research, it is recommended to apply this hybrid model to other mine sites with different geological conditions to test its robustness. Furthermore, incorporating geomechanical variables (e.g. rock mass rating, joint properties) as inputs could further enhance the model's accuracy. Finally, the performance of the Honeybee algorithm could be benchmarked against other state-of-the-art metaheuristic algorithms to explore further potential for optimisation.

9. References

Adhikari, G. R. (1999). Studies on Flyrock at Limestone Quarries. *Rock Mechanics and Rock Engineering, 32*, 291-301. doi:10.1007/s006030050049

Ampazis, N., & Perantonis, S. (2000). Levenberg-Marquardt algorithm with adaptive momentum for the efficient training of feedforward networks. *Proceedings of the IEEE-INNS-ENNS International Joint Conference on Neural Networks. IJCNN 2000. Neural Computing: New Challenges and Perspectives for the New Millennium, 1*, 126-131. doi:10.1109/IJCNN.2000.857825

Bhatawdekar, R., Kumar, R., Sabri Sabri, M., Roy, B., Mohamad, E., Kumar, D., & Kwon, S. (2023). Estimating Flyrock Distance Induced Due to Mine Blasting by Extreme Learning Machine Coupled with an Equilibrium Optimizer. *Sustainability, 15*, 3265. doi:10.3390/su15043265

Ding, X., Jamei, M., Hasanipanah, M., Abdullah, R., & Le, B. (2023). Optimized Data-Driven Models for Prediction of Flyrock due to Blasting in Surface Mines. *Sustainability, 15*, 8424. doi:10.3390/su15108424

Ebrahimi, E., Monjezi, M., Khalesi, M. R., & Armaghani, D. J. (2016). Prediction and optimization of back-break and rock fragmentation using an artificial neural network and a bee colony algorithm. *Bulletin of Engineering Geology and the Environment, 75*, 27-36. doi:10.1007/s10064-015-0720-2

Ghasemi, E., Sari, M., & Ataei, M. (2012). Development of an empirical model for predicting the effects of controllable blasting parameters on flyrock distance in surface mines. *International Journal of Rock Mechanics and Mining Sciences, 52*, 163-170. doi:10.1016/j.ijrmms.2012.03.011

Hecht-Nielsen, R. (1987). Kolmogorov's mapping neural network existence theorem. *In Proceedings of the international conference on Neural Networks* (pp. 11-14). New York: IEEE.

Hornik, K., Stinchcombe, M., & White, H. (1989). Multilayer feedforward networks are universal approximators. *Neural Networks, 2*(5), 359-366. doi:10.1016/0893-6080(89)90020-8

Hosseini, S., Poormirzaee, R., Hajihassani, M., & Kalatehjari, R. (2022). An ANN-Fuzzy Cognitive Map-Based Z-Number Theory to Predict Flyrock Induced by Blasting in Open-Pit Mines. *Rock Mechanics and Rock Engineering, 55*, 4373–4390. doi:10.1007/s00603-022-02866-z

Hudaverdi, T. (2022). Prediction of flyrock throw distance in quarries by variable selection procedures and ANFIS modelling technique. *Environmental Earth Sciences, 81*, 281. doi:10.1007/s12665-022-10408-7

Kaastra, I., & Boyd, M. (1996). Designing a neural network for forecasting financial and economic time series. *Neurocomputing, 10*(3), 215-236. doi:10.1016/0925-2312(95)00039-9

Kanellopoulos, I., & Wilkinson, G. G. (1997). Strategies and best practice for neural network image classification. *International Journal of Remote Sensing, 18*(4), 711-725. doi:10.1080/014311697218719

Karaboga, D. (2005). *An idea based on honey bee swarm for numerical optimization.*

Karaboga, D., & Basturk, B. (2007). A powerful and efficient algorithm for numerical function optimization: artificial bee colony (ABC) algorithm. *Journal of Global Optimization, 39*, 459–471. doi:10.1007/s10898-007-9149-x

Khajevand, S., Rezakhah, M., Monjezi, M., & Manríquez León, F. A. (2025, 5 1). Enhancing Transportation Fleet Efficiency in Open-Pit Mining via Simulation: a Case Study. *Journal of Mining and Environment, 16*(3), 997-1007. doi:10.22044/jme.2024.15094.2889

Laguna, M., & Martí, R. (2002). Neural network prediction in a system for optimizing simulations. *IIE Transactions, 34*, 273–282. doi:10.1023/A:1012485416856

Masters, T. (1993). *Practical neural network recipes in C++.* Morgan Kaufmann.

Mirzehi Kalateh Kazemi, M., Nabavi, Z., Rezakhah, M., & Masoudi, A. (2023, 12 1). Application of XGB-based metaheuristic techniques for prediction time-to-failure of mining machinery. *Systems and Soft Computing, 5*, 200061. doi:10.1016/j.sasc.2023.200061

Mirzehi, M., Rezakhah, M., Mousavi, A., & Nabavi, Z. (2023). New MIP model for short-term planning in open-pit mines considering loading machine performance: a case study in Iran. *International Journal of Mining and Mineral Engineering*, 341-364. doi:10.1504/IJMME.2023.137375

Monjezi, M., Bahrami, A., & Yazdian Varjani, A. (2010). Simultaneous prediction of fragmentation and flyrock in blasting operation using artificial neural networks. *International Journal of Rock Mechanics and Mining Sciences, 47*(3), 476-480. doi:10.1016/j.ijrmms.2009.09.008

Monjezi, M., Goshtasbi, K., Rezakhah, M., & Singh, T. N. (2007). Design of stable slopes for Songun copper mine. *Mining Technology, 116*(3), 146-152. doi:10.1179/174328607X228901

Moreno, E., Ferreira, F., Goycoolea, M., Espinoza, D., Newman, A., & Rezakhah, M. (2015). Linear programming approximations for modeling instant-mixing stockpiles. *Application of computers and operations research in the mineral industry-proceedings of the 37th international symposium, APCOM, 2009*, 582-587.

Murlidhar, B. R., Nguyen, H., Rostami, J., X. Bui, A. J., Ragam, P., & Mohamad, E. T. (2021). Prediction of flyrock distance

induced by mine blasting using a novel Harris Hawks optimization-based multi-layer perceptron neural network. *Journal of Rock Mechanics and Geotechnical Engineering, 13*(6), 1413-1427. doi:10.1016/j.jrmge.2021.08.005

Noroozi Ghaleini, E., Koopialipoor, M., Momenzadeh, M., Sarafraz, M. E., Mohamad, E. T., & Gordan, B. (2019). A combination of artificial bee colony and neural network for approximating the safety factor of retaining walls. *Engineering with Computers, 35*, 647-658. doi:10.1007/s00366-018-0625-3

Paola, J. (1994). *Neural network classification of multispectral imagery.* (Doctoral dissertation, MSc thesis, The University of Arizona, USA).

Raina, A. (2023). *Flyrock in Surface Mining: Origin, Prediction, and Control.* Boca Raton: CRC Press. doi: 10.1201/9781003327653

Rezaei, M., Monjezi, M., & Varjani, A. Y. (2011). Development of a fuzzy model to predict flyrock in surface mining. *Safety science, 2*, 298-305. doi:10.1016/j.ssci.2010.09.004

Rezakhah, M., & Moreno, E. (2019). Open pit mine scheduling model considering blending and stockpiling. In E. Topal (Ed.), *Proceedings of the 28th International Symposium on Mine Planning and Equipment Selection - MPES 2019* (pp. 75-82). Perth: Springer Cham. doi:10.1007/978-3-030-33954-8

Ripley, B. D. (1993). Statistical aspects of neural networks. *Natworks and Chaos-Statistical and Probabilistic Aspects*, 40-123.

Sayadi, A., Monjezi, M., Talebi, N., & Khandelwal, M. (2013). A comparative study on the application of various artificial neural networks to simultaneous prediction of rock fragmentation and backbreak. *Journal of Rock Mechanics and Geotechnical Engineering, 5*(4), 318-324. doi:10.1016/j.jrmge.2013.05.007

Tajik, S., Monjezi, M., Rezakhah, M., & Amiri Hosseini, M. (2023). Development of a Mathematical Model for Predicting Blast-Induced Fragmentation Considering Elastic Wave Velocities. *JOURNAL OF ROCK MECHANICS, 7*(2), 71-82. doi: 10.22034/IRSRM.2023.21255.2222

Wang, C. (1994). *A theory of generalization in learning machines with neural network applications.* Pennsylvania: University of Pennsylvania.

Wang, X., Hosseini, S., Jahed Armaghani, D., & Tonnizam Mohamad, E. (2023). Data-Driven Optimized Artificial Neural Network Technique for Prediction of Flyrock Induced by Boulder Blasting. *Mathematics, 11*(10), 2358. doi:10.3390/math11102358

Yari, M., Armaghani, D., Maraveas, C., Ejlali, A., Mohamad, E., & Asteris, P. (2023). Several Tree-Based Solutions for Predicting Flyrock Distance Due to Mine Blasting. *Applied Sciences, 13*(3), 1345. doi:10.3390/app13031345

Zorlu, K., Gokceoglu, C., Ocakoglu, F., Nefeslioglu, H., & Acikalin, S. (2008). Prediction of uniaxial compressive strength of sandstones using petrography-based models. *Engineering Geology, 96*(3-4), 141-158. doi:10.1016/j.enggeo.2007.10.009

SAŽETAK

Integriranje procjene umjetne neuronske mreže s optimizacijom algoritmom pčela za smanjenje izlijetanja komada stijena pri miniranju u površinskome kopu

Leteći komadi stijena (*flyrock*) neželjena su i opasna pojava koja nastaje tijekom miniranja u površinskim kopovima, a mogu imati ozbiljne posljedice na okoliš i sigurnost ljudi. Zbog tih rizika nužno je provesti detaljno istraživanje ovoga fenomena kako bi se smanjili njegovi negativni učinci. U ovome se radu predstavlja novi hibridni inteligentni model koji omogućuje predviđanje i smanjenje udaljenosti izlijetanja stijena kombiniranjem umjetne neuronske mreže (ANN) s optimizacijom algoritmom pčela. Analiza je provedena na temelju skupa od 334 zapisa miniranja prikupljenih iz površinskoga kopa rudnika bakra Sungun. Razvijeni su različiti modeli neuronskih mreža koji su potom vrednovani. Nakon procjene modela pomoću formalnoga sustava bodovanja odabran je najuspješniji model za optimizaciju. Taj odabrani ANN model pokazao je izvrsna prediktivna svojstva s koeficijentima determinacije (R^2) od 0,8930 za fazu treniranja i 0,8874 za fazu testiranja te s vrijednostima srednje kvadratne pogreške (RMSE) od 0,2486 i 0,2512. Time je postigao bolje rezultate u odnosu na klasične empirijske modele. Za dodatnu optimizaciju obrasca miniranja i povećanje sigurnosti korišten je algoritam pčela s ciljem minimizacije predviđene udaljenosti letećih komada stijena. Kao rezultat optimizacije utvrđena je optimalna udaljenost izlijetanja stijena od 7,25 metara, što predstavlja smanjenje od 27,5 % u odnosu na najmanju zabilježenu vrijednost u skupu podataka. Ti rezultati potvrđuju učinkovitost predloženoga hibridnog pristupa u poboljšanju sigurnosti i učinkovitosti miniranja u površinskim kopovima.

Ključne riječi:
procjena izlijetanja komada stijena, optimizacijski algoritam, model miniranja, algoritam pčela, metaheuristički algoritmi

Author's contribution

Mojtaba Rezakhah: conceptualization, data curation, formal analysis, investigation, resources, software, supervision, and writing – original draft. **Erfan Nemati**: formal analysis, investigation, methodology, software, validation, and writing – original draft. **Amir Batarbiat**: formal analysis, investigation, methodology, resources, software, validation, visualization, and writing – original draft. **Manoj Khandelwal**: data curation, methodology, resources, supervision, validation, visualization, and writing – review & editing
All authors have read and agreed to the published version of the manuscript.

RGNZ/MGPB

Mechanical activation and geopolymerisation of Taiwanese fly ash

Rudarsko-geološko-naftni zbornik
(The Mining-Geology-Petroleum Engineering Bulletin)
DOI: 10.17794/rgn.2025.5.12

Original scientific paper

Fanni Dolgos[1]*, Roland Szabó[1], Wei-Ting Lin[2], Gábor Mucsi[1]

[1] *Institute of Raw Materials Preparation and Environmental Technology, University of Miskolc, Egyetem út 1., Miskolc, 3515, Hungary.*

[2] *Department of Civil Engineering, National Ilan University, No.1, Sec. 1, Shennong Rd., Yilan City, Yilan County 260, Taiwan (R.O.C.).*

Abstract

The use of raw fly ash in the production of cement and geopolymer products is limited due to its low reactivity. However, the reactivity of fly ash can be increased through a mechanical activation process, allowing for its wider use. This study focused on the mechanical activation and geopolymerisation of coal fly ash originating from Taiwan. The mechanical activation was carried out by grinding in a batch-stirred media mill for 1, 3 and 5 minutes. The fineness and specific surface area significantly increased after 1 minute, and then only slightly decreased with further milling. The lime absorbance test showed significant improvement in pozzolanic activity (130-140% increase) after mechanical activation. For geopolymer synthesis, a 10M NaOH solution was used as an alkali activator with a liquid/solid ratio of 0.35. The geopolymer containing 3-minute fly ash grind produced the highest 28-day compressive strengths (36.1 MPa). The structural characterisation of fly ash and geopolymer was carried out by Fourier Transform Infrared (FTIR) spectroscopy. Changes in the FTIR spectra of fly ashes indicated the formation of amorphous aluminosilicate gel, a new reactive product as a result of geopolymerisation. Based on the strength development of geopolymers, mechanical activation enhanced the reactivity of fly ash, resulting in rapid setting and higher strength development during the early stages of geopolymerisation. The results clearly showed that, after mechanical activation, fly ash became a more reactive raw material, offering greater application potential than its current uses in cement production, road construction, and soil stabilisation.

Keywords:

fly ash, geopolymer, mechanical activation, pozzolanic activity

1. Introduction

The cement industry is one of the main contributors to climate change, accounting for 5-8% of the annual global anthropogenic CO_2 emissions. Due to growing populations and economic development, resulting in increasing demand for housing and infrastructure, the global cement demand is still estimated to rise by 12-23% above 2020 levels by 2050 (**Cheng et al., 2023**). In their study, **Flower and Sanjayan (2007)** found that during the production of typical commercial concrete mixes, Portland cement is responsible for 74-81% of the total CO_2 emissions, followed by the production of coarse and fine aggregates. As the production of traditional Portland cement is getting increasingly unsustainable due to the high energy demand and the use of non-renewable raw materials, there is a pressing need to develop more environmentally friendly and sustainable construction materials.

Geopolymerisation of silica- and alumina-rich industrial by-products is one of the most heavily researched areas today, with significant progress being made in the field. The term "geopolymer" was first coined by Davidovits to describe the inorganic polymeric material, which is the product of the reaction between aluminosilicate-oxides with silicate under highly alkaline conditions (**Das and Rout, 2021; Xu and Van Deventer, 2000**). Geopolymers are considered synthetic analogues for natural zeolitic materials with similar hydrothermal conditions required for their synthesis (**van Jaarsveld et al., 1998; Xu and Van Deventer, 2000**). Contrary to zeolites' regular and highly crystalline structures, the much faster geopolymer reaction results in amorphous to semi-crystalline three-dimensional aluminosilicate materials (**Xu and Van Deventer, 2000**). The mechanism of the geopolymer reaction is still not fully understood to this day, however, the most proposed three main stages are: dissolution, transportation or orientation and reprecipitation/polycondensation (**Xu and Van Deventer, 2000; Das and Rout, 2021**). In simple terms, geopolymers are the product of the reaction of alumina- and silica-rich solids with alkaline solution. The alkaline solution can be sodium hydroxide (NaOH), potassium hy-

* Corresponding author: Fanni Dolgos
e-mail address: dolgosfanni@gmail.com

Received: 30 April 2025. Accepted: 16 July 2025.
Available online: 21 October 2025

droxide (KOH), sodium silicate (Na_2SiO_3), potassium silicate (K_2SiO_3) solutions or various combinations (**Das and Rout, 2021**). The presence of these alkali salts/hydroxides is crucial in the geopolymerisation reaction, as they are needed for the dissolution of the silica and alumina (first stage of geopolymerisation), as well as for the catalysis of the condensation reaction (final stage). The geopolymer reaction begins with the dissolution of aluminosilicate solids, resulting in the formation of a gel layer on the surfaces of the particles. This gel then diffuses outwards, filling out the spaces between the particles through the precipitation of the gel and the dissolution of new solids. The aluminosilicate particles are bound together by the hardened gel phase which acts as a binder (**Xu and Van Deventer, 2000**). The geopolymerisation reaction takes place at temperatures lower than 100°C, making it an economically and environmentally more sustainable alternative to traditional concrete materials. Geopolymers also possess similar or superior mechanical and chemical properties, thermal resistance, fire and chemical resistance compared to traditional concretes (**Mucsi et al., 2015; Islam et al., 2025; Xu and Van Deventer, 2000**). Geopolymer technology was originally developed as the chemical activation of natural raw materials rich in Al_2O_3 and SiO_2 such as kaolin, metakaolin, silica fumes and calcined clay (**Farhan et al., 2020**). Geopolymerisation synthesis is also suitable for the high-rate utilisation of industrial by-products with high alumina and silica content, such as fly ash, ground granulated blast furnace slag (GGBS), red mud and mine tailings (**Ambrus and Mucsi, 2023; Nath et al., 2016; Kumar et al., 2010; Aziz et al., 2020; Kumar and Kumar, 2013; Mucsi et al., 2019; Manjarrez and Zhang, 2018; Moukannaa et al., 2018**). In conclusion, geopolymer technology greatly reduces the environmental impact of both traditional Portland cement-based concrete production and industrial by-products, helping the transition toward environmentally sustainable construction materials (**Ali et al., 2025; Liu et al., 2024; Islam et al., 2025**).

Among the above mentioned industrial by-products, fly ash is one of the most researched materials as a geopolymer precursor due to its easy availability, low cost and suitable chemical and mineralogical composition. Fly ash properties are highly dependent on the characteristics of the fired coal (e.g. origin, type, carbon content, particle size) and the combustion technology used (e.g. boiler configuration, temperature, gas cleaning equipment) (**Bhatt et al., 2019**). Fly ash has a high degree of pozzolanic reactivity due to its high SiO_2, Al_2O_3 and Fe_2O_3 content, which can cumulatively exceed 70%. The construction sector already applies fly ash as a cement substitute; however, its use is limited due to its relatively low pozzolanic activity compared to other cementitious materials, which can be detrimental to the quality of the produced concrete (**Hamada et al., 2024**). **Ali et al. (2025)** demonstrated the effectiveness of adding fly ash to concrete composites to counteract the detrimental effects of recycled coarse aggregate (RCA) on concrete quality. They found that substituting the cement with just the inactivated fly ash can improve the strength; however, this improvement in early strength development was lower than that of concretes containing mechanically and chemically activated fly ash. Adding either the mechanically or chemically activated fly ash further improved the properties of both fresh and hardened concrete. Their use enhanced the formation of C-S-H gel, resulting in a denser, stronger matrix. The best properties, including strength, permeability and density, were obtained by using chemically activated fly ash, as the highly alkaline environment accelerated the pozzolanic reaction and the formation of hydration products. Fly ash can also be used in combination with other waste materials, such as waste glass and GGBS, to produce foams with desirable properties (**Fóris and Mucsi, 2023; Liu et al., 2025**). Additionally, the low calcium content of fly ash was found to be particularly beneficial in terms of sulphate resistance as it reduces the formation of expansive products such as ettringite, which can be detrimental to the quality of geopolymers (**Islam et al., 2025**).

Similarly to concrete, the characteristics of fly ash particle size have a significant effect on the setting behaviour, strength development and microstructure of geopolymers (**Kumar and Kumar, 2011**). Both **Zhang et al. (2012)** and **Gao et al. (2024)** found that the particle size characteristics, specific surface area, and mineral and chemical composition had a combined effect on the reactivity of the examined fly ashes. They concluded that while the surface area is not the main determining factor in terms of reactivity, it is important for the dissolution mechanism of fly ash, since the initial key reactions between the raw material and the alkaline solution occur on the surface of the particles. **Gao et al. (2024)** also noted the critical role of the optimal distribution of fine and coarse particles in the geopolymerisation process. The importance of fly ash fineness to geopolymer properties was also highlighted by **Das (2024)**. Particle size has a strong influence on the microstructural development of the geopolymer matrix, which is closely related to the development of mechanical properties. Using fine fly ash resulted in a more compact and homogenous matrix, implying the formation of more sodium aluminosilicate hydrate (N-A-S-H) gel. This is because the fine fly ash particles are more reactive and can be almost completely dissolved in the highly alkaline activator.

The reactivity of fly ash can be improved by thermal activation, mechanical activation and chemical activation (**Ali et al., 2025**). Mechanical activation is carried out by milling in high-energy mills, such as ball mill, planetary ball mill, vibratory mill and stirred media mill in both wet and dry modes (**Fu et al., 2008; Nath and Kumar, 2020; Ambrus and Mucsi, 2023; Marjanović et al., 2014; Temuujin et al., 2009; Kumar et al. 2017; Molnár et al.,**

2014; Yang et al., 2019). Mechanical activation reduces the particle size of fly ash and increases its specific surface area, thereby accelerating the precipitation and reaction rates, as well as increasing the dissolution rate of the SiO_2 and Al_2O_3 components. The reduced particle size enhances the formation of the N-A-S-H gel and other hydration products, resulting in a denser structure (**Debnath et al., 2022; Dong et al., 2025; Liu et al., 2024**). It was proven that geopolymers made from mechanically activated fly ash have higher mechanical strength and improved properties than those made from untreated fly ash (**Kumar and Kumar, 2011; Zhao et al., 2015; Chu et al., 2019; Mucsi et al., 2014a; Mucsi et al., 2014a; Somna et al., 2011**). The material properties and the grinding conditions (grinding media, grinding method, use of chemical additives) greatly influence the particle size distribution, the macroscopic and microscopic properties of the material (**Dong et al., 2025**).

Kumar and Kumar (2011) mechanically activated fly ash in a vibratory mill and investigated the effects on geopolymerisation at ambient (27°C) and elevated (60°C) temperatures. Mechanical activation was found to increase the reaction rate and decrease the reaction time. As the duration of mechanical activation increased, the compactness of the geopolymers also increased, which could be explained by the formation of a greater amount of aluminosilicate gel. A strong relationship was established between the geopolymer properties (setting time and compressive strength), and the reactivity and median particle size of fly ash.

Marjanović et al. (2014) studied the influence of mechanical activation on the properties of fly ash and the synthesised geopolymers. Four different Serbian fly ashes were ground in a planetary ball mill for 15, 30, 45 and 60 minutes. Based on the particle size distribution results, it was determined that 15 min was the optimum duration of mechanical activation ($x_{50} \sim 3$ μm), as the agglomeration of particles was observed with prolonged grinding times. The compressive strength of geopolymers made from raw fly ash was low (< 5 N/mm^2), then following mechanical activation, the strength of the geopolymers exceeded 50 N/mm^2. The improvement in strength can be attributed to the greater formation of geopolymer gel resulting from the increased availability of alumina through mechanical activation. Agglomeration during milling can be caused by irregular fragments adhering to particle surfaces and small particles bonding together via weak van der Waals forces. These phenomena can be inhibited by adding grinding aids such as triethanolamine (TAE), as presented by **Dong et al. (2025)**. TAE not only enhanced the fragmentation of large particles, but XRD analysis also implied that it decreased the interaction forces between particles.

Mucsi et al. (2015) carried out a comparative study on the mechanical activation of a landfilled brown coal fly ash in a ball mill, vibratory mill and stirred media mill. Based on the results, there was a strong correlation between the grinding conditions (mill type and residence time), the ground material characteristics (x_{50} and specific surface area (SSA)) and the resulting geopolymer properties. The finest fly ash product (x_{50} = 5.2 μm, SSA = 21116 cm^2/g) was achieved by using a stirred media mill, which also proved to be the most efficient grinding method in terms of grinding energy and kinetics. The increased SSA also resulted in a more than 10 times higher uniaxial compressive strength of the geopolymer, which can be attributed to the better solubility and the filler effect of the finer fly ash particles.

The objective of the present study is the mechanical activation (MA) in stirred media mill and geopolymerisation of Taiwanese coal combustion fly ash (FA). MA was systematically performed in a laboratory batch-stirred media mill in dry mode for different grinding periods. Particle size and geometric specific surface area (SSA) were determined to study the effect of mechanical activation. The pozzolanic activity of raw (RFA) and mechanically activated fly ash (MFA) was determined by the lime absorption method. The structures of the fly ashes and the synthesised geopolymers were monitored by Fourier Transform Infrared Spectroscopy (FTIR). Geopolymers (GP) were made from RFA and MFA, and their average 7- and 28-day compressive strength and apparent density were determined.

2. Materials and methods

The fly ash (RFA) used in this study was collected from the Linkou Power Plant, which is located in the Linkou District of New Taipei City, Taiwan (see **Figure 1**). The plant has three pulverised coal-fired units with ultra-supercritical (USC) steam boiler technology. Australian and Indonesian high-quality bituminous and subbituminous coal are used, preferably with low sulphur content, suitable for USC boilers.

The chemical composition of the RFA was determined by X-ray fluorescence analysis (XRF), the result of which is presented in **Table 1**. The total SiO_2, Al_2O_3 and Fe_2O_3 content is 81.46%, which exceeds the minimum 70% oxide content limit required for pozzolanic materials (**Hamada et al., 2024**) and can be classified as Class F based on the ASTM C618 classification (**Ambrus and Mucsi, 2023**). Loss on ignition (LoI) was measured at 950°C with a heating time of 90 minutes and a residence time of 60 minutes. Due to its properties, this fly ash is used in cement production, road construction and soil stabilisation. It is also used to replace cement by 10-25 wt%, based on the requirements of ASTM C618.

The particle size distribution and geometric specific surface area (SSA) were measured using a HORIBA LA-950V2 laser particle size analyser in wet mode. Distilled water was the dispersing media and Na-pyrophosphate was the dispersing agent for the measurements. The particle size of RFA is between 0.20 and 200 μm,

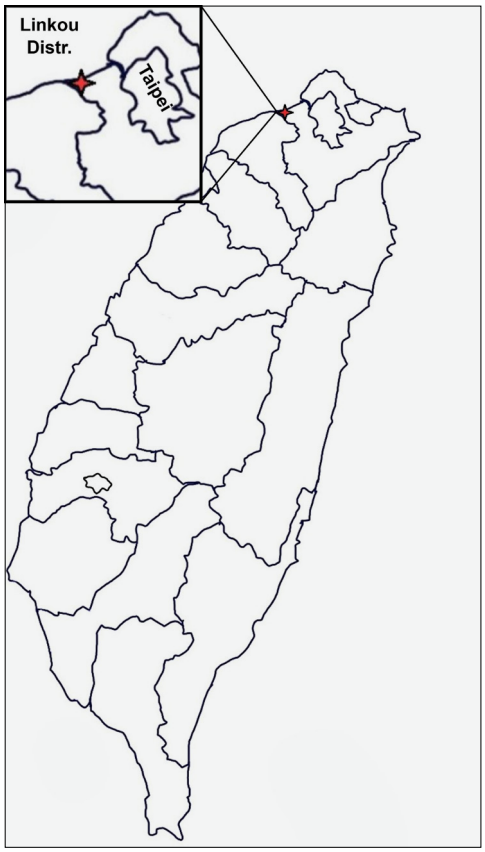


Figure 1. Location of Linkou Power Plant in Taiwan

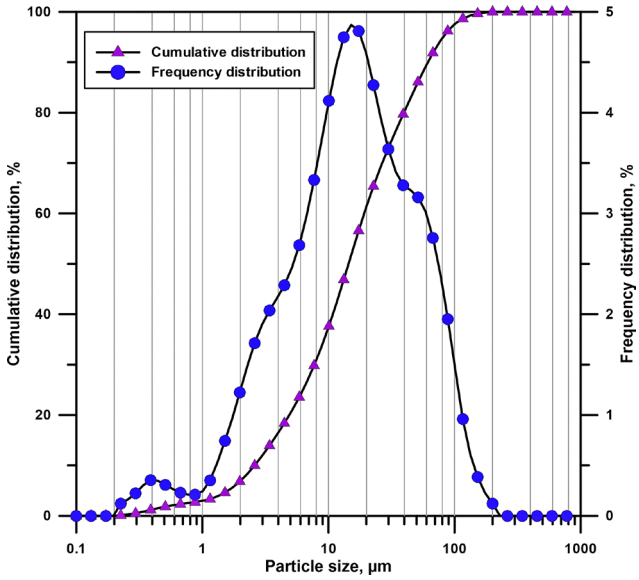


Figure 2. Cumulative and frequency distribution curves of particle size of RFA

with two main peaks located at around 0.40 and 15 μm on the frequency distribution curve (see **Figure 2**). The characteristic particle sizes of the RFA are the following: x_{10} = 2.60 μm, x_{50} = 14.44 μm, x_{80} = 39.69 μm, and the SSA was calculated to be 4736 cm^2/g.

The particle density was determined by the pycnometer method using isopropyl alcohol. The particle density of RFA was 2.42 g/cm^3.

The mechanical activation of the RFA was carried out by dry grinding in a laboratory batch-stirred media mill at a peripheral speed of 6 m/s. The lining of the mill and the grinding discs are made of a high-wear resistant Al_2O_3 material. The mill is also equipped with a water-cooling system to prevent the lining from overheating during milling. The used grinding media were SiLibeads ZY-type ceramic beads with a diameter of 0.8-1.0 mm and specific weight of 6 kg/l. The beads are made of yttrium stabilised zirconium oxide, making them highly resistant to wear and tear, ensuring low contamination of the milled product. Two batches of grinding beads were used in rotation. For each milling round, the media filling and the material filling ratios were constant at 0.7 and 0.8, respectively. The milling was carried out for 1, 3, and 5 minutes. The grinding media and the milled product were separated using a 500 μm sieve. While the degree of wear and breakage of the grinding media was negligible, emptying the mill and sieving resulted in a loss of beads. To ensure consistency, the mass of the grinding media batch was measured before each grinding session and supplemented accordingly.

The FTIR spectra of the fly ash samples and the geopolymer matrices were measured using a JASCO FT/IR 4220 spectrometer equipped with a diamond ATR accessory. The spectra data were collected in the range of 4000-400 cm^{-1} at a resolution of 4 cm^{-1} and baseline corrected.

The method described in the standard MSZ 4706–2:1998 "Complements for cement. Natural pozzolanic complements (trass) for cement." was used to study the effect of mechanical activation on the pozzolanic activity of fly ash. For the test, 100 ml of saturated lime solution was added to 2 g of material then sealed and shaken. The solution was shaken every day. Titration was performed every other day by taking 50 ml of the solution, to which methylene orange indicator was added and then 0.05 mol/L HCl solution was slowly added to the lime solution until the colour of indicator changed. Following the titration, 50 ml of fresh lime solution was added to the base solutions. The measurement took 30 days in total. Using the HCl solution loss, the lime uptake per 1 g of material can be determined.

NaOH solution with a molarity of 10 M was used for geopolymer synthesis. The liquid/solid ratio was kept at a constant 0.35 for all geopolymer mixtures. The solid and liquid components were mixed manually, then the pastes were cast into a polyvinyl chloride mould divided into 20×20×20 mm cubes. The specimens were manually compacted by gently dropping the mould at least 10 times to remove air bubbles. The geopolymers were stored hermetically sealed in the mould at room temperature for six days. Once removed from the mould, the hardened specimens were stored in separate Ziploc bags for each mixture at room temperature until the day of the compressive strength measurements.

Table 1. Chemical composition (weight %) of the Taiwanese FA

Oxide	SiO_2	Al_2O_3	Fe_2O_3	CaO	MgO	TiO	P_2O_5	Na_2O	K_2O	LoI
wt%	50.96	23.89	6.61	8.38	1.48	1.21	1.49	0.72	0.88	2.29

The uniaxial compressive strength (UCS) measurements were carried out 7 and 28 days after preparation using a SZF-1 type hydraulic compression-testing machine with a maximum load capacity of 25 kN. For each age, the average USC values of three cube specimens (see **Figure 3**) are given. Prior to the UCS tests, the size and mass of the specimens were measured to determine their specimen density.

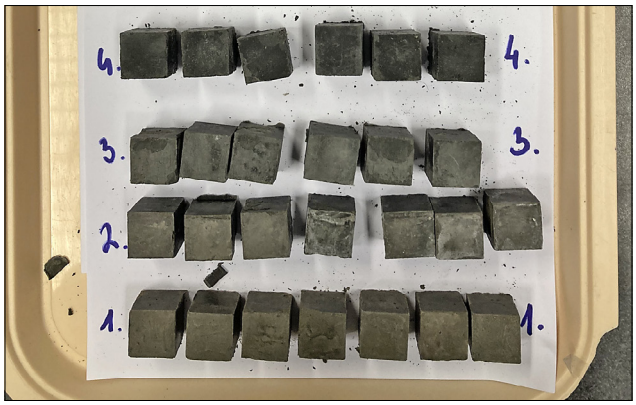


Figure 3. Prepared GP specimens

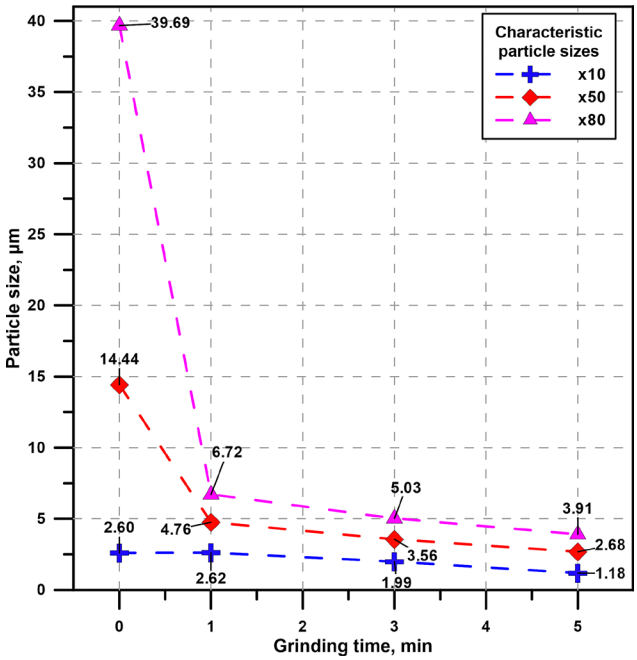


Figure 4. Characteristic particle sizes as a function of grinding time

3. Results and discussion

3.1. Particle size and specific surface area

The effect of mechanical activation in the stirred media mill on the characteristic particle sizes (x_{10}, x_{50} and x_{80}) are shown in **Figure 4**. There is technically no deviation in the x_{10} value following 1 min of mechanical activation; however, with prolonged grinding the size reduction is higher. Contrary to the x_{10}, the initial x_{50} and x_{80} values decreased considerably (by 67% and 83%), but the decrease was less with further grinding, only 22-25%. These observations correlate well with the findings of **Kumar and Kumar (2011)**, **Fu et al. (2008)** and **Nath and Kumar (2020)**, who also found that the increase in fly ash fineness is more prominent in the initial stages of grinding, which slows down in later stages.

The change in the frequency distribution after mechanical activation in the stirred media mill can be well observed in **Figure 5**. As a result of 1 minute of grinding, the first mode of the RFA frequency curve below 1 µm disappeared and became monomodal, with the second mode of ~11 µm shifting to a higher frequency at a smaller particle size range from 1 to 20 µm. On the MFA3 curve, the submicron particles reappear between ~0.2-1 µm and the sharpest peak shifts to a smaller particle size with a slightly increased frequency. This indicates a higher degree of fragmentation of coarse particles and deagglomeration. This process with higher grinding time further intensified as the mode associated with the ultrafine particle fraction became more prominent, also in good correlation with the significant increase in geometric SSA (see **Figure 6**).

In general, the geometric SSA increased exponentially with prolonged grinding time (see **Figure 6**). The

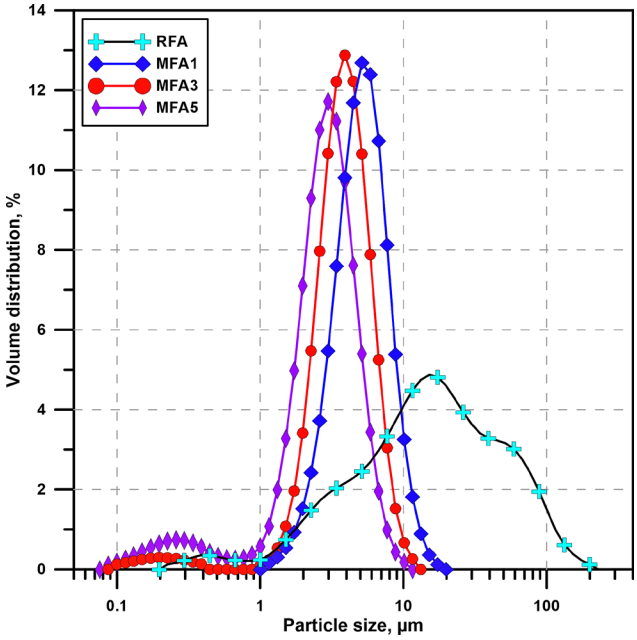


Figure 5. Frequency curves of the RFA and MFA samples

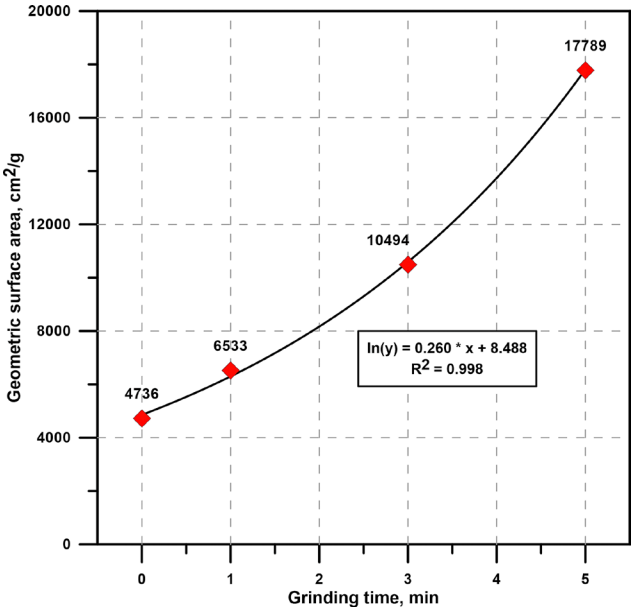


Figure 6. Geometric surface area as a function of grinding time

sharp increase in the geometric SSA between 1 and 3 minutes of grinding suggests the formation of ultrafine particles, as evidenced by the reappearance of the first mode and the slight shift toward finer particle size on the frequency curve. The highest SSA was obtained after 5 minutes of mechanical activation, resulting in a 70% increase compared to MFA3. The geometric SSA increased almost 4 times from 4736 cm^2/g to 17789 cm^2/g after 5 minutes of grinding compared to the RFA.

3.2. Pozzolanic activity

Pozzolanic reaction is defined as the interaction between the amorphous silica and alumina content of materials and the calcium hydroxide ($Ca(OH)_2$) formed during cement hydration, which promotes the formation of additional cementitious compounds (**Hamada et al., 2024**). The pozzolanic activity of fly ash is much lower than traditional natural pozzolanic materials (i.e. trass) and other "manufactured" pozzolanic materials like silica fume, as the pozzolanic reaction takes place extremely slowly on the glassy outer shell of fly ash particles (**Opoczky, 2001**). The mechanical activation of fly ash by fine grinding breaks the particle's vitreous outer layer (surface activation) and liberates the inner part with a high glassy phase, thereby increasing the proportion of the glassy phase participating in the pozzolanic reaction, resulting in a stronger geopolymer (**Opoczky, 2001; Mucsi et al., 2015; Gao et al., 2024**). The pozzolanic activity of fly ash can be enhanced by increasing its surface area, as this improves the reactivity with $Ca(OH)_2$ in the cement paste, leading to improved concrete strength and durability (**Hamada et al., 2024**).

It is evident from the lime absorption test results (see **Figure 7**) that by grinding in the stirred media mill, the pozzolanic activity of the fly ash was significantly improved. The initial 40.2 mg/g FA total lime uptake of the untreated fly ash was raised to between 93.3-96.4 mg/g FA, the highest lime absorption achieved by the 3-minute grinding. This improvement can be attributed to the increase in surface area and the breakdown of the vitreous outer layer of the fly ash. Initially, the dissolution of the active components of the raw material by the alkali activator occurs on the particle surface, during which the vitreous outer layer is gradually destroyed. However, this process is relatively slow, which inhibits the depolymerisation-condensation polymerisation reaction of FA (**Liu et al., 2025**). To enhance the reactivity of FA, it is necessary to destroy the glassy structure of the particles, as described in detail through the geopolymerisation process by **Liu et al. (2025)**. Mechanical grinding destroys the vitreous outer layer of the FA, exposing the inner alumina and silica compounds that participate in geopolymer or cementitious reactions. Thus, the higher absorption of lime by MFAs is due to the increased availability of these compounds, as well as the increased surface area of the active sites compared to RFA.

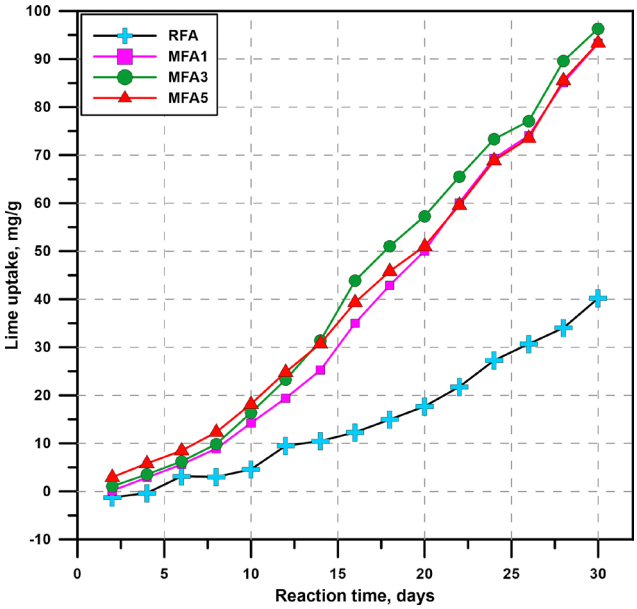


Figure 7. Lime uptake of the RFA and MFAs

3.3. Compressive strength and specimen density

The average UCS results presented in **Figure 8** show that the mechanical activation of the RFA significantly enhanced the compressive strength of the MFA-based geopolymers. Compared to the RFA-based geopolymer (RFAGP), the increase in the 7-day compressive strength was more than 200% even after only 1 minute of milling (MFA1GP). The rate of improvement is much lower for the 28-day UCS values but still ranges from 53-91%. Overgrinding resulted in a decrease of USC. The MFA1GP and MFA5GP specimens yielded similar compressive strength results at both ages. The geopolymer

made from the MFA3 achieved the highest compressive strength at both ages, reaching maximum strengths of 26.2 MPa and 36.1 MPa at 7 and 28 days of age, respectively. **Mucsi et al. (2015)** found that after increasing the fineness of FA by grinding in a high-energy mill, the solubility of SiO_2 and Al_2O_3 in the NaOH solution can be enhanced, resulting in a higher amount of GP gel. They also suggest that the <1 μm unreacted size fraction can act as a filler, playing a role in improving the geopolymer strength.

For RFAGP, the compressive strength improved by 361% between 7 and 28 days, indicating a prolonged strength development and longer setting time (**Nath and Kumar, 2020**). Meanwhile, the rate of strength development during this period is much lower in the case of MFA-geopolymers, suggesting that the majority of the geopolymerisation of FA occurs in the earlier stages of geopolymer formation and slows down over time. These differences in strength development demonstrate the enhancing effects of mechanical activation on the reactivity of FA, resulting in the more rapid dissolution of FA, leading to faster setting and higher strength development at the earlier stages (**Temuujin et al., 2009**).

The specimen density values at 7 and 28 days ranged from 1.874-1.917 g/cm^3 and 1.803-1.932 g/cm^3, respectively. The particle size reduction did not cause a substantial change in the specimen density of the geopolymers. The MFA3GP had the highest specimen density at both ages, but the increase is considerably lower, only 2%, compared to the UCS values.

As a result of the rapid setting caused by mechanical activation, the workability of the fresh geopolymer paste deteriorated as the grinding time increased. This resulted in difficulties during the moulding and the compaction of the specimens. The morphology and fineness of fly ash are important factors in terms of its use in the production of ordinary Portland cement concretes. The spherical FA particles and the wide size distribution contribute to lower water demand and better workability, as well as higher packing density of the concrete, resulting in higher strength. During grinding, this spherical morphology of FA is destroyed and the range of sphere sizes is reduced, which could also be the cause of the lower workability of the fresh concrete (**Temuujin et al., 2009; Felekoğlu et al., 2009**). Raising the fly ash content can also affect the fluidity of fly ash-slag geopolymer foam concrete, which increases due to the low surface tension of the spheroidal glassy microstructure of the raw fly ash particles. With mechanical activation, this structure is damaged, leading to reduced surface tension and increased cohesion between particles, resulting in the decreased flow of the slurry (**Liu et al., 2025**). In conclusion, the decrease in UCS and specimen density between MFA3GP and MFA5GP can be partially explained by the inadequate compaction of the specimens caused by the combined effects of rapid setting and poor workability of the geopolymer paste.

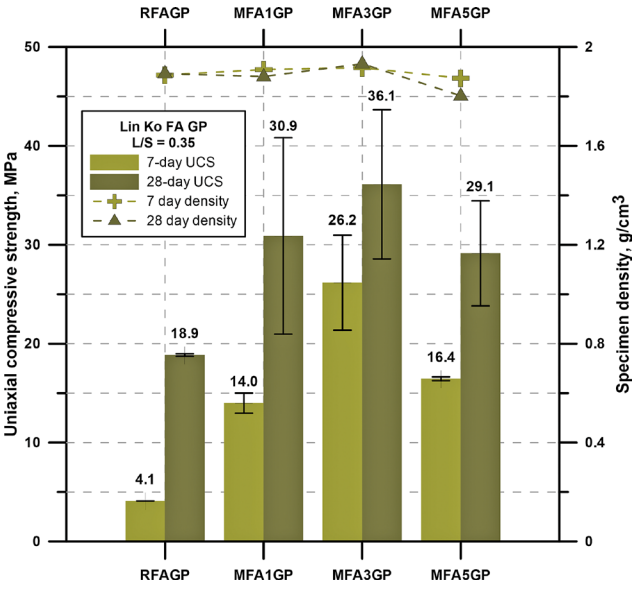


Figure 8. Compressive strength and specimen density of Taiwanese fly ash-geopolymers

3.4. FTIR spectroscopy

The FTIR spectra of RFA and the three MFAs are presented in **Figure 9**. The high-intensity broad band at ~1054 cm^{-1}, present in the spectra of both RFA and MFAs, is attributed to the asymmetric stretching vibrations of T – O – Si (T = Al or Si). This band is characteristic of fly ashes and is the result of the combined vibrations of the quartz, mullite and vitreous components. The presence of quartz also contributes to the band at 698 cm^{-1} and the double band at 795-777 cm^{-1} (**Marjanović et al., 2014**). The intensity of the double peak increases as the grinding time increases. These bands are characteristic of the bending vibrations of Si–O–Si bonds of quartz, and the higher intensity can be explained by the breakdown of the covalent bond in the silicate network of fly ash (**Ambrus and Mucsi, 2023; Djobo et al., 2016**). The peak at 556 cm^{-1} is related to the symmetric stretching vibration of Si – O – Si and Al – O – Si (**Panias et al., 2007**). Milling weakens the bonds within the particles, making them more reactive with alkali activators during geopolymerisation (**Debnath et al., 2022**). In general, the spectra of fly ash were not significantly altered by mechanical activation, although the prominent peaks shifted to higher intensities, which is the result of higher infrared absorbance due to higher specific surface area (**Mucsi et al., 2015; Debnath et al., 2022**). However, it shows remarkable differences in the band sharpening observed in the silicate mineral region (around 1200–1000 cm^{-1}), which provides insight into the concentration and structural order of the silicate mineral. According to **Hamada et al. (2024)**, the increase in peak intensity is due to the disintegration of larger particles into finer particles, as well as the breakdown of molecular bonds. The observed sharpening of the band indicates an increase in the concentration of

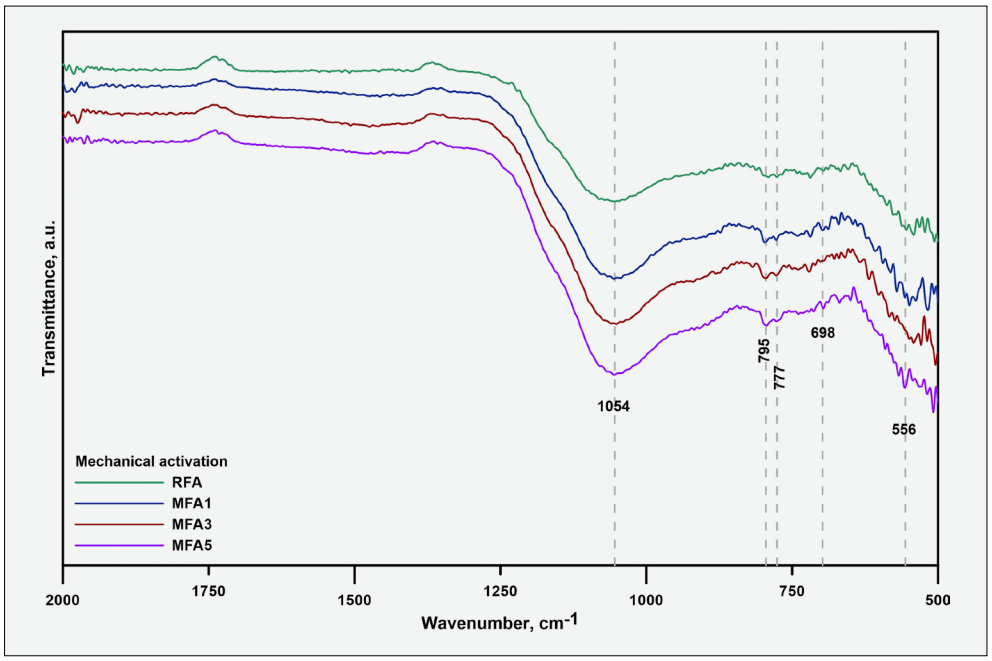


Figure 9. FTIR spectra of the RFA and MFAs

reactive material and silica content (SiO_2), both of which can be attributed to grinding activity.

Several new peaks and bands appeared as a result of the geopolymerisation of fly ash as can be seen in **Figure 10a**. The most prominent change can be observed in the peak attributed to the asymmetric stretching vibrations of Si – O – T (T = Al or Si) bonds. The main band at ~1050 cm^{-1} on the spectra of fly ashes shifts to a lower wavenumber at ~970 cm^{-1} with higher intensity, resulting in a sharp peak on the spectra of fly ash geopolymers. This prominent shift signifies structural reorganisation and the formation of new reaction products, namely, the amorphous aluminosilicate gel. This can be the result of the dissolution of the amorphous phase of fly ash in the strong alkaline activating solution (**Kumar et al., 2017; Panias et al., 2007**). The series of small bands located between ~795 and 690 cm^{-1} is associated with the presence of quartz (**Marjanović et al., 2014**), the change in intensity is similar to those located in the spectra of the fly ashes. A broad band with a peak located at 3300 cm^{-1} and a low-intensity peak at ~1650 cm^{-1} appear in the spectra of both the RFA and MFA geopolymers. These peaks are attributed to the stretching vibrations of O–H bonds of adsorbed water and the bending vibrations of H – O – H bonds of water molecules enclosed within the aluminosilicate structure, respectively (**Kumar et al., 2015; Kumar et al., 2017**). **Panias et al. (2007)** found a correlation between the intensity of the water-related peaks and the compressive strength of geopolymers. A higher intensity of these peaks indicates a greater degree of water adsorption, as can be seen on the RFAGP spectrum (**Kumar et al., 2015; Kumar and Kumar, 2011**), which also had the lowest 7-day UCS. However, the intensity of both bands significantly decreased for MFA3GP, which had the highest 7-day UCS. The band appearing at ~1400 cm^{-1} in every spectrum, is characteristic of the stretching vibrations of C = O, indicative of carbonate groups (i.e. Na_2CO_3) in the structure which is the product of the atmospheric carbonation of NaOH aqueous phase. The highest and lowest intensities of this band were detected for RFAGP and MFA3GP, respectively, indicating a higher degree of carbonation due to the unreacted alkali in the geopolymer matrix containing untreated fly ash (**Kumar et al., 2015; Panias et al., 2007**).

On the spectra collected after prolonged curing of geopolymers (see **Figure 10b**), considerable change can be observed in the bands related to the structural water content (3700-3000 cm^{-1} and 1650 cm^{-1}). Both of these peaks appeared at a higher intensity for MFA3GP, for RFAGP, these peaks shifted to a significantly lower intensity after 28 days. The peak attributed to the C=O bond also shifted towards lower intensity, indicating a lower rate of carbonisation. This decrease could be due to the increased involvement of fly ash in the hydration reaction over a longer curing period. This inhibits the carbonisation process due to the reduced availability of free alkali (**Liu et al., 2024**). This correlates well with the change observed in Si – O – T (T = Al or Si) peak at 970 cm^{-1} in the geopolymer spectra, which became much sharper over time, indicating greater polymerisation (**Kumar and Kumar, 2011**. The peak at 970 cm^{-1} on the spectrum of MFA3GP shifted to the highest intensity which also had the highest 28-day UCS.

3.5. *Relationship between compressive strength, SSA, x_{50} and lime absorption*

The 7-day and 28-day compressive strengths as a function of SSA, median particle size (x_{50}) and lime uptake are presented in **Figure 11**. The relationship between these parameters was examined based on the best

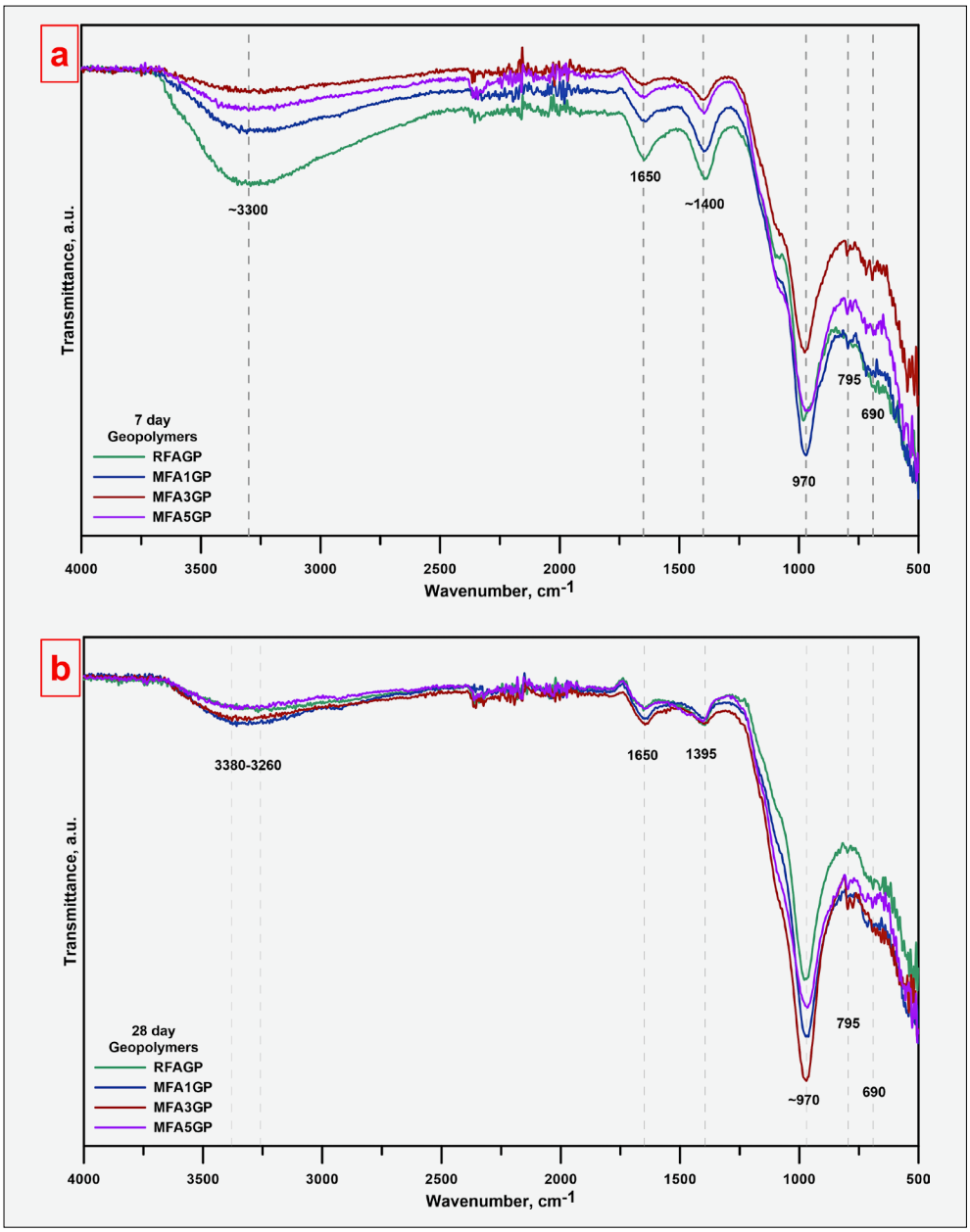


Figure 10. FTIR spectra of GPs at the age of (a) 7 days and (b) 28 days

fit function to the points. The weakest correlation was found with the SSA of the FA. Higher coefficient of determination fit was observed between the 7-day UCS and the SSA (R^2 = 0.513), indicating that the SSA may have a bigger influence – although weak – on the earlier stages of strength development, as a higher SSA can enhance the dissolution rate of FA in the initial stages of geopolymerisation (**Zhang et al., 2012**). Stronger correlation was found between the UCS and the x_{50}, and between the UCS and the amount of lime absorbed, both of which follow an exponential trend. **Gao et al (2024)** observed a similarly strong relation between the compressive strength of geopolymers and the median particle size of FA. The authors, along with **Kumar and Kumar (2011)**, suggest that x_{50} more accurately characterises the particle size distribution when the reactivity of FA is considered.

4. Conclusions

The following conclusions can be drawn from the experimental results presented above:

- Mechanical activation had a significant effect on the reactivity of the investigated Taiwanese fly ash. The pozzolanic activity of MFAs, determined by lime uptake test, increased by 130-140% compared to the RFA.
- However, overgrinding resulted in a smaller increase in the pozzolanic activity of FA, which also affected the compressive strength of the geopolymer.

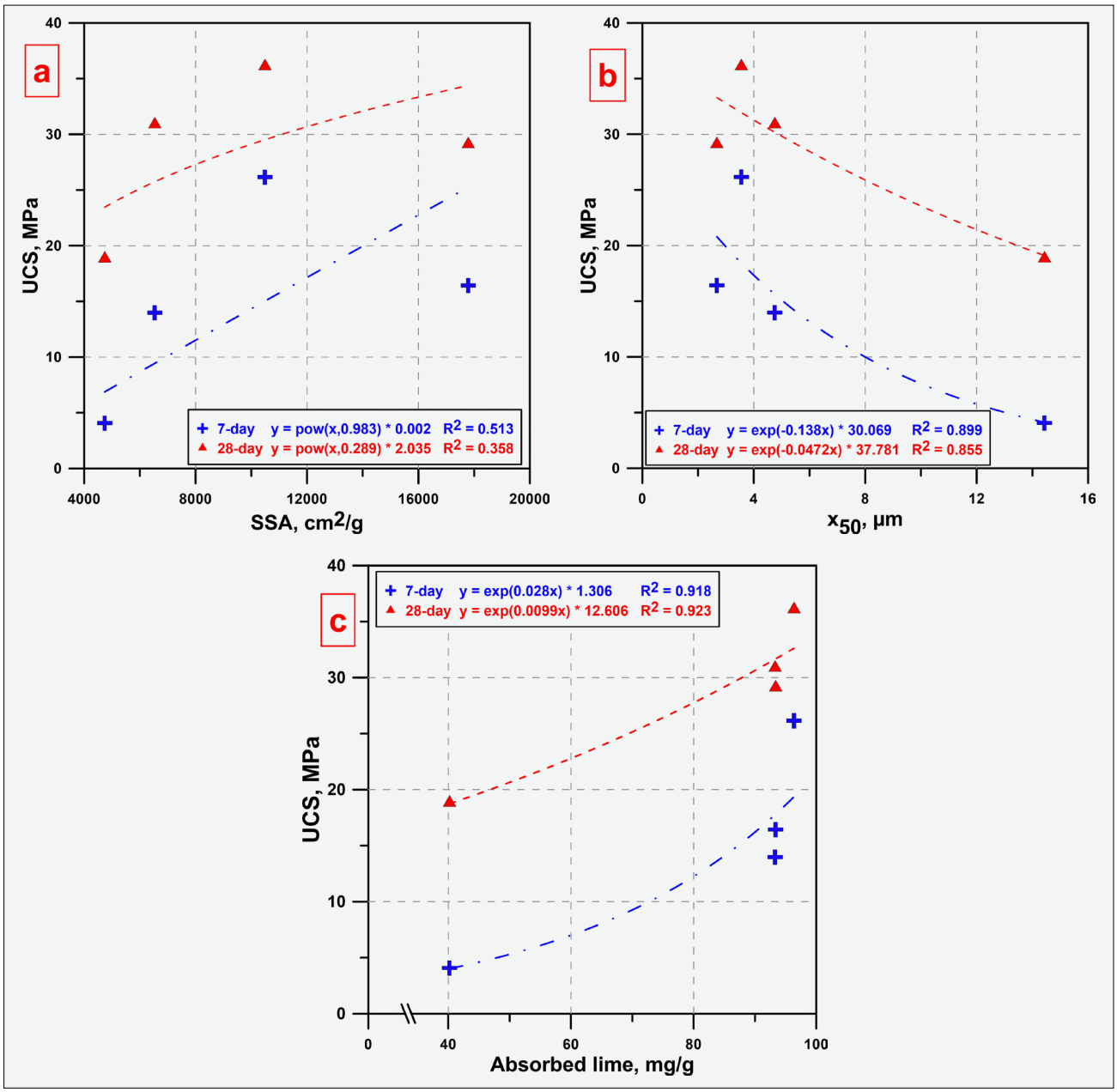


Figure 11. UCS as a function of (a) SSA, (b) x_{50} and (c) absorbed lime

- Optimal fineness was found to be at 3 min residence time mechanical activation where median particle size and specific surface area were 3.56 µm and 10494 cm^2/g, respectively.
- A strong correlation was found between the lime uptake results of the ground fly ash and the resulting geopolymer compressive strength. The MFA3 had the highest total lime uptake (96.4 mg/g FA), from which the geopolymers with the highest compressive strength (36.1 MPa at the age of 28 days) were produced.
- FTIR results show that after mechanical activation, the prominent peaks on the spectrum of RFA shifted to higher intensities, which is the result of higher infra-absorbance due to higher specific surface area as well as the breakdown of molecular bonds. The shift of the main peak at ~1054 cm^{-1} in the FA spectra shifted to lower wavenumbers after geopolymerisation, indicating structural reorganisation and formation of new reaction products (amorphous aluminosilicate gel).
- In order to better support the results of FTIR measurements and understand the structural changes that occur as a result of milling and geopolymerisation, XRD and SEM measurements are necessary.
- Overall, it can be concluded that the mechanical activation of Taiwanese fly ash can significantly enhance its pozzolanic activity, decreasing reliance on traditional cement manufacturing processes and helping to lower CO_2 emissions. Therefore, it pro-

vides an environmentally friendly alternative to traditional materials and helps to reduce the global environmental impact.

Acknowledgement

The authors would like to thank Dr. Ferenc Móricz associate professor for the XRF measurement and Dr. Ákos Debreczeni associate professor for conducting the compressive strength tests.

Funding

This study was carried out within the framework of project no. 2019-2.1.7-ERA-NET-2022-00051 entitled "Foamed Geopolymer Made by Additive Manufacturing for the Construction Technology Applications" with support from the National Research, Development and Innovation Fund of the Ministry of Culture and Innovation and Hungarian Organizations, in the financing of the ERA-NET COFUND/EJP COFUND Programme with co-funding from the European Union Horizon 2020 research and innovation programme.

5. References

Ali, T, Qureshi, M. Z., Onyelowe, K. C., Althaqafi, E., Deifalla, A., Ahmed, H., & Ajwad, A. (2025). Optimizing recycled aggregate concrete performance with chemically and mechanically activated fly ash in combination with coconut fiber. *Scientific Reports,* 15, https://doi.org/10.1038/s41598-025-92227-x

Ambrus, M. and Mucsi., G. (2023). Advanced processing of high Ca fly ash for enhanced reactivity and improved high value-added application possibilities. *Case Studies in Construction Materials*, 18, https://doi.org/10.1016/j.cscm.2023.e02214

Aziz, I. H., Abdullah, M. M. A. B., Salleh, M. A. A. M., Azimi, E. A., Chaiprapa, J. & Sandu, A. V. (2020). Strength development of solely ground granulated blast furnace slag geopolymer. *Construction and Building Materials*, 250, https://doi.org/10.1016/j.conbuildmat.2020.118720

Bhatt, A., Priyadarshini, S., Mohanakrishnan, A. A., Abri, A., Sattler, M. & Techapaphawit, S. (2019). Physical, chemical, and geotechnical properties of fly ash: A global review. *Case Studies in Construction Materials*, 11, https://doi.org/10.1016/j.cscm.2019.e00263

Cheng, D., Reiner, D. M., Yang, F., Cui, C., Meng, J., Shan, Y., Liu, Y., Tao, S. & Guan, D. (2023). Projecting future carbon emissions from cement production in developing countries. *Nature Communications*, 14 (1), https://doi.org/10.1038/s41467-023-43660-x

Chu, Y., Davaabal, B., Kim, D., Seo, S., Kim, Y., Ruescher, C. & Temuujin, J. (2019). Reactivity of fly ashes milled in different milling devices. *Reviews on Advanced Materials Science*, 58 (1), 179–188, https://doi.org/10.1515/rams-2019-0028

Das, D. (2024). Role of particle size on the mechanical and microstructural properties of fly ash-based geopolymer. *Interactions,* 277, https://doi.org/10.1007/s10751-024-02117-3

Das, D. and Rout, P. K. (2021). Synthesis, Characterization and Properties of Fly Ash Based Geopolymer Materials. *Journal of Materials Engineering and Performance,* 30, 3213–3231, https://doi.org/10.1007/s11665-021-05647-x

Debnath, K., Das, D., & Rout, P. K. (2022). Effect of mechanical milling of fly ash powder on compressive strength of geopolymer. *Materials Today: Proceedings,* 68, 242–249, https://doi.org/10.1016/j.matpr.2022.08.321

Djobo, J. N. Y., Elimbi, A., Tchakouté, H. K. & Kumar, S. (2016). Mechanical activation of volcanic ash for geopolymer synthesis: effect on reaction kinetics, gel characteristics, physical and mechanical properties. *RSC Advances*, 6, 39106 –39117, https://doi.org/10.1039/C6RA03667H

Dong, Y., Ning, X., Han, T., Hou, H., Zang, M., Lu, H., & He, X. (2025). Triethanolamine assisted ball milling activation of high alumina fly ash: Grinding kinetics, activation mechanism. *Ceramics International,* 51 (4), 4168–4177, https://doi.org/10.1016/j.ceramint.2024.11.393

Farhan, K. Z., Johari, M. A. M. & Demirboğa, R. (2020). Assessment of important parameters involved in the synthesis of geopolymer composites: A review. *Construction and Building Materials*, 264, https://doi.org/10.1016/j.conbuildmat.2020.120276

Felekoğlu, B., Türkel, S. & Kalyoncu, H. (2009). Optimization of fineness to maximize the strength activity of high-calcium ground fly ash – Portland cement composites. *Construction and Building Materials*, 23 (5), 2053–2061, https://doi.org/10.1016/j.conbuildmat.2008.08.024

Flower, D. J. M. and Sanjayan, J. G. (2007). Green house gas emissions due to concrete manufacture. The International Journal of Life Cycle Assessment, 12, 282–288, https://doi.org/10.1065/lca2007.05.327

Fóris, I., and Mucsi, G. (2023). Influence of raw material properties on waste-based glass foam. *Rudarsko-geološko-naftni zbornik, 38* (4), 75–83, https://doi.org/10.17794/rgn.2023.4.7

Fu, X., Li, Q., Zhai, J., Sheng, G. & Li, F. (2008). The physical-chemical characterization of mechanically-treated CFBC fly ash. *Cement and Concrete Composites*, 30 (3), 220–226, https://doi.org/10.1016/j.cemconcomp.2007.08.006

Gao, R., Zhou, Z., Yang, J. & Zhang, J. (2024). Innovative assessment of reactivity in fly ash: The role of particle size distribution characteristics. *Open Ceramics*, 20, https://doi.org/10.1016/j.oceram.2024.100680

Hamada, H. M., Abed, F., Al-Sadoon, Z. A. & Alashkar, A. (2024). Enhancing pozzolanic activity of fly ash via dry and wet milling: A comparative study for sustainable construction material enhancement. *Journal of CO2 Utilization*, 83, https://doi.org/10.1016/j.jcou.2024.102811

Islam, I., Khattak, S. A., Petrounias, P., Asif, A. R., Al Shah, S. S., Turrakheil, K. S., Ahmed, W., Ur Rashid, M., Ur Rehman, Q. & Khan, M. N. (2025). Experimental Investigation of Mechanical Properties and Durability of the Self-Compacting Geopolymer Mortar using various Mineral Additions. *Rudarsko-geološko-naftni zbornik*, 40(1), 13–27. https://doi.org/10.17794/rgn.2025.1.2

Kumar, S., Kristály, F. & Mucsi, G. (2015). Geopolymerisation behaviour of size fractioned fly ash. *Advanced Powder Technology*, 26 (1), 24–30, https://doi.org/10.1016/j.apt.2014.09.001

Kumar, A. and Kumar, S. (2013). Development of paving blocks from synergistic use of red mud and fly ash using geopolymerisation. *Construction and Building Materials*, 38, 865–871, https://doi.org/10.1016/j.conbuildmat.2012.09.013

Kumar, S., Kumar, R. & Mehrotra, S. P. (2010). Influence of granulated blast furnace slag on the reaction, structure and properties of fly ash based geopolymer. *Journal of Materials Science*, 45 (3), 607–615, https://doi.org/10.1007/s10853-009-3934-5

Kumar, S. and Kumar, R. (2011). Mechanical activation of fly ash: Effect on reaction, structure and properties of resulting geopolymer. *Ceramics International*, 37 (2), 533–541, https://doi.org/10.1016/j.ceramint.2010.09.038

Kumar, S., Mucsi, G., Kristály, F. & Pekker, P. (2017). Mechanical activation of fly ash and its influence on micro and nano-structural behaviour of resulting geopolymer. *Advanced Powder Technology*, 28 (3), 805–813, https://doi.org/10.1016/j.apt.2016.11.027

Liu, X., Jiang, T., Li, C., Wan, M., Xuan, W., & Wang, X. (2024). Effect of Precursor Blending Ratio and Rotation Speed of Mechanically Activated Fly Ash on Properties of Geopolymer Foam Concrete. Buildings, 14(3), 841. https://doi.org/10.3390/buildings14030841

Manjarrez, L. and Zhang, L. (2018). Utilization of copper mine tailings as road base construction material through geopolymerization. *Journal of Materials in Civil Engineering*, 30 (9), https://doi.org/10.1061/(ASCE)MT.1943-5533.0002397

Marjanović, N, Komljenović, M., Baščarević, Z. & Nikolić, V. (2014). Improving reactivity of fly ash and properties of ensuing geopolymers through mechanical activation. *Construction and Building Materials*, 57, 151–162, https://doi.org/10.1016/j.conbuildmat.2014.01.095

Molnár, Z., Kristály, F. & Mucsi, G. (2014). Mechanical activation of deposited brown coal fly ash in stirred media mill. *Acta Physica Polonica A*, 126, 988–993, http://dx.doi.org/10.12693/APhysPolA.126.988

Moukannaa, S., Loutou, M., Benzaazoua, M., Vitola, L., Alami, J. & Hakkou, R. (2018). Recycling of phosphate mine tailings for the production of geopolymers. *Journal of Cleaner Production*, 185, 891–903, https://doi.org/10.1016/j.jclepro.2018.03.094

Mucsi, G., Kumar, S., Csőke, B., Kumar, R., Molnár, Z., Rácz, Á., Mádai, F. & Debreczeni, Á. (2015). Control of geopolymer properties by grinding of land filled fly ash. *International Journal of Mineral Processing*, 143, 50–58, https://doi.org/10.1016/j.minpro.2015.08.010

Mucsi, G., Lakatos, J., Molnár Z. & Szabó, R. (2014a). Development of geopolymers using industrial waste materials. In: Cygas, D. and Tollazzi, T. (Eds.), *9TH International Conference Environmental Engineering (9TH ICEE) - Selected Papers.* Vilnius, Lithuania, http://dx.doi.org/10.3846/enviro.2014.039

Mucsi, G., Molnár, Z., Rácz, Á., Faitli, J., Gombkötő, I. & Ráczkevi, B. (2014b). High energy density milling as a tool for improving the properties of fly ash based geopolymers. In: Yianatos, J., Doll, A. and Gomez, C. (Eds.), *IMPC 2014 - 27th International Mineral Processing Congress,* October 20–24. 2014, Santiago, Chile.

Mucsi, G., Szabó, R., Rácz, Á., Kristály, F. & Kumar, S. (2019). Combined utilization of red mud and mechanically activated fly ash in geopolymers. *Rudarsko-geološko-naftni zbornik*, 34, 27–36, https://doi.org/10.17794/rgn.2019.1.3

Nath, S. K. and Kumar, S. (2020). Role of particle fineness on engineering properties and microstructure of fly ash derived geopolymer. *Construction and Building Materials*, 233, https://doi.org/10.1016/j.conbuildmat.2019.117294

Nath, S. K., Maitra, S., Mukherjee, S. & Kumar, S. (2016). Microstructural and morphological evolution of fly ash based geopolymers. *Construction and Building Materials*, 111, 758–765, https://doi.org/10.1016/j.conbuildmat.2016.02.106

Opoczky, L. (2001). A pernyék szilikátkémiai tulajdonságai (The silicate-chemical proper-ties of fly ashes). *Építőanyagok*, 53 (4), 105–108. (in Hungarian).

Panias, D., Giannopoulou, I. P. & Perraki, T. (2007). Effect of synthesis parameters on the mechanical properties of fly ash-based geopolymers. *Colloids and Surfaces A: Physicochemical and Engineering Aspects*, 301 (1–3), 246–254, https://doi.org/10.1016/j.colsurfa.2006.12.064

Somna, K., Jaturapitakkul, C., Kajitvichyanukul, P. & Chindaprasirt, P. (2011). NaOH-activated ground fly ash geopolymer cured at ambient temperature. *Fuel*, 90 (6), 2118–2124, https://doi.org/10.1016/j.fuel.2011.01.018

Temuujin, J., Williams, R. P. & van Riessen, A. (2009). Effect of mechanical activation of fly ash on the properties of geopolymer cured at ambient temperature. *Journal of Materials Processing Technology*, 209 (12-13), 5276–5280, https://doi.org/10.1016/j.jmatprotec.2009.03.016

Van Jaarsveld, J. G. S., Van Deventer, J. S. J. & Lorenzen, L. (1998). Factors affecting the immobilization of metals in geopolymerized flyash. *Metallurgical and Materials Transactions B,* 29, 283–291, https://doi.org/10.1007/s11663-998-0032-z

Xu, H. and Van Deventer, J. S. J. (2000). The geopolymerisation of alumino-silicate minerals. *International Journal of Mineral Processing,* 59 (3), 247–266, https://doi.org/10.1016/S0301-7516(99)00074-5

Yang, J., Huang, J., Su, Y., He, X., Tan, H., Yang, W. & Strnadel, B. (2019). Eco-friendly treatment of low-calcium coal fly ash for high pozzolanic reactivity: A step towards waste utilization in sustainable building material. *Journal of Cleaner Production*, 238, 117962, https://doi.org/10.1016/j.jclepro.2019.117962

Zhang, Z., Wang, H. & Provis, J.L. (2012). Quantitative study of the reactivity of fly ash in geopolymerization by FTIR. *Journal of Sustainable Cement-Based Materials*, 1 (4), 154–166, https://doi.org/10.1080/21650373.2012.752620

Zhao, J., Wang, D. & Liao, S. (2015). Effect of mechanical grinding on physical and chemical characteristics of circulating fluidized bed fly ash from coal gangue power plant. *Construction and Building Materials*, 101, 851–860, https://doi.org/10.1016/j.conbuildmat.2015.10.144

SAŽETAK

Mehanička aktivacija i geopolimerizacija letećega pepela s Tajvana

Uporaba sirovoga letećeg pepela u proizvodnji cementa i geopolimernih proizvoda ograničena je zbog njegove niske reaktivnosti. Međutim, reaktivnost letećega pepela može se povećati postupkom mehaničke aktivacije, čime se omogućuje njegova šira primjena. Ovo istraživanje usmjereno je na mehaničku aktivaciju i geopolimerizaciju letećega pepela dobivenoga iz ugljena s Tajvana. Mehanička aktivacija provedena je mljevenjem u mlinu s miješanim medijem u trajanju od 1, 3 i 5 minuta. Finoća i specifična površina znatno su se povećale već nakon 1 minute, a s daljnjim mljevenjem tek su se neznatno mijenjale. Test apsorpcije vapna pokazao je znatno poboljšanje pucolanske aktivnosti (povećanje od 130 do 140 %) nakon mehaničke aktivacije. Za sintezu geopolimera korištena je otopina natrijeva hidroksida (NaOH) koncentracije 10M kao alkalni aktivator, s omjerom tekućina / čvrsta faza od 0,35. Geopolimer koji je sadržavao pepeo mljeven 3 minute postigao je najveću tlačnu čvrstoću nakon 28 dana (36,1 MPa). Strukturna karakterizacija letećega pepela i geopolimera provedena je Fourierovom transformacijskom infracrvenom (FTIR) spektroskopijom. Promjene u FTIR spektrima letećih pepela upućivale su na to da se geopolimerizacijom stvara novi reaktivni produkt amorfni alumosilikatni gel. Na temelju snage razvoja geopolimera mehanička aktivacija povećala je reaktivnost letećega pepela, što je dovelo do brzoga vezivanja i većega razvoja čvrstoće u ranim fazama geopolimerizacije. Rezultati jasno pokazuju da je nakon mehaničke aktivacije leteći pepeo postao reaktivnija sirovina nudeći veći potencijal primjene nego što je to slučaj u njegovoj trenutačnoj upotrebi u proizvodnji cementa, izgradnji cesta i stabilizaciji tla.

Ključne riječi:
leteći pepeo, geopolimer, mehanička aktivacija, pucolanska aktivnost

Author's contribution

Fanni Dolgos (department engineer): data curation, investigation, visualization, writing – original draft and writing – review & editing. **Roland Szabó** (research fellow): conceptualization, investigation, methodology, supervision, writing – review & editing. **Wei-Ting Lin** (professor): resources and writing – review & editing. **Gábor Mucsi** (professor): conceptualization, methodology, resources, supervision and writing – review & editing.
All authors have read and agreed to the published version of the manuscript.

RGNZ/MGPB

Seed-Guided, Fault-Aware Horizon Tracking via Greedy Propagation for Geological Modelling

Rudarsko-geološko-naftni zbornik
(The Mining-Geology-Petroleum Engineering Bulletin)
DOI: 10.17794/rgn.2025.5.13

Original scientific paper

Ana Brcković[1]*, Marko Cvetković[1], Josipa Kapuralić[1], Ivan Medved[1]
[1] *Faculty of Mining, Geology and Petroleum Engineering, University of Zagreb, Pierottijeva 6, 10000 Zagreb, Croatia.*

Abstract
The Gola Gas field in the northwestern Drava Basin lies within the structurally complex petroleum system. Its sandstone reservoirs exhibit spatial heterogeneity due to deltaic fan sedimentation, necessitating robust interpretation tools. We present a fully Python-based seismic horizon extraction and 3D geological modelling workflow tailored to this challenge. The method leverages the greedy propagation method to track horizons with optimal reflector continuity, overcoming limitations of manual interpretation and traditional auto-pickers in faulted or noisy zones. An initial approximation is provided via seed-guided interpolation. Around this surface, a seismic sub-volume is extracted and flattened to align reflections. Within this volume, the greedy algorithm identifies a locally optimal path, maximizing continuity and amplitude strength. Our implementation extends the cost-based framework with slope guidance, local correlation, and robust outlier filtering to ensure geologic realism and repeatability. Surfaces are converted to 3D meshes using interpolation and smoothing, and the results are integrated into an interactive 3D geological model of the Gola field. For the first time in the research area, the model was built entirely in Python, enabling automated horizon extraction, geobody visualization, and seismic interpretation within a flexible, open-source environment.

Keywords:
seismic horizon, geological model, greedy propagation, dynamic programming, Gola field

1. Introduction

The Gola Gas field, located in the northwestern Drava Basin, lies within the "Deep Drava" petroleum system, a structurally complex zone shaped by syn-rift tectonics from the Early to Middle Miocene (**Lučić et al., 2001; Pavelić, 2001; Royden, 1988**) (see **Figure 1**). Miocene sediments, unconformably overlying Mesozoic basement, include bioclastic limestones, lithic sandstones, and fine-grained conglomerates deposited in marine and deltaic environments. In the NW part of Gola, sandy conglomerate sequences and bioclastic limestones dominate, with evidence of high-density turbidity currents depositing coarse detritus on delta slopes (**Lowe, 1982**). Gas reservoirs occur mainly in Lower and Middle Miocene clastic units at depths of 1800–3950 m (**Saftić et al., 2003**), with lateral and vertical heterogeneity reflecting variable depositional settings – from continental to shallow marine. These units exhibit significant lithological variability and reservoir quality, with bioclastic carbonates forming key gas-bearing intervals. Although some conglomerates and sandstones lack fossils, their sedimentological features suggest subaqueous deposition in a proximal prodelta to shallow marine setting (**Tadej, 2011**). The importance of the selected research area lies in the fact that the deeper subsurface is known for its gas bearing calcitic reservoirs in Early to Middle Miocene and has therefore been explored (**Tadej, 2011**). However, it has been established that the shallow, Upper Miocene reservoir sandstones of the Gola field were deposited within the sedimentary channels and lobes of prograding delta fans and are classified as stratigraphic traps (**Brcković et al., 2024**). The importance of delineating sandstone reservoirs lies in the heterogeneity of their spatial distribution and complex sedimentation in deltaic fan environment. The reservoir properties, such as porosity and permeability, have been determined using the core measurements (**Tadej, 2011**). However, due to intertwined layering of sandstones and shales, the reservoir connectivity is still to be determined and described. The reservoir sandstones have been established in well data (**Brcković et al., 2024; Tadej, 2011**). However, limitations of traditional seismic interpretation methods provides the space for the application of machine learning methods assisted interpretation. This is why the aim of the article is to present a reproducible Python-based framework combining local greedy propagation method for seismic interpretation, leading to the geological modelling of the research area. Horizons

* Corresponding author: Ana Brcković
e-mail address: ana.brckovic@rgn.unizg.hr
Received: 12 June 2025. Accepted: 26 June 2025.
Available online: 21 October 2025

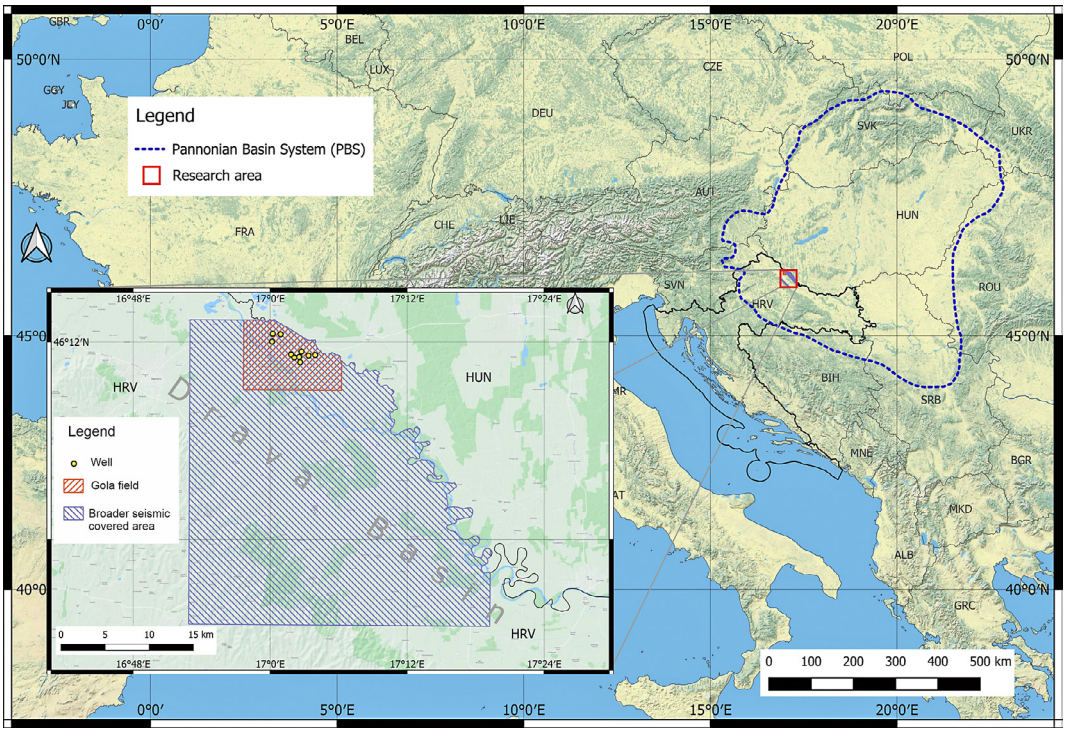


Figure 1. Geographical position of the main research area (Gola field), broader area with seismic data containing the main research area, wells position (well top data) on a map of central Europe with Panonnian Basin System borders delineated.

themselves are not isolated artifacts but are essential inputs to stratigraphic modelling and the basis for understanding reservoir architecture. To illustrate the broader geological utility of the extracted horizons, independently derived geobodies were integrated with stratigraphic surfaces to construct a more comprehensive subsurface model.

Seismic horizon interpretation is a basic step in geological modelling framework, which is essential for characterizing structural and stratigraphic frameworks in the subsurface. Traditionally, horizons are identified manually by interpreters who follow coherent reflectors in seismic sections. While this approach can provide geologically valid results, it is often subjective, labor-intensive, and limited in resolution and consistency, especially in large 3D seismic datasets or in structurally complex areas with faults, noise, or stratigraphic discontinuities (**Yan & Wu, 2021**). Recent methodological innovations have aimed to automate horizon picking to overcome these limitations. Among them, slope-based methods use local dip estimates to propagate horizon picks (**Wu & Fomel, 2018**). While robust in relatively continuous settings, they struggle with abrupt terminations of horizons such as those formed by faulting. To address this, **Wu & Fomel (2018)** proposed multigrid correlations to enhance continuity, and **Bugge et al. (2019)** introduced non-local trace matching to better capture lateral reflection relationships in discontinuous settings. A major leap in horizon extraction has come with the use of deep learning. For instance, **Bi et al. (2021)** developed a volume-to-volume convolutional neural network that estimates a relative geologic time (RGT) volume from seismic data. This RGT volume can simultaneously capture horizons and faults by treating them as isosurfaces and discontinuities, respectively. The approach leverages synthetic training data and structural similarity-based loss functions to generalize across various seismic settings (**Bi et al., 2021**). Others similarly used U-Net architectures for direct horizon extraction from seismic amplitudes, showing that neural networks can handle complex geometries and discontinuities when trained appropriately (**Tschannen et al., 2020**) . Despite the efficiency of deep learning, it remains computationally expensive, data-hungry, and often difficult to interpret or control. As a complementary alternative, dynamic programming (DP) offers an efficient, deterministic method for extracting optimal seismic paths and surfaces. **Yan & Wu (2021)** proposed a DP-based refinement method that starts from a coarse initial horizon and searches for the optimal amplitude-consistent surface within a defined window. This approach does not rely on continuous slopes alone, making it particularly adept at following reflectors through structurally disturbed zones such as faults or unconformities. Moreover, it integrates user guidance through sparse control points or seed values, which enhances interpretability and flexibility (**Yan & Wu, 2021**). In contrast to deep networks, dynamic programming is not data-driven but instead exploits local correlation structure and global optimization to ensure geological real-

ism. It is computationally lightweight and interpretable, making it a valuable tool for semi-automatic workflows or for use alongside machine learning where ground truth is limited. By combining these approaches – traditional slope estimation, non-local matching, and dynamic programming – modern seismic interpretation frameworks can achieve unprecedented precision and reliability in horizon tracking. This enables more robust geobody extraction, reservoir modelling, and subsurface analysis, especially in complex geologies where manual or purely slope-based methods fail to trace seismic horizons adequately.

Recent research in 3D geological modelling reveals a strong trend toward combining open-source tools, machine learning, and structured geological logic. Many studies focus on hierarchical or stochastic modelling strategies, often relying on geological rules or learning from data (**De La Varga et al., 2019; Feng et al., 2024; Marquetto et al., 2024**). A wide range of studies emphasize hybrid methodologies that combine traditional interpretation with computational models, often using decision trees, support vector machines, or unsupervised clustering to improve reservoir prediction and structural modelling accuracy (**Chen et al., 2024; Otmane et al., 2025**). While **Shahbazkia et al. (2025)** further demonstrated the robustness of hybrid approaches like Quick Invariant Signature and Dynamic Time Warping (DTW) for handling noisy seismic data. These papers show a broader shift toward modular, flexible modelling workflows. Our approach in this article is simple, modular, deterministic and fully Python-based. It combines interpretable seed-guided surface extraction with structured hexahedral meshing. Our emphasis was on bridging semi-automated interpretation with geobody extraction and volumetric mesh creation, and doing so entirely with accessible, open-source libraries.

2. Materials and methods

The methodology implemented for seismic horizon extraction implements the greedy propagation method (GP) to refine or generate geologically consistent surfaces that follow seismic reflectors with optimal continuity. This approach was motivated by the limitations of both manual interpretation, which is subjective and time consuming, and traditional automated methods, which often struggle in the presence of structural discontinuities like faults or noisy reflections. Traditional methods include but are not limited to the methods such as Maximum Amplitude Picking, Zero-Crossing or Peak/Through Picking, Tracking Using Instantaneous Attributes and Dip-Steered Auto-picking (Gradient-Based), which have been tested throughout our research as well (see **Table 1**). The proposed methodology applies a greedy algorithm in line with principles of greedy optimization strategies (**Lu et al., 2016; Nie et al., 2023**).

For seismic horizon picking in Gola field, several seismic attributes were utilized to enhance reflector continuity and improve the reliability of the greedy approach. The core attribute used during tracking was the seismic amplitude, specifically focusing on peak or trough continuity, depending on reflector polarity. However, amplitude alone can be ambiguous in areas of structural complexity, so this was supplemented with the instantaneous phase and local similarity (correlation) attributes to guide the algorithm through low signal-to-noise regions. Amplitude values were extracted directly from the seismic cube and used to identify local maxima or minima as target reflection events. To improve lateral continuity, local similarity (computed via a windowed normalized cross-correlation) was applied in the inline and crossline directions. This measure acted as a confidence mask during DP pathfinding, preferring paths with consistent waveform shapes. Slope estimates were optionally calculated using gradient filters, allowing the algorithm to enforce realistic dip constraints, especially important near faults. All attribute calculations and tracking were implemented in Python, allowing full reproducibility and seamless integration with the automated interpretation framework. These attributes collectively ensured robust and geologically valid horizon extraction even in structurally deformed or noisy seismic sections. The process begins with an initial approximation of the horizon, typically interpolated from sparse seed points or derived through a separate coarse tracking mechanism. This preliminary surface does not need to be precise; it merely guides the subsequent refinement. Around this surface, a sub-volume of seismic amplitudes is extracted, which is flattened relative to the initial horizon to align local reflections. Within this sub-volume, the dynamic programming algorithm searches for a path that maximizes the global consistency of reflection events, typically focusing on peaks, troughs, or zero crossings, while accounting for local continuity and amplitude strength. The DP algorithm ensures a globally optimal solution by avoiding local minima that might mislead simpler tracking methods. A crucial strength of this approach lies in its ability to follow reflectors through complex structures, including faults and noisy regions, by treating horizon tracking as a global optimization problem. This is supported by the previous work by **Yan & Wu (2021)**, who demonstrated how dynamic programming can overcome the shortcomings of slope-based and correlation-based horizon tracking. Their formulation interprets the horizon as an optimal path through a 2D or 3D cost function, where the cost is inversely related to desirable seismic features, such as high correlation or strong amplitude alignment. Our implementation extends this idea by also incorporating local slope guidance, where available, and by using efficient neighbourhood correlation schemes to provide local predictive depth shifts. The method has been enhanced to preserve determinism, ensuring repeatable

Table 1. Results of modification for automatic horizon picking functions, with increasing version number meaning better geological plausibility

Version	Added Method	Core Feature	Advantage
v0	Max amplitude	Simple peak detection on each trace	Fastest and simplest baseline method
v1	Slope based	Picks guided by local structural dip	Improves structural realism and continuity
v2	DTW based	Cross-trace reflector alignment	Adapts to variable and non-flat reflectors
v3	DTW based refined	Local peak alignment refined per trace	Faster and more geologically realistic than full DTW
v4	Median filter	Post-processing smoothing	Produces smoother and cleaner horizons
v5	Median + Gaussian filter	Dual-pass smoothing (median + Gaussian)	Further noise suppression and continuity improvement
v5.1	+ Local continuity refinement	Adjusts picks based on 3×3 neighbourhood if deviation > threshold (e.g. 15 m)	Respects geological trends; tolerant to structural breaks
v5.2	Attribute masking (chaos-guided)	Attribute thresholding to mask noisy picks	Suppresses chaotic or structurally incoherent reflectors
v5.3	Attribute + slope guidance	Combines slope steering with attribute masking	Better tracking through dipping zones and faults
v6.0	Dynamic programming (DP)	Global trace-by-trace optimization with amplitude + smoothness cost	Enforces horizon continuity across long lateral distances
v6.1	DP + slope jump limit	Adds constraint on steep lateral depth jumps	Improves tracking in high-dip zones; avoids aliasing
v7	Local search window	Narrows DP search to region near previous best pick	Greatly reduces compute time; more robust to vertical noise
v8	Outlier filtering + surface mesh	Removes statistical outliers and interpolates smooth surface	Converts raw picks into clean, interpretable 3D surfaces
v9	Greedy propagation seed-based tracking (1D)	Tracks from seed in single direction using local peaks	Anchors horizon to known markers (e.g. well tops); improves realism
v10	Greedy propagation seed-based tracking (2D)	Expands seed tracking to via local amplitude search	Propagates surfaces consistently from sparse seed input
v11	Seed + correlation + slope (GP)	Combines seed guidance, slope prediction, and trace similarity matching	Produces geologically plausible, slope-consistent, seed-anchored horizon surfaces

results, and to filter out physically implausible outliers in the resulting surface. Additionally, by transforming the extracted horizon into a point cloud and applying robust outlier filtering and smoothing (via interpolation and Gaussian filtering), we generate a final continuous surface that is both geologically plausible and visually consistent. Complementing this, recent advances in deep learning-based approach-es, as presented by **Bi et al. (2021)**, offer a data-driven alternative using Relative Geologic Time (RGT) estimation. These methods predict RGT volumes from seismic data using encoder-decoder neural networks, allowing simultaneous interpretation of horizons and faults. While such methods are powerful, especially when large training datasets are available, our dynamic programming method provides a transparent, interpretable, and user-guided alternative that does not rely on black-box models or extensive training data – making it particularly suitable for exploratory interpretation or projects with limited labelled datasets. Together, these methodologies establish a robust, reproducible, and interactive horizon extraction workflow that balances automation with interpretability and adapts well to varying geologic scenarios and data qualities.

The starting point of this workflow is the function that extracts horizon (see **Appendix A.1**), which implements a robust seed-based greedy algorithm. It propagates from one or more user-defined seed points, each defined by an inline, crossline, and depth value, and traverses neighboring traces to determine the best-matching horizon location. The match is based on correlation of trace segments within a depth window to ensure that the local waveform shape is preserved. Importantly, the method does not match each trace to its immediate neighbor. Instead, it compares all segments to the reference pattern taken from the seed trace, promoting geological consist-

ency across a larger area. Local slope estimates help steer the search direction to follow natural reflector trends, while a depth penalty discourages large vertical jumps, preventing the algorithm from locking onto strong but unrelated reflectors. These combined strategies ensure that the extracted horizon honors both signal similarity and geological structure. After the horizon is extracted, it is typically noisy or contains small-scale deviations caused by trace-level inconsistencies or interference. The next step uses the filtering function to identify and remove extreme outlier values in the horizon surface. This step uses a z-score analysis to quantify how much each depth value deviates from the statistical trend of the rest of the surface. Traces that deviate beyond a user-defined threshold are masked, removing the influence of extreme values without erasing genuine geological variation. This smoothed horizon can now be safely used for surface reconstruction. To move from a scattered set of horizon points to a continuous surface, the function was defined (see **Appendix A.2**) that converts the 2D DataArray (with inline, crossline, and depth) into a point cloud. It can apply an optional amplitude threshold filter to reject regions with low signal strength, reducing noise propagation into the surface. The resulting dataset contains structured coordinates of interpreted horizon points, which form the basis for gridding and smoothing. The core gridding and smoothing are performed with smoothing function (see **Appendix A.3**) that transforms irregular horizon point clouds into continuous surfaces. This function supports flexible interpolation methods and applies rigorous quality control, including filtering by z-score and global depth deviation. Users can opt to fill missing gaps using the nearest-neighbor interpolation and apply a Gaussian smoothing filter to gently remove noise while preserving regional structure. This creates clean, geologically plausible surfaces that are ready for visualization, modelling, or comparison with known horizons.

The seismic interpretation workflow developed here revolves around the automation and enhancement of one of the most fundamental tasks in subsurface characterization, which is horizon mapping. Through numerous modifications (see **Table 1**), it was determined which was the best approach for horizon extraction in our research area. This workflow is structured to bring repeatability, robustness, and geological plausibility into the interpretation process by combining dynamic programming, local dip guidance, amplitude-based correlation, and surface smoothing techniques. The process ultimately produces high-confidence horizon surfaces that reflect subsurface structure with minimal manual intervention and are suitable for subsequent geological modelling. To create geological model and interactive visualization workflow in Python, a combination of specialized scientific, geospatial, and visualization packages was used (see **Appendix B**). Data was uploaded and processed by using mostly numpy (**Harris et al., 2020**), xarray (**Hoyer & Hamman, 2017**), pandas (**The pandas development team, 2024**) and scipy (**Virtanen et al., 2020**). Rasterio was used for reading and interpreting the DMR surface from GeoTIFF format (**Gillies et al., 2013**). To build a 3D geological model, a structured grid was created by layering known surfaces from top to bottom: starting with the digital elevation surface (DMR), followed by a sequence of interpreted horizon surfaces, and finally a user-defined bottom surface. A regular grid was constructed horizontally (X and Y directions), and for each layer, the corresponding depth (Z value) was calculated using surface data. Between each pair of adjacent surfaces, the model volume was filled to represent realistic geological intervals. This layered grid structure reflects the true geometry of the subsurface and can serve as a foundation for simulations, property modelling, or further geological analysis. For the interactive geological model, pyvista was utilized (**Sullivan & Kaszynski, 2019**).

Together, these functions form a modular and adaptable workflow for seismic horizon interpretation. The workflow emphasizes clarity and determinism, with each step explicitly grounded in seismic amplitude patterns and geological structure. It is equally suited for isolated surface extraction or large-scale horizon mapping. Compared to manual picking, which is time-consuming, user-biased, and often inconsistent if multiple people are working on a bigger area, this approach provides rapid, reproducible, and explainable results in Gola field area and even in the wider are of research (see **Figure 1**). This methodology has been validated on the wider area of our Gola field, making it a powerful foundation for modern geological modelling.

In order to reliably showcase the spatial distribution of extracted horizon surfaces, a geological model of the research area has been built.

3. Results

3.1. Greedy propagation guided horizon extraction

The proposed methodology of local greedy propagation initially based on a dynamic programming approach, has been proven to reliably and semi-automatically extract seismic horizons throughout the seismic volume. The goal was to extract seismic horizon surfaces in order to build an interactive 3D geological model of the research area using free and open-source Python tools.

The development of the horizon extraction workflow followed a stepwise refinement from simple amplitude-based picking to more geologically realistic and robust methods (see **Table 1**). The earliest versions (v0–v1) focused on trace-wise strategies such as selection of maximum amplitude or inclusion of local dip information to follow structurally plausible trends. While these methods offered fast results, they were structurally inaccurate

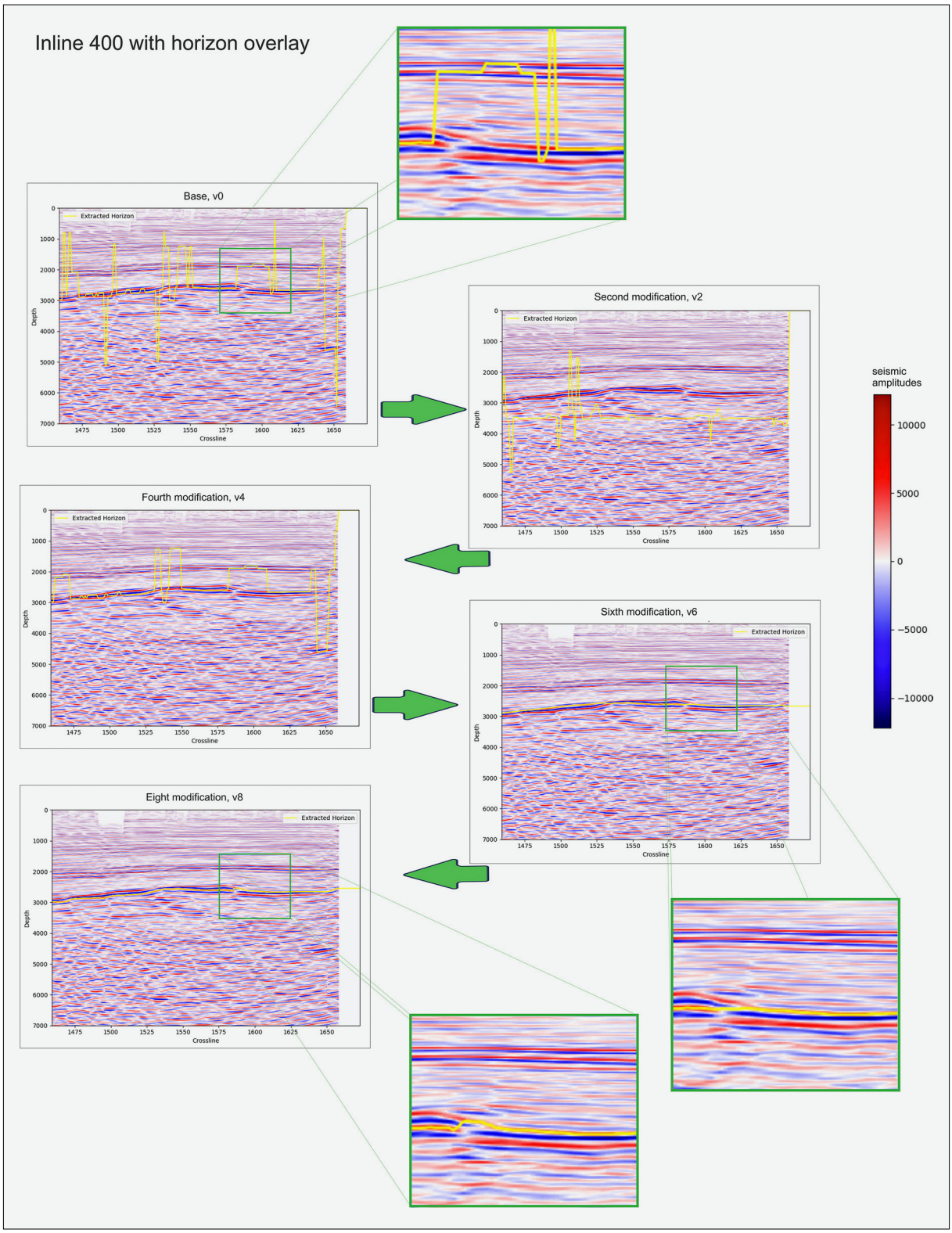


Figure 2. Results of modification to automatic horizon picking functions with some of the modification (versions) from **Table 1** being shown. Higher version numbers show better geological reliability in an automatic horizon extraction (more observable on the magnified panels in green).

and unreliable. Since they were based on the amplitude values and with no restraint, the horizon line was visibly connecting similar amplitude strengths on different locations and depths which lead to unexpected peaks in the line (see **Figure 1**). Subsequent versions (v2–v3) utilized Dynamic Time Warping (DTW) to improve reflector alignment across traces and better handle lateral reflector variability, while versions v4–v5 incorporated

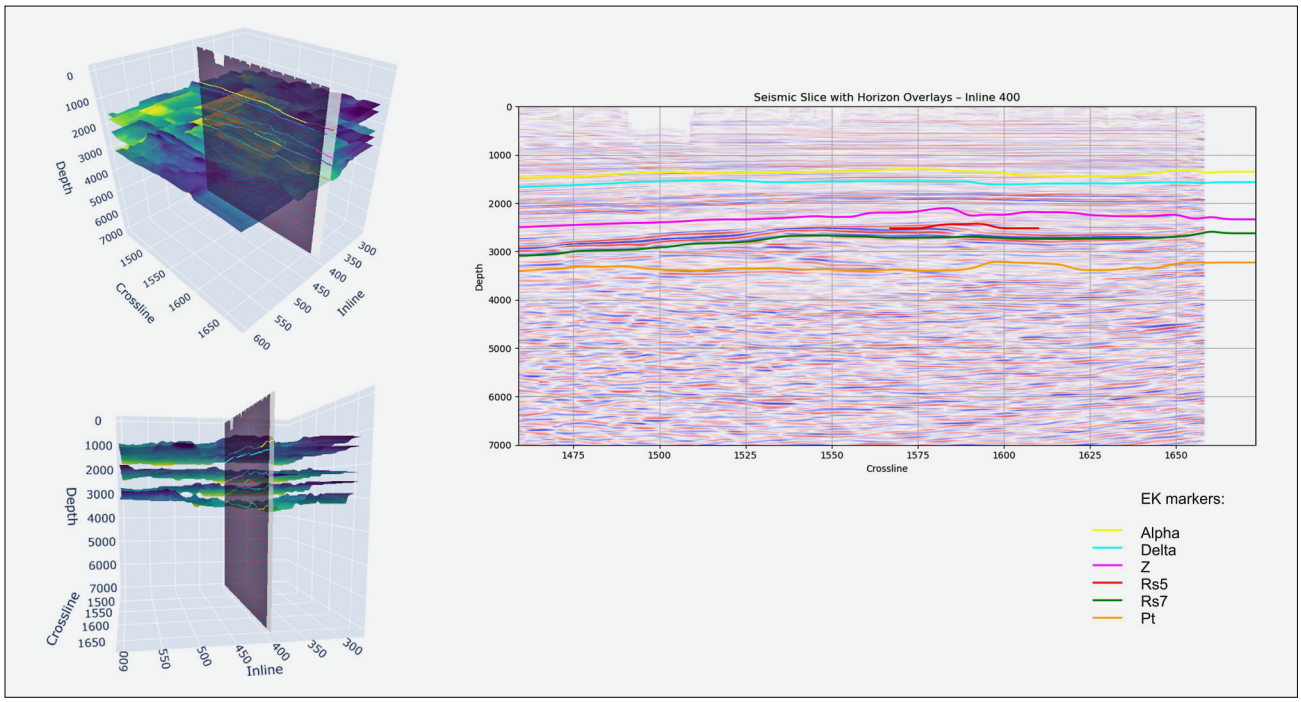


Figure 3. Automatically picked horizons that represent different well tops spatially propagated over the seismic volume

smoothing and attribute-based masking to enhance surface continuity and suppress noise from potentially chaotic or faulted zones. The improvement in horizon tracking seemed more stable but the depth was translated and thus the horizon detection was unreliable (see **Figure 1**). Subsequent versions (v6–v8) introduced dynamic programming (DP) as a global optimization strategy, in which the horizon was treated as a path across traces that minimizes a cost function combining amplitude and smoothness. DP proved to be a powerful tool for enforcing lateral continuity and global structural coherence. It greatly reduced the erratic behaviors seen in previous versions and the selected horizon is tracked well (see **Figure 1**). However, a critical limitation persisted: DP has no notion of geological relevance. It finds the best path, based on signal, but not necessarily the desired reflector. Seismic data often contains multiple reflectors of similar amplitude, and not all of them are stratigraphically or reservoir relevant. Without a way to guide DP toward a specific reflection of interest, the method could select unintended features, especially in layered or noisy intervals. This challenge was resolved by shifting to a seed-guided approach (v9–v11), which means that one or more known horizon points can be defined, either from well data or from visual inspection of strong reflectors. The final method (v11) implemented greedy seed-based propagation. From each seed point, the method expands outward by choosing the best-matching depth position in adjacent traces, guided by a reference pattern and informed by local dip. This design not only respects structural trends but ensures that only the desired reflector is followed, solving the ambiguity that DP struggled with. This ensured the possibility of extracting horizons for different well tops from well data, in total six of them (see **Figure 2**).

The decision to adopt greedy local propagation over global optimization was grounded in both methodological and practical considerations. While DP ensures global continuity, it is computationally expensive, especially in 3D volumes or large 2D sections, and it lacks the flexibility to adapt to faults, reflector terminations, or seed constraints. In contrast, greedy propagation is computationally lightweight and directionally flexible. Just by comparing the time needed for execution of the code for one (same) horizon extraction, it is visible how much easier the GP approach is for the end user (in our case around ten times faster). By expanding from seeds using local rules and updating only what is needed, it achieves high performance and scalability, especially when working in interactively defined zones. It also adapts naturally to discontinuities, when a fault or reflector break is encountered, correlation falls below a set threshold, and the propagation halts. This makes the method fault-aware without requiring explicit fault detection. This is a key strength, as many workflows either ignore faults or require a separate, often complex, fault-picking step. This is especially interesting for our research, as there are only few known and detected faults, while discontinuities in reflections are usually due to the stratigraphical and structural complexity of the area.

To ensure the reliability of the extracted horizons, a thorough visual validation process was carried out using an interactive 2D seismic viewer (see **Figure 3, Figure 4**). This custom-built tool allowed for a detailed inspection of both inline and crossline slices, overlaid with the interpreted horizon surfaces (see **Appendix A.4**). Each

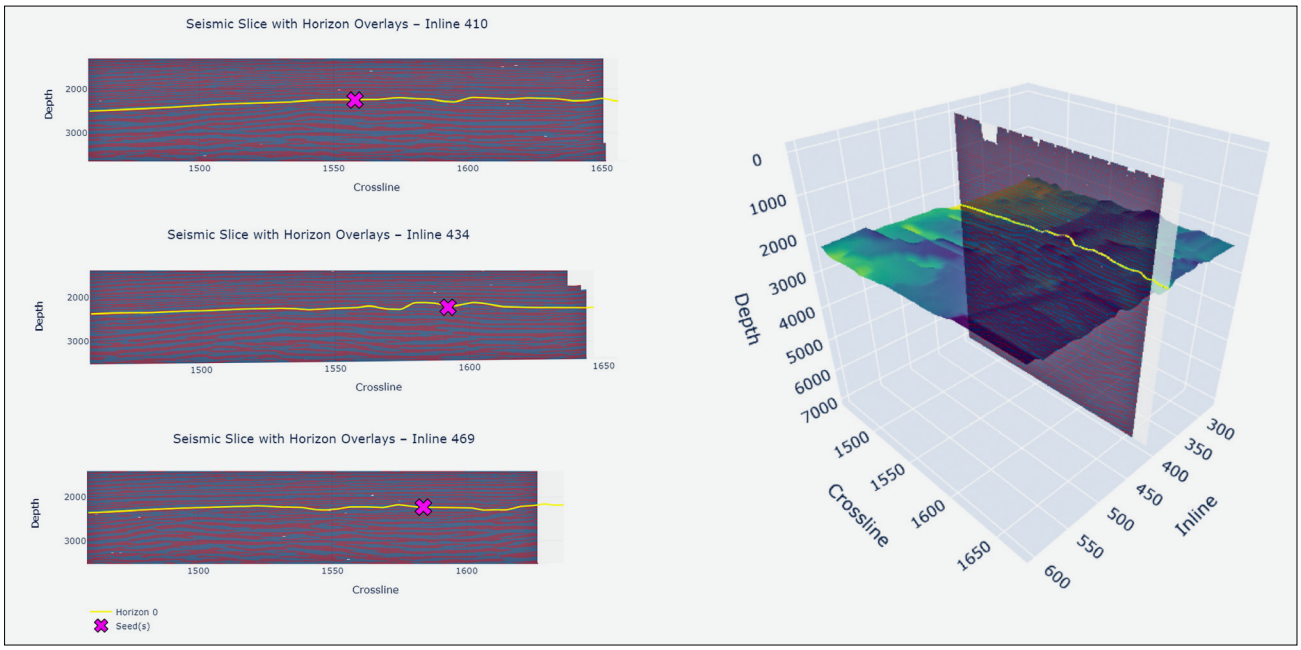


Figure 4. Horizon Z picking results – tracking was done based on dynamic programming (DP) with the initial seeds from well data (well top position). The results were visually validated and tracking is within the seismic resolution as well as within the expected manual interpretation of the experts.

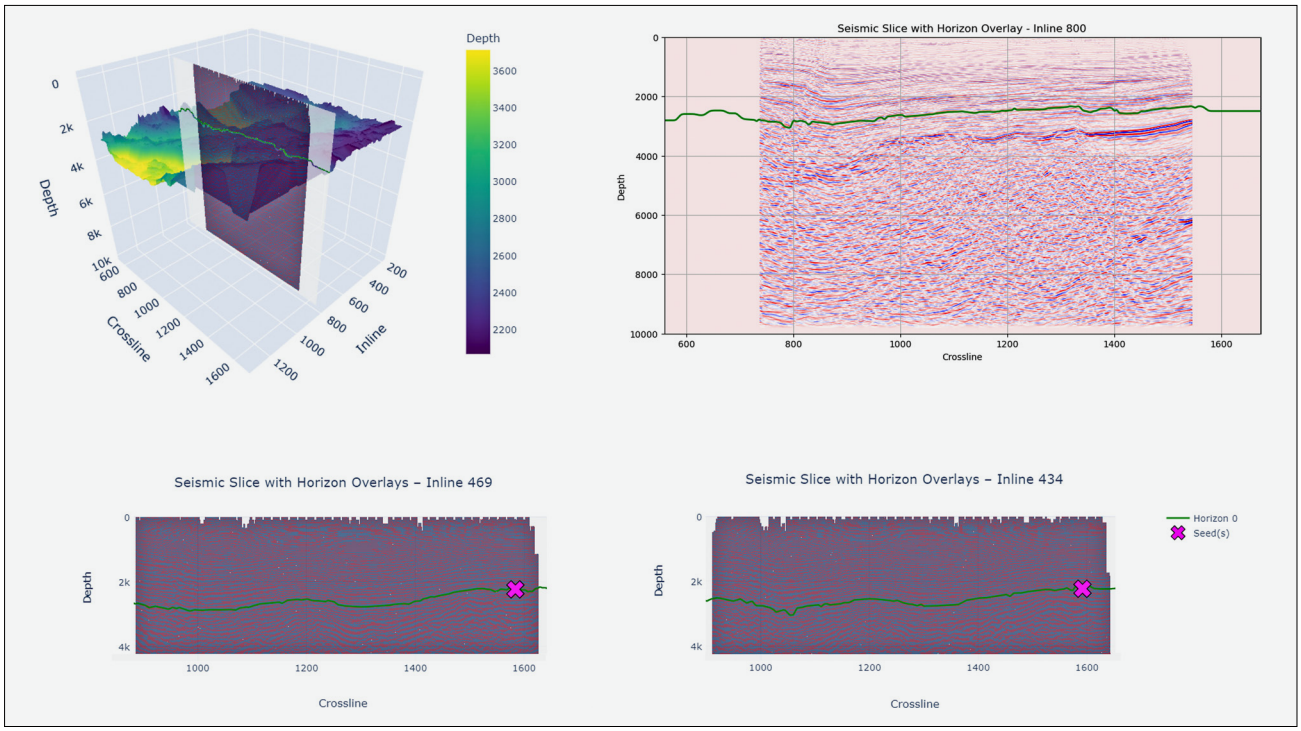


Figure 5. Horizon Z picked in a wider area that includes our research area, Gola field

horizon derived from well tops was tracked and systematically verified across the full seismic volume. By interactively scrolling through inlines and crosslines, interpreters were able to confirm that the extracted surfaces consistently followed the expected reflector patterns and aligned with geological features observed in the well log data. This visual quality control step was crucial in identifying and correcting any inconsistencies, and it reinforced the accuracy and geological realism of the interpretation workflow.

Using the same sparse set of seed points (between one and five seeds per desired horizon) derived from the test dataset, the proposed methodology successfully scaled to a broader seismic volume that encompassed the origi-

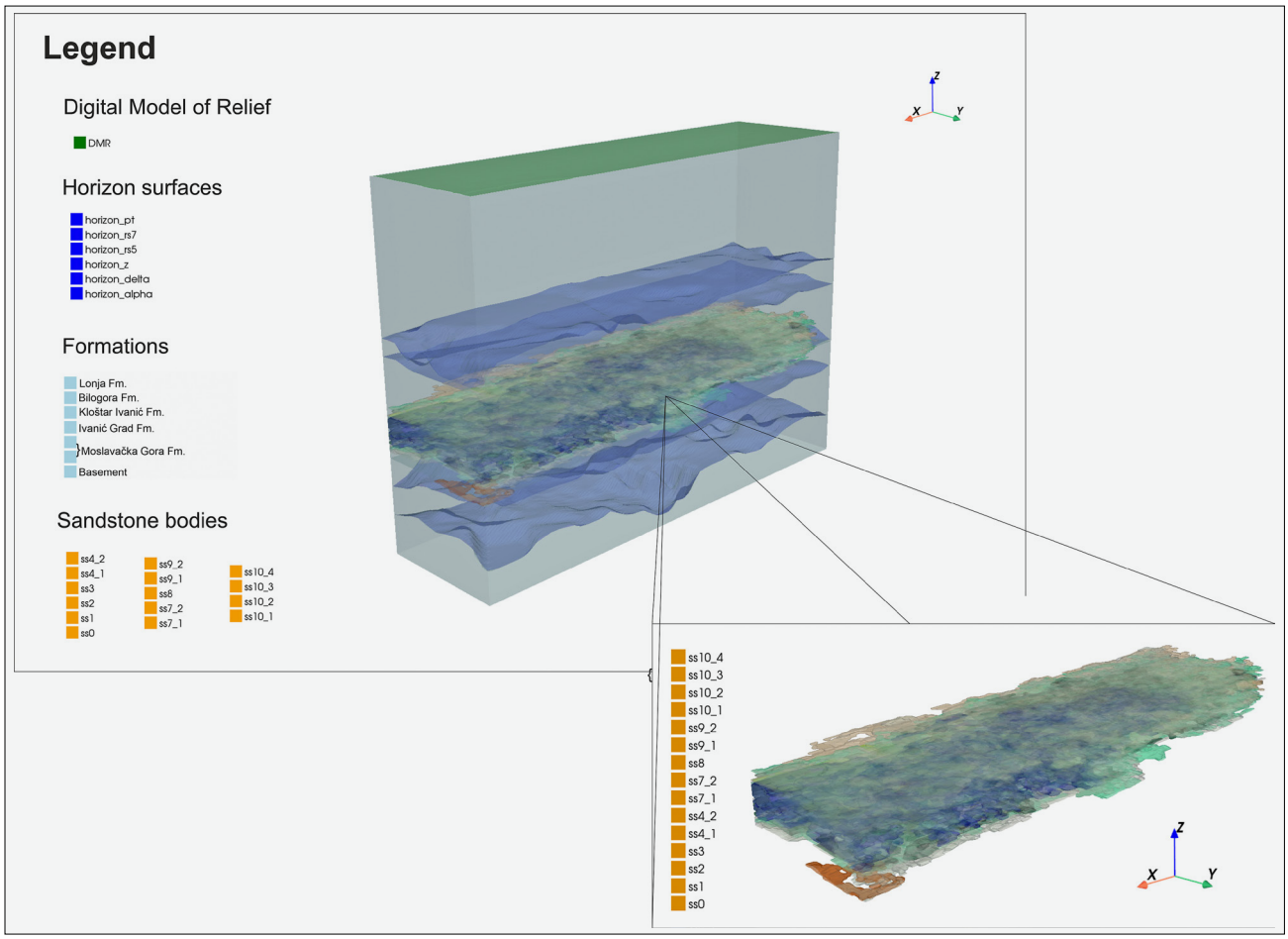


Figure 6. Geological model of the Gola field retrieved with a full python framework, containg DMR (uploaded), horizon surfaces (automatically extracted with dynamic programming) and 14 geobodies presenting potential reservoir sandstones with different petrophysical properties (extracted with unsupervised learning methods (unpublished manuscript).

nal area (see **Figure 1, Figure 4**). Despite being calibrated on a smaller subset (Gola field, 7 x 7 x 7 km seismic volume), the greedy seed-based horizon tracking approach maintained geological consistency and structural coherence when applied to the larger dataset (broader seismic covered area containing Gola field, 25 x 25 x 10 km seismic volume) (see **Figure 1**). This outcome highlights the method's robustness and generalizability. It demonstrates that a carefully selected seed, whether from well data or visual interpretation, can guide horizon extraction effectively across extended spatial extents, even when the seeds have local distribution. Such transferability is particularly valuable for regional interpretation, where limited ground truth exists but broader coverage is desired.

3.2. Interactive geological model (Python-based)

One of the key outcomes of this work is the construction of an interactive 3D geological model of the research area (Gola field) (see **Figure 5**). This model integrates multiple data sources and is built on the extracted seismic horizon surfaces from this study, publicly available Digital Model of Relief (DMR) for topographic context, and geobodies previously extracted through semi-automated analysis (unpublished manuscript). These constructive elements (horizons, geobodies) were processed, interpreted, and visualized using fully open-source Python tools. Unlike the usual modelling that relied on proprietary software or merely visualization of the externally prepared models, this project demonstrates a complete open-source workflow from uninterpreted 3D seismic data to geological insight. The model provides an intuitive, high-resolution view of the subsurface architecture while the Python-based workflow offers established workflow for new data generation and insertion (see **Appendix B**). This is particularly valuable given that the area remains actively investigated, with limited previous modelling attempts. By offering both transparency and interactivity, the model enhances accessibility for geoscientists and stakeholders, while also giving a foundation for future updates as new data become available.

4. Discussion

The developed methodology is centered around a semi-automated, seed-guided horizon tracking function

that applies a greedy expansion logic (**Lu et al., 2016**). It mimics the cognitive process of human interpreters by matching local waveform patterns and following anticipated reflector dips. Specifically, the function extracts a waveform pattern from a seed location and performs trace-by-trace pattern matching using correlation within a defined depth window. A vertical deviation penalty ensures geological continuity, while optional slope steering biases the vertical search window to favor structurally consistent reflectors. Faults are not explicitly detected as some methodology suggestes (**Nayak & Nayak, 2025**), yet the method exhibits natural fault-tolerance.

Discontinuities are respected due to the local nature of the correlation window, a strict minimum correlation threshold, and the use of a visited mask to prevent backtracking or looping. This reflects how human interpreters hesitate or revise their interpretations near fault zones.

Originally motivated by the dynamic programming (DP) principle, the implementation evolved into a greedy expansion approach for both memory efficiency and geophysical realism. This concept has also been emphasized in seismic applications of dynamic programming by **Yan & Wu (2021)** and in general algorithmic optimization strategies like those described by **Goldner et al. (2013)** and **Nie et al. (2023)**. The greedy approach focuses only on reflectors of interest, with no need to explore the entire volume. This stepwise evolution of the method is also reflected in the functional versions developed during this study. Early versions relied on basic amplitude picking and slope guidance. The final version implemented a greedy seed-guided expansion with slope and pattern constraints that offer the best balance between interpretive control, geological consistency, and computational efficiency. The visual validation step ensured that each surface consistently honored the original seed and followed the targeted log marker or reflector over the full seismic volume. Notably, the method generalized well, even when seeds were placed in a smaller test dataset, they were successfully used to extract geologically viable horizons in a much larger surrounding volume.

Strengths of the workflow lie in its reproducibility, interpretability, and full automation potential. With only a single seed, surfaces can be propagated through large volumes, as can be seen in our results. First, we adapted the methodology for Gola field and the results were geologically plausible, especially given the seismic resolution that is around 30 m. Similar integration of automated horizon tracking into regional stratigraphic frameworks has been explored in recent works as well (**Chang et al., 2024; Feng et al., 2024; Marquetto et al., 2024**). The method is especially attractive to both academia and industry due to its ability to run interactively in modern Python environments. The integration with geobody extraction (unpublished manuscript), 3D surface reconstruction, and topographic data further allows complete subsurface modelling, all within a free and open framework. However, some challenges could be acquainted. They are primarily related to parameter tuning (e.g. depth window, correlation threshold, dip weighting), which can impact stability in structurally complex or noisy areas, but are easily modified. In regions with multiple competing reflectors or low signal-to-noise ratios, the method may still require expert supervision to adjust parameters or validate seed placement. Ambiguity in such areas is inherent to seismic interpretation and not unique to this method.

Ultimately, an interactive geological model was built, constructed entirely using open-source tools, from surface horizons to previously extracted geobodies. This model represents the first fully open-source 3D geological interpretation of the Gola field area, offering valuable insights for research, education, and ongoing industry exploration.

5. Conclusions

This study presents a fully open-source workflow for semi-automatic seismic interpretation and 3D geological modelling, applied for the first time to the Gola gas field. At its core is a seed-guided horizon extraction method that mimics human interpretation logic by applying local pattern matching, vertical continuity constraints, and optional dip steering. The approach balances geological realism with computational efficiency through a greedy expansion algorithm, as a robust, scalable tool. The final implementation successfully tracks geologically consistent surfaces through structurally complex zones without requiring full-volume analysis.

Our results show that even a single seed can initiate reliable surface propagation across large seismic volumes, enabling reproducible, geologically plausible interpretation. When combined with geobody extraction, topography, and interactive visualization, the method forms a complete modelling workframe. Although some parameter tuning is still necessary in complex geological settings, this limitation is minor thanks to the method's transparency and adaptability. The resulting interactive 3D model marks the first fully open-source structural representation of the Gola field and serves as a valuable resource for research, education, and exploration.

Acknowledgement

The authors would like to thank INA-Industrija nafte d.d. for providing data. All the analyses, interpretation and modelling have been done using Python.

Funding

This research received no external funding.

6. References

Bi, Z., Wu, X., Geng, Z., & Li, H. (2021). Deep Relative Geologic Time: A Deep Learning Method for Simultaneously

Interpreting 3-D Seismic Horizons and Faults. *Journal of Geophysical Research: Solid Earth*, 126(9). https://doi.org/10.1029/2021JB021882

Brcković, A., Orešković, J., Cvetković, M., & Marić-Đureković, Ž. (2024). Enhancing the Understanding of Subsurface Relations: Machine Learning Approaches for Well Data Analysis in the Drava Basin, Pannonian Super Basin. *Applied Sciences (Switzerland)*, 14(14). https://doi.org/10.3390/app14146039

Bugge, A. J., Lie, J. E., Kjelsrud Evensen, A., Faleide, J. I., & Clark, S. (2019). Automatic extraction of dislocated horizons from 3D 2 seismic data using non-local trace matching 3 4 Right-running head: Seismic horizon correlation. http://library.seg.org/

Chang, P. Y., Puntu, J. M., Lin, D. J., Amania, H. H., Chen, W. S., & Lin, A. T. shun. (2024). Application of machine learning and resistivity measurements for 3D apparent geological modeling in the Yilan plain, Taiwan, at the SW Tip of the Okinawa trough. *Geoscience Letters*, 11(1). https://doi.org/10.1186/s40562-024-00339-5

Chen, Z., Wang, R., Xu, B., & Zhu, J. (2024). Research on Oil and Gas-Bearing Zone Prediction and Identification Based on the SVD–K-Means Algorithm – A Case Study of the WZ6-1 Oil-Bearing Structure in the Beibu Gulf Basin, South China Sea. *Energies*, 17(22). https://doi.org/10.3390/en17225771

De La Varga, M., Schaaf, A., & Wellmann, F. (2019). GemPy 1.0: Open-source stochastic geological modeling and inversion. *Geoscientific Model Development*, 12(1), 1–32. https://doi.org/10.5194/gmd-12-1-2019

Feng, Y., Wen, G., Shang, J., Wen, S., & Wu, B. (2024). Research on 3D geological modeling based on boosting integration strategy. *Ore Geology Reviews*, 171. https://doi.org/10.1016/j.oregeorev.2024.106157

Goldner, E., Silva, P. M. ´ A., & Gattass, M. (2013). 2D Horizon Tracking Using Dynamic Programming.

Harris, C. R., Millman, K. J., van der Walt, S. J., Gommers, R., Virtanen, P., Cournapeau, D., Wieser, E., Taylor, J., Berg, S., Smith, N. J., Kern, R., Picus, M., Hoyer, S., van Kerkwijk, M. H., Brett, M., Haldane, A., del Río, J. F., Wiebe, M., Peterson, P., Gérard-Marchant, P., Sheppard, K., Reddy, T., Weckesser, W., Abbasi, H., Gohlke, C.,… Oliphant, T. E. (2020). Array programming with NumPy. In Nature (Vol. 585, Issue 7825, pp. 357–362). *Nature Research*. https://doi.org/10.1038/s41586-020-2649-2

Hoyer, S., & Hamman, J. (2017). xarray: N-D labeled Arrays and Datasets in Python. *Journal of Open Research Software*, 5(1), 10. https://doi.org/10.5334/jors.148

Lowe, D. R. (1982). Sediment gravity flows: II: Depositional models with special reference to the deposits of high-density turbidity currents. *Journal of Sedimentary Petrology*, 52, 279–297.

Lu, G., Xiong, Y., Ding, C., & Wang, Y. (2016). An optimal schedule for urban road network repair based on the greedy algorithm. PLoS ONE, 11(10). https://doi.org/10.1371/journal.pone.0164780

Lučić, D., Saftić, B., Krizmanić, K., Prelogović, E., Britvić, V., Mesić, I., & Tadej, J. (2001). The Neogene evolution and hydrocarbon potential of the Pannonian Basin in Croatia. *Marine and Petroleum Geology*, 18(1), 133–147. https://doi.org/10.1016/S0264-8172(00)00038-6

Marquetto, L., Jüstel, A., Troian, G. C., Reginato, P. A. R., & Simões, J. C. (2024). Developing a 3D hydrostratigraphical model of the emerged part of the Pelotas Basin along the northern coast of Rio Grande do Sul state, Brazil. *Environmental Earth Sciences*, 83(10). https://doi.org/10.1007/s12665-024-11609-y

Nie, J., Graizer, V., & Seber, D. (2023). A greedy algorithm for wavelet-based time domain response spectrum matching. *Nuclear Engineering and Design*, 410. https://doi.org/10.1016/j.nucengdes.2023.112384

Nayak, B., & Nayak, P. (2025). Optimal fault detection from seismic data using intelligent techniques: A comprehensive review of methods. *Journal of Groundwater Science and Engineering*, 13(2), 193–208. https://doi.org/10.26599/JGSE.2025.9280049

Otmane, M., Imtiaz, S., Jaluta, A. M., & Aborig, A. (2025). Boosting Reservoir Prediction Accuracy: A Hybrid Methodology Combining Traditional Reservoir Simulation and Modern Machine Learning Approaches. *Energies*, 18(3). https://doi.org/10.3390/en18030657

Pavelić, D. (2001). Tectonostratigraphic model for the North Croatian and North Bosnian sector of the Miocene Pannonian Basin System. *Basin Research*, 13(3), 359–376. https://doi.org/10.1046/j.0950-091x.2001.00155.x

Royden, L. (1988). Late Cenozoic tectonics of the Pannonian Basin system. In L. H. Royden & F. Horvath (Eds.), The Pannonian Basin: A study in basin evolution. *AAPG Memoir* 45. AAPG.

Saftić, B., Velić, J., Sztanó, O., Juhász, G., & Ivković, Ž. (2003). Tertiary subsurface facies, source rocks and hydrocarbon reservoirs in the SW part of the Pannonian Basin (Northern Croatia and south-western Hungary). *Geologia Croatica*, 56(1), 101–122. https://doi.org/10.4154/232

Gillies, S. and others. (2013). Rasterio: geospatial raster I/O for Python programmers. https://github.com/rasterio/rasterio

Shahbazkia, H. R., Khosravani, H. R., Pulatov, A., Hajimani, E., & Kiazadeh, M. (2025). A Comprehensive Comparative Study of Quick Invariant Signature (QIS), Dynamic Time Warping (DTW), and Hybrid QIS + DTW for Time Series Analysis. *Mathematics*, 13(6). https://doi.org/10.3390/math13060999

Sullivan, C., & Kaszynski, A. (2019). PyVista: 3D plotting and mesh analysis through a streamlined interface for the Visualization Toolkit (VTK). *Journal of Open Source Software*, 4(37), 1450. https://doi.org/10.21105/joss.01450

Tadej, J. (2011). Evolution of the Early and Middle Miocene sedimentary environments in the north-western part of the Drava depression based on the well analysis data (Razvoj ranomiocenskih i srednjomiocenskih taložnih okoliša sjeverozapadnog dijela Dravske depresije na temelju podataka iz dubokih bušotina). *Faculty of Mining, Geology and Petroleum Engineering*.

The pandas development team. (2024). pandas-dev/pandas: Pandas. *Zenodo*.

Tschannen, V., Delescluse, M., Ettrich, N., & Keuper, J. (2020). Extracting horizon surfaces from 3D seismic data

using deep learning. *Geophysics*, 85(3). https://doi.org/10.1190/geo2019

Virtanen, P., Gommers, R., Oliphant, T. E., Haberland, M., Reddy, T., Cournapeau, D., Burovski, E., Peterson, P., Weckesser, W., Bright, J., van der Walt, S. J., Brett, M., Wilson, J., Millman, K. J., Mayorov, N., Nelson, A. R. J., Jones, E., Kern, R., Larson, E., … Vázquez-Baeza, Y. (2020). SciPy 1.0: fundamental algorithms for scientific computing in Python. *Nature Methods*, 17(3), 261–272. https://doi.org/10.1038/s41592-019-0686-2

Wu, X., & Fomel, S. (2018). Least-squares horizons with local slopes and multi-grid correlations. http://library.seg.org/

Yan, S., & Wu, X. (2021). Seismic horizon extraction with dynamic programming. *Geophysics*, 86(2), IM51–IM62. https://doi.org/10.1190/geo2020-0039.1

SAŽETAK

Kartiranje seizmičkih horizonata temeljeno na inicijalnim točkama, uz toleranciju na rasjede, za potrebe geološkoga modeliranja

Plinsko polje Gola u sjeverozapadnome dijelu Dravske depresije smješteno je unutar strukturno složenoga naftnog sustava. Njegovi pješčani rezervoari pokazuju prostornu heterogenost uzrokovanu deltnom lepezastom sedimentacijom, što zahtijeva robusne alate za interpretaciju. Ovdje predstavljamo cjeloviti proces ekstrakcije seizmičkih horizonata i 3D geološko modeliranje, u potpunosti razvijen u Pythonu, a prilagođen ovom izazovu. Metoda se temelji na lokalno optimalnoj propagaciji (*greedy algorithm*) koja omogućuje praćenje horizonta s naglaskom na kontinuitet reflektora nadilazeći ograničenja ručne interpretacije i tradicionalnih automatskih algoritama u područjima s rasjedima ili šumom. Inicijalna aproksimacija dobiva se interpolacijom oko zadanih početnih točaka (*seed*), nakon čega se izdvaja podvolumen seizmičkih podataka koji se zatim splošti kako bi se refleksije poravnale. Unutar toga volumena algoritam pronalazi lokalno optimalnu putanju maksimizirajući kontinuitet i amplitudu reflektora. Naša implementacija proširuje standardni okvir vođen dodatkom nagiba, lokalne korelacije i filtriranja odstupanja, čime se osigurava vjerna i ponovljiva geološka interpretacija. Dobivene površine horizonata zatim se interpoliraju, izglađuju i pretvaraju u 3D mreže koje se integriraju u interaktivni geološki model polja Gola. Prvi put u ovome istraživanom području geološki model izrađen je u potpunosti korištenjem Python okruženja omogućujući automatiziranu ekstrakciju horizonta, vizualizaciju geoloških tijela i seizmičku interpretaciju u fleksibilnome, otvorenome sustavu.

Ključne riječi:
seizmički horizont, geološki model, *greedy* algoritam, dinamičko programiranje, polje Gola

Author's contribution

Ana Brcković (Assistant, MSc): conceptualization, data curation, formal analysis, investigation methodology, software, visualization and writing – original draft. **Marko Cvetković** (Associate professor, PhD): conceptualization, data curation, methodology, resources, supervision, validation and writing – review & editing. **Josipa Kapuralić** (Assistant professor, PhD): methodology, resources, validation and writing – review & editing. **Ivan Medved** (Assistant professor, PhD): methodology, resources, software and writing – review & editing.
All authors have read and agreed to the published version of the manuscript.

RGNZ/MGPB

A Sustainable and Practical Machine Learning Approach Using Scikit-Learn for Predicting Stope Instability: Identification of Critical Geotechnical Factors

Rudarsko-geološko-naftni zbornik
(The Mining-Geology-Petroleum Engineering Bulletin)
DOI: 10.17794/rgn.2025.5.14

Original scientific paper

Amos Bemo[1], Deji Olatunji Shonuga[2], Tawanda Zvarivadza[3], Moshood Onifade[4], Manoj Khandelwal[4]*

[1] *Department of Mining Engineering, Midlands State University, Gweru, Zimbabwe.*
[2] *Victoria Institute of Technology, Melbourne VIC 3000, Australia.*
[3] *Department of Civil, Environmental and Natural Resources Engineering, Luleå University of Technology, Luleå, Sweden.*
[4] *Institute of Innovation, Science and Sustainability, Federation University Australia, Ballarat, Victoria 3350, Australia.*

Abstract

Stope instability remains a persistent and hazardous challenge in underground mining, impacting safety, efficiency, and sustainability. Traditional stability assessment methods, while valuable, are often limited by site-specific calibration, simplifications, and adaptability issues in dynamic underground conditions. While machine learning shows potential for improved accuracy, a critical gap persists in understanding how geotechnical factors interact in practice. This study introduces a novel, practical machine learning framework (Scikit-Learn) to predict stope instability, and crucially, to quantify the nuanced, non-linear influence and interaction of critical geotechnical factors in a shallow gold mine. Comprehensive geotechnical investigation (observations, lab tests, rock mass classifications, blast damage assessments) and advanced data analysis (Random Forest feature importance, RFE, decision boundary analysis) identified water ingress, blast-induced damage, and rock mass quality (RMR) as the most significant instability factors. Water ingress profoundly impacted stability, with moderate blast damage exacerbating instability under high water ingress. Rock strength showed comparatively lower significance. The developed model achieved robust predictive performance (accuracy: 0.83, precision: 0.88, recall: 0.83, F1-score: 0.83). Based on these insights, tailored support patterns (e.g. 22mm/16mm cone bolts, timber props) are proposed to mitigate specific risks. This research significantly advances targeted rock mechanics solutions by providing a deeper, quantifiable understanding of complex instability mechanisms, enhancing mine safety and operational efficiency in shallow gold mining.

Keywords:
geotechnical factors, stope instability, machine learning, rock mass classification, shallow mining, rock support

1. Introduction

Stope instability remains a critical issue in underground mining, directly impacting both safety and production efficiency. The stability of a stope is intrinsically linked to the mechanical properties of the surrounding rock mass. Rock strength parameters, including uniaxial compressive strength (UCS), tensile strength, and shear strength, are fundamental in determining the potential for failure (**Cai, 2016; Alzoubi et al., 2009**). Specifically, UCS plays a critical role in defining overall stability and supporting requirements for stopes (**Li et al., 2019; Madzivire et al., 2018**). *In situ* and induced stress fields significantly influence stope stability, with the relative orientation of stopes to these stress fields being a crucial factor (**Karimzadeh et al., 2020; Mortazavi et al., 2018; Jaouhari et al., 2017**). Rock mass classification systems, such as the Rock Tunneling Quality Index (Q) and the Rock Mass Rating (RMR), provide quantitative measures of rock mass quality and facilitate the prediction of potential failure mechanisms (**Brown et al., 2015; Lato et al., 2015; Smith et al., 2007; Cai et al., 2004; Hoek et al., 1997**). Additionally, the Rock Quality Designation (RQD) of the rock mass surrounding a stope is a critical indicator of its stability, with lower RQD values signifying a more fractured and jointed rock mass (**Bai et al., 2022; Karimzadeh et al., 2020**).

Water ingress and water logging can severely compromise stope stability by reducing the effective cohesion and friction angle of the rock mass and increasing effective stresses on stope walls (**Wang et al., 2019; Joughin et al., 2012; Potvin et al., 2001**). Additionally, blast-induced damage, characterized by physical and structural alterations in the rock mass, contributes significantly to instability. While blasting is essential for hard rock mining, it can result in overbreak, slabbing,

* Corresponding author: Manoj Khandelwal
e-mail address: m.khandelwal@federation.edu.au
Received: 5 October 2024. Accepted: 15 January 2025.
Available online: 21 October 2025

and peripheral damage (**Smith et al., 2018**). Optimizing blasting practices to minimize damage and dilution is crucial for maintaining stope stability.

Excavation stability in underground mining is influenced by a complex interaction of geological and operational factors. While open stope mining enhances productivity and reduces worker exposure to hazardous environments, it also introduces risks such as overbreak-where unstable rock displaces beyond the planned excavation boundary, often due to weak or unfavourably oriented hangingwalls (**Li et al. 2023; Capes, 2009**). Such occurrences increase operational costs, disrupt production, and compromise safety. The main contributors to instability include stress relaxation, which alters rock mass behaviour (**Jorquera et al. 2023; Diederichs and Kaiser, 1999**), as well as mining techniques, extraction rates, rock strength, geological features, and stope dimensions.

Faults, which represent fractures in the Earth's crust with relative movement along their planes, are another critical consideration. Their orientation, movement type, and associated stress regimes significantly affect surrounding rock stability (**Szmigiel et al. 2024; Zhou et al., 2022**). Furthermore, the management of post-mining voids - commonly addressed through backfilling with materials like cemented rock fill or paste backfill (**Skrzypkowski, 2021a, 2021b; Lingga and Apel, 2018**) is essential to maintain long-term ground integrity. It is also vital to consider the influence of adjacent stopes, as stress redistribution from neighbouring excavations can pose significant stability challenges (**Vinay et al. 2023**). Proper control of excavation edges through methods such as controlled blasting and the application of support systems is necessary to minimize overbreak and ensure design compliance.

Classical methods for assessing stope stability have long served as foundational tools in underground mining, offering critical insight into rock mass behaviour. These traditional approaches, grounded in empirical formulas and extensive field and laboratory data, have been instrumental in evaluating excavation stability. Among these, the stability graph method developed by **Mathews et al. (1981)** stands out for its widespread use. This technique integrates rock mass classification systems, such as the Q system by **Barton et al. (1974)** and the Rock Mass Rating (RMR) system by **Bieniawski (1973)** and incorporates key adjustment factor such as rock stress (A), joint orientation (B), and surface orientation (C) to compute the stability number (N), a key parameter for stope design and support.

Machine learning techniques have emerged as powerful tools for predicting stope instability by analyzing complex datasets and identifying non-linear relationships between geotechnical parameters. Algorithms such as Random Forest and Support Vector Machines (SVMs) have been successfully applied to predict stope instability from various geotechnical inputs (**Li et al. 2023; Vinay et al. 2023; Bui et al., 2020; Pham et al., 2017**). These techniques can handle large datasets and identify patterns that are often obscured by traditional statistical methods. While these classical approaches remain relevant, the advent of machine learning has introduced powerful new tools for assessing stope stability (**Szmigiel et al. 2024; Jorquera et al. 2023; Qi et al. 2018**). For instance, a study by **Adoko et al. (2022)** demonstrated the application of feed-forward neural network classifiers, achieving a 91% prediction accuracy using a dataset of 225 stope cases from three Ghanian mines. This highlights the potential of machine learning in capturing complex interdependencies among the many variables influencing stability.

Traditional empirical and analytical methods, while foundational, often face limitations such as dependency on site-specific calibration, inherent simplifications of complex rock mass behaviour, and a lack of adaptability to dynamic underground conditions. For example, the Stability Graph Method by **Mathews et al. (1981)** provides a robust framework but relies on simplified adjustment factors that may not fully capture the nuanced interactions of multiple geotechnical parameters in highly variable rock masses. Numerical simulations offer detailed insight into stress distribution and deformation, but they are computationally intensive, require extensive input data, and often involve significant simplification of geological structures. Conversely, machine learning models, particularly those leveraging Scikit-Learn, offer distinct advantages. They can process large, heterogeneous datasets, identify non-linear relationships without explicit mechanistic models, and adapt to diverse geological settings with appropriate training data. Their ability to learn complex patterns directly from data makes them particularly suitable for problems like stope instability prediction where multiple interacting factors are at play. This study aims to showcase the practical value of integrating such advanced data-driven techniques into mine design and operational decision-making, leading to enhanced safety, reduced operational costs, and improved resource utilization in the mining sector.

Building on this, this study aims to investigate the geotechnical factors influencing stope instability in the 2North Section of a gold mine using machine learning techniques. By leveraging these advanced analytical methods, this research seeks to develop a predictive model that accurately forecasts stope instability, contributing to improved safety and productivity. The integration of machine learning with traditional geotechnical analysis offers a comprehensive understanding of stope instability, enabling the development of effective rock mechanics solutions. By incorporating parameters such as rock mechanical properties, blast damage, rock mass quality, and water effects, we aim to improve prediction performance and deepen our understanding of the critical factors affecting stope stability.

2. Materials and Methods

2.1. Geology and Mining Overview of the Study Area

The mine exploits auriferous sulfide mineralization within shear zones hosted by the Archaean Iron Mask Formation, located in the Harare-Bindura-Shamva greenstone belt of the Zimbabwe Craton (>2.5 Ga) (**Blenkinsop et al., 1999**). The Iron Mask Formation consists of metamorphosed felsic volcanics (dacite, meta-andesite, meta-rhyolite), with gold mineralization primarily associated with arsenopyrite, pyrrhotite, and pyrite. The ore zones, averaging 1m in width and 3.7 g/t Au, dip variably (10°-70°, mean 40°). The mine utilizes sublevel stoping with random pillar support. Stope dimensions range from 1-3m wide and 10-30m high. Detailed discontinuity mapping and rock mass characterization are essential, considering the lithological variability of the Iron Mask Formation and its impact on rock mass strength and deformation. Notably, a period of stope flooding, followed by resumed mining without a documented geotechnical assessment, necessitates a thorough evaluation of potential water-induced instability. This includes assessing water pressure effects on joint strength and potential pore pressure development.

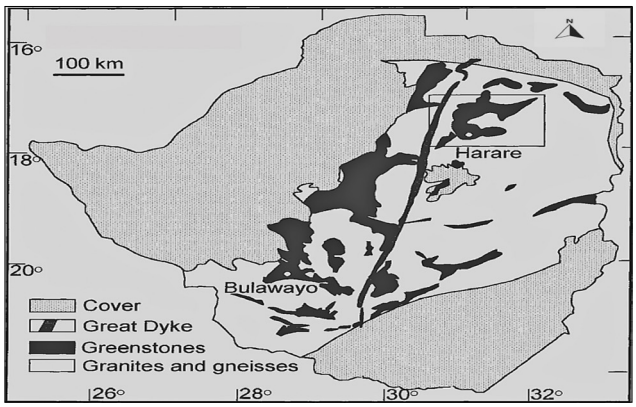


Figure 1. Simplified geological map of the Zimbabwe Craton, showing major lithological units. Adapted from **Blenkinsop et al. (1999)**.

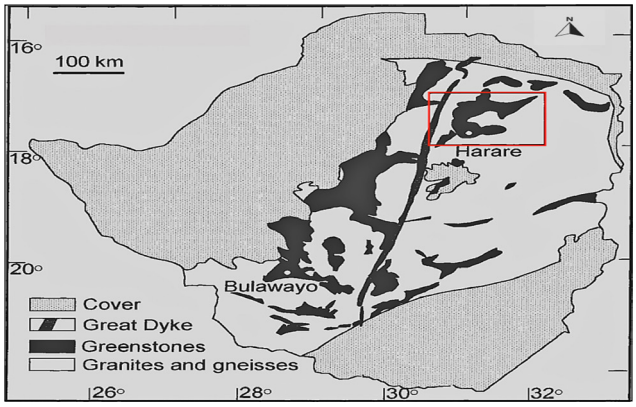


Figure 2. Regional geological map of the Zimbabwe Craton highlighting the Harare-Bindura-Shamva Greenstone Belt. The red rectangle indicates the approximate location of the greenstone belt. Adapted from **Blenkinsop et al. (1999)**.

The regional geological setting of the Zimbabwe Craton, highlighting its major lithological units, is illustrated in **Figure 1**.

The Harare-Bindura-Shamva Greenstone Belt, a significant mineralized zone within the Zimbabwe Craton, is delineated by a red rectangle on the regional geological map shown in **Figure 2**.

Detailed mapping within the Harare-Bindura-Shamva Greenstone Belt has revealed several significant geological structures that control mineralization. These key structures are presented in **Figure 3**. For instance, the major shear zones are evident.

2.2. Rock Strength Determination

Circular cylindrical core samples were prepared for uni-axial and tri-axial tests from areas under study. The samples were cut to 1150mm size using a diamond saw. For the Brazilian tensile strength test, samples were cut to 16mm length, and all specimens were given identity numbers. The samples were supplied for laboratory testing.

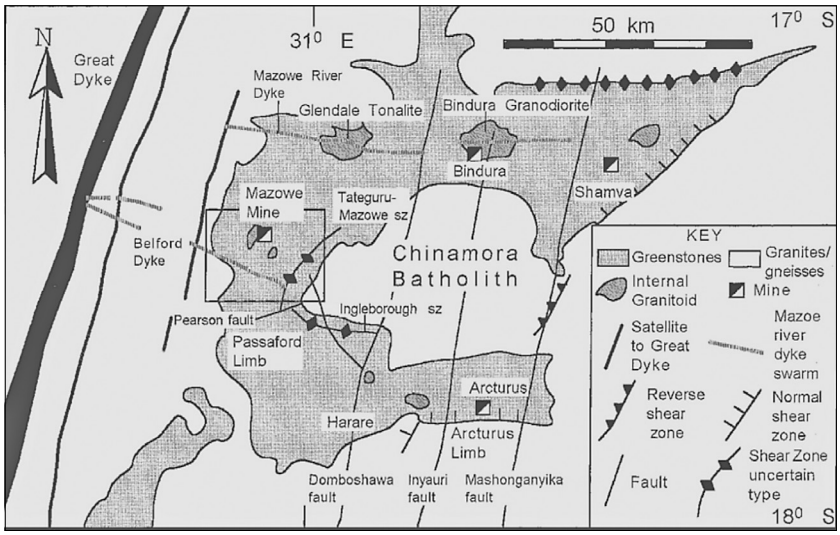


Figure 3. Detailed map illustrating significant structures within the Harare-Bindura-Shamva Greenstone Belt. Adapted from **Blenkinsop et al. (1999)**.

2.3. Rock Mass Classification

The ground water conditions, discontinuity direction, thickness, infill type, joint set number, spacing, roughness, and other geotechnical characteristics impacting rock mass performance at certain places were measured and documented in the study. Field estimates were used to estimate the strength of the rock, and data from uniaxial compressive strength (UCS) tests was added. The joint frequency approach suggested by **Palstrom (1982)** was utilized to determine the RQD rating because the drill core was not available. The volumetric joint count, $\mathbf{J}_v$, was first calculated using the joint spacing per interval as stated in **Equation 1**.

$$Jv = \frac{1}{j1} + \frac{1}{j2} + \frac{1}{j3} \tag{1}$$

where joint sets 1, 2, and 3 are represented by J1, J2, and J3 respectively.

Additionally, information was gathered in compliance with the RMR system of rock mass classification specifications (**Bieniawski, 1989**).

2.4. Evaluation of Stope Stability

Stability graphs, originally introduced by **Mathews et al. (1981)**, are among the most widely adopted empirical methods for evaluating stope stability in underground mining. This approach was developed using established rock mass classification systems, notably the Q-system by **Barton et al. (1974)** and the Rock Mass Rating (RMR) system by **Bieniawski (1973)**. The Mathews stability graph focuses on identifying the main factors that influence rock mass stability through specially designed charts that correlate various rock mass properties. These charts incorporate parameters such as the rock stress factor (A), joint orientation adjustment factor (B), modified rock tunneling index (Q') and surface orientation factor (C). These factors are used collectively to compute the stability number (N'), a significant metric in the design of stope dimensions and support systems. The stability number serves as a quantitative measure of the rock mass conditions and stope stability and is determined using the relationship in **Equation 2**.

$$N' = Q' ABC \tag{2}$$

The Mathews' stability graph method proposed by **Mathews et al., (1981)** was used to evaluate the stope stability of the stopes. The average of the Q-system data generated for every stope was used to calculate the Q' value. Potvin factor analysis was performed at each stope's specific places where the RMR Q-system had been concluded. The modified stability number N' of each and every stope was computed using the modal Potvin factor values, as well as their respective hydraulic radii. The stope dimensions, thus width and height were measured using a distometer so as to determine the hydraulic radii of the stopes. These values were used to determine the stope stability on the stability graph and the maximum tolerable unsupported length. For each stope under investigation, the modified stability number N' and the hydraulic radius was determined using **Eqaution 2**.

A vital element in the accurate assessment of stope stability is the shape factor, commonly known as the hydraulic radius (HR), which links the geometric dimensions of the opening. The hydraulic radius is a major parameter that characterizes the shape of the stope and plays a significant role in determining its structural stability. It is typically defined as the ratio of the area of the exposed hanging wall to its perimeter. In the case of inclined stopes - where the excavation is not perfectly vertical - the hanging wall exposure becomes the most important consideration for calculating the HR. The HR calculation incorporates the stope's span along both the dip (h) and strike (w) directions (**Tishkov, 2018**) as shown in **Equation 3**.

$$Hydraulic\ \ Radius = \frac{wh}{2(w+h)} \tag{3}$$

2.5. Assessment of Blast Damage

The measuring tools Peak Particle Velocity (PPV) and Half Cast Factor were employed to evaluate blast damage. Vibration sensors were installed at strategic locations to measure the PPV generated by the blast. PPV values were recorded at each sensor location during the blast event. The PPV was determined using the formula proposed by **Singh (1994)** in **Equation 4**.

$$Vmax = K\left(\frac{R}{\sqrt{Q}}\right)^{-¿\beta¿} \tag{4}$$

where Vmax is the PPV, from an explosive charge, Q, at a known distance R.

The half cast factors (**Equation 5**) were calculated by measuring the length of half cast barrels in the designated areas that remained after the blast:

$$\textbf{Half Cast Factor} = \\ = \frac{\sum Lengths\ of\ \ visible\ blastholes(after\ \ explosion)}{\sum Lengths\ of\ \ perimeter\ \ blastholes(befor\ \ eexplosion)} \tag{5}$$

2.6. Data Analysis

The collected data from field investigations, laboratory experiments, and an extensive literature review were subjected to systematic analysis using a combination of established geotechnical and empirical techniques. Rock strength parameters were evaluated through both uniaxial compressive and triaxial compressive strength tests to determine the mechanical behaviour of the intact rock under varying stress conditions. Rock mass quality was assessed using the RQD and RMR classification systems, providing insight into the struc-

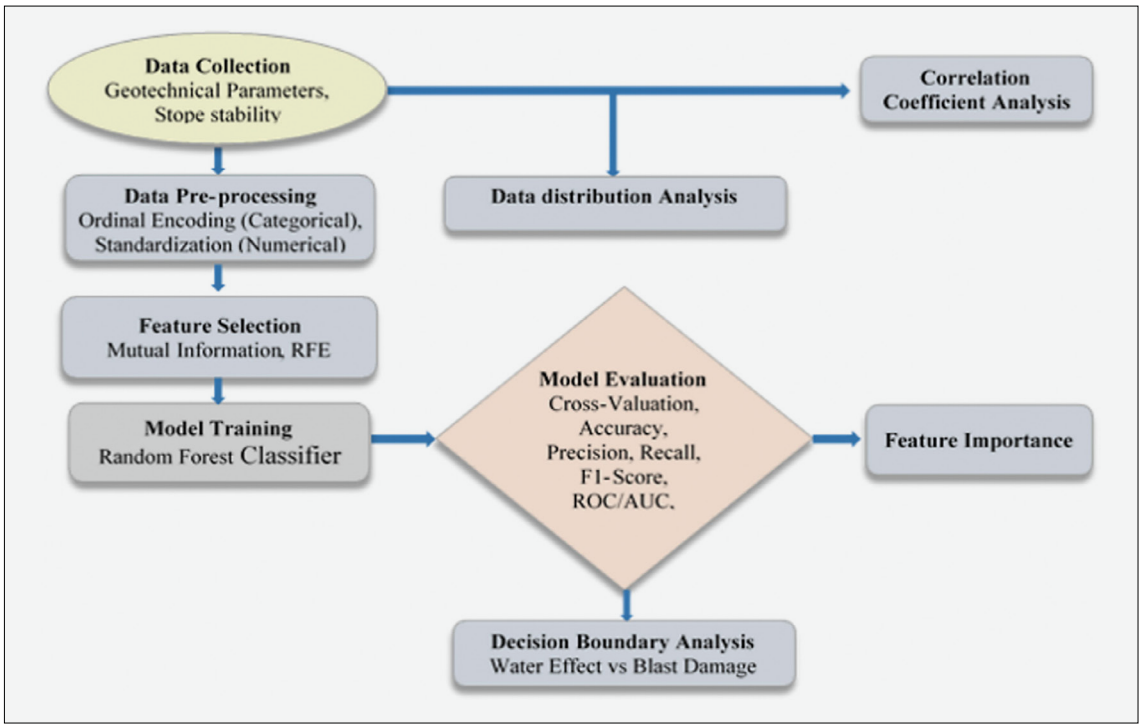


Figure 4. Workflow Diagram of the Machine Learning Process for Stope Instability Prediction

tural integrity and geomechanical characteristics of the rock mass. Stope stability was analyzed utilizing the Mathews' stability graph method, an empirical tool that relates rock mass conditions, geometry, and support requirements to the potential for stable excavation. Blast-induced damage was assessed by analyzing PPV data and the Half Cast Factor, both of which are indicators of blast performance and fragmentation control. This multifaceted analytical approach ensured a comprehensive understanding of the subsurface conditions and their implications for excavation and support design.

2.7. Factor Analysis

Machine learning techniques were applied to analyze the dataset, encompassing processes such as feature selection, feature importance evaluation, and decision boundary visualization. The analysis was conducted using Scikit-learn, a widely adopted machine learning library in Python, on a dataset integrating geological, geotechnical, and mining-related parameters. Feature selection was carried out using mutual information and recursive feature elimination (RFE) to identify the most relevant variables contributing to model performance and predictive accuracy. Feature importance was assessed using the Random Forest Classifier, which provided insight into the relative significance of each input variable in the classification tasks. To visualize model behaviour and class separation, decision boundary plots were generated using Support Vector Machines (SVMs). Additionally, feature distribution plots were employed to explore the distribution and potential interactions among variables. To further understand the interrelationships among geotechnical factors, correlation coefficients were computed and analyzed. **Figure 4** summarizes the whole factor analysis process.

2.7.1. Feature Importance Analysis

As previously described, the Random Forest Classifier was used for feature importance analysis. The core of the Random Forest lies in the aggregation of multiple decision trees. Each tree T_j in the forest $\{T_1, T_2, \ldots, T_m\}$ is built on a bootstrap sample of the training data and considers a random subset of features at each split. The prediction of the forest for a given input x is often based on the majority vote of its individual decision trees. This ensemble prediction, $\hat{y}(x)$, can be expressed as shown in **Equation 6**:

$$y(x) = mode\{T_j(x)\}_{j=1}^{m} \quad (6)$$

Where $\hat{y}(x)$ is the final predicted output of the Random Forest model, mode denotes the statistical mode, which is the value that appears most frequently, $T_j(x)$ is the prediction of the jth individual decision tree for a given input x and j is the total number of trees in the Random Forest.

The importance of a feature X_k is quantified by observing how much the prediction accuracy (or impurity) decreases when that feature is randomly permuted. A feature is considered important if its permutation leads to a significant drop in model performance. The importance score $I(X_k)$ for a feature X_k can be expressed as shown in **Equation 7**:

$$I(X_k) = \frac{1}{m}\sum_{j=1}^{m}\left(e_j - e_{j,k}^{perm}\right) \quad (7)$$

where e_j is the out-of-bag (OOB) error for tree T_j and $e_{j,k}^{perm}$ is the OOB error of T_j after the values of feature X_k have been randomly permuted. The OOB error is calculated on the data points not used to train that specific tree. Categorical variables (water effect and blast damage) were encoded using ordinal encoding, and numerical features (RQD, Rock Strength, Rock Mass Rating) were standardized using the *z*-score as shown in **Equation 8**:

$$z_i = \frac{x_i - \mu_X}{\sigma_X} \quad (8)$$

where z_i is the standardized value of the i^{th} data point, x_i is the original value of the i^{th} data point, μ_x is the mean of the feature X and σ_x is the standard deviation of the feature X.

The *z*-score: ensures that the variance across features is comparable, which can be important for distance-based algorithms (though Random Forest is less sensitive to feature scaling).

2.7.2. Recursive Feature Elimination Analysis

Recursive Feature Elimination (RFE) is a feature selection technique that recursively removes the least important features until a specified number of features is reached. The process can be described as follows:

1. Train a model on the entire set of features and calculate the importance of each feature.
2. Remove the least important feature(s) based on a predefined criterion.
3. Repeat steps 1-2 until the desired number of features is reached.

The importance of each feature in the Recursive Feature Elimination (RFE) process was calculated using **Equation 9**:

$$I(X_k) = |w_k| \quad (9)$$

where $I(X_k)$ is the importance of feature X_k and is the w_x weight assigned to feature X_k in the model.

The RFE process can be mathematically represented by **Equation 10**:

$$RFE(D,K) = X_1, X_2, ..., X_K \quad (10)$$

where *RFE(D, K)* is the set of K features selected from the original dataset D.

2.7.3. Decision Boundary Analysis

Decision boundary plots were generated using the Random Forest Classifier to visualize the classifier's predictions across the feature space of the two most significant factors: water effect and blast damage. The decision boundary B for separating the feature space into regions corresponding to different class predictions is defined as shown in **Equation 11**:

$$B = \{x \in R^d \mid f(x) = c\} \quad (11)$$

where x is a vector of the 'Water Effect' and 'Blast Damage' features (after encoding), d is the dimensionality of this subspace (here, $d=2$),R^d I the Euclidean space and c is the class boundary (e.g. the point where the probability of 'Stable' equals the probability of 'Unstable'). For probabilistic classifiers like Random Forest (which can output class probabilities), the decision boundary can be defined at a specific probability threshold (e.g. 0.5).

2.7.4. Data Distribution Analysis

Feature distribution plots were used to visualize the distributions of individual geotechnical factors and the relationships between pairs of factors. The relationships between pairs of variables were explored using joint probability distributions and the Pearson correlation coefficient – The Pearson correlation coefficient, r, between two variables X and Y is defined as shown in **Equation 12**:

$$r_{XY} = \frac{E\left[(X - \mu_X)(Y - \mu_Y)\right]}{\sigma_X \sigma_Y} \quad (12)$$

where E is the expectation operator, μ_x is the mean of variable X, μ_x is the mean of variable Y, σ_x is the standard deviation of variable X and σ_y the standard deviation of variable Y.

2.7.5. Correlation Coefficient Analysis

Correlation coefficient results were used to determine linear relationships among the geotechnical factors, specifically focusing on the correlation between water effect, blast damage, and rock quality (represented by RQD and Q). The t-statistic for assessing the significance of a correlation coefficient is given by **Equation 13**:

$$t = r\sqrt{\frac{n-2}{1-r^2}} \quad (13)$$

where n is the number of data points, t is the t-statistic value, r is the Pearson correlation coefficient and n is the number of data points.

The resulting p-value indicates the probability of observing such a correlation if there were no true linear relationship between the variables.

2.7.6. Model Evaluation

The performance of the Random Forest Classifier was evaluated using standard classification metrics, including accuracy, precision, recall, and F1-score. For the 'Unstable' class:

The overall accuracy of the model, precision, recall and F1-score was calculated as shown in **Equation 14, 15, 16** and **17.**

$$Accuracy = \frac{Number\ of\ Correct\ Predictions}{Total\ Number\ of\ Predictions} \quad (14)$$

$$Precision = \frac{True\ Positives}{True\ Positives + False\ Positives} \quad (15)$$

$$Recall = \frac{True\ Positives}{True\ Positives + False\ Negatives} \quad (16)$$

$$F1-score = 2 \times \frac{Precision \times Recall}{Precision + Recall} \quad (17)$$

To ensure the model's robustness, 5-fold cross-validation was performed. The dataset was divided into 5 folds, and the model was trained and evaluated 5 times, each time using a different fold as the validation set. The average performance across the folds provided a more reliable estimate of the model's generalization ability. The average metric across K folds in cross-validation was computed using **Equation 18**:

$$\overline{Metric} = \frac{1}{K}\sum_{i=1}^{K} Metric_i \quad (18)$$

where K is the number of folds used in cross-validation, $Metric_i$ is the value of the evaluation metric on the i[th] validation fold.

ROC Curve for Logistic Regression

Furthermore, the ROC curve used was to evaluate the performance of a logistic regression model. The Receiver Operating Characteristic (ROC) curve is a graphical representation of the performance of a binary classifier. It plots the True Positive Rate (TPR) against the False Positive Rate (FPR) at different thresholds.

The TPR and FPR can be calculated using **Equation 19** and **20**:

$$TPR = \frac{TP}{TP + FN} \quad (19)$$

$$FPR = \frac{FP}{FP + TN} \quad (20)$$

where TP is the number of true positives, FN is the number of false negatives, FP is the number of false positives, and TN is the number of true negatives.

The area under the ROC curve (AUC) was calculated using **Equation 21** to quantify the overall performance of a logistic regression model.

$$AUC = \int_0^1 TPR\left(FPR\right) dFPR \quad (21)$$

The AUC value ranges from 0 to 1, where 1 represents perfect classification and 0.5 represents random guessing.

The logistic regression model can be represented mathematically as shown in **Equation 22**:

$$P\left(Y = 1 \middle| X\right) = 1/\left(1 + e^{(-z)}\right) \quad (22)$$

where $P(Y=1|X)$ is the probability of the positive class given the input features X, and z is a linear combination of the input features (see **Equation 23**):

$$z = w_0 + w_1 X_1 + w_2 X_2 + ... + w_n X_n \quad (23)$$

Where w_i are the weights assigned to each feature X_i.

3. Data Analysis

This study evaluates the stability of underground mine stopes in the 2North Section by examining the effects of rock mechanical properties, blast-induced damage, rock mass quality, and water presence. A combined approach involving laboratory tests, field observations, empirical classification systems, and machine learning methods was employed to provide an integrated assessment of stope stability and support design requirements.

3.1. Rock Mechanical Properties

The mechanical properties of intact rock are fundamental in assessing the overall stability and deformation behaviour of underground excavations. In this study, laboratory tests were conducted on representative rock samples to determine key strength parameters, including Uniaxial Compressive Strength (UCS), Triaxial Compressive Strength (TCS), and tensile strength, providing insight into the inherent competence of the rock materials.

The UCS results demonstrated a relatively wide but consistently high strength range, with values spanning from 167 MPa in the ore zone to 215 MPa in the granodiorite unit (see **Table 1**). These values clearly classify both lithologies as strong to very strong rocks based on standard rock strength classification systems (ISRM). Such high compressive strengths imply that, under unconfined loading conditions, the intact rock is unlikely to fail or undergo significant deformation, even when subjected to the stresses typically encountered in underground mining environments.

Table 1. Summary of Rock Mechanical Properties

Rock Type	UCS	TCS	Tensile Strength
Metabasalt	172	NA	NA
Metaandesite	175	NA	NA
Granodiorite	215	NA	12.2
Ore zone	167	93.2	11.6

Note: Triaxial Compressive Strength Test was only done on the ore zone and the Tensile Strength Test only on granodiorite and the ore zone.

Further testing on ore zone samples revealed a TCS of 93.2 MPa, which, while lower than the UCS, reflects the increased confinement typical of in-situ conditions and demonstrates the material's capacity to sustain stress un-

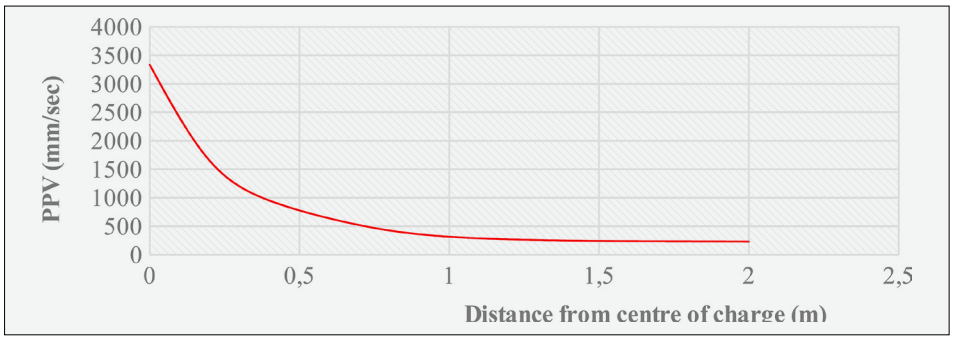


Figure 5. PPV versus Specific Charge for 1.5m Charge Length

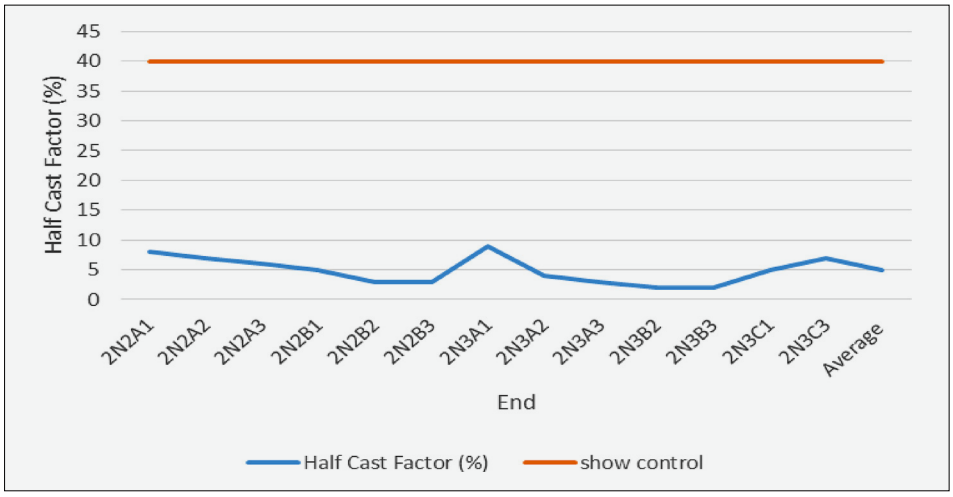


Figure 6. Half-Cast Factor Measurements for Different Stope Ends

der triaxial loading. This value is within the expected range for strong, brittle rock and supports the conclusion that the ore body itself, when intact, is mechanically robust.

The tensile strength values were also notably high, with the ore zone recording 11.6 MPa and granodiorite slightly higher at 12.2 MPa. Tensile strength is critical in determining the rock's resistance to crack initiation and propagation, especially in the presence of blast vibrations or stress redistributions. These values suggest that the intact rock would not readily fracture under tensile loading, further reinforcing its competent mechanical nature.

However, despite these strong intact rock properties, field observations and empirical assessments indicate instability in certain stopes. This discrepancy points to a key understanding in rock mechanics: while laboratory strength data provides valuable baseline information, rock mass behaviour in situ is dominantly controlled by discontinuities (such as faults, joints, fractures, and bedding planes) rather than the properties of the intact rock alone (**Li et al. 2023; Vinay et al. 2023**). The presence of geological discontinuities can dramatically reduce the effective strength of the rock mass, acting as planes of weakness along which shear displacement, dilation, or separation may occur. This is particularly relevant in jointed or faulted ground, where intact rock strength becomes a secondary consideration (**Qi et al. 2018**). As a result, the rock mass strength is governed not only by the intact strength but also by the orientation, persistence, spacing, and surface conditions of these discontinuities.

In the context of the studied stopes, it is reasonable to conclude that failure mechanisms are likely driven by structural weaknesses rather than by the degradation of the intact rock. This assertion is supported by other findings in the study, such as moderate to high levels of fracturing (as evidenced by RQD values) and elevated blast-induced damage (high PPV values). These factors collectively reduce the overall rock mass quality and increase the likelihood of instability, despite the high laboratory-derived strength values.

3.2. Blast Damage Assessment

Blasting is an essential component of underground mining, enabling efficient rock breakage and extraction. However, improper blast design or execution can result in excessive damage to the surrounding rock mass, compromising excavation stability. One of the most reliable indicators of blast-induced damage is PPV - a dynamic measurement of the vibration intensity caused by explosive charges.

In this study, PPV values recorded during stope development ranged from 229.5 mm/s to 3335 mm/s (see **Figure 4**). This considerable variation in PPV reveals inconsistent control over blast energy dissipation, with values at the higher end far exceeding typical thresholds associated with safe excavation practices. According to various em-

pirical guidelines and case studies, PPV values exceeding 1000 mm/s are often associated with severe stress redistribution, overbreak, and long-term deterioration of rock mass properties, particularly in jointed or fractured ground. The observed upper range of 3335 mm/s is therefore indicative of substantial blast-induced stress and potential rock mass degradation in affected areas.

Further compounding this issue is the mean half-cast factor, a metric used to evaluate the effectiveness of perimeter control blasting. In this case, the half-cast factor was calculated at only 4.92% (see **Figure 6**) - a value considerably lower than the acceptable range for well-controlled blasting. The half-cast factor essentially reflects the proportion of blast holes that produce smooth, half-round impressions on the final excavation perimeter. Low percentages indicate poor energy confinement, excessive rock spalling, and a lack of controlled fracturing at the boundary, leading to unintended overbreak and increased wall damage.

The combination of high PPV values and a low half-cast factor strongly suggests that blast damage is a significant contributor to the deterioration of stope walls, beyond what might be explained solely by geological factors such as naturally blocky ground or fault structures. While the presence of pre-existing discontinuities undoubtedly plays a role in how energy is transmitted and fractures propagate, the primary mechanism of instability in this case appears to be anthropogenic - specifically, suboptimal blasting practices.

It is also important to note that high PPV values have a cumulative effect on the rock mass, especially in zones with repeated blasting cycles. Damage induced by vibration may not be immediately visible but can manifest over time as gradual loosening, slabbing, or rockfall. In addition, blast-induced microcracks reduce the rock's elastic modulus and shear strength, thereby lowering the overall stability of the excavation even in the absence of visible failures.

3.3. Rock Mass Classification

The quality of the rock mass was evaluated using the RQD and the Q-system, both of which are widely accepted empirical classification methods in geotechnical engineering. These assessments provided quantitative measures of the rock mass integrity and structural competence. The results of this analysis are presented in **Table 2**.

3.3.1. Evaluation of Rock Mass Quality Using RQD

The Rock Quality Designation (RQD) serves as a key indicator of the degree of fracturing within a rock mass and is widely used in empirical rock mass classification systems, including the Q-system. In this study, RQD values were assessed across four stopes to evaluate the integrity, continuity, and competence of the rock mass, all of which are critical factors for ensuring the stability of underground excavations.

Table 2. Summary of the rock classification results

Stope	RMR	RQD	Q	Q'	Comment
2A	61	73	3.8	6	Good
3C	66	70	4.9	8	Good
2B	83	90	16.9	19	Very good

The results indicate that Stopes 2A and 3C exhibited RQD values of 73% and 70% respectively, which classify them as moderately fractured rock masses, as shown in **Table 2**. These values suggest the presence of frequent jointing and discontinuities, which can compromise the structural behaviour of the stope walls and roofs, making them more susceptible to instability and overbreak. The moderate RQD values in these stopes are symptomatic of less competent rock that may require additional support measures to ensure safe stope development and long-term excavation performance.

The lower RQD values observed in Stopes 2A and 3C can be attributed to a combination of blast-induced damage and hydrogeological effects. Excessive blasting, especially in poorly controlled rounds, can create new fractures and extend existing ones, thereby deteriorating the surrounding rock mass. Moreover, elevated water pressure within joints and fractures can further degrade rock quality by reducing effective stress and contributing to joint dilation and weakening. These factors act synergistically to exacerbate pre-existing geological weaknesses, leading to the observed reduction in RQD.

In contrast, Stope 2B recorded a significantly higher RQD, indicating improved rock mass quality and reduced fracture density. This suggests a more intact and cohesive rock structure, which enhances load-bearing capacity and decreases the likelihood of shear or tensile failure along joint planes. As such, Stope 2B is expected to exhibit better performance in terms of ground control, reduced support requirements, and lower risk of overbreak. Notably, Stope 2B exhibited the highest RQD at 90%, denoting a very competent and unfractured rock mass. Such high values are indicative of minimal discontinuities, with long, continuous core pieces recovered during drilling, reflecting superior geological conditions. This degree of rock mass integrity is typically associated with enhanced stope stability, increased safety, and more cost-effective excavation due to lower support demands.

This interpretation is further supported by field observations and geotechnical logs, which noted signs of water ingress and irregular fracture patterns in these stopes. The presence of water not only promotes mechanical deterioration but can also lead to chemical alteration of joint infill, compounding the loss in structural cohesion. As a result, the stope stability in these areas is compromised, and targeted mitigation strategies (such as improved blast control, pre-drainage techniques, and localized support installation) may be necessary.

3.3.2. Evaluation of the Rock Mass Quality Using the Q-system

In this study, the Q-system analysis yielded distinct variations across the analyzed stopes, revealing significant differences in rock mass conditions and their implications for stope stability. Stope 2B recorded the highest Q-value of 16.9, categorizing it as a good quality rock mass, as shown in **Table 2**. This high value is primarily attributed to favourable geological conditions, specifically the absence of groundwater and the presence of clean, clay-free joint infill. The lack of water is particularly significant, as water acts as a destabilizing agent by reducing effective stress, lubricating joint surfaces, and weakening rock-bridging elements. Moreover, clay-free joints contribute to better interlocking and higher shear resistance, both of which are essential for maintaining the structural integrity of excavated openings.

The elevated Q-value for Stope 2B directly correlates with its observed stability and larger tolerable unsupported span, suggesting that it may require minimal ground support, thereby offering potential cost and operational efficiency advantages during mining operations. These findings underscore the importance of dry conditions and joint cleanliness as critical contributors to excavation stability.

In contrast, Stopes 2A and 3C exhibited significantly lower Q-values of 3.8 and 4.9, respectively, placing them in the fair to poor rock quality category. These values reflect moderate stability conditions that warrant more conservative excavation designs and likely necessitate reinforced support systems. A key factor influencing the reduced Q-values in these stopes is the presence of groundwater, which adversely affects several Q-system parameters. Water reduces the Jw factor, indicating wet or saturated conditions, and contributes to the alteration of joint infill materials, thereby decreasing the Ja and potentially increasing joint activity and deformation risk. In such environments, joints are more likely to become critically stressed, leading to increased dilation, rock block detachment, and potential stope wall instability.

Interestingly, Stope 3C displayed a slightly higher Q-value than Stope 2A, which can be attributed to its higher joint friction, represented by a greater Jr value. Joint roughness enhances mechanical interlocking between rock blocks, providing increased resistance to shear failure even in the presence of water or other weakening agents. This factor offers marginally better performance in Stope 3C, although not sufficient to significantly alter its classification within the Q-system. The influence of joint friction also highlights the multifactorial nature of rock mass behaviour, where improvements in one parameter may partially offset deficiencies in others.

Overall, the Q-system analysis provided quantitative insight into the geomechanical performance of the various stopes. The results emphasize that Stope 2B offers a more stable mining environment, while Stopes 2A and 3C require additional engineering interventions. These findings reinforce the value of the Q-system in pre-mining assessments and its ability to guide risk-informed stope design, ground support selection, and excavation sequencing in underground mining operations

3.3.3. Use of the Q results to evaluate stope stability

The maximum tolerable unsupported span, derived using the Q-system empirical design method, serves as a critical parameter in assessing the relative stability of underground stopes. This span refers to the largest excavation width that can be safely maintained without the use of additional ground support, based on the rock mass quality and structural conditions. It is directly influenced by the Q-value, which integrates key factors such as RQD, joint set number, joint roughness, groundwater conditions, joint alteration, and stress reduction due to excavation geometry.

In the context of this study, Stope 2B exhibited the highest tolerable unsupported span, reflecting its superior rock mass conditions and overall stability, as shown in **Table 3**. This result is consistent with its higher Q-value and RQD, which indicate a competent rock mass with fewer fractures, clean joint surfaces, and minimal water ingress. The ability of Stope 2B to support a larger span without reinforcement suggests that the rock mass is well-interlocked and capable of withstanding the induced stresses from mining without immediate risk of collapse or significant deformation.

Table 3. Maximum tolerable unsupported length of the stopes

Stope	ESR	Q	Maximum tolerable unsupported length(m)
Stope 2A	1.6	3.8	5.5
Stope 3C	1.6	4.9	6.0
Stope 2B	1.6	16.9	9.9

Table 4. The calculated Modified Stability Number and Hydraulic radius

		STOPE DIMENSIONS		POTVIN FACTORS				STABLE STOPE SPAN	
Stope	Joint Orientation °	Width(w) m	Height(h) m	A	B	C	Q'	N	Hydraulic Radius
2A	45	31	37	1	0.5	6	6	13.5	8.43
3C	30	36	40	1	0.2	6	8	15.2	9.47
2B	30	29	35	1	0.2	6	19	26.2	7.93

In contrast, Stopes 2A and 3C demonstrated considerably lower maximum unsupported spans, signaling reduced stability and a higher probability of requiring artificial support systems. These stopes also recorded lower RQD values (73% and 70%, respectively), indicating more intense fracturing and possibly blast-induced damage or degradation due to groundwater pressure. The reduced span capacity in these areas implies that the rock mass cannot reliably sustain large openings, as discontinuities such as joints, fissures, and weakened zones may serve as planes of failure, especially under the influence of gravity and mining-induced stress changes.

The strong correlation between RQD and the calculated unsupported spans emphasizes the significance of rock mass fragmentation and structural integrity in stope design. RQD, as a measure of the degree of fracturing in the core samples, directly impacts the overall Q-value and, subsequently, the recommended excavation span. This highlights the necessity of accurate geotechnical logging and sampling in the early stages of mine design to ensure safe and efficient stope development.

Furthermore, the variation in span tolerances among the stopes suggests that site-specific ground control strategies are essential, rather than relying on a generalized design approach. While Stope 2B may safely accommodate wider openings, Stopes 2A and 3C would benefit from narrower spans or the implementation of support systems such as cable bolts, mesh, or shotcrete to mitigate the risk of overbreak and ensure worker safety.

3.4. Stope Stability Assessment

To assess the stability of the evaluated stopes, the modified stability number (Q′) and hydraulic radius were calculated, as summarized in **Table 4**. These parameters are central to the Mathews Stability Graph method, where the stability number (Q′) incorporates key rock mass quality factors such as joint condition, groundwater influence, and joint orientation, while the hydraulic radius reflects the geometry of the excavation.

Among the analyzed stopes, Stope 2B demonstrated the highest Q′ value, indicating the most favourable rock mass conditions overall. Interestingly, this high stability number was maintained despite a relatively low joint orientation factor (B). This suggests that the inherent rock quality (reflected in parameters like intact rock strength, joint spacing, and absence of water) played a dominant role in promoting stability. In other words, while unfavourable joint orientation typically reduces stability, the overall robustness of the rock mass in Stope 2B was sufficient to offset the negative influence of joint orientation. This finding highlights the complex interplay between geological and structural factors in influencing excavation performance, where strong, dry, and tightly interlocked rock masses can compensate for less-than-ideal joint alignments.

However, the analysis also reveals a critical point regarding the mechanism of potential failure. In stopes with lower Q′ values and less favourable geometrical or structural conditions, such as 2A and 3C, failure is likely to initiate along joints that intersect the free face at small angles. These low-angle joints act as potential sliding surfaces, especially when oriented sub-parallel to the excavation walls or roof. Such orientations reduce the shear resistance along the joint planes, particularly when combined with stress relief from excavation or the presence of water, which can lower effective stress and lubricate joint surfaces. This failure mechanism is consistent with observed overbreak patterns in similar mining settings and underscores the importance of joint orientation analysis in ground control planning.

Furthermore, the relationship between Q′ and HR on the Mathews Stability Graph places these stopes within the potentially unstable region, suggesting that while outright failure may not be imminent, there is an elevated risk that warrants attention. In practice, this means that additional support measures or modifications to stope dimensions may be required to maintain stability, particularly in areas where joint geometry and excavation layout intersect unfavourably.

3.4.1. Mathews Stability Graph

The results derived from the Mathews Stability Graph (see **Figure 7**) reveal that all analyzed stopes plot within the "*potentially unstable*" zone of the graph. This zone, positioned between the empirically defined stable and failed regions, represents a range of hydraulic radius and stability number (N) combinations where stope performance is highly sensitive to local geological, structural, and operational conditions. It indicates that the analyzed stopes, while not necessarily prone to immediate failure, exhibit a heightened risk of instability and would likely require additional support measures or design modifications to maintain structural integrity.

Among the evaluated stopes, Stope 2B demonstrates the highest relative stability, as indicated by its location within the potentially unstable zone at a higher Stability

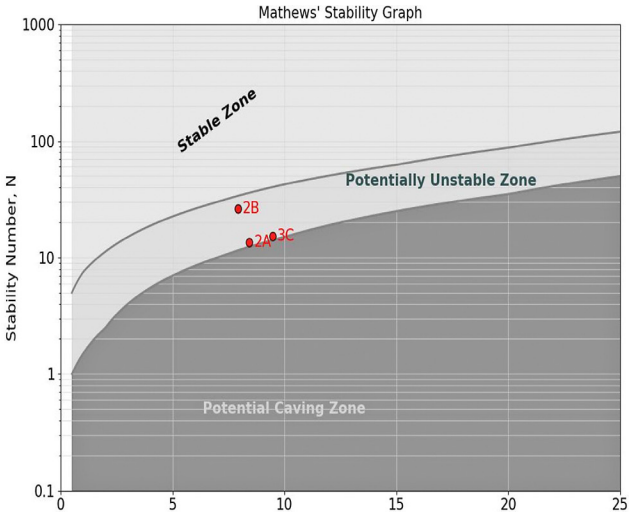


Figure 7. Stop Stability Results on Mathews' stability graph

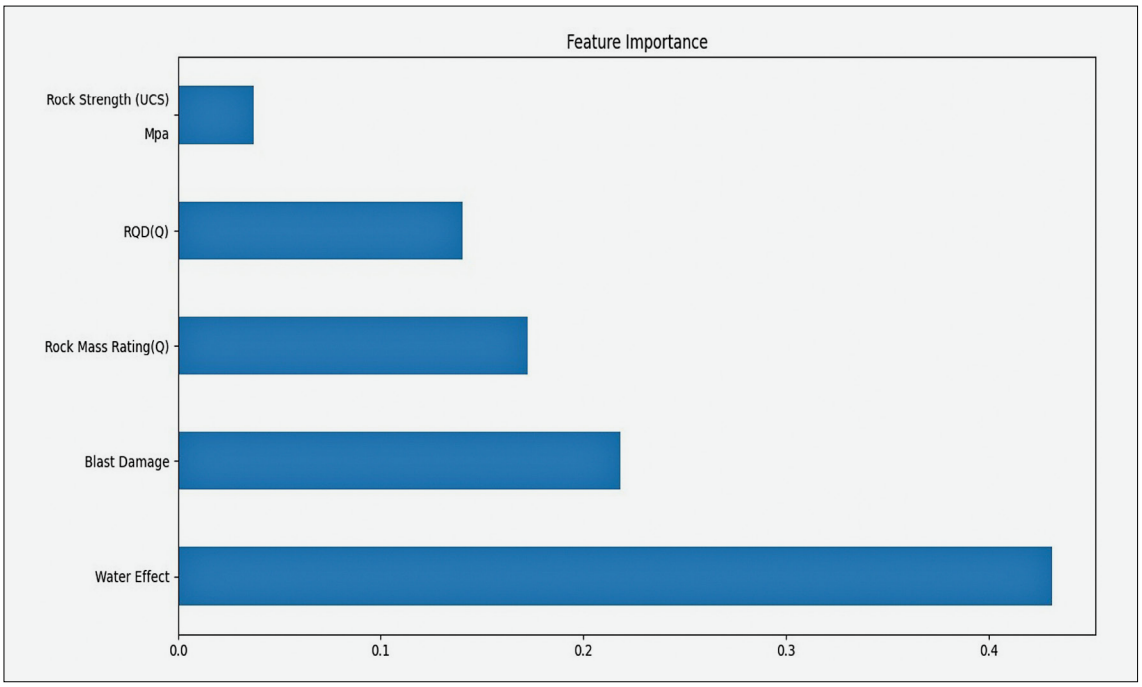


Figure 8. Feature importance scores obtained from the Random Forest Classifier

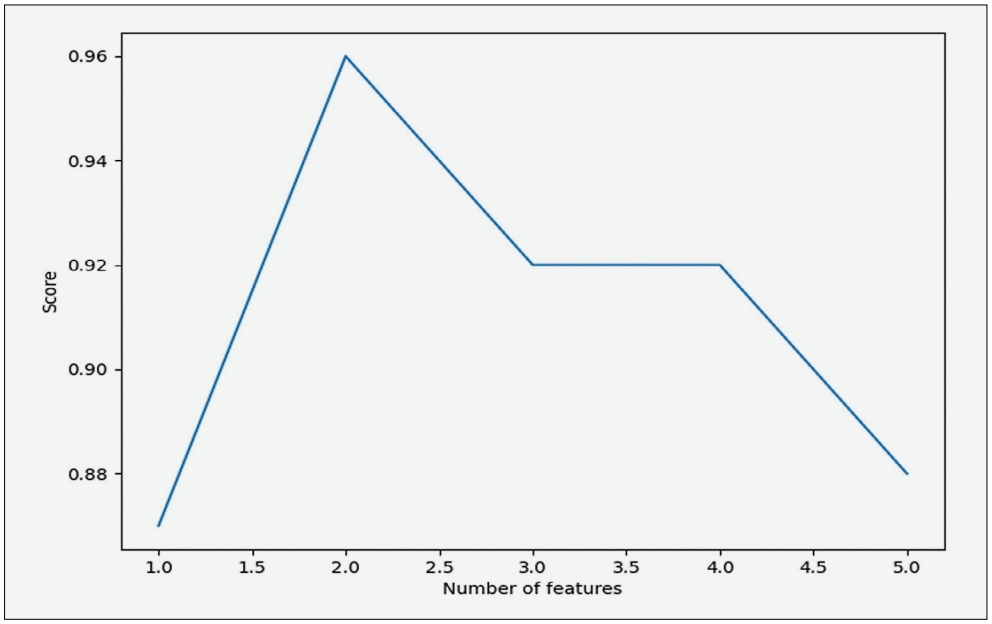


Figure 9. The Recursive Feature Elimination (RFE) process

Number (N), positioning it closer to the stable region. This observation is supported by its comparatively higher Q-value, which reflects more favourable rock mass conditions, and a greater RQD, suggesting a higher degree of intact rock within the core samples. The Q-value, which incorporates factors such as joint set number, joint roughness, joint alteration, and groundwater conditions, plays a direct role in the computation of the stability number (N). A higher Q-value in Stope 2B therefore results in a higher N, shifting its plot point further to the right on the stability graph and indicating improved stability.

This trend validates the underlying empirical relationships embedded in the Mathews Stability Graph method. The graphical output aligns well with the field data and quantitative input parameters, especially in the case of Stope 2B, where the correlation between good rock mass quality and predicted stability is clearly evident. However, the fact that all stopes fall within the potentially unstable region (even those with moderate to high rock quality) emphasizes the critical role of stope geometry, particularly the hydraulic radius, in influencing stability outcomes.

3.5. *Machine Learning Analysis Using Scikit-Learn*

Machine learning analysis was conducted using the Scikit-learn library, a robust and widely adopted frame-

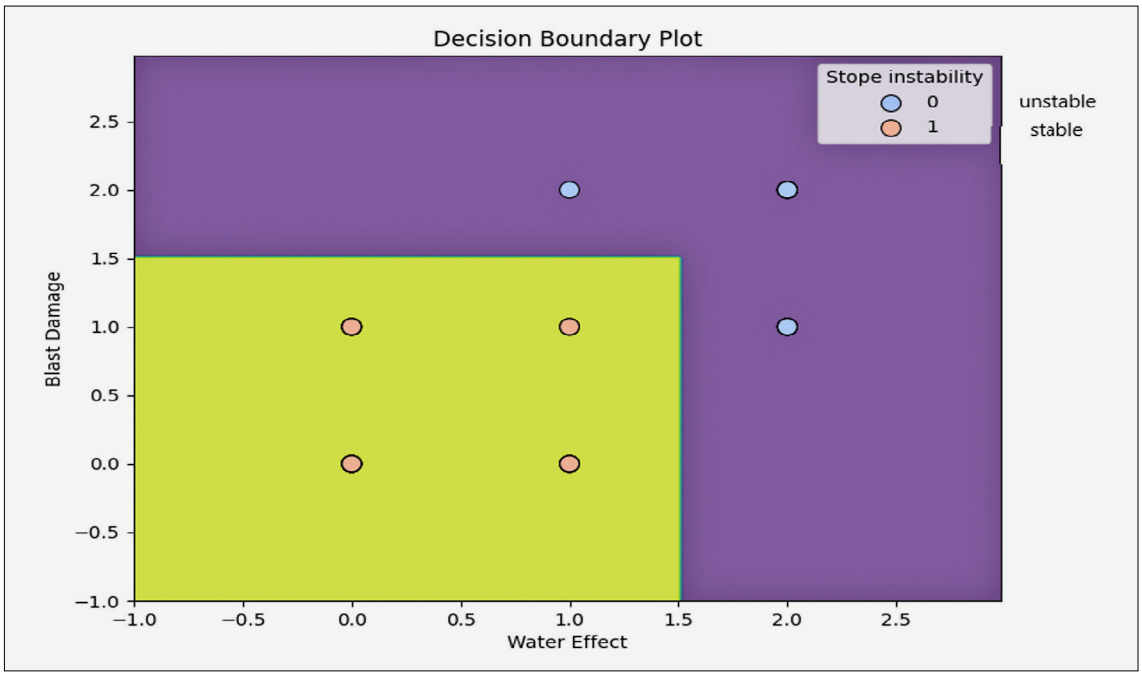


Figure 10. Water Effect against blast Damage Decision Boundary Plot

work in Python for building and evaluating machine learning models. The workflow began with data preprocessing, which involved handling missing values, encoding categorical variables, and scaling features to ensure uniformity across the dataset. Following preprocessing, the dataset was split into training and testing subsets to facilitate fair model evaluation and eliminate overfitting. Model evaluation metrics including accuracy, precision, recall, F1-score, were calculated to compare algorithm performance and select the most effective model for the task. Visual tools such as confusion matrices and ROC curves were used to interpret classification results.

3.5.1. Feature Importance Analysis

To understand the relative influence of various geotechnical factors on stope instability, the Random Forest Classifier from the Scikit-Learn library was employed to perform feature importance analysis. The choice of Random Forest was motivated by its ability to handle both categorical and numerical data, its robustness against overfitting, and its capacity to provide feature importance scores based on the mean decrease in impurity.

Prior to model training, categorical variables (water effect and blast damage) were encoded using ordinal encoding, assigning numerical values representing the severity levels (e.g. low=0, medium=1, high=2). Numerical features (RQD, Rock Strength, RMR) were standardized using Scikit-Learn's StandardScaler to ensure consistent scaling.

The feature importance scores, as visualized in **Figure 8**, revealed that water effect was the most influential factor in predicting stope instability, followed by blast damage and RMR. RQD and Rock Strength exhibited comparatively lower importance. This suggests that the presence of water and the extent of blast damage significantly contribute to instability, potentially by exacerbating existing discontinuities and reducing the effective strength of the rock mass.

It is important to note that the feature importance scores are relative and should be interpreted within the context of the dataset. While Rock Strength showed low importance, it does not imply it's entirely negligible; rather, its variability within the dataset might be less influential compared to other factors.

3.5.2. Recursive Feature Elimination Analysis

The Recursive Feature Elimination (RFE) process was used to evaluate the importance of each feature in predicting stope stability (see **Figure 9**). The results showed that water effect, blast damage, and RMR were consistently ranked as the top features, indicating their high importance in predicting stope stability. When these features were removed from the model, the performance dropped significantly, further confirming their importance. The RFE analysis provided further insight into the relationships between the geotechnical factors and stope instability, and supported the findings of the feature importance analysis.

3.5.3. Decision Boundary Analysis

To further explore the interaction between the two most significant factors, water effect and blast damage, we performed a decision boundary analysis. This technique visualizes the classifier's predictions across the feature space, illustrating how different combinations of water effect and blast damage influence stope stability.

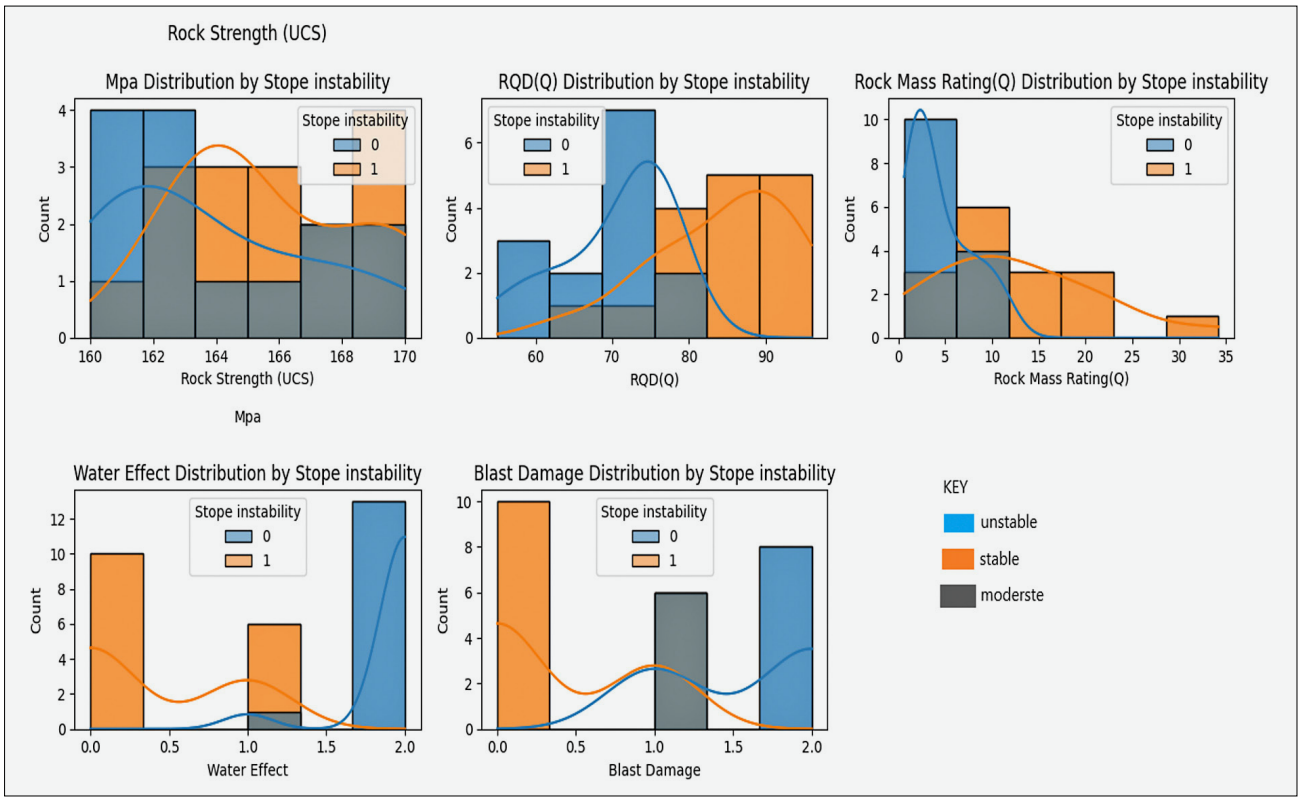


Figure 11. Feature distribution plots for the five factors under investigation

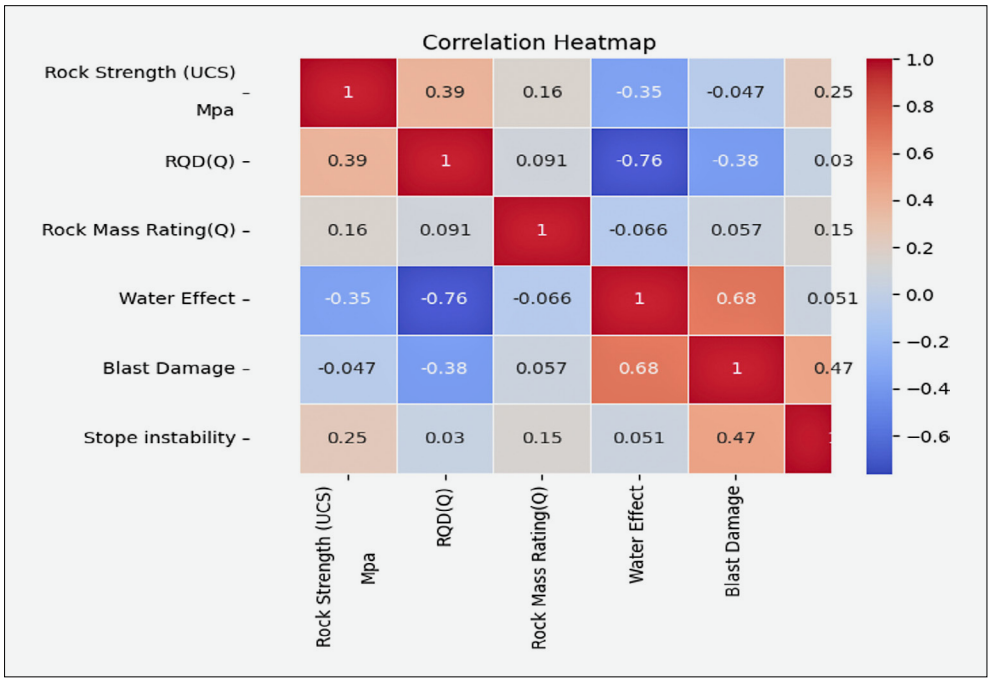


Figure 12. Correlation Heatmap

Figure 10 shows the decision boundary generated by the Random Forest Classifier. The yellow area represents the region where the model predicted "Stable" stope conditions, while the purple area represents "Unstable" conditions.

The analysis revealed that:

Water effect is a dominant predictor: when water effect is low (0) or medium (1), the classifier predicts "Stable" regardless of blast damage severity. This suggests that in the absence of significant water influence, even high levels of blast-induced damage are unlikely to compromise stope stability.

High water effect increases instability risk: when water effect is high (2), the classifier predicts "Unstable" for medium (1) and high (2) blast damage levels. This indicates that elevated water influence substantially increases the risk of instability, particularly when combined with blast damage.

Interaction effect: the decision boundary analysis underscores a strong interaction between water effect and blast damage. Specifically, a high-water effect amplifies the destabilizing impact of blast damage, pointing to a compounded influence on stope stability.

3.5.4. Data Distribution Analysis

Feature distribution plots (see **Figure 11**) reveal a positive correlation between rock strength and RMR, indicating that higher-strength rocks are generally associated with better rock mass quality. Additionally, a positive correlation was observed between water effect and blast damage, suggesting that the presence of water may exacerbate the extent of blast-induced damage. This distribution analysis is critical for understanding the interrelationships among geotechnical factors and plays a vital role in informing the design of appropriate ground support systems.

Classification Report:

	precision	recall	f1-score	support
0	0.75	1.00	0.86	3
1	1.00	0.67	0.80	3
accuracy			0.83	6
macro avg	0.88	0.83	0.83	6
weighted avg	0.88	0.83	0.83	6

Figure 13. Classification report extract

3.5.5. Correlation Coefficient Analysis

The correlation coefficient analysis shows a strong negative linear relationship between water effect and rock quality, and a moderate negative linear relationship between blast damage and rock quality (see **Figure 12**). This suggests that the presence of water is associated with a decrease in rock quality, and that blast damage is also associated with a decrease in rock quality. The correlation coefficient analysis is essential in understanding the relationships between the factors and designing appropriate support systems.

3.5.6. Model Evaluation and Limitations

The performance of the Random Forest Classifier was evaluated by using multiple metrics, achieving an accuracy of 0.83, precision of 0.88, recall of 0.83, and an F1-score of 0.83, as illustrated in **Figure 13**. To assess the model's robustness and its ability to generalize to unseen data, a 5-fold cross-validation procedure was conducted. In this process, the dataset was randomly partitioned into five equal subsets; in each iteration, four subsets were used for training and the remaining one for testing, ensuring that each subset served as the test set exactly once. The performance metrics averaged across the five folds were consistent with those obtained from the initial model evaluation. This consistency indicates that the model does not suffer from overfitting and demonstrates reliable generalization capability. Such validation strengthens confidence in the model's predictive

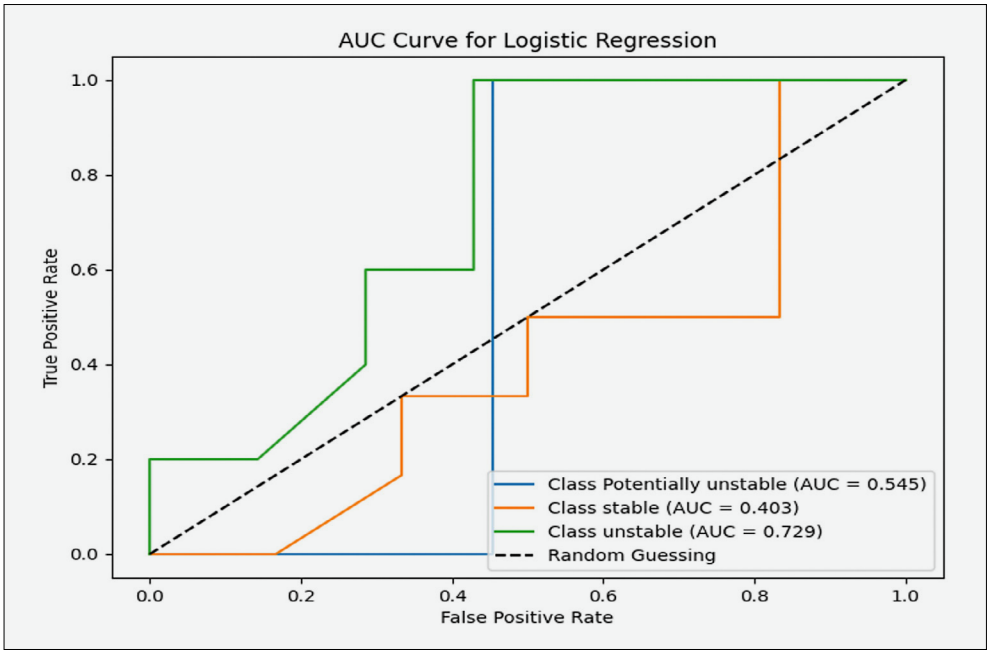


Figure 14. Receiver Operating Characteristic (ROC) Curve for Logistic Regression

reliability when applied to new or unseen geotechnical datasets.

It is important to acknowledge several limitations associated with this analysis. First, the dataset used for training the machine learning model was relatively limited in size, which may constrain the model's ability to fully capture the underlying complexity and non-linear interactions among geotechnical features. This limitation could affect both the generalizability and robustness of the predictive outcomes. Second, while categorical encoding was employed to represent variables such as water effect and blast damage, this approach simplifies the inherently complex and continuous nature of these factors. Although effective for initial modelling purposes, such simplification may lead to a loss of nuanced information. Future research could benefit from the use of more advanced encoding methods, such as ordinal encoding, one-hot encoding with domain-specific thresholds, or even continuous variable modelling, to better reflect the true variability and interactions of these parameters.

Furthermore, the data used in this study were collected exclusively from the 2North Section of the mine. As a result, the model's applicability may be limited to this specific geological and operational context, and its predictions may not be directly transferable to other sections of the mine with differing geotechnical or hydrological conditions. To enhance the model's predictive power and generalizability, future studies should consider expanding the dataset, incorporating additional features such as joint orientation, stress regime, or time-dependent effects, and applying the model across multiple zones of the mine. These improvements would allow for a more comprehensive assessment of stope stability and broader applicability of the model outcomes.

Figure 14 displays the Receiver Operating Characteristic (ROC) curve for the trained Logistic Regression model. The ROC curve plots the true positive rate (sensitivity) against the false positive rate (1 - specificity) at various classification thresholds. The Area Under the Curve (AUC) provides a single scalar value summarizing the overall performance of the classifier for different classes. The AUC values for Class Potentially unstable, Class stable, and Class unstable are 0.545, 0.403, and 0.729, respectively.

The ROC curve and AUC values provide insight into the model's ability to balance true positives and false positives, which is crucial for practical applications in mining engineering. The results indicate that the model performs relatively well in predicting "unstable" stopes (AUC = 0.729), suggesting that it can effectively identify instances that are likely to be unstable. However, the model's performance for "stable" stopes is poor (AUC = 0.403), indicating that it struggles to distinguish between stable and other classes. The model's performance for "potentially unstable" stopes is moderate (AUC = 0.545), suggesting that it can identify some instances that are potentially unstable, but with limited accuracy.

The varying AUC values across classes suggest that the model may be biased towards certain classes or that the features used to train the model are not equally informative for all classes. To improve the model's performance, it may be necessary to collect more data, particularly for the classes with lower AUC values, or to explore alternative feature engineering strategies. Additionally, hyperparameter tuning or the use of ensemble methods may help to improve the model's overall performance.

4. Discussion

This study applied a machine learning approach to predict stope instability, building upon and contrasting with traditional empirical and analytical methods. While classical approaches like the Mathews Stability Graph (**Mathews et al., 1981**) and rock mass classification systems (**Bieniawski, 1973; Barton et al., 1974**) provide foundational insight, their inherent limitations often arise from their reliance on simplified parameters and site-specific calibrations. For instance, the stability graph method, while widely used, may not fully capture the complex, non-linear interactions between multiple geotechnical factors. Our findings, particularly the strong influence of water ingress and blast-induced damage identified by the Random Forest model, underscore the need for models that can discern such intricate relationships more effectively than traditional empirical formulas alone.

Previous studies, such as **Adoko et al. (2022)**, have successfully demonstrated the application of neural networks for stope design, achieving high prediction accuracies. Similarly, **Li et al. (2023)** and **Vinay et al. (2023)** highlight the effectiveness of Random Forest and Support Vector Machines in predicting stope instability. The strength of our approach lies in its practical application of the Scikit-Learn library to a specific shallow gold mining environment, providing a granular analysis of feature importance that quantifies the relative impact of each geotechnical factor. While other studies may focus on broader datasets or different mining contexts, our work offers a tailored solution directly applicable to the identified challenges in the 2North Section.

A significant advantage of the machine learning approach over purely empirical methods is its capacity to handle large, heterogeneous datasets and identify subtle, non-linear patterns that might be overlooked by simplified models. For example, the decision boundary analysis clearly illustrated the amplifying effect of high water ingress on instability when combined with moderate blast damage – a synergistic interaction that empirical formulas might struggle to quantify precisely. This directly translates to practical benefits for end-users in the mining sector, enabling more proactive and precise interventions. By accurately predicting high-risk areas, mine op-

erators can optimize the deployment of support systems, leading to reduced material consumption, improved safety by minimizing exposure to unstable ground, and ultimately, enhanced operational efficiency and mineral reserve optimization through reduced dilution and downtime. This also extends to machinery maintenance, as a more stable ground reduces the risk of equipment damage from rockfalls and ground movement.

However, this study also presents limitations. The relatively limited dataset size inherently restricts the model's generalizability beyond the specific geological and operational context of the 2North Section. While the 5-fold cross-validation indicated robust performance within this dataset, applying the model directly to other mine sections without further training or validation could yield inaccurate predictions. Furthermore, the use of categorical encoding for water effect and blast damage, while practical, simplifies the continuous nature of these phenomena. Future research should explore larger, more diverse datasets and advanced encoding techniques (e.g. continuous variables or more granular ordinal scales) to enhance model robustness and transferability. Incorporating additional features such as joint orientation, in-situ stress regimes, and time-dependent effects would also further refine predictive accuracy, leading to more comprehensive ground control solutions.

Table 5. Fall out heights and support demand of the stopes under investigation

Stope	Density Kg/m³	Fall Out Height No.	Fall Out Height m	Support Demand kN/m²
Stope 2A	2700	1	1.17	31
	2700	2	1.27	34
	2700	3	1.21	32
Average			**1.22**	**32**
Stope 3C	2700	1	1.25	33
	2700	2	1.29	34
	2700	3	1.21	32
Average			**1.25**	**33**
Stope 2B	2700	1	0.77	20
	2700	2	0.68	18
	2700	3	0.72	19
Average			**0.72**	**19**

4.1. Stope Failure Analysis

Rock falls with medium and high hazard intensity are dominating stopes 2A and 3C, indicating the failure of support systems. The support system consists of natural in-situ pillars left randomly in stopes, relying on the excellent rock mass quality of the stopes. The adopted support design from 2South Section, had a maximum tolerable unsupported length of 7.5m which deviated from the calculated values. The maximum tolerable unsupported length for stope 2A and 3C deviated negatively with a magnitude of 2.5m and 1.5m respectively. This entails the deterioration of the rock mass quality in these stopes. As the rock mass quality was altered, the stope shape factor became insignificant for the design thus the stope stability decreased. As a result, new support requirements which may include artificial support are now necessary.

4.2. Support Demand and Pattern

The analysis of support demand and support pattern indicates that the proposed support configuration is adequate for maintaining the stability of the stopes, as detailed in **Tables 5** and **6**. The support demand was quantitatively estimated based on established rock mass classification systems (RMR and Q-system) and evaluated using the Mathews' stability graph method, which integrates rock quality, stope geometry, and excavation span to determine required support levels.

The proposed support pattern was designed to ensure an even distribution of load and to accommodate localized stress concentrations, particularly around larger load-bearing pillars. This design approach considers both the mechanical properties of the rock mass and the empirical stability zones defined in the stability graph. The pattern aims to transfer and distribute loads effectively, minimize deformation, and prevent progressive failure, thereby ensuring the long-term structural integrity of the stopes under anticipated mining conditions.

The support demand was calculated using **Equation 24**.

$$Support\ \ Demand\ \ per\ m^2 = pgh \tag{24}$$

where ρ is the verage density of the overlying rock mass, g is the acceleration due to gravity and h is the Fall-out height.

Table 6. The tributary area for rock fall conditions and the corresponding support spacing

Stope	Support Unit	Support Ressistance kN	Support Demand kN/m²	Tributary Area for rock falls m²	Support Spacing M
Stope 2A	22mm cone bolt	190	32	5.9	2.4
	16mm cone bolt	100	32	3.1	1.8
Stope 3C	22mm cone bolt	190	33	5.8	2.4
	16mm cone bolt	100	33	3.0	1.8
Stope 2B		80	19	4.2	2.1

5. Conclusions

Stope instability remains a critical challenge in underground mining, often leading to hazardous conditions, production delays, and financial losses. Traditional empirical and numerical methods, while effective, are limited by site-specific constraints and require extensive calibration. This study presents a practical machine learning (ML) approach for predicting stope instability by analyzing the main geotechnical parameters. The following are the findings of this study:

- **a)** the primary geotechnical factors influencing stope instability in the 2North Section of the mine are water effect, blast damage, and poor rock mass quality, with water effect being the most significant factor.
- **b)** stopes 2A and 3C have lower rock quality (RQD and Q-system values) compared to Stope 2B, indicating higher potential for instability.
- **c)** blast damage assessment revealed significant damage to the remaining rock mass, with a lack of proper perimeter control during blasting operations.
- **d)** the analysis using the Scikit-Learn Machine Learning Library confirmed that water effect, blast damage, and RMRs are the most important factors affecting stope instability, while rock strength has the least influence.
- **e)** the Random Forest Classifier demonstrated strong predictive performance, achieving an accuracy of 0.83, precision of 0.88, recall of 0.83, and an F1-score of 0.83. This performance was consistent across 5-fold cross-validation, indicating the model's reliability and generalization capability.
- **f)** the stopes are all situated in the potentially unstable zone on the stability graph, with Stope 2B being more stable than the other two.
- **g)** the adopted support design from 2South Section has been considered insufficient due to changes in rock mass quality, necessitating new support requirements for an effective ground support system. The maximum tolerable unsupported lengths of the stopes had significantly reduced, stopes 2A by 29% and 3C by 21%.
- **h)** the proposed machine learning approach offers a robust and practical tool for mine operators, allowing for more accurate predictions of stope instability, thus enabling optimized resource allocation for support systems and enhanced safety by reducing exposure to hazardous conditions.
- **i)** future research should focus on expanding the dataset to include a wider range of geological and operational conditions from multiple mine sections, exploring continuous variable modeling for factors like water pressure and blast intensity, and incorporating additional parameters such as joint orientation and in-situ stress regimes to further enhance the model's generalizability and predictive accuracy.
- **j)** the current state of the ground welcomes the application of additional mining techniques to improve the stability of the stopes, thus providing a secure working environment for employees, and supervision.

Funding

We declare that no funding was received during the preparation of this manuscript.

6. References

Adoko, A.C., Saadaari, F., Mireku-Gyimah, D., Imashev, A. (2022). A feasibility study on the implementation of neural network classifiers for open stope design. Geotech. Geol. Eng. 40 (2), 677–696. https://doi.org/10.1007/s10706-021-01915-8.

Barton, N., Lien, R., Lunde, J. (1974). Engineering classification of rock masses for the design of tunnel support. Rock Mech. 6 (4), 189–236. https://doi.org/10.1007/ BF0123 9496.

Barton, N., & Grimstad, E. (2014). The Q-system following thirty years of development and application in tunnelling projects. Tunnel and Underground Space Technology, 39, 49-69.

Bieniawski, Z.T. (1973). Engineering Classification of Jointed Rock Masses, vol. 15. Transaction of the South African Institution of Civil Engineers, pp. 335–344.

Blenkinsop, T.G., Oberthür, T., and Mapeto, O. (1999). Gold mineralization in the Mazowe area, Harare-Bindura-Shamva greenstone belt, Zimbabwe: I. Tectonic controls on mineralization: Mineralium Deposita, v. 34, p. 382–392.

Capes, G.W. (2009). Open Stope Hangingwall Design Based on General and Detailed Data Collection in Unfavourable Hangingwall Conditions. The University of Saskatchewan, Canada. NR62618 Ph.D.

Deere, D. U., & Deere, D. W. (1967). Rock quality designation (RQD) after twenty years. In Proceedings of the 8th US Symposium on Rock Mechanics (pp. 138-152).

Diederichs, M.S., Kaiser, P.K. (1999). Tensile strength and abutment relaxation as failure control mechanisms in underground excavations. Int. J. Rock Mech. Min. Sci. 36 (1), 69–96. https://doi.org/10.1016/S0148-9062(98)00179-X.

Houghton, D. A., & Stacey, T. R. (1980). A review of the design of temporary mine openings. Journal of the South African Institute of Mining and Metallurgy, 80(9), 274-279.

ISRM (International Society for Rock Mechanics) (1978). Suggested methods for determining the uniaxial compressive strength and deformability of rock materials. International Journal of Rock Mechanics and Mining Sciences & Geomechanics Abstracts, 16(2), 135-140.

Jones, A., et al. (2015). "Evaluation of Blast Damage Control Measures in Underground Hard Rock Mines." Mining Engineering Journal, 67(3), 45-52

Jorquera, M., Korzeniowski, W., Skrzypkowski, K. (2023). Prediction of dilution in sublevel stoping through machine

learning algorithms. In: IOP Conf Ser: Earth Environ Sci, vol. 1189, 012008. https://doi.org/10.1088/1755-1315/1189/1/012008.

Jones, A., & Wang, L. (2018). "Assessment of stope stability using the modified stability graph method in narrow vein mining." International Journal of Rock Mechanics and Mining Sciences, 105, 123-130.

Laubscher, D. H. (1990). "A geomechanics classification system for the rating of rock mass in mine design." Journal of the South African Institute of Mining and Metallurgy, 90(10), 257-273.

Li, C., Zhou, J., Du, K., Dias, D. (2023). Stability prediction of hard rock pillar using support vector machine optimized by three metaheuristic algorithms. Int. J. Min. Sci. Technol. 33 (8), 1019–1036. https://doi.org/10.1016/j.ijmst.2023.06.001.

Lingga, B.A., Apel, D.B. (2018). Shear properties of cemented rockfills. J. Rock Mech. Geotech. Eng. 10 (4), 635–644. https://doi.org/10.1016/j.jrmge.2018.03.005.

Mathews KE, Hoek E, Wyllie DC, Stewart SBV (1981). Prediction of stable excavation spans at depths below 1000m in hard rock mines. CANMET Report, DSS Serial No. OSQ80-00081

Palmstrom, A., & Broch, E. (2006). "The RMCS - Rock Mass Characterization System." Proceedings of the International Symposium on Rock Engineering for Underground Excavation.

Palmström, A., & Stille, H. (2007). Ground behaviour and rock engineering tools for underground excavations. Tunnelling and Underground Space Technology, 22(3), 363-376.

Periasamy, R. & Mohanta, D. (2024). Carbon emission assessment of energy generation in India. In: Energy and Climate Change. ScienceDirect. Vol 5. pp 100140. https://doi.org/10.1016/j.egycc.2024.100140.

Skrzypkowski, K., (2021a). Determination of the backfilling time for the zinc and lead ore deposits with application of the BackfillCAD model. Energies 14 (11), 3186. https://doi.org/10.3390/en14113186.

Skrzypkowski, K., (2021b). 3D numerical modelling of the application of cemented paste backfill on displacements around strip excavations. Energies 14 (22), 7750. https://doi.org/10.3390/en14227750.

Smith, J., et al. (2015). "Application of the modified stability graph method for stope design in deep-level gold mines." Mining Engineering, 67(3), 42-48.

Smith, J., Doe, J., & Johnson, A. (2018). Assessment of Blast Damage in Underground Hard Rock Mines: A Case Study. Journal of Mining Engineering, 10(2), 123-136.

Raimi, M., Oluwasegun, O. O., & Akerele, T. (2022). Global Energy Supply. In: The Palgrave Handbook of Climate Resilient Societies. Palgrave Macmillan, Cham. https://doi.org/10.1007/978-3-030-80255-9

Szmigiel, A, Apel, D. B., Pourrahimian, Y., Dehghanpour, H.,Pu, Y., (2024). Exploring machine learning techniques for open stope stability prediction: A comparative study and feature importance analysis. Rock Mechanics Bulletin; https://doi.org/10.1016/j.rockmb.2024.100146

Tishkov, M., (2018). Evaluation of caving as a mining method for the Udachnaya underground diamond mine project. In: Proceedings of the Fourth International Symposium on Block and Sublevel Caving. Australian Centre for Geomechanics, Perth, pp. 835–846.

Qi, C., Fourie, A., Du, X., Tang, X. (2018). Prediction of open stope hangingwall stability using random forests. Nat. Hazards 92 (2), 1179–1197. https://doi.org/10.1007/s11069-018-3246-7.

Vinay, L.S., Bhattacharjee, R.M., Ghosh, N., Kumar, S. (2023). Machine learning approach for the prediction of mining-induced stress in underground mines to mitigate ground control disasters and accidents. Geomech. Geophys. Geoenerg. Georesour. 9 (1), 159. https://doi.org/10.1007/s40948-023-00701-5.

Zhou, Q., Liu, D., Lin, X. (2022). Pre-evaluation of fault stability for underground mining based on geomechanical fault-slip analysis. Geomat. Nat. Hazards Risk 13 (1), 400–413. https://doi.org/10.1080/19475705.2022.2032401.

SAŽETAK

Održiv i praktičan pristup strojnom učenju pomoću Scikit-Learn baze za procjenu nestabilnosti čela radilišta: identifikacija ključnih geotehničkih čimbenika

Nestabilnost čela radilišta i dalje je stalan i opasan izazov u podzemnoj eksploataciji, s negativnim utjecajem na sigurnost, učinkovitost i održivost. Tradicionalne metode procjene stabilnosti, iako korisne, često su ograničene potrebom za baždarenjem na specifičnome lokalitetu, pojednostavnjivanjem i slabom prilagodljivošću u dinamičnim podzemnim uvjetima. Iako strojno učenje pokazuje potencijal za poboljšanu točnost, i dalje postoji velik nedostatak razumijevanja kako geotehnički čimbenici međusobno djeluju u praksi. Ovo istraživanje predstavlja novu, praktičnu okosnicu strojnoga učenja (Scikit-Learn) za procjenjivanje nestabilnosti čela radilišta te ključnoga kvantificiranja suptilnoga nelinearnog utjecaja i međudjelovanja ključnih geotehničkih čimbenika u plitkome rudniku zlata. Sveobuhvatno geotehničko ispitivanje (opažanja, laboratorijska ispitivanja, klasifikacije stijenskih masa, procjene oštećenja uslijed miniranja) i napredna analiza podataka (*Random Forest*, *Recursive Feature Elimination*, *Decision boundary analysis*) identificirali su najvažnije čimbenike nestabilnosti: prodor vode, oštećenja uzrokovana miniranjem i kvalitetu stijenske mase (RMR). Prodor vode imao je velik utjecaj na stabilnost, pri čemu su umjerena oštećenja od miniranja dodatno pogoršavala nestabilnost u uvjetima visokoga prodora vode. Čvrstoća stijenske mase pokazala se relativno manje važnom. Razvijeni model postigao je snažnu prediktivnu učinkovitost (točnost: 0,83, preciznost: 0,88, odziv: 0,83, F1 mjera: 0,83). Na temelju tih znanja predloženi su prilagođeni oblici podgrade (npr. konusna sidra 22 mm / 16 mm, drvena podgrada) kako bi se ublažili specifični rizici. Ovo istraživanje znatno doprinosi ciljanom rješavanju problema u mehanici stijena pružajući dublje, kvantificirano razumijevanje složenih mehanizama nestabilnosti, čime se poboljšava sigurnost i operativna učinkovitost kod plitke eksploatacije zlata.

Ključne riječi:
geotehnički čimbenici, nestabilnost čela radilišta, strojno učenje, klasifikacija stijenske mase, plitko rudarenje, podgrada

Author's contribution

Amos Bemo: conceptualization, formal analysis, methodology, software, investigation, visualization, data curation, and writing - original draft preparation. **Deji Olatunji Shonuga**: visualization, writing - original draft preparation and, writing - review and editing and supervision. **Tawanda Zvarivadza**: methodology, visualisation, writing and editing and supervision. **Moshood Onifade**: formal analysis, methodology, investigation, and writing - original draft preparation. **Manoj Khandelwal**: conceptualization, software, writing - review and editing. and supervision.
All authors have read and agreed to the published version of the manuscript.

RGNZ/*MGPB*

Radovi/*Papers*

1.	Evaluating Liquefaction Susceptibility Through HVSR and MASW Methods: A Case Study in Mamuju, West Sulawesi, Indonesia *(Andri Moh. Wahyu Laode; Muh. Altin Massinai; Muhammad Fawzy Ismullah Massinai; Erfan Syamsuddin)*	1-18
2.	Magnetic and Geochemical Studies of Iron sand Deposits around Tambora Volcano in Sumbawa, Indonesia: A proxy for search high quality iron sand *(Putu Billy Suryanata; Adella Ulyandana Jayatri; Satria Bijaksana; Silvia Jannatul Fajar; Ulvienin Harlianti)*	19-30
3.	Application of Artificial Intelligence in Reservoir Simulation for Characterizing Multi-Phase Fluid Flow through Petroleum Reservoirs *(Viswakanth Kandala; Suresh Kumar Govindarajan; Tummuri Naga Venkata Pavan; Swaminathan Ponmani; Srinivasa Reddy Devarapu)*	31-42
4.	MAETEC: An Optimized MATLAB-Based Approach for Accurate and Efficient Terrain Correction in Complete Bouguer Anomaly *(Indra Arifianto; Jun Nishijima; Rahmat Catur Wibowo)*	43-56
5.	Unveiling the dynamics of deep-focus earthquakes: Insights from the 2020 Jepara event Mw 6.7 and subduction processes beneath Java *(Tio Azhar Prakoso Setiadi; Anne Meylani Magdalena Sirait; Yehezkiel Halauwet; Andrean Vesalius Hasiholan Simanjuntak; Adi Susilo)*	57-66
6.	An investigation on the potential recovery of copper from a low-grade copper resource containing high silica content *(Milad Abbassi; Asghar Azizi)*	67-82
7.	Geology and mineralogy of Fe-Sn deposit in Batubesi, Belitung Island, Indonesia *(Aryo Dwi Handoko; Mochamad Slamet Sugiharto; Syafrizal; Alfend Rudyawan; Benyamin Sapiie)*	83-98
8.	Anthropogenic Hazards Assessment of Mining Activities in Surghar Range, Punjab, Pakistan *(Syed Sajjad Ahmad; Hafiz Muhammad Zaheer Afzal; Hafiz Zeeshan Akram; Sajjad Khan; Ihtisham Islam; Salman Ahmed Khattak)*	99-113
9.	Combining the 3D geological and geostatistical modelling of gypsum concentration, using historical borehole and blasthole information *(Stefano Merli; Sara Kasmaee; Cristina Barbalucca; Vanessa Cellini; Francesco Tinti)*	115-126
10.	Concentrating the Zn-Pb sample from Nignan ore deposit *(Maryam Abedi Moghadam; Marzieh Hosseini Nasab; Mohammad Noaparast)*	127-140
11.	Integrating ANN Prediction with Honeybee Optimisation for Flyrock Minimisation in Open-Pit Mining *(Mojtaba Rezakhah; Erfan Nemati; Amir Batarbiat; Manoj Khandelwal)*	141-152
12.	Mechanical activation and geopolymerisation of Taiwanese fly ash *(Fanni Dolgos; Roland Szabó; Wei-Ting Lin; Gábor Mucsi)*	153-165
13.	Seed-Guided, Fault-Aware Horizon Tracking via Greedy Propagation for Geological Modelling *(Ana Brcković; Marko Cvetković; Josipa Kapuralić; Ivan Medved)*	167-178
14.	A Sustainable and Practical Machine Learning Approach Using Scikit-Learn for Predicting Stope Instability: Identification of Critical Geotechnical Factors *(Amos Bemo; Deji Olatunji Shonuga; Tawanda Zvarivadza; Moshood Onifade; Manoj Khandelwal)*	179-198

ISSN 0353-4529